

PCTWORLD INTELLECT
Inte

INTERNATIONAL APPLICATION PUBLISHED



WO 9604409A1

(51) International Patent Classification ⁶ :

C23C 14/14, 14/22, C22C 23/06, 45/00

A1

(43) International Publication Date: 15 February 1996 (15.02.96)

(21) International Application Number: PCT/EP95/02882

(22) International Filing Date: 19 July 1995 (19.07.95)

(30) Priority Data:

94111991.9

1 August 1994 (01.08.94)

EP

(34) Countries for which the regional or
international application was filed:

AT et al.

(71)(72) Applicant and Inventor: HEHMANN, Franz [DE/DE];
Iburger Strasse 151, D-49082 Osnabrück (DE).

(72) Inventor; and

(75) Inventor/Applicant (for US only): WEIDEMANN, Michael
[DE/DE]; Berliner Strasse 8, D-30916 Isernhagen (DE).(74) Agent: GRAMM, LINS & PARTNER; Theodor-Heuss-Strasse
1, D-38122 Braunschweig (DE).(81) Designated States: AU, CA, CN, JP, KR, RU, US, European
patent (DE, FR, GB).

Published

With international search report.

(54) Title: SELECTED PROCESSING FOR NON-EQUILIBRIUM LIGHT ALLOYS AND PRODUCTS

(57) Abstract

Methods to produce corrosion resistant wrought light alloys and products, in particular aluminium and magnesium alloys, the latter containing 0.1-0.2 to 30-35 wt.% light rare earth metals and/or corresponding misch-metals and/or Y (and Eu) and/or 0.1 to 40 wt.% early transition metals and/or metalloids, by appropriate extension of corresponding latitude of alloying made possible by very extreme processing conditions of rapid solidification techniques via vapour deposition using thermal evaporation and/or plasma and magnetron sputtering methods. Engineering solutions are described to control productivity, quality and yield, via melt spinning, planar flow casting, laser beam surface melting and ball milling techniques including five particular methods for mechanical alloying, mechanical grinding and/or reaction milling, all employed to achieve the unique microstructures required for superior property profiles. These are followed by consolidation procedures including extrusion, rolling, forging, drawing and superplastic forming. The alloys show surprising resistance to corrosive attack even under the exposure to saline environments containing hydrogenperoxide (H₂O₂). The alloys may contain (depending on the alloy synthesis method employed) further minor and major additions of transition and simple metals as well as metalloids with similar characteristics as rare earth and early transition metals regarding passivation of the alloyed surface.

FOR THE PURPOSES OF INFORMATION ONLY

Codes used to identify States party to the PCT on the front pages of pamphlets publishing international applications under the PCT.

AT	Austria	GB	United Kingdom	MR	Mauritania
AU	Australia	GE	Georgia	MW	Malawi
BB	Barbados	GN	Guinea	NE	Niger
BE	Belgium	GR	Greece	NL	Netherlands
BF	Burkina Faso	HU	Hungary	NO	Norway
BG	Bulgaria	IE	Ireland	NZ	New Zealand
BJ	Benin	IT	Italy	PL	Poland
BR	Brazil	JP	Japan	PT	Portugal
BY	Belarus	KE	Kenya	RO	Romania
CA	Canada	KG	Kyrgyzstan	RU	Russian Federation
CF	Central African Republic	KP	Democratic People's Republic of Korea	SD	Sudan
CG	Congo	KR	Republic of Korea	SE	Sweden
CH	Switzerland	KZ	Kazakhstan	SI	Slovenia
CI	Côte d'Ivoire	LI	Liechtenstein	SK	Slovakia
CM	Cameroon	LK	Sri Lanka	SN	Senegal
CN	China	LU	Luxembourg	TD	Chad
CS	Czechoslovakia	LV	Latvia	TG	Togo
CZ	Czech Republic	MC	Monaco	TJ	Tajikistan
DE	Germany	MD	Republic of Moldova	TT	Trinidad and Tobago
DK	Denmark	MG	Madagascar	UA	Ukraine
ES	Spain	ML	Mali	US	United States of America
FI	Finland	MN	Mongolia	UZ	Uzbekistan
FR	France			VN	Viet Nam
GA	Gabon				

Selected Processing for Non-Equilibrium Light Alloys and Products

Technical Field

This invention relates to new magnesium and aluminium alloy articles consisting of a non-equilibrium matrix phase of essentially early, i.e. light rare earth and/or transition metals and/or metalloids made by non-equilibrium methods such as rapid solidification from the melt and from the vapour phase and by solid state synthesis with an essentially homogeneous distribution of the major part of the alloying elements on an atomic length scale of the eventually purified alloy matrix. More particularly, it relates to economically viable wrought magnesium and aluminium alloy articles made by selected processing routes and useful as extruded, forged or rolled products for space, ballistic, airframe and other aero nautical as well as for terrestrial applications such as in trains and automobiles, the products thereby achieved by novel methods to control the alloy synthesis, alloy conversion and alloy joining.

Background Art

Reference is made and priority is claimed with regard to EP-application n° 94111991.9 from 1 August, 1994.

Corrosion resistant commercial magnesium alloys such as the new high purity version of the Mg-Al base AZ91-alloy, i.e. AZ91E¹⁾ or the new Mg-Y base WE43²⁾-alloy are comparable with the corrosion rates of pure magnesium, of aluminium alloys A357 and A206 (all with corrosion rates of the order of 0.25 - 0.51 mm/year (10 - 20 mils per year [mpy]) in a salt fog test after ASTM B117) and they are about two orders of magnitude better than previous magnesium alloy families (cf. [2]). Another new magnesium alloy showing about 0.25mm/year (10 mpy) in standardized test conditions is the rapidly solidified magnesium alloy EA55RS³⁾ which has been made available quite recently as a wrought alloy product in extruded, rolled and forged form and which allows due to the fine grain structure for superplasticity and an alloy forming operation at about 150°C lower temperatures than conventionally cast magnesium alloys so retaining the refined microstructure and the resultant improvement of engineering properties in the final product [3]. On the aluminium side, many new alloy compositions with superior properties have been developed, but the methods to synthesize them from the vapour and solid state are not mature and controllable as is required by (pilot) production scale.

Aerospace applications require metallic materials with self-healing surface films to protect the interior, i.e. the bulk material when exposed to air (including rain independent on environmental particulars). None of the existing magnesium engineering alloys exhibit a surface passivation upon exposure to normal atmospheres containing saline species as it is known for titanium and aluminium alloys. For iron it is the allotropy which allows for passivation by equilibrium alloying austenitic and ferritic iron with chromium, for example. The absence of allotropy for aluminium,

¹⁾ 8.3 - 9.7 Al, 0.35 - 1.0 Zn, < 0.15 Mn, < 0.1 Si, balance Mg.

²⁾ 3.7 - 4.3 Y, 2.4 - 4.4 Nd and heavy rare earth misch-metal, 0.4 - 1.0 Zr, < 0.2 Zn, balance Mg.

³⁾ 5.1 Al, 4.9 Zn, 5.0 Nd, balance Mg. **SUBSTITUTE SHEET (RULE 26)**

for example, results in deterioration of corrosion behaviour of aluminium upon equilibrium alloying and this applies more seriously to magnesium alloys. Magnesium alloys yet represent the worst case among structural metals for aeronautical applications, since magnesium has not only no allotropy as titanium and iron, but Magnesium does also not develop a passive surface film on exposure to normal atmospheres as is evident for pure titanium and pure aluminium. None of the existing conventional magnesium alloys have yet shown pronounced passivation behaviour by alloying as - by definition - becomes evident upon a significant decrease in corrosion rates compared to the pure metal. Hehmann et al. have shown [5], however, that significant passivation is possible by alloying the α Mg solid solution with at least 17 wt.% Al in the supersaturated state. This type of passivation, however, was not obtainable unless very extreme conditions of rapid solidification from the melt were applied and it was therefore restricted to thin cross-sections and not obtainable by conventional ingot metallurgy. An engineering solution to this problem would provide the driving force to resolve many of the obstacles for the introduction of advanced light alloys, but the solution to this problem has not been recognized as a combined problem of the development of non-equilibrium new and/or established light alloys as well as of corresponding processes.

As long as 75 years ago, Tammann [4] and later Gerischer et al. [5] reported increasing pitting potentials and decreasing anodic current densities of the equilibrium Cu-Au and Ag-Au solid solutions with increasing levels of gold representing the more noble and passivating constituent. The majority of the equilibrium phase diagrams of binary Mg-alloys shows, however, a very restricted solubility range in the cph-Mg solid solution due to the formation of strong compounds suppressing equilibrium solubility in cph-Mg [6]. Only the so-called "yttrics" exhibit relatively large equilibrium solid solubilities in cph-Mg. This group consists of yttrium and the heavy rare earth metals Gd, Tb, Dy, etc. as well as scandium which, due to their physical commonalities, are found in nature as a mixture, the so-called (heavy) rare earth (HRE) mischmetals and which have led to the most heat resistant Mg-based alloys on record. Heavy rare earth metals and scandium are relatively expensive alloying additions to magnesium. Sm and Gd represent the most economically viable individual heavy rare earth alloying additions with relatively large equilibrium solid solubility in cph-Mg. If Sm and Gd are employed via a cheaper mischmetal, they may co-exist with a considerable amount of yttrium. Yttrium, however, was reported [7,8] not to result in the required improvement of corrosion behaviour when dissolved in cph-Mg compared to pure magnesium. Mg-HRE alloys require also relatively laborious solution and ageing treatments when made by conventional casting methods (cf. [9,11a]).

In 1987, Hehmann and co-workers found [7,8] that the rapidly solidified (RS) solid solutions of La and Ce in the as-quenched supersaturated cph-Mg were very effective in order to passivate magnesium and to reduce corrosion rates compared to the pure metal. Only very small levels of La and Ce, i.e. 0.4 at.% La or Ce (2.2 wt.% La or Ce) in cph-Mg were required to arrive at uniform corrosion rates as low as 0.04 mils / yr (1 μ m / year) compared to 15 - 20 mils / yr (350 - 500 μ m / year) for pure magnesium by using a 1 emol aerated NaCl aqueous solution of

pH = 4.9 (cf. [7,8]). Similar effects were observed before during the polarization of 7075 aluminium alloy in an electrolyte that was doped with La- and Ce-salts [10]. By contrast, the passivation of an cph-Mg-base solid solution containing Al required an Al-level of more than 16 wt.% in the supersaturated cph-Mg-state in order to arrive at 7 mils / yr (200 $\mu\text{m}/\text{yr}$) and corresponding solid solutions were thermally very unstable [11]. Light RE-metals are not only cheaper than heavy RE-metals. They also showed a better performance compared to the passivation effects obtainable by heavy RE elements in cph-Mg via conventional casting methods (cf. [7] vs. [6,11a]). Alloying of the cph-Mg based solid solution with light RE elements seems to provide a very effective alternative to passivate magnesium metal used as a matrix material.

For passivation of magnesium, the details of the microstructure appeared to be crucial in addition to the solute selected for solid solution alloying with cph-Mg and to the concentration range of corresponding solid solution. The reduction in corrosion current by several orders of magnitude compared to corresponding ingot castings and prior-art Mg engineering alloys was considered (cf. [7,8]) to originate in the complete absence of second phases, i.e. when the volume fraction of equilibrium dispersoids separated from the melt upon solidification was virtually 0.0 and the RE elements virtually completely held in the cph-Mg solid solution. However, relatively early pitting corrosion was also observed despite significant reduction in the more uniform corrosion rate. A precise correlation between the various nonequilibrium microstructures of these alloys and their response to corrosive attack has yet not been forwarded. Moreover, the corrosion behaviour of these microstructures upon exposure to test conditions which are accepted by industry has also not yet been presented.

A similar behaviour was observed with Al-Cr-Fe alloys made by vapour deposition. These alloys do not know any larger volume fraction of second phases as would apply to the equilibrium state of corresponding compositions [59-61]. While (all) Al-alloys show deterioration of the corrosion resistance relative to (commercially and/or high and/or ultra-) pure aluminium due to the microgalvanic effect(s) at the alloy surface, the PVD- Al-Cr-Fe alloys showed threefold improved corrosion resistance over pure aluminium.

The extension of equilibrium solid solubility of light rare earth elements in cph-Mg require high front velocities to suppress microsegregations upon solidification of the melt due to low partition coefficients $k_0(T)$. $k_0(T)$ is defined as the ratio C_S/C_L at a given temperature T, where C_S = solidus concentration and C_L = liquidus concentration of an initial alloy concentration c_0 . Corresponding values range from 0.05 for Mg-Eu to 0.1 for Mg-Sm (cf. [12,13]). Hypoeutectic Mg-Sr alloys with coefficients k_0 of 0.005 were shown to require front velocities of 2 to 4 m/s corresponding to laser withdrawal velocities of 3 to 6 m/s in order to achieve solidification without microsegregations [14]. The conditions to extend the equilibrium solid solubility of light RE metals in cph-Mg by liquid quenching methods are therefore not readily available.

Corresponding one phase as-solidified microstructure was observed in a surface chill zone of width 20 - 30 μm of piston-and-anvil (PA) splats of overall thickness 150 μm [7,8]. The reminding cross-section of dendritic growth of equilibrium phases was a result of the recalescence triggered by internal release of latent heat that occurs when the solidification front traverses the cross-section of the volume flattened by "splatting". PA-splat cooling is a discontinuous method to produce small volumina of material. In order to achieve a surface chill zone of width 20 - 30 μm in a sample of size 50 mg, pressures up to 5 bar for pneumatic acceleration of the piston were required (cf. [15]). Due to the variety of microstructures accrued to the high pressure available, PA-splat cooling is a very useful method to evaluate the departure from microstructural and structural equilibrium required for the economically viable production of passive magnesium alloys by using continuous RS-manufacturing methods. However, the high quality of these microstructural portions were instrumental for the present invention.

One RS-processing method that could continuously produce metastable phases and microstructures is vapour deposition. Bray et al. reported [16,17] on extension of prior-art by the effect of titanium in extended solid solution of cph-Mg made by thermal evaporation on to a collector which was temperature-controlled at between 100° - 150° C. The Mg-Ti system was identified [17] to develop annual corrosion rates between 330 $\mu\text{m}/\text{yr}$ for Mg-2.0 wt.% Ti over 30 $\mu\text{m}/\text{yr}$ for Mg-22 wt.% Ti and 5 $\mu\text{m}/\text{yr}$ for Mg- 47 wt.% Ti compared to 490 $\mu\text{m}/\text{yr}$ for evaporated pure magnesium and 420 $\mu\text{m}/\text{yr}$ for WE43, for example, as was derived from weight loss experiments after immersion for 7 days in 0.6 mol NaCl aqueous solution. The disadvantages of vapour deposition of Mg-Ti base alloys appeared to include 1. a thermally relatively unstable solid solution of at least a substantial part of Ti in cph-Mg, i.e. not much higher than 200°C, 2. that significant passivation required Ti-levels as high as 22 wt.% where the density of the overall alloy had already exceeded a value of 2.0 g/cm^3 and 3. that Ti is very different from magnesium in that it provides a much higher vapour pressure so evaporating not as easily to provide an economically viable major alloying addition to cph-Mg. Ti is a representative for early transition metals to produce new and corrosion resistant magnesium base alloys showing the importance to develop relevant vapour deposition processes.

The non-equilibrium microstructures offered by the umbrella of rapid solidification processing (RSP) have yet not been explored systematically in order to develop magnesium alloys and applications with significantly improved surface passivity. The alloy compositions and the possibilities for conversion of non-equilibrium Mg-alloys into products of which corrosion resistance, mechanical properties, the stability and the transformation behaviour of the metastable non-equilibrium state are of prime concern, have also not been explored to date. This concerns wrought products with a fine grain size inside the bulk material and which are suitable for low and elevated temperature applications as well as for weathered applications.

Disclosure of the Invention / Part I

It is the object of the inventions disclosed herein to take the above limitations systematically into account in order to provide magnesium and aluminium alloys with superior corrosion behaviour and modulus of elasticity due to a non-equilibrium alloy surface and/or - depending on the employed RSP-method - due to a non-equilibrium alloy bulk for superior mechanical properties compared to the available commercial magnesium alloys by using economically feasible production methods combined with an alloy conversion procedure which have yet not been applied for such alloys. In order to achieve such improvements it is important to reduce the susceptibility to weight loss in saline and other corrosive environments and to retain corresponding microstructures in final product form. The challenges in order to surpass in prior-art magnesium alloys include:

1. the reproducibility of the reported results for the extended solid solutions of rare earth elements in cph-Mg by employing test conditions accepted by industry;
2. the discrimination of the effect of second phases resulting from microsegregations and artificial overageing in order to identify precisely the passivation effect obtained by microstructural departure from equilibrium;
3. the methods and conditions to reproduce the required non-equilibrium microstructure by using continuous production methods and
4. the identification of the conditions (eg. temperature) of alloy conversion (i.e. extrusion, forging, rolling, isostatic pressing) and the degree of affordable ageing and/or microsegregations to retain the effect of the non-equilibrium microstructure in the final product.

The inventions claimed herein are magnesium and aluminium alloys synthesized and produced by rapid solidification from the melt including melt-spinning, planar flow casting or laser beam surface melting and from the vapour phase including vapour deposition by using diaphragmas to control productivity and yield of elemental and alloyed vapour throughputs synthesized by thermal evaporation methods and/or by plasma and magnetron sputtering methods as well as by solid state synthesizing techniques now controllable by the operator independent on the milling technique employed. While the non-equilibrium alloy development is demonstrated along selected experiments, alloy compositions and established and critically reviewed selection criteria towards superior properties, the controlling variables and engineering solutions to continuously produce such alloys are shown in the last part of the invention and coupled with the hierarchy for more effective realization including rapid prototyping alloys, alloy products and corresponding processes if not yet available. The alloys contain 0.1 or 0.2 wt.% up to 30 or 40 wt.% La, Ce, Pr, Nd, Sm, Ti, V, Cr, Mn, Zr, Nb, Mo, Hf, Ta, W, Al, Ga, Si, B, Be, Ge, Sb all evidencing similar and/or complementary oxidation and passivation characteristics or a combination of these alloying additions with up to 35 wt.% such as available via selected (light rare earth) misch-metals and also via commercially available alloys WE43, AE42, QE22, and ZE41, for example and/or via a commercial mischmetal including (heavy) rare metals, yttrium and/or

transition metals, within which either individual alloying additions or a combination of them is substantially held in solid solution of cph-Mg or another non-equilibrium (ne) phase after solidification and solid state synthesis then followed by conversion of these alloys into semi-finished or final wrought products by including microstructural transformation and hardening processes upon shaping and deliberate annealing treatments.

Corrosion behaviour upon immersion in aqueous solutions of the extended solid solution (TSSE) of light rare earth metals in cph-Mg

A marked improvement in corrosion resistance of these alloys was obtained in comparison to prior art magnesium alloys containing alloying elements such as aluminium, yttrium, other transition metals such as manganese and simple metals such as zinc by using standardized test conditions and in comparison to experimental alloys containing corresponding equilibrium microstructures consisting of dendritic growth with relatively large volume fractions of microsegregations delineating corresponding cell or grain boundaries.

A first series of the claimed alloys was made by piston-and-anvil (PA) splat cooling in an argon atmosphere using a pressure of 5 bar to pneumatically accelerate the moving piston (cf. [15]). A number of advantages are offered by PA-splat cooling compared to continuous production methods currently available for the development of passive magnesium alloys. Unlike for non-consolidated vapour deposited solid solutions made by low temperature thermal evaporation (cf. [16,17]) and sputtering , PA-splats have the advantage to represent fully dense material without the porosity entrapped upon vapour deposition (see below) or conventional casting due to the high impact pressure of the moving piston(s) (hammer) providing conditions which render this technique superior to pressure die-casting in order to assess small quantities on a short time scale basis. Another advantage of PA - splats is to provide sufficient equidistant 2 - dimensional length scale in order to prepare standard samples of 20 mm * 20 mm or of diameter about 30 mm which is not readily available by melt-spinning, for example. An equidistant 2-dim length scale is important to avoid irreproducible gradients in surface potential [18]. The feathered rim of PA-splats (cf. Fig. 1 - 5) was cut off to ensure reproducibility.

Examples of the microstructure of the transverse cross-section of such splats mounted edge-on are shown in Figs. 8 - 10. Typical for the resulting PA-splats is a two-zone microstructure with a strikingly sharp transition from featureless or nearly featureless planar or nearly featureless columnar growth to a zone of segregated dendritic or cellular growth (Figs. 8 - 10). Two zone microstructures without columnar growth in the chill zone, but with a planar and sharp transition to a dendritic zone manifest a negative temperature gradient there. The planar growth was therefore controlled by solute trapping (Fig. 6 ; n.b. absolute stability would require a positive temperature gradient and would appear as featureless columnar growth in the chill zone). As a result, the featureless chill zones represent a microstructure with a random and entirely homogeneous distribution of the alloying atoms on an atomic length scale as is otherwise only possi-

ble by vapour deposition techniques allowing for fragmentation on the level of a single atom (Fig. 7 and below), but in our case here certainly without any porosity similar as upon pressure die casting. All results on the response on natural and artificial ageing in the present invention do confirm the homogeneous distribution of alloying elements on an atomic length scale. The two zone microstructure is only available in the center of the PA-splats where the contact between piston (hammer) and melt is best, while reduced thickness towards the rim of the splat results in reduced contact so reduced / less efficient heat transfer and increased microsegregations there.

Predendritic surface features coexisting with the featureless zone were also observed (cf. Figs. 9c and 10a). They can result from uncontrolled fluid flow upon "splating" resulting in less stringent heat extraction and forming a circle of circular islands of microsegregations on solidification which are finer than the microsegregations in the dendritic chill-off zone as indicated by optically not resolvable dendritic interspacings. Predendritic features became macroscopically evident by etching the PA-splat surface with hydrofluoric (HF) and phosphatic (H_3PO_4) acids resulting in dark discs of diameter 1 - 2 mm around the central PA - splat portion, i.e. corresponding surface oxide appeared optically dark compared to the metallic shiny solid solution (cf. Fig. 11a). These islands may have resulted in early pitting upon potentiodynamic polarization despite the up to 3 orders of magnitude lower corrosion rates of the featureless zone of PA Mg-La and PA Mg-Ce splats compared to prior art alloys and corresponding segregated zones (cf. Figs. 8 - 10 n.b. PA-splat fragments of size 10 mm * 10 mm were used in [7,8]). However, even after 8 years of exposure to inland atmosphere (Paris) the segregationfree chill-zones did not show any sign of corrosion, though the neighbouring segregated and/or dendritic microstructures showed white, grey and black corrosion products as was expected for pure magnesium after such a long time exposure to air (cf. Figs. 1 to 5 and R.S. Busk, Mg Product Design).

Industrial test conditions for quantification of the earlier observations by Hehmann et al. [7,11] has to refer to macroscopic corrosion tests, since electrochemical methods overrun quite easily passivation due to the effect of microstructural artefacts resulting in pitting despite improved uniform resistance to corrosion. Initial tests were performed by employing an immersion test developed by Machu [19]. The test simulates the conditions of a salt spray test (5% NaCl at 35°C) by reducing the required time intervall from 300 hrs of the spray test down to 16 hrs for the immersion test by employing a solution of 5 wt.% sodium-chlorid (NaCl) together with the addition of 1 wt.% hydrogen-peroxide (H_2O_2) solution (30 wt.%) added to this solution at 23°C. One modification of this immersion test is the DIN 50947 test developed for Al-based alloys. Another modification was developed by AHC Oberflächentechnik (see [20]) which employs 5% of the H_2O_2 -solution (30 wt.%) and 1 wt.% NaCl. The test provides a relatively

aggressive medium and is used [19] to reduce the standardized interval of 16 hrs time to an interval of 2 hrs time. The test is particularly useful to simulate the corrosion behaviour on long-term salt spray tests such as after ASTM B117 which uses only the NaCl-addition. The test is applicable to Mg-based alloys and was used for the piston-and-anvil splats of the claimed alloys and on reference casting alloy AZ91.

Macroscopic surface attack was recorded optically after 0.5, 1, 2 and 3 hours immersion into a solution of 5% H_2O_2 (30 wt.%) and 1 wt.% NaCl. Supersaturation of the metallic shiny surface zone was confirmed by X-ray diffraction showing a pair of each (hkl)- reflection corresponding to either the equilibrium cph-Mg solid solution or to corresponding supersaturated solid solution (cf. [8,12,13]). Results of the AHC-modified immersion test are shown in Figs. 11 - 19 and they are summarized graphically in Figs. 20 - 22.

The supersaturated featureless surface (cf. Figs. 8 - 10) of as-solidified PA Mg-splats with 2.2 and 4.2 wt.% La showed less than 5% of attacked surface area (Figs. 11 and 12). This was a smaller surface area fraction than the surface area of predendritic surface islands (about 15%) coexisting with the featureless surface zone. The surface glamour of the featureless chill-zone was hardly attacked after the modified Machu-test employed. By contrast, the surface of the microsegregated dendritic chill-off side of PA-Mg splats with 2.2 to 6.9 wt.% La showed vigorous corrosive attack for 100% of the surface after 2 hrs immersion (Figs. 11 and 12). By contrast, predendritic features did not show corrosive attack indicating that the size, composition and/or structure of these microsegregations had not passed the critical conditions to trigger corrosion under the above conditions.

A heat treatment for 1 h at 400°C ensured the nucleation of La-containing precipitates from the supersaturated solid solution of La in αMg without resulting in excessive growth and/or coarsening of this particular type of precipitation (cf. DSC-part below). This heat treatment increased the observable attack of the primarily featureless surface zone from <5% to about 35%, while the heat treatment was not observed to affect the corrosion behaviour of the dendritic zone (Figs. 13 and 14). The corrosive attack on the heat treated featureless surface was triggered by the edges of the rim where surface contact was between the supersaturated chill zone and the segregated chill-off zone due to the cut (see above) through the cross-section. Predendritic surface features did not appear to have triggered the surface attack observed on supersaturated featureless surfaces of heat treated PA Mg-La splats.

The employed PA Mg-Ce splats showed an area fraction of about 20% predendritic surface islands coexisting with corresponding featureless surface zone (Fig. 15). The corrosive attack on the supersaturated featureless surface of as-solidified Mg-Ce splats was observed to start off from corresponding rim of the PA-splats (Figs. 15 and 16). The splats did not show any corrosive attack on the side of the supersaturated featureless chill zone including coexisting

pre-dendritic features after 2 hours immersion in the aqueous solution containing 5% H_2O_2 (30 wt.%) and 1 wt.% NaCl. If corrosion was not triggered by other regions, the side of as-solidified PA Mg-splats with 2.2 and 6.0 wt.% Ce dominated by featureless growth remained unattacked (Figs. 15 and 16). They retained their metallic glamour there even after 3 hours immersion (Fig. 15d). After 3 hrs immersion the attacked overall surface area of the chill side did not exceed 15%. This was more than 5% smaller than the area of the coexisting predendritic features.

After heat treatment for 1h at 400°C, initiation of corrosive attack on the featureless surface zone of PA Mg-Ce splats could not be traced back to a specific microstructural site coexisting with that zone (Figs. 17 and 18). That is: artificial ageing has resulted in the formation of precipitates of a size (i.e. above an atomic length scale) which was sufficient to render the material susceptible to corrosion. After 1 h exposure to the Machu-immersion test modified by AHC, a large scatter of 4 to 40% in attacked surface area of the featureless surface zone was observed. After 3 hours immersion the attacked area of the side of primarily featureless growth was observed to increase from <15% before heat treatment to 40 to 60% after heat treatment. Both the large scatter and the relatively large increase in corrosive attack indicated that microstructural inhomogeneities were responsible for the observed degradation of corrosion resistance after heat treatment. The observed microstructural inhomogeneities at the splat alloy surface result from microsegregations delineating columnar growth (cf. Fig. 9c) or from predendritic features due to uncontrolled fluid flow (ditto).

The comparison of the response to macroscopic corrosive attack of the featureless relative to the microsegregated zone shown in Figs. 20 - 22 appears as a conservative estimation of what can be obtained by segregation-free alloying the (extended) solid solution of cph-Mg or any other non-equilibrium Mg-base matrix phase. Microsegregations have evidently exaggerated pitting and the surface area of the featureless chill zone attacked by corrosion. The response of predendritic features and heat treatment to the employed immersion test indicates that a certain size and nature of second phases and a certain degree of ageing can be afforded without triggering corrosive attack. By contrast, overageing as employed for high strength 7000 Al-alloys for aerospace applications undermined the improved resistance to corrosion obtained by the extended solid solution of La and Ce in cph-Mg.

The impurity analysis of the Mg used for preparation of the alloys was 0.0034 +/- 0.003 wt.% Fe, 0.0005 wt.% Cu, 0.010 wt.% Si, < 0.005 wt.% Al, 0.0004 wt.% Mn and 0.001 wt.% Ni. Alloy preparation did not increase the level of the more critical impurities Fe, Ni, Si and Cu, since pure Ta was used as crucible material. Despite the relatively high Fe-level, it was possible to discriminate the microstructural effects for PA Mg-Nd (Fig. 23) and PA Mg-Sm splats (Fig. 24) with a particular strong advantage of the supersaturated segregation-free chill zone relative to the heat-treated so coarsened dendritic chill-off zone (cf. Fig. 25), for Mg-Mn splats (Figs. 26 - 30) and Fig. 87 and p. 56 showing an increasingly and more uniform

dispersion of second phases separated from the melt above 6 wt.% Mn (and which is consistent with what is expected from solidification kinetics) and the development of a black tarnish after heat treatment for 4 hours at 350°C (see Fig. 29, i.e. a condition which was elsewhere identified [45] to assure the solid state precipitation of β Mn from corresponding supersaturated cph-Mg-base solid solution, see below), for PA Mg-Si splats in the range from 0.5 to 5.0 wt.% Si (Figs. 31 to 35) with the same trends as for Mg-Mn, but with more detrimental effect of the Mg_2Si -type of solid state precipitates by heat treatment and melt-separated Mg_2Si -dispersoids than the elemental β Mn, for PA Mg-Sb splats of which the result for two concentrations (2.46 and 7.09 wt.% Sb) are shown (Figs. 36 to 39), for heat-treated PA Mg-Ca splats with 2.0 to 5.0 wt.% Ca (Figs. 40 to 42), for as-solidified and heat-treated PA Mg-Sr (Fig 43) and heat-treated PA Mg-Ba splats (not shown here), for PA Mg-Pd and PA Mg-Au splats (cf. Figs. 44 to 46) as well as for Mg-Y splats (Fig. 19). The immersion test of the extended solid solution of yttrium in α Mg made by PA splat-cooling did not show the improvements in corrosion resistance over prior-art alloys as was obtained by the solid solution of rare earth metals in cph-Mg (Fig. 19). This is in agreement with the earlier observations made by polarization tests indicating that microsegregations (avoidable by PVD-methods, for example, see below) are particularly harmful in the system Mg-Y(cf. [7,8]).

The systems Mg-Ca, Mg-Sr and Mg-Ba provide a particular family of Mg-based alloys which is discussed in the chapter on n-conduction (see below). These elements do not provide sufficiently stable Mg-based ne-phases (amorphous Mg-10wt.% Ca, for example, transformed at 110°C, see also the work by Mordike et al. on corresponding extended solid solution in cph-Mg, below). The particular role of the alkaline earth elements is that they are less noble than Mg on the one hand so providing an electron pressure on the MgO surface oxide film so a micro-cathodic protection within a size regime of solid state precipitates on the other. This is most effective directly after formation of such second phases from the solid state (cf. work by Pechiney, below), not from the liquid. That is, not the Mg_2Ca phase is a problem triggering eventually corrosion in an Mg-matrix, but its size. When separated from the melt, the size is too large. If formed from the solid state, however, attention is required to avoid overageing of this particular type of second phases. The results for heat-treated and/or as-solidified splats of the systems Mg-Si, Mg-Sb and Mg-Mn showed that no such "size-window" for improved corrosion resistance of Mg exist when the precipitates contain more noble elements than Mg.

All results are consistent in that the homogeneous distribution of the solutes (and solvent Mg, a term which is extended here for non-equilibrium Mg-base phases as well) on an atomic length scale (that is the topological or spatial distribution of different atoms in the surface plane) is the universal pre-requisite for enhancement of the MgO surface film prior to allow individual elements to develop particular advantages with respect to particular environments including the passivation of Mg in environments with higher concentrations of Cl^- -ion (see "Hierarchy of Relevant Criteria", below). All results are also consistent in that larger levels of

alloying the Mg-based matrix cannot be achieved by processing from the melt even if there was sufficient solubility in the melt as for the investigated systems. This was evident with the systematic decrease in corrosion resistance in the systems Mg-Si, Mg-Sb and Mg-Mn with increasing alloy concentration and the marked reduction of corrosion resistance afforded by a heat treatment and resulting solid state precipitates and/or coarsening of corresponding dispersoids in PA Mg-Si and Mg-Sb splats all evidencing that the homogeneous distribution of alloying elements on an atomic length scale the universal pre-requisite for Mg-alloy passivation. If the PA-splats showed a distinct two-zone alloy microstructure as to Figs. 8 - 10, corrosion on the (macroscopic) side of the featureless chill zone started from the rim of the splat (where the dendritic zone was co-exposed to the 5 wt.% H_2O_2 -1 wt.% NaCl aqueous solution with the featureless zone due to the cut-off feathered edges) and continued to travers the cross-section until eventually stopped from further expansion towards the supersaturated inner circle as was evident for PA Mg-5.0 wt.% Si splats (Figs. 33 and 34). The question whether the enhanced alloying afforded by selected non-equilibrium techniques (see below) provides a passive MgO-based surface oxide film is related to the question whether the alloying addition supports or suppresses the tendency of the MgO-film to transform to the more vulnerable $Mg(OH)_2$ -surface film. The Mg-Mn system, however, is at the borderline to the early transition metals which cannot be added by processing from the melt due to liquid immiscibility.

Vapour deposition is a very effective method to suppress microsegregations so to improve microstructural homogeneity. Vapour deposition is considered to result in cooling rates of the order of 10^{10} to 10^{12} K/s [21]. More importantly, vapour deposition has the general advantage over liquid quenching that fragmentation occurs on the level of an individual atom where no latent heat evolving upon solidification can be dissipated back into the fragmented volume. This is indicated by a columnar featureless microstructure of the deposit indicating that a positive temperature gradient had occurred upon condensation, i.e. when the latent heat is directed towards the cooling substrate and the deposit has a lower temperature than the vapour arriving at the deposit surface (cf. [22,23]; n.b. equiaxed growth would indicate the reverse).

Vapour deposition incorporates two processing families, namely thermal evaporation and (magnetron) sputtering methods. The sources used for thermal evaporation include resistance, induction, electron beam and microwave heating as well as sublimation, laser beam and arc evaporation methods [24]. Another form of vapor deposition is the sputter removal of a certain number of atoms sputtered from the material per incident ion [25]. Vapour deposition is therefore the ultimate solution of fragmentation via RS-processing without embracing any uncontrolled fluid flow and / or recalescence resulting in micro-segregations as upon liquid quenching even when the employed conditions of heat transfer were very extreme. A substantial increase in the limit of supersaturation can also be obtained by vapor deposition compared to liquid quenching. Maximum equilibrium solid solubility of Cr in fcc-Al, for example, was increased from 0.7 to about 2.5 wt.% Cr by using RSP, but to 10.7 wt.% Cr by employing PVD

[26,27]. The microstructure of binary PVD Al-Cr alloys was completely free of second phases.

The improvements in corrosion behaviour reported by Bray et al. [16,17] on vapour deposited solid solutions of Ti in cph-Mg were reproduced by Hirota et al. [28] via magnetron sputtering to obtain the extended solid solution of 8 - 47 Ti [at.%] in cph-Mg. Subsequent anodic polarization in 1 mol HCl aqueous solution resulted in Ti-cation- and corresponding O^{2-} -anion enrichment and in Mg^{2+} -cation and OH^- -anion depletion of the surface oxide underlying the passivation in this electrolyte which observed at potentials above the observed corrosion potentials at -0.68 (eg. for Mg-47 Ti) with respect to the standard calomel electrode potential.

A series of alloyed vapour deposits of Mg-8 (1.5) Ce and Mg-4 (2.1) Ti [wt.% (at.%)] was prepared by vapour sputtering employing a deposition rate of about 50 $\mu\text{m/h}$. The deposition was intercepted when the deposits had reached a thickness of 250 - 300 μm . Initial tests were performed by continuous immersion of test coupons of size 60 mm * 40 mm of the VD-alloys into the aqueous solution of the modified Machu-test containing 5% H_2O_2 (30 wt.%) and 1 wt.% NaCl at 27°C. Reference alloy AZ91 and vapour deposited Mg-4 wt.% Ti was attacked uniformly over the entire surface (Fig. 47). When the substrate temperature was held at 60°C, the VD Mg - 8 Ce alloy showed only very localized pitting corrosion embedding surface areas which were not attacked by the electrolyte (Fig. 47). The non-affected areas of the VD Mg - 8 Ce alloy retained their metallic shiny glamour even after 2 hours immersion. Ce appeared as a more effective alloying element than Ti for passivation of magnesium alloys by alloying the cph-Mg solid solution so confirming the observations reported in [7,8] compared to those in [16,17].

Pitting corrosion, however, was not observed for the featureless chill zone of PA-Mg-Ce splats under the conditions of the modified Machu-test. Fig. 48 shows the optical microstructure of the resultant Mg - 8 wt.% Ce alloy made by sputtering compared to corresponding chill-cast alloy. After 60 sec chemical etching in 5% picral (plus 0.5% glacial acetic acid) the as-sputtered microstructure of Mg - 8 Ce showed a featureless columnar grain structure without any response to indicate microsegregations over the entire cross-section of 250 μm , while the as-cast version responded instantly to chemical etching as for the dendritic chill-off zone of PA-splats. Comparison with previous work (cf. [8,13]) of the lattice parameter 'a' and 'c' obtained by X-ray diffraction indicated that all Ce was tied up in the extended cph-Mg-base solid solution without the microsegregations present even after extreme liquid fragmentation and quenching.

The overall microstructural homogeneity of the claimed alloys was improved substantially by vapour deposition using the sputtering method compared to solidification processing from the liquid phase. Sputtering leads to less porosity compared to thermal evaporation, but it embeds also the ions used for the bombardment of the target [29]. The porosity in as-deposited alloys is a result of protuberances that grow upon condensation of the alloy vapour resulting in shado-

wing and pores that oxidize in vacuum and under subsequent exposure to normal atmosphere [30]. The observed pitting corrosion has thus resulted from the porosity due to deposition of the alloys at 60°C triggering artefacts equivalent or worse compared to microsegregations so to obscure the surface conditions in real life (cf. [17], p. 163). The absence of porosity in as-deposited supersaturated cph-Mg-base solid solutions is therefore at least as important as the suppression of microsegregations to develop magnesium alloys with substantially improved surface passivity. It can be achieved by in-situ consolidation and / or by vapour deposition at elevated temperatures [29,30] which must not be as elevated to trigger disintegration of the supersaturated solid solution.

Obviously, the effect on corrosion behaviour of both microsegregations and porosity form the crucial, but yet underestimated quality parameters of high performance passive magnesium alloys. The most important result obtained here is that microsegregations can be suppressed effectively by vapour deposition, since the growth normal of the metastable solid solution, i. e. the vector normal to the continuously advancing growth front by vapour deposition (as indicated for 8 wt.% Ce in cph-Mg) is practically unlimited.

Thermal Stability by Differential Scanning Calorimetry (DSC) of the extended solid solution (TSSE) of light rare earth metals in cph-Mg

The advantage over transmission electron microscopy (TEM) of DSC-analysis of rapidly solidified (RS) metastable phases is that it operates on a macroscopic scale and tells with certainty whether the investigated material represented the metastable phases concerned, while TEM is subjected to statistics of sampling and therefore never representative for a metastable RS-material that was subjected to recalescence.

In PA-splat cooling, the sharp transition from featureless to dendritic microstructure results from recalescence which triggers a dramatic decrease of several orders of magnitude in front velocity compared to the initial velocity after traversing about 20 to 40 μm of the cross-section (cf. Fig. 8 - 10 and [32,33]). Microstructural modelling [34] including external heat flow and dendritic and planar crystal growth showed that the width of extended solid solutions of various elements in cph-Mg is limited to some 20 μm by employing a heat transfer coefficient $h = 2 - 3000 \text{ [kW / (K m}^2 \text{)]}$. This value is one of the highest obtainable values for quenching from the liquid phase. The predictions, however, are in good agreement with the observations of such microstructures (cf. [7,13]). The growth normal of supersaturated one phase microstructures obtained by liquid quenching is limited to some microns even under relatively extreme heat transfer conditions. Note that the growth normal is the vector of solid growth perpendicular to the growth front of segregationless or nearly segregationfree solidification. Fragmentation down to a droplet size of about 20 μm is therefore inevitable to avoid microsegregations which interfere with DSC-analysis of the supersaturated cph-Mg-base solid solution.

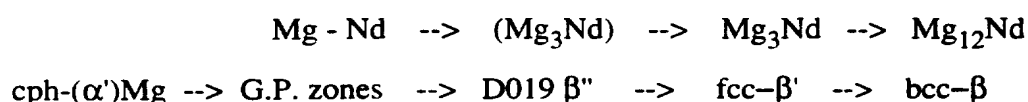
In order to examine the transformation behaviour of the cph-Mg solid solution by DSC it was thus necessary to refer to the gun technique for quenching from the liquid phase (cf. [31])

and to vapor deposition. Both methods provide a high degree of fragmentation coupled with sufficient heat transfer required for a microstructure without substantial microsegregations. Otherwise, small thermal effects of the metastable proportion of the microstructure cannot be discriminated from those thermal effects arising upon heating from the re-dissolution in the solid state of the second phases forming due to recalescence upon and/or ageing after solidification (cf. [6]). The DSC-analyses shown in Figs. 50 - 58 were done on a Dupont 910 analyser. The exothermal effects are plotted upwards in Figs 50 - 58.

The gun splats employed were of diameter <0.5 to 1.5 mm and of thickness <0.1 μm to 40 μm which represents a wide range of cooling rates from 10^5 to 10^{10} K/s [31]. A large majority of the population of droplets made by the gun-technique, i.e. > 90% by weight, was of thickness < 20 μm . The microstructure of gun splats indicated a transition from featureless growth to very fine banded cellular structure of cell size usually < 1 μm (Fig. 49). Banded microstructures are a result of velocity oscillations near the velocity for absolute stability (which is the front velocity for segregationfree growth). They are one evidence that growth in the cellular zone was not controlled by recalescence [35]. Accordingly, the degree of supersaturation of gun-splats is relatively high compared to corresponding cell boundary segregations.

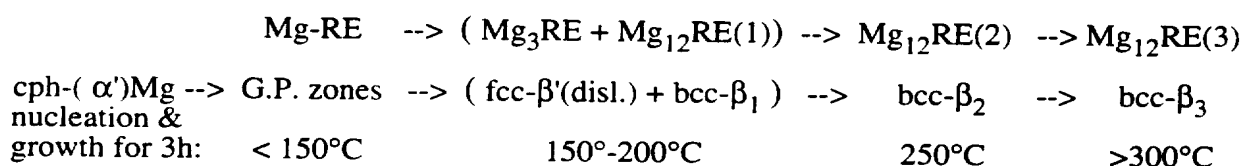
Fig. 50 shows three exothermal effects of gun splats of a Mg - 8 Ce alloy [nom. wt.%] with regard to the baseline (dotted), i.e. a flat spectrum between 150° and 200°C, an exothermal peak at 350° C and a relatively large and wide thermal effect between 400° and 500°C. Calibration and evaluation of the activation energy for transformation results in some 60° C lower temperatures for isothermal transformation and growth temperatures (see below). The heat flow of exothermal effect n° 3 was reduced when a tantalum foil was employed to getter residual oxygen in the 5N argon used as a purge gas for the DSC-cell (Fig. 51; n.b. gun splats form a relatively large surface area per unit volume of material exposed to the purge gas). The same sequence of these three exothermal effects was observed for Mg-gun splats of nominal composition 1 wt.% La and 1 wt.% Nd (Fig. 52). The sequence of exothermal transformation peaks was virtually independent on type of light rare earth solutes in the αMg solid solution.

A similar series of exothermal effects was observed on DSC-analysis of Mg-Y splats and ribbons including an exothermal spectrum n° 1 at around 160°C representing the formation of a bcc- β'' phase followed by an exothermal effect n° 2 at around 260°C representing the combined formation of a transgranular β' -phase and of the equilibrium β -phase at cell boundaries then followed by an exothermal effect n° 3 for transgranular formation of equilibrium $\alpha+\beta$ at around 350°C [36]. According to Karimzadeh [37], the transformation sequence of the supersaturated solid solution of conventionally cast Mg - 3 wt.% Nd alloy, i.e. cph-Mg, was observed to follow upon isothermal ageing:



nucleation temperatures: < 175°C 175°-200°C 200°-300°C >300°C

Omori et al. reported [38] the transformation sequence of the equilibrium solid solution of 1.3 wt.% Ce in cph-Mg to follow precipitation at 150°C of intermediate phases at grain boundaries and dislocations followed by transgranular precipitation at 200°C of intermediate phases which were found to be responsible for hardening the alloy and by formation of the equilibrium phases at temperatures above 250°C. Wei and Dunlop [39] showed in more detail that the combined effect of RE-elements does not change the precipitation sequence of an Mg - 1.3 wt.% misch-metal alloy compared to the sequence of the solid solution of elemental RE additions in cph-Mg after isothermal heat treatment for 3h following:



where:

β_1 = hexagonal prism Mg_{12}RE - particles of height 35 nm * diameter 50 nm and considered to be responsible for age-hardening the alloy by obstruction of dislocations in the basal plane.

β_2 = Mg_{12}RE - particles of irregular morphology stemming from the transformation of fcc- β' at dislocations into the β_2 -phase.

β_3 = Mg_{12}RE - particles of height 250 nm * length 100 nm.

For the commercial alloy WE43, the β' -phase was proposed [40] to correspond to Mg_{12}NdY and the β -equilibrium phase to correspond to $\text{Mg}_{12}\text{Nd}_2\text{Y}$. In all cases, three distinct reactions were observed with increasing temperature involving age hardening by the intermediate and/or transgranular β'' , β' - and fine β -phases after formation and/or dissolution of GP-zones, but prior to formation of transgranular equilibrium phases. That is, that no hardening was observed by the formation of GP-zones at temperatures < 150°C and that hardening does not require the entire transformation of the passivating extended solid solution of light rare earth elements in αMg leaving ample freedom for alloy conversion of these microstructures into final product form. Furthermore, Wei and Dunlop considered [39] that:

1. transgranular GP-zones dissolve rather than transform at the transition from temperatures < 150°C to temperatures above this threshold.
2. nucleation and growth of the fcc- β' - and the bcc- β_1 - phase was not only promoted by dislocations, twin and grain boundaries, but also by compound-type of heavy rare earth nuclei that might have already formed in the melt and that did not dissolve during solution treatment.

Form and magnitude of the observed thermal effects are therefore largely dependent on the microstructure induced by the RS-method employed. A large concentration of dislocations,

grain boundaries, microsegregations along these microstructural features and of HRE-nuclei would thus favour the exothermal reactions n° 1 and 2 at lower temperatures at the expense of the reaction at above 300°C and vice versa. In rapidly solidified Mg-Y alloys, for example, 11 microstructural evolutions were introduced by rapid quenching from the melt and which were identified to result in a distinct separation of transformation processes of cph-Mg at grain and cell boundaries below 300°C (corresponding to about 20% of the overall transformation of cph-Mg) and in the interior of grains above 300°C (corresponding to about 80% of the overall transformation of cph-Mg) resulting in two independent microstructural evolutions (cf. [36]).

The individual evaluation of the observed exothermal effects of Mg - 8 Ce [nom. wt.%] yields about 7 J/g for exotherm n° 1 (attributable to the formation of D019 β'' and/or fcc- β' -Mg₃RE), about 10 J/g for exotherm n°2 (attributable to growth of β' and the formation of β at grain boundaries) and about 32 J/g for exotherm n°3 (attributable to formation and growth of equilibrium- β in the interior of the grains and cells) (Fig. 53). As for the extended solid solution of Y in α Mg, the major transformation of the supersaturated solid solution of Ce in cph-Mg occurred at higher temperatures, here above or around 400°C. The enthalpy of transformation of exothermal effect n° 2, $\delta H(\text{exo}2)$, of the Mg-La samples, however, was observed to amount to 45 J/g compared to about 10J/g for Mg-Ce and Mg-Nd gun-splats.

The observed peak temperature T' of the exothermal effects n° 2 was found at $T = 355^\circ\text{--}358^\circ\text{C}$ for a heating rate of 40 K/min independent on the type of rare earth metal and concentration (Fig. 54). The observation of a nearly constant peak temperature of the exothermal effect n° 2 independent on light RE solute and concentration underlines that cell boundaries and resultant microsegregations control the exothermal reaction n° 2 of the gun splats and that the volume fraction of microsegregations was particularly high for Mg-La gun splats. The Mg-La system was reported to develop more easily microsegregations compared to Mg-Sm splats of equivalent levels of alloying when made under constant conditions of quenching from the melt and this was coupled to a smaller cell size and a smaller width of the featureless chill zone of Mg-La splats compared to Mg-Sm splats ([8,12,13]). The volume fraction of microsegregations separated from the melt and the volume fraction of precipitates subsequently formed upon solid state precipitation was observed to increase with increasing cell boundary area within the regime of cellular growth from the liquid phase [36]. Obviously, the scatter in cooling conditions upon gun splatting (see above) is of minor significance here compared to the solidification kinetics of the specific alloy systems concerned and which control the formation of the microstructure (cf. [41,42]).

The individual evaluation of the observed exothermal effects of Mg - 8 Ce [nom. wt.%] yields about 7 J/g for exotherm n° 1 (attributable to the formation of D019 β'' and/or fcc- β' -Mg₃RE), about 10 J/g for exotherm n°2 (attributable to growth of β' and the formation of β at grain boundaries) and about 32 J/g for exotherm n°3 (attributable to formation and growth of

equilibrium- β in the interior of the grains and cells) (Fig. 53). As for the extended solid solution of Y in α Mg, the major transformation of the supersaturated solid solution of Ce in cph-Mg occurred at higher temperatures, here above or around 400°C. The enthalpy of transformation of exothermal effect n° 2, $\delta H(\text{exo2})$, of the Mg-La samples, however, was observed to amount to 45 J/g compared to about 10J/g for Mg-Ce and Mg-Nd gun-splats.

The observed peak temperature T' of the exothermal effects n° 2 was found at T = 355°-358°C for a heating rate of 40 K/min independent on the type of rare earth metal and concentration (Fig. 54). The observation of a nearly constant peak temperature of the exothermal effect n° 2 independent on light RE solute and concentration underlines that cell boundaries and resultant microsegregations control the exothermal reaction n° 2 of the gun splats and that the volume fraction of microsegregations was particularly high for Mg-La gun splats. The Mg-La system was reported to develop more easily microsegregations compared to Mg-Sm splats of equivalent levels of alloying when made under constant conditions of quenching from the melt and this was coupled to a smaller cell size and a smaller width of the featureless chill zone of Mg-La splats compared to Mg-Sm splats ([8,12,13]). The volume fraction of microsegregations separated from the melt and the volume fraction of precipitates subsequently formed upon solid state precipitation was observed to increase with increasing cell boundary area within the regime of cellular growth from the liquid phase [36]. Obviously, the scatter in cooling conditions upon gun splatting (see above) is of minor significance here compared to the solidification kinetics of the specific alloy systems concerned and which control the formation of the microstructure (cf. [41,42]).

An anomalous doublet in exothermal n° 3 was observed in Mg-Ce gun splats indicating that an endothermal reaction was superimposed to the exothermal phase transformation at above 400°C (cf. Fig. 53c). This endothermal effect increased with increasing degree of fragmentation. Fig. 55a shows the result of the DSC-analysis of Mg - 8 Ce gun splats of thickness below 2 μm and Fig. 55b shows the DSC analysis of vapour deposited Mg - 8 Ce made at a relatively high substrate temperature. At a deposit temperature of 60°C, however, this endothermal effect dominates the transformation behaviour of PVD Mg - 8 Ce over the exothermal reactions at lower temperatures, which then became negligible (Fig. 56).

Endothermal effects can only result from the transformation of an ordered into an disordered phase or from the dissolution of second phases. Previous DSC-analyses of the solid solution of Mg-Sm and Mg-Gd alloys have shown relatively broad endothermal effects resulting from the dissolution at heating rates as high as 40 K/min of very fine ($<<1 \mu\text{m}$) second phase dispersions [6]. These second phase dispersions were a result of separation from the melt due to insufficient initial undercooling and subsequent recalescence (as indicated by the increase in scale with increasing foil thickness of splats, for example) or they resulted from long term natural ageing of the corresponding solid solutions [6].

The peak-shaped form and the magnitude of the large endothermal effect at above 400°C observed upon DSC-analysis of vapour deposited Mg - 8 Ce alloy corresponds to those transformation peaks which were frequently observed for metastable metallic matrix phases such as metallic glasses obtained by rapid quenching from the melt [43]. They did not correspond to the less sharp effects observed upon dissolution of second phases. The high reproducibility of this endothermal effect by sampling from a plate of length 65 mm * width 90 mm and of thickness 300 µm combined with increasing evidence of this effect with increasing degree of fragmentation prior to solidification confirmed that corresponding material was not subjected to the often irreproducible effect on microstructure of recalescence. The endothermal effect appears therefore to be related to the transformation of a metastable one phase matrix of Ce in cph-Mg (see Fig. 64) of which the structural difference to solid solution remains to be identified.

Temperature calibration of the Dupont 910 analyser was done by employing the equation

$$T = T' * m + b$$

where T = real temperature, T' = recorded temperature resulting in the following coefficients m and b for calibration as a function of heating rate H:

H [K/min]	m [/]	b [K]
20	1.0011	-2
40	0.9905	-4.5

The real endothermal peak temperature of the vapour deposited Mg - 7.2 Ce alloy arrived at 414.5°C for a heating rate H = 20 K/min (n.b. T' = 414.5°C) and at 423°C for a heating rate H = 40 K/min (n.b. T' = 431.5°C) corresponding to an activation energy E_A of 113 kJ/(mol K) and a quasi-isothermal transformation temperature at between 360°C (H = 0.1 K/min) to 382°C (H = 1 K/min) by using the Kissinger method [44] . The real temperature of the exothermal peak N° 2 of Mg-1 wt.% La splats made by the gun technique was 342.4°C for H = 20 K/min (n.b. T' = 344°C) and 350°C for H = 40 K/min (n.b. T' = 358°C) corresponding to an activation energy E_A of 83.3 kJ/(mol K) and a quasi-isothermal transformation temperature at 292.6°C (H = 0.1 K/min) by using the Kissinger method.

Fig. 56a shows an integral enthalpy of transformation of 54 J/g of PVD Mg - 8 Ce in the temperature range between 100° and 540°C. The integral value is the sum of an exothermic evolution of -14 J/g between 100° and 393°C and of the above discussed endothermal peak with an endothermal enthalpy of + 68 J/g between 393° and 540°C. In terms of absolute values, the exothermic spectrum represents 20.6 % of the integral value over a temperature intervall of 293°C or 0.7% per 10 K, while the endothermal effect represents 5.4 % of the integral value per 10 K. It is evident that the endothermal effect at above 400°C represents the transformation of

metastable into the equilibrium phases. This transformation seems to be somewhat superimposed by an exothermal reaction immediately starting after the onset of the endothermal peak and increasingly separating the endothermal peak as the heating rate decreases (Fig. 57). The transformation sequence of the endothermally transforming phase obtainable with increasing degree of fragmentation such as vapour deposition seems to pass through the phases formed by liquid quenching (cf. Figs. 57 and 55a). The observed fraction of partial exothermal to endothermal enthalpies of PVD Mg - 8 Ce was fully reproducible independent on sampling and heating rate employed (Fig. 58).

The vapour deposited solid solution of Ce in α Mg was close-packed hexagonal (Fig. 64), but it represented a more ordered phase than the resultant equilibrium phases for which the change in entropy provides the driving force for transformation, since:

$$\Delta G < 0$$

$$\text{so that } |\Delta H| < |-T\Delta S|$$

where ΔG : Gibbs free energy, the driving force for phase transformation, ΔH : the recorded enthalpy of transformation and ΔS : entropy of transformation non-recordable by DSC. The increasing departure from equilibrium appeared to increase the degree of ordering dramatically when fragmentation arrives at the level of individual atoms. The fragmentation down to the level of a single atom, however, appeared as a *conditio sine qua non* for the formation of a 100% or nearly 100% volume fraction of metastable MgRE phases upon change of matter, i.e. when the recalescence leads to segregation upon solidification and resulting in insufficient metastable volume fraction. The present observations are also not forthcoming from advanced solid state processing without change of matter such as mechanical alloying, which incorporates limitations upon purity and phase homogeneization as is set by processing conditions and resultant shear stress imposed on dislocation movement resulting in a multi-phase and which makes it attractive to employ vapour deposition instead, if possible. The mechanical alloying / ball and/or bar milling route, however, provides promising results in the more immediate period of time (see below).

Natural Ageing Behaviour

After eight years of room temperature (natural) ageing including temperature cycles from below zero celsius to above 40°C and humidity alterations from below 40% to above 90% splat cooled cph-Mg solid solutions supersaturated with La, Ce, Sm and Gd showed two endothermal effects at 120° to 150°C and at between 350° to 450°C (Figs. 59 to 60). If not indicated otherwise, these splats were made by the rotating splat cooling technique (RW) which provides cooling rates of the order of 10^7 to 10^9 K/sec and a levels of fragmentation allowing to form "splatted" cross-sections in the range of <1 to 50 μ m. The RW splats investigated were all below 25 μ m and their microstructure corresponded to the microstructure shown in Fig. 49.

Endothermal effects can only result from the transformation of an ordered into an disordered phase or from the dissolution of second phases within the non-equilibrium and/or equilibrium solid solution or any other phase. The change in entropy provides the driving force in both cases. The second phases must be very fine ($< 1 \mu\text{m}$) in order to be completely dissolved at heating rates as high as 40 K/min (cf. Figs. 59 to 62). The enthalpy of transformation of the endothermal effect n° 1 at around 150°C increased with increasing levels of La and Gd, but a concentration effect on enthalpy was not evident for Mg-Ce splats:

Alloy /Splat Thickness [wt.%] / [μm]	Heat of transformation of endothermal effect at 150°C by using a heating rate $H = 40 \text{ K/min}$	Corresponding Transformation Temperature
Mg - 3.9 La / <20	> +30 J/gram	at about 145°C
Mg - 6.8 La / <20	> +40 J/gram	at about 130°C
PA Mg- 4 La / 140	absent	
Mg - 3.65 Ce / <20	> +85 J/gram	at about 150°C
Mg - 13.2 Ce / <20	> +50 J/gram	at about 140°C
PA Mg- 4 Ce / 140	absent	
Mg - 4.6 Sm / 20	> +50 J/gram	at about 150°C
Mg - 7.5 Gd / 30	60 J/gram	at about 148°C
Mg - 17.9 Gd / 30	125 J/gram	at about 140°C
PA Mg- 8 Gd / 200	about 3 J/gram	at about 150°C

Selected splat thicknesses had assured that the alloying elements were essentially tight up in solid solution when they were made almost ten years ago. The absence of an exothermal effect after this period of exposure to ambient temperature conditions suggest that the extended solid solutions have entirely transformed into an ordered (room temperature) phase of which the endothermal effect represents either the dissolution and/or transformation into more stable structural configurations finally transforming into the equilibrium microstructure at 420°C as is shown by the (usually larger) second endothermal effect at around 350° to 400°C. The endothermal transformation effects were sharp (i.e. forming "glass"-like peaks) at temperatures around 130° - 150°C. They decreased with increasing alloying content suggesting the presence of a metastable intermediate phase in a more complex overall precipitation sequence.

Hehmann observed [11] such endothermal effects after 7 and 12 months room temperature ageing of the extended solid solution of Al in cphMg. These endothermal effects were identified [11] to represent the transformation of an ordered γ -superlattice preferentially forming at the boundaries of cells of size $<< 1\mu\text{m}$, i.e. of some 5 to 100 nm (Fig. 63). The endothermal

effect n° 1 observed in the alloys claimed by this invention, however, were not evident after such relatively short durations of natural ageing. In aerospace applications, however, it is important to know the behaviour of metastable alloys and phases over much longer periods. The endothermal effects were related to the transformation sequence of the metastable solid solution of La, Ce, Sm and Gd in cph-Mg and are therefore expected to universally occur in other systems such as Mg-early transition metal base alloys of which the major onset of phase transformation (equilibrium phase formation) occurs at even lower temperatures than in the Mg-early rare earth base alloys. Mg-based solid solutions containing rare earth elements were reported to form atomically thin layers of GP- (i.e. γ -) type of precipitation zones ([44-1,44-2]). They might transform to (1) a more disordered and eventually more incoherent phase including the possibility of (2) dissolution within the metastable supersaturated Mg-based solid solutions for which the change in entropy provides the driving force for transformation and for which dislocations and grain boundaries as well as second phases separated during solidification (a problem which is better controlled by PVD) act as the preferred nucleation sites. The occurrence of the endothermal effect at around 150°C, however, requires homogeneity of the alloying additions on an atomic length scale of an disordered phase before, the largest length scale of which corresponding to the minimum length scale of the γ -phase (i.e. 5nm or so, see above)

It was interesting to note that a small endotherm at 150°C was observed for Mg-Gd splats made by using the PA-technique, but not for PA-Mg-splats containing La or Ce (Figs. 59 to 62) (n.b. the employed PA-technique is the most "clean" chill block technique concerning the featureless chill zone, but not for the entire splat cross-section). This is consistent with a k_0 -value nearer to unity in the Mg-Gd system allowing for supersaturation during solidification from the melt for relatively large cross-sections. The small heat of transformation of the first endothermal effect in PA-Mg-Gd shows in fact that other factors such as grain boundary concentration and/or coarsening of co-existing dispersoids / microsegregations have "eaten away" the GP-zone type of solid state phases on long term exposure to natural ageing conditions. That is, the larger the (volume fraction of) uncontrolled second phases upon solidification including impurities (and this is to be generalized for corresponding alloys made by PVD-techniques), the larger the natural ageing rate. This is consistent with the results for PA Mg-La and PA Mg-Ce splats of which the second endothermal effect obscured to discriminate the first one.

The first endothermal effect represented a phase transformation that can lead to grain boundary embrittlement and loss of strength due to a reduction in transgranular coherence. From the observations made herein it is now possible to derive an annealing treatment after forming, solutionizing and quenching operations that does not trigger an undesired transformation of phases forming upon natural ageing. Any annealing treatment of the metastable supersaturated state should therefore be performed in the temperature range below the observed endothermal peak n° 1 (i.e. at $T < 130^\circ$), while a GP-dissolution treatment (provided that other second phases including microsegregations are absent) at around 150°C. The magnitude of the second

endothermal effect of the as-solidified, i.e. non-solution treated version of the claimed alloys increased with increased thickness of the traverse cross-section of the splats so with the volume fraction of second phases separated from the melt during solidification. It is concluded from these observations that actual time and temperature for solution treatments of the rapidly solidified (as-deposited) condition of the claimed alloys can be reduced to less than 1 hr at temperatures below 400°C opening an avenue to retain the refined grain structure and strength increment in the final product.

The occurrence of distinct endothermal effects at temperatures between 120° to 150°C which are related to the transformation of GP-zones formed after long-term natural ageing allow also for identification of the claimed optimum temperatures and the claimed optimum durations of the (i) forming procedures, (ii) intermediate heat- and homogeneization- or solution-treatments between forming operations, (iii) ageing conditions and (iv) annealing treatments for stress relief without undue damage to the protective surface film afforded by the elements enhancing the MgO-surface oxide. Temperature and time of annealing procedures and/or solution heat treatments can be markedly reduced compared to conventionally synthesized and/or processed light alloys due to their extremely fine microstructure resulting in an increase in surface area of second phases providing the increase in driving force for second phase dissolution. Any annealing treatment for stress relief of the supersaturated solid solutions should according to the invention not exceed temperatures of 140°C for short term exposures of the order of 2 hrs or 110°C for longer exposures in order to avoid that the transformations of the supersaturated solid solutions or of GP-zones, formed within the solid solutions, reduce corresponding passivating effect.

Intermediate Summary of the Invention on Thermal Stability

The results show that the transformation sequence of the extended solid solution of light RE elements in cph-Mg with a random, ordered or quasi-ordered distribution of the light RE atoms is the yet reported most thermally stable cph-Mg base solid solutions of an alloying addition in in as-solidified (as-deposited) magnesium:

1. The transformation temperatures of MgRE alloys are at some 30° to 60° C higher temperatures than corresponding microstructural evolutions observed for RSP Mg-Y alloys (cf.[36]).
2. The onset of the formation of equilibrium phases from the extended solid solution of light RE metals in cph-Mg occurs at some 90° to 120° C higher temperatures than the transformation of the extended solid solution of manganese in cph-Mg [45] .
3. The optically columnar VD-microstructure without boundary phases evidencing the absence of any recalescence and microsegregations as obtained by vapour deposition appears to result in a further increment of thermal stability of the extended solid solution with an equilibrium phase transformation peak dominating the overall transformation at an isotherm of some 360°C. This isotherm appears to be around 150° to 180°C thermally more stable than an hypothetical isothermal transformation temperature of the extended solid solution of Ti in

cph-Mg which was also obtained by vapour deposition (cf. [17]).

4. In summary, the thermal stability of rare earth elements in the cph-Mg base solid solution is at least some 100°C higher compared to that of the yet published transition metals.
5. From the viewpoint of the thermal stability of the final transformation of liquid and vapour processed solid solutions of light RE metals in cph-Mg it appears of secondary importance for subsequent consolidation and alloy conversion of the as-solidified material whether this reaction is exo- or endotherm. By contrast, fine microsegregations in corresponding liquid quenched material appeared to render the material susceptible to ageing at room temperature as indicated by a value of activation energy, E_A , of 83 kJ / (mol K) which is below the threshold of 100 kJ / (mol K) for ageing processes at ambient [46].
6. The magnitude of thermal effects and the ratio of the magnitude of these effects depends on the processing route for the synthesis of the alloying elements rather than on the light RE metal employed (cf. Figs. 50 - 54 vs. 56 to 58). The vapour deposition route was observed to favour microstructural evolutions at higher temperatures at the expense of thermal effects at lower temperatures via segregation-free microstructures of the extended solid solution of Ce and other light RE metals in cph-Mg compared to liquid processing so to preserve the homogeneity on an atomic length scale in the final product.
7. Vapour deposition makes the extended solid solution of (light) RE elements in cph-Mg a very attractive material for corrosion demanding applications in which further transition metal (TM) additions can be added deliberately to strengthen the material upon alloy conversion by precipitation of these TM at significantly lower temperatures than required for formation of the equilibrium phases from the extended solid solution of RE metals in cph-Mg.

Commercialization

The wrought Mg alloy market is currently lingering on the 7000 t.p.a. level which is 2% of the overall Mg-market or 0.04% of the wrought Al alloy market. This situation is mainly related to the poor passivation characteristics of the available cast and wrought Mg alloys. In order to take advantage of the present invention for the development and commercialization of Mg-base alloys and products with passivating alloy surfaces it is necessary to :

- (i) employ suitable conditions of alloy conversion including appropriate transformation temperatures in order to retain the novel structure in the final product,
- (ii) enhance the mechanical properties such as via synergistic hardening effects of the employed alloying additions without break-down of the passivity of the surface film and
- (iii) to use continuous production techniques to arrive at economically viable product forms.

Alloy conversion of RSP light alloys

According to ASM handbooks [47,48], hot forming operations of commercial Mg-based alloys include extrusion at temperatures ranging from 360° to 440°C, rolling at temperatures between 420° to 500°C and forging often within some 50°C of the liquidus temperature of corresponding

magnesium alloy. From the DSC-analyses it is evident that these conditions would destroy the supersaturated cph-Mg base solid solution and the resultant passivation effect due to the low equilibrium solid solubility of light RE metals in cph-Mg (cf. [5,49]). Emley had shown [50], however, that a grain size of less than about 8 μm represents the threshold for increasing deformability and ductility of hexagonal magnesium, which is one factor required to reduce the forming temperature and/or to avoid failure upon extrusion, rolling and forging so to allow for higher productivity in terms of extrusion speed, metal yield and quality of the final product. The refined microstructure of RS Mg-alloys does not only increase hardness and strength (see below), it also allows for "cold" extrusion, rolling and forging at some 100° to 300°C lower temperatures than applied to ingot processed magnesium alloys.

Microcrystalline Mg-alloys

This has been demonstrated by Isserow and Rizzitano as long as twenty years ago for microcrystalline ZK60A (Mg - 6.0 Zn - 0.45 Zr, in [wt. %]) powders made by the rotating electrode process (REP) [51]. The spherical powder was kept under refrigeration before being extruded preferably at temperatures as low as 65°C then waterquenched to avoid overageing and subsequently aged for 24 hours at 120° to 150°C. The strength increment of up to 427 MPa UTS (422 MPa tensile yield strength TYS) originated in a grain size of 1 to 10 μm . Though care must be exercised due to delamination along the fibred fracture paths (the size of intermetallic compounds were of size 0.1 μm), this fibred structure also doubled fracture time and impact energy in charpy specimen leading to consideration of REP-ZK60A for large body applications such such as via rolling for sheet products in aerospace applications [51].

More recently, Das et al. [52-55] and Nussbaum et al. [56-58] have demonstrated that the effect of microstructural refinement of Mg-Al-Zn-base alloys afforded by RSP resulted in excellent formability at temperatures as low as 150°C making such alloys useful for near-net shape operations including rolling and forging. The increased freedom in processing conditions was largely dependent on fine intermetallic second phase dispersions to pin the growth of grain boundaries of RS Mg-Al-Zn base alloys upon alloy forming operations, since the RSP-refined microstructures are otherwise thermally very instable so to result in degradation of the resultant properties. Large grains would also result in failure such as by blistering, hot shortness and structural changes as often encountered upon extrusion, rolling and forging of ingot processed magnesium alloys.

The details of alloy conversion of microcrystalline RS Mg-Al-Zn base alloys include:

1. superplastic forming of consolidated alloy Mg - 0-14Al - 0-4Zn - and 0.2-3 X (X = Mn, Ce, Nd, Pr and yttrium) (in [at. %]) comprising a microstructure of a solid solution phase of size 0.2 to 1.0 μm together with precipitates of Mg- and Al-containing intermetallic phases of size less than 0.1 μm using a forming rate ranging from 0.01 mm/sec to 0.21 mm/sec at 160° to

- 275° C (U.S. patent 4,938,809 [52]);
2. as for 1., but with the proviso that the sum of Al and Zn ranges from about 2 to 15 at.% and deforming corresponding consolidated alloy (preferably cylindrical) billet(s) by over 80% at temperatures ranging from 200° to 300°C by employing a closed-die or an open-die forging to arrive at minimum UTS-values 378 MPa (U.S. patent 5,071,474 [53]);
3. alloy(s) as for 1. and 2., but forming such alloy billet(s) into a rolling stock which is then preheated to temperatures ranging from 200° to 300°C followed by rolling the heated stock at a rate of 25 to 100 rpm by adjusting the gaps of the preheated rolls of diameter 5" (5 inch, i.e. about 13 cm) so to reduce thickness by 2 to 25% per pass and to arrive sheet thickness 0.014 to 0.095" with minimum UTS-values 400 MPa (U.S. patent 5,087,304 [54]); for comparison, the strength values of conventional Mg-based alloy sheets at ambient temperature were reported by the ASM handbook [47] to range from 260 to 290 MPa UTS and from 140 to 220 MPa TYS at elongation values between 8 and 24%;
4. alloys and sheets as for 3., but forming such sheets into a complex shape by employing strain rates ranging from 10^{-1} to 10^{-2} /sec at temperatures ranging from 275° to 300°C eventually arriving at elongations > 300% and a grain size up to 5 μm (U.S. patent 5,129,960 [55]);
5. extrusion of the alloy(s) Mg - 2-11Al - 0-12Zn - and 0-0.6Mn and 0-7Ca (in [wt.%)) comprising a microstructure of mean particle size less than 3 μm and a dispersion of inter-metallic compounds of size less than 1 μm such as Al_2Ca which delineate grain boundaries so to stabilize such microstructures against growth and coarsening by exposures for 24 h at 200°C and allowing for extrusion at temperatures of 200° to 350°C with an extrusion ratio of 10:1 to 40:1 (preferably 10:1 to 20:1) and a forward ram speed of 0.5 to 3 mm/sec (or 5 mm/sec with higher Ca-contents) to result in rupture strength values of at least 290 to 320 MPa, the extrusion performed with melt-spun ribbon either directly, after pre-compaction the ribbon to billets or after vacuum-degassing the ribbon (U.S. patent 4,997,622 [56]);
6. thermal deformation including extrusion (EP 0414620A1 [57]), drawing and forging or a combination of the two latter at between 200° and 350°C of spray-deposited alloy(s) Mg - 2-9Al - 0-4Zn - 0-1Mn - 0.5-5Ca and 0-4RE (in [wt.%)), where RE is yttrium, Nd, Ce, La, Pr, misch metal (MM) and mixtures thereof, the alloys comprising a homogeneous magnesium matrix of grain size 3 to 25 μm and intermetallic phase dispersions including $\text{Mg}_{17}\text{Al}_{12}$, Al_2Ca , Mg_aRE_b and Al_aRE_b of size < 5 μm , the thermally deformed product then followed by selected solution treatments and temper hardening or by temper hardening only in order to arrive at fracture toughness values of 30 to 35 MPa m^{0.5} at UTS-levels of 480 to 365 MPa (U.S. patent 4,997,622 [58]).

It is interesting to note that only a deposition route has led to fracture toughness values of RSP-Mg alloys acceptable for aerospace applications. In RSP-deposition routes, the fragmentation is inverted in-situ so circumventing exposure of excessive surface area to oxygen and resultant oxide formation. Vapour deposition (VD) provides therefore also a perspective for crucial

mechanical properties of Mg-base aerospace applications with satisfying surface passivity.

Nanocrystalline VD-Al alloys

Rapidly solidified aluminium-base alloys made by melt-spinning, planar flow casting and gas atomization are usually consolidated (extruded etc.) at temperatures between 350° and 400° C. By contrast, vapour deposits of Al - 2.8-6.3Cr and Al - 2.5-6.1Cr - 0.45-0.92Fe (in [at. %]) alloys of columnar grains of diameter 1 µm and of thickness 0.1 µm with the chromium entirely tied up in the fcc-Al solid solution and the iron to form Al₇(CrFe) precipitates of size 3 to 5 nm (i.e. at least by a factor 10 finer than in Al-alloys made by RSP-methods from the liquid and which were preferentially formed at cell boundaries) were rolled at temperatures between 20° and 420°C [59], preferably at between 190° or 250° and 290°C [60] to produce sheet of thickness 1.6 to 1.7 mm with the highest ever reported strength levels of a crystalline engineering Al-alloy (UTS : 848 MPa at a fairly convenient ductility of 8 %) followed by annealing treatments that affected the dislocation substructure only at temperatures where the solid solution of Cr in fcc-Al and the resultant properties were degraded [61].

Nanocrystalline PVD Mg - alloys

Microstructural refinement improves systematically the deformability of Mg- and Al-base alloys (see below) and this effect is more evident for Mg-alloys. Microcrystalline Mg-alloys provide the most superplastic light alloys and a larger reduction in forming temperatures than microcrystalline Al - alloys made by the same RSP-methods. Microcrystalline light alloys require a fine dispersions of second phases to suppress growth and coarsening of RSP-refined matrix grains upon alloy conversion into product or semi-finished product form. In nanocrystalline light alloys, however, the virtual absence of such particles facilitates the conversion of the microstructure into final product form. The degree of homogeneity obtained by the refinement on the nanostructural length scale allows to reduce more effectively the required forming temperatures and offers diffusion as the material parameter to take over the control of microstructural modifications upon alloy conversion into final product form. This is coherent with the requirements for alloy conversion of metastable Mg-alloy products with sufficient surface passivity as in the case of the extended solid solution of (light) RE metals in cph-Mg.

Mg - (light) RE metal base alloys offer an additional reduction in forming temperatures from the alloy chemistry point of view. Krishnamurthy et al. reported [62,63] on ultrasonic gas atomization (UGA) of Mg - 3.2Nd - 1.1Pr - 1.5Mn [wt. %] alloy and subsequent consolidation at lower temperatures compared to RS Mg-Al-Zn base alloys. Much better tensile strength at room temperature and improved corrosion resistance were achieved compared to the strongest ingot processed alloy ZK60, although this alloy did not contain any of the classical solid solution strengthening elements such as Al and Zn. Satisfying interparticle bonding without porosity was attained after degassing for 1 h at 250°C, preheating for 2 hrs at 250°C, hot-

isostatic pressing for 6 h at 250°C followed by preheating for 2 hrs at 250°C and extrusion at reduction ratios between 12:1 and 20:1 (for 150 to 250°C) or 8 : 1 (for 100° to 250°C). The employed extrusion temperatures were thus lower for microcrystalline Mg-LRE base metals than for nanocrystalline VD Al-alloys (see above). No satisfying consolidation was possible for the UGA Mg - 3.2 Nd - 1.1 Pr - 1.5 Mn alloy outside these conditions (cf. [51]).

The advantages of an insitu-consolidation-type of RSP-route such as vapour deposition over UGA, for example, are evident: VD does not impose the need for degassing or pressing so reducing the number of processing steps and improving the overall economics of VD-alloy conversion significantly compared to the more traditional powder metallurgy routes. Vapour deposition offers all the advantages of spray deposition from the liquid phase with the additional advantage of the formation of metastable structures allowing for passive magnesium alloys.

Nanocrystalline Mg-LRE alloys with the LRE held in extended solid solution thus represent a philosophy that is different from previous avenues for the development and application of high performance light alloys. It is part of the invention that vapour deposited Mg-LRE based alloys are transformed into product form at temperatures where no detrimental effect on passivation occurs due to susceptibility to the formation of compound nuclei in the melt (cf. [39]) and the resultant acceleration of solid state precipitation and hardening by exposure to natural and artificial ageing conditions. It is therefore part of the invention to consolidate the claimed alloys at temperatures ranging from ambient (i.e. 15°C) up to 370°C, preferably in the range from 50° to 200°C and using extrusion ratios, for example, which range from 3 : 1 to 45 : 1.

Engineering Properties including Damage Tolerance

Vapour deposited Mg - (light) RE binary alloys

Grain size refinement does not only accrue to the conversion of the extended solid solution of (light) RE metals in cph-Mg into wrought product forms without substantial loss in surface passivity. Grain refinement also entitles selected RSP-routes to result in superior mechanical properties via Hall-Petch grain boundary strengthening the (super-) saturated passive cph- and/or ne-Mg-alloy matrix without detrimental effect upon passivation by (enhanced) alloying. Initial microhardness tests were performed on the two regimes of grains of size of the as-cast alloy Mg-8 Ce (cf. Fig. 48) as well as of corresponding vapour deposited version resulting in following Vicker's hardness numbers (VHN) as a function of grain size:

<u>Alloy</u>	<u>Size of Secondary Dendrite Cells [µm]</u>	<u>VHN</u>	<u>UTS [MPa]</u>
Conventional Casting	20-30	64.7 +/- 5.5	207
	5-12	82.7 +/- 9.5	264
PVD	(X-ray: 0.025)	148.5 +/- 12.3	540

The nanocrystalline subcell structure of the vapour deposited material was derived from the full intensity mean half width (FMHW) of the (002) reflection shown in Fig. 64. Under the assumption that no residual stresses were involved, the use of the Debye-Scherer formula

$$d = k \lambda / \Delta(2\Theta) \cos \Theta$$

yields a subgrain size of 25 nm. The Hall-Petch proportionality constant k_y of the two-phase binary Mg - 8 wt.% Ce casting alloy is in good agreement with that of other Mg - LRE based metals such as the rapidly solidified alloy EA55RS (see Fig. 65). The results support the hypothesis that grain boundaries provide the rate controlling mechanism for plastic deformation of the Mg - (light) RE alloys when made by ingot processing. Significant deviation from this Hall-Petch relationship is indicated however, by the results for the vapour deposited version of Mg - 8Ce. Such deviation were frequently observed in nanocrystalline metals such as Ti and Pd owing to the fact that diffusion took over the rate controlling mechanism of plastic deformation (cf. [65]).

According to US. patent 5 118 368 [66], the coupling factor between ultimate tensile strength UTS and VHN for metastable magnesium-based phases ranges from 3.2 to 3.5 indicating quite a considerable strength value of the order of 540 MPa or more for the vapour deposited alloy Mg - 8 wt.% Ce. This is a high value for a simple binary Mg-alloy and embraces encouraging significance for the further development. Vapour deposited binary Al - Cr alloys in which the Cr was entirely accomodated by the supersaturated α Al solid solution resulted in tensile yield strengths of 400 MPa. The addition of only 0.4-0.8 at.% Fe led to VD Al alloys with 4-6 at.% Cr in solid solution and the Fe forming precipitates of size some 3 - 5 nm. They are the best Al-engineering alloys ever reported with UTS values ranging from 635 to 818 MPa and values of elongation-to-fracture at between 6 and 10% (cf. [26,27]). The initial microstructure of VD Al-Cr-Fe alloys allowed for tailorability and an optimization of properties which rendered the resultant property profiles superior compared to all other metallic materials. The solid solution and the combined effect of dislocations and fine grain structure contributed to about 60% of the strengthening effect of these vapour deposited alloys [27]. The solid state second phases obtained by subsequent thermomechanical processing of VD Al-Cr-Fe alloys are so fine that a maximum efficiency of strengthening mechanisms was achieved without reduction in toughness which is so important for aerospace applications (see above).

Evidently, these attributes accrue to the Mg-Ce system as well. Ce and the other light (and heavy) rare earth metals represent not only a very thermally stable solid solution in cph-Mg or any other metastable Mg-rich Mg-light RE phase as Cr does in fcc-Al especially when made via the PVD-route, they also represent an effective solid solution hardener so opening avenues for a promising development. Subsequent precipitation of selected alloying additions to the solid solution of light RE metals in cph-Mg via selected alloy forming operations should improve

hardness, strength and the operative Hall-Petch proportionality constant k_y (and the intercept $\Delta\sigma_0$ of the Hall-Petch-relationship) of corresponding wrought alloy products even further.

Improved Damage Tolerance by Processing for "Clean Grain Refinement"

(Effect of Purified and Purification of Feedstock and Impurity Size)

As for other reactive materials, the properties and in particular the damage tolerance of Mg- and Al-based alloys depend on their impurity content. It shall be noted that spectacular failures occurred in aviation and automobile applications due to catastrophic corrosion of Mg-alloys after a while of use in service which resulted from microgalvanically active inclusions such as Fe-, Ni- and/or Cu- (containing) inclusions and/or second phases, for example. In their classical paper, Hanawaldt et al. have demonstrated [67] the particular tolerance limit of 0.017 wt.% Fe in the presence of Mn and of 0.005 wt.% Fe in the presence of Al in casting alloys above which catastrophic failure results upon immersion in salt-solution. Most critical (and relatively independent on deliberate alloying additions) was the Ni-content of Mg-castings with a maximum threshold as low as 0.001 wt.% Ni prior to a dramatic increase in the susceptibility to corrosion.

The world, however, has ignored and/or underestimated the significance of the "Hanawaldt"-thresholds for more than 40 years. Between the 1950s and 1980s it was common use to either employ a 2N8 (i.e. 99.8 % purity by weight) feedstock for magnesium with certified trace analyses of individual maximum impurities (by weight) in the range of [68,69]:

0.002% Ni
0.05% Fe
0.02% Cu
0.01 - 0.04% Si
0.1% Mn
0.04% Al
0.05% others, balance Mg,

i.e. without providing any guarantee against "Hanawaldt"-type of critical impurity levels and resulting failure, - or the higher purity version of 3N-Mg-feedstock (99;90) of that period which represented a better alternative, but not a solution to the corrosion problem, since in particular the iron-content was still very critical (cf. Table 1, Part 1 and [68,70]):

0.001% Ni
0.02 - 0.003% Fe
0.002 - 0.005% Cu
0.01% Si
0.01 - 0.05% Mn
0.01% Al
0.01% others, balance Mg,

i.e. still without providing the guarantee required against "Hanawaldt"-type of corrosion failure.

It was only relatively recently that the "Hanawaldt"-type of thresholds were sufficiently taken into account in the fabrication of engineering alloys such as AZ91 and other Mg-Al-based casting alloys (cf. Table 1, part 2). Along with the introduction of high purity Mg-alloys, Closset and Dimayuga have shown [71] that the further reduction of critical impurities from 0.015 wt.% Cu and 0.004 wt.% Fe down to the level of 0.001 to 0.0015 wt.% Cu and Fe and a constant level of max. 0.001 wt.% Ni results in a further reduction of the annual corrosion rate of AZ91 alloy from 12 down to 3 mpy (cf. Table 1, part 2). Such results are possible by using 3N8 Mg feedstock providing the following trace analysis of maximum impurity content [72]:

Al 0.003 %
 Mn 0.0016 %
 Ni 0.0005 %
 Si 0.002 %
 Ca 0.001 %
 Cd <0.0001 %
 Zn 0.004 %
 Fe 0.0013 %
 Cu <0.0005 %
 Pb 0.001 %
 Sn <0.001 %

Other important impurity-thresholds in Mg include the Na-level which should be below 0.003 wt.% to avoid (grain boundary) embrittlement and the oxygen content in ingot processed Mg-alloys (i.e. with a grain size > 20µm) to avoid deterioration of fracture toughness, for example [50]. An analysis of sublimed grade ("SM") of magnesium feedstock resulted [73] in:

0.004% Fe
 0.004% Mn
 0.002% Al
 0.003% Si
 <0.0005% Cu
 <0.0005% Ni
 < 0.0005% Na
 < 0.0005% Ca

so 99.985 (4N) magnesium by weight. Mg-feedstock impurities are therefore a reference for further Mg-based alloy development. Mg-feedstock impurities represent the minimum contamination in Mg-alloy synthesis from/via condensed matter such as by casting methods, ball, bar and other milling techniques employing the solid state and PVD via (magnetron) sputtering methods on the one hand and they represent a maximum contamination in Mg-alloy synthesis by using thermal evaporation methods due to the involved distillation and resulting purification effect (see below).

The processing of Mg-alloys via/from condensed matter is unique in the sense that the impurity

level of the feed stock is inevitably retained and/or increased in the final alloy and alloy product depending on the processing conditions employed. Feed stock and processing conditions must avoid critical levels of critical impurities with regard to novel Mg-alloys and Mg-alloy chemistry, which in return must retain the low density of magnesium. The impurity level of the feed-stock therefore determines and/or co-determines the final property profile, in particular the profile of the electro-chemical and/or corrosion properties. In order to develop superior Mg-alloys it is therefore not only necessary to choose a suitable feedstock, but also to retain the degree of purity supplied by way of the feedstock, i.e. to keep further contamination as low as possible. Therefore, it is inevitable to employ a number of pre-cautions:

1. Condensed Matter Processing and Sputtering

- 1.1 usage of a refractory metal such as Hf, V, Ta, Nb, Mo, W, Cr, Re, Zr (or a refractory metal based alloy, intermetallic, ceramic) as crucible material to avoid any reaction between Mg-melt and crucible. Mg-melts must not only avoid (contact with) iron-based crucibles (cf. above). In the case of an alloying additions such as (heavy) rare and alkaline earth metals such as (elemental) calcium, alumina, magnesia, zirconia, i.e. oxides cannot be used as crucible materials, either, since they are reduced by calcium, for example, and the resultant oxide products embedded in the Mg-matrix trigger local pitting of the Mg-alloy. Graphite must also be excluded due to the susceptibility of liquid magnesium to form Mg-carbides which are (as are Al-based carbide) easily dissolvable in aqueous solutions. The most versatile, since shock-resistant crucible material was identified to be tantalum. It is therefore also very useful to employ Ta (or W) (- based alloys) as a material for the milling container and/or its surface layer of a defined (eg/. sputtered thickness) (eg. 5 nm to several millimeter, eg. 5 mm using PVD-, CVD and plating techniques) as well as for the milling projectiles / bodies (balls, bars etc.) and their surface layer of a defined thickness (eg. 1 nm to eg. 20% of corresponding overall cross-section).
- 1.2 inert gas atmosphere such as argon to protect the liquid at highest possible atmospheric pressure to minimize losses o the melt due to evaporation. Note that the use of a flux endangers contamination of the melt with Na, K, Cl etc.

2. Vapour Deposition using Thermal Evaporation Methods

Thermal evaporation of pure Mg-feedstock represents effectively a co-evaporation situation with respect to the involved impurities such as Fe, Ni, Cu, Si etc. which - due to their distinctively different vapour pressures compared to Mg - are overproportionally retained either in the liquid Mg-bath or the solid feedstock following the law by Hertz-Knudsen:

$$\begin{aligned}\Delta\Gamma^{[mol]} &= \Delta(dN_v/A_v dt) \\ &= (2\pi mk_B T)^{-1/2} (\Delta p^* - p) \alpha_v\end{aligned}$$

where dN_v = number of evaporated atoms per unit time, A_v = amount of evaporated surface employed, p^* = saturation pressure of the element concerned, p = (static) pressure at

evaporation surface, k_B = Boltzmann's constant and α_v = evaporation coefficient which depends upon surface conditions and which are depending on T and P in turn. The distillation effect does not replace the need to use Ta (-based) materials and/or coatings for the crucibles to protect the (molten) Mg-feedstock (eg. as a Mg-bath) against Fe-contamination. Certain trace elements of the Mg-feedstock such as Na, K and Ca will be co-evaporated without (essential) distillation effect. Their impurity level has to be minimized in the very first Mg-feedstock employed. Others such as oxygen and carbon are easily introduced upon thermal evaporation and/or sputtering due to the risk to absorb oxygen and/or carbon as a result of the fact that with evaporation a fragmentation level on a mono-atomic length scale so the highest surface-to-volume ratio of matter in nature is attained. Already the fabrication of Mg-Ca based casting alloys had led to to a combination of 0.0021 to 0.0236 wt.%C due to the affinity of Ca with atmospheric carbon resulting in Ca-carbides at surface and in the bulk of corresponding slabs [73].

The further Mg-alloy development may relax the conditions on the critical level of critical impurities in magnesium feed-stock, but it does not make the requirements on Mg-alloy purity redundant, since the majority of atoms in possible contact with the impurity atoms remains Mg-atoms. One of the prime objectives of micro-alloying by *conventional* processing is micro-structural refinement to increasing strength, thermal stability of strength and deformability as well as to reduce micro-shrinkage of corresponding Mg-alloys. Many elements considered (cf. [74, 75]) for microalloying, however, are low melting point trace elements with the potential effect to recontaminate the recently established high purity ingot Mg-alloys by formation of microgalvanically active second phases. Moreover, micro-alloyed constituents have a tendency to be re-distributed on grain boundaries when processed by conventional casting methods as a result of partition coefficients below unity.

It was possible to improve the corrosion behaviour of Mg-Al-Zn-base alloys instead by micro-structural refinement down to the degree that was achieved by impurity reduction of Fe, Ni and Cu in ingot processed Mg-Al-Zn-based alloys, but without the need to recur to high purity standards. From earlier work it is known [7,12, 13] that microstructural scale including porosity, grain size and size of second phases as well as choice of higher order additons for resultant type of solid state precipitates are crucial to improve the corrosion resistance of an advanced Mg-alloy. Cotton and Jones, for example, reported [76,77] one to two orders of magnitude lower corrosion rates of RS Mg-15 wt.% Al splats over I/M AZ91 as a function of Fe-impurities and explained their results on the basis of (i) matrix ennoblement with Al (cf. Fig. 68) and (ii) a reduced rate of proton discharge around the refined Fe-inclusions. While conventional micro-alloying increases the susceptibility of high purity Mg-alloys to corrosion, RSP increases damage tolerance of non-high purity Mg alloys and would improve the corrosion resistance of high purity Mg alloys even further.

Under compressive loading and under tensile loading at hydrostatic pressures (HP) of 230 to 700 MPa RS AZ91 was found [78] to show macroscopic and localized shear bands without premature grain boundary fracture nor with any evidence by TEM of twinning. Grains were of size $1.2 \pm 0.5 \mu\text{m}$ being decorated by $\text{Mg}_{17}\text{Al}_{12}$ -particles of size $0.1 - 0.3 \mu\text{m}$. I/M AZ91 of grain size $8 - 15 \mu\text{m}$, however, showed ample evidence of twinning under such conditions. The observed shape change and resulting microscopic strain of the $1 \mu\text{m}$ -grains were smaller than the imposed macroscopic strain. At room temperature using a strain rate $\dot{\epsilon} = 10^{-4}$ [78], true (engineering) strain to fracture of RS AZ91 increased from 0.1 (10.5%) (for HP = 0 MPa) to up to 1.6 (400%) (for HP = 700 MPa). Grain *refinement* down to about $1 \mu\text{m}$ was therefore considered to activate new deformation mechanisms allowing for grain boundary sliding and new flow processes at ambient temperature so substantially improving *ductility* of wrought Mg-alloys. Not only that these results confirm the ductility transition in the grain size regime of $5 - 10 \mu\text{m}$ (Fig. 69) as was shown by Emley [50] in 1966 for pure Mg (see below.) and which is relatively independent on composition and alloy system. The results also suggest that such grain refinement is difficult to be achieved without recurs to the techniques according to the invention.

Microstructural refinement by rapid solidification method down to $< 1 \mu\text{m}$ does not only result in more effective grain refinement than micro-alloying by conventional means ($10 - 30 \mu\text{m}$, cf. Figs. 66 and 67). Obviously, it also embraces the advantage of higher chemical homogeneity so avoiding undesirable and unpredictable microgalvanic and other detrimental effects than those introduced by conventional micro-alloying. This is particular relevant for non-equilibrium Mg- and Al-based alloys eventually consisting of a high grain boundary and/or dislocation density in which impurities (such as by micro-alloying) may act as nuclei to trigger natural ageing via GP-zones and other second phases (cf. above). The employed feed-stock therefore allows to discriminate beneficial from detrimental alloying and microstructural effects upon corrosion behaviour and/or damage tolerance of non-equilibrium Mg- and Al-alloys so to surpass in the usual conclusion that the anode-to-cathodic surface area controls the observed results (cf. [11] and "Hierarchy of Relevant Criteria ", below).

The combined effect of impurity reduction and microstructural refinement should therefore render Mg- heavy rare earth metal alloys to candidates for a superior alternative to current established Mg-alloys for more demanding applications by replacing the thermally less stable Al and Zn in Mg-Al-base alloys including the rapidly solidified magnesium alloy EA55RS. This particular alloy development should allow for more corrosion resistant magnesium engineering alloys by casting routes so superceding current development for corrosion resistant cast and wrought magnesium alloys. The alloy compositions and the treatments for transforming such alloys into products where corrosion resistance and the stability and transformation behaviour of the metastable state is of prime concern have yet not been explored. This concerns wrought products and thin-walled castings with a fine grain size and which are suitable for low temperature applications.

One of the consequences is that microstructural refinement is essential for advanced Mg-alloys processed via condensed matter for demanding aeronautical applications in order to provide satisfying damage tolerance. Apart from alloy compositions the following parameters are essential, i.e. grain size, size of precipitates and dispersoids, the degree of purity and the size of impurities and/or impurity phases. The combined effect of impurity control and/or reduction and microstructural refinement allows for superior corrosion resistance via condensed matter processing and in particular via thermal evaporation methods. Once a productive thermal evaporation process is established, vapour - deposited Mg-feedstock can be used for mechanical alloying without undermining economical viability of the final product.

Table 1 Purity of Primary Mg Feedstock and AZ91 Reference Alloy

Part 1: Primary Magnesium Ingot / Chemical composition in wt. %

	<u>ASTM 9980A</u>	<u>Mg-1</u>	<u>Mg-2</u>	<u>Mg-3</u>
Aluminium, Max.				0.003%
Copper, Max.	0.02%	0.02%	0.02%	0.004%
Iron, Max.			<u>0.05%</u>	<u>0.04%</u>
Lead, Max.	0.01%	0.01%	0.01%	0.005%
Manganese, Max.	0.10%	0.10%	0.01%	0.006%
Nickel, Max.	0.001%	0.001%	0.001%	0.001%
Silicon, Max.				0.005%
Tin, Max.	0.01%	0.01%	0.01%	0.005%
Calcium, Max.		0.0015%	0.0015%	0.0015%
Sodium, Max.		0.003%	0.003%	0.003%
Boron, Max.				0.00007%
Other Impurities each Max.	0.05%	0.05%	0.05%	0.01%
Magnesium by Diff., Min.	99.80%	99.80%	<u>99.90%</u>	<u>99.90%</u> !
Comments		Same As ASTM 9980A	Low Mn	Low Mn and Al

Table 1 / Part 2 Chemical Specifications for AZ91 Casting Alloys

Alloy	Cu %max	Ni %max	Fe %max	Mn %min	Designation
AZ91 A	0,10	0,03	(0,3)*	0,13	ASTM Die Cast
AZ91 B	0,35	0,03	(0,3)*	0,13	ASTM Die Cast
AZ91 C	0,10	0,01	(0,3)*	0,13	ASTM Gravity Cast
AZ91 D	0,015	0,001	0,004	0,17	ASTM HP Die Cast
AZ91 E	0,015	0,001	0,005	0,17	ASTM HP Gravity Cast

* No max. Fe is specified; included in others

Table 1 / Part 3 Annual Corrosion Rates of AZ91 as a Function of Impurity Content

Alloy	Cu % max	Ni % max	Fe % max	Mn % min	Corrosion Rate (mils/y)
AZ91D	0,015	0,001	0,004	0,17	25
AZ91X *	0,003	0,001	0,004	0,17	12
AZ91SX *	0,0024	0,0010	0,0024	0,17	5
AZ91UX*	0,0010	0,0010	0,0015	0,17	3

* Timminco Metals generic designation.

Hall-Petch Strengthening of High Performance Light Alloys

If intragranular grain boundary failure was suppressed via grain refinement, localized shear at stresses of the order of theoretical shear strength were considered [78] to become the limiting strengthening mechanism. The compressive stress to fracture of RS AZ91 was found to amount to 650 to 750 MPa at $T = 77 - 273$ K and a strain rate $\dot{\epsilon}$ of $0.1 \times 10^{-3} \text{ s}^{-1}$. At room temperature using a strain rate $\dot{\epsilon} = 10^{-4}$ [78], tensile stress to fracture of RS AZ91 increased from 400 MPa (for HP = 0 MPa) to up to > 900 MPa (for HP = 700 MPa), the latter corresponding to a value of $E/70$. The validity of such postulations can be examined by the response of the Hall-Petch proportionality constant k_y on grain refinement. Pechiney established [79] a Hall-Petch-type of relationship for yield strength TYS of the unmodified RS AZ91 composition as a function of grain size d following

$$\text{TYS} = \sigma_0 + k_y \cdot d^{-1/2}$$

with $\sigma_0 = 130$ MPa and locking coefficient $k_y = 210 \text{ MPa mm}^{0.5}$. Jones suggested [80] that the TYS-data for Si- and RE-containing RS Mg-Al-Zn based alloys developed by Allied Signal are in agreement with these values by Pechiney. In fact, the values by Allied indicated somewhat higher σ_0 and k_y - values (see Figs. 66 to 72). Evidently, Si and RE act not only as the often quoted (cf. [81]) microstructural stabilizers via formation of T-stable dispersoids to pin the motion of dislocation and grain boundaries upon consolidation of pulverized ribbons, flakes and droplets, but also as nucleants and catalysts for more effective grain refinement itself during both solidification and/or consolidation. The first and basic effect of such additions is thus to increase the *boundary* strengthening effect afforded by grain refinement upon the entire processing route cf. those alloys without such additions.

Already as long as twenty years ago, Isserow and Rizzitano reported [82] on the effect on grain refinement of RS as one of the dominant factors to improve strength of ZK 60 alloy by "micro-quenching". Corresponding k_y -value was in the regime of that reported by Pechiney, while corresponding intercept σ_0 , however, appeared to be significantly higher than for

Mg-Al-Zn alloys (Figs. 66,67). A k_y -value of $185 \text{ MPa } \mu\text{m}^{0.5}$ is evident from the literature on Mg-alloy QE22 (cf. [83]). Meschter reported [84] a strength increment of 68 MPa for solution treated RS Mg-10.9 Al over ingot processed Mg-9 Al (wt.%) which was consistent with the grain size reduction from about 100 to $11 \mu\text{m}$ (i.e. factor 10) assuming an Hall-Petch factor k_y of $337 \text{ MPa } \mu\text{m}^{0.5}$. While the k_y -values for the above precipitation-hardened Mg-Al-Zn-based and ZK60 alloys are significantly lower compared to pure Mg ($280 \text{ MPa } \mu\text{m}^{0.5}$, see Figs. 66 and 67) [85], the value for the monophase Mg-Al alloy is above that for pure Mg and conventional Mg alloys, i.e. $280 \text{ MPa } \mu\text{m}^{0.5}$ [86]. The data Meschter reported [84] for multiphase RS Mg - 13Al - 1.2Si alloy are in excellent agreement with the values for binary Mg - 10Al alloys as corresponding extrapolation to smaller grain sizes shows (Figs. 66,67). Finally, the reported data for Mg-Li based alloys result in $100 \text{ MPa } \mu\text{m}^{0.5}$ for the $(\alpha+\beta)$ -Mg-9 wt.% Li base alloys by Meschter and O'Neal [87,88] and in $58 \text{ MPa } \mu\text{m}^{0.5}$ for the bcc- β Mg -40Li - 2H (at.%) by Haferkamp et al. [89] (Figs. 66,67). These are the lowest k_y -data yet observed for an Mg-alloy resulting in softer alloys than pure Mg for a grain sizes below 40 to $50 \mu\text{m}$.

Mechanical Particulars: Mg vs. Al

Mg has attracted much attention to study the nature of ideal metallic or free electron bonding [90]. The free $3s^2$ valence electron structure excludes pure Mg per se from any covalent bonding phenomena resulting in the lowest average valence electron binding energies and the weakest interatomic cohesion of a structural metal [91]. The additional covalent $3p^1$ - bond of pure Al develops larger moduli of elasticity E (71 GPa) and of shear K (26 GPa) and a larger *specific* modulus of elasticity E/ρ (27 GPa cm^3/g) compared to Mg ($E = 45 \text{ GPa}$, $K = 17 \text{ GPa}$, $E/\rho = 25 \text{ GPa } \text{cm}^3/\text{g}$) [85]. The operative slip distance in Mg is as for Al, but the operative slip normal (that is the perpendicular distance between two adjacent slip planes) is about four times longer. Both the theoretical and the operative Peierls-Nabarro stress on the close-packed (0001)-plane of pure Mg are thus orders of magnitude lower than on the (111)-planes of pure Al. *Perfect* lattice dislocations in pure Mg and conventional Mg-alloys would have therefore a relatively *wide* strain field and a much *higher* mobility than in pure Al and Al-alloys. Despite of this higher mobility, however, pure Mg is moderately *harder* than pure Al resulting in 40 over 15 Brinell Hardness Numbers BHN [92] and a Hall-Petch coefficient k_y of $280 \text{ MPa } \mu\text{m}^{1/2}$ which is four times *larger* cf. that of pure Al ($68 \text{ MPa } \mu\text{m}^{1/2}$) [93].

Below 498 K, plastic deformation of polycrystalline cph-Mg is *limited* to basal (0,0,0,1) $\langle 1,1,-2,0 \rangle$ slip and to pyramidal (1,0,-1,2) $\langle 1,0,-1,1 \rangle$ twinning [50] (Fig. 70). The Mg-crystal has thus only 3 geometrical and 2 independent slip systems, while the Al-crystal has 12 (1,1,1) $\langle 1,-1,0 \rangle$ geometrical and 5 independent slip systems for general shape change [94]. The maximum (polycrystal: mean) value of ($\cos \phi \cos \lambda$) between slip orientation and tensile axis of Mg is therefore smaller than corresponding value for Al. Following Schmid's law ($\sigma_y = \tau_{\text{crss}}/(\cos \phi \cos \lambda)$) shows that the relatively low ($\cos \phi \cos \lambda$)-value is one reason (see above)

for the larger hardness number and Hall-Petch coefficient of Mg cf. Al, but it is also one reason why polycrystalline Mg and its alloys do not develop macroscopic yielding and, instead, large stress concentrations at grain boundaries. Pure Mg and conventionally cast Mg-alloys thus present a tendency to embrittlement due to intergranular failure, but also localized transcrystalline fracture either along twinned regions in particular upon compression or along basal (0001) planes for very large grains [50]. Prismatic $(1,0,-1,0)<1,1,-2,0>$ slip planes are not active in pure Mg (Fig. 70). The addition of Li and In can activate such slip planes by using conventional casting methods [95 - 97]. Activation of prismatic $(1,0,-1,0)<1,1,-2,0>$ slip renders Mg-alloys more ductile at lower temperatures without the need to recur to the required grain refinement as is affordable by rapid solidification. Unfortunately, however, such conventional alloys are associated with extremely low solid solution and cold hardening response as well as with poor corrosion resistance despite of their large solid solubility and this has already misled and thus frustrated a number of research programmes for different motivations. Unless sufficient grain refinement was introduced to reduce back stresses and to enhance crystalline rotation via grain boundary gliding, however, deformation of *structural Mg alloys* at ambient show *always* a tendency to twinning (see below).

Obviously, *grain refinement* of Mg-alloys embrace a larger potential to improve strength and ductility as compared to Al-alloys and an interesting question is why this advantage has yet been left so untouched compared to the advantages of other materials. Furthermore: what degree of grain refinement substitutes for the missing independent slip system? Grain refinement is certainly one of the more important factors for the further development of Mg. The comparison of modulus, operative slip normal vector and resultant Peierls-Nabarro stresses on the one hand with hardness and boundary strengthening capacity on the other indicates quite clearly that the mechanical behaviour of Mg is dictated by preferred *dislocation reactions* as it is for other materials. Such dislocation reactions can take over the control of mechanical properties otherwise dictated by Peierls stresses, for example. If not, grain refinement of Mg would do the reverse and pure Mg would be softer than pure Al without showing better ductility.

Rate - Controlling Dislocation Reaction in cph-Mg

The *scope* of dislocation slip planes in the cph-lattice embraces basal, prismatic and first order pyramidal slip planes with Burgers vector $1/3 \mathbf{a} <1,1,-2,0>$ and first and second order pyramidal systems with Burgers vector $1/3 (\mathbf{c}+\mathbf{a}) <1,1,-2,3>$ (Fig. 70). The $1/3 \mathbf{a} <1,1,-2,0>$ vector is the shortest Burgers vector in the cph-lattice (cf. Fig. 71). The rate controlling mode for plastic deformation is therefore dictated by the lattice friction experienced by the structure of the core of the $1/3 \mathbf{a} <1,1,-2,0>$ screw dislocation. Screw dislocations move slower than edge dislocations, since they are always present on two crystallographic planes and form sessile dislocation jogs upon propagation and intersection with other screws (cf. [98,99]). The structure of the dislocation core tells with certainty whether (i) energy is to be gained upon dissociation of perfect dislocation movements into imperfect or partial dislocation movements which leaves a trace in the translational lattice, i.e. a stacking fault (SF) related to a given slip plane and (ii)

whether *sessile* SF-components are involved. The *operative* slip mode of cph-metals is confined *either* to the basal plane (simple metals like Mg and Be) *or* to the prismatic plane (transition metals, see Table 2). The *c/a*-ratio does not control activation of prismatic slip as misleading literature tells (cf. Table 2). Any comparison of the mechanical properties of Mg-based alloys has therefore to be made on the basis of the structure of the core of the $1/3 \mathbf{a} < 1,1,-2,0 >$ screw dislocation.

The basal dissociation of the $1/3 \mathbf{a} < 1,1,-2,0 >$ screw dislocation (Fig. 70) follows [100,101]:

$$1/3 \mathbf{a} < 1,1,-2,0 > \quad \text{---} \rightarrow \quad 1/6 \mathbf{a} < 1,0,-1,0 > + 1/6 \mathbf{a} < 0,1,-1,0 >$$

and corresponds to a SF-energy γ_h of the order of 10 mJ m^{-2} (cf. [102]). The prismatic SF-energy γ_p is about seven times larger underlying that no cross-slip occurs at ambient (see above.). For comparison, the SF-energy γ_{111} of unalloyed Al is even larger (eg. 200 mJ m^{-2} , cf. [103]). The low basal stacking fault energy thus results (i) in a low number of operative slip modes, but it also allows for a larger dissociation of the rate-controlling $1/3 \mathbf{a} < 1,1,-2,0 >$ basal screw than the corresponding screw in pure Al. The dissociated basal screw is a moderately harder transcrystalline obstacle for the motion of further dislocations allowing to pile-up more dislocations in pure Mg than in an hypothetical Al-crystal without activated cross-slip. This is the second factor contributing to the moderately higher values of hardness and k_y and to intergranular embrittlement of *pure* Mg, though Peierls stresses are much lower than in *pure* Al. The cold working capacity of pure Mg is thus slightly better than that of *pure* Al. For reasons of crystal symmetry it was postulated [102], however, that any further dissociation such as by intersection with other dissociated dislocations cannot introduce sessile edge components into the basal plane. Basal stacking faults might always be *glissile* as is evidenced by the relatively low work hardening response of Mg-alloys compared to Al-alloys.

Effect of Grain Size and Thermal Activation on Deformation Modes

Mg shows a marked ductility transition when twin formation is suppressed by grain refinement and by *pyramidal* $(1,0,-1,1) < 1,1,-2,0 >$ slip at temperatures at around 225°C (Fig. 69) [50]. Twinning is an athermal shear deformation process involving mirrored movement of several thus reduce the large Peierls stresses associated with the large $1/3 (\mathbf{c}+\mathbf{a}) < 1,1,-2,3 >$ Burgers vector (Fig. 70). Any increase in the susceptibility to thermal activation would therefore render *slip* deformation modes more competitive and would decrease the likelihood of twinning. There are three factors to increase the susceptibility to thermal activation of slip: (i) grain refinement reducing boundary back stresses so allowing easier accommodation of a) the overlap or void displacement between two adjacent grains (i.e. grain boundary sliding and/or rotation) as well as of b) the transcrystalline twinned volume, (ii) alloying elements with low melting points such as Li and (iii) increasing the temperature itself. It is thus kind of an adventure to attribute the enhanced deformability of Mg-Li alloys to twinning [104]. By

contrast, twinning is frequently observed at high deformation rates such as under cyclic loading of conventionally processed Mg-Al based alloys [105]. Grain refinement of such alloys then results in significantly improved resistance to fatigue (cf. [105]).

Grain refinement below a grain size of 8 μm of pure Mg reduces the ductility transition down to room temperature (Fig. 69). The critical resolved shear stress for pyramidal slip in Mg was found [106] to peak at around 100°C then followed by decreasing pyramidal crss towards higher temperatures. Alloying with Al and Zn slightly reduces the brittle-to-ductile transition temperature (eg. AZM with peak at 212°C) [50]. When both suitable alloying and grain size refinement come together, however, Mg alloys such as RS AZ 91 with a grain size of about 1 μm become superplastic even at room temperature (i.e. > 1000%) [78]. Novel micro-grained Mg-alloy compositions obtained by rapid solidification contain more T-stable dispersions impeding grain boundary sliding processes at lower temperatures. Their grain size is between 0.1 and 1 μm and they show a 400% superplasticity at around 548 - 573 K [107] which is better than for any of the other light alloys.

Prismatic or Basal Slip? The Activation Issue for Polycrystalline Mg

The alternative and/or complementary method to enhance the deformability of Mg-alloys by non-equilibrium techniques is to trigger prismatic slip in the (eg.) cph-Mg-matrix (super-) saturated with selected elements. Prismatic slip in polycrystalline pure Mg has been observed at very low temperatures between -4°C and -195°C and at 260°C [50, p. 486/7]. At temperatures around ambient prismatic slip was only evident in single crystals of pure Mg under preferred orientations of loading to avoid basal slip [108]. By contrast, conventional cast Mg-Li and Mg-In alloys show high room temperature ductility due to activation of prismatic slip. Mg-Li alloys show a decreasing axial ratio c/a with increasing Li-content, but Mg-In alloys do not [95 to 97]. Be has the lowest axial ratio of all cph-metals (see Table 2), but it deforms by basal slip as Mg and does not exhibit any prismatic slip at room temperature in polycrystalline form [108 to 110]. There is no point to believe that a simple metal like Be or the addition of a simple metal like Li to Mg enhances prismatic slip and deformability because of a lower c/a-ratio. Obviously, the geometrical ratio c/a is a phenomenon that correlates with slip activity for a given cph-metal within certain limits of alloying, but it does not provide any interpretation for the activation of prismatic slip and better deformability at all. However, the c/a-ratio it is a widespread concept to mislead alloy selection and design criteria (cf. [104]).

Legrand has shown [109] the consequences of orbit anisotropy on the $1/3 \text{ a} <1,1,-2,0>$ core structure and the resultant principal glide mode. The principal slip plane of simple cph-metals like divalent Be, Mg, Zn and Cd is the closed packed basal plane due to the isotropy of corresponding valence electron structure. Easy prismatic slip is only evident for transition metals and yttrium so for rare earth metals (Table 2). The anisotropy of d-orbits is essential for activation of prismatic slip and it increases with decreasing degree of (filled) d-band states, Z suggesting

Table 2 Glide Systems and Particulars of Close-Packed Hexagonal (cph) Metals.
After Legrand (1984) [109].

cph-Element	Principal Glide Mode ¹⁾	Secondary Glide Mode ¹⁾	Value $R^{2)}$	γ_{\min} [mJ/m ²] ³⁾ and γ_p/γ_b	Axial Ratio c/a
Cd	B	Π_1, Π_2, P	0.2	15 / 10.0	1.886
Co	B	Π_2	0.2	45 / 5.1	1.624
Zn	B	Π_2, P	0.25	35 / 6.0	1.856
Mg	B	Π_2, P	0.25	30 / 4.2	1.624
Be	B	P, Π_2	0.6	390 / 1.6	1.568
Re	B/P	-	0.9	540 / 1.1	1.615
Tc	-	-	1	440 / 0.94	-
Tl	B/P	-	-	-	1.598
Ru	P	-	1.7	520 / 0.59	1.582
Os	-	-	1.8	600 / 0.57	-
Hf	P	B, Π_2	2.1	185 / 0.47	1.581
Zr	P	Π_1, B, Π_2	2.3	150 / 0.44	1.593
Ti	P	Π_1, B, Π_2	2.6	110 / 0.38	1.588
Y	P	B	3.5	60 / 0.29	1.571

¹⁾ B = basal plane; P = prismatic plane; Π_1 and Π_2 are first and second order pyramidal planes. respectively.

²⁾ $R = (C_{66} * \gamma_b / C_{44} * \gamma_p)$, where C_{ij} elasticity constants with C_{66} not equal C_{44} for departure from ideal close packing and γ_b and γ_p are stacking fault energies in the basal and prismatic plane. respectively.

³⁾ If principal slip mode B, then $\gamma_{\min} = \gamma_b$, otherwise $\gamma_{\min} = \gamma_p$.

that also f-orbits affect prismatic slip. The anisotropy results in two maxima in γ_b (TM) for Z of about 2 and 7 and in two minima in γ_b (TM) for Z of about 4 and 9 (Fig. 73). Corresponding γ_p (TM)-values, however, are relatively constant (Fig. 73). The tendency for prismatic slip thus increases with decreasing ratio γ_b / γ_p (Table 2). Incorporation of the ratio of the elasticity constants C_{66} and C_{44} completes the classification of cph-slip modes following:

$$R = (C_{66} * \gamma_b / C_{44} * \gamma_p)$$

(Table 2). The R-parameter is the only yet reported parameter to give a consistent interpretation of the principal, i.e. active slip mode in hexagonal materials. R is always < 1 for divalent metals with operative basal slip, while it is > 1 for transition metals for which prismatic slip is the principal mode of deformation (Table 2). R is (near) 1, however, when both basal and prismatic modes are active such as for Re. Re is in fact the most ductile cph-metal despite of its high Young's modulus and resultant high melting point while Be is not.

From Table 2 it is evident that early transition metals, yttrium (so also "early" (= light) rare earth metals) provide the electronic structure to induce prismatic slip in Mg via major so non-equilibrium alloying (eg. via the role of mixtures or deviation from it to reduce the R-value of (cph-) Mg, the effect of the electronic structure on the ne-Mg-based matrix thereby being assured by the homogeneous distribution of the d-band early transition and early rare earth metals on an atomic length scale. This was confirmed by the PA-splats supersaturated with yttrium and rare earth metals which were very ductile on bending while those with Ca (made under same conditions also decreasing c/a in supersaturated Mg, see [6,12]) were very brittle. That is, the elements enhancing passivation of Mg by alloying (see below) correspond to those elements useful to induce prismatic slip into Mg of cph-crystal structure or of a variant.

Alloy selection for superior VD Mg-base Higher Order Alloys with a Passive cph and/or Non-equilibrium metastable One-Phase or Nearly One-Phase Matrix Self-healing in Air and Other Environments

Any hardening of the extended solid solutions of (light) rare earth metals in cph-Mg and/or in any other metastable Mg-rich Mg-(light) RE matrix phase with either random, ordered or quasi-ordered distribution of the (light) RE atoms by second phase dispersions has to satisfy the following conditions:

1. the second phase dispersion must not destroy the self-healing passivating capacity of the surface oxide;
2. the nucleation and growth of second phases should therefore be controlled by solid state precipitation;
3. such solid state precipitates must form at distinctively lower temperatures than the temperatures at which corresponding metastable Mg-rich Mg-(light) RE phase transform into corresponding equilibrium phases. These limiting-type of temperatures were identified to be

- at around 300° to 360°C depending primarily on alloy synthesis employed (see above);
4. these precipitates should be essentially inert with the metastable Mg-rich Mg-(light) RE matrix phase from the electro-chemical point of view.

Two families of ternary additions distributed in a random, ordered or quasi-ordered way on the atomic length scale of corresponding metastable Mg-rich Mg-(light) RE matrix phases are selected here as the base for reinforcement at temperatures in the projected regime for alloy conversion without harmfully affecting the passivating film capacity of the claimed alloys.

Minor additions of simple and transition metals and metalloids

One base ternary addition for the formation of the required reinforcement is aluminium. Aluminium was reported to form galvanically inert aluminides with the (light) RE metals and alkaline earth (AE) metals [112]. Their inertness is believed to origin in either suitable electro-chemical potentials or in favourable surface film formation on Al_xRE_y and Al_xAE_y -type of aluminides when co-exposed with the magnesium matrix to atmospheric conditions (cf. [112]). Nussbaum et al. [113] reported on the most corrosion and likewise heat resistant RS-Mg-Al-Zn based alloy by adding up to 6.5 %Ca resulting in a fine dispersion of Al_2Ca of size 0.05 μm . The formation of such aluminides does not adversely affect the corrosion resistance of magnesium alloys. Hehmann et al. have shown [114] that the addition of Ca can increase the corrosion resistance in other alloy systems such as in Mg-Cu-Ca alloys most probably due to a reduction in cathodic area. Das et al. [115] and Hehmann [7] demonstrated that the addition of the rare earth elements Ce, Nd, Pr etc. to RS Mg-Al-Zn-based alloys did not degrade the corrosion resistance compared to RS Mg-Al-Zn-based alloys without such additions, since the resultant dispersions of fine Mg_xRE_y and/or Al_xRE_y phases were found to be micro-galvanically essentially inert with the cph-Mg-matrix. The alloys claimed herein are based on an reciprocal alloying strategy with regard to the RS Mg-Al-Zn-based alloys containing rare earth elements such as Ce, Nd, Pr, i.e. using light (or early) rare earth and transition metals (see below) as the major alloying element and adding Al, Ga etc. for pptn.-hardening instread.

In RS Mg-Al-Zn-based alloys, aluminium is the major solid solution hardening element of an otherwise non-passive overall Mg-alloy matrix, while the minor rare earth additions are primarily used for the formation of fine second phase dispersions to stabilize the refined matrix by delineating cell and grain boundaries upon alloy conversion and to increme the resultant strength at room temperature. The basis of this is that Al has a relatively large equilibrium solid solubility of 12 at.% in cph-Mg [49] and that the applied conditions of RSP are not sufficient to achieve a microstructure essentially consisting of an extended solid solution of the alloying additions in the cph-Mg matrix and which is essentially free of microsegregations.

In the claimed alloys, however, the (light) rare earth additions are only or primarily used as solid solution alloying elements to passivate and to strengthen the magnesium alloy matrix,

while the aluminium (and alkaline earth and the other minor higher order additions, see below) are primarily used for the formation of a (compared to more recent RSP light alloys) relatively moderate volume fraction of thermally stable solid state precipitates to improve the mechanical properties. In the claimed alloys, aluminium, alkaline earth and the other minor higher order additions provide an ideal instrument to reinforce the supersaturated solid solution of (light) RE metals in cph-Mg with the resulting second phase dispersion independent on grain size and the rate controlling plastic deformation mechanism concerned (see above).

The rare earth or alkaline earth aluminides provide also a useful alloying route for improved properties at elevated temperatures. Aluminides are thermally very stable leading to reduced stress relaxation at elevated temperatures and and to improved resistance to secondary creep when finely distributed in the alloyed Mg-matrix. Nussbaum and co-workers reported [116,117] on a more detailed analysis of high temperature properties of RS and ingot processed AZ91 alloy. Under given conditions, both variants did not show any grain growth suggesting that creep controls the high temperature properties of AZ91. Under an applied stress of 50 MPa at 150°C, the RS-version (grain size: 1.5 μm) showed a 100fold higher secondary creep rate and an 150% higher stress relaxation compared to conventional AZ91 (grain size 12 μm).

The addition of 2.3 wt.% Ca to RS AZ91 showed the prime significance for high temperature properties of the combined effect of the overall microstructure *and* composition of Mg-alloys relative to the employed grain size alone: although RS AZ91 + 2.3 Ca had the smallest grain size (i.e. 0.6 μm) of the three variants so structurally providing the largest concentration of internal surface area or easy-diffusion paths, its secondary creep rate was 400 times smaller than for RS AZ91 and 5 times smaller than for ingot processed AZ91 [116,117]. Stress relaxation for 100 hrs at 150°C was improved by 20% compared to ingot processed AZ91. The fine dispersion of Al_2Ca of mean size 0.05 μm was observed both in trans- and in intragranular areas. The fine size rendered the Al_2Ca -phase therefore instrumental to pin the motion of dislocations and grain boundaries so suppressing both creep and grain boundary sliding even in the presence of relatively temperature-unstable $\text{Mg}_{17}\text{Al}_{12}$ -phases. Relatively high *initial* stress relaxation rates in both RS-versions indicated grain boundary sliding to control the *begin* of high temperature deformation before transgranular creep appeared to take over the rate-controlling mechanism. That is, that the otherwise diffusion controlled properties of the claimed alloys can be improved by a suitable size of corresponding aluminide and/or simple metal containing dispersion.

The feasibility of this higher order alloying approach, i.e. the reinforcement of passive Mg-(light) RE based alloys with simple metal additions while the RE metal is essentially held in solid solution is largely supported by the transformation behaviour of the extended solid solutions of corresponding elements such as Al and Ca in cph-Mg upon DSC-analysis. The transformation behaviour of binary alloys is a valid reference for corresponding behaviour in

more complex alloys, since diffusion is the rate-controlling material parameter for the transformation process. Diffusion, however, is a local and kinetic microscopic process independent on macroscopic thermodynamic properties.

Hehmann reported [118] that the (extended) solid solution of 9 to 23 at.% Al in cph-Mg is thermally relatively unstable leading to the formation of corresponding equilibrium phases at temperatures between 120° and 180°C, i.e. at some 200°C lower temperatures than equilibrium phases would form from the extended solid solution of (light) RE elements in cph-Mg. This result was consistent with the observation in AZ91 (which is essentially a quaternary Mg-Al-Zn-Mn alloy) that creep strength increased with decreasing Al-content and resulting decrease of volume fraction of the relatively coarse (i.e. 0.5 µm-) $Mg_{17}Al_{12}$ -grain boundary precipitates for a given grain size [116,117]. Obviously, such particles are too large to pin the motion of dislocations and grain boundaries and increase the mobility of grain boundaries instead due to their low melting point.

P. Vostry et al. reported [119] on the transformation of the extended solid solution of 1, 3 and 10 wt.% Ca cph-Mg to occur at temperatures T_{transf} at between 160°C (for 1Ca) and 120°C (for 10 Ca). These observations confirm the feasibility of the formation of fine Al_2Ca -type of precipitates from the extended solid solution of (light) RE element(s), Al and alkaline earth elements such as Ca in cph-Mg at temperatures where the passivity of cph-Mg due to the dissolved (light) RE metals remains unaffected by corresponding precipitation. The resultant precipitates may or may not incorporate further elements such as Mg and RE after the formula $(Al_aMg_b)_x(AE_cRE_d)_y$ and where suffix a, b, c, d, x, and y are stoichiometric variables (see [120] by Zarechnyuk and Kripyakevich who reported on $Al_2(Ce,Mg)$ in the cph-Mg matrix). The advantage of such (complicated) compositions of solid state precipitates with regard to the need of microgalvanically inert second phase dispersions in passive cph-magnesium base alloys is that they provide a tailorable "buffering" effect. This "buffering" effect can be estimated in a first approach via the rule of mixtures applied to the galvanic potentials of the involved components.

The feasibility of precipitation of more complex aluminides in Mg-alloys is also supported by the existence of more complex silicides such as Mg_2CeSi_2 (cf. [121]). Silicides play a major role in conjunction with transition metals in advanced aluminium (see below). Borides provide similar opportunities with the advantage of even lower density compared to silicides of same stoichiometry (cf. [123]). The affinity of elements and the resultant thermal stability of equilibrium phase dispersions is in fact decoupled from corresponding atomistic mobility (diffusion) in solid solution so from the thermal stability of corresponding extended solid solutions. Otherwise would the major transformation process of Ti in cph-Mg, for example, start at higher temperatures than that of Ce in cph-Mg etc., while aluminides such as Al_2Ca solid state precipitates could not be a thermally stable phase in an Mg-alloy matrix. The

inventions, however, show the reverse.

Other minor quantities are zirconium and manganese to be added as quaternary additions to the extended solid solution(s) of (light) RE metals or (light) RE-based misch-metals (MM) in conjunction with ternary aluminium in cph-Mg. In their classical paper Busk and Leontis reported [124] that these alloying additions were instrumental to suppress the tendency to stress corrosion cracking and to improve extrudability of AZ-type of alloys via co-extrusion of blends of suitable prealloyed atomized powders rather than ingot. This was related to solid-state inter-diffusion which resulted in "interference hardening" by the precipitation of finely dispersed, insoluble Al_3Zr - and/or Al_xMn_y - type of compounds leading to the best thermal stability and strength improvements of up to 430 MPa reported in the 1950s as well as to applications such as support beams used for floor or built-in loading ramps of the C 133-transport plane involving 40% increase in compressive yield strength, for example.

Zinc was reported [125] to be embedded in Mg-RE-precipitates decorating the grain boundaries of Mg- alloy ZE63 with 5.3 Zn, 2.5 RE-mischmetall (MM) and 0.7 Zr (all in [wt.%]). This alloy shows better resistance to secondary creep at 150°C than AZ91 and ZE41 T5, for example, due the absence of any low melting point second phases on the grain boundaries. Minor zinc additions may therefore be considered to trigger preferential grain boundary precipitation from the extended solid solution of (light) RE metals in cph-Mg without disintegration of corresponding supersaturation beyond the level of RE-additions required to complete volume fraction and stoichiometry of corresponding Mg-RE-Zn-precipitation.

The amount of aluminium and alkaline earth elements (required to reinforce the claimed alloys by the aforementioned solid state precipitates including RE- and AE- aluminides and corresponding silicides or borides) should be kept small to avoid that larger levels of the passivating (light) RE metals in cph-Mg are tight up in such dispersions. Under the maxim that none of these minor additions must unduly degrade the passivating capacity of the extended solid solution of (light) RE-metals in cph-Mg, a rule-of-thumb-formula for the amount of Al (in [at.%]), Al%, claimed herein is $Al\% = k_1 * AE\% + k_2 * xRE\%$ where x = excess fraction RE metal required to complete the volume fraction of precipitates of stoichiometry defined by parameters, k_1 and k_2 . The alloys claimed herein should therefore contain between 0.2 and 10 wt.% aluminium and between 0 and 10 wt.% alkaline earth (AE) metals, preferably 0.5 and 4 wt.% aluminium and between 0.1 and 1.5 wt.% alkaline earth (AE) metals (Ca, Sr, Ba) held essentially in the extended solid solution of (light) RE elements in cph-Mg with a random, ordered or quasi-ordered distribution of the (light) RE atoms and/or the alkaline earth and the aluminium atoms in the as-deposited and/or as-solidified state.

Selection of Rare Earth Metals for Mg-base Higher Order Alloy Compositions

The present invention embraces the potential for a "technology shock" for magnesium based

alloys and products including a universe of new alloying possibilities by selected new methods of processing via synthesis and thermo-mechanical alloy conversion. It is therefore advisable to employ also established commercial alloys and techniques such as mechanical alloying (see below) in order to spur the realization of corresponding processing technologies.

Commercial "E"-type of Mg-alloys

"E" is the ASTM-designation for rare earth additions without yttrium ("W") to Mg-alloys. The commercial alloys claimed for processing by the new continuous production methods selected for extended solid solutions in cph-Mg are as following (including approximate compositions):

Alloying addition Alloy	Al	Zn	Mn	Zr	Y	RE	AE	Ag	Si
WE54				0.45	5.25	3.5 ¹⁾			
WE43				0.4	4	3.5 ²⁾			
ZE63		5.3		0.7		2.5			
ZE41		4.0-4.2		0.7		1.2 - 1.3			
EZ33		2.5		0.6		3			
EZ32		2.2		0.6		2.7			
AE41	3.9	0.01	0.35			0.64			0.1
AE42	3.9	0.02	0.35			1.4			0.1
QE22				0.7		2.1		2.5	
EQ21				0.7		2.1		1.3	

¹⁾ 1.5 -2Nd, 1.5 - 2HRE (heavy rare earth metals, i.e. other yttrics than yttrium)

²⁾ 2-2.5Nd, 0.75-1HRE

Misch-metals

The misch-metals (MM) for structural magnesium alloys often quoted in the literature include "Ce"-misch-metal with approximately 49 Ce, 26 La, 19 Nd, 6 Pr or "Nd"-mischmetal with 80 Nd, 16 Pr, 2Gd and 2 other RE (all in [wt.%)] [39,50] . The use of a specific MM for structural magnesium is primarily dictated by price and availability considerations rather than by engineering properties related to a specific MM-composition. That is why patents for applications of misch-metals in magnesium alloys do usually not refer to the particular composition of the misch-metal to be used in magnesium nor do they specify the precise technological advantage of misch-metals over individual rare earth elements in order to justify the use of MM from an engineering point of view (cf. [17]). From the aforementioned studies and (the present invention it is evident, however, that yttrium (which is a regular member of RE%minerals) should not be used excessively for melt-processed magnesium alloys with the RE metals essentially held in solid solution. The costs for the required feedstock of RE metals

for structural aerospace products based on passive Mg alloys will largely be compensated for by the return to be realized by the application itself.

RE metals are extracted from RE-oxide containing minerals and ores which represent mixtures of the oxide of virtual ly all or the majority of the available RE metals. The most common minerals include the following approximate composition of individual RE metals or RE groups:

RE-content [wt.%]	La	Ce	Nd+Pr	yttrium	other yttrics (HRE)
Ore composite					
Monazite	23	45	24	2.5	4.5
Bastnaesite	32	49	17	2	
Long Wan	3	1.5	5	62.5	28
Xin Fong	19	2	32	25	22
Wan An	8	1.5	8.5	49	33
Xun Wu	30	7	39	9	15
Din Nan	26	3	25	28	18

Selected extraction of preferred RE metals can change the composition of the final MM relative to the composition of the ore used for extraction. One of the cheapest method, however, is the extraction of all or a maximum of RE metals from an abundantly available RE ore without undue numbers of operations due to specific MM-selektion criteria. The use of "light" RE metals for passive magnesium (see "Disclosure") exludes consideration of larger quantities of misch-metals stemming from and/or corresponding to the ore composition of Long Nan - and Wan An-type of RE-ores. Monazite- and Bastnaesite-type of ores are the most abundantly available and currently most used ores for the extraction of RE-metals and MM-metals. MM-metals of compositions stemming from and/or corresponding to the ore composition of Monazite-, Bastnaesite- and Xun Wu-type of RE-ores are therefore the most preferable misch-metals for use in passive magnesium alloys with the MM essentially held in extended solid solution of cph-Mg or corresponding structural derivatives.

Ti and metalloids (Si, B, Sb)

The majority of transition metals and metalloids show very high vapour pressures and this is one reason why they do not or not readily alloy with magnesium via liquid processing. The only solution in this case is mechanical alloying and vapour deposition, the latter with the advantages discussed already on page 9 and on page 15 below. If the alloying of magnesium with high melting transition metals and metalloids is possible via the liquid phase, galvanically active (micro-) segregations may result quite easily and exclude these elements from major additions to passive Mg alloys by processing from the melt.

A combination of essentially monophasic Mg-(light) RE alloys with high melting transition and

metalloid additions via vapour deposition is representative for the fundamental principle of advanced processing: While equilibrium microstructures and properties are dominated by the *physical differences* of individual alloying elements as to the Hume-Rothery rules, non-equilibrium microstructures and properties result from the *cooperative performance* of quite different constituents providing a yet entirely unexplored wealth of innovations.

1. The use of one or more transition metals alone in cph-Mg or the use of TM such as Ti as a ternary addition for precipitation hardening from the extended solid solution of (light) RE elements in cph-Mg with a random, ordered or quasi-ordered, but in any case essentially homogeneous distribution of the light RE and the Ti atoms includes the following disadvantages:

- 1.1. The equilibrium Ti-precipitates in the binary system Mg-Ti were elemental Ti [126] as Mg-precipitates were in Ti-base Ti-Mg alloys [127]. That is that no intermetallic phases form in the equilibrium binary phase diagram Mg-Ti (or Ti-Mg) (a dilemma which applies to other binary Mg-TM phase diagrams such as Mg-Mn) and that a relatively high level of alloying would be necessary to achieve sufficient age hardening response, for example, on either side of the (binary section of the) Mg-Ti phase diagram.
- 1.2. Mg- containing oxides were observed in VD Ti-Mg alloys and this was attributed to the oxygen diffusion in Ti [127] so they will appear especially in high Ti Mg-base Mg-Ti alloys. Oxides, however, are known to degrade the properties of high performance Mg alloys and in particular their damage tolerance [112].

2. The advantages of Ti as a minor alloying addition to the extended solid solution of (light) RE elements in cph-Mg with a random, ordered or quasi-ordered distribution of the light RE and the Ti atoms include the possibility for a deliberately manipulated precipitation route of Ti (-containing) precipitates from cph Mg - (light) RE metastable phases at temperatures around 200°C upon thermo-mechanical alloy conversion, i.e. where Ti is (partially) taken out of the solid solution for precipitation hardening, while the passivating effect of RE-metals in solid solution remains essentially unaffected. since:

- 2.1. Ti forms very stable solid state precipitates of pure Ti once they have formed at around 200°C or so from the extended solid solution in cph-Mg. In VD Mg-17wt.% Ti alloy exposed for 4h to 500°C. for example, the observed size of the Ti- precipitates was 10 - 15 nm [126].
- 2.2. Ti-containing precipitates offer to act as hardening base via solid state precipitation at 200°C. since this precipitation reaction appears already as a major phase transformation upon DSC-analysis (cf. [17]) so the possibility to decouple this precipitation from nucleation of a major RE-containing precipitation process (cf. Disclosure of The Invention).
- 2.3. VD Mg-Ti alloys were reported [17] to retain their improved resistance to corrosion upon ageing at temperatures up to 250°C without any major degradation compared to the corrosion resistance before ageing, i.e. Ti does not cause the disastrous effect on

corrosion behaviour as Fe does

The alternative of Ti in an extended solid solution of cph-Mg is (i) to produce another non-equilibrium (eg. amorphous) Mg-Ti base matrix phase and/or (ii) to alloy Ti together with a Ti-affinitive element on top of an extended solid solution of rare earth elements in cph-Mg or any other Mg-base non-equilibrium phase in order for a more complex precipitation involving Ti. Prime candidate is aluminium largely known to result in the fascinating world of titanium aluminides which form currently one of the largest research activities in the world of materials. The addition of quaternary aluminium to ternary titanium (or vice versa) to the claimed metastable Mg-(light) RE alloys (see above) spurs the precipitation kinetics and leads to a doubled (via TiAl-type of precipitates) or even quadrupled volume fraction (via Ti_3Al or Al_3Ti) compared to elemental Ti in VD Mg-Ti alloys via the affinity between titanium and aluminium.

These aluminides can be rendered more effective with regard to temperature stability and volume fraction by the addition of metalloids such as silicon, boron, germanium or antimon transforming corresponding aluminides in corresponding metalloid containing precipitates such as Al-rich silicides of the form $Al_{13}(Fe,V)_3Si$, the latter being known as the most temperature stable solid state precipitates ever reported for a high performance high temperature aluminium base alloy. The phase was achieved by the more extreme conditions of rapid solidification affordable by planar flow casting (PFC) [128] resulting in simultaneous supersaturation of fcc-Al with the alloying additions Fe, V and Si and in separation from the melt of melt-spun RS- $Al_{13}(Fe,V)_3Si$. This phase is icosahedrally disordered of near spherical morphology and of size 20 to 100 nm decorating the boundaries of both grains and subgrains of size 0.5 to 2.0 μm in Al-Fe-V-Si alloys [128]. The phase is of bcc crystal structure with lattice parameter 1.25 nm showing an (intermetallic) coarsening rate of $2.9 \cdot 10^{-26} m^3h^{-1}$ which is about 3 orders of magnitude smaller than for AlFe-phases, for example (cf. [129]). The phase leads to a nano-dispersion of round-shaped precipitates in the as-extruded condition [128] which is a particularly attractive morphology for mechanical properties such as plane strain fracture toughness, yield strength and Young's modulus which are all of prime interest for HT-sheet applications [130].

For all of the Mg-alloys claimed herein, the iron (Fe) of the aluminides known from RSP-processing of advanced Al-alloys (such as for $Al_{20}Fe_5Ce$, $Al_{10}Fe_2Ce$, Al_6Fe of size 100 - 300 nm and of $\Theta'Al_3Fe$ and also the relatively coarse equilibrium Al_3Fe particles reported for advanced high temperature Al-alloys (cf. [131])) and of the known silicides may be replaced by titanium (n.b. Ti evaporates also more easily than Fe). Instead of Fe or Ti, however, other transition metals such as Mn (and Cr) can be used for $Al_aTM_bSi_c$ -type of silicides due to the relatively low temperature of a major onset of transformation of corresponding extended solid solution in cph-Mg (cf. [17,45]) and/or their stabilizing (cf. [132]), but also enoblin and/or passivating effect on such intermetallics.

Binary, ternary and quaternary extended solid solutions of rare earth-, transition- and/or simple metals in cph-Mg

However, the entity of the extended solid solutions of transition metals in cph-Mg is far from being explored yet. Shaw et al. reported [133] on the corrosion behaviour of the extended solid solutions of 2.4 - 13.3 Cr, 0.9 - 2.4 Mo, 2.7 - 13.0 Ta and 1.0 - 7.4 tungsten (W) in cph-Mg-deposits of thickness of $< 2 \mu\text{m}$ as well as for the ternary single phase (amorphous or crystalline) alloy $\text{Mg}_{67.8}\text{Al}_{15.5}\text{W}_{17.6}$ after deposition onto a graphite substrate, all of which made by magnetron sputter deposition. Pronounced passivation was observed for the extended solid solution of 2.7 ($\rho = 2.14 \text{ g / cm}^3$) to 8.2 ($\rho = 3.1 \text{ g/cm}^3$) at.% Ta in cph-Mg and for the metastable ternary MgAlW-alloy ($\rho = 5.0$) with the first ever reported active-to-passive transition for an Mg-alloy similar to those observed for Cr-steels, for example. All transition metals employed were reported to increase the corrosion potential so enoble corresponding Mg-alloys with increasing levels of alloying. At solute concentrations $> 2 \text{ at.}\%$, however, Cr was observed to result in the highest rate of ennoblement followed by W.

The results by Shaw et al. [133] were confirmed by Hirota et al. who reported [28] also on the corrosion behaviour of the extended solid solution of 20 - 77 Zr, 14 - 72 Nb and 18 - 77 Ta [at.%] in cph-Mg. The anodic polarization in 1 mol HCl aqueous solution resulted systematically in TM-metal cation- and corresponding O^{2-} -anion enrichment and in Mg^{2+} -cation and OH^- -anion depletion of the surface oxide and lead to passivation in this electrolyte at potentials above the observed corrosion potentials at -0.3 V for Mg-57Nb and -0.25 V for Mg - 38 Ta, for example (all with respect to the standard calomel electrode potential and in [at.%]). The thickness of corresponding air-formed oxides was 2nm, while that formed in the electrolyte not more than 4.5 nm. Annual corrosion rates for solute concentrations $> 40 \text{ at.}\%$ decreased from $30 \mu\text{m / yr}$ for the Mg-Ti system (see page 7) down to as low as $1.5 \mu\text{m / yr}$ for the Mg-Ta system [28] (cf. Figs. 74 to 76).

On the basis of these observations it is then straight-forward to see these improvements in the light of a universal consequence of passivating components in Mg as it was first shown by Hehmann et al. [11] for the extended solid solution of Al in cph-Mg and in more general predicted for the first time by Tamman already in 1919 [4], i.e. an homogeneous distribution of the alloying elements on an atomic length scale. On top of this first topological criterion (see below), the efficiency of light rare earth and/or early transition metals and/or metalloids to substantially enhance the corrosion behaviour of magnesium alloys by passivation the Mg-alloy surface might result from their ability to:

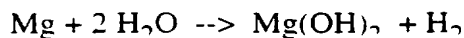
- a) form a variety of oxides of different stoichiometry without large changes in the enthalpy of formation [123] (cf. Tables 3 and 4);
- b) to donate a relatively large number of electrons upon substitution of Mg-ions of the MgO surface oxide by RE_2O_3 , TM_2O_3 , RE_xO_y , TM_xO_y , met_xO_y where $x < y$ to the otherwise non-conductive MgO so providing a higher surface potential eventually rendering the alloy

surface inert by an increase in electron concentration at the very top layer of the oxide repelling O^{--} -ions there so transforming the MgO into an n-conductor (cf. Tables 3 - 6) known to suppress the diffusion eg. of magnesium to the surface (cf. [28]).

It is evident that these criteria apply particularly to the transition metals Ti, V, Cr and Mn as well as to the elements of the same sub-group of following periods of the atomic table and this is in full agreement with the present observations and the observations made by the British, American and Japanese laboratories. The supra-periodical coherency of these observations, however, was not obvious prior to the present invention. The relatively low vapour pressure of transition metals impose a general limitation for economically viable VD-processing compared to that with rare earth metals which provide a relatively large vapour pressure. Alloying additions such as vanadium, however, are known to provide at least six different oxide modifications (rare earth three to four) and V as well as Cr and Mn (see Fig. 87 and page 56) are therefore very attractive alloying additions for passivation of the magnesium alloy surface [123]. The ability to form a variety of oxides can be explained by the ability of the element to provide different states of oxidation, but also on the basis of the flexibility to provide different proportions of ionic and covalent bonding with oxygen and this ability was considered to result in amorphous oxides [145]. Amorphous oxides can suppress diffusion topologically, since they usually do not develop or they reduce grain boundary diffusion paths, for example. In the present invention this ability to modify the Mg-oxide was demonstrated by the colour that appears on the surface of the extended solid solution of Si (pink-to-blue shiny, see Fig. 1), Ge (green) and Sb (red-to-violet) in cph-Mg and this was observed for the first time for the extended solid solutions in cph-Mg and the colour remained there even after eight years of exposure to normal atmosphere without forming a tarnish or other surface film products. The addition of TM with relatively high evaporation rates in conjunction with RE and simple metals such as aluminium as well as metalloids are therefore a very useful alloying supplement when held in solid solution of cph-Mg or a metastable structural variant of Mg which supplies the topological criterion to cover the Mg-alloy surface most homogeneously. Homogeneity on the atomic scale, however, is the most important criterion as evident from the invention and this is not surprising regarding the extreme position of magnesium in the electrochemical series.

Hierarchy of Relevant Criteria for Stainless Mg-Alloys via Single, i.e. One-Phase and/or Duplex Non-Equilibrium Mg-base Matrices

The following alloy development criteria are relevant to complete (not to substitute) the high purity alloying concept to provide even better corrosion resistance and eventually relaxing the requirements on purity of Mg-alloys and feedstock as well as on the refinement of essentially inert and/or second phases being critical for the protection of the Mg-base bulk afforded by the surface film (see above). One of the most remarkable and widespread assumption is that the corrosion of Mg is controlled by the reaction



(cf. [134 to 136]). This assumption ignores the reality and is one example for the origins why the literature on the corrosion of Mg comprises a list of incoherent and undigested statements seducing to class room methodology on microgalvanic and other cells (cf. [137]). The assumption that pure Mg "corrodes" suggest the absence of a surface reaction and/or oxidation product on the Mg-(alloy) bulk prior to transforming into Mg-hydroxide. The same authors outline (cf. [136]), however, that a magnesium oxide film forms at higher temperatures which (eventually) develops a Pilling-Bedworth ratio, i.e. a ratio of the molar volume of the surface oxide MgO to that of the substrate (bulk) metal Mg of $V_{\text{MgO}}/V_{\text{Mg}} = 0.81$ without referring to the apparent contradiction. The MgO-oxide surface film is considered to be non-protective as a result of pores and fissures forming diffusion paths between metallic bulk and environment. In practise, however, Mg and its alloyed surfaces are always exposed to casting temperatures above 450°C and/or vapour deposition and/or eg. ball milling environments with more or less dry air before being exposed to humid environments (at lower temperatures). Therefore, the MgO-surface film forms first prior to other reaction products including Mg-base hydroxides frequently observed after exposure to humid environments. The Pilling-Bedworth ratio of the $\text{Mg}(\text{OH})_2$ on pure Mg, however, is 1.73. The $\text{Mg}(\text{OH})_2$ -crystal has a layered rhombohedral structure providing easy basal cleavage so dissolution in acids ($\text{pH}_{\text{crit}} \leq 8.5$) all indicating the poor adherence forthcoming from the fissures forming under expansion and resulting micropressures so developing the problems similar to the MgO-film (which is subjected to microstresses under tension), but the other way around. One of the resulting misconceptions is to improve the corrosion behaviour of Mg by *suppressing* the formation of MgO as the initial product in the reaction chain of Mg-based surface films (and if only in the interpretation) so to improve the properties of the $\text{Mg}(\text{OH})_2$ -based hydroxide rather than vice versa. The prime question is therefore (i) why and under what conditions transforms the MgO-film to the Mg-hydroxide and (ii) how can this transformation be replaced by a more efficient surface protection with the MgO as the basis (see schematic, Fig. 77).

The MgO \rightarrow Mg(OH)₂ - Transformation

One of the reasons why attention is focussed on the modification and/or stabilization of the Mg-hydroxide $\text{Mg}(\text{OH})_2$ rather than on that of the oxide MgO is the comparison of the free energy of formation of both species, i.e. ΔG for MgO is 136 kcal/gmol and ΔG for $\text{Mg}(\text{OH})_2$ is 142.6 kcal/gmol leading to the conclusion that $\text{Mg}(\text{OH})_2$ should form more easily since being thermodynamically more stable on a macroscopic scale. In fact, what is overlooked here is that the formation of $\text{Mg}(\text{OH})_2$ requires a molecule of water the ΔG of which also enters the energy balance $\delta\Delta G$ following:

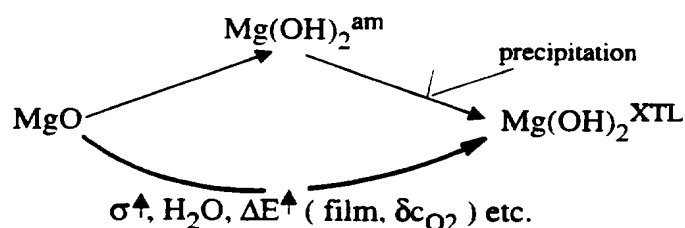
	$\text{MgO} + \text{H}_2\text{O} \rightarrow \text{Mg}(\text{OH})_2^{\text{XTL}}$			$\delta\Delta G$ [kcal/gmol]
ΔG	-136		-142.6	-6.6
ΔG		-68.3		+61.7

How is this transformation of MgO into Mg(OH)_2 then nonetheless possible ? Uniform formation of Mg(OH)_2 requires a humidity of a minimum of 80% without being sufficient, while it is possible locally already at 30% humidity. While the misleading comparison of ΔG of MgO and Mg(OH)_2 suggests a small driving force towards formation of the Mg(OH)_2 due to the negative difference of $\delta\Delta G = -6.6 \text{ kcal/gmol}$, the reality is that, on a macroscopically homogeneous scale this reaction cannot occur as the balance with ΔG for water shows and resulting in a positive value of $\delta\Delta G = 61.7 \text{ kcal/gmol}$. The latter is confirmed by the observation reported in the Pourbaix-Atlas that dense MgO -plates are hardly attacked upon immersion in water, while MgO -powder dissolves rapidly in water (as a result of the increase in stored energy including a surface term here) and showing that the macroscopic energy balance is hardly the origin of the corrosion behaviour of magnesium and its alloys and that - contrary to widespread belief - Mg(OH)_2 does not necessarily destabilize MgO , but that microscopic factors including surface energy, concentration of H_2O , microgalvanic effects under the surface film, film-characteristics including microstresses under tension and/or pression as well as the formation of aeration cells forming local elements externally including oxygen gradients in the electrolyte, δc_{O_2} , (cf. Figs. 78 to 80). They are all contributing to an increase in ΔG on the left hand side of the above reaction so contributing to increase the driving force to a transformation of MgO to other products including Mg(OH)_2 instead. In fresh water, for example, Mg does not corrode. (Accumulation of) Water *droplets* on the surface of Mg , however, can provoke catastrophic corrosion effects showing the commonality of the corrosion characteristics of Mg with those of iron and/or steels (cf. Fig. 78 to 80) including the significance of local rather than macroscopic conditions).

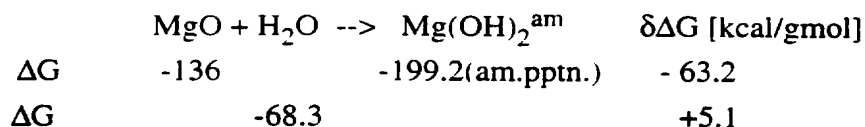
It is therefore not surprising that the actual transformation of MgO to crystalline Mg(OH)_2 is frequently observed to be associated with the transformation to amorphous Mg(OH)_2 -islands and/or precipitations via condensation of droplets in relatively low humidity, the amorphization increasing the entropy of transformation following

$$\delta\Delta G = \delta\Delta H - T\delta\Delta S$$

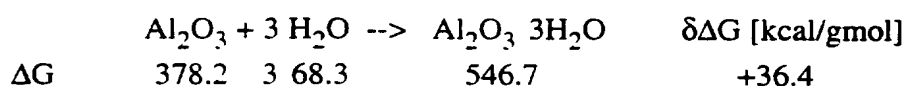
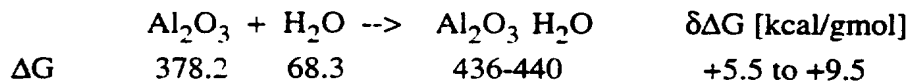
i.e. nature mobilizes the excess term ΔS in view of corresponding low $\delta\Delta H$ -balance and driving forces $\delta\Delta G$ to finally arrive at the crystalline Mg(OH)_2 - endproduct. It is therefore wrong to direct Mg alloy development towards modification and/or stabilization of amorphous Mg(OH)_2 rather than to avoid it totally, since once being formed, the transformation into crystalline Mg(OH)_2 becomes inevitable unless the hydroxide was washed away before:



(where $E =$ (local strain) energy here). A revision of the available thermodynamical data shows that also the transformation of MgO into amorphous $\text{Mg}(\text{OH})_2$ (the most stable $\text{Mg}(\text{OH})_2$ - configuration) is thermodynamically, i.e. macroscopically not evident (cf. [123]):

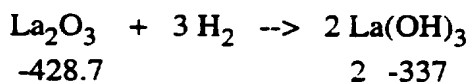


so requiring further (energy / enthalpy) contributions. For comparison, the reaction

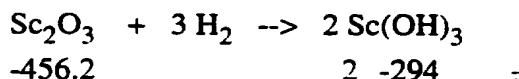


would require the same order of magnitude microscopic activation (energy) to occur. In practise, however, Al_2O_3 does not transform as easily into corresponding hydroxide as Mg does and this confirms that microscopic energy contributions are the rate-controlling energy criteria among the overall criteria controlling the transformation of MgO to $\text{Mg}(\text{OH})_2$ or another hydroxide - derivative, for example.

It is also evident, however, that the beneficial effect of the very homogenous distribution of rare earth elements on the corrosion behaviour of Mg in a H_2O_2 -based solution does not result from macroscopic energy criteria, since the free energy balance of the transformation of corresponding oxides into hydroxides, i.e. eg.



or



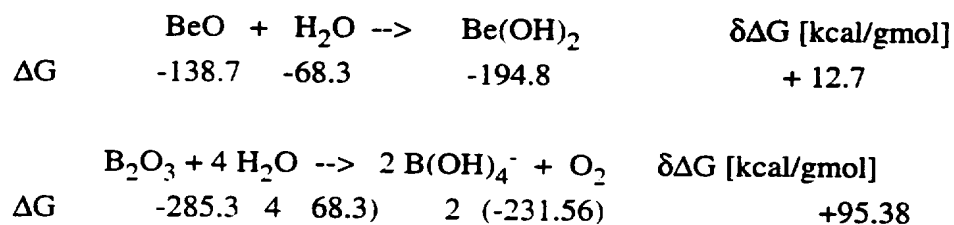
(as representatives which shall be sufficient here, cf.[123]) is not only very exotherm providing a potentially large driving force. it increases the susceptibility of a mixture with MgO to excess-hydrogen at the surface as is easily available in H_2SO_4 -, HCl - and/or HNO_3 -based acid solutions (see claim 1.16). The same trend is given by the balance of corresponding crystal lattice energies (cf. [123]). The involvement of rare earth elements in Mg-base surface oxides thus increases its macroscopic susceptibility to the transformation to a(n eventually mixed) hydroxide in more aggressive media providing a hydrogen-controlled reaction eventually leading to incorporation of anions such as SO_4^{--} , Cl^- and $(\text{NO}_3)^{3-}$ in the surface film so increasing its vulnerability to corrosive attack.

The oxides of transition metals and metalloids, however, do not transform (as easily as those of rare earth elements) into corresponding hydroxides. In fact, no hydroxides were reported for the following elements (cf. [123]): Ce (an interesting CeCrO_3 -oxide was reported instead), for Cr, Ge, Hf, Mo, Nb, Re, Rh, Si, Ta, Tc, Ti, W, V, yttrium, and Zr, all in full agreement with the

observations by Hirota et al., see above). Most of the rare earth metals such as Gd, Dy, Pr, Ho etc. may absorb water instead (cf. reaction for aluminium and [123]), while the late transition metals form systematically hydroxides, i.e. $\text{Co}(\text{OH})_2$, $\text{Cu}(\text{OH})_2$, $\text{Au}(\text{OH})_3$, $\text{Mn}(\text{OH})_2$, $\text{Ni}(\text{OH})_2$, $\text{Os}(\text{OH})_4$, $\text{Pd}(\text{OH})_4$, $\text{Pt}(\text{OH})_2$ and $\text{Zn}(\text{OH})_2$, for example. The different behaviour of the early and late transition metals was explained [139] on the basis of their different metal oxygen bond strength ΔH_{ads} providing the energy for oxygen dissociation ($\text{O}_2 \rightarrow 2\text{O}$; $\delta\Delta H(\text{O}_2)$: 498 kJ/mol) prior to formation of oxide nuclei (Fig. 81) being dictated by like-like metal bond strengths $\epsilon_{\text{M-M}}$ operating as nucleation barriers for oxide formation so (pure) metal passivation (Fig. 81). Passivity promoters are characterized by high ΔH_{ads} - low $\epsilon_{\text{M-M}}$ -values. The synergistic effect of both criteria classifies passivation behaviour of pure metals which provide per se a one-phase microstructure. The extrapolation of this classification to the corrosion problem of magnesium (i.e. the $\text{MgO} \rightarrow \text{Mg}(\text{OH})_2$ -transformation) shows (i) that Al and early transition metals are prime candidates for passivation of magnesium, (ii) why H_2O_2 -based electrolytes as employed in the invention discriminate topological from chemical passivation effects (i.e. the use of H_2O_2 reduces and/or replaces $\Delta H_{\text{ads}}(\text{req})$ for O_2 -dissociation catalytically and rendering Mg-alloys passive provided, that the surface film is topologically dense (see next chapter) and (iii) that percolation analysis according to which a chain of metal-oxides are formed without breaking metal-metal bonds is not sufficient to explain the passivation of magnesium. ΔH_{ads} is related to the metal-oxygen bond strength following

$$\epsilon_{\text{M-O}} = 0.5 [\Delta H_{\text{ads}}(\text{ox}) + \delta\Delta H(\text{O}_2)]$$

while $\epsilon_{\text{M-O}}$ is proportional to the lattice energy of the oxides (Table 3). Accordingly, all elements forming oxides with higher lattice energies than MgO provide improved O_2 -dissociation and oxides with $x < y$ for which a jump in lattice energies towards higher values is evident) are particular useful (Table 3). Also the oxides of Be and B are stable in view of the reactions:



i.e. without significantly (Be) modifying the macroscopic energy balance when involved in MgO and/or without favouring (B) the formation of corresponding hydroxide (Be, B). The beneficial effect of a homogeneous distribution of rare earth elements including yttrium and/or scandium on solid Mg-based surfaces in other environments is evidently based on parameters which are different from macroscopic equilibrium conditions calling for an analysis of the microscopic and more local effect they have on MgO (and Al_2O_3) for example.

Table 3 Lattice Energies of Oxides (Highlighted (eg. by flash), if larger than for MgO)

Oxide	Calculated lattice energy [kJmol ⁻¹]	Literature source	Thermochemical cycle lattice energy [kJmol ⁻¹]
Li ₂ O	2799	Baughan (1959)	
Na ₂ O	2481	Baughan (1959)	
K ₂ O	2238	Baughan (1959)	
Rb ₂ O	2163	Baughan (1959)	
Cu ₂ O	3273	Mamulov (1961)	
Ag ₂ O	3002	Mamulov (1961)	
Tl ₂ O	2659	Mamulov (1961)	
LiO ₂	(878)	D'Orazio, Wood (1965)	(872)
NaO ₂	799	Yatsimirskiii (1959)	796
KO ₂	741	D'Orazio, Wood (1965)	725
RbO ₂	706	D'Orazio, Wood (1965)	695
CsO ₂	679	D'Orazio, Wood (1965)	668
Li ₂ O ₂	2592	Wood, D'Orazio (1965)	256
Na ₂ O ₂	2309	Wood, D'Orazio (1965)	2305
K ₂ O ₂	2114	Wood, D'Orazio (1965)	2078
Rb ₂ O ₂	2025	Wood, D'Orazio (1965)	2006
Cs ₂ O ₂	1948	Wood, D'Orazio (1965)	1861
MgO ₂	3356	Wood, D'Orazio (1965)	3526
CaO ₂	3144	Wood, D'Orazio (1965)	3133
SrO ₂	3037	Wood, D'Orazio (1965)	2849
KO ₃	697	Wood, D'Orazio (1965)	-
→ BeO	4293	Huggins, Sakamoto (1957)	4443
MgO	3795	Huggins, Sakamoto (1957)	3791
CaO	3414	Huggins, Sakamoto (1957)	3401
SrO	3217	Huggins, Sakamoto (1957)	3223
BaO	3029	Huggins, Sakamoto (1957)	3054
→ TiO	3832	Huggins, Sakamoto (1957)	3811
→ VO	3932	Ladd, Lee (1961)	3863
MnO	3724	Ladd, Lee (1961)	3745
FeO	3795	Ladd, Lee (1961)	3865
CoO	3837	Ladd, Lee (1961)	3910
NiO	3908	Ladd, Lee (1961)	4010
PdO	3736	Ladd, Lee (1961)	-
CuO	4135	Mamulov (1961)	4050
ZnO	4142	Ladd, Lee (1961)	3971
CdO	3806	Ladd, Lee (1961)	-
HgO	3907	Ladd, Lee (1961)	-
GeO	3919	Ladd, Lee (1961)	-
SnO	3652	Ladd, Lee (1961)	-
PbO	3520	Ladd, Lee (1961)	-

continued on next page

Table 3 Lattice Energies of Oxides/continued

Oxide	Calculated lattice energy [kJmol ⁻¹]	Literature source	Thermochemical cycle lattice energy [kJmol ⁻¹]
↓ Sc ₂ O ₃	13557	Gasharov, Sovers (1970)	13708
Y ₂ O ₃	12705	Gasharov, Sovers (1970)	-
La ₂ O ₃	12452	Johnson (1969)	-
Ce ₂ O ₃	12661	Johnson (1969)	-
Pr ₂ O ₃	12703	Johnson (1969)	-
Nd ₂ O ₃	12736	Johnson (1969)	-
Pm ₂ O ₃	12811	Johnson (1969)	-
Sm ₂ O ₃	12878	Johnson (1969)	-
Eu ₂ O ₃	12945	Johnson (1969)	-
Gd ₂ O ₃	12996	Johnson (1969)	-
Tb ₂ O ₃	13071	Johnson (1969)	-
Dy ₂ O ₃	13138	Johnson (1969)	-
Ho ₂ O ₃	13180	Johnson (1969)	-
Er ₂ O ₃	13263	Johnson (1969)	-
Tm ₂ O ₃	13322	Johnson (1969)	-
Yb ₂ O ₃	13380	Johnson (1969)	-
Lu ₂ O ₃	13665	Ladd, Lee (1961)	-
Ac ₂ O ₃	12573	Krestov, Krestova (1969)	-
Ti ₂ O ₃	-	-	14149
V ₂ O ₃	15096	Mamulov (1961)	14520
Cr ₂ O ₃	15276	Mamulov (1961)	14957
Mn ₂ O ₃	15146	Mamulov (1961)	15035
Fe ₂ O ₃	14309	Mamulov (1961)	14774
Al ₂ O ₃	15916	Yatsimirskiii (1961)	-
Ga ₂ O ₃	15590	Yatsimirskiii (1961)	15220
In ₂ O ₃	13928	Yatsimirskiii (1961)	-
Ti ₂ O ₃	14702	Mamulov (1961)	-
Pb ₂ O ₃	(14841)	Van Gool, Picken (1969)	-
CeO ₂	9627	VanBaur (1961)	-
ThO ₂	10397	Ladd, Lee (1961)	-
PaO ₂	10573	Ladd, Lee (1961)	-
VO ₂	10644	Ladd, Lee (1961)	-
NpO ₂	10707	Ladd, Lee (1961)	-
PuO ₂	10786	Ladd, Lee (1961)	-
AmO ₂	10799	Ladd, Lee (1961)	-
CmO ₂	10832	Ladd, Lee (1961)	-
TiO ₂	12150	Ladd, Lee (1961)	-
ZrO ₂	11188	Ladd, Lee (1961)	-
MoO ₂	11648	Ladd, Lee (1961)	-
MnO ₂	12970	Ladd, Lee (1961)	-
SiO ₂	13125	Ladd, Lee (1961)	-
GeO ₂	12828	Ladd, Lee (1961)	-
SnO ₂	11807	Ladd, Lee (1961)	-
PbO ₂	11217	-	-

Table 4 Oxides Grouped according to their Tendency to form Hydroxides*TM forming oxides with small tendency to form hydroxides*

Ti	TiO, TiO ₂ , Ti ₂ O ₃
Zr	ZrO, ZrO ₂ , ZrO ₃
V	VO ₂ , V ₂ O ₃ , V ₂ O ₄ , V ₃ O ₅ , V ₄ O ₇ , V ₆ O ₁₃
Cr	Cr ₂ O ₃ , Cr ₂ O ₇ ⁻²
Hf	HfO, HfO ₂
Nb	Nb, NbO ₂ , Nb ₂ O ₅
Re	ReO ₂ , ReO ₃
Rh	RhO, RhO ₂ , Rh ₂ O ₃
Ta	TaO ₂ , Ta ₂ O ₅
(Mn	MnO, MnO ₂ , Mn ₂ O ₃ , Mn ₃ O ₄)

Others forming oxides with relatively small tendency to form hydroxides

Ce	CeO, Ce ₂ O ₃
Sb	Sb ₂ O ₃ , Sb ₂ O ₄ , Sb ₂ O ₅
Be	BeO, BeO ₂ ⁻
B	B ₂ O ₃
Ga	GaO, Ga ₂ O, Ga ₂ O ₃
Al	Al ₂ O ₃
Ge	GeO, GeO ₂
Si	SiO, SiO ₂
P	PO, P ₄ O ₆ , P ₄ O ₁₀
Sn	SnO, SnO ₂

TM forming oxides with a tendency to form hydroxides

Co	Co ₃ O ₄
Cu	CuO, Cu ₂ O
Au	AuO ₃ ⁻
Fe	FeO, Fe ₂ O ₃ , Fe ₃ O ₄
Ni	NiO, Ni ₂ O ₃
Os	OsO ₃ , OsO ₄
Pd	PdO
Pt	PtO ₂ , Pt ₃ O ₄
Ag	Ag ₂ O, Ag ₂ O ₃
Cd	CdO

Others forming oxides with a tendency to form hydroxides or absorbing H₂O

RE ¹⁾	RE ₂ O ₃
Ba	BaO ₂
Ca	CaO ₂ , CaO, CaMgC ₂ O ₆
In	InO, In ₂ O ₃
Li	LiO, Li ₂ O, LiO ₂
Se	SeO, SeO ₂
Na	NaO, Na ₂ O, NaO ₂
Sr	SrO, Sr ₂ O, SrO ₂

¹⁾RE = rare earth, see Table 3

Topological Non-Permeability and Adherence of the Enhanced MgO-based Surface Oxide as the Basic (but not Sufficient, see above) Requirement for Passivation of Magnesium

The advent of RSP evidenced significant drawbacks on the theory of the formation of self-healing passive alloy surface films. No consistent metallurgical relationship has yet been reported between composition, microstructure and crystal structure on the one hand and *passivability* of the alloy surface overlayer on the other¹⁾. The literature on passivability of pure Fe, Cr, Ni, Ti and Al as well as on FeCr- and FeCrNi-steels concentrates on *surface* mechanisms and structures of the *surface layer*. Topological coherency or non-permeability of the surface oxide of conventionally processed "equilibrium" alloys has always been discussed as a result of the oxide itself or of its contact to the environment, for which a unique discription with respect to the problem is given by the pK_s -value = $-\log K_s$ where $K_s = (H_3O^+) A^- / HA$ with HA = acid, H_3O^+ and A^- the resulting hydronium ion and corresponding anion. However, the passivating *alloy* surface film is a result of the (details of the) environment on the one

¹⁾ A consecutive (i.e. chronological so inversed hierarchical) order of pre-requisites for alloy passivation of non-passive metals (Fe, Mg) is given by (i) *chemical*, then (ii) *physical* criteria followed by (iii) *topological* considerations. Chemical conditions include adsorption of *mono-molecular layers* of O^{2-} or OH^- -ions to tie up metallic valencies in the unfilled continuum of conducting bands as a necessary, but not sufficient pre-requisite n°1 for atmospheric growth of a surface oxide in order to retain the beneficial effect of many 3d- (ie. TM-) or 4f- (ie. RE-) elements, for example, on their own corrosion resistance or when alloyed to another, more easily corroding metal or alloy (cf. yttrium in thermal barrier coatings). Physical criteria (pre-requisite n°2) include a) the crystal or non-crystalline *structure of the surface oxide* (suppressing ionic diffusion paths such as for (metallic) anions or O^{2-} -cations so including (anodic) polarization prior to thermodynamic equilibrium with the environment; eg. Al_2O_3 , Cr_2O_3 , disordered Fe_3O_4 in acids, ($Fe_2O_3 + Cr_2O_3$)-spinells) and / or b) its *e^- -conductivity* (eg. Al_2O_3 and TiO_2 are insulators so also suppressing cathodic partial reactions, while the oxides of Fe, Cr and Ni do not). Topological *non-permeability* of the resultant surface film is the last, but not least pre-requisite n°3 for passivation. If the oxide is a) *free of diffusion paths/pores* (eg. Ti_2O_3 , Cr_2O_3 , Al_2O_3 , ($Fe_2O_3 + Cr_2O_3$)-spinells), it leads on to a thin (< 10 nm) and metallically shiny passive film (--> Def. of "passive" = orders of magnitude lower corrosion rates than expected being stable over a range of applied potentials) which can be reinforced by further anodizing (eg. Al, Ti: strictly speaking, n°3 a) does not require the exact knowledge on n°2). If the oxide is b) *porous* (i.e. semipermeable, eg. Fe_2O_3 , Ti_2O_3 , Mo-oxides, MgO), often a sponge-like tarnish is formed including complicated corrosion mechanisms that eventually stop the further attack after a while (eg. Fe in SO_2 -atmospheres, selective corrosion generating surface zones depleted with the less noble constituent (CuAu, CdMg and MgAl solid solutions) and eventually oxidized pores such as AgO on CuAg-solid solutions to result in a coherent surface film).

hand and the details of the microstructure on the other. As a given alloy microstructure such as a given (extended) solid solution reacts different in different acids, this principle is reversible in that different (extended) solid solutions (provided, that no local elements such as pores and Fe-inclusions are rate-controlling) will react quite similar in different environments (acids). The invention has shown that the universal effect of a solid solution, amorphous or non-equilibrium crystalline phase with a homogenous distribution of the alloying elements on an atomic length scale controls this behaviour independent on alloy purity and environment, i.e. even when the tendency to destabilize the Mg (-based) surface oxide is increased. Such a universal effect was not discriminated before in the presence of Cl^- -ions for which the use of hydrogen peroxide (H_2O_2) was crucial (see above). As a result, any non-equilibrium Mg-based product retaining this atomic homogeneity for topologically dense and adherent oxide stabilization must be thermally stable and that is why the rare earth elements play an important role for passive Mg-alloys + products.

Current R&D thus tends to overlook the interface function of the passivating alloy surface film. The best example is that of stainless steel. The *composition* of the bulk (eg. Cr or Ni) was the only metallurgical criterion reported in the literature, while the underlying *microstructures* were always taken for granted. Fig. 82 indicate that the equilibrium microstructure of stainless steels consists of mono- or two-phase matrices with large solid solubilities of either phase so no large microgalvanic gradients to be neutralized and withstood by the surface film. While passivity of Cr-containing stainless steels is based on the ferritic α -phase field extension, that of Cr/Ni- containing stainless steels is built upon the austenitic γ - and resultant martensitic phase field extension. The significant Cr_2O_3 -enrichment of the Fe_2O_3 -surface oxide at 12 to 13 wt.% Cr is considered of major importance, but it is in fact of secondary importance in view of the stainless steels already existing at below this compositional threshold [140]. The effect of Cr in stainless steels is based on *one-phase field extensions* by equilibrium alloying exploring largely the allotropy of Fe. The resultant small microgalvanic microstructural effects leave formation, coherency and stability of the surface overlayer practically untouched.

The reason to overlook this important pre-requisite for alloy passivity is simple: the underlying microstructure of stainless steels is already attainable by *equilibrium processing* so nobody needs to bother about its conditions of formation. Overlooking this pre-requisite, however, can have fatal consequences on the further R&D aimed at passive alloys, in particular when the passive *alloy* bulk is not attainable by equilibrium processing. The opposite to Fe and its steels holds for Al and its alloys. While Fe is *passivated* by selected equilibrium alloying via exploring its allotropy, almost each equilibrium alloying of Al *deteriorates* the effect of the perfect passive film on high-purity Al due to the formation of galvanically active microstructural second phases destabilizing the Al_2O_3 surface film. In contrast to Ti, Al cannot take advantage of allotropy in order to *maintain* its passivity by one-phase field extension upon equilibrium

alloying the underlying microstructure. For Mg base-metals, the consequences on R&D by ignoring microstructural effects on passivity are even worse, since pure Mg has no (i) allotropy or (ii) a perfect self-healing passive surface oxide film in the high-purity state or on any of its equilibrium-alloys and almost none of its all-liquid processed alloys. Furthermore, (iii) low solid solubility at thermodynamic equilibrium due to large electrochemical effects between Mg and many alloying elements makes the development of stainless mono-phase Mg-matrices impossible by using an *equilibrium* approach.

<div style="text-align: center;"> ← Rank of Passivability of "Equilibrium" Alloys </div>			
1. Ti-base	2. Al-base →	← 3. Fe-base Mg-base
passive & allotropic base-metal	passive base-metal	allotropic base-metal	----

All other approaches have failed to achieve a passive Mg-base material. Is it not surprising that equilibrium processing will never lead to stainless Mg-alloys. The impact of non-equilibrium processing illustrates the embarrassing dilemma of the absence of stainless Mg-alloys by other means. "Non-equilibrium processing to compensate for missing metallic passivity and allotropy, low melting point and strong electrochemical effects" is the name of the game and requires for the first time a self-consistent *theory of corrosion* relating *microstructure* and *corrosion* properties. The need for the development of stainless Mg requires more efficient *non-equilibrium processing* for one-phase alloy matrices with minimum galvanic gradients. The "one-phase"-microstructure allowing for coherent non-permeability of passivating oxides is crucial before structure and properties of surface oxides *become effective*. In the first place, this means that equilibrium-processing is "out" in order for the development of stainless Mg and this is not surprising at all. Ultimate development goal n°1 is therefore an *alloyed monophase matrix* with least microgalvanic gradients in order to generate an alloyed MgO-surface film without permeability both on the atomic and microstructural scale. Prime objective is the *coherency* of an MgO-base spinell and/or ad-mixture, not the existence of the spinell and/or ad-mixture itself. and sufficient resistance to passivate galvanic microstructural & surface layer gradients. The objective calls for terminal solid solubility extension (TSSE) of element X in monophase Mg-alloy matrices or any other non-equilibrium (ne) Mg-base phase in order to establish a new generation of Mg-alloys by non-equilibrium processing. One alternative is a dual-phase ($\alpha+\beta$ -) Mg-alloy matrix with extended solid solubility of B and A in ($\alpha+\beta$)-Mg or a β -monophase Mg-alloy matrix as to the Cr/Ni-austenitic-type of stainless steels. Without undue increase in density, however, such microstructures are most obtainable by non-equilibrium crystalline and/or amorphous phase microstructures of higher order Mg-alloys (Fig. 83).

Modification of the Pilling-Bedworth Ratio of Magnesium

The Pilling-Bedworth ratio is a topological criterion. Under the condition that the micro-structural details are sufficiently topologically dense (see above), it is then the Pilling-Bedworth ratio (see above) which takes over control of the topological permeability due to cracks and fissures (unlike chemical permeability due to diffusion through a (ordered or disordered) crystal) of the surface oxide. According to Pilling-Bedworth (PB) the volume ratio of the MgO surface-oxide -to- the Mg-bulk is 0.81. The reduction of the molar volume of the surface oxide relative to the Mg (alloy) bulk induces cracks, fissures etc. resulting in an increase in the surface energy, microstresses and topological inhomogeneity by opening up diffusion paths between environment on the one hand and crack tip (oxide) and adjacent metallic bulk on the other. This is the practical origin why an increasing concentration of moisture in air (i.e. > 30 %) and aeration cells (local exterior elements) such as droplets and condensed humidity including the resulting oxygen concentration gradients at the oxide surface, i.e. δc_{O_2} or $\delta c_{O^{2-}}$ destroy the MgO-film and leading finally to the formation of unprotective $Mg(OH)_2$ or a derivative. It explains why passivation of Mg towards more aggressive media containing large(r) quantities of excess hydrogen such as for pH < 7 requires in the first place a modification of the MgO-surface film in that the PB-ratio is increased towards a value of 1 and/or above this value up to a certain threshold (beyond which the increasing PB-ratio becomes counter-productive, cf. PB of $Mg(OH)_2$) this effect becomes counter-productive) via an homogeneous distribution of the oxide-modifying and/or -stabilizing element with a topologically homogeneous distribution on an atomic length scale, i.e. normal to the surface projected to the environment to allow to be accordingly homogeneously incorporated in the resulting modified oxide and for tight growth of the surface film as is given by the law by Tamman for oxide growth, i.e.

$$d = (2 k t)^{0.5}$$

where k a constant and d = film thickness, of which the PB is defined following

$$V(Mg_a-X_b-Y_c-Z_d)_e - O_f / V_{Mg^{ne}} \rightarrow 1.0$$

and/or > 1.0 where ne = non-equilibrium and x,y and z ternary, quaternary and quinary alloying addition where b to d are suffixes according to homogeneous and/or stoichiometric distribution of element X, Y and Z in the (cation-sub-) lattice of the (mixed / alloyed) MgO-base surface oxide of which the ratio of overall cation to anion is denoted by suffix "e" and "f" here.

Evidently, (early, cf. next p.s) transition metals and metalloids are most effective in increasing the PB-ratio and the electron concentration in MgO. The PB-ratio provides an excellent concept for more protective MgO/Mg ratios towards unity, since the PB of Mg is smaller than 1, the MgO is non-conductive and provides an NaCl-type of crystal which allows kations with higher oxidation states such as Al, Ti, Ce and the other early transition and rare earth elements (see Table 3 to 6) to modify the MgO to an n-conductor (nb. the oxygen cations in the oxides of

Table 6 Pilling-Bedworth ratios of Pure Elements and Range of Oxidation States (cf. **Table 5**)

Element	PB-ratio	Range of Oxidation States
K	0.45	+1
Li	0.57	+1
Na	0.57	+1
Mg	0.81	+2
Cd	1.21	+2
Ce	1.23	+3/+4
Al	1.28	+3
Pb	1.40	+2/+4
Ni	1.52	+2/+3
Ag	1.59	+1
Pd	1.60	+2/+4
Cu	1.68	+1/+2
Al	1.68	+3
Fe	1.77	+3
Mn	1.79	+2 to +7
Ti*	1.95	+2 to +4
Cr*	1.99	+2 to +6
Co	1.99	+2/+3
Si*	2.27	+2/+4
Ta*	2.33	+5
Sb	2.35	+3/+5
Nb*	2.61	+3/+5
V*	3.18	+2 to +5
W*	3.40	+6

to an non-equilibrium matrix phase.

2. Li (and K and Na) cannot improve the PB-ratio of Mg and this is consistent with the poor corrosion resistance of one- and two-phase equilibria α - and $(\alpha+\beta)$ -MgLi alloys despite their topologically homogenous (disordered) distribution of Li-atoms in α Mg and β Mg on an atomic length scale.

3. The elements with resistance to form hydroxides provide the most effective tool to close microcracks and fissures in MgO due to very large PB-ratios R_{PB} becoming effective in a first approach via the role of mixtures and/or deviations from it by following

$$R_{PB} = [(1 - \alpha x) V_{MgO} + \alpha x V(Me_aO_b)] / [V_{Mg} + \Delta V_{Mg^{ne}}]$$

where V_{MgO} and V_{Mg} as previously and $V(Me_aO_b)$ the molar volume of the oxide of an alloying element. $\Delta V_{Mg^{ne}} = V_{Mg^{ne}} - V_{Mg}$ the difference of the molar volume of the ne-phase and pure Mg and α a coefficient describing the deviation from the role of mixtures in a certain composition range of interest.

Ultra-high purity was one factor to reduce the corrosion rate of AZ91 alloy castings down to 3 mpy (see above). If the alloying elements were distributed homogeneously as is possible by PVD, PA-splat cooling etc. (without sufficient thermal stability) the resulting PB-ratio would eventually increase towards 1.0 so providing a higher non-permeability of the surface oxide

and relaxing the conditions for alloy purity to arrive at the same results. The H_2O_2 -solution applied in the invention provided an excellent test bed to discriminate the effect of MgO-oxide modification when the formation of corresponding hydroxide cannot be excluded (presence of Cl^- -ions, possibility to absorb water).

n-Conduction, Flexible Bonds, Amorphous Oxides

The Pilling-Bedworth ratio is not the only microscopic = local criterion to accrue for passivation of (non-equilibrium) Mg-alloys. Its significance for equilibrium Mg-alloys stems from the non-conductivity of the NaCl-type of MgO-(surface) crystal. While the MgO-(surface) crystal is ideally non-conductive, the metallic Mg-bulk provides ideally free-electron conduction resulting in an increasing electrical field gradient with decreasing thickness of the MgO surface oxide film. Provided that a topological homogeneous surface oxide with PB-ratios around and/or above unity protects the metallic interior (i.e. without local elements outside, eg. due to water droplets and/or inside due to noble second phases such as Fe-inclusions, for example), the substitution of Mg-atoms in the MgO-surface crystal lattice with alloying elements of valencies > 2 (which is possible due to the stoichiometric NaCl-type of crystal structure) would reduce this gradient by an increasing electron concentration of excess-elements at the oxide surface, repelling O^{2-} -ions there so reducing the (driving force for) diffusion of Mg-atoms to corresponding surface (cf. Fig. 84). The ability to induce n-conduction is shown (Table 4) by the smaller number of RE-, TM- and metalloid atoms compared to oxygen atoms per molecule ($g \cdot atom$) of corresponding oxide, eg. TM_aO_b with $a < b$ etc., since oxygen is (usually) divalent (in these oxides). Enhanced corrosion resistance by the introduction of n-electrons into the MgO-base surface film requires a topologically tight oxide with PB-ratio close(r) to or above unity, while the reduction of the electrical field gradient due to increasing e^- -concentration relaxes in turn the requirement for the topological tightness of this oxide so for PB-ratios versus optimum values.

Both factors are provided by the (combined) use of early transition, early (= light) rare earth metals (in particular Ce, see Table 3) and metalloids all providing high positive valencies (i.e. relatively large oxidation states so donation of electrons to the Mg(-based) surface oxide, cf. Tables 3 and 4), the rare earth elements with the advantage to provide high evaporation rate, the transition metals (. Ce) and metalloids with the supplementary advantage to suppress the (local) transformation of MgO to a hydroxide so enhancing the corrosion behaviour of Mg in particular in more aggressive media (see above) as well as the particular advantage of the early transition metals (not readily alloyable to Mg due to liquid immiscibility) to provide a large number of oxides indicating high electron bond flexibility and/or susceptibility to substitute with Mg in the MgO-lattice. Khan and co-workers, for example, found that a mixture of Y, Hf and small amounts of Si provided superior protection against corrosive attack, where the small amount of Si was instrumental for a major improvement. From the hierarchy of parameters it is evident that the effect of rare earth metals to improve the corrosion resistance of Mg-alloys

originates in microscopic parameters including the PB-ratio and/or an increased electron concentration in the MgO-surface oxide, both representing complementary rather than exclusive parameters (cf. Table 3 - 5, as is with purity and the rest), while the overall $\delta\Delta G$ -balance at the surface becomes more negative (less favourable) for protection in this alloy case. The hierarchy of instrumental parameters for passivation of magnesium thus suggests a combination of transition and rare earth metals as well as metalloids to be alloyed together to magnesium using PVD-methods and/or mechanical alloying. While productivity of the available production facilities is crucial for the selection of whether transition metals, rare earth metals and/or metalloids dominate the resulting alloy composition, the application (indoor or outdoor) decides over the more concrete level of individual alloying elements. Aviation, however, provides the largest readily available fuel saving potential by employing high performance Mg-alloys instead of conventionally processed aluminium alloys (Fig.100 - 104).

Alloy chemistry does not provide mobile anions and/or cations inside the alloy as is possible in an electrolyte *in front of* an alloy. Equivalent mobility *inside* the alloy (i.e. between microstructural cathodes and anodes) is only provided by electrons. However, impurities such as Ni and Fe do not act catastrophically ("though" being more noble than Mg) because they easily discharge H^+ -ions, they act catastrophically because the MgO-surface oxide allows the Fe-agglomeration to create an electron underpressure (cloud) so electron suction driving positive Mg^{++} -atoms to the surface at a different site. This is only possible above a certain size (see Jones and Cotton, above). The opposite is with less noble elements (Ca, Sr, Ba) and resulting precipitates (Mg_2Ca) providing microgalvanic protection the other way around as was demonstrated in this invention by the improved resistance to corrosive attack of certain heat-treated Mg-Ca based splats *after* supersaturation of the cph-Mg matrix with an homogeneous distribution on an disordered atomic length scale. *Surface* precipitates with less noble corrosion and/or electrode potential than the (non-equilibrium) Mg - alloy matrix provide electrons to the Mg-based bulk increasing the free electron pressure onto the surface oxide. Again, this is only possible above a certain size. Already Newmann and co-workers have shown [144] that for a given overall current density the distribution of current density on a conducting particle in a non-conducting matrix depends only on geometrical factors following

$$I = I_{\text{overall}} / [2\pi (1-r^2/a^2)^{0.5}]$$

where r = particle radius and a = position on particle with regard to particle center. Therefore microcathodic protection by Al_2Ca -type of surface precipitates is most effective once such precipitates have formed and becomes less effective with increasing size of the surface precipitates (see invention, above).

With enhanced n-conduction of the MgO-based surface oxide the effect of (refined) Fe- (and Ni etc.) impurities including their distribution on an atomic length scale will change and the result will primarily depend on the question whether the MgO-based surface oxide is more

stable over the competing $\text{Mg}(\text{OH})_2$ -derivative or not, all depending on segregation-free, but alloyed microstructure, overall alloy chemistry and environment. Fine-scale microcathodic protection may therefore neutralize the entire effect of impurities providing a useful supplement to stabilize surface oxide(s). "Microgalvanically" less noble (surface) precipitation (in the above sense) provides an ideal supplement to reduce the tendency of Mg-atoms to diffuse to the surface where O^{2-} -ion are otherwise waiting for it including the case when this oxide provides n-conduction due to incorporation of elements such as Ti, Ce, Al and other (early transition and/or rare earth) metals belonging to their groups. The efficiency to contribute to n-conduction by microcathodic surface precipitation, however, depends on the freedom to modify the effect of an undeliberately added alloying element such as Fe being prone to H^+ -ion discharge rather than improving the MgO-oxide including content and size of the Fe- (- inclusion). The efficiency increases with how the other factors of the hierarchy of relevant criteria (the latitude of which being enormously increased by alloy synthesis with fragmentation on an atomic length scale) allow it to do so.

Intermediate alloy summary

The significance of higher order extended solid solutions with regard to passivate the surface of magnesium alloys lets to claim the following groups of more complex Mg-alloys:

1. Mg-RE - plus alloying additions for (partial) precipitation in order to improve the Hall-Petch-relationship including proportionality constant k_y and intercept $\Delta\sigma_0$ via selected conditions of thermo-mechanical processing:
 - 1.1. Mg - RE - Al
 - 1.2. Mg - RE - alkaline earth (Ca, Sr, Ba)
 - 1.3. Mg - RE - Zn
 - 1.4. Mg - RE - metalloids (Si, Ge, B, Sb etc.)
 - 1.5. Mg - RE - Al - alkaline earth (Ca, Sr, Ba), where $\text{Al} = 2 \text{ to } 3 * \text{AE}$ and $\text{AE} \ll \text{RE}$
 - 1.6. Mg - RE - Al - metalloids
 - 1.7. Mg - RE - Al - transition metals (TM, eg. Zr, Mn), where $\text{Al} = 2 \text{ to } 4 * \text{TM}$ and $\text{TM} \ll \text{RE}$
 - 1.8. As for 1.1. to 1.7., but using defined misch-metals instead of individual RE.
2. Commercial alloy compositions with and without the complementary additions to Mg - RE as to 1.1. to 1.8..
3. Mg - RE as for 1, but using
 - 3.1. Mg - RE - TM, where $\text{RE} > \text{TM}$
 - 3.2. Mg - RE - Al - TM as for 1.7, but using one or more individual TM
 - 3.3. Mg - RE - Al - TM - metalloid, where $\text{Al} > \text{TM} > \text{metalloid}$ and TM represent one or more than one individual TM
 - 3.4. As for 3.1. to 3.3., but using defined misch-metals instead of individual RE.

4. As for 3.1 to 3.4. , but keeping the higher order additions essentially in solid solution of cph-Mg.
5. Mg - TM based alloys with the transition metals held in the extended solid solution
 - 5.1. Mg - TM - RE
 - 5.2. Mg - TM - Al
 - 5.3 Mg - TM - TM
 - 5.4 Mg - TM - TM - RE
 - 5.5 Mg - TM - TM - Al
 - 5.3. Mg - TM - Al - metalloids
 - 5.4. Mg - TM - Al - AE
 - 5.5. Mg - TM - Al - RE. where Al > RE and TM >> Al
6. Mg-metalloid based alloys with the metalloids held in extended solid solution. From mechanical alloying it is known that boron increases the cristallization temperature of amorphous Fe₇₅Zr₂₅ from 450° to 550°C. Evidently, metalloids in Mg-based ne-phases provide thermally very stable transformation temperatures so a basis to built up corresponding alloys. The selection of higher order additions to Mg-metalloid based ne-alloys can take advantage of the results obtained by mechanical alloying of Mg-10Ti-5B alloys (cf. below):
 - 6.1 Mg - met
 - 6.2 Mg - met - TM
 - 6.3 Mg - met - RE
 - 6.4 Mg - met - TM - TM
 - 6.5 Mg - met - TM - RE
 - 6.6 Mg - met - TM - Al
 - 6.7 Mg - met - TM - TM - RE
 - 6.8 Mg - met - TM - RE - Al

The more concrete compositions derived from the aformentioned observations are given in claims 5, 6 and 9.

Identification of continuous production techniques

Principal

RSP renders useful elements in magnesium more effective via microstructures not obtainable by conventional means. The universal consequence of RSP is the increased microstructural homogeneity underlying all improvements achieved by advanced solidification methods to date. However, processing has yet not reached out to control this homogeneity on the atomic length scale including the absence of microsegregations and porosity which were both underestimated and / or ignored with regard to the need of the passivation of magnesium and its alloys. Microstructural control on the atomic length scale are possible by:

1. Marginal stability sustained by a large temperature gradient across the liquid - solid interface (cf. [14])
2. Absolute stability sustained by very high front velocities (RSP) in combination with capillarity effects at the liquid - solid interface (cf. [13])
3. Solute trapping achieved by both high front velocities and a relatively low liquid diffusivity due to increased viscosity etc. (cf. [13])
4. Condensation of alloy vapours.

The laboratory-scale discontinuous methods used in the invention have shown the limitations for 2. and 3. with regard to continuous production of metastable phases, i.e. an ubiquitous inefficiency to suppress microsegregations unless the most extreme conditions available for fragmentation and heat extraction were applied. From microstructural modelling it is evident (see [14]) that principal 1. is impractical for the production of the desired microstructures due to the high required temperature gradient / low velocity of the growth fronts concerned.

Any control of microstructural homogeneity on an atomic length scale including the absence of microsegregations and porosity requires an outstanding degree of control over the applied non-equilibrium process in order to control the reproducibility of an extreme departure from equilibrium. The two principal axes to be explored are represented by (i) most effective *heat extraction* and by (ii) the highest possible degree of *fragmentation* and (iii) methods that *couple* improvements in both directions. Rapid solidification from the *liquid* require to explore primarily the possibilities to increase heat extraction for a useful degree of fragmentation which is not explicitly and / or precisely predictable, while rapid solidification from the *vapour* phase incorporates already the ultimate degree of fragmentation so degrading heat extraction capacity to a question of secondary importance for the control of vapour technology. Vapour deposition is free of the constraints set by solidification kinetics so immediately subjected to the available degree of productivity and quality of the processing method concerned. Both vapour deposition and mechanical alloying can be run semi-continuously or continuously depending on alloy quantity and/or productivity employed and/or required as well as on the applied processing principles and how these principles are operationalized.

Liquid processing at its extrema

Atomization

Not only are conventional ingot metallurgy and casting methods, but also almost all (inert) gas atomization methods for the production of powders are not potent to produce the required non-equilibrium microstructures of Mg-(light) RE-metal based alloys. Hehmann showed [32] that the observed sharp microstructural transition from the supersaturated chill zone to dendritic growth at a cross-sectional thickness 30 out of 150 μm requires an initial undercooling of at least 150 K in order to result in 30% of recalesced partitionsless growth and resultant supersaturation of the light rare earth elements La, Ce, Pr and Nd in cph-Mg.

Levi et al. have shown [146], however, that initial undercoolings above 150 K are available by the electrohydrodynamic (EHD) atomization method. EHD-atomization is run continuously by a using a wire-type of feed-stock molten by a laser beam. The particle size distribution of EHD-atomized powders ranges from some nm to up to 100 μm . The available minimum of the upper level of the particle size distribution is about 5 μm [147]. Al-Fe alloy droplets were observed to require a degree of fragmentation down to 200 nm to yield 100% volume fraction supersaturated microstructure by partitionless solidification. The maximum of frequency of the particle size distribution was at around one micron. That is that this method would allow for about 20% overall volume fraction of partitionless growth (as for the PA-splats used in the invention) of Al-Fe base powders clearly showing that even the extreme conditions of EHD-processing are not sufficient in order to obtain a segregation-free overall microstructure in Al-Fe base powders.

As for Al-alloys (cf. [146]), it was evident that the volume fraction of segregation and dendrites at the chill-off side of liquid-quenched Mg-base thin foils, ribbons and powders decreases primarily with increasing solid solubility at equilibrium and the resulting increase in partition coefficients $k_0(T)$ (cf. [12-14, 32, 36]). Alloy systems like Mg-Nd and Mg-Sm (or corresponding misch-metals like a Nd-base MM), however, should be suitable candidates for partitionless growth in about 100% volume fraction of the overall powder, since there partition coefficients $k_0(T)$ are about one order of magnitude larger than for the Al-Fe system.

Melt spinning and planar flow casting

Melt spinning (MS) and planar flow casting (PFC) are continuous production methods of the chill-block type of liquid quenching methods. Their characteristics include a more effective heat extraction compared to gas atomization methods so allowing for wider cross-sections of partitionless growth or larger growth normals of metastable one-phase solidification structures (cf. Disclosure of the Invention) than obtainable by atomized powders solidifying in flight.

A discussion of the operative heat transfer coefficients h showed, however, that splat cooling techniques provide much larger h -values than MS-techniques [148]. It is therefore inevitable to identify the methods to maximize h for MS- and PFC techniques and to constrain fluid flow in such a way that the maximum growth normal is limited to the extend of the growth normal of the required metastable one-phase solidification structure. In free jet MS, no such constraints are imposed to the melt puddle between nozzle and rotating wheel (cf. [149], p. 274) and the thickness of the ribbon is to a large extend dictated by the employed wheel surface velocity. More extreme conditions of rapid solidification are affordable by PFC [150] including constraint melt puddles and improved control upon resultant ribbon dimensions (thickness and width). PFC is performed by using a rectangular slot orifice used as a casting nozzle in close proximity to the rotating chill wheel. A shroud allows a jet of inert gas to stabilize the shape of the molten pool of metal on the rotating chill block [150], while a scraper is used behind the melt puddle to

reduce the gas film between liquid and wheel so improving contact and heat transfer. Furthermore, the melt puddle is confined to the gap left between planar orifice and chill so arriving at smaller thicknesses and larger widths of the resultant ribbons than is possible by free jet-casting or melt-spinning.

According to the invention, the metastable growth normal of the required extended solid solutions of (light) RE metals in cph-Mg by chill-block quenching methods is of the order of $20\text{ }\mu\text{m}$ (see above). It was therefore necessary to identify the processing conditions required to improve heat extraction and constraints imposed on the size of the melt puddle relative to the conditions usually applied to this processing family so to allow for metastable growth normals of the order of $20\text{ }\mu\text{m}$. For comparison, Rohklin et al. reported [151] dendritic growth traversing the entire cross-section of melt-spun Mg-La ribbon without showing any supersaturated cph-Mg-base solid solution at all by employing an estimated cooling rate of 10^5 K/s .

MgRE-ribbons of width 2 mm and of thickness $20\text{ }\mu\text{m}$ were made in an helium atmosphere at a wheel surface speed $4\text{--}5000\text{ rpm} \cdot \pi d$, where d = diameter 30 cm of a Cu-wheel of surface finish $1\text{ }\mu\text{m}$ to maximize heat extraction by the chill. Such conditions were considered to result in cooling rates of the order of 10^6 K/s [152,153]. The distance between nozzle orifice and rotating wheel surface was limited to 2 to 2.5 mm in order to simulate near-PFC-conditions. A columnar microstructure was found to traverse almost the entire cross-section of the resulting ribbons indicating that a positive temperature gradient was maintained when the solidification front traversed the cross-section of the ribbon as for the vapour deposits of this invention (cf. Fig. 85 vs. Fig. 48 (top)). That is, that recalescence did not control the formation of the microstructure, though some second phases were found to delineate the columnar grains. Consequently, DSC-analysis of the transformation behaviour of supersaturated cph-Mg-RE-ribbons was not interfered with endothermal dissolution effects stemming from a pronounced segregated dendritic zone and forming the major proportion of PA-splats, for example (see above).

Ribbons with larger levels of rare earth elements (i.e. $> 10\text{ wt.}\%$) exhibited a relatively large exothermal peak at around 400°C depending on the heating rate employed. Fig. 86 shows an exothermal peak-effect of as-spun Mg - 17 Ce alloy at 422°C (note that the exothermal effects are plotted downwards in this particular case) by employing a heating rate of 40 K/min and using a Perkin-Elmer DSC 2. The enthalpy of transformation of this exothermal effect amounts to 400 J/mole . This of the order of magnitude of corresponding effects in the system Mg-Y where they represent the transformation of the supersaturated solid solution of yttrium in cph-Mg into the equilibrium phases cph-Mg and Mg_{25}Y_4 [36]. In rapidly solidified Mg-Y alloys relatively large exothermal effects were observed at 150° to 280°C and they were identified to represent the formation of the hardening intermediate phase β'' and of β' (cf. [36]).

Melt-spun ribbons of Mg-(light) RE alloys, however, did not show such low-temperature effects when made under the above conditions. As-spun Mg - 17 wt.% Ce ribbon showed a

rather flat exothermal spectrum instead as it was observed for vapour deposited Mg-RE alloys (see above) indicating a low transformation activity in this temperature range (Fig. 86). As for VD Mg-RE deposits of columnar microstructure, the major transformation of the super-saturated solid solution of RE (Ce) in cph-Mg occurred at temperatures $> 400^{\circ}\text{C}$. The absence of larger exothermal effects at and below 290°C for the columnar microstructure of the melt spun ribbons shows the possibility of alloy conversion of the extended solid solution of (light) RE in cph-Mg continuous ribbons into the final product at this and lower temperatures and without the (further) formation of interfering intermediate and / or equilibrium phases.

Alloy compositions to be employed, however, should be kept simple and / or involving partition coefficients near unity (i.e. $= 1$) to avoid excessive formation of microsegregations increasing the alloys' susceptibility to natural ageing processes.

Laser beam surface melting

It is evident from more recent microstructural modelling (cf. [13,14, 32-35]) that the available fragmentation within the regime of liquid processing does not allow for growth of substantial volumes or volume fractions of the desired metastable one-phase cph-Mg base solid solutions even under extreme conditions of heat transfer. The required material is only available instead in form of thin layers due to the limitations imposed by recalescence, while the chill-off side even of finely divided volumes shows dendritic structures, especially when the operative partition coefficient is small (for eutectic phase diagrams, i.e. $\ll 1$) or very large (for peritectics, i.e. $\gg 1$).

An enhanced response to anodic polarization was reported for the solid solution of 2.7 wt.% Zr in cph-Mg made by laser cladding on pure magnesium and resulting in improved resistance to corrosion as compared to alloy AZ91B, for example, by employing a beam withdrawal speed of 6.35 mm/sec [154]. The advantage of laser or electron surface beam melting or traversing is that the solidification front velocity is directly coupled so controlled by the withdrawal speed (see [23]). In contrast to all other RSP-methods from the melt, laser surface processing does not involve a nucleation barrier so resulting in epitaxial growth of the (re-) molten layer on the solid underlayer. Systematical experimental work has resulted in microstructural selection diagrams showing (cf. [41,42]) that the velocity required for the formation of segregation-free solids (and solid surfaces) increases with decreasing partition coefficient for eutectic binary alloys such as Al-Cu, Al-Mn and Al-Fe and ranging from some mm/sec to up to 2 m/sec or more. Excellent agreement was also reported between predicted and actual velocities of the order of 2.5 to 3.2 m/s for the formation of an extended solid solution of strontium in cph-Mg by processing without nucleation barriers such as by using a laser technique [12,14].

Also the mechanical properties can be improved by the formation of quasieutectic and / or banded (cf. [155 to 157]) microstructures which occur at sufficiently high levels of (complex) alloying or somewhat lower withdrawal speeds of the laser or electron beam. Kalimullin et al.

reported [95-97] laser surface treatment of Mg-8 Li-5 Al-4 Cd-1 Zn-0.4 Mn alloy [wt. %] (sowjet designation MA21) to improve resistance to (i) creep and to (ii) corrosion (one order of magnitude in 3% NaCl solution) due to a fine quasi-eutectic surface structure. The micro-hardness of laser treated binary Mg-8Li alloy was found to increase by 40% over corresponding underlayer and by more than 600% if prior-cladded with pure Al [158].

The readily available alloys to explore improved mechanical and corrosion properties by thin surface films of metastable microstructures according to the invention include laser or electron beam surface remelting or traversing of commercial alloys AE41, AE42, QE22, EQ21, ZE41, EZ33, EZ32, WE43, WE54, but also AM-, AS- and AZ-type of Mg-base engineering alloys, since Al (cf. [11,159]) and Mn (see Fig. 87) were also found to improve surface passivity within certain microstructural limits. Particularly, the surfaces of the RE-metal containing Mg-base engineering alloys should be less susceptible to natural ageing or even immune as compared to Mg-Li base alloys subjected to laser surface treatments (cf. [50,64]). They are also prime candidates for the extended solid solutions involving more than one alloying element with the possibility to form an active-to-passive transition as for ternary VD MgAlW-alloys and for Cr-steels, for example (cf. pages 38/39).

Vapour deposition

From the invention it is evident that a segregation-free microstructure and not the choice of the alloying composition is the crucial factor to achieve a substantial improvement in the corrosion resistance of the Mg-alloy matrix including passivation of the MgO-surface oxide film. The effect of most attractive alloying elements was yet obscured, however, due to their immiscibility in liquid magnesium and due to unfavourable solidification kinetics. Both problems are inter-related with each other (i) via the need for processing without recalescence and (ii) via the dilemma that no process including solid state synthesis methods exists on earth which provides the required control and productivity. That is, both problems are faced with a strategic dilemma in order to arrive at outstanding light alloys the world is waiting for. Insofar as is evident from the invention that a *productive* method which decouples the synthesis of magnesium with light rare earth and/or early transition metals and/or metalloids from solidification kinetics including the partition coefficient k_0 would be the solution with regard to corrosion resistance of light alloys and superior strength, ductility and toughness. Alloy compositions can be more complicated then without restrictions imposed by partition coefficients far away from unity (i.e. $k_0(\text{eut.}) \ll 1 \ll k_0(\text{per.})$) so to avoid excessive formation of microsegregations which increase the alloys' susceptibility to natural ageing processes [39] and which are particularly damaging to passivity and/or damage tolerance of magnesium alloys.

Vapour deposition integrates the 4 historical development philosophies for Mg-alloys in one alloy synthesis operation:

1. *Highest possible quenching rates* ($> 10^{10}$ K/s) combined with Ultra-Homogeneity (UH), i.e. homogeneity on an atomic length scale due to condensation of monoatomic (or cascades of atoms of) metallic gases, which embrace an *infinitely small heat of transformation* (= *sublimation or condensation*). RSP-engineering alloys quenched from the liquid show not much more than a volume fraction of 20% UH in corresponding chill zone. A 100% UH-type of microstructure is the origin of superior = tailorable property profiles of FVD-Mg-alloys without which no sustainable wrought Mg-market can be established
2. It opens a *universe of new alloying possibilities* ($> 10^{100}$) including Li-equivalent ultra-light surface oxide-modifiers such as Be and Bor. The ineffective use of expensive alloying constituents such as Ag, rare earths and yttrium, which were the final approach via conventional ingot metallurgy to make Mg competitive, can be replaced by a more efficient use of these and all other elements including those with restricted solubility in the solid state due to the formation of strong compounds suppressing equilibrium solubility (see above), but also in the liquid alloy phase due to the formation of large immiscibility gaps with more than twenty important elements such as Be, B, Ti, V, Cr etc.
3. *Ultrapurity* due to adaptability of the process to the partial vapour pressure of elements employed (and which represent a free-of-charge supplement vs. conventional high purity technology). This renders *total recycling* possible and avoids simultaneously catastrophically acting impurities such as Fe & Ni which can destroy passivating surface films.
4. Items 2. - 4. make laborious and expensive *surface protection schemes* (prone to cause dangerous and difficultly handable waste) *redundant* and reduces macrogalvanic corrosion more effectively than suggested by the difference in the actual Galvani-potentials concerned.

Therefore, vapour deposition is superior to chill-block quenching methods such as PFC. A productive, i.e. economically viable VD-method to produce controlled alloy compositions, however, has yet not been developed, although it could be immediately employed for more conventional, i.e. established E-type of Mg-alloys series where the use of RE-metals concentrates on improved elevated temperature properties via T-stable phases separated from melt and/or from the solid by precipitation. If these alloys were made by VD, however, an effective precipitation via the solid state alone and in underaged condition could be provided that is more stable due absence of nuclei triggering microstructural transformations at lower temperatures and simultaneously retaining sufficient passivation eg. by extended solid solubility (cf. above).

Novel alloy compositions are currently the prime objective of VD-development instead without addressing the basic problems sufficiently including productivity, yield and quality of the resultant massive preforms. For magnesium, Bray et al. reported [16,17] thermal evaporation by using an electron gun as the heating supply source for the high-melting component. This method is 1. an uncontrolled evaporation method driven by a relatively unproductive temperature gradient providing the driving force for the deposition of the vapour trajectories

between evaporation surface and chilled substrate and / or deposit and resulting in 2. pan cake-shaped deposits and 3. relatively low yield of the deposited fraction compared to the overall evaporated vapour.

Both magnesium as the base metal and the (light) RE-metals have relatively low vapour pressures providing an attractive alloy chemistry for economically viable products by a vapour deposition method employing the relatively inexpensive sources of resistance and induction heating in conjunction with:

1. controlled evaporation and deposition characteristics including high productivity due to a high vapour throughput, a continuous vapour throughput independent on the discrete charge per operative crucible and per operative substrate,
2. a high vapour yield and
3. a controlled geometry of the resultant deposit.

so to replace Al and Zn in Mg-Al-base alloys including the rapidly solidified magnesium alloy EA55RS by passive magnesium engineering alloys and superceding current developments.

New Vapour Deposition Process / Second Part of the Invention

Until today, no evaporation process has been developed for the production of economically viable materials from the vapour phase such as via vapour deposition, which (naturally) controls (large quantities of) vapour throughput including its physical state, i.e. concentration, temperature and pressure. What is claimed here is a continuous vapour deposition process of which the driving force for gravity independent mass transport from evaporation source(s) to deposit(s) is provided by an external pumping system and of which the actual overall throughput Q_v is controlled, for a given pumping speed S , by at least one heated, heatable and/or superheated (wrt. vapour temperature) interface (membrane) which separates (cf. schematic in Fig. 88) :

- a) two adjacent evaporation chambers n and $(n+1)$ containing at least one individual evaporation source each or
- b) an evaporation chamber n with at least one individual evaporation source and a mixing chamber $(n+1)$ containing no or at least one individual evaporation source or
- c) an evaporation chamber as under a) or b). but followed by a chamber providing a fascility for the deposition of the vapour and which follows into the direction of vapour flow lines (vapour trajectories).

allowing local driving forces to be controlled by vapour pressure. all of the solutions a) through c). however, employing *interfaces* (*membranes*) which are characterized as following:

- a) the interface generating a profile of at least one *discontinuous* pressure gradient $(\int \sum_{i=1}^N (dP_i/dx_i))$, where $N = n, n+1, n+2, n+3, \dots, n+k$ between the at least one evaporation source and/or the at least one substrate provided for vapour deposition of the alloyed and/or

unalloyed (i.e. essentially pure elemental) vapour of the vapour deposited alloy of the required resultant, final overall composition, while the at least interface is constructed in such a way that it takes over the function of a diaphragma used in nature for the osmosis¹⁾ of liquids or in technology applied to the *separation* of chemical constituents, but here without the need for and/or without actual change of composition of the vapour(s) and used for the *synthesis* of metallic gases or vapours and the interface is being called *diaphragma* in the following,

- b) the diaphragma thereby actively providing and/or controlling a pressure gradient (dp°/dx) across the interface separating two adjacent chambers, which is *steeper* (larger in amount) than the pressure gradients within the adjacent evaporation and/or deposition chambers so that either (in isolated cases such as for Mg) the vapour (over-)pressure of a preceeding (in the sense of the direction of the vapour flow, lines or trajectories) chamber and/or the vapour underpressure of the next following chamber acts as the specific driving force, i.e. the "osmotic" pressure being able to overrun without triggering condensation the effect of decreasing and/or increasing temperature (gradients) across the interface of diaphragmas separating evaporation and deposition chambers without condensation by:

The principal idea is to separate at least one pair of adjacent chambers n and $(n+1)$, i.e. designated by suffix "1" and "2" in the following, if not indicated otherwise, of temperatures T_1 and T_2 by employing a distinct temperature gradient which requires a steep and controlled pressure gradient across the interface separating both chambers, thereby the temperature gradient is either negative, i.e. the temperature increases with vapour flow so that $T_1 < T_2$ or it is positive, i.e. the temperature decreases with vapour flow so that $T_1 > T_2$, while the pressure gradient is always negative, i.e. $P_1 > P_2$ on the understanding that the overall system is driven by a pumping system outside the evaporation and deposition system concerned, that is that the imposed overall pressure gradient is the controlling process variable $n^\circ 1$.

The overall process is subjected to the law(s) by Boyle-Mariotte following:

$$(p_1 V_1) / T_1 = (p_2 V_2) / T_2 \quad (1)$$

- 1) For analogy reasons, the term "osmosis" is used here (if not indicated otherwise) for controlled separation of matter via means of a new class of membranes, the separation being driven by forced convection:

---> **Definition:** osmosis is referred here to the selection and/or transfer of a controlled quantity of vapour *mass* and/or gaseous matter without selection of the components involved in the vapour and/or gas traversing the membrane. While classical osmosis is triggered by chemically different solutions being separated via a semi-permeable diaphragma building up a chemical pressure against the pressure provided by the height of the solution, the new process is based upon forced convection resulting from the underpressure between adjacent vapour chambers being sufficient to overrun increasing temperatures.

which becomes translated, according to the invention, into:

$$(P_n V_n) / T_n = (P_{n+1} V_{n+1}) / T_{n+1} \quad (2)$$

Since any (pilot-) process is limited in scale, for a first approach it is assumed that $V_1 = V_2$ so that process control is subjected to

$$P_1 / T_1 = P_2 / T_2 \quad (3)$$

which becomes translated, according to the invention, into:

$$P_n / T_n = P_{n+1} / T_{n+1} \quad (4)$$

The more general driving force to control gaseous flow in the orifice(s) of the interface (membrane) which forms part of the overall diaphragma design and which overrides the effect of thermal gradients, is the static pressure difference between chamber 1 (or n) and chamber 2 (or n+1), i.e. $\Delta P(\Delta T) = k (P_1 - P_2)$, or $\Delta P_n(\Delta T_n) = k(\Delta T_n) (P_n - P_{n+1})$, which is controlled by the interplay of depression (underpressure) depending on pumping speed provided by the external pumping system and which should have the principal intake behind the deposition level of the deposition zone and/or suitable separation walls (see next PCT-application following this one), i.e. in a position where the vapour concerned cannot penetrate the pumping system. The more specific driving force (with regard to the question of positive or negative T-gradient) between the adjacent chambers is dictated by the difference of corresponding pressure-to-temperature ratios

$$\Delta F(\Delta P_n, \Delta T_n) = k(\Delta P_n, \Delta T_n) (P_n / T_n - P_{n+1} / T_{n+1}) \quad (5)$$

where T_{n+1} corresponds to the evaporation temperature of the higher melting component and where the change of state of the gas / vapour involving a (in reality) polytrope (or ideally an adiabatic) gas transformation or change of state following:

$$T_n^\nu P_n^{1-\nu} = T_{n+1}^\nu P_{n+1}^{1-\nu} \quad (6)$$

where ν is the coefficient for the polytrope change of state of the gas or vapour with

$$\kappa > \nu > 1$$

and κ = coefficient for adiabatic change of state (cf. [160], p. 145/6). As a result, a dynamic equilibrium is built up between the effect of suction due to macroscopic underpressure between adjacent vacuum chambers on the one hand and the local power interaction between the diaphragma and the vapour (gas) flow on the other, the latter including thermal power input due to heat transfer and/or mass separation and/or constitutional change upon interfacial mass transfer, friction and thermal power extraction by the diaphragma.

An attempt to establish such an interface was made by introducing a "resistor to flow" under patent application n° P 44 06 333 4 [161]. This "resistor to flow is formed as" (n.b. "formed as" is not the same than "consisting of") a "matrix of flow channels, which are" (i.e. the individual flow channels (which tunnel the vapour to the adjacent chamber in direction of vapour flow), not the matrix!) "distributed over a predominant fraction of the cross-section of the chimney of evaporation" (i.e. the projection of the x-dilation of the evaporation chamber onto the "resistance to flow") "in such a way that a *monotonic* decrease in pressure results between the evaporation zone and the at least one surface of condensation".

In the more general description of the patent it was said that the matrix of flow channels " consists (!) preferably of a bunch of equi-distant *tubes and jets/nozzles*, which result in a sort of 'clogging flow' covering at least the majority of the cross-section of flow " (this cross-section was not defined, but corresponds obviously to the projected surface area of the overall resistor to flow) and which was made responsible to avoid back-diffusion of the higher melting components. Under claims 14 to 18 the resistor to flow is defined as a "net or grid", "tubes with equi-distant hollow spaces" of an "inner" (!) diameter of these hollow spaces which is claimed at most 20%, preferably 10% of the length of the tubes, L, and that these channels are preferably fabricated as a jet nozzle (which is not the same than a jet nozzle geometry). The figures and drawings of this patent suggest indeed that the resistor to flow concerned consists of "hollow spaces" rather than of a resistor or of an arrangement of individual flow resistors (cf. [160,161]). Hollow spaces appear as "pen stocks", for example (cf. drawings in [160] and Fig. 89).

It must be resumed here:

1. A matrix of flow channels forms only the "conductance of flow", while the "resistor to flow" is made by individual elements or a network surrounding corresponding "flow channels" (Fig. 34). Obviously, the only resistance provided by patent application P 44 06 333 4 stems from the thickness or cross-section of the resistor to flow corresponding - according to the drawings - to the length of the tubes, L, acting as the flow channels [160]. This suggests, however, that the vapour is considered to be wet or at least half-way condensed to provide internal friction so providing laminar flow as to a (real) liquid. This is also suggested by the "clogging flow" ("Pfropfströmung") quoted in the description of the patent application, but the "Pfropfströmung" is not claimed to be an explicit part of the process, though it is the only solution left for what was claimed under P 44 06 333 4.
2. The decrease in pressure between evaporation source and substrate / deposit is indeed monotonic, if there was only a resistance to flow and if only the matrix of the flow channels was defined, i.e. the *specific conductance*. The specific conductance is of secondary importance for a resistor to aero- and hydrodynamic flow, while a resistor to aerodynamic flow is not sufficient to *control* the aerodynamic flow of an ideal gas or a gas which is half-way condensed.

3. A resistor to (gaseous or vapour) flow does not generate the required steep and controlled pressure gradient across the interface between two adjacent chambers 1 and 2 (or n and n+1) unless condensation occurs at the orifice(s) of corresponding interface (cf. also Venturi-nozzle, [161]) or unless vapour velocity is limited by the speed of sound (n.b. a liquid is pushed by P_1 (or P_n), while a gas or a vapour is attracted by P_2 (or P_{n+1}) or, in both cases pushed or attracted by the gradient resulting from both P_1 and P_2 (see below), respectively.

4. A jet nozzle is an *apparatus* for an *active* increase of the overall pressure inside the flow channel (eg. the by-pass) of a jet nozzle. The increase in pressure inside the flow channel of a resistor to flow, however, is produced in a "passive" way, since the driving force for vapour or gaseous flow is provided *externally*. In case of a continuous vapour deposition process, this driving force stems directly from a dynamic equilibrium between the adjacent chambers via the polytrope working function given in eq.n (6) and which is maintained by an external pumping system (see above).

The driving force ΔF (or ΔP , see above) controlling the local change of pressure in an individual flow channel so also the decrease in *static* pressure, $\Delta p_{o,s}$, and the increase in *hydrodynamic* pressure, $1/2\Delta(\rho v)^2_o$, inside an individual flow channel of the "resistor to flow ", is proportional to the change of the overall pressure in corresponding flow channel following:

$$\Delta p_o^{\text{overall}}(T) = \Delta p_{o,s}(T) + 1/2\Delta(\rho v)^2_o \quad (7)$$

where $\Delta p_o^{\text{overall}} = \text{const.}$ for $T = \text{const.}$ and ρ and v the density and velocity, respectively, of the elemental or prealloyed vapour or gas. The critical overall change of pressure $\Delta p_{o,\text{crit}}^{\text{overall}}$ without condensation can be increased by superheating the " resistor to flow " relative to T_1 and/or T_2 of the adjacent operating chambers, but this does not affect the limiting physics of a "resistor to flow " as an interface between two evaporating chambers designed to result in an alloy deposit of controlled microstructural homogeneity on the atomic length scale of at least two components with (very) different evaporation (or vapour saturation) pressure. The rearrangement of eq.n (7) following:

$$\Delta p_{o,s}(T) = - 1/2\Delta(\rho v)^2_o + k(T) \quad (8)$$

results in *two limiting physics* of the "resistor to flow" given by:

1. condensation as dictated by van der Waals' equation (cf. [160], p. 148) resulting in two limiting sub-cases:

1.1. $p_{o,s}(T) < P_{\text{crit}}(T)$ due to $\rho_{\text{Gas}} \rightarrow \rho_{\text{Liquid}}$, where $P_{\text{crit}}(T)$ is/are the critical pressure(s) of condensation of a given isotherm $T(p,V)$, where condensation occurs, for example, when the laminar flow of the gas is condensed into an orifice of size being too small or when turbulences arise behind the " resistor to flow ", i.e. the interface (see below).

1.2. Stop of the gas flow due to $v = 0$, i.e. have clogging of orifice and of the " flow channel " due to 1.1 and process has to be interrupted eventually.

2. If case 1.1. and 1.2. can be avoided eg. by superheating the " resistor to flow ", then $\Delta p_{o,s}(T)$ is limited by the speed of sound, i.e. have only $v < v_{\text{sound}}$ available in order to
 - 2.1. decrease the static pressure inside the orifice
 - 2.2. manipulate P_2 as a function of pumping speed S via the pressure gradient (dp°/dx) across the " resistor to flow ".

The limiting physics of a " resistor to flow " cast considerable doubt on the possibilities to maintain the continuity of the process claimed under P 44 06 333 4 as well as to control the process as a whole, since:

1. A decrease in (static) pressure in the orifice would require a definition of the " resistor to flow " in patent application P 44 06 333 4 [161], especially the coefficient of flow resistance, c_F , (i.e. for flow surrounding a deliberately shaped geometrical element) as well as the ratio of the surface area of the sum of the orifices of the flow channels, i.e. ΣA_o , relative to the surface area of the overall resistor, A_R . However, these parameters were not defined or claimed.
2. Even if there was a (local) decrease, $\Delta p_{o,s}(T)$, inside the orifice this decrease does not give any guarantee for a decrease $\Delta P(\Delta T) = k (P_1 - P_2)^{1)}$ corresponding to the sharp, gradient $(dp^\circ/dx)^{1)}$ across the interface of a diaphragma allowing for the required discontinuity in the overall profile of pressure along the x-component of the dimension of the overall process, i.e. between evaporation sources on the one side and substrate and deposits, respectively, on the other. Only this gradient (dp°/dx) across the interface allows for the required control of the evaporation of constituents of (very) different evaporation pressures. Patent application P 44 06 333 4 [161], however, claims that the " resistor to flow " should contain a " matrix of orifices " instead of a " matrix of resistors ". Consequently, the resultant pressure gradient between evaporation sources and between deposit(s) / substrate(s) was claimed to be " monotonic " instead of " discontinuous ". Such possibilities include the Venturi-type of jets, but then again it would be necessary to define the decrease in cross-section and / or surface area of outlet relative to intake and which was not done.

Therefore, the process claimed under P 44 06 333 4 [161] is limited (in the case of absence of condensation) by the speed of sound leaving no manoeuvrability for an in-situ control other than condensation. Condensation between evaporation source and deposition level, however, is a contradiction to the fundamental requirement of the process itself which was claimed to be designed for economically viable products from the vapour phase so to explore the productivity of vapour deposition technology.

¹⁾ for clarity: dP/dx is the macroscopic pressure gradient across the interface at any given point. $\Delta P(\Delta T) = k (P_1 - P_2)$ is the resultant, but not operative driving force for vapour flow and (dp°/dx) is equivalent to the local driving force at the flow channel which becomes operative due to the characteristics of the interface there including the engineering solutions claimed below.

A process which is controlled by condensation or by the speed of sound or by both is not controlled by a " resistor to flow " which is the principal claim in P 44 06 333 4 [161]. The principal objective of a continuous vapour deposition process, however, is to avoid condensation other than on the substrate(s) / deposit(s), the latter particularly being a transformation from the vapour to the solid phase, i.e. any formation of a liquid phase must be avoided in the overall process in order to achieve sufficient productivity and quality. Condensation and speed of sound are not patentable unless an engineering solution to control condensation and / or speed of sound was claimed. This is not evident from patent application P 44 06 333 4 [161], the application is thus not patentable.

The only solution to generate a pressure gradient (dp°/dx) according to the required gradient $\Delta P(\Delta T) = k (P_1 - P_2)$ by using a " resistor to flow " would be case 1.1 of the limiting physics (p. 61). This was obviously meant to be, since vapour was shown to be evaporated "upwards " , i.e. against the forces of gravity, but this was not explicitly defined or claimed and would require again the definition of an engineering solution. Any control of a continuous vapour deposition process involving interfaces to separate evaporation chambers should provide superheated vapour at rear of the interface, i.e. at the outlet to avoid condensation in the adjacent chamber resulting from turbulent flow (see below).

Possible solutions, however, include a membrane or diaphragma as claimed in this invention which provides a high coefficient c_F *in front of* the " resistor to flow ", i.e. at its intake to increase turbulent flow there even further, but it also requires a device allowing to collect condensed droplets when falling down so allowing for the re-use of material and rendering local condensation in front of the " resistor to flow " instrumental to a " mass filter " according to a diaphragma, but this was then not a characteristic of the " resistor to flow " itself and consequently it was not claimed and would be only readily applicable to alloy vapours of an alloy phase diagram without showing an immiscibility gap in the melt.

If condensation was a solution to the problem in patent application P 44 06 333 4, i.e. a method to generate a pressure gradient (dp°/dx) across the separating interface, it is very doubtful whether this process will work without further engineering solutions and, more importantly, whether it provides a good solution.

The Diaphragma: Principal Engineering Solution to Control Continuous Vapour Deposition
The force of the " resistor to flow " in aero- and hydrodynamics is defined as [160]:

$$F_F = F_P + \Sigma F_{Fr} \quad (9)$$

where F_F : force of a resistor to flow occurring upon turbulent flow, i.e. at velocity v beyond the critical velocity v_{crit}

- F_P : force of a resistor to pressure
- ΣF_{Fr} : force of (internal) friction for laminar flow of a liquid in a cylindrical tube, i.e. $\Sigma(8\pi\eta lv)$ with η = coefficient of *internal* friction (dynamic viscosity), l = length of individual tube (flow channel) and v = mean velocity inside tube (channel); for gases, however, η_{gas} is about 0, since laminar gas flow does not generate flow contact of the individual atoms, while turbulent flow should be minimized particularly *behind* the interface of the diaphragma, i.e. in chamber $n+1$, to avoid condensation there; therefore, ΣF_{Fr} = negligible (i.e. approaching 0).

while:

$$F_P = c_p \frac{1}{2}(\rho v)^2 A \quad (10)$$

- with c_p : coefficient of pressure resistance of the resistor to flow (or a diaphragma), which is different from the pressure resistance of an interface without flow channels. c_p is a function of the mean velocity in front of a resistor or an individual resistor element as well as of the intensity of turbulences at rear of an resistor element and insofar c_p is a function of the geometry of the resistor element(s) employed
- A : front surface of a resistor or an individual resistor element facing the approaching laminar flow.

Note that the hydrodynamic pressure, $\frac{1}{2}(\rho v)^2$, is preset by the pressure difference as to eq.ns (5) and (6) so by the required pressures of two adjacent chambers. That is why A and c_p must be adjusted to the required alloy composition and productivity (i. e. the throughput Q_v). Since ΣF_{Fr} = negligible (i.e. about 0) here, the coefficient of flow resistance (cf. above, i.e. for flow surrounding an element of given geometry), $c_F = c_p$ and eq.n (9) can be written as

$$F_F = c_F \frac{1}{2}(\rho v)^2 A \quad (11)$$

Physically speaking, the resistor to flow transforms incoming lamellar flow (and/or under vacuum also incoming molecular flow) into outgoing turbulent flow of a gas or a liquid by narrowing down the distribution of flow lines into the "hollow" space made available by the flow channels [161]. In fact, the continuous evaporation process needs an interface between two successive evaporation chambers with exactly the opposite characteristics compared to a resistor to flow claimed in [160]: the incoming vapour (i.e. incoming from chamber 1 or n) is inevitably turbulent and/or undirected due to evaporation by thermal or magnetron sputtering methods and/or stirring actions resulting from the mixing zone (cf. [160]) and must provide macroscopically (i.e. over the cross-section of the entire resistor to flow) a parabolic distribution in the density of flow lines, since the matrix of flow channels does not cover 100% of the resistor to flow according to patent application P 44 06 333 4. The outgoing vapour (i.e. out-

going towards the deposition chamber 2 or n+1), however, must achieve a maximum degree of laminar and/or molecular flow to avoid turbulences (which are the loci of forced atomic collisions, pressure increase and resulting nuclei for condensation) and to result in a uniform distribution (density) of flow lines there for a number of reasons including the risk of condensation in conjunction with incomplete adiabatic processing resulting in an undue local decrease of coefficient γ of the polytropic change of state of corresponding vapour particularly for negative temperature gradients across the interface of the resistor to flow and insufficient adjustment / control of local pressure differences particularly for positive temperature gradients across the interface of the resistor to flow required to produce a uniform thickness of the resultant deposit. An interface which provides the opposite, of course, is no more a resistor to flow, but a diaphragm as is evaluated in the following.

The force of the resistor to an *undefined* type of flow is not only not important with regard to the required diaphragm, it also has to be kept as low as possible in order to minimize the resistance to *undefined* flow when the vapour crosses the interface of the required diaphragm. More particularly, turbulences *in front of* (not within) the diaphragm increase the pressure locally so increasing the local driving force for transfer of vapour from one into the following evaporation or deposition chamber. That is, the freedom in control variables is increased by turbulent flow *in front of* the interface and/or by a *homogeneous flow line density of directional laminar and/or molecular flow* behind the interface as is evaluated in the following. Inso-far, what is needed here is a *resistor to turbulent and/or undirected flow* combined with a *conductor for lamellar and/or molecular flow* to bridge dynamic equilibria of a polytropic change by sophisticated local control of the gaseous state of matter as is dictated by a sharp positive static pressure gradient required according to processed material and/or required productivity (i.e. decreasing static pressure in the direction of x-translation of vapour flow lines) and in order to override negative (increasing) and positive temperature gradients without condensation so solving the problem of process control of continuous vapour deposition. However, this is the opposite of the established definition of a resistor to flow (see [161]) and a very interesting, since unorthodox and inverted problem with regard to classical aerodynamics.

Mathematically speaking, eq.n (11) does not apply anymore and eq.n (9) must be evaluated on the understanding that F_F should be very small (not negligible), while F_P is relatively large and a third term is to be introduced for the required diaphragm which compensates for the difference between the two former following:

$$F_F = F_P - F_D \quad (12)$$

where F_D refers to any type of "mass filter" without compositional change (see below) including those arising from a "clogging flow " due to condensation at an interface that is designed to separate adjacent evaporation chambers. Eq.n (12) shows the physical meaning

of what results into the sum of the required forces to control the process:

$$F_P = F_F + F_D \quad (13)$$

where in particular

$$F_D > F_F \quad (14)$$

involving a change from the control of a "clogging"-type of process via the resistance to an undefined type of vapour flow to control via the forces of pressure differences which not only incorporate the forces of the invented diaphragma, but which are in particular dominated by them. What is F_D physically ? And how does it physically relate to F_F ?

A diaphragma is used to be defined by a (semi-permeable and/or porous) wall separating (i.e. keeping separately, not filtering and/or not necessarily filtering !) two different substances or matters, which can be either a liquid mixture or a gas mixture, by allowing for a (directed) throughput from one into the adjacent substance, i.e. by a flow into one direction, a directional flow which corresponds to laminar flow in aero- and hydrodynamics and to laminar and/or molecular flow in our new process. The classical, membrane-controlled process is used to be called "osmosis" which represents an adjustment of the concentration of one substance with respect to the other (which are at the same time kept apart by the membrane) via a flow of mean velocity being significantly smaller than without diaphragma. That is: a (usually aqueous) solution (eg. water) is moved from a dilute state (eg. pure water) into the more concentrated solution (eg. polluted HCl takes water up to the top of a tree). The driving force to adjust the concentration accordingly, i.e. to fulfill its functional purpose is proportional to the local flow velocity and is called "osmotic pressure".

The driving force for the classical osmosis, i.e. the osmotic pressure of liquids and gases of different composition depends on the transmembranic pressure gradient $\Delta P(T,V)$ *as well as* on the concentration difference, Δc , across the (interface of the) membrane resulting in the osmotic pressure, $\Delta \pi(\Delta c)$, following

$$\Delta F_{Os} = \Delta P(T,V) - \Delta \pi(\Delta c)$$

(n.b. the interface of the diaphragma in the present invention is assumed to represent the shortest distance of separation of the two different substances which is not the same than the overall dimensions of the claimed individual elements of the diaphragmas invented here, see below), i.e. the normal separating both mixtures. In the present process, however, there is no transmembranic "osmotic" barrier in the classical sense, since the exchange of gas and/or vapour is independent on concentration and subjected to an entirely different objective (i.e. not to the separation, but to the synthesis of matter and materials). Since there is no control of transmembranic mass transfer by the chemistry of the vapour concerned, there is also no classical "osmotic" pressure. "Osmotic"-type of barriers are provided instead by an increasing

temperature across the interface of the diaphragma, for example, i.e. a physical type of osmosis in which the variable vapour temperature is controlled by employing suction flow driven by underpressure, the final underpressure in the deposition unit being controlled by the pumping speed of the vacuum pumping system employed. Unlike for the process of gas permeation, for example (where $\delta\Delta P$ is triggered by fluctuations in front of the membrane), the *overall* pressure difference in the present vapour deposition process invented here so $\delta\Delta P$ is therefore not (apart from local exceptions including individual evaporation / vacuum chambers) controlled by a vapour pressure building up due to the (eg. vapour) pressure of the vapour sources in front of the diaphragma, but as a result of suction at least behind the last membrane prior to vapour deposition.

The resultant physical-type (i.e. *independent* on concentration of both adjacent mixtures for a given temperature) of osmosis of a gas or vapour, however, is only a function of pressure following (cf. [161], p. 97):

$$E = (dV / V dp) = 1/P \quad (15)$$

with E = expandability of the gas. This was derived from the law by Boyle-Mariotte following:

$$V dp = \text{const. } dm \quad (16)$$

where dm is assumed here to represent the mass exchanged per unit time over the interface of the diaphragma. In order to define a universal diaphragma that is independent on either an increasing temperature (i.e. a negative temperature gradient $-\Delta T$) or a decreasing temperature (positive temperature gradient $+\Delta T$) across the interface of the diaphragma, eq.n (16) has to be transformed to

$$\text{const. } dm_D < (V dp)_D \quad (17)$$

Obviously, macroscopic control of vapour mass exchange between two evaporation chambers or an evaporation and a deposition chamber requires that the effectively released mass

$$dm_D < dm \quad (18)$$

where dm represents the exchanged mass of a "resistor to flow", for example. F_D is therefore proportional to corresponding difference, i.e. $F_D = k (dm - dm_D)$.

That is, in order to control mass flow between two adjacent chambers even for increasing temperature, the effectively released mass dm_D has to be decoupled kinetically from $dp = f_n (S, \Delta T)$ without affecting (i) the proportionality between dm_D and the velocity of vapour flow between both chambers *or* (i.e. (ii) is alternative) (ii) the wake effect of the pumping system. Instead of draining the evaporation sources by excessive acceleration (speed of sound) and bunching of vapour flow lines via Venturi-type of nozzles (including the "resistor to flow" made up by a matrix of flow channels directing the vapour towards the adjacent chamber) so eventually triggering condensation, a dynamic equilibrium of mass exchange is generated

involving (see below) 1) expansion and 2) acceleration of a *discrete* mass of vapour dm_D towards the substrate and growing deposits, but already within the diaphragma. Decoupling of the resulting vapour throughput Q_v (in [W], [Pa m³/s], [Nm/s]) from pumping speed S , however, is per se an osmotic problem and requires the use of a membrane. The resultant physical-type of osmosis (essentially without chemical change) for vapour deposition takes advantage of macroscopic static pressures and resultant pressure gradients, microscopic hydrodynamic pressures, local vapour velocity and the momentum of the vapour to provide the required transmembranic change of state of matter and process control.

Due to the laminar and/or molecular flow inside a cylindrical flow channel between two adjacent vacuum chambers separated by a membrane, eq.n (7) can be re-written as:

$$\Delta p_o^{\text{overall}}(T,S) = (p_1(T) - p_{o,s}(T)) + 1/2 (\rho_1 - \rho_{o,s}) [(v_1 - v_{o,s})]^2 \quad (19)$$

The continuously maintained static pressure drop between the two adjacent chambers requires that $p_o = P_2$. This cannot be achieved by lamellar and/or molecular flow through an (undefined) matrix of flow channels even via Venturi-type of jet nozzles providing a reduction in throughput area. $\Delta p_o^{\text{overall}}(T,S)$ is given by the pumping speed of the system and the alloy to be processed, the term $p_1(T) - p_{o,s}(T)$ should be controlled in such a way that $p_o = P_2$ and P_1 and v_1 are also assumed to be preset by the system. The remaining variables are $\rho_{o,s}$ and $v_{o,s}$. One way to evaluate the transmembranic state of gas (flow) as a function of macroscopic conditions is:

$$\begin{aligned} 1/2 (\rho_1 - \rho_{o,s}) [(v_1 - v_{o,s})]^2 &= - (p_1(T) - p_{o,s}(T)) + \text{const.} \\ &= p_{o,s}(T) - p_1(T) + \text{const.} \\ 1/2 (\rho_1 v_1^2 - 2\rho_1 v_1 v_{o,s} + \rho_1 v_{o,s}^2 - \rho_{o,s} v_1^2 + 2\rho_{o,s} v_1 v_{o,s} - \rho_{o,s} v_{o,s}^2) &= p_{o,s}(T) + \text{const.} \\ - k_1 v_{o,s} + k_2 v_{o,s}^2 - k_3 \rho_{o,s} + k_4 \rho_{o,s} v_{o,s} - \rho_{o,s} v_{o,s}^2 &= p_{o,s}(T) + \text{const.} \end{aligned}$$

The transmembranic vapour and/or gas transfer, i.e. the throughput under the maxim of vapour deposition process control by means of a membrane, is thus controlled by the P_1 -independent term $\rho_{o,s} v_{o,s}^2$, i.e. a decreasing static pressure in an individual flow channel, $p_{o,s}(T)$, requires an increasing product (!) of density and velocity, $\rho_{o,s} v_{o,s}^2$ as a result of an increasing term $v_{o,s}^2$ and a decreasing density, $\rho_{o,s}$, (see term $k_3 \rho_{o,s}$) itself, of the traversing vapour. While the local density of the gas (flow) controls the reduction of static pressure locally, the velocity v_o is required to compensate for this decrease by an increase in directional momentum of the (evt. monoatomic) gas species. The decrease in density of traversing vapour inside the diaphragma is the most important parameter to be controlled in order to provide a universal diaphragma that is independent on either an increasing or decreasing temperature. Therefore, the design should allow for a substantial reduction in the density of flow lines within the diaphragma between intake and outlet while providing possibilities to accelerate them at the same time so relaxing the requirements for local density (pressure) reduction upon transmembranic vapour transfer.

As a result, the employed suction flow overruns the possibility of osmotic pressure gradients in their classical = chemical sense, i.e. there is essentially no difference in the chemical potential across the interface in the very vicinity of a transmembranic flux channel (or pore). This is, however, the working principle of the diffusion pump, but without premature condensation. The compositional gradient over the interface of a classical membrane for the separation of chemically different constituents/species is replaced by a local gradient in density and/or temperature. The locus of the characteristic boundary layer (in the classical sense) is thereby removed from the front of the interface to any transmembranic position between front face over center-line of the transverse cross-section (i.e. perpendicular to the local x-normal independent on whether the diaphragma has a curved surface or not) and/or up to the rear of the interface (see Fig. 88).

Engineering Solutions for the Diaphragma

The exchanged mass dm_D is proportional to the magnitude of traversing laminar and/or molecular flow, while the turbulent fraction of traversing laminar and/or molecular flow is proportional to the (risk or probability of) condensation so composition fluctuations to take over control of vapour flow. The resulting consequences for an appropriate engineering solution include:

1. The turbulent fraction of traversing laminar and/or molecular flow has to be minimized by an appropriate engineering solution in any case.
2. A continuous increase in vapour temperature within the diaphragma should improve the control of the required (laminar and/or molecular) mass exchange for increasing temperatures.
3. Vapour acceleration should be coupled with superheat sufficient to compensate for vapour cooling resulting from radiation prior to atomic attachment at the deposit.

There are several engineering solutions available to provide a diaphragma for the synthesis of metallic vapours in a continuous vapour deposition process:

- 1) *Single and multiple (series of) bifurcations* as an anti-nozzle system (Fig. 90). Bifurcations represent the opposite of jet nozzles applied to gas atomization of liquids, for example, in order to maximize fragmentation. In vapour deposition, fragmentation is maximized by nature and requires control of condensation. The bifurcations are constructed in such a way that the pressure of each individual outlet for backstreaming vapour, P_B , is smaller than the pressure at the intake, P_I , i.e. $P_I > P_B$ so to allow for partial backstream of a substantial fraction of dm , i.e. the difference $dm_B = dm - dm_D$ into any of the preceding chambers where the vapour comes from. The advantage of bifurcations: they provide an elegant basic solution without excessive turbulent flow inside the diaphragma and in conjunction with the use of flow line elements as outlet configuration at rear of the diaphragma or in conjunction

with a trumpet-like outlet which again represents the opposite to the nozzle design used in gas-atomization (Fig. 91) and can involve angular and smoothed out single and multiple conductances with and without confined gaseous flow (eg. to accelerate vapour velocity towards the deposit) arriving at the use of multiple octopus-like configurations (i.e. configurations including diffuser -to- jet nozzle transitions (Fig. 91).

- 2) The use of *constructional elements with large c_F -values* to generate turbulences at medium distance from the intake by simultaneously avoiding them directly at the orifice and at the outlet of the traversing flow channel so to create relatively large static pressure in front of the orifice of corresponding flow channel, i.e. away from the interface of the diaphragma as to Fig. 92, the turbulences, thereby reducing the laminar and/or molecular flow in any of the evaporation chambers n (or $n^\circ 1$), $(n+2)$ or $n^\circ 2$ etc. so "filtering" directional flow down to a fraction compared to that without the use of corresponding constructional elements, of which the corresponding c_F -values ranging from 0.25 to 5, in particular between 1.1 and 3, the higher values thereby obtained by a combination of individual elements comprising *to suppress turbulent flow* at rear of the diaphragma as well as at the immediate intake area include trumpet-shaped in- and outlets of which the resulting coefficients of flow resistance, c_F , shall be not larger than 0.25.
- 3) If the force of diaphragma, F_D , is large as to (a combination of) claimed solutions of 1) and 2), a relatively large internal resistor to flow , F_F , is affordable by the diaphragma (see eq.n (14)). This is particularly useful for large P- and T-gradients to be achieved. Instead of a single matrix of flow tunnels (cf. [161]) which is not a very efficient resistor to flow according to a parallel electrical switch, a *series of successive resistors to flow* is orders of magnitude more efficient by superimposing various resistors to flow which can consist of a matrix of resistor elements which are arranged equidistantly between the flow channels or not and which embrace the following characteristics (cf. Fig. 93):
 - a) the overall resistance to flow increases with increasing number m of resistor levels employed (Fig. 93) and/or
 - b) the local laminar and/or molecular velocity of vapour inside the flow channel, v_o , can be increased by reducing the relative orifice area (projection of available flow lines). i.e. the surface area fraction (ratio) of intake-to-resistor, $\Sigma A_o / \Sigma A_R$ decreases progressively with increasing numbers of resistor level m , and/or
 - c) v_o can be increased by keeping the relative orifice area $\Sigma A_o / \Sigma A_R$ constant, but increasing the temperature differentially with each discrete level of m , and/or
 - d) v_o can be increased by a combination of b) and c) and/or
 - e) but p_o has to be decreased at the same time. so must decouple the absolute amount of projected inlet-area from projected outlet area per resistor level and this can be done by
 - e1) a progressive increase of the absolute surface area of the orifices of level $m+1$ with regard to that of level m and/or
 - e2) the introduction of an increasing overall area $\Sigma A_o + \Sigma A_R$ and/or

- e3) the introduction of a differential volume in front of level m which acts as a differential vapour reservoir likewise allowing the vapour to adapt the required partial temperature increase and which may include heating serpentine here which are traversed by the vapour volume dm_D or dm , and/or
- f) while all of the solutions 3a) to 3e) can be achieved with and without turbulences, the amount of required turbulent flow being optimized with regard to the required gradient dP/dx and dT/dx across the interface of the diaphragma by introducing flow line elements in front of the differential resistor elements or in front of part of the resistor elements of a selected fraction of m-levels as well as at rear of the final outlet level m^{\max} .
- 4) Finally, any combination of the principal engineering solutions 1) to 3) as indicated in Figs. 90 to 93 and resulting in overlapping simple or more complicated solutions as reproduced schematically in Figs. 90 to 94. should provide a satisfying solution for the required engineering alloy composition at a given productivity.

Maintenance of Driving Force Suction Flow

A comparison shows the hierarchy of functional levels patented so far:

<u>Rank</u>	<u>Functional Level</u>	<u>Patent by</u> <u>[100]</u>	<u>This Patent</u>
1	Driving Force for Productivity: Underpressure in Deposition Unit maintained by Vacuum Pumping System	no	yes
2	Maintenance of Driving Force (Form of Control of rank 1)	no	(see below)
3	Principal Engineering Solution to Realize the Maintenance of The Driving Force: Diaphragma	no	yes
4	Principal Membrane - Elements: eg. Bifurcations, Geometrical Elements at Rear with low c_F -values	no	yes
5	Secondary Membrane - Elements eg. series resistors, whirley elements in front of diaphragma	no	yes
6	Controlling elements of rank 5: resistor surface and c_F -values	no	yes
7	Non-controlling elements for rank 5: eg. length of straight tube sections, conductance	partially	partially

In analogy to the movement of the melt extraction drum in the melt extraction process(cf. [102], for example, the movement of the surface of the growing deposit of the condensor and collector system has to provide the conditions for diaphragma-controlled extraction of vapour throughput from the final evaporation and/or vapour mixing chamber, i.e. the final (alloyed) vapour reservoir on the one hand and the at least one deposition unit on the other in order to maintain the pressure gradient between both chambers (eg. between the (n+1)- and the (n+2)-unit) which then controls and/or communicates with (the throughput of) all other units of the overall vapour deposition process by suction flow.

The operative vapour accommodation factors α_T on the deposit surface are a function of the vector sum (parallelogram) of the velocity of the vapour (trajectories) emerging from rear of the (final) diaphragma on the one hand and the velocity of the deposit surface on the other. In a first approach both velocity vectors are assumed to be constant. For molecular flow conditions it is then evident that the (perpendicular) distance h between rear surface of the final diaphragma and deposit surface opposite to the rear surface must not exceed a value which is a function of the mean free path MFP of the vapour concerned where

$$\text{MFP} = kT / (2^{0.5} \pi a^2 p)$$

with p = overall pressure in flow channel, a = diameter of atoms or vaporized molecule concerned, T = vapour or gas temperature and k and π = constants (Boltzmann and 3.14, respectively). For both the lamellar and molecular flow condition, the use of a rotating (circular) disc and/or deposition surface (cf. [100]) introduces a third component into the vector balance between final diaphragma and deposition surface and would require a definition of how the effect on accommodation factor of the change in deposit surface velocity with distance from the rotating axis (pivot) is controlled by transmembranic vapour momentum in order to achieve uniform conditions of vapour accommodation on the deposition surface. These details are part of an additional patent to be laid down within the next ten days after deposition of this patent.

The operative accommodation factor dictates the degree of decoupling of $Q_v(x)$ from pumping speed S and is a function of the volume fraction of vapour reaching the deposit surface as well as the (loss of) momentum of the vapour after passing through the final diaphragma prior to deposition. In the most simple case of a straight cylindrical flow channel, the balance of the momentum forces within the hypermembranic distance h (i.e. the distance h between (rear) surface of diaphragma and deposition front surface) depends (for a given vapour state in the preceding evaporation and/or mixing chamber) on the diameter d_z of the cylindrical flow channel, since the further variables to control h_{eff} (for a required = given α_T), i.e. p , ρ , and v and the resultant nature of turbulent-free transmembranic vapour flow is directly controlled by d_z . That is, h_{eff} is a function of d_z unless a specific control of the transmembranic momentum was defined. The condition for laminar flow is

$$(d_z/2) \text{ MFP} \gg 1 \quad (1)$$

that for molecular flow is

$$(d_z/2) \text{ MFP} \ll 1 \quad (2)$$

and for the transition between both regimes:

$$0.1 \leq (d_z/2) \text{ MFP} \leq 10 \quad (3)$$

from these relationships it is evident that the maximum hypermembranic distance, h_{\max} , between (rear) surface of final diaphragma and (front of) deposition surface (and therefore the control of decoupling $Q_v(x)$ from S_{req}) is for lamellar flow a function of d_z , for molecular flow a function of MFP and for mixed vapour flow through the final diaphragma a function of a dimensionless value, which varies by two orders of magnitude.

The use of the geometrical flow elements with low c_F -values suppress the formation of turbulences within the distance h_{eff} . Under this condition, the vapour stream is eventually deflected laterally by collision with atoms moving with vector - components into y- and z-direction and which are eventually controlled by the velocity and roughness of the deposit surface and by the density of protrusions on the deposit surface. The lateral deflection per atom increases with decreasing pressure (i.e. increasing underpressure for a given pressure gradient) in the vacuum chamber /-system accomodating the deposit and with decreasing distance $h_{\text{eff}}(F_0)$ where F_0 = transmembranic vapour momentum. On the other hand, the number of collisaons decreases with decreasing pressure / increasing underpressure in the final vacuum unit. Consequently,

$$h_{\text{eff}}(F_0) < h_{\max}(\alpha_{A,\text{crit}}) \quad (4)$$

where $h_{\max}(\alpha_{A,\text{crit}})$ is a function of lateral deflection which allows impingement of a critical volume fraction $\alpha_{A,\text{crit}}$ of vapour stream on the deposition surface. Since

$$\alpha_T = (E_v - E_r) / (E_v - E) = (T_v - T_r) / (T_v - T) \quad (5)$$

where

E_v = kinetic energy of atom impinging on substrate surface

E_r = energy of desorbed atom prior to achieve equilibrium with bulk underlayer

E = energy of desorbed atom after equilibrium with bulk underlayer was established

an atom is reflected from the deposition surface when $\alpha_T < 1$. For a given α_A -value arriving at the deposition surface (for a moving substrate the corresponding level is the velocity layer building up in front of the surface, since the velocity of the substrate may under optimized conditions control the effective accomodation according to the melt extraction by the surface of the melt extraction drum, see above), the relative accomodation coefficient $\alpha_T(\alpha_A)$ decreases

with decreasing h_{eff} and increasing α_A -values. For $\alpha_T = 1$, $\alpha_T(\alpha_A)$ is directly proportional to h_{eff} . Therefore, h_{eff} must not remain under a certain value $h_{\text{min}}(\alpha_{T,\text{crit}})$, at which α_T falls below a critical value $\alpha_{T,\text{crit}}$, i.e.

$$h_{\text{min}}(\alpha_{T,\text{crit}}) < h_{\text{eff}}(F_0) < h_{\text{max}}(\alpha_{A,\text{crit}}) \quad (6)$$

While condition (4) assures that h_{eff} controls the vapour fraction impinging on the deposition surfaces, it is the difference $h_{\text{max}}(\alpha_{A,\text{crit}}) - h_{\text{eff}}(F_0)$ which controls α_T and hence the fraction of $Q_v(x)$ deposited on the surface, i.e. Q_A . Optimization of or versus

$$\alpha_A(h) = \alpha_T(h) = 1 \quad (7)$$

allows for a large Δh_{eff} -range so maximum efficiency of the process. The ratio of both functions, i.e. $(\alpha_T/\alpha_A)(h)$ depends on dp/dx , dT/dx , F_D (see above, i.e. the local manipulation of traversing vapour stream parameters p , ρ and v) and the lateral velocity and surface quality including roughness and temperature of the deposition surface. Claim 7 shows the range of conditions for controlled vapour deposition, i.e. controlled and optimized yield $Q(A)$ of $Q_v(x)$ of the invented process and therefore a controlled decoupling of $Q_v(x)$ and S_{req} following

$$Q(A) = \Delta P_1 * q(x) * \alpha_A * \alpha_T$$

with the resulting differential

$$(\delta/\delta'x) * Q(A) = Q(A) = \Delta P_1 * q(x) * [(\delta \alpha_T/\delta'x) \alpha_A * (\delta \alpha_A/\delta'x) \alpha_T]$$

where $\delta'x = \delta x + h_{\text{eff}}(F_0)$ with δx = transmembranic cross-section, i.e. $\delta'x$ embraces $h_{\text{eff}}(F_0)$.

Engineering Solutions for the Overall Process

The best control of deposited vapour yield and/or the resulting efficiency per diaphragma element of a vapour deposition process overall driven by suction flow is given by a continuous batch process of planck collectors/condensors in the deposition level, the batch collector process thereby employing rectangular and flat condensors and resulting deposition surfaces, each of which partly covered by the overall diaphragma-outlet per pass (cf. Figs. 95, 96) and moving, in a given horizontal or vertical plane, either clockwise or anti-clockwise, i.e. in only one sense of the resulting circuit (cf. Fig. 97) and thereby describing a movement around the central axis of the overall deposition process (horizontal condensor plane) outside the range where the vapour is deposited, at least around the central axis of the deposition unit (which may be inclined at angle $0^\circ < \delta_{\text{dep}} \leq 90^\circ$ (cf. Fig. 98) with regard to final evaporation and/or mixing chamber and/or corresponding diaphragma). Compared to a reciprocating planck-collector, for example, the continuous batch process moving in one sense assures constant ΔT -intervalls between "exposure" to impinging vapour and outside, i.e. $\delta \Delta T = 0$ (cf. Fig. 97). Compared to a (rotating - collector drum and collector disc, the continuous planck process provides uniformity and maximization of vapour accomodation factors due to constant deposition surface velocities and constant angles of

impingement, i.e. minimization of components of different velocity vectors in the moment of atomic impact. The resultant deposit does not explicitly provide curved surfaces so no need for pre-forming operations prior to conventional alloy conversion procedures into semi-finished and/or (final) product form. That is, the continuous batch process employing flat and rectangular (plate-(like)) collector / condensor provides the best conditions to control decoupling of throughput $Q_v(x)$ and underpressure in the final vacuum unit so near-net shape production (eg. of sheet, plate etc.) at relatively high deposition rates, technically easy combinations of constructional variants of individual vacuum chambers and in particular the combination of one single and large final evaporation and/or mixing chamber with several individual, but communicating deposition units so a large variety of possibilities to control the overall process by fine tuning the involved parameters (transmembranic gradients of vacuum state, local deposit surface velocities etc., see above).

The technical details of the collector batch process are shown in Figs. 96 - 103. According to Figs. 96 - 103, the condensers and/or deposits are accommodated by a vacuum chamber of the sections designated with (31) and (34), which move in (a) ring-like or (a) multi-angular (cf. 21a) vacuum chamber(s), the latter being positioned around a coaxial (hollow) shaft (13j) which accommodates a propulsion shaft (13i) for the transport of the overall collector system, the operation of transport thereby supported by pushing stamps (24), pushing and/or pulling jaws (25), claws (26) and other gripping devices as well as rolling tables (27). The hollow shafts are eventually accommodated in a coaxial tube (55) accommodating rotating/rotatable anti-friction bearings (56). The propulsion shaft (axle-tree) (13i) rotates around a rotation axis A_R with an orientation which is independent on gravity vector g and being connected with the condensators by conductances for a chill medium, in particular a liquid such as nitrogen, water and/or oils, the conductances located concentrically in the internal cross-section of the tubes (not shown here). The chill-medium is distributed via a rotating distribution and collector (13d) to conduct it to the condensators and to return it to the refrigerating aggregat (13f).

The condensers embrace chill tunnels being eventually arranged in form of a meander (rectangular condensor and disc and drum) and/or by a circular conducting sheet (disc-type of condensor) allowing for optimized conductance efficiency and/or contact of the flow of the chill medium within the condensor (rectangular or disc) with the deposit (preform, layer, etc., see claim 1). The bottom of (53) of the vacuum chamber(s) in the deposition level is adopted to the form of the vapour chimney, their transition from the evaporation- and/or mixing zone (cf. 19, 19b and 19c) towards the final diaphragma and the form of corresponding (final) diaphragma prior to deposition. Smaller and eventually pilot-plants with disc-type (circular) condensor(s) embrace a small concentric aperture in the vacuum chamber (51) for penetration of the hollow shaft (54). By contrast, the part (level) of the vacuum chamber (34) for the condensor - batch process comprises a slit-type and vacuum-tight, here not further described guide rail, in which the conductance for the supply of the condensor(s) with the chill medium moves by means of rotation

around corresponding supply shaft. Accordingly, the entire distribution system for the chill medium including 13a to 13d and 13i is accommodated by one or two vacuum chamber(s) (cf. 13o) which increases, on the one hand, (dramatically) the overall volume of the vacuum chamber on the deposition/condensor level of the process, but makes on the other hand - the guide rail redundant. Both solutions combined so that the overall vacuum chamber system in the deposition level comprises several chambers, the resulting multiple vacuum chamber system with gradually decreasing vacuum pressures towards a) the deposition zone (21) (see also side view (31)), which is separated from b) the zone of in-situ consolidation (21a) by (eventually movable/moving) separation walls (17) and by (eventually movable/moving) separation segments (33) as well as from c) the lower part of the vacuum chamber (34) and finally from d) vacuum chamber (13o), which accommodates the supply system and conductances for the chill medium by providing a lowest possible vacuum chamber height and thereby either connecting the lower part of the vacuum chamber or being separated from them.

The large advantage of this condensor-batch circuit process is the application of constant lateral velocities v_{Kon} of the deposition surface in contrast to the significantly varying surface velocities ω_{Kon} of a circular condensor. As a result, the process is controlled by constant $h_{eff}(F_0)$ -values as a function of the y- and z-translation, i.e. the surface coordinates of the diaphragma, providing larger Δh_{eff} -ranges for the condition $\alpha_A = \alpha_T = 1$ and, accordingly, better controllable throughput and deposition powers $Q_v(x)$ and Q_A , respectively (see above).

Consequences / Conclusions

The claimed alloys were not only highly supersaturated, but they were also very ductile on bending as is indicated by the entire absence of second phases. Vapour deposition for supersaturated solid solutions of light rare earth and/or early transition metals and/or metalloids as well as selected simple metals in magnesium thus provides an outstanding avenue to develop passive magnesium alloys with a perspective for economically viable products.

Limited reproducibility of the resultant alloy composition has so far limited the productivity of vapour deposition. The diaphragma for the physical-type of gaseous osmoses by employing forced convection over the entire evaporation and vapour deposition process renders the reproducibility of alloy composition so final quality directly proportional to $dm = fn(dp)$ for $S = \text{const.}$ so to the imposed pumping speed S and the resultant productivity of a given evaporation system. That is, an appropriate interface which is able to control $dm_D = fn(dp)$ increases alloy quality with increasing (imposed) pumping speed and productivity and this is the key point for vapour deposition technology to become industrialized. High productivity vapour deposition processes are applicable to the distillation of condensed matter including water, aqueous waste solutions including the more awkward cases involving poisonous constituents as well as for purification of metallic and other elemental species such as (commercially) pure magnesium, alkaline earth metals such as calcium, rare earth metals and aluminium, for example.

Vapour deposition is an "Umklapp" process of the fragmentation-growth normal issue in rapid solidification processing: the efficiency of non-equilibrium processing increases dramatically at the frontier of fragmentation on the atomic level and is given for granted by evaporation techniques. Front velocities are orders of magnitude larger than the sustainable growth velocity of the preform, plate, disc, layer, film, or whatever form of deposit. The more consequent methods to control vapour deposition processing therefore invert the principles used for rapid solidification from the melt: instead of control of fragmentation (which can never be done as good as by nature itself), vapour deposition requires rigorous control of condensation. The key of this control is the diaphragma which opens the commercial avenues into a new era of alloy synthesis and transformation. The ultimate barrier to succeed with rapid solidification is set by the competition between the degree of mass fragmentation and in-situ consolidation to form bulk components without the need to recur to powders. In-situ consolidation of a given non-equilibrium structure is limited by the effective scale of the growth normal which becomes practically identical with the growth normal of the deposit. Therefore, consideration of cooling rates and equilibrium thermodynamics have yet obstructed the view for the real potential of rapid solidification including in-situ consolidation to reverse fragmentation in a single operation. The era of rapid solidification is obliged to a major breakthrough. The productivity of optimum fragmentation and consolidation is directly coupled. Vapor deposition is the ultimate solution in materials science, since it involves atomic scale solidification paths so approaching zero-latent heat per discrete volume transformed, hence zero-recalcence and, as a universal consequence, practically unlimited scale of corresponding growth normals even for the largest possible departures from equilibrium.

The absence of recalcence not only allows for property jumps, it obliges to mass production of corresponding "super"materials. Vapour deposition is a continuous growth process along the normal to the solidification front, while rapid solidification from the melt is always a discontinuous process. Small childs know the analogy: the chill effect of a condensed substance such as ether etc. on the skin does not disappear before the substance itself has disappeared.

As a result, thermal evaporation is inevitably linked with a distillation effect and this is given for granted as stainless steels by equilibrium ingot metallurgy. The invented process may therefore be considered as another form of "clean room" technology, an never underestimatable attribute in particular for those materials which are known to require demanding long term properties such as the resistance against fatigue, creep, damage tolerance and corrosion in weathered environments and which will improve phase selection by controlled nucleation in the future and which is a subject with particular importance for the production of semi-conductors such as porous silicon.

For reactive materials such as Mg, Al and Ti, alkaline and rare earth metals, for example, however, subsequent in-situ consolidation provides protection against contamination of the other-

wise relatively unlimited surface area of the deposit and evaporated powder, respectively, by oxidization, inclusions due to processing etc. Therefore, any of the claimed process combinations of evaporation and/or mixing chamber units on the one hand and collector-containing units on the other transforms the materials property issue of advanced processing into a productivity-quality issue of advanced processing. The invented process configurations represent the most effective, i.e. the most productive and best quality fragmentation-consolidation configuration yet available independent on inherent materials parameters such as vapor pressure, specific heat, reactivity with O_2 etc..

The high-productivity evaporation is the inherent characteristic of the invented process and is independent on the vapour pressure of the elements due to control of operating vapour pressures by means of diaphragmas. The universal consequences of rapid solidification processing are dictated by the efficiency in materials fragmentation, chemical and structural homogeneity and subsequent consolidation. Evaporation and deposition of vapor constitutes the ultimate level, since fragmentation so latent heat extraction arrives at the atomic length scale resulting in theoretically unlimited growth normal n per unit surface of metastable metallic alloyed and unalloyed phases. Therefore, evaporation and deposition of vapor represents a dramatic threshold (an "Umklapprozess") for the efficiency of advanced processing.

With the invented process it is now possible to explore and exploit this potential for the first time. Physically speaking, vapour deposition isolates the property-controlling alloy conversion step and reduces phase transformation during the change of the physical state down to an individual atom. Isolation during processing of the individual atom, however, provides the universal threshold compared to conventional materials and composites: the constituting forces between the components controlling material properties move from the never satisfying phase boundaries to the interatomic forces controlled by the electronic structure of the involved components in the translational lattice or amorphous structure thereby overrunning equilibrium thermodynamics. Characteristic length scales move from the micron - range into the Angström-range and this explain partly the technology jumps bound to come and which deviates from the rule of mixtures. The permutation possibilities of materials enhanced by conventional composite technology are thereby not limited, but increased even further. A material as simple as magnesium allows already 10^{36} completely new alloy systems and reaches more than 10^{100} new alloy systems when including established alloy chemistry. Refractory atoms supersaturated in solid Mg-base non-equilibrium structures allow to supercede any form of increase in Young's modulus via the rule of mixtures and this has strong implications for the entire industry. However, the chemical aspect has so far entirely obscured that the alloy-independent microstructure controls the rest of it. The historical superlatives bound to be realized with the present technology include:

- Economically viable nanocrystalline materials
- Economically viable massive parts via the vapour phase
- Economically viable ultra-pure alloys

- Economically viable high performance magnesium
- Rapid increase of the diversity and availability of economically viable high performance structural and functional materials such as "solar silicon", in particular for light (and reactive) metals.

The innovative value and depth of the is reflected in the claims at the end of this document. The entire absence of vapour depositon in the real world of alloy synthesis requires to explore conventional casting opportunities and justifies to employ solid state syntheses methods.

However, nobody has yet forwarded a universally applicable method to patent materials and processes made by solid synthesis techniques. As for passivation of magnesium alloys, the key to solve the problem to patent ball milled (i.e. mechanically alloyed) (light) alloys in a unique way is to derive an hierarchy of operating variables which control the process. This is done in the third part of the invention (see below).

Casting Alloys including Spray Forming

Kamado et al. reported [11a] on the effect of solution treatment and ageing of Mg-Gd and Mg-Dy solid solutions in 3 wt. NaCl aqueous solution. After ageing at 200°C, the alloys showed the best improvements and this is consistent with the observations made in the present study with Mg-calcium splats, for example (see above) due to the more negative standard electrode potential of the alloying addition concerned. Kamado et al. did not report, however, on the effect of porosity of their alloys, though the alloys were in the as-cast (i.e. as-poured (microstructural) ingot-) shape without having been subjected to mechanical working by (hot or cold) forming operations. Furthermore, Kamado et al. did not report on the size of the employed melt, resultant ingot size including cross-section, slab thickness and resultant effect on microstructural scale, but they concluded instead that corrosion resistance increased with decreasing volume fraction of "eutectic compound". The comparison of the corrosion resistance of the as-cast vs. peak-aged Mg-Gd and Mg-Dy (based) alloys showed, however, that second phase separation from the ingot-processed melt is detrimental compared to corresponding solutionized and (peak-) aged condition in any case independent on whether the separated compound is "eutectic" in nature or not. A size effect on corrosion behaviour was evident instead in that the as-cast microstructure with a grain size well above 100 µm (and resultant intra- and transgranular phase separated from the melt) appeared relatively coarse, while corresponding type of solid state precipitates in the peak-aged condition are inevitably 2 to 3 orders of magnitude smaller. Size effects of compounds on corrosion behaviour were reported earlier for the Mg-Ysystem (cf. [12]). Kamado et al. did not separate the effect of individual alloying elements from the effect of impurities on resultant corrosion. It was interesting to see, however, that the work by Kama do et al. confirmed earlier work by the author in that yttrium kept in solid solution of Mg is not beneficial compared to precipitation of yttrium by way of fine $Mg_{23}Y_6$ -dispersoids such as obtainable upon "peak"-ageing. Attractive casting alloys in view of the aforementioned relevant criteria for stainless magnesium are offered by the quaternary Mg-Sc-Mn-Zr system eventually doped with aluminium and alkaline

earth of the type $[\text{at.\%Al}] = 2 [\text{at.\%Ca}]$ to develop finely dispersed alkaline earth aluminides. Sc is light and may provide the surface characteristics of titanium in magnesium. On the other hand, Zr and Mn are peritectic systems as Mg-Sc without restricting the large solubility of Sc in cph-Mg at lower levels (see phase diagram review by Rohklin et al.). The unstable solid solution of Ca and Al provides the increment in corrosion resistance by microcathodic protection (see above) as is required for engineering alloys of the otherwise soft Mg-Sc solid solution. The d coupling of precipitation from the eventual effect of homogenous solute distribution of the Pilling-Bedworth ratio of the MgO-based oxide was yet not pursued by the Japanese collaborators.

It has been tried to introduce Al-base powders made from spray-formed billets for almost 10 years now, but major success is yet to be seen. A pilot production plant for the manufacturing of as-sprayed Al-sheets is currently being aimed at exploring this low cost / high volume route via optimized design and operating conditions of linear atomization systems. Reduced numbers of hot rolling steps combined with more effective use of feed stock of spray-formed Al-alloys were considered to result in a total cost saving of 13% over the conventional ingot casting and hot rolling route. Attractive combinations of yield strength (521 MPa in longitudinal direction), thermal stability of yield strength (400 MPa at 200°C) and stress rupture resistance was recently reported for SF Al-6.2Cu-1.8Mn-0.4Mg-0.3Zr-0.3V-0.4Ag extrusions as well as for 2618-extrusions made from spray formed billets, but fracture toughness (eg. 17 MPa m^{0.5}) for the former alloy was rather poor in the high strength condition. The alloys did not show susceptibility to stress corrosion cracking, however, and were considered for HT airframe applications and, after optimization, for strength and durability critical airframe components. Fracture toughness values > 30 MPa m^{0.5} were reported [60] for SF Al-5Cu-0.5Mn at yield strength 430 MPa as well as for SF Al-10Zn-2Mg-1Cu-0.2Zr with 34 MPa m^{0.5} at yield strength 560 MPa in the as-extruded condition, for example. From Figs. 141 to 144 it is evident, however, that the driving force to employ advanced magnesium alloys instead of aluminium alloys is about four times larger provided, the corrosion problem was solved as to the present invention(s).

Ball, Bar and Rod Milling (Mechanical Alloying, Mechanical Grinding and/or Chemical (i.e. Reaction) Alloying) for Non-Equilibrium Phases / Third Part of the Invention

1. Limitations of the Mg alloy development by all-liquid processing and by vapor deposition

The motivation to employ mechanical alloying to develop corrosion resistant Mg-alloys with improved modulus of elasticity stems from the limitations in the alloy synthesis set by processing from a) the liquid phase (which is mainly related to the constitution of the (available) Mg-based phase diagrams, i.e. the low solubility of useful elements in (i) the liquid excluding them from all-liquid synthesis and (ii) in the solid resulting in partition coefficients k_0 far from unity) and b) from the vapor phase which is mainly related to the absence of any relevant and economically viable VD-process to date (cf. [162].). Furthermore, MA leads eventually to a

nanocrystalline microstructure of equilibrium and/or non-equilibrium matrix phases and/or second phase dispersions so fulfilling in particular the three conditions for commercialization of non-equilibrium Mg-alloys (cf. above on p.18 - 38). The segregations in the predendrites of Figs. 8 - 10 triggering the corrosion in corresponding alloys are orders of magnitude larger than the limit for microstructural refinement set by shear stress occurring upon ball milling, for example (cf. p.15 above).

The more sophisticated route of rapid solidification processing (RSP) of Mg-Al-Zn based alloys from the melt has arrived at the following advantages over conventionally processed Mg-alloys and the available Al-alloys ([959.163]):

1. An improvement of 40 to 60 % in room temperature ultimate tensile strength (UTS) over conventional ingot processed Mg-alloys and the specific UTS of the strongest Al-alloys.
2. An increase in the ratio of compressive-to-tensile yield strength from 0.7 to a value of >1.1.
3. The resultant *specific* yield strengths of RSP Mg-base engineering alloys exceed those of I/M Mg- and Al-alloys by 52 - 98% in tension and 45 - 230% in compression.
4. The resultant elongations-to-fracture are within 5 and 15% for the as-extruded state and can be tailored to 22% by subsequent thermo-mechanical processing at the expense of moderate losses in strength. However, corresponding strength values are then still 150 - 200 MPa higher than for I/M Mg-alloys.
5. The atmospheric corrosion behaviour of the RSP Mg-alloys is in the range of the new high purity and conventionally alloys AZ91 E and WE43 and the corrosion resistant Al-alloy 2014-T6. Corresponding corrosion rates are two orders of magnitude smaller than for those Mg-alloys that have caused spectacular failure in the 1950s to the 1970s.
6. RS Mg-base alloys show superior superplastic deformation behaviour at temperatures above 100°C as compared to other light alloys and doubled resistance to fatigue as a result of substantial grain refinement cf. ingot metallurgy.

Chill-block, i.e. rapidly quenched Mg-Al-Zn base alloys are therefore primarily designed for applications at ambient temperature and where compressive loading is of major concern, while galvanic problems and resistance to (long-term) atmospheric corrosion, fracture and fatigue may eventually be solved otherwise. It shall be noted that none of the research programmes on RSP Mg-Li alloys have yet attained the specific strength levels of RS Mg-Al-Zn-base alloys. The specific strength formed prime motivation for RS Mg-Li research projects (cf. [164]).

Results from metastable non-equilibrium Mg-phases, however, were particularly promising at least in this respect, but they were not yet sufficient to solve the corrosion problem of magnesium. Hehmann and co-workers found exceptionally high hardness values in splat-cooled and partially amorphous Mg-Ni and Mg-Ce foils [165], which then led to the development of fully and partially amorphous Mg-Ni-Ca alloys with outstanding UTS-values of up to 1150 MPa or the highest specific strength values ever reported for a metallic material (i.e. up to 600 MPa / g

cm^{-3} , see Fig. 104) [166-168]. Subsequent work by Inoue et al. [169-173] and by Masumoto et al. [174] in similar ternary systems by adding Sr, Ga, La, Ce, misch-metal and Y to RS Mg-Ni and Mg-Cu base alloys led to UTS-values above 1000 MPa with a specific tensile strength of $436 \text{ MPa} / \text{g cm}^{-3}$ for amorphous $\text{Mg}_{90}\text{Ni}_5\text{La}_5$ (cf. Fig. 104). The observed coupling factor k_H for $\text{UTS} = k_H$ microhardness ranged from 3.3 - 3.7. Other features include (i) crystallization doublets at temperatures T_x between 120° and 200°C upon DSC indicating the high susceptibility to natural ageing, (ii) pronounced glass transition temperatures as were evident for more thermally stable glasses with $T_x > 200^\circ\text{C}$, (iii) relatively large T-intervalls of up to 60 K between the observed glass transition and crystallization temperatures and (iv) significant softening prior to crystallization at temperatures above 50°C . It is questionable whether these amorphous alloys will find applications in view of their low thermal stability, high susceptibility to corrosion after transformation into the heterogenous phase mixture and/or higher densities relative to pure Mg (i.e. to some extent far above that of Al).

The development of metastable phases has since concentrated on amorphous Mg-Ni and Mg-Cu base alloys by chill-mold type of casting methods, for example, which was reported to be sufficient to yield amorphous cross-sections of critical thickness up to 4.0 mm in $\text{Mg}_{80}\text{Y}_{10}\text{Cu}_{10}$ - [172] and 3.5 mm in amorphous $\text{Mg}_{65}\text{Ni}_{20}\text{Nd}_{15}$ -alloys [175]. The structural state of the undercooled liquid including (i) the large increase in viscosity with increasing undercooling as is given by the Vogel-Fulcher-type of viscosity and (ii) dissimilarity in short-range ordering of the liquid compared to corresponding equilibrium crystalline long-range orders have supported easy glass formation in these Mg-base systems [176]. Due to the large increase in viscosity, the growth models by Kurz and Trivedi [177,178] showed a dramatic decrease with increasing levels of alloying to Mg in front velocity required to generate massive solidification [159,179].

From an atomistic point of view, the addition of refractory metals such as Ti, Nb, Ta, Mo, W, Zr, Cr, Mn, Hf etc. would not only increase the viscosity of the Mg-melt, but in particular the thermal stability, the modulus of elasticity and the resistance to corrosion of corresponding solid non-equilibrium Mg-phases due to the electronic structure and resultant high melting point of these TM, for example. Unfortunately, these TM are not soluble in liquid Mg above negligible alloying levels. While the above advantages n° 1. - 6. originate in the refined microstructure including temperature-stable intermetallic dispersions, mechanical alloying not only embraces such advantages as a universal consequence, but it also offers particular promising avenues for metastable Mg-base phases incorporating the above refractory metals for a cost-effective advantage over carbon-reinforced organic matrix composites (CFC) provided, that an hierarchization and quantification of corresponding universally applicable milling parameters can be identified (cf. below).

The major merit of RSP has been to show the limitations imposed by *all-liquid* processing on the properties of Mg-alloys. Choice and level of useful alloying to Mg are more restricted than

for Al and steel and require concerted Mg-development programmes which will have to be independent on traditional all-liquid processing for the metallic Mg-matrix (!). Together with minor relaxations of regulations for use of Mg in aerospace vapor- and solid state synthesis by VD- and MA-technologies will initialize an era of important use of Mg in aerospace *and* elsewhere (cf. [180]). Numerous applications as summarized in claim 15 are possible by non-equilibrium methods such as MA and VD (cf. [181]). Prime barrier & challenge remain the absence of a self-healing passive surface film of current Mg-alloys that provides better corrosion resistance than *high-purity* magnesium as the reference coupled with improved modulus of elasticity. From the view-point of magnesium, this situation embraces strong similarities to that of steel-development more than hundred years ago and the prime question is how rapidly the "champion" based on Mg can be achieved.

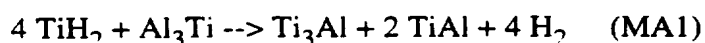
2. Status of Mechanical Alloying of Light Alloys

The motivation to employ mechanical alloying as the alternative route towards improved corrosion resistance, elastic modulus and thermal stability of structural (non-equilibrium) Mg-alloys and to produce a more cost-effective material than CFC includes mechanical working of solid Mg-base mixtures by ball milling, mechanical grinding and/or chemical (i.e. reaction) alloying is to increase the latitude of (i) alloying elements, (ii) metastable matrix phases and (iii) microstructures of existing and novel alloys as to (i) and (ii). Mechanical alloying has the advantage to readily include alloying additions such as metalloids and transition (Zr, V, Ti, Nb, Ta, Mo, W, Hf etc.) and rare earth metals with high melting points to Mg. They were shown (see above) to be important elements in order to solve the corrosion problem of Mg-alloys likewise combined with the attractive mechanical properties reported for all-liquid processed metastable non-equilibrium phases (see above) when homogeneously distributed on an atomic length scale. The experimental and/or processing conditions to achieve metastable (non-equilibrium) phases are more readily available by mechanical alloying. Alloying elements with very low vapour pressures such as Ta and Mo as well as high-melting (and boiling) intermetallic compositions can be readily employed and embedded in metastable phases by mechanical alloying. Fabrication of relatively large MA powder quantities represents a particular advantage over current vapour deposition technology for massive components for which no productive and economically viable method has been developed to date. The up-scaling of a (pre-) industrial pilot plant for mechanical alloying of corrosion resistant (non-equilibrium) Mg-alloys involves less unknown parameters as compared to a condensation-free vapour deposition process of controlled productivity (cf. [162]). However, the development of Mg alloys by mechanical alloying has been limited to date to isolated studies without achieving the development stage of Al- and Ti-based alloys.

Mechanical alloying (ball, bar and rod milling involving chemical reactions and/or grinding or not) helps in many ways to complete the solid parts of the equilibrium and non-equilibrium phase diagrams that are obscured to date due to liquid immiscibility excluding the production

of corresponding alloys via the liquid state. Recent structural results include the extended solid solubilities of up to 6 at.% Mg in solid solution of α Ti [182] as well as glass formation ranges in binary and ternary Ti-systems that were expanded with regard to corresponding rapidly solidified Ti-alloys [183]. Mechanical alloying of more dilute Ti-alloys containing 6 at.% Mg and 10 at.% Cu resulted in grains of size 6 to 15 nm [184,185]. Microstructural refinement of the crystalline state was considered [186] to be limited by the shear stress imposed on dislocation movement. Amorphous $\text{Ti}_{42}\text{Al}_{58}$ made by sputtering transformed into crystalline grains of size 10 nm [187], while refinement of $\text{Ti}_{42}\text{Al}_{58}$ by MA without formation and devitrification of an amorphous precursor reached a grain size of 20 nm or so [188]. Amorphous Ti-base phases were achieved after 9 h for Ti-10 Cu over 11 to 64 h for Ti - 15 to 50 Ni, 17 h for Ti - 15 to 50 Pd and 25 h for Ti - 25 to 50 Si to up to 64 h for Ti - 50 Co and Ti - 50 Fe (all in [at.%]) [189].

Ball milling of Ti-based intermetallic phases by MA was possible, for example, either directly from elemental powders via (i) moderate milling conditions applied to Ti-50 at.% Al alloy [190] and (ii) by chemical or reaction milling a mixture of $\text{TiH}_2 + \text{Al}_3\text{Ti}$ [191]:



for which the formation of TiAl provides the major driving force so corresponding volume fraction to increase to 95% on subsequent HIP'ing and indirectly via (iii) heat treatment of the extended solid solution of 24 to 33 wt.% Al in α Ti or of an amorphous Ti-powder containing 50 to 55 at.% Al where the conditions of milling were more extreme than for (i) [192].

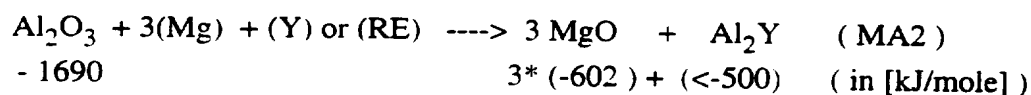
Ball milling of Al-base alloys includes the development of an Al-Li-Mg-O-C alloy with fracture toughness K_{IC} 45 MPa $\text{m}^{0.5}$ at tensile yield strength 450 MPa and 100fold reduced corrosion rate cf. IM7075-T73 as well as MA Al-Ti alloys with ultimate tensile strength 500 to 550 MPa and 7 to 15% ductility at ambient (cf. [193]). Complex amorphous MA-Al-based alloys containing transition metals were reported to show crystallization temperatures as high as 600°C (Fig. 105). The as-extruded MA-material showed remarkable mechanical properties at room temperature [194]. Amorphous Al-base Al-transition metal phases were achieved after milling periods ranging from 23h for more complex Al-base alloys [194] over 15-40 h for amorphous Al - 25at.% Nb [195], 60 h for amorphous Al-50 at.% Nb [196] and 180 - 450 h for amorphous Al - 10 to 50 at.% Fe alloys and up to 300 h for amorphous Al-Ta alloys [196].

A frequently employed method for ball milling of engineering Al-based alloys is to add a carbon (- bearing) constituent as a lubricating agent to the precursor (pre-alloyed, eg. powder) charge in order to facilitate a reaction effect and/or to increase the yield of the operation (cf. [139,197,199]). It has been reported [197] on Al-based alloys containing 0.5 - 4.0 wt.% C, 0.5 wt. oxygen, 12 - 20 wt.% Si and eventually 5 wt.% Fe. These MA Al-based alloys do not

contain the more expansive transition metals Ni, Cu, Cr, Ti, Zr and/or Ag and also no (equilibrium) solid solution hardening elements such as Mg and/or Zn. Oxygen in MA light alloy powders can either stem from the surface oxides of atomized and other (pre-alloyed) presursors and/or from the (inert) atmosphere employed upon milling and subsequent powder handling. Obviously, the relatively cheap alloying additions Si and Fe provide (i) a more effective and/or sufficient improvement of engineering properties by ball milling with carbon and oxygen /oxides as compared to employing spray forming and composites, for example, and/or (ii) the need and/or possibility to minimize the cost for the employed feed stock in conjunction with the available (productivity of) ball milling plants. However, all is not aluminium that glitters.

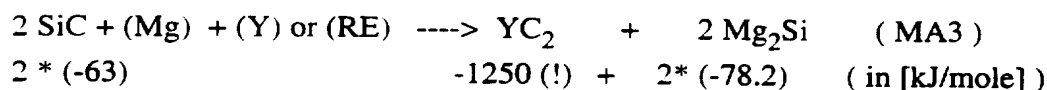
The potential for metastable phase formation of Mg-based alloys has been demonstrated by (i) cold-rolling of alternating Mg-Ni multilayers [200] and by (ii) mechanical alloying of pre-alloyed crystalline Mg-30at.% Zn [201] and a mixture of elemental Mg-Al-Ca powders [202]. More recently, Hehmann reported [194] on a systematic study to achieve thermally stable non-equilibrium phases based on magnesium. Following the work on amorphous Al-based alloy with the highest ever reported crystallization temperature of 620°C for an Al-base alloy (cf. [194]), a partially amorphous WE54-base material was developed of which the crystallization peaks were reported [203] to extend to temperatures between 480° and 614°C (Fig. 106). The results were made possible after planetary ball milling a mixture of (WE54 + 3 to 9 wt.% Al₂O₃) to powders of particle size between 10 to 400 µm, while ball milling of WE54 doped with SiC was reported [203] to show weaker and thermally less stable non-equilibrium phase formation. No exact milling conditions (milling time etc., see below) were published yet.

Initial strength values of corresponding as-extruded alloys were above 400 MPa at ambient with values of elongation-to-fracture between 3 and 8% and above 200 MPa at 250°C (elongations 50 - 60 %) without having optimized any of the processing steps including thermomechanical processing [194]. A dispersion of yet unidentified precipitates of size < 1 µm was observed to suppress recrystallization upon extrusion at 380°C. It was suggested that exothermic in-situ reactions between the alloyed constituents allows for the formation of novel refractory dispersions with more than a doubled volume fraction compared to the unmilled blend of powders [194]. The possibilities to tailor the microstructure by internal reaction included dispersion strengthening by chemical phase transformation via an oxidation-redox-reaction of the form



and resulting in a heat of reaction of -600 [kJ/mole]. Neglecting the heat of formation of the solid solution of Y in α-Mg, corresponding enthalpy of reaction is clearly exotherm. Activation of this reaction may increase with increasing degree of microstructural refinement, homogeneity

and amorphization for a given alloy concentration and with increasing volume fraction of Al_2O_3 for a given set of experimental conditions as to the increase in heat flow of corresponding exothermal effects observed between 510° and 620°C. A very exothermic reaction of the type



was also possible resulting in an enthalpy of reaction value of -1280 [kJ/mole]. Other reactions involving the use of a lubricating agent were not yet reported. The resultant Mg-alloys, however, represent a second generation of Mg-metal matrix composites, since they combine the nanometer length scale of the microstructure of ODS-alloys with the reinforcement of the first Mg-MMC's, but without corresponding interfacial problems.

By using a 'Rpulverisette 5' - apparatus by Fritsch, FRG with 4 symmetrically arranged rotating cylindrical steel containers (i.e. vials) being double-rotating around their common pivot and around the pivot of each individual vial which were of external diameter 10 cm by height external 5 cm (see Fig. 107 and [204]) and employing an alloy charge of not more than 8g magnesium while the closing and re-opening the attritor containers was done in an Ar-glove box continuously flushed with 4N8 argon at 1 bar, it was possible to:

1. circumvent atomizing the precursor alloy (usually required to facilitate mechanical alloying (cf. [198]) by transforming (pre-alloyed) WE54 alloy chips and (bent) turnings machined from ingot bar directly into MA WE54 powder particles of size 80 to 500 μm which makes MA for non-equilibrium alloys even more attractive, but corresponding milling conditions including the employed chip size were not published yet.
2. increase the volume fraction and (irreversible) transformation temperature of an yet unidentified non-equilibrium matrix phase as well as the welding of resultant powder to the surface of the milling containers (vials, cf. Figs. 106,107) by increasing rotational speed (often referred to as "milling intensity") of the apparatus so increasing the loss of powder and decreasing the yield with increasing milling speed by employing 3 to 9 wt.% Al_2O_3 of size 3 micron to the WE54 chips, but the exact milling conditions including milling time and/or milling intensity as a function weight ratio of balls-to-charge required for a given volume fraction amorphous were not reported yet.
3. increase the yield of a mechanically alloyed WE54-base powder doped with 3 micron Al_2O_3 - and 3 micron SiC powders to up to 95 to 99% by either using a relatively low rotational speed without lubricant resulting in powder size 80 - 250 μm or by relatively high rotational speeds including the use of a lubricant (powder size 10 - 400 μm), thereby allowing for consolidation to a dispersion strengthened Mg-base matrix made from MA-powder without the need of degassing the powder, but no details on milling time and speed, type and quantity of lubricant and associated charge including the size of WE54-chips and number and size of milling balls were disclosed yet.

Provided, that substrate temperature (distribution) was controlled, the occurrence of non-equilibrium phases upon VD is given for granted due the absence of recalescence, but productivity depends on other factors (see above). Formation of non-equilibrium phases by mechanical alloying in particular with an homogenous distribution of the alloying elements on an atomic length scale, however, requires a relatively precise definition of the milling variables for the operator including a unique hierarchy of the parameters to be controlled. Chen et al. summarize [205] eight factors "known to affect the milling process":

1. milling equipment (eg. attritor, planetary ball mill or vibrating mill)
2. "milling intensity" (velocity of the balls and resulting impact energy, frequency of impact and resulting impact power)
3. milling temperature (hot, cold etc.)
4. milling atmosphere (vacuum, Ar, air, N₂, control agent)
5. ball-to-powder (charge) weight ratio
6. filling fraction of the volume of the milling container
7. constitutive material of the milling device (WC, (type of) steel, ceramics) and
8. milling time.

It would be interesting to see what other authors have to publish in this respect (cf. [206]).

3. Disclosure of the Invention: Qualitative and Quantitative Parameters (for the Operator) to Achieve the Required (Micro-) Structural Transformation into Non-equilibrium Mg-alloys by Ball Milling including MA

It is the objective of this part of the invention to identify the required milling technique(s) and variables as well as the type of the initial precursor material required to produce fully or nearly fully non-equilibrium Mg-base matrix phases by MA within economically viable milling periods. However, no hierarchy of ball milling techniques, milling variables and precursor material has yet been established for the selection and production of (light) non-equilibrium phases of a given alloy system and in particular not for homogeneous non-equilibrium Mg-alloys rather than composite materials by ball milling.

3.1 Formability of (Homogeneous) Non-Equilibrium (ne-) Phases by Mechanical Alloying and/or Ball Milling

Solid state amorphization (as well as the formation of other competing non-equilibrium phases, eg. crystalline, quasi- and/or nanocrystalline and/or terminal solid solubility extension) by ball milling was considered until recently to depend on a negative heat of mixing of corresponding liquid, ΔH^{mix} , and on a large difference in diffusivity of the involved constituents, ΔD (cf. [207,208]). The coincidence of solid state amorphization by ball milling with amorphization by rapid quenching (RSP) from the liquid in the same alloy system was thought (cf. [209,210]) to prove the importance of macroscopic thermodynamics (free energy ΔG) and the ΔH^{mix} -criterion, while deviations and extension of the concentration range of amorphization

of a given alloy system by ball milling compared to that by RSP was considered to show superior non-equilibrium phase formability by ball milling due to less effective kinetic barriers (eg. ΔD) as compared to RSP (eg. freezing range).

The effect of ball milling to overrun barriers for non-equilibrium phase formation as preset by equilibrium alloy constitution is inherent to the process. Extension of an amorphous one-phase field was reported for TiAl-base alloys in the range from 45 to 65 wt.% Al, i.e. in the concentration range where rapid solidification such as by melt spinning does only allow for an amorphous phase at Al-levels > 60 at.% (cf. [211]) due to unfavourable solidification kinetics at lower levels. A large number of non-equilibrium phases made of two transition metals (i.e. TM(1)-TM(2) where TM(1) is Cr, Mn, Fe, Co, Ni, Cu, Pd or Re, i.e. so-called "late" transition metals, and TM(2) is Zr, Ti, Nb or Hf, i.e. so-called "early" transition metals) was summarized [211]. In 3d-systems with relatively small negative or positive ΔH^{mix} -values (eg. V-Ti, Cr-Zr, V-Zr, Fe-Nd), ball milling was believed to exclusively result in crystalline instead of amorphous alloys [210,211].

ΔG - and ΔD -criteria have found widespread attention to predict more concentrated amorphous and non-equilibrium metallic materials, but they remained without practical benefit for non-equilibrium phase formation and selection by the operator. Consequently, a large proportion of the publications on ne-phases by ball milling is devoted to ΔG -interpretations of the observed results without analysis of the applied parameters and operating variables. In the meantime, however, amorphous phases by ball milling were observed in systems with positive ΔH^{mix} -values such as Cu-W, Cu-Ta, Cu-V, Si-Zn, Si-Sn [213-216] and with small differences ΔD such as V-Zr [217] as well as in pure and alloyed components involving a diamond crystal structure such as in Si, Ge, $\text{Ge}_x\text{Si}_{1-x}$ and GaAs [218-221].

Obviously, ball milling can always lead to the formation of a non-equilibrium phase independent on alloy system and composition provided, that the milling conditions are correct. The prime question is: "What are the operating variables to increase and optimize the transformation rate, yield, purity and homogeneity of the as-milled powder product?" The driving forces for ne-phase formation by ball milling were yet related to alloy constitution and formability kinetics without incorporating the form in which the energy was supplied to the material. The energy for non-equilibrium phase transformation by ball milling of the solid state is supplied by shock and friction. ΔG -related phase diagram calculations, however, are yet a function of temperature without incorporating mechanical shock energy. Therefore, they can not supply more than supplementary aspects to explain non-equilibrium phase formation by ball milling. If they are applied to exclude the formation of a non-equilibrium phase, however, they provide a misleading analysis of the (operative = mechanically sensitive) driving forces for non-equilibrium phase formation via solid state synthesis by ball milling (cf. [222]), since the maxim for phase transformation without change of the (macroscopic) state of matter is to avoid proces-

sing without (excessive) heating and without overriding the time required for the (milling) operation (see above).

The main interpretations of ne-phase formation by mechanical alloying are (cf. [223]):

1. Local melting in analogy to a rapid quench or anneal
2. Effect of plastic deformation
3. Thermal and athermal diffusion, the latter in analogy to the effect of irradiation (Fig. 108).
According to Gaffet and co-workers [225,264], the microstresses introduced by various ball milling techniques correspond to the same order of magnitude than the microstresses introduced by static and dynamic mechanical loading and irradiation by electrons, neutrons etc..
4. Chemical diffusion across (thin) multi-layers of different components A and B, being interpreted eg. as a function of difference in diffusivity, ΔD , esp. in the non-equilibrium state.
5. Effect of nano-scale crystal (grain) refinement (lattice instability and amorphization resulting from decrease in grain size and expansion of corresponding lattice parameter).

All authors agree in that the increase in free energy of the ball milled material is a direct result of the increase in structural faults with milling time (energy storage in the form of atomic disorder) resulting in stabilization of the structure of a high temperature, disordered crystalline or amorphous phase(s) according to the degree of the resultant increase in energy. This phase competes with an increase in temperature (due to adiabatic deformation work, compression and/or shear all increasing corresponding c_p -value) - and the tendency to (re-)transform to corresponding equilibrium phase(s) and/or to minimize its free energy via relaxation by diffusion. Many authors have attributed the increase in (stored) free energy to an increase in elastic energy (cf. [226,227]). An increase in elastic energy may occur upon static loading such as in tension, compression, torsion and shear, but ball milling represents a dynamic loading subjected to repeating impacts of an *individual energy at a given impact frequency*. Furthermore, the dynamic loading upon ball milling occurs in the moment of impact (which is of the order of 10^{-5} sec) and is orders of magnitude smaller than the period between two impacts. Therefore, ball milling is different from fatigue upon which dynamic loading occurs during the entire cycle between two amplitudes. Finally, the ability to absorb impact energy via shock and friction was related to a viscous resistance (cf. [228,229]), but no physical criteria were yet attributed to the viscous resistance.

Evidently, milling and constitutional variables for non-equilibrium phase formation by MA have yet been presented in a reductive rather than complementary way which would be the basis to create a universal hierarchy of corresponding parameters (cf. claim 2). While selected shock power set by operator and ball milling technique may eventually overrun constitutional barriers in order to result in a non-equilibrium phase as solute trapping would do upon rapid solidification, material parameters (such as the ΔD -criterion) and/or resultant (initial) materials selection remain rate-controlling and crucial for the economically viable products. Amorphous phase formation in systems without fast diffuser (eg. Zr-V) is relatively rare, while it is relatively easy in the Ni-Ti and Fe-Zr system (which represents a combination of early and late

transition metals with very different diffusivities) compared to glass formation in the Cr-V and Zr-V system with relatively similar diffusivities. all evidencing at least some significance of the ΔD -criterion. Progress was made, however, in the quantification of operating variables required for ne-phase formation and which are universally applicable from one ball mill to another.

3.2 Advantages of Planetary Ball Milling: Highest Degree and Latitude of Power Control for the Formation of Homogeneous Non-Equilibrium Phases

A planetary ball mill consists of a (central) rotating holder (disc, table) upon which a defined number N_{MV} of rotating milling containers (i.e. the (milling) vials, here denoted with suffix MV) are mounted bottom-on [204]. The vials are usually mounted on the rotating table in such a way that the normal on the plane of the (orifice of the) opening of the vial to fill it with the corresponding (mixture of the) initial (i.e. precursor) material(s) and to remove the ball-milled end-product after a defined milling cycle $C_M = f_n$ (number of parameters, N_P) from the vial(s) is pointing upwards. in particular perpendicular to the plane in which the rotating table is moving. If the rotating table of the planetary ball mill rotates clock-wise, the vials rotate anti-clockwise and vice versa (for a schematic with (/ indicating) four vials, see Fig. 109). In commercially available planetary ball mills, the minimum number of vial holders per rotating holder disc is two, i.e. $N_{MV}(\min) = 2$. Hypothetically, however, $N_{MV}(\min)=1$, since the weight of one vial can be outbalanced by an equivalent weight on the opposite side of the holder disc.

Control of Detachment and Kinetic Energy E_K per Milling Ball

The milling balls inside the vial of a planetary ball mill either (i) roll or slide along the internal wall surface and/or (ii) they are ejected towards the opposite internal wall surface of the vial (cf. Fig. 109) and/or (iii) they undergo more complex movements at higher filling fractions of the vial volume. The (ii)-type of milling ball movement allows to explore the centrifugal forces provided by planetary ball milling which are in (commercially available planetary ball mills) up to twentyfive times larger than the force of gravitation [204]. However, the (ii)-type of ball movement is only possible, if the centrifugal force created by the rotation of the holder disc is larger than the centrifugal force created by the rotation of the vial, i.e.

$$\Omega^2 R > \omega^2 r^* \quad (\text{MA4})$$

where

1. Ω the rotation speed of the rotating holder disc (vial holder table) of given distance R for the at least one vial.
2. $R = \overline{O_D O_{MV}}$, i.e. the separation distance between the center O_D of the rotating holder disc and the center of the at least one rotating vial, O_{MV} , on the rotating disc on which the vial holders are fixed.
3. ω the rotation speed of the at least one vial of a given radius "r" mounted on the rotating holder disc.

4. "r" the internal vial radius and resultant effective radius $r^* = r - r_{b,i}$, with $r_{b,i}$ = milling ball radius.

For $(\omega^2 r^* / \Omega^2 R)$ -ratios > 1 , however, planetary ball milling can result in rapid "caking" (build up of material to the wall of the vials) and/or frustrates the operation due to absence of milling effect (i.e. refinement of microstructure and/or fabrication of a powder, see below). The (ii)-type of movement allows to control a discrete value of kinetic energy (vector notation: E_K) per ball in flight (i.e. after detachment) following (cf. [224] and Fig. 112):

$$E_K = (m_b / 2) * (V_d^2) \quad [J / impact] \quad (MA5)$$

where V_d is corresponding ball velocity given by (for mathematical details, see [224]):

$$V_d = [- R\Omega + r^* \omega \sin(\alpha_d)] \underline{I} - r^* \omega \cos(\alpha_d) \underline{J} \quad [m/s] \quad (MA6)$$

where $\sin(\alpha_d) = (-r^* \omega^2 / R\Omega^2) = C$ = detachment angle for movement (ii) resulting in the absolute value (which is independent on $\alpha_d = \omega t(\alpha)$, see eq. MA8), i.e.

$$E_K = m_b / 2 * [- R\Omega + r^* \omega * (-r^* \omega^2 / R\Omega^2)]^2 \quad [J / ball] \quad (MA7)$$

Fig. 110 shows the effect on the amplitude of V_d (i.e. under condition MA4) of vial rotation ω at a given disc rotation Ω and the effect of disc rotation Ω at a given vial rotation ω by using R and r^* -values of commercially available planetary ball mills [204]. Evidently, the increase in Ω is far more effective than the increase in ω in order to increase the amplitude of V_d , while the increase in ω is rapidly limited by criterion MA4, i.e. $(r^* \omega^2 / R\Omega^2) < 1$. Fig. 111 shows a more complete set of results using eq. MA7. Evidently, a large R -value (G5) relaxes the conditions required for rotation Ω (eg. from 1 to 2) and/or ω (from position 3 to 4) in order to achieve the same or a much larger impact (kinetic) energy than by employing a relatively small R -value (G7). Furthermore, vial rotation velocity ω is only effective to control the E_K -value for planetary ball mills by using very small R -values (Fig. 111) [223].

*Control of Effective Impact Power P^**

As a result of the high centrifugal forces operating during the (ii)-type of movement it is valid to assume that $V_d = V_c$ (velocity at collision, cf. Fig. 112) and the vector $E_K(V_d)$ being equal to the kinetic energy of the ball at impact, i.e. $E_c(V_c)$, where

$$|E_c(V_c)| = E_c = K_a * (m_b / 2) * [V_c]^2 \quad [J / ball] \quad (MA7)$$

and K_a ranging from 0 for totally elastic to 1 for totally inelastic collision, that is that E_c is roughly proportional to Ω^2 and $\Omega^2 R$. Iasonna and Magini have shown experimentally that a small layer of powder on the internal vial surface is enough to attain K_a -values close to 1 [230]. The actually occurring impact frequency per milling ball, f , is controlled by the flight time t_1 and the time t_2 during which the ball is attached to the vial surface after a first collision:

$$f = 1 / (t(\alpha)) = 1 / (t_1 + t_2) \quad (\text{MA8})$$

where t_1 is obtained numerically when the two conditions cf.[224]):

$$[-R\Omega + r^* \omega C] t_1 + r^* (1 - C^2)^{1/2} = R \cos(\Theta) + r^* \cos(\alpha) \quad (\text{MA9})$$

$$[-r^* \omega (1 - C^2)^{1/2}] t_1 + R + r^* C = R \sin(\Theta) + r^* \sin(\alpha) \quad (\text{MA10})$$

are satisfied, where $\Theta = \pi/2 + \Omega t_1$ and detachment for $t_1 = 0$. The solution for flight time t_1 is obtained by scanning $\Delta\alpha$ (Abdellaoui and Gaffet propose (cf.[224]) $\Delta\alpha = 0.01^\circ$) from 0 to 2π for a given Δt_1 -increment. The solution of eq.s MA9 and 10 provides the flight time t_1 between detachment and collision (impact) of the milling ball with the internal vial surface and Θ_c (i.e. the position of impact of the milling ball with regard to the reference frame) and α_c (i.e. the position of impact in the vial). The two latter are then employed to calculate t_2 using:

$$t_2 = [3\pi - (\Theta_c - \alpha_c) + \arccos(r^* \omega^2 / R \Omega^2)] / (\Omega + \omega) \quad (\text{MA11})$$

(cf. [224]). The number of collision events per vial and unit time with the vial surface (and/or material, cf. below), i.e. the frequency f of collision events per vial is sub-controlled by the number n_b of the milling balls employed per vial, i.e.

$$f = f^* \cdot n_b \quad (\text{MA12})$$

Figs. 113 and 114 show the numerical results of frequency f as a function of Ω and ω for $n_b = 5$ and $R = 13$ cm (G5), $R = 7.5$ cm (G7) and $r^* = 1.35$ cm [223]. Evidently, the vial rotation velocity ω (does not only affect E_c , see Figs. 110 and 111, but it) is particularly relevant for frequency f and f of the actual impacts of the milling ball(s) upon vial surface and/or material on the vial surface (Fig. 113) and the resulting impact power P' and P (in [W]), i.e.

$$P' = E_c \cdot f \quad \text{and} \quad P = E_c \cdot f \quad (\text{MA13a,b})$$

(cf. Fig. 114). The vial rotation speed ω provides a discrete impact frequency f (f) for a given disc rotation speed Ω (and R at lower Ω), i.e. f (f) is proportional to ω and relatively independent on R at higher values of Ω (Fig. 113). Iasonna and Magini have shown [230] that f obtained via eq.s MA9 and 10 is in excellent agreement with experimental observations for filling fractions of milling balls, $f_{nb} < 0.5$, where

$$f_{nb} = n_b / n_b(\text{max}) \quad (\text{MA14})$$

with $n_b(\text{max})$ = maximum number per vial independent on size of milling balls and independent on whether collision cascades instead of individual (ii)-type of ball movements occur (as is likely at higher velocities). Due to the effect of distance R on E_c , however, an increase in R from 7.5 to 13 cm results in an increase of impact power P by a factor of about 2 for $\Omega=400$ rpm to up to 3 for $\Omega = 500$ rpm at a given vial rotation $\omega = 300$ rpm (Fig. 114), for example. The effective mean impact frequency f^* of events per unit mass or mole of initial material per

vial is also controlled by the absolute weight of the initial (precursor) charge per vial, i.e.

$$f^* = f / \Sigma m_{\text{charge}} \quad [\text{Hz} / \text{gram}] \quad \text{and} \quad f^* = f / \Sigma n_{\text{charge}} \quad [\text{Hz} / \text{mole}] \quad (\text{MA15a,b})$$

providing a large range of discrete values of impact power, i.e.

$$P^* = E_c \cdot f^* \quad [\text{W/gram}] \quad \text{and/or} \quad [\text{W/mole}] \quad (\text{MA16})$$

It is the effective mechanical impact power P^* which has to match the required power $P_{\text{req}}(T,x)$ for non-equilibrium phase formation and which is imposed by the constitution of a given alloy system. The resulting control of a discrete and eventually very high P^* -value (cf. next paragraph) makes planetary ball milling the most interesting ball milling technique for solid state synthesis of (in particular Mg-base) non-equilibrium phases which require an homogeneity on an atomic length scale to provide sufficient corrosion resistance (see above) and which incorporates powder and/or microstructural (second phase and/or grain) refinement afforded by alternative ball milling techniques (cf. next paragraph). The control of the transfer of impact power P into the ball-milled material is important, for example, for the volume fraction of non-equilibrium phase formation by (planetary) ball milling. Chen et al. reported [205] a minimum threshold in mechanical impact power P to be required in order to achieve the transformation of crystalline NiZr alloys into fully amorphous (i.e. 100 vol.% non-equilibrium) phase formation (Fig. 115 and below). The (steady state) amorphization rate was observed to increase with increasing shock power for a given milling temperature within the temperature range allowing for amorphization (cf. Figs. 115 and 121).

Effect of Size, Material, resulting Weight and Filling Fraction of Milling Balls

Evidently, the ratio $\Sigma n_b / \Sigma m_{\text{charge}}$ is not a weight ratio and the ratio of weight of milling balls-to- Σm_{charge} is not a very useful parameter, since it allows for numerous unidentified materials and ball quantities to enter the milling process unless size, material (composition and resulting density) and resulting weight per milling ball were defined. The choice of size, material and resulting weight of (commercially available) milling balls is of secondary importance for the choice of R, Ω, r^* and ω in a planetary ball mill in order to obtain $P_{\text{req}}(T,x)$ for the non-equilibrium phase concerned (nb. for a given n_b , the impact frequency f per vial and energy per impact $E_{K,s}$ and the resulting power (eq.MA13a,b) are uniquely defined by ω and Ω , cf. below), but is of prime significance wrt. alloy purity and affordable (type of) contamination of the ball-milled material such as the required non-equilibrium Mg-alloys, for example. The methods to avoid iron contaminations, for example, include to employ high $F_{c,s}/F_{c,f}$ -ratios (cf. next section), lubrifiers (see below), for example, and a small number of WC-balls in WC-vials was also reported [231] to reduce contaminations without entirely excluding such them.

The number n_b of milling balls employed per milling container (vial) depends on the size of the milling container as Σm_{charge} does. n_b is specified by the range of applicable and/or

tolerable (wrt. contamination of end-product, and by commercially available) materials $\Delta\Sigma_k$ for a) milling containers and/or container surface (planetary: vial) and for b) milling balls resulting in specific weight $\rho_{b,j}$, by the radius $r_{b,i}$ and $(m_b)_{i,j}$ = resulting absolute weight of an individual milling ball of resulting number $(n_b)_{i,j}$ or (eg. the overall number of a mixture, i.e.) $\Sigma(\Sigma(n_b)_{i,j})$ per milling container (vial). This notation is particularly important with respect to abrasion occurring upon ball milling and inevitably changing $r_{b,i}$ as a function of milling time. The materials of commercially available milling balls include SiO_2 (achate, density: 2.6 g/cm^3), "Syalon" (90% Si_3N_4 , 3.24 g/cm^3), sintered corundum (99.7% Al_2O_3 , 3.7 g/cm^3), tungsten carbide (96%WC + 3%Co, 14.75 g/cm^3), hardened Cr-steel (7.85 g/cm^3), stainless Cr-Ni-steel (7.89 g/cm^3), Teflon with core of steel (3.0 g/cm^3) and 97% pure zirconia (ZrO_2 , 5.7 g/cm^3) [204]. For a given $\rho_{b,j}$ and $r_{b,i}$, $(n_b)_{i,j}$ or $\Sigma(\Sigma(n_b)_{i,j})$ are limited by $f_{nb}(\text{crit})$ above which the efficiency of power (transfer) decreases (Fig. 116) and which is about 0.5 (cf. [230]). The available size $r_{b,i}$ of these materials ranges from 5 over 10 and 15 to 20 mm.

Frequency f and E_K are coupled by secondary parameters such as the specific weight $\rho_{b,j}$ and the size $r_{b,i}$ of milling balls defining both $(m_b)_{i,j}$ and $(n_b)_{i,j}$ at the same time. It was shown [230] that the increase in $r_{b,i}$ within the above range of ball sizes $\Sigma r_{b,k}$ increases the energy transfer E_c and decreases frequency f showing that the same impact power can be transferred by different number of balls of different diameter. Therefore, the available parameter window E_c vs. f^* for non-equilibrium phase formation by planetary ball milling can be increased within certain limits independently on the ratio of ω/Ω (see below), since impact frequency per vial can be controlled independently on impact energy by the number of milling balls per vial:

$$f^* = \Sigma \Sigma f^*_{i,j} = \Sigma \Sigma f^* \cdot (n_b)_{i,j} / \Sigma m_{\text{charge}} \quad [\text{impact}/(\text{sec gram})] \quad [\text{Hz / gram}] \quad (\text{MA17})$$

Under the condition that ball weight does not affect ball velocity during the entire flight, a decrease in E_c by decreasing $(m_b)_{i,j}$ can result in an increase of f , but the effect of fine-tuning E_c and f by ball weight $(m_b)_{i,j}$ remain subjected to the control by Ω and ω for a given apparatus and R and size of vial and r all controlling impact energy per ball via:

$$E_c = \Sigma \Sigma E_{c,i,j} = \Sigma \Sigma (m_b)_{i,j} / 2 \cdot ([- R\Omega + r^* \omega \cdot (-r^* \omega^2 / R\Omega^2)]^2) \quad [\text{J/impact}] \quad (\text{MA18})$$

The freedom to manipulate E_c per impact with the weight of the milling ball for a given Ω and ω is more restricted relative to manipulate the frequency with type and/or number of milling balls for a given Ω and ω of vials of industrial planetary ball mills yet to come with very large internal radii, since acceleration and resulting flight velocity V_d of a billet can change due to the effect of gravity over long flight distances. The relative effect to increase the processing window $E_c = f_n(f^*)$ by manipulation of number $(n_b)_{i,j}$ and/or weight of milling balls $(m_b)_{i,j}$ is reproduced graphically in Fig. 117.

*Decomposition of Discrete Kinetic Energy Value E_c and resulting Mode of Power Transfer: Control of Transfer Efficiency, resulting Milling Time and Temperature for a given P^**

The impact of the milling balls results in local elastic and plastic deformation of the material (i.e. vial, precursors and/or ne-phase) and friction. Under the assumptions that (i) no slip between milling ball and vial surface or material upon detachment and collision and (ii) no collision between milling ball(s) and/or between milling balls and material during flight occurs and that (iii) the effect on velocity of weight of the milling ball is negligible, the discrete E_c -value decomposes into the following two components (cf. Fig. 112):

$$E_c = |E_c(V_c)| = m_b/2 * (V_{c,p}^2 + V_{c,\alpha}^2) = E_{c,s} + E_{c,f} \quad [\text{J/impact}] \quad (\text{MA19})$$

where $V_{c,p}$ the normal velocity (which induces primarily deformation energy by shock) and $V_{c,\alpha}$ the tangential velocity (which induces primarily heat by friction). In order to calculate both relative velocities quantitatively, it is necessary to transform eq.MA6 from cartesian into the local tangential (u_α) and perpendicular (u_p) components at impact by using¹⁾

$$u_p = \cos(\alpha)I + \sin(\alpha)J \quad \text{and} \quad u_\alpha = -\sin(\alpha)I + \cos(\alpha)J$$

resulting in

$$I = \cos(\alpha)u_p - \sin(\alpha)u_\alpha \quad \text{and} \quad J = \sin(\alpha)u_p + \cos(\alpha)u_\alpha \quad (\text{MA20a,b})$$

Substitution of eq.sMA20a,b with eq.MA6 results in the normal and tangential velocities of a milling ball in the moment of impact at the surface of the vial of which the absolute values are defined as (for the details of the mathematical treatment, see [223,224]):

$$V_{c,p} = [(-R\Omega + r^*\omega C)\cos(\alpha) - r^*\omega(1-C^2)^{0.5}\sin(\alpha)] \quad [\text{m/s}] \quad (\text{MA21})$$

$$V_{c,\alpha} = - [(-R\Omega + r^*\omega C)\sin(\alpha) + r^*\omega(1-C^2)^{0.5}\cos(\alpha)] \quad [\text{m/s}] \quad (\text{MA22})$$

Fig. 110 shows the results for $V_{c,p}$ and $V_{c,\alpha}$ as a function of $\alpha = \omega t$ under the assumptions of $R = 12.5$ cm, $r^* = 2.775$ cm, $\Omega = 206$ rpm (3.43 Hz), $\omega = 80$ rpm (1.3 Hz) resulting in $C = (-\omega^2 r^*)/\Omega^2 R = -0.0335$.

The angle of impact, α , is obtained numerically via eq.s MA9 and 10. Subsequent substitution of eq.s MA21 and 22 with eq.MA19 results in corresponding (a) ratio of shock-to-friction energy induced into the material, (b) corresponding fraction of shock and friction powers, and (in practise) the (c) resulting elastic and plastic deformation of the material and the (d) resulting local, mean and maximum temperature. Fig. 118 shows a decreasing friction-to-shock energy ratio with increasing disc rotation velocity Ω for a given vial rotation velocity ω and $R = 13$ cm and $r^* = 1.35$ cm. The possibilities to increase the ratio of $E_{c,s}$ over $E_{c,f}$ include the reduction of vial velocity ω for a given disc velocity Ω , but also to decrease the ratio $(\omega^2 r^*/\Omega^2 R)$ (cf. criterion MA4) by increasing R or decreasing r^* . The angle α and the resulting Ω/ω -couples

required for maximum shock energy and zero friction is obtained numerically by the derivatives

$$d\bar{E}_{c,s}/d\alpha = m \left[(-R\Omega + r^* \omega C) \cos(\alpha) - r^* \omega (1-C^2)^{0.5} \sin(\alpha) \right] \\ \left[-(-R\Omega + r^* \omega C) \sin(\alpha) - r^* \omega (1-C^2)^{0.5} \cos(\alpha) \right] \quad (\text{MA23})$$

$$d\bar{E}_{c,f}/d\alpha = m \left[(-R\Omega + r^* \omega C) \cos(\alpha) - r^* \omega (1-C^2)^{0.5} \sin(\alpha) \right] \\ \left[-(-R\Omega + r^* \omega C) \sin(\alpha) - r^* \omega (1-C^2)^{0.5} \cos(\alpha) \right] \quad (\text{MA24})$$

Friction represents the work required for embedding a hard (and eventually brittle, see following paragraphs) precursor constituent such as a transition metal or a metalloid in magnesium e.g. at the beginning of the milling cycle, shock represents the work required for constitutional change including grain refinement and formation of (metastable) non-equilibrium phases. In their classical paper Benjamin and Volin [232] reported on five periods during mechanical alloying of a powder including (i) particle flattening resulting from plastic deformation, (ii) particle welding increasing mean particle size, while particle number decrease, (iii), formation of equiaxed particles when welding and fracturing rate is about equal, though the microstructure consists of a lamellar alignment of the precursors, followed by (iv) more random welding including the formation of lamellar colonies and (v) the final refinement of microstructural and/or particle refinement. Materials parameters promoting powder and/or alternating layer formation, i.e. the milling effect independent on size and shape of precursor include the operative engineering properties such as ductility or brittleness, hardness, and shock-resistance of the employed precursor material linking milling variables with the as-milled powder product. Provided, that the correct material for milling balls and/or (surface coating of the) vial(s) was selected, an increase in friction may be induced deliberately by relatively large ω/Ω -ratios (cf. Fig.118, 119) at the beginning of the milling cycle during stage (i) to (iii) to enhance the repeated fracture and welding of (elemental and/or pre-alloyed) precursors (i.e. the welding-to-fracture cycle of

¹⁾Footnote to page 115:

The flight trajectory of a milling ball (cf. Fig. 112) obtained by sufficient rotational speed Ω at rotational distance R_Ω is defined by a relative movement in flight with regard to the holder disc (i.e. by vector U_p) and the vial (by vector u_p). Due to the (assumed) absence of the effect of gravitation, the relative movement of the milling ball lies in the two-dimensional plane of the rotating holder disc for the vials and is therefore completely defined by only two (and not three) components following:

$$U_p = \cos(\Theta)I + \sin(\Theta)J \quad \text{and} \quad u_p = \cos(\alpha)I + \sin(\alpha)J$$

where $\Theta = \Omega t$ and $\alpha = -\omega t$, t = time (intervall) of planetary ball milling passed by and I and J the reference vectors defining the plane of the holder disc. The vectors U_p and u_p provide a unique definition of the movement of milling balls relative to the movement of the apparatus and to the resultant effects they introduce into the initial (precursor) material including effective shock energy, frequency and power required per unit mass of non-equilibrium material.

clean interfaces generating alternating layers in the (sub-) micron range in time $t(\text{me})_{\text{req}}$ prior to trigger non-equilibrium (ne. i.e. matrix and/or one-) phase formation in $t(\text{ne})_{\text{req}}$ via mutual in-diffusion of the involved (elemental) components with an homogeneity on an atomic length scale). but also at the end of the milling cycle in order to explore in-situ heating for an increase in the formation rate of the corresponding non-equilibrium phase (cf. §MA3.9), all resulting in the overall milling time required

$$t_{\text{req}} = t(\text{me})_{\text{req}} + t(\text{ne})_{\text{req}}$$

Friction has to be minimized, however, during the cycle for ne-phase formation, $t(\text{ne})_{\text{req}}$ in order for (i) full exploitation of the power supplied by the machine and to maximize the efficiency of impact power for ne-phase formation following

$$t(\text{ne})_{\text{rc}} = P_{\text{req}}(T, x) / E_{\text{c.S.c}}$$

where $E_{\text{c.S.c}}$ the shock energy cumulated during the milling operation, as well as for (ii) lowest possible contamination with Fe, for example (if contamination cannot be avoided otherwise such as by the choice of the milling ball material and vial, type of alloying additives, lubricifiers, etc., see below). Unless Ω and ω are chosen as such that $dE_{\text{c.f}}/d\alpha = 0$ and $d^2E_{\text{c.f}}/d^2\alpha = \text{negative}$, $E_{\text{c.f}}$ friction, so grinding and thus heating is inevitably involved and T-control may eventually require a cooling system. Evidently, classical terms such as "mechanical grinding" (used for ball milling from one single type of pre-alloyed precursor to produce non-equilibrium alloys) and "mechanical alloying" (used for ball milling for an alloy by using different precursor components) are useless for the operator in order to arrive at homogeneous non-equilibrium phases, since it is evident that a precursor charge of various elemental components requires primarily friction (as indicated by the term grinding¹⁾) at the beginning before shock takes over rate-control for homogeneous transformation to the required (one-phase or essentially one phase) non-equilibrium structure and eventually including (chemical) reaction without the need for long range order atomic displacements. The choice of (i) and (refractory-) dispersion strengthened Mg-base alloy with an equilibrium Mg-base matrix phase or for (ii) a metastable Mg-base bulk alloy with a non-equilibrium and eventually very corrosion resistant matrix phase, i.e. the constitutional effect, and/or with a non-equilibrium microstructure involving at least one of both type of phases, is depending on the mode of impact power of a given precursor charge and no other technique gives such as freedom to control them than type I of PBM.

Accordingly, the operative P_{req} -thresholds required for homogeneous non-equilibrium phase formation by (planetary) ball milling may change with Ω and/or ω and resulting impact energy and/or frequency f , since the type of the transfer of E_K , i.e. the operative $E_{\text{c.s}}/E_{\text{c.f}}$ -ratio controls

¹⁾ A mixture of milling balls including two larger WC balls of radius 1/4inch (6mm) was recommended [204] to improve the efficiency of milling power for sufficient grinding action.

the local, mean and maximum temperatures all depending on the number of collision events per ball and unit time f with the vial surface and/or the material to be milled, i.e. on time $t(\alpha) = t_1 + t_2$ between two impacts. The injected power increase with increasing rotation velocities Ω and/or ω and make planetary ball milling a high power and eventually hot milling equipment (the heat of which controlled deliberately by $\omega = fn(\Omega.R.r^*)$ and/or cooling and/or additional artificial heating). For the fabrication of economically viable non-equilibrium Mg-alloys with superior corrosion resistance by planetary ball milling it is therefore inevitably to employ planetary ball mills in which Ω and ω are decoupled (see below).

Limited Control on $E_{c,f}$ and Power-Transfer by Commercial Planetary (Type-II) Ball Mills

One important limiting parameter on the control of injected power by using commercially available (type-II of) planetary ball mills is their interdependence/proportionality of rotation velocity of the vial(s), ω , to the rotation velocity of the holder disc, Ω , following:

$$\omega = -k_{\Omega/\omega} \Omega \quad (\text{MA25})$$

where $k_{\Omega/\omega} = \text{const.}$ coupling parameter, that is, the rotation velocity of the vial(s) increases (nearly or almost nearly) linearly with increasing rotation velocity of the holder disc so being preset by Ω (Fig. 119 and [204]). In planetary ball mills for which Ω and ω are mechanically coupled (i.e. only one motor), a large impact power is thus inevitably linked with relatively high shock frequencies per milling ball eventually overrunning the required control of non-equilibrium phase formation and selection via the (ii)-type of milling ball movement by excessive friction resulting in unfavourable $E_{c,f}/E_{c,s}$ -ratios, for example (cf. straight line for $k_{\Omega/\omega}$ of planetary II-type planetary ball milling in Fig. 119 as well as corresponding line in Figs. 119, 120). Furthermore, the (ii)-type of milling ball movement in commercially available planetary ball mills is limited (last, but not least due to the detachment condition, see above) to relatively small radii R so "r" of the vial and consequently, it was yet impossible to apply this technique to a larger production volume of homogeneous non-equilibrium phases. Type-II of ball mills therefore allow for limited control on the $E_{c,s}/E_{c,f}$ -ratio so on $P^*(T)$ and milling time and resulting cumulative energy required, i.e.

$$E_{c,c} = P^*(T) * t_{\text{req}} \quad (\text{MA 26})$$

Therefore, impact frequency f per vial (for a given ω and/ or given Ω so for a given impact energy E_c) of a commercially available planetary ball mill is controlled entirely by the number of milling balls, n_b (cf. eq.MA12). At $n_b = n_{b(\text{crit})}$ where $n_{\text{crit}} = fn(f_{nb})$, however, an increase in filling fraction of the vials with milling balls and/or material results in undue friction so heating.

Results by Planetary Ball Mills with ω Decoupled from Ω (Type-I)

It was only very recently that a thorough control of rotation speed Ω , ω and T independent

from each other as well as the effect of separation distance R on impact energy and impact frequency required for ne-phase formability was employed more systematically. Gaffet et al. reported [224,233,234] the formation of amorphous $\text{Ni}_{10}\text{Zr}_7$ at room temperature to require 48 h by employing an upper Ω -threshold at 600 rpm and a lower Ω -borderline at 500 rpm employing $R = 7.5$ cm or by using $\Omega = 380 - 410$ rpm for $R = 13$ cm resulting in ω_{req} ranging from about 50 (127) rpm to 360 rpm by using $r^* = 1.35$ cm in both cases (Figs. 121, 122). The resulting E_c - and f^* -values required for amorphization by the two planetary ball mills were quite different (Fig. 122, 123) showing that neither the impact energy nor the frequency controlled solid state ne-phase formation (Fig. 123) and that only the product of both, i.e. the resulting impact power $P^*(T)$ controls the formation of the non-equilibrium amorphous phase (Fig. 124). At the lower Ω -bound, amorphization was considered to be limited by insufficient impact (= activation) power (or energy) for ne-phase formation below which only partial amorphization and/or microstructural refinement was possible, while amorphization at the higher Ω - and the higher ω -bound was considered to be limited by excessive power input resulting in excessive (local) heating [220,225]. The interpretation is supported by similar observations by other authors (cf. [235]) and by the shrinking size of the Ω/ω -window for amorphization of $\text{Ni}_{11}\text{Zr}_9$ alloy at higher vial (i.e. macroscopic) milling temperatures before disappearing completely at milling temperatures above 300°C. Within the actual parameter window for amorphization, however, the rate to induce structural defects arrives at a steady state at which the impact energy is consumed by atomic movements to form and (after completion of phase transformation) to move within a structurally homogeneous ne-phase [224].

Table 7 summarizes the quantitative milling conditions employed by Gaffet and co-workers on non-equilibrium phase formation by planetary ball milling of $\text{Ni}_{11}\text{Zr}_9$ and other metallic systems and materials, (ii) the resultant windows ΔP_{req} as well as (iii) the resulting cumulative impact energy $E_{c,c} = f_n(P,t)$. The employed impact energies E_c range from 0.07 to 0.25 J/impact (by assuming $K_a = 1$), the employed frequencies were between 24 and 130 Hz, and the resulting impact powers were from 0.3 to 2.2 W/g resulting (by employing milling times between 40 and 480 h) in cumulative energies ranging from 0.05 to 1.0 GJ/g. n.b. where such high energies are consumed it is evident that the materials of milling body and container must be compatible with the end-product. in particular for aeronautical applications. The special merits of the work by Gaffet et al. were to show (cf. Table 7):

1. That the supratechnological milling variables controlling ball, bar and/or rod milling are (i) injected milling power and (ii) the ratio of shock-to-friction which uniquely define the operating conditions to control the non-equilibrium state of a given (precursor) material. The control of these parameters allows to overrun "frontiers" such as ΔH^{mix} -criterion etc. until recently being considered to limit non-equilibrium phase formation by solid state synthesis such as ball milling including mechanical alloying (cf. amorphous Cu-W, Si [218] and Ge).

2. For planetary ball milling, a separate and quantitative control on two process parameters, i.e. (i) disc rotation frequency Ω for a given R , m_b and resulting E_c and (ii) vial rotation velocity ω for a given r^* and n_b and the resulting impact frequency f for a given alloy charge, all at a given milling temperature as well as the milling temperature itself allow to control the absolute value and the nature of the required power-input for ne-phase-formation, $P^*(T,x)$.
3. For the first time, a quantitative effect of R and Ω_{req} for non-equilibrium phase formation was reported following approximately the equation $(\Omega^2 R)_1 = (\Omega^2 R)_2$.
4. The advantage of planetary ball mills to offer the largest latitude of $P(T)$ and of control on $P(T)$ and on corresponding nature of $P(T)$, i.e. the ratio of shock-to-friction power as compared to competing ball milling technologies such as vibrating or horizontal or attritor ball mills all being associated with undue levels of friction (cf. next paragraph).

It was interesting to note that there was no significant effect of ball milling conditions - within the employed range of parameters - on the critical values of the destabilization of the diamond structure of pure Ge (and Si, not shown in Table 7) which were reported [219] to result from a refinement of the crystallite and a resulting expansion of the crystal lattice parameter. It was also interesting to note that amorphization of Cu-W alloys (which are characterized by a positive heat of mixing up to 35.5 kJ/mole [236] require relatively high milling times and resulting cumulative energies and this appears to be consistent with equivalent Al-base systems such as Al-Nb (see above). In contrast, the system NiZr does not only allow for relatively short milling times and resulting cumulative impact energies, but also for a relatively large ΔP -window ranging from 400 to 820 mW/g (cf. Table 7, Fig. 124 and [240]). This may be related to a relatively large negative heat of mixing, ΔH^{mix} of the system Ni-Zr, since although the ΔH^{mix} -criterion may not serve as a criterion to exclude amorphous and/or non-equilibrium phase formation (see above), it may serve as a reference for ne-phase formation rate and for the extension of the ΔP -window for non-equilibrium phase formation by ball milling and corresponding $P_{req}(T,x)$ -domain provided by nature.

Low ΔH^{mix} -values were considered to favour extended solid solutions over amorphous phases upon non-equilibrium (matrix) phase formation by mechanical alloying (cf. above and [211]). Low ΔH^{mix} -values, however, are a universal consequence for terminal compositions which is consistent with the requirement to retain the low density of Mg in the disclosed Mg-alloys made by non-equilibrium processing such as by vapour deposition and ball milling. Both technologies overrun the constitution of the alloy system preset by macroscopic thermodynamics independently on whether reactive constituents such as Al and/or Mg are involved and independently on relatively large (negative and low positive) ΔH^{mix} -values for concentrated alloy compositions (such as $Mg_{50}X_{50}$, [236,241]). For ball milling including mechanical alloying and/or mechanical grinding and/or chemical reaction milling, however, the required time to produce the more relevant microstructural control for passivation of corresponding

Table 7 Quantitative Conditions for Non-Equilibrium Phase Formation by Type-I PBM

System	NE-Phase	R	Ω	r^*/r_b	ω	m_b	n_b	m_{charge}	t	Atmosph.	E_c	f	P	$E_{c,c}$
	[wt.%] (if not indicated otherwise)	[mm]	rpm	[mm]	rpm	[g]		[g]	[h]		[J/ impact]	[Hz]	[W/g]	[GJ/ 10g]
Ni-Zr [224,233 .234]	amorph. (at.) Ni ₁₀ Zr ₇	75	500 - 600	13.5 / 7.5	50-360	14	5	10	40 - 48	static Ar	0.11 - 0.16	30 - 55	0.3 - 0.9	0.48 - 1.52
	amorph. (at.) Ni ₁₀ Zr ₇	132	380 - 410	13.5 / 7.5	50-360	14	5	10	48	static Ar	0.194 - 0.227	24 - 41	0.5 - 1.0	0.8 - 1.45
Cu-Fe [237]	TSSE of 27 Cu in Fe 65 Fe in Cu	132	305	13.5 / 7.5	675	14	5	10	240	Air + 1ml ethanol	0.16	60	1.0	8.3
Cu-W [213]	part. am. Cu- 30-100 W and TSSE of 5-25 W in Cu	120	340	13.5 / 7.5	765	14	5	10	140 - 180	static Ar	0.2	69	1.4	7 - 9
Ge-Si [220]	part. am. Si-Ge: Si-52.2Ge Si-35Ge	120	200	13.5/7.5	450	14	5	10	-	static Ar	0.07	44	0.3	-
		120	340	13.5/7.5	765	14	5	10	-	static Ar	0.2	69	1.4	-
Ge [219]	amorph. Ge	75	700	13.5/7.5	1400	14	5	10	96	static Ar	0.25	130	2.2	10.4
		120	340	13.5/7.5	765	14	5	10	72	static Ar	0.20	70	1.4	3.6
		120	200	13.5/7.5	450	14	5	10	150	static Ar	0.07	42	0.3	1.6
Fe-Si [189]	TSSE of 16 Si in Fe	120	340	13.5 / 7.5	765	14	5	10	168	static Ar	0.2	70	1.4	8.5
	part. am. Fe - 26-36 Si	75	600 - 700	13.5 / 7.5	250	14	5	10	168	static Ar	0.17 - 0.18	47 - 52	0.8 - 0.9	4.8 - 5.7
Si-B [239]	amorph. Si - 0 to 90 B	120	200	13.5 / 7.5	450	14	5	10	233 - 1480	static Ar	0.07	44	0.3	2.6 - 5.4
Si-C [239]	amorph. Si - 30 to 70 C	120	200	13.5 / 7.5	450	14	5	10	-	static Ar	0.07	44	0.3	-

PBM: planetary ball milling.

NE : non-equilibrium.

part. am.: partially amorphous.

at.: atomic ratio.

TSSE: terminal solid solubility extension.

other symbols: see text

Mg-base alloy due to homogeneization of the involved alloying elements on an atomic length scale and degree of suppression and resulting tailoring by subsequent thermo-mechanical processing of second phase dispersions appears to be well covered by the E_c -, f -, P^* - and $E_{c,c}$ -values required for the systems summarized in Table 7.

The separate control of ω independent on Ω of planetary ball mills leaves particular possibilities for the operator to control E_c and f^* in order to enhance non-equilibrium phase formability by the operator:

1. to provide high activation energies for ne-phase formation even for large milling quantities without excessive power and/or friction input (i.e. gravitational forces can be overcome over large flight distances at relatively low impact frequencies (and local temperatures) per milling ball independent on whether the milling container is chilled or not (n.b. excessive power inputs were shown [233] to stabilize an inhomogeneous matrix without the possibility to return to the homogeneous ne-phase during the milling operation.) Planetary ball mills with ω decoupled from Ω provides a more efficient use of impact power and non-equilibrium phase formation by the operator than all other types of the existing ball milling techniques.
2. more efficient milling histories from initial charge to the non-equilibrium powder end-product including the in-situ change (i.e. during the milling operation without interruption of the milling procedure and/or exposure of the material to a different atmosphere) of f^* without affecting E_c and vice versa.

The available impact power of planetary ball mills is uncritical for formation of homogeneous ne-phases such as corrosion resistant non-equilibrium magnesium alloys, but the available technology is not sufficient to allow the required control for the production of economically viable quantities (cf. next chapter).

3.3 Degree of Control and Latitude of Shock Power vs. Productivity :

Comparison and Hierarchization of Ball Milling Techniques for ne-phase formation

Tables 8 and 9 show a comparison of the characteristics of the main milling techniques.

Type-I (and -II) of planetary ball milling provide impact powers covering the power regime of all other ball milling techniques. This includes (i) control of a discrete value of kinetic energy E_c per collision between milling ball and internal vial surface, which is proportional to Ω^2 for a holder disc of given R so being controlled by the product $\Omega^2 R$ and (ii) to provide this control over a large range of Ω -values and impact frequencies resulting in a large range of discretely controlled mechanical shock powers with (iii) a controlled degree of friction to be transferred from the at least one milling ball per vial (after detachment from the internal vial surface) upon collision with the ball-milled material at the (opposite side of the) internal vial surface (cf. Fig. 109) thereby allowing power levels to trigger atomic jumps as in an irradiation process [225]. The control of a discrete E_c -value over a wide range of impact powers makes planetary ball milling a superior ball milling technique for non-equilibrium phase formation which

incorporates microstructural (second phase and grain) refinement afforded by the other types of ball milling such as attrition or vibrating ball mills in which (i) the control and/or (ii) range of the available shock energy and resulting shock power(s) is substantially smaller compared to the operating shock energy in a planetary ball mill (cf. [205,224]).

Vibrating ball mills are divided in "cold", low power frame grinders (eg. Pulverisette O) and in "hot", high energy mills (eg. SPEX), the latter with a vibrating frequency of about 20 Hz and about half the impact energies of planetary ball mills due to smaller milling balls employed (Table 8). The frame of the frame grinder including the grinding stock is moved vertically up and down (by an electromagnetic coil) against a single grinding ball of diameter 30-70 mm of which the big mass allows for plastic strain at low impact velocities (cf. [205]). Figs. 127 and 128 show a schematic of three versions of the high energy vibrating mills including one, two and three degrees of freedom in ball movement directionality. The impact frequency in high energy vibrating mills increases naturally with increasing weight ratio of milling balls (of given size) -to- (alloy) powder charge, but it was shown [242] that the impact between two colliding balls entrapp less powder volume (height) than between a single milling ball and the wall of a milling container showing a significant disadvantage compared to planetary ball milling due to a lower efficiency of the ball/wall collisions compared to ball/ball collisions and which is directly related to the high filling fraction f_{nb} ususally encountered in vibrating ball-mills. In the 1D-version, the energy is transferred into the powder only by shock, but in the 2D- and 3D-version friction is involved in the transformation of impact energy. The energy absorbed by the powder (alloy) is assumed to increase with increasing coefficient of viscosity of the powder, but no clear physical meaning has yet been attributed to this coefficient (cf. [228,229]).

Attrition ball milling (horizontal or vertical), often referred to as "high energy" ball milling, involves the rotation of stirring arms (impellers) at relatively high rotation frequencies Ω_A through a stationary vertical or horizontal tank filled with balls and material (powder), the vertical tank accomodating a vertical shaft, the horizontal technique accomodating a horizontally rotating shaft (Figs. 125 and 126) [243,244]. The stirring action of the impellers triggers - for a given Ω_A -value - a range of relatively low impact velocities of relatively small balls actually resulting in a range of - contrary to popular belief - very low impact powers at relatively high impact frequencies and mean tank temperatures (in fact, an energy form that is inevitably discernable) due to the friction that results primarily from the rotation of the billets, i.e. attrition ball milling is always confronted with a relatively high wear problem independent on the material used for impellers, balls, tank and their coatings. Commercial attritors provide rotation frequencies Ω_A in the range of 30 - 700 rpm for tanks of diameters up to about 1 m and filling volumes up to 1100 l (for larger volumes, $\Omega_A < 100$ rpm) [243]. The high impact frequencies at relatively low kinetic energies make attritor ball milling attractive for relatively fast refinement of precursors and/or microstructures, but the absence of the control of a discrete kinetic energy (due to the range of operative impeller arm distances R_A) and the relatively low

values of kinetic energy provided by attritors exclude them from the controlled formation of non-equilibrium phases unless the alloy concerned provides a large E_c -window at relatively low E_c -levels with regard to the shock energies occurring at a given impeller frequency Ω_A . The so-called "high energy" - type of attrition ball milling does not allow a precise control of shock power and of the rate of structural faults, mechanical working, local deformation and resulting non-equilibrium phase formation induced into the initial pre-cursor material as well as eventual reduction of yield due to "caking" by external milling variables set by the operator. A recently up-dated horizontal attrition ball milling technique was considered [244] to significantly (i) increase the impact energy and (ii) to decrease the variation in energy employed and (iii) to eliminate the problems relative to gravity in a vertical attritors (i.e. dead zones, density gradients in resultant powder material employed). Unlike for planetary and the classical type of horizontal ball milling (see below), however, this attritor variant is not sufficient to solve the relatively inefficient cooling associated with attritor ball milling as a result of the poor contact of the ball-milled product with the container wall.

Table 8: Characteristics I of laboratory mills. From [205].

	Attritor	Planetary mill	Vibration mill	
			Pulv. O	SPEX
Nbr of ball	>1000	5-12	1	4-10
Diameter of ball (mm)	2-10	10-20	20-70	-10
Movement of ball	roll	roll + shock	shock	shock
Velocity of ball (ms ⁻¹)	0-0.8 (a)	2.5-4. (b)	0.14-0.24 (f)	< 3.9(a)
Kinetic energy (10 ⁻² J ball ⁻¹)	< 1	1-40	0.3-3	<12
Frequency of shock (Hz)	> 1000 (h)	~100 (h)	15-50 (f)	200 (d)
Power(W/g/ball)	< 0.001	0.01-0.8	0.005-0.14	<0.24
Mean Temperature of vial (°C)	150(c)	50-120(b)	< 35 (c)	60 (g)
Peak Temperature ΔT_{max} (°C)	< 1 *	287(b)	< 1 *	170*
T_{max} (°C)	150	300	35	230
Atmosphere	GAS	GAS	GAS VACUUM	GAS

Table 1. Some characteristics of common laboratory mills:
ref.: a:[36], b:[48], c:[39], d:[35], e:[26], f:[21], g:[32],
h:[49]. *:calculated by the authors using Schwarz' formula[34].

Table 9: Characteristics II of laboratory mills. From [224].

Table 1. Documented [24] and calculated values (*: this work) of the kinetic energy, the shock frequency and the shock power for the different ball mills

	Attritor	Vibratory mills		Planetary ball mills		
		Pulv. O	SPEX	Pulv. P5	G7	G5
Velocity of balls (m/s)	0-0.8	0.14-0.24	<3.9	2.5-4	0.24-6.58	0.28-11.24
Kinetic energy (10 ⁻³ J/hit)	< 10	3-30	<120	10-400	0.4-303.2	0.53-884
Shock frequency (Hz)	> 1000	15-50	200	~100	5.0-92.4	4.5-90.7
Power (W/g/ball)	<0.001	0.005-0.14	<0.24	0.01-0.8	0-0.56	0-1.604

Horizontal ball mills used for industrial milling of composite-type of dispersion-strengthened materials consists of diameters $D = 2R = 1$ to 2 m accomodating typically 1 ton of powder and up to 10^6 milling balls corresponding to about 10 tons [245, 246]. Wall detachment of the milling balls from the internal container wall (cf. Fig. 129) occurs at rotating velocities of the cylinder ω . for which

$$\omega^2 R < g \quad (\text{MA27})$$

with g = acceleration by gravity allowing for $\omega_{\max} = 0.7$ to 0.5 Hz followed by a parabolic trajectory of the ball before impact at velocities (cf. [247])

$$v_h = 2 (gR)^{0.5} \quad (\text{MA28})$$

of values 4.4 to 6.3 m/s all of which at $D = 2R = 1$ to 2 m. The velocity of milling balls in horizontal ball mills, v_h , consists of a tangential component $v_t = \omega R = (gR)^{0.5}$ and of a normal component $v_g = (2gz)$ with z = normal component of parabolic flight trajectory (cf. [247]). The frequency of impacts per ball to the powder is of the order of ω resulting in relatively low impact powers even for high weights per milling ball (eg. $(m_h)_{i,j} = 50g$ gives $0.9J/\text{impact}$ at $v_h = 6.3$ m/s or 0.9 MJ per (above) cylinder (conditions) so (maximum) impact powers in the range below 0.45 W/g, i.e. not enough for most of the ne-phases shown in Table 7. Horizontal ball milling has attracted the attention of so-called "low energy" ball milling. Evidently, this term is as useless as the term "high energy" attrition ball milling (unless the conditions (for the operator) were defined more precisely). Horizontal ball mills with their easily obtained large container volumes are limited to ne-phase formation in systems requiring relatively low impact powers (<0.5 W/g) instead. Also milling bars can be used in horizontal ball mills to increase impact surface so milling efficiency per unit volume of milling body [223].

Ball milling by vibrating, attrition and gravity ball mills thus represent three technologies in which non-equilibrium phase formation leaved uncontrolled volume fractions of initial material and/or non-equilibrium phases due to uncontrolled and/or small impact frequencies and/or energies resulting in all cases in a limited freedom in the choice of operational variables, the resulting impact power for and control on non-equilibrium phase selection and formation. The absence of a categoric need for more substantial property improvements via phase selection by ball milling (as is offered by non-equilibrium phase formation for Mg-base alloys) and reduction upon the operating factors controlling non-equilibrium (matrix) phase formation of a given material or group of materials by ball milling have obstructed the view for a systematic control on non-equilibrium phase selection by ball milling (cf. the above reported milling times for non-equilibrium phase formation of Ti- and Al-base alloys) to date, i.e. after 20 years of world-wide ball milling. Until recently no appreciation was given to the significance of shock power controlling occurrence and formation rate of non-equilibrium (matrix) phases of a given material (see above). The natural acceleration of a milling ball by gravitation was considered

instead to provide an inherent advantage for ball milling of advanced light alloys with refined and novel microstructures and/or phase selection. However, ball milling by gravitational-type of acceleration of milling balls imposes an inherent limitation on the available shock power scale and the selection and fabrication of non-equilibrium phases by solid state synthesis (see above).

The most important limiting parameter with regard to commercialization of planetary ball mills and corresponding products is the distance R . R is of prime importance for the further up-scaling towards industrialization of planetary ball milling for non-equilibrium (matrix phase) alloys such as those based on magnesium. The potential volume to be accommodated by the overall apparatus, the resulting freedom in filling fraction and overall weight of charge with regard to centrifugal forces sustainable by the holder disc and the maximum impact energy E_c^{\max} for a given Ω^{\max} all increase with increasing R . Today, $R = \text{const.}$ for a given holder disc (table) of a given planetary ball mill, i.e. R may only vary from one type of a planetary ball mill and/or corresponding laboratory and/or supplier to another, but planetary ball mills yet to come may provide facilities to vary R for a given disc as depending on the required impact powers P_{req} to be introduced into the material. Ω and ω remain the major independent milling variables of a given planetary ball mill to control the selection of non-equilibrium phases and this remains true even if planetary ball mills with flexible and/or relatively large R -values become available to accommodate larger milling containers and milling volumes at a given filling fraction for industrialization and commercialization of planetary ball milling technology and resulting materials. The industrialization and commercialization of planetary ball milling for non-equilibrium phases and/or alloys requires the definition and minimization of the applicable scale of Ω and ω due to the operating forces and limitations set by the available materials and assembling techniques and the resulting costs for planetary ball mills.

The advantages and disadvantages of ball milling techniques regarding the fabrication of non-equilibrium alloys and the need to control a discrete value in shock power and resulting processing windows results in the following hierarchy of preference:

1. Planetary ball milling with ω decoupled from Ω (Planetary I - type) embracing practically unlimited control of ω and/or Ω and the resultant scale of shock energy E_K , shock frequency f and shock power P^* so providing higher shock-to-friction ratios and incorporating all the advantages of other ball milling techniques for the fabrication of non-equilibrium phases, matrix phases and alloys, but vial volumes are yet limited to $<200 \text{ ml}$ (cf. [220]).
2. Planetary ball milling with ω coupled to Ω (Planetary II) providing subcontrol of f and P^* for a given Ω and ω by $(n_b)_{i,j}$ or $\Sigma(\Sigma(n_b)_{i,j})_j$ and Σm_{charge} alone, but available volume limited to 500 ml/vial [204].
3. Vibrational ball milling with f -control by ω and $(n_b)_{i,j}$ or $\Sigma(\Sigma(n_b)_{i,j})_j$ and Σm_{charge} , but the resulting filling fraction f_{nb} limits the available ΔE_c - and shock power range ΔP (cf. Table

- 8 vs. 7) The resulting possibilities for (control of the volume fraction f_v^{ne} of) non-equilibrium matrix phase formation, resulting milling time t_{req} and formation rate are thus limited, but the available container volumes are of pilot or larger scale [229].
4. Attrition or Attritor Ball milling provides a large range of impact energies ΔE_c which are discretely uncontrolled for a given rotation velocity of corresponding attrition and/or stirring arms. The available volumes of milling containers are up to 1100 l (cf. [243,244]).
 5. Horizontal ball mills with vertical rotation planes limited range (and control) of f , f^* , E_c , therefore limited range and control on P and the resultant fabrication of non-equilibrium matrix phases and alloys so primarily used for the refinement of advanced alloys. Practically no limitations in container volume (cf. [245 - 247]).

3.4 Machined Mg-based Chips and Turnings Co-milled with Hard and eventually Brittle Precursor Constituents under Dry and Wet Conditions

This hierarchy was taken into account in the present invention. The characteristics of the applied apparatus (i.e. a Pulverisette 5^R) included the distance $R = 12.5$ cm, vial radius $r = 3.275$ cm, coupling parameter $k_{\Omega/\omega} = 1.17$ (cf. Fig. 119, 120) and $n_b(\max) = 124$ for the employed steel balls (cf. Table 10). Particular attention was given to the effect of the (initial) alloy charge required to obtain non-equilibrium Mg-alloys and microstructure. The actual details employed to achieve the metastable WE54 base MA-Mg alloy (which represented a relatively difficult case, see below) serve to provide the more specific milling conditions required to develop non-equilibrium Mg-base matrix alloys including extended solid solutions, amorphous and non-equilibrium crystalline, quasi- and/or nanocrystalline Mg-base phases by ball milling.

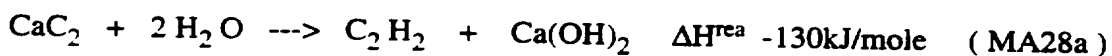
Since MA of light alloys is usually starting off from atomized powders (cf. [198]), prime question to start the investigation was: "Under what conditions can the powder atomization step be left out (in view of the additional increment on cost and surface-to-volume ratio so contamination with oxygen it confers on the overall processing route and material), i.e. can machined (pre-alloyed, in particular dilute) Mg-base chips and (bent) turnings directly be transformed to the required MA-powders?". Therefore, the selection of the initial (precursor) material is particularly important and allows to provide the information whether the initial (precursor) material can be homogenized fine enough (often interpreted as alternating (sub-) micron layers as the preliminary condition) to trigger (in a reasonable time scale) an homogeneous phase transformation for an even more homogeneous non-equilibrium matrix phase by MA.

As-cast ingot material of pure magnesium and of the magnesium alloy WE54 was used as a test bed to narrow down the required milling parameters. They were machined to chips and/or turnings of size of the order of 1 to 10 mm prior to ball milling the employed (pre-alloyed) and

Since MA of light alloys is usually starting off from atomized powders (cf. [198]), prime question to start the investigation was: "Under what conditions can the powder atomization step

be left out (in view of the additional increment on cost and surface-to-volume ratio so contamination with oxygen it confers on the overall processing route and material), i.e. can machined (pre-alloyed, in particular dilute) Mg-base chips and (bent) turnings directly be transformed to the required MA-powders?". Therefore, the selection of the initial (precursor) material is particularly important and allows to provide the information whether the initial (precursor) material can be homogenized fine enough (often interpreted as alternating (sub-) micron layers as the preliminary condition) to trigger (in a reasonable time scale) an homogeneous phase transformation for an even more homogeneous non-equilibrium matrix phase by MA.

As-cast ingot material of pure magnesium and of the magnesium alloy WE54 was used as a test bed to narrow down the required milling parameters. They were machined to chips and/or turnings of size of the order of 1 to 10 mm prior to ball milling the employed (pre-alloyed) and elemental milling charge (Figs. 130 a-f). For further details, see Table 10, below. A 2 hour - milling cycle was usually employed to compare the results obtained by MA of Mg with the published results on other metallic materials. Under these conditions, ball milling at a wide range of rotational milling speed, milling time and/or weight ratios of milling balls-to-machined chips of pure Mg and of WE54-ingot did not result in the formation of a mechanically alloyed powder (i.e. a milling effect, see overnext section) when adding a) sub-micron graphite powder and/or graphite lumps and/or b) (liquid) hexan (i.e. C_6H_{14}) or c) neither graphite nor hexan, (n.b. graphite and eg. ethyle acetate are frequently employed for mechanical alloying of Al-base alloys [269]). The use of a carbon-bearing constituent represents also a risk of formation of Mg(-base) carbides (Mg_2C / Mg_2C_3) known to be easily washed away by aqueous solutions such as water via reactions similar to (cf. [248]):



so eventually deteriorating quite significantly the corrosion resistance of the resultant MA Mg-alloys and obscuring the beneficial effects of corresponding non-equilibrium phase, while the use of an alcohol embraces the double-risk for formation of carbides and oxides and/or hydroxides due to the (-OH) subgroup of the CH_3-CH_2OH molecules involded in alchools. The addition of ethanol to ball milled Cu-Fe alloys was reported [237] to result in Fe_3O_4 - and Fe_3C -dispersions representing an hardening advantage in that case. More particular, the addition of ethanol (i) reduced and suppressed the sticking of powder to the milling ball and/or vial wall surfaces, (ii) to reduce the contamination of the MA-powder product from abrasion of milling ball and vial surfaces due to reduction of corresponding friction (coefficient) by a factor of > 2.5 for Cu-20wt.% Fe to > 25 for Cu-40wt.%Fe and (iii) improved the homogeneity of non-equilibrium Cu-base Cu-Fe-phases [237].

WE54 is a commercially established and ductile Mg-allgy composition and therefore a representative base in order to develop an extended solid solution or anot`er non-equilibrium phase

without undue increase in density due to mechanical (and/or chemical) alloying by ball milling, for example. Unlike for mechanical alloying of aluminium, for which carbon or a derivative is not only used as a lubricifier, but also in order to form a controlled volume fraction of carbides to improve their thermal stability, it is therefore more critical to use a carbon-bearing lubricifier for MA of Mg-alloys and (if a milling effect was to be obtained from machined pure Mg- and/or dilute Mg-alloy chips and/or turnings) eventually inevitable to exclude graphite and/or hexan from the milling operation unless selected precursors were added instead reducing "caking" and improving homogeneization.

A powder production (i.e. a milling effect) was obtained instead by the addition of hard and eventually brittle powder precursor constituents such as 3-micron BN, SiC, Al_3Ti and Al_2O_3 .

Table 10 Employed Initial Charges and Milling Variables

Variables	Alloys	1 Fig.3	2 Fig.9	3	4	5	6
1. Selection of End-Product and Initial Charge							
1. (Pre-alloyed) Base of Initial Charge including absolute quantities [g and cm^3]	WE54	6 / -	4.5 / -	4.5/2.5	6 / -	8 / -	8 / -
2. 1. Form of (Pre-alloyed) Base of Initial Charge (for machined chips/turnings: diameter or width [mm] length [mm])	Fig.20c	Fig.20d	Fig.20a	Fig.20b	Fig.20e	Fig.20f	
2.2 Alloying Additive I [g and wt.%] (i.e. absolute and relative quantity)	5 5-6 25*10	<1 5	5 5-10	5 5-6	20-30 8-12		
2.3 Form of Alloying Additive I	0.54/9.0	0.113/2.5	0.13/2.8	0.18/3.0	0.24/3.0	0.24/3.0	
3. Atmosphere ¹⁾ (of Milling Container) (i.e. Static/purged - inert gas/vacuum)	Al_2O_3	Al_2O_3	Al_2O_3	Al_2O_3	SiC	SiC	
4.1 Lubrifying Additive I (absolute [ml] and relative [wt.%] quantity)	- 3 μm -powder	5N Ar					
4.2 Purity of Lubrifying Additive I	static/1 bar						
	none	none	none	hexan	none	hexan	
	n.a.	n.a.	n.a.	1.0/11.6	n.a.	0.5/5.0	
	n.a.	n.a.	n.a.	>95%	n.a.	>95%	

(continued on next page)

reinforcements (called "alloying additives" in the following) to the machined Mg- and WE54-chips and turnings prior to the milling operation. The results showed that the use of at least one of the hard and eventually brittle precursor constituents BN, SiC and Al_2O_3 instead of a classical lubricifier such as graphite or hexan was inevitable to obtain a "milling effect", i.e. a mechanically alloyed (overall) powder from machined Mg- and WE54-chips and turnings. A high temperature metastable phase (see above) was obtained after ball milling for only 2 hrs. when 3-micron Al_2O_3 was added to the machined WE54-chips without the addition of a lubricifier (Figs. 106 and 131). However, the milling operation with Al_2O_3 and without lubricifier led to substantial welding and smearing of the alloy charge to both the (interior) surface of the vials and to the surface of the milling balls when employing $\Omega > 190$ rpm. As for the ball-milled Cu-base Cu-Fe alloys (cf. [237]), the welding and smearing of the resultant alloy to vial and milling ball surface was reduced by the addition of a lubricifier, here hexan, but in a

Table 10 / Cont'd





II. Selection of Apparatus

5. Volume of Milling Container [l]	0.133	→
6. Ball Milling Technique	Planetary II	→
7.1 Rotational Separation Distance R' (R) [m]	0.125	→
7.2 Range Ω^{\min} to Ω^{\max} (i.e. $\Delta\Omega$) [rpm]	80 - 360	→
7.3 Range ω^{\min} to ω^{\max} (i.e. $\Delta\omega$) [-rpm]	179 - 716	→
7.4 T-control and/or Range T^{\min} to T^{\max} [°C]	none	→
7.5 Coupling parameter (eg. $k_{\Omega/\omega}$)	$k_{\Omega/\omega} = 1.17$	→
8. (Range of) Material of Milling Container	Fe - 13Cr - 0.4Mn - 0.3C [wt. %]	→
9. (Range of) Material of Milling Balls	Fe - 6Cr base [wt. %]	→
10. Radius of Milling Container r [mm]	32.75	→

III. Selection of First Order Milling Variables

11. Ω [rpm +/- 10%]	206	206	168	264	160	293
12. ω [-rpm +/- 10%]	241	241	197	310	187	343
13. T [°C]	22° to 70° →					

IV. Selection of Second Order Milling Variables

14.	i/j	1/1						
15.1	$\rho_{b,1}$ [g/cm ³]	7.60						
16.1	$r_{b,1}$ [mm]	5.0						
17.1	$(m_b)_{1,1}$ [g]	3.98						
18.1	$(n_b)_{1,1}$	18	10	10	18	17	18	
19.	f_{nb} [%]	14.5	8.1	8.1	14.5	13.7	14.5	
20.	$\Sigma m_{charge} = \Sigma m_{alloy} + \Sigma m_{(alloying\ additives)}$ [g]	6.54	4.61	4.63	6.18	8.24	8.24	
21.	$\Sigma(\Sigma(m_b)_{i,j}) / \Sigma m_{charge}$	10.95	8.63	8.63	11.59	8.21	8.694	

V. Results

22. E_c (for $K_a = 1$) [mJ/impact]	17	17	10	26	10	45
23. $f^* - f^*$ [Hz] - [Hz/gram]	97/15	54/11.7	40/8.64	115/18.6	61/7.4	126/15.3
24. $P^*(T)$ [W/g]	0.26	0.20	0.09	0.48	0.07	0.69
25. Powder Yield f_v^y	0.5	0.2	0.9	0.98	0.95	0.99
26. Powder size [μ m] (mean, if not otherwise)	-	-	200	95% < 315	170	100
27. Volume fraction non-equilibrium phase f_v^{ne}	0.5	0.6	<0.1	none	<0.1	none
28. T_{transf} of ne-phase [°C]	500	613	(600)	n.a.	(<300°)	n.a.
29. $t_{req}(f_v^y, f_v^{ne})$	2 h →					

1) Various authors recommend the use of teflon or indium rings to seal the milling container (vial). However, no effect was discovered over the use of conventional O-rings.

relatively large quantity (i.e. 5 - 12 wt.%). This addition reduced and/or suppressed the formation of the high temperature non-equilibrium metastable phase within a 2 hour milling intervall.

The details of the milling variables to obtain a milling effect with a yield of 95 to 99% or a non-equilibrium phase of about 60 vol.% after 2 hrs of ball milling are shown in Table 10. The results on ball-milling (WE54 + Al₂O₃) are consistent with rapid amorphization in a P*-window around 0.20 - 0.26 W/g employing dry milling conditions. This P*-window appears relatively narrow at a lower level compared to the P*-window for amorphization of Ni₁₀Zr₉.

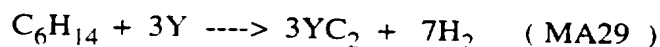
suggesting the fabrication of Mg-base ne-phases by other ball milling techniques (see above). The evolution of heat of transformation (which is related to the volume fraction of corresponding non-equilibrium phase) with milling time represents a non-linear phenomenon (cf. Figs. 115 and 132a-c and [205]). Weeber et al. recorded [249] the crystallization enthalpy ΔH_x of ball-milled $\text{Fe}_{20}\text{Zr}_{80}$ as a function of ball milling time showing saturation of the increase in ΔH_x after about 30 hours (Fig. 132 a). The results were confirmed by the entire absence of (crystalline) hkl-reflections for as-milled $\text{Fe}_{50}\text{Zr}_{50}$ after ball milling times > 16 hours (Fig. 132 b). It was concluded that amorphization in the latter occurred after 4 to 16 hrs of ball milling after an average layer thickness of about 100 nm of crystalline Fe and Zr had formed. Similar results were reported on MA of elemental (Ni and 2 Ti) and after mechanical grinding of crystalline NiTi_2 intermetallic alloy for the formation of amorphous NiTi_2 alloy (cf. Fig. 132 c and [207]).

If the reduction in X-ray peak intensity is associated with increasing irreversible exothermal effects on differential scanning calorimetry (DSC), the reduction in X-ray intensity can be considered proportional to the reduction of corresponding (equilibrium) crystalline phases. Fig. 133 shows a non-linear extrapolation of the volume fraction metastable phase estimated from the reduction in corresponding X-ray peak intensity according to Fig. 131. The extrapolation results in an estimated milling time required of about 8 h for the formation of 100% or nearly 100% volume fraction of corresponding metastable phase obtained by MA of WE54-chips and turnings by using (hard) Al_2O_3 -alloying additions at a low yield ($< 50\%$) due to "caking". Evidently, the addition of Al_2O_3 promotes the ne-phase formation of dilute Mg-base alloys by ball milling. One possibility to interpret these results is the large negative heat of formation of Al_2O_3 among the more common reinforcements, i.e.

SiC : - 64.4 kJ/mole
 Mg₂Si : - 78.2 kJ/mole
 Al₂Y : $< - 500$ kJ/mole (i.e. $> - 500$ kJ/mole)
 MgO : - 597.5 to - 602.5 kJ/mole
 Al₂O₃ : - 1663.5 to - 1690 kJ/mole

eventually providing a shorter milling cycle from "3" to "2" than is possible from "1" to "2" in Fig. 134. It shall be noted that during the 2 h milling cycle the temperature of the vials was measured to have increased to up to 70°C depending on the number of milling balls and the rotational speed employed.

From Table 10 it is evident that the addition of hexane increases yield, but also milling time required to achieve a given volume fraction non-equilibrium Mg-base phase structure provided that the (hard and/or brittle) Al_2O_3 -precursor powder of size 3 micron was added to the machined Mg-base chips. According to the extrapolation shown in Fig. 133, a milling time of $>> 10$ h would be required to obtain a fully non-equilibrium phase of (about) 100% yield made from machined WE54-chips and turnings plus 3 wt.% Al_2O_3 powder of size 3 micron. It appeared that the lubricant reacted with yttrium following



and/or the rare earth metals and eventually suppressed the formation of the non-equilibrium phase due to the very negative value in the enthalpy of formation ΔH^{for} of YC_2 (cf. eq.s MA2 and MA3) when WE54 was ball-milled with hexan resulting in a reaction enthalpy ΔH^{rea} which is about 3580 kJ/mole more negative than without hexan and eventually leading to a dealloying effect on the Mg-matrix with yttrium (n.b. the ΔH^{for} -value of hexan is 170 kJ/mol). The development of non-equilibrium Mg-alloys without excessive "caking", minimized contamination and inhomogeneities (cf. [207]), high powder yield and alloy performance on the one hand and sufficient volume fraction and formation rate of corresponding ne-phase, i.e. without (excessive) formation of carbides (and/or (hydro-) oxides) and milling time required for ne-formation on the other require:

1. smaller fractions of friction-to-shock energy as forthcoming from the coupling factor $k_{\Omega/\omega}$ and resulting high vial velocities ω (see above).
2. a sophisticated choice of precursor constituents to avoid competition from competing phase formation (see above), and
3. the use of small(er) quantities (fractions) of lubricifiers such as hexane.

3.5 Hard and Brittle "Alloying Additives" to Reduce $t(\text{me})_{\text{req}}$

The addition of a hard and eventually brittle precursor constituent was shown to be crucial to obtain a ball-milled Mg-base powder from machined precursors within a reasonable milling period (i.e. < 2 h) independent on whether a lubricifier (hexane) was added or not making it necessary to address the effect the engineering properties of selected elemental and/or compound based "alloying additives". The addition of at least one hard and brittle precursor was shown to substantially reduce the milling time required for formation of Mg-base ne-phase and/or suitable powder by ball milling, since they rapidly provided a dynamic equilibrium between welding and fracture (or shear) when ductile Mg-base alloy chips were employed. The hard and relatively brittle γ -TiAl alloys, for example, showed a rapid refinement in microstructural length scale down to 40 nm or so (and which corresponds to the formation of alternating layers) after MA for $t(\text{me})_{\text{req}} < 2\text{h}$ (cf. Fig. 135 and [192,232]). This is in agreement with the invention that the addition of Al_2O_3 results in a significant volume fraction of non-equilibrium WE54-base phase formation after 2 hrs of planetary ball milling, i.e. when using ductile precursors.

The use of Mg-powders instead of machined chips to obtain high-performance Mg-alloys including materials for hydrogen storage (see below) by ball milling is also possible, but it provides a number of disadvantages. Dilute Mg-alloys such as Mg-TM based systems (TM = Ti, V, Zr, Cr, Mn, Nb, Mo, Ta, Hf etc.. and also B and Be, all with almost complete immiscibility in liquid Mg) and the Mg-met based systems (where met = Si, Ge, Sb etc. with their very low solubility in the equilibrium solid cph-Mg), for example, do not or merely possess the

possibility for pre-alloying from the liquid to provide a one phase field at equilibrium so pre-alloyed topological, i.e. atomic structural and/or microstructural configurations to minimize $t(\text{me})_{\text{req}}$ for the required non-equilibrium, Mg-base powder end-product. As elemental powder, magnesium and many other alloying additions such as V are either not easily commercially available, prone to absorb intolerable oxygen levels and/or very toxic (upon inhalation, for example). It is therefore very attractive to start the milling procedure from machined (if possible, prealloyed) chips and turnings instead of employing corresponding powders and to extend this approach to ductile alloying elements such as V and/or Zr or very pure Ti (and, if a (major) TM-alloying component(s) such as Ta is shock-resistant and/or - for a given set of milling variables - not hard and/or brittle enough) by adding a hard and brittle (third) alloying additive such as Al_2O_3 instead of using (eg. impure) elemental V, Zr etc.. Alternatives include co-milling with BN due to the boron, with SiC due to the silicon and with Al_2O_3 and/or $\text{Ti}_x\text{Al}_y\text{Al}_3\text{Ti}$ due to the aluminium and/or Ti (cf. previous chapters).

Masumoto et al. have recently taken up [250] the advantage to employ a compound-element mixture including aluminium and monoclinic $\text{Al}_{13}\text{Co}_4$ or aluminium and orthorhombic $\text{Al}_{11}\text{Mn}_4$ -powders in order to obtain amorphous $\text{Al}_{85}\text{Co}_{15}$ and amorphous $\text{Al}_{85}\text{Mn}_{15}$ which were claimed not being obtainable by using corresponding elemental precursors alone. More detailed observations by Courtney and co-workers have shown [251] that ductile-brittle precursor mixtures are more effective for powder particle refinement so reduced welding by ball milling at higher ball velocities (cf. Fig. 136). The higher velocity-regime, however, is the required avenue for the economical viable fabrication of non-equilibrium phase resulting from activation energy and/or power thresholds and time-constraints set by amortization of equipment and affordable acquisition costs.

The addition of hard, eventually brittle refractory compounds with elements likewise contributing to the passivation of the resulting Mg-alloy surface accelerates the overall formation of the envisaged non-equilibrium phase formation due fracture of the more ductile precursor constituents such as pure and/or pre-alloyed Mg and to suppress excessive welding (i.e. "caking") at the same time, i.e. to accelerate the formation of alternating layers and the start of more global interdiffusion and metastable phase formation in particular. The homogeneization of the initial chips, turnings, precursor powders etc. is directly related to the formation rate of powder particles of final composition before the local configuration of the initial precursors, i.e. before structural faults introduced by shock power start to control the rate (and yield) of non-equilibrium (eg. Mg-based phase formation during $t(\text{ne})_{\text{req}}$. Oxides such as Al_2O_3 , carbides such as SiC, nitrides such as BN and aluminides such as Al_3Ti , have evidenced their ability to introduce the "milling effect" and to reduce the time required to start (interdiffusion-controlled) Mg-base phase formation (i.e. within less than 2 hrs in the case of WE54-chips and -turnings together with Al_2O_3). Therefore, an "alloying additive" has to play two roles upon MA for non-equilibrium

brium (matrix and/or one-) phase Mg-base (and other) alloys:

1. facilitating fracture and welding on a sub-micron scale to reduce the time required to trigger the onset for non-equilibrium phase formation as is induced by shock-assisted and structural fault enhanced interdiffusion without loss of material by "caking".
2. thereby being "consumed", i.e. alloyed "away" and eventually (co-) passivating the Mg-base (non-equilibrium) matrix phase.

Ductile precursors such as pure Mg and/or terminal Mg-alloys such as WE54 and/or ductile and shock-resistant passivating components such as Ta or V do not fulfill requirement N°1 for an "alloying additive" and remain simple precursor (initial) materials. Most of the passivating components are likewise hard and brittle providing an ideal basis for requirement n° 1, i.e. to fracture terminal so ductile Mg-base precursor constituents without the need to employ (larger quantities of eventually contaminating) lubricifiers.

Mechanical alloying and/or ball milling of (terminal, i.e.) Mg-based precursors together with a brittle "alloying additive" instead of using classical lubricifiers (alone) reduces the required milling time to generate alternating layers in the (sub-) micron range prior to trigger mutual (thermal and athermal) interdiffusion of the involved components so circumventing the particular drawback set by the available equilibrium constitution of Mg-alloys (cf. above) and the resultant need to employ elemental and/or Mg-free precursors with an eventually very different chemistry and crystal structure instead of pre-alloyed precursors better corresponding to chemistry and structure of an homogeneous non-equilibrium Mg-base end-product. Choice and level of the "alloying additive" in order to rapidly obtain the "milling effect" without "caking" belong to the prime parameters for the development of economically viable Mg-base engineering alloys by ball milling. The conditions (milling variables and selected precursors) for Mg-base powder production by ball milling without "caking" on the surface of vials and milling balls of the resultant (dilute) Mg-alloys by starting from machined (prealloyed) Mg-base chips and turnings as well as from atomized Mg-base powders, all without undue increase in density due to (mechanical) alloying in order to produce equilibrium and non-equilibrium Mg-base alloys with superior engineering properties, are given in claim n°2.

3.6 Attributes of Alloying Additions to Reduce $t(ne)_{req}$

While the selection of the "alloying additive" (i.e. the chemistry and/or (crystal) structure) did not (appear to) affect by very much the resultant "milling effect" (i.e. the production of powder due to alternating layer formation by (interparticle) welding and fracture without substantial "caking"), the choice of the "alloying additive" significantly affected the rate of non-equilibrium phase formation. Al_2O_3 was found to be more effective in this respect for ball milling of pre-alloyed WE54-chips (and turnings) than BN and SiC. Al_2O_3 appears to be an attractive "alloying additive" to corrosion-resistant non-equilibrium Mg-alloys containing alloying elements with an incompletely occupied electron shell such as transition metals (eg.

Ti, Ta, V, Nb, Mo, Hf, Cr, Mn, etc.) and rare earth metals (see previous chapter), i.e. to reduce the milling time required for (a given volume fraction of) non-equilibrium phase formation by acceleration of a constitutional change for the matrix phase after the milling effect, i.e. after alternating layers and the start of more general interdiffusion had occurred, since Al_2O_3 appears to be very effective in order to trigger Mg-base ne-phase transformation (cf. § 3.3 of this third part of the invention).

Mg is a generally attractive candidate for non-equilibrium phase formation by ball milling on this particular aspect, since it provides a relatively high (self-) diffusivity due to a high lattice vibration (literally, Mg has a "blown-up" atomic volume relative to its atomic core charge and weight) and thus relatively high resultant ΔD -values with many of the more useful alloying additions for corrosion resistant Mg-alloys, in particular with TM and metalloids due to their high melting points (cf. Table 11). The temperature range in which diffusivity data for TM and metalloids were recorded, however, were usually significantly higher than the melting point of pure Mg. $\Delta D = D_T(\text{Mg}) - D_T(\text{X})$ is therefore only obtainable from more universal empirical relationships for diffusion in solids such as

$$D_T = 2.3 \cdot 10^{-7} \exp [- (Q_D / RT)] \quad [\text{m}^2/\text{s}] \quad (\text{MA } 30)$$

where $Q_D = 17.7 T_m$, T_m the melting point of the component concerned and T = service or milling temperature, eg. ambient (all in [K], cf. [252]). Therefore, the difference in melting point is sufficient to assess the effect of alloying additions on rate-control for Mg-TM and/or Mg-met based ne-phase formation by ball milling (cf. Table 11).

The melting point of an element is also proportional to mechanical properties such as hardness and modulus of elasticity, for example [255,256]. The elastic modulus represents a pure mechanical, i.e. athermal contribution to the power required for propagation of mechanical shock waves, i.e. (cf. [257]):

$$P(E) = 1/2 C A \rho (\omega_E)^2 s^2 \quad (\text{MA31})$$

where C = phase velocity of the mechanical wave following:

$$C = (E/\rho)^{0.5} \quad (\text{MA32})$$

A = propagation front surface, ρ = density and ω_E and s the frequency and amplitude of the mechanical shock wave. In analogy to the ΔD -criterion, differences in elastic modulus provide a local driving force for homogenization of the mechanical impact power provided by ball milling so another, but important and consistent criterion regarding previous constitutional material parameters to promote the formation rate of Mg-based over other ne-phases following

$$\Delta P(E) = (E_p(\text{X}))^{0.5} - (E_p(\text{Mg}))^{0.5} \quad (\text{MA33})$$

Ball milling of Mg-based precursors with TM- and/or met-based precursors should therefore

Table 11 Selected Properties at Ambient Temperature of Early Transition Metals and Metalloids for Mechanical Alloying of Mg-Alloys (from Smithells [253], Johnson Matthey's [72] and Weast [254])

Metal	ρ [g/cm ³]	Hardness ¹⁾	Ductility ³⁾ [%El.]	Young's Modulus E [GPa]	E/ ρ [GPa/ g/cm ³]	T _m [°C]	T _m ρ [°C]
Mg	1.74	35-45 B ²⁾ 2.0 M	ductile	45	25.9	650	-
α Ti	4.51	60 V	ductile	112	24.8	1668	746
V	6.11	-	very ductile	138	22.6	1900	724
Cr	7.19	9.0 M	brittle	248	34.5	1875	709
Mn	7.43	5.0 M	brittle	-	-	1245	678
α Zr	6.51	110-170 V	18	93	14.3	1852	715
Nb	8.57	200 V	2	103	12.0	2468	719
Mo	10.22	250 B	1 - 5	293	28.7	2610	710
Hf	13.1	152 V	ductile	40	10.7	2222	686
Ta	16.6	150-200 B	1 - 2	188	11.3	2966	690
W	19.3	488 B	1	360	18.7	3387	691
Re	21.0	-	24 A	468	22.3	3180	684
Be	1.85	106-130 V	0 - 3	300	162.2	1283	-
B	2.34	9.3 M	brittle	-	-	2100	1302
Si	2.33	7.0 M	brittle	-	-	1410	984
Ge	5.32(?)	-	brittle	-	-	937	671

¹⁾ B : Brinell hardness, V : Vickers hardness, M : Mohs hardness: data are for commercially pure metals, if not indicated otherwise.

²⁾ extruded bar

³⁾ in "hard" condition, if not indicated otherwise; A : annealed

result relatively rapidly in corrosion resistant ne-phases with high modulus and/or strength as a result of the rule of mixtures at least. That is, that the attributes to rate-control ne-phase formability tend to coincide with the requirements for attractive engineering properties in the particular case of ball-milling for selected Mg-based ne-phases, and are primarily dependent on the involved constituents and less dependent on concentration.

An increase in crystallization temperature T_x of amorphous $\text{Fe}_{75}\text{Zr}_{25}$ of around 100°C by the addition of 15 wt.% boron was reported, for example (cf. [211]). The effect of boron was considered to enhance vacancy-based interdiffusion of boron into amorphous FeZr-layers during milling and in particular after milling during heat treatment for 2 hrs at 550°C . There is no evident obstacle why the hard boron material should not produce similar effects such as an increase in the transformation temperature of non-equilibrium Mg-Zr and other Mg-TM alloys, for example, which would then, in return, allow for higher milling temperatures and shorter milling times required. A universally applicable criterion to predict the maximum milling temperature for ne-phase formation by ball milling is (in a first approach) the Kauzmann criterion [258] to predict the alloy glass temperature T_g , i.e.

$$T_{\text{transf}} = k_{\text{transf}} * T_g = k_{\text{transf}} (0.22 - 0.25 T_m) \quad (\text{MA34})$$

where k_{transf} is an empirical constant to quantify the effect of phase selection by the system.

The DSC-analysis of ball-milled Mg-10 wt.% Ti doped with 5 wt.% brittle boron lumps of size of some mm results in fact in a significant shift of the onset of the irreversible exothermic transformation temperature from some 240°C to (for a heating rate of 40 K/min) as high as 550°C (Fig. 137) and was directly followed by an endothermal melting above this transformation (Fig. 137). That is, ball milling of Mg-Ti with boron results in a non-equilibrium Mg-base phase with the same very high transformation temperature as ball milling of WE54 with Al_2O_3 . The conditions employed were $R = 13 \text{ cm}$, $r = 3.3 \text{ cm}$, $r_b = 0.75 \text{ cm}$, $m_b = 14 \text{ g}$, $n_b = 5$, $\omega = 200 \text{ rpm}$ and $t = 12 \text{ h}$. The only variable was Ω with 180, 260, 380 and 456 rpm resulting in a ball-milled end-product which was not tight up by "caking" of 1, 30, 80 and 80-90 volume %, respectively, and in a gradually increasing magnitude of the exothermal effect around 600°C . That is, for a given milling time (i.e. here of 12 hours) both the magnitude of the irreversible high temperature exotherm and yield of the resultant ball-milled end-product are directly coupled to each other and decreased with decreasing ratio of the employed shock-to-friction ratio (Fig. 137). It is concluded that ball milling of the relatively dilute terminal so ductile Mg-based alloys containing passivating components such as light/early rare earth and/or transition metals and/or metalloids require either:

1. to perform the milling operation at a relatively high absolute value of shock energy and resultant power and/or
2. to employ a relatively high ratio of shock-to-friction to avoid excessive "caking" and/or retardation/delay in non-equilibrium phase formation and/or

3. to decrease the size of the brittle precursor (eg. use of B- or BN-powder instead) and/or to increase the volume fraction of any type of brittle alloying addition such as B, BN, Al_2O_3 etc. to reduce (excessive) welding and/or "caking" during the milling operation and to increase the freedom to increase factors 1. and 2., for example,

so increasing non-equilibrium phase formation rate at high yield and/or the yield itself. That is, the requirements for phase stability and productivity are directly interrelated and/or equivalent within a certain regime of selected precursor mixtures and corresponding operating variables as summarized in claim 2.

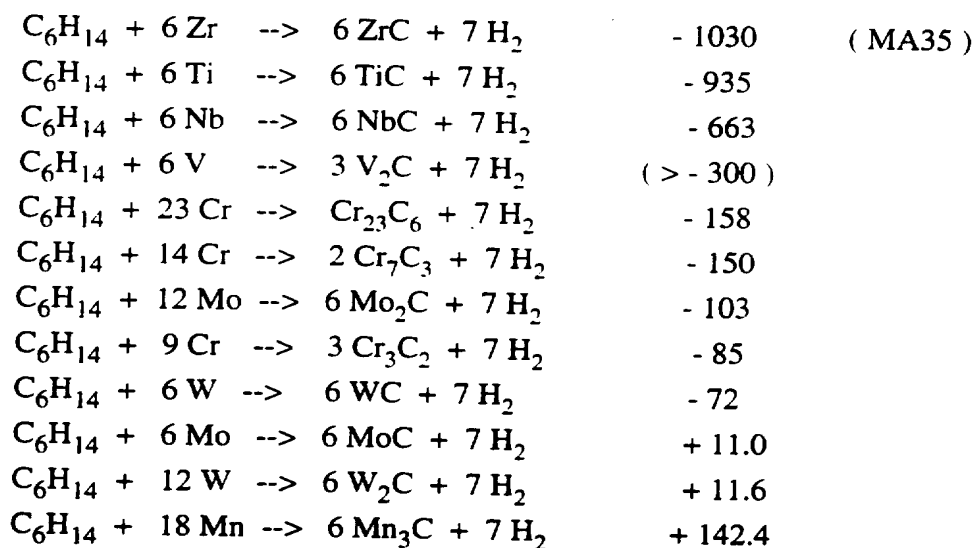
Evidently, not only hardness, modulus of elasticity and interdiffusivity, but also the onset of non-equilibrium phase transformation are atomistic properties and in some cases, as for metalloids such as boron, all related to the (mean) melting (and boiling) point of the involved alloying elements making the claimed combinations of selected transition metals and metalloids attractive candidates for non-equilibrium processing of thermally stable Mg-based ne-phases with high modulus and corrosion resistance. A mixture of Mg-Ta-Ti-Mo and/or Mg-V-Cr (or other higher order Mg-TM-TM-TM alloy combinations) relaxes the choice and quantity of alloying and/or lubricifier additions, since alloying elements such as Cr and Mo are brittle, while the addition of a metalloid such as Si and/or SiC (and/or B and/or BN, Al_2O_3 etc.) enhances not only the brittle-to-ductile fraction when employed in conjunction with ductile Mg-base precursors, but in particular the specific modulus. Evidently, the combination of these elements provide ideal combinations of alloying additions to accelerate the formation of non-equilibrium Mg-base alloys by MA due to their very different ductility, melting points and elastic moduli.

3.7 Use of Lubrifiers

Classical lubricifiers (carbon, alcohols) appear only ineffective to increase yield of terminal Mg-base alloys in combination with hard and eventual brittle "alloying additives". The quantity of the lubricifier such as hexan is to be minimized with regard to the eventually resulting formation of micro-galvanically active dispersions such as carbides or other reactands in the as-milled powder and their affordable volume fraction with regard to the level of alloying additive and/or milling time employed. If the resulting dispersion is micro-galvanically inert, a controlled and eventually moderate addition of lubricifiers such as hexan (or silan) allows to tailor in-situ-wise corresponding as-milled microstructure which is to be explored further on subsequent consolidation and forming operations.

The combination of "alloying" and "lubrifying" additives has to energetically allow for the formation of the required non-equilibrium Mg-base alloy. Reaction milling of aluminium base alloys involves the controlled addition of oxides and/or oxygen and/or the addition of carbon-bearing lubricifiers to be directly converted into an Al-base oxide or carbide dispersion (cf. [269]) and represents a quite straightforward approach for which it is sufficient to employ less sophisticated ball milling techniques such as horizontal ball mills. In the redoxation milling for equilibrium and non-equilibrium Mg-base alloys, however, "alloying" and "lubrifying"

additives are consumed (away) by a redox-reaction induced by the milling operation in order to trigger a non-equilibrium Mg-matrix phase transformation instead. An hexane/TM part of Mg-base precursor mixtures shows significantly smaller (partial) heats of reactions, ΔH^{rea} , due to substantially lower ΔH^{for} -values for the formation of corresponding carbides than hexane with rare earth and/or yttrium so increasing the probability of alternative reactions including the formation of a (disordered) homogeneous non-equilibrium Mg-base one-phase matrix induced by shock energy (here with $d\Delta H^{\text{rea}} = \Delta H^{\text{for}}(\text{TM}_a\text{C}_b) - \Delta H^{\text{for}}(\text{C}_6\text{H}_{14})$, in [kJ/mole]) in following order [259]:



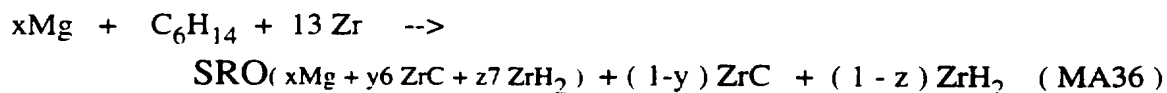
The use and involvement of an initial TM-compound (with negative ΔH^{for}) instead of elemental TM and/or the additional use of a ceramic compound (negative ΔH^{for}) would increase non-equilibrium phase formability due to reduced (macroscopic) enthalpy (less driving force) for carbide formation (cf. eg. MA29), since corresponding left hand side of the reaction would be more stable if (a controlled quantity of) hexane was employed as a lubricifier and the $d\Delta H^{\text{rea}}$ - balance would shift to more positive values so increasing the (constitutional) window for formation of a non-equilibrium Mg-base matrix phase with decreasing heat of formation of the potential carbide (here with Mn least disturbing in this respect). Among the common reinforcements, Al_2O_3 provides the largest destabilization effect on the reaction (less than 1 mole Al_2O_3 compensates for the tendency of 1 mole hexane to form Zr-carbides).

However, Mg (-Zr based) alloys are known to undergo self-degassing via the formation of hydrides such as ZrH_2 [260]. Self-degassing is therefore also possible in other Mg-transition, Mg- rare earth and eventually Mg-metalloid based metals. The formation of hydrides (and/or related short range orders) increases the exothermic nature of eq. MA35-type of reaction:



and would therefore energetically support the tendency for ne-phase formation by ball milling, since the system Mg-Zr-ZrC-ZrH₂ represents effectively a pseudo-quaternary system with two

compounds reducing dramatically corresponding free energy according to the situation shown in Fig. 134. On a microscopic scale, the ne-phase formation is supported kinetically by a tendency to form short range orders (SRO) dissimilar from the crystal structure of an equilibrium phase of same composition following



and which may act as a nuclei for an homogeneous ne-matrix phase eventually involving interstitial atoms such as hydrogen and/or carbon homogeneously distributed on an atomic length scale or not. The Zr in eq.MA36 is representative for other TM and metalloids (cf. Table 11). The tendency to support ne-phase formation via SROs has been observed in other Mg-based systems such as Mg-Ni [261] and was considered to be inducible by hydrogen in compounds such as C15 Laves phases [262]. The corrosion properties of the final ball-milled Mg-alloys is further improved by replacing hydrocarbons with silanes (eg. SiH_4) to entirely circumvent the formation of carbides including corresponding SRO, but this would require special safety precautions to prepare and handle the involved products.

The potential of silans and/or hydrocarbons such as those of the C_nH_{n+2} -series to induce ne-phases with an homogeneous distribution of alloying additions on an atomic length scale, i.e. on the constitutional side is reduced by the introduction of slip so efficiency of the mechanically introduced impact power. One way to increase the operative efficiency of a ball mill for ne-phase formation of a given "wet" alloy charge is to maximize the ratio of shock-to-friction energy as is possible in particular by using planetary ball mills (see previous chapters). If hard and/or eventually brittle "alloying additives" are involved in the wet alloy precursor charge, the use of selected "lubrifying additives" relax the milling conditions allowing for more extreme mechanical impact power cycles such as at the beginning of the operation to improve powder quality (control of powder size and and corresponding frequency distribution, cf. [194,203]) without reducing the formation of metastable phases achieve of a given powder yield. If hydro-carbon(s) is/are employed, the milling operations should ensure to complete both (i) the redoxation reaction of the hydrocarbon(s) or similar lubrifiers including self-degassing via transition and/or rare earth and/or metalloid metals and/or (ii) to let the (excess) hydrogen and/or hydrocarbon essentially escape from the material before finishing the milling operation so allowing for consolidation operations without the need for degassing the (precompact) powder (cf. [194,203]).

3.8 Choice of Milling Atmosphere and Further Ball-Milled Materials

The repeated exposure of fresh, rough and highly activated metallic interfaces to atmospheric gases renders ball milled materials, in particular reactive metals for aerospace applications such as Al, Ti and Mg very sensitive to absorb atmospheric gases such as oxygen and nitrogen [205]. It is therefore straightforward to employ inert and very pure protective atmospheres of

helium, argon, hydrogen, krypton, neon, and/or xenon, for example, and/or a vacuum in the milling container concerned prior to start the milling operation.

By contrast, reactive milling in an oxygen and/or nitrogen or carbonized atmosphere is deliberately used for the fabrication of nitrides such as TiN, ZrN, BN, Mo₂N, Si₃N₄, AlN, Cu₃N and/or W₂N, for example, but is also extendable to the fabrication of oxides and carbides including SiO₂, ZrO₂, Ta_xC_y etc. which will then serve as a base material to fabricate temperature stable and thermally resistant diaphragmas for controlled vapour deposition processes as to the invention (see above) [205]. These materials are homogeneous, since the chemical reaction can continue in the interior of the material, while the reaction rate is enhanced by high milling powers, the increase in milling temperature and the quantity of gas supplied to the milling container as all is possible via planetary ball milling, for example.

The advantages to provide high rates of defect formation makes planetary ball milling also very interesting to fabricate more economically more effective hydrogen storage materials. Terzieva et al., for example, reported [266] on an improvement of hydrogen storage capacity, hydriding and dehydriding kinetics of mixtures of magnesium and a LaNi₅ type of MM'₅ alloy where M is a mischmetal consisting of La, Ce, Pr and Nd and M' is nickel with Al, Co and Mn impurities, the MM'₅ content at levels of 30wt.% or so, after planetary ball milling by using milling balls of mass 12 grams or so. From the invention it is evident that the mass of the milling ball is of secondary importance relative to the discussed hierarchy of parameters controlling the rate of the introduction of structural defects including ne-phase formation and/or the milling effect, i.e. the injected impact power and not the mass of milling balls is controlling hydrogen storage capacity and fabrication of Mg-based materials made by ball milling. Recent development, however, concentrated on the effect of Ni-concentration in ball-milled Mg-alloys and the effect of catalysts such as Pd to improve the hydrogen storage characteristics of ball-milled Mg-base alloys [267, 268]. From this invention, however, it is evident that the micro-structural refinement and the increase of structural defects to increase the hydrogen storage capacity of such materials does not require very large P* and E_{c,c}-values, but that the hydrogen storage capacity increases with increasing P* and E_{c,c}-values. This aspect is taken into account in claim 2 of the invention.

3.9 In-situ and Post-Milling Annealing, Milling Alternatives

Post-milling isothermal annealing for 24h at 500°C of initial alloy Si-33.3at.%Fe consisting of a mixture of elemental iron, silicon, FeSi, crystalline α -FeSi₂ plus an amorphous phase in the as-milled state was reported [189] to increase the volume fraction of the amorphous phase at the expense of the (elemental) crystalline phases with decreasing grain size. Similar mechanically activated annealing and/or solid state diffusion processing was observed in MoSi₂ and WSi₂ [265]. Ball milled Al-Fe base alloys [269] were subjected to a first milling cycle of 8h using a weight ratio of ball-to-alloy precursor charge of 10:1, the ball-milled Al-Fe

base alloys consisting of an solid solution supersaturated with Fe (and/or Mn), which decomposed during subsequent annealing into metastable Al_6Fe (at 320°C) or equilibrium $\text{Al}_{13}\text{Fe}_4$ (at 400°C) of size up to $40\text{ }\mu\text{m}$ followed by a second milling cycle of 6-8 h in order to enhance homogeneity and microstructural refinement of the resulting second phase intermetallic dispersion of size 0.1 to $0.6\text{ }\mu\text{m}$ with grain size 0.1 to $0.5\text{ }\mu\text{m}$ (Fig. 138).

The invented Mg-TM-met alloys provide excellent candidates for homogeneization by in- and ex-situ (post-milling) heat treatments in order to take undissolved constituents into (crystalline or amorphous) solid solution, i.e. either during and/or after a controlled milling cycle due to the above ΔD - and ΔE -criteria compensating for the positive heat of mixing as forth-coming from the large immiscibility gaps of the Mg-alloy systems for passive surface oxides and providing a barrier to economically viable processing (that is, that unlike (elemental) precursor mixtures increase $t(\text{me})_{\text{req}}$ and the tendency to form like-like atomic pairs (A-A and B-B etc.) so $t(\text{ne})_{\text{req}}$ for the formation of ne-phases with an homogeneity on an atomic length scale compared to pre-alloyed precursors with corresponding improved topological similarity). When solid state synthesis of different elements is controlled by interdiffusion of the constituents involved in the alloy charge, acceleration of interdiffusion would then be achieved by a controlled temperature and/or heating cycle after and/or during the milling operation provided, that at least one of the precursor constituents of the employed mixture of precursor powder and/or machined chips and/or turnings is brittle enough and sufficiently available in order to avoid "caking". Ball-milled Mg-base ne-phases require lower annealing temperatures for homogeneization after a first milling cycle than those applied to develop dispersion strengthened Al-base alloys (see claim n° 2). In-situ annealing is particular possible by PBM due to its unlimited latitude to control the ratio of the injected friction-to-shock power. Also the carbide and/or hydride (and/or corresponding SRO) formation (and destabilization) is best controlled externally by planetary ball mills with Ω decoupled from ω which allows for deliberate milling cycles including selected change of P^* and friction-to-shock ratios and supported by homogeneization treatments including in-situ and post-milling annealing to relax defect concentrations and eventually expelling hydrogen so to suppress formation of hydrides, if necessary. Planetary type I of ball milling is the most flexible ball milling technique so allowing, due to the decoupling of ω from Ω , to employ more often, eventually shorter more effective and more variable in-situ annealing, i.e. T/t-cycles (Fig. 139) than by external annealing cycles proposed by [269].

3.10 Powder Processing

This paragraph deals with the consolidation of ball milled Mg- and/or Al-base base and other ball milled powders including diaphragma-materials which are accessible by ball milling techniques. Ball milled materials were generally observed to provide (surface) activated so better densification characteristics (reduced consolidation temperatures and pressures) than powders from other processes [265]. The resultant redox-reaction process for the invented

Mg-alloys then incorporates all current evolutions in the development of advanced light alloys by ball milling (cf. [198]):

- no degassing required or if (a reduced need for) degassing, need XS-alloying to compensate for the dealloying effect by carbide formation and to avoid formation of light alloy carbides due to their susceptibility to (aqueous) corrosion.
- no residual hydrogen, i.e. removal of (liquid) hexane or H_2 during or by evaporation in vacuum for eg. 0.5 h at temperatures up to 480°C depending on transformation temperature (cf. [194, 203])
- hot pressing at around $T = T_{transf} - 30^\circ C$ ([263])
- can employ low extrusion ratios (better avoiding localized melting, eventually localized formation of (evt. embrittling) shear bands
- large cross-sections of as-extruded products possible
- direct powder forging possible (cf. [198]).
- (one-step) explosive and/or shock (self-propagating) consolidation methods to better conserve the ne-structure in the final product [207], a method being particular useful for consolidation of nano-crystalline intermetallics (Ti-Al, Fe-Al, Nb-Al), nanostructured SiC_xN_y powders, non-equilibrium $Cu_{1-x}Ta_x$ alloys, nanocrystalline oxide materials such as TiO_2 , $SrTiO_3$, $KNbO_3$, dense $MoSi_2$, $TiNiSi$, TiB_2 , TiC , Si_3Ni_4 , TiC , TiN , TiO_2 , $TiC-MgO$ composites, CrO_2 , CrB_2 , for example [271], VC , Fe_3C , Al_2O_3 , SiC , Ta_2C , B_4C , Cr_3C_2 , $SiAlON$ and Cr-base, Nb-base, Ta-base, Mo-base and W-base alloys.

SPEX mill powders, for example, were observed to be smaller with a more refined micro-structure so also harder than those by attritor ball milling [247] and requiring higher consolidation (eg. HIPing) temperatures for a given consolidation pressure and/or time or vice versa, but they are all amenable to successful consolidation by

- metal powder injection molding providing parts of high complexity and accuracy at low costs, a method which is particular useful for ball milled powders exhibiting good sintering characteristics in combination with binders that hold the particles in place for mass transfer during molding, the binder thereby acting as a flow and carrier agent with good wettability, progressive decomposition during debinding and non-toxicity, all of which at temperatures between 150° and 600°C or so (thermal debinding) to be enhanced by contact with porous materials to promote capillary flow, by solvent to dissolve the binder and by catalytic extraction in which the binder is rapidly hydrolyzed to corresponding monomer so finally leading to homogeneous microstructures and density affording superior engineering properties compared to conventional press-and-sinter products and allowing a wide range of geometric options including undercuts, tapered surfaces and cross holes (see claim n°15).

3.11 Conclusions

Each ball mill and/or ball milling operation provides the possibility of different milling condi-

tions as was shown above. The injected impact power, eventually dividing in shock and friction, is the universally applicable parameter to control ne-phase formation independent on the ball milling technique employed and independent on and likewise instructive for the operator. The disclosed empirical data and empirically proven relationships show the scope of the processing variables and their operating regime required to achieve the structural changes for corrosion resistant non-equilibrium Mg-alloys and other light alloys by ball milling including the fully transformed metastable state such as a Mg-base amorphous and/or non-equilibrium crystalline matrix free or essentially free of second phase dispersions which are eventually harmful to the corrosion resistance of the corresponding alloy. Under the maxim of MA for non-equilibrium and corrosion resistant Mg-base phase formation, the prime parameters to optimize powder yield (i.e. to avoid "caking") and subsequent powder MA-Mg-base consolidation and forming operation are:

1. the hard and/or brittle-to-ductile precursor ratio (by weight and/or by volume) and/or
2. the rotational milling speed(s) and impact energies and/or
3. the filling fraction of milling balls and/or precursor charge and resulting effective impact powers and/or
4. the resulting ratio of friction-to-shock energy
5. the type and quantity of lubricating agent eventually required and/or
6. the resultant milling time cumulative impact energy required.

Claim n° 2 is a consequence of the observations made in this invention and includes a summary of the combinations of brittle elemental (Cr, Mo, ... Si, B, Be) on the one hand and ductile elemental (V, Ta, Zr, cf. Table 11) refractory additions on the other. Hardness, brittleness and their effect on the operative interdiffusivity in the terminal MA Mg-base alloy by using selected elemental and compound-type of "alloying additives" represent prime selection criteria to reduce the welding part of the milling cycles so t_{req} for interesting non-equilibrium Mg-base matrix phases by ball milling.

The time intervalls required to achieve the relevant constitutional effects are dictated by economics, while the large ΔD - and ΔE -values of the Mg-systems concerned provide a useful criterion to compensate for the relative small contribution to the overall driving force preset by the (terminal) ΔH^{mix} -values. In conjunction with a hard and eventually brittle precursor elemental and/or compound "alloying additive" as well as a lubricant in the initial ball milling charge and the controlled addition of impact power to the initial precursor charge it is possible to reduce the milling periods required to achieve the structural ne-state to between 0.2 and 250 hours, in particular to between 0.3 and 40 hours.

Joining Techniques for Non-Equilibrium Alloys

Unlike for Mg-casting alloys, most of the non-equilibrium alloys made by vapour deposition

and mechanical alloying cannot be joined by liquid metal methods such as (arc, gas metal etc.) welding and/or brazing, since it would destroy the non-equilibrium (micro-) structure so favouring mechanical joints (rivets, screws, bolts, self-clinching devices, HT-interference fits) and adhesive bonding methods (rubber and/or epoxy base resin, ethoxyline resin, phenolic base materials) including their advantages (established design, versatility, large choice of adhesive and strengths, no stress concentrations, good fatigue strength, no water penetration) and disadvantages (risk of galvanic corrosion, limited shear strength, laborious operations) [272].

The materials for mechanical joints are made from the same or similar VD- and/or ball milled Mg-base materials themselves providing like-like joints, since they will provide sufficient strength, notch-impact sensitivity and fatigue resistance due to the high microstructural homogeneity so replacing dissimilar metals such as steels and likewise being fabricated as relatively

cheap by-products, allowing for relatively cheap mechanical joint procedures and adhesive bonding methods, reduced waste disposal and recycling problems. Evolving methods in solid state joining useful for non-equilibrium Mg-base alloys include diffusion bonding (at low T and/or pressures as high as > 10 MPa as was applied to high strength Al7475, to AlLi alloys 8090 and 2091, cf. [274]), inertia and linear friction welding for high quality welds (as eg. for Al-Fe-Ce, Al-Fe-Mo-V and Al-Fe-V-Si alloys) and joints (as eg. for SiC-particulate reinforced Al-Fe-Si-V such as Al8009 and Al6061-T6 tubings with 10 vol.% Al_2O_3 [273]).

The galvanic corrosion and joining problem is further reduced by thermal spraying (eg. on top of dissimilar metals and/or passive Mg-components and Mg-joints all coping with like-unlike mechanical joints), employing high purity joint surfaces, appropriate design including adhesive interlayers, cleaning, degreasing, thin coatings including anodizing (the affordable shear in the coating increases with decreasing coating thickness), pickling and priming (eg. with chromate and dichromate), if not replaceable by other means.

Overall Balance: a First Approach

The economical and ecological significance of the impact of the new generation of Mg-alloys (and to a lesser extent of the new Al-base alloys) is summarized in a first approach in Figs. 141 to 144. As time goes by, a tremendous potential is left out as is indicated by the decline of Mg-applications in the aeronautical domain. With the realization of the processing methods selected in this invention it will be possible to provide a pivot in this evolution.

Literature

1. F. Hehmann. Diversity and Innovations: Key to the Structural Magnesium Market, JOM 45 (11). 1993, p. 27 - 29.
 2. J.F. King, New advanced magnesium alloys, in " Advanced materials technology int. ". 1990, pp. 12 - 19.
 3. S.K. Das, C.F. Chang and D. Raybould, in "PM in Aerospace and Defense Technologies", edt. F.H. Froes. MPIF, Princeton. NJ 08540. 1989, pp. 63 - 66.
 4. G. Tammann. " Die chemischen und galvanischen Eigenschaften von Mischkristallen und ihre Atomverteilung ". Leipzig. 1919.
 5. R.P. Tischer and H. Gerischer. Z. Electrochem. 62. 1958, p. 50.
 6. L.A. Carapella. " Fundamental Alloying Nature of Magnesium", Met. Progress 48, Aug. 1947, pp. 297 - 307.
 7. F. Hehmann, R.G.J. Edyvean, H. Jones and F. Sommer. Effect of Rapid Solidification Processing on Corrodability of Magnesium Alloys, Conf. Proc. PM Aerospace Materials '87, eds. B. Williams and G. Dowson, Met. Powder Report Publishing Services, Shrewsbury, England, p. 46/1.
 8. F. Hehmann, 'Rasch Erstarrte Magnesium-Mischkristalle und Ihr Umwandlungs- und Korrosionsverhalten' , Doctoral Thesis, University of Stuttgart, published in Fortschrittberichte VDI', Reihe 5, N° 155: Grund- und Werkstoffe', VDI-Verlag, Düsseldorf, F.R.G., Jan. 1989.
 9. M.E. Drits, L.L. Rohklin and N.P. Abručina, Metallovedenie i Termicheskaya Obrabotka Metallov 17, 1985, 27 - 28.
 10. B.R.W. Hinton, N.E. Ryan, D.R. Arnott, P.N. Trathen, L. Wilson and B.E. Williams, Corrosion Australasia 10, vol. 3, 1985, pp. 12 - 17.
 11. F. Hehmann, H. Jones, F. Sommer and R.G.J. Edyvean, Corrosion Inhibition in Magnesium-Aluminium Based Alloys Induced by Rapid Solidification Processing, J. Mater. Sci. 24, 1989, pp. 2369 - 2379.
 - 11a. S. Kamado, Y. Kojima, Y. Negishi and S. Iwasawa. R. Ninomiya. Light Metals Processing and Applications, Quebec City, Quebec Canada, 29 Aug. - 1 Sept. 1993, Canadian Institute of Mining, Metallurgy and Petroleum. Montreal, Quebec H3Z 3B8, Canada, 1993, pp. 849 - 858.
 12. F. Hehmann, F. Sommer and H. Jones, Extension of Solid Solubility of Yttrium and Rare Earth Metals in Magnesium by Rapid Solidification', eds. F.H. Froes and S.J. Savage, American Society for Metals. Metals Park, OH, 1987, pp. 379 - 398.
 13. F. Hehmann, F. Sommer and B. Predel, Extension of Solid Solubility in Magnesium by Rapid Solidification, Mat. Sci. Engng. A125 (2), 1990, pp. 249 - 265.
 14. F. Hehmann and P. Tsakiroopoulos. Microstructural Modelling of Laser Glazing, Gas-Atomization and Spray Forming for the Development of Magnesium Alloys, Conf. Proc.
- SUBSTITUTE SHEET (RULE 26)

- " Magnesium Alloys and Their Applications ", DGM. Oberursel, Oct. 1992.
15. H. Gronert. Dipl. Thesis. University of Duisburg. 1984.
 16. D.J. Bray, R.W. Gardiner, B.W. Viney and H.M. Flower, as ref. [11], pp. 159 - 166.
 17. D.J. Bray, R.W. Gardiner and B.W. Viney, GB-Patent 2.262.539 A. 23 June, 1993.
 18. D. Remppel. Dr. Thesis. Fachbereich Chemie, University of Stuttgart, FRG, 1987.
 19. Angewandte Oberflächentechnik für metallische Werkstoffe, eds. Harald Simon and Martin Thoma, Carl Hanser Verlag, 1985, p. 302.
 20. AHC-Oberfläche, AHC-brochure for corrosion tests, AHC-Oberflächentechnik. Friebe & Reininghaus GmbH. Kerpen. FRG, p. 111, priv. communication, March 1986.
 21. L. Bianchi, Journal of Metals 5, 1991, pp. 45 - 47
 22. J.A. Thornton. "High Rate Thick Film Growth", Ann. Rev. Mater. Sci. 7, 1977, p. 214.
 23. W. Kurz and D.J. Fisher. " Fundamentals of Solidification ". Trans Tech Publications 1989. Switzerland. Germany. UK, USA, 3rd edition, 1989.
 24. R. Glang, "Handbook of Thin Film Technology", eds. L.I. Maissel and R. Glang, McGraw Hill 1970, pp. 1 - 7.
 25. W.D. Westwood, MRS Bulletin 12, 1988, pp. 46 - 52.
 26. R.L. Bickerdike et al., Int. J. Rapid Solidification (2), 1986, pp. 1 - 19.
 27. M.C. Connell and P.G. Partridge, Acta metall. 35 (8), 1987, pp. 1973 - 1980; b) pp. 1981 - 1993.
 28. E. Hirota, H. Habazaki, A. Kawashima, K. Asami and K. Hasimoto, Scientific Report A38, 1 March, 1993, The University of Tohuko, Japan.
 29. S.M. Rossnagel and J.J. Cuomo, MRS Bulletin 12, 1988, pp. 40 - 45.
 30. R.W. Gardiner, U.S. Patent 4,976,995, Dec. 11, 1990.
 31. P. Duwez and H. Willens, TMS - AIME 227, 1963, p. 362.
 32. F. Hehmann, Terminal Solid Solubility Extension in Magnesium by Rapid Solidification, Proc. 47th Int. Magnesium Conference, May 29 - 31, 1990, Cannes, Int. Mag. Association, VA, pp. 76 - 82.
 33. F. Hehmann and P. Tsakirooulos, Prediction of Temperature Stable Aluminium Alloys Made by the Osprey Process (I): Supersaturation of Binary Eutectic Additions in α Al by Recalesced Free Adiabatic Growth, Proc. First Int. Conf. on Spray Forming, eds. J. Wood et al., The Inst. of Metals. London, Dec. 1990, page 16-1 - 16-15.
 34. M. Müller, J. Wachter and F. Sommer. Proc. Conf. " Mg-Alloys and Their Applications. eds. B.L. Mordike and F. Hehmann. DGM, Oberursel, Oct. 1992, pp. 527 - 534.
 35. M. Carrard, M. Gremaud, M. Zimmermann and W. Kurz, Acta metall. mater. 40 (5), 1992, pp. 983 - 996.
 36. F. Sommer, F. Hehmann and H. Jones. Transformation Behaviour of the Extended Solid Solution of Yttrium in Magnesium by Rapid Solidification, J. Less Common Metals 159 (1990), pp. 237 - 259.

37. H. Karimzadeh. " The Microstructure and Mechanical Properties of some Mg-Alloys Containing Yttrium and Heavy Rare Earth Metals ", PhD Thesis, University of Manchester, Oct. 1985.
38. G. Omori, S. Matsuo and H. Asada. "Precipitation process in Mg-Ce-Alloys". Trans JIM. Vol. 16, 1975.
39. L.Y. Wei and G.L. Dunlop, as ref. 13, pp. 335 - 342.
40. M. Ahmed, G. W. Lorimer, P. Lyon and R. Pilkington, as ref. 13, pp. 301 - 308.
41. H. Jones. Metallurgical Science and Technology 7 (1) 1989, pp. 63 - 75.
42. H. Jones. Mat. Sci. Engng A137, 1991, pp. 77 - 85.
43. F. Sommer, G. Bucher and B. Predel. J. Physique 41, 1980, pp. C8-563 - 566.
44. H.E. Kissinger. J. Res. Nat. Bureau of Standards 57 (4), 1956, p. 217.
45. N.I. Varich and B.N. Litvin. Fiz. Met. Metallov. 16, 1963, pp. 526 - 529.
46. J.W. Christian, "The Theory of Transformations in Metals and Alloys", Pergamon, New York, 2nd edition, 1975.
47. ASM Metals Handbook, Properties of Magnesium Alloys, Vol. 2, 9th edition, ASM Metals Park, 1979, Ohio, 44073-9989, USA.
48. ASM Metals Handbook, Forming and Forging, Vol. 14, 9th edition, ASM Metals Park, 1979, Ohio, 44073-9989, USA, pp. 259 - 260.
49. Phase Diagrams of Binary Magnesium Alloys, eds. A.A. Nayeb-Hashemi and J.B. Clark, ASM Materials Park, 1988, Ohio 44073-9989, USA.
50. E.F. Emley, Principles of Magnesium Technology, Pergamon Press, 1966.
51. S. Izzetow and J. Rizzitano, Int. J. Powder Met. & Pow. Techn. 10 (3), 1974, pp. 217 - 225.
52. S.K. Das, C.F. Chang and D. Raybould, U.S. Patent 4 938 809, July 3, 1990.
53. D. Raybould, C.F. Chang and S.K. Das, U.S. Patent 5 071,474, Dec. 10, 1991.
54. C.F. Chang and S.K. Das. U.S. Patent 5 087 304, Feb. 11, 1992.
55. C.F. Chang and S.K. Das, U.S. Patent 5 129 960, July 14, 1992.
56. G. Regazzoni, G. Nussbaum and H.T. Gjostland. U.S. Patent 4,997,622, March 5, 1991.
57. J.F. Faure, G. Nussbaum and G. Regazzoni, EP - Patent 0 414 620, 27. 02. 1991.
58. J.F. Faure, G. Nussbaum and G. Regazzoni, U.S. Patent 5,073,207, Dec. 17, 1991.
59. M.C. McConnell and P.G. Partridge, as ref. 12, pp. 143 - 153.
60. R.L. Bickerdike, D. Clark, G. Hughes, M.C. McConnell, W.N. Mair, P.G. Partridge and B.W. Viney, Int. Conf. "Rapidly Solidified Materials". San Diego, ASM Metals Park, 1986, pp. 145 - 151.

61. P.G. Partridge, as ref. 12, pp. 155 - 162.
62. S. Krishnamurthy, I. Weiss and F.H. Froes, Key Engng. Mat. 29-31, 1989, pp. 135 - 146.
63. S. Krishnamurthy and Y.W. Kim, in " Magnesium Developments ", Proc. World Materials Congress, Sept. 1988, Chicago IMA, ASM International, pp. 11-16.
64. F. Hehmann, METALL 5, 1994, pp. 377 - 381.
65. J. R. Weertman and P.G. Sanders, Proc. Int. Conf. "Dislocation '93", Aussois, March-April 1993, Trans Tech Publications Ltd, Aedermannsdorf, Switzerland.
66. T. Masumoto, A. Inoue, T. Sakuma and T. Shibata, U.S. patent 5 118 368, 1992.
67. J.D. Hanawaldt, C.E. Nelson, J.A. Peloubet, Tran AIME 147 (1942), pp. 273 - 299.
68. Fachausschuss Nichteisenmetalle, DNA, 1961, p.318.
69. E. Bissig, Alcan Chemical Ltd., Dow Magnesium Analysis Sheet, 23 February, 1993.
70. **Former Italian producer, to be supplied later**
71. B. Closset and F. Dimayuga, in Proc. Conf. " Mg-Alloys and Their Applications ", 10-12 April, 1992, DGM, Oberursel, RFA, pp. 143 - 150.
72. Johnson Matthey GmbH, Finest Inorganic Research Chemicals and Materials, Handbook, 1995/96, Karlsruhe, RFA.
73. F. Hehmann, Consultancy Work, Report to AFWAL, Wright-Patterson Air Force Base, 8 November, 1985.
74. M.Ö. Pekgülyüz and M.M. Avedesian, as ref. FH22, pp. 213.
75. M.Ö. Pekgülyüz, A. Luo, P. Vermetta and M.M. Avedesian, Proc.50th Int. Mg Conf., IMA, McLean, VA 22101, May 1993.
76. J.D. Cotton and H. Jones, J. Electrochem. Soc. 136(11), 1989, pp. 523C-527C
77. J.D. Cotton and H. Jones, Int. J. Rapid Solidification, Int. J. Rapid Solidification 6, 1991, p. 155.
78. D. Lahaie, J.D. Embury, M.M. Chadwick and G.T. Giray, Scr. Metall. Mater. 27 (2), 1992, pp. 139-142.
79. G. Nussbaum, P. Saintfort, G. Regazzoni and H. Gjestland, Scripta Met. 23 (1989), p.1079.
80. H. Jones, Mater. Sci. Engng. A137 (1991), pp. 77-85.
81. Project MAIE / 0053 / F: Rapid Solidification of Magnesium, EURAM-BRITE Workshop, 26-27 Nov. 1990, Louvain-la-Neuve, Belgium.
82. S. Isserow and J. Rizzitano, Int. J. Powder Met. & Pow. Techn. 10 (3) (1974), p. 217.
83. P.J. Vervoort and J. Duszczek, PM Aerospace Materials 1991, Lausanne Switzerland, Nov. 4 - 6, 1991, MPR Publishing Services Ltd., Shrewsbury SY1 1HU, UK, 1992, paper N° 30.
84. P.J. Meschter, Met. Trans. 18A (1987), pp. 347 - 350.
85. A. Cottrell, An Introduction to Metallurgy, 2nd edition, Edward Arnold Publishers, 1975, p. 398.
86. E.O. Hall, in "Yield Point Phenomena in Metals and Alloys", Plenum Press, New York, 1970.

87. P.J. Meschter and J.E. O'Neal. Met. Trans. 15A, 1984, pp. 234-240.
88. P.J. Meschter. Mc Donnel Douglas Research Laboratories, priv; communication, 1986.
89. H. Haferkamp, Fr.-W. Bach, P. Bohling and C. Willems, as ref. FH19, pp. 829 - 836.
90. G.V. Raynor, The Physical Metallurgy of Magnesium and Its Alloys. Pergamon Press, London, 1959.
91. C. Kittel, Introduction Into Solid State Physics, 5th Edition. John Wiley & Sons Inc., New York, 1976.
92. C.J. Smithells. Metals Reference Book. 2nd Edition. Interscience Publishers, 250 Fifth Avenue, New York 1. 1955: 6th edition. Butterworth, London and Boston, 1983.
93. T.H. Courtney, Mechanical Behaviour of Materials. Mc Graw Hill, 1990, p. 171.
94. R. Von Mises. Z. Angew. Math. Mech. 8, 1928, p. 161.
95. P. Bach, PhD Thesis. Nancy, 1969.
96. R. Karney and G. Sachs. Z.Phys. 49 (1928), p. 480.
97. F.E. Hauser, P.R. Landon and J.E. Dorn, Trans. ASM 50, 1958, p. 856.
98. N.K. Chen and R.B. Pond, Trans. AIME 194, 1952, p. 1085.
99. W.G. Johnston and J.J. Gilman. J. Appl. Phys. 30, 1957, p. 121.
100. F.R.N. Nabarro, Theory of Crystal Dislocations, Clarendon Press, Oxford, 1967.
101. J.P. Hirth and J. Lothe, Theory of Dislocations, Mc Graw Hill Book Co., New York, 1968.
102. V. Vitek and M. Igarshi, Phil. Mag. 63 A (5), 1991, pp. 1059 - 1075.
103. G.E. Dieter, Mechanical Metallurgy, 3rd edition, McGraw Hill Int., Singapore, 1986, p.137.
104. K. Schemme, Doctoral Thesis, University of Bochum, 1993, p. 52.
105. N. Attari, C. Robin and G. Aluvinage, in "Advanced Aluminium and Magnesium Alloys", eds. T. Khan and G. Effenberg, ASM International, June 1990, p. 837.
106. J.F. Stohr and J.P. Poirier, Philos. Mag. 25. 1972, p. 1313.
107. S.K. Das, C.F. Chang, D. Raybould, J.F. King and S. Thistlethwaite, Proc. Conf. " Mg-Alloys and Their Applications, eds. B.L. Mordike and F. Hehmann, DGM, Oberursel, Oct. 1992, pp. 487-494.
108. A. Couret, D. Caillard. W. Püschl and G. Schoeck, Philos. Mag. A 63 (5), 1991, pp.1045 - 1057.
109. B. Legrand, in "Dislocations 1984", eds. P. Veyssi re. L. Kubin and J. Castaing, Colloque International du C.N.R.S., Edition du Centre National de la Recherche Scientifique, 15 Quai Anatole France, 75700 Paris.
110. M.S. Duesbury, The Dislocation Core and Plasticity, in "Dislocation in Solids, Vol. 8: Basic Problems and Applications". ed. F.R.N. Nabarro, Elsevier Science Publishers. B.V., North-Holland, 1989.
111. N.K. Chen and R.B. Pond, Trans. AIME 194, 1952, p. 1085.
- 111a. W.G. Johnston and J.J. Gilman. J. Appl. Phys. 30, 1957, p. 121.
112. F. Hehmann and H. Jones. Rapid Solidification of Magnesium Alloys: Recent

- Developments and Future Avenues. in 'Rapid Solidification Technology', eds. T.S. Sudarshan and T.S. Srivatsan, Technomic Publishing Co., Inc., Lancaster, Basel, 1993, pp. 441-487.
113. G. Nussbaum, G. Reggazoni and H. Gjestland, in "Science and Engineering of Light Metals", Proc. Int. Conf. "RASELM", JILM, Tokyo 1991, pp. 115 - 120.
 114. F. Hehmann, S. Krishnamurthy, E. Robertson, A.G. Jackson, S.J. Savage and F.H. Froes, in "Horizons of Powder Metallurgy", Part II, Verlag Schmid, Freiburg 1986, pp. 1001 - 1008.
 115. C.F. Chang, S.K. Das and D. Raybould, Met. Powd. Rep. 41, 1986, pp. 302 - 308.
 116. H. Gjestland, G. Nussbaum, G. Regazzoni, O. Lohne and O. Bauger, Mat. Sci. Engng. A134 (1991), pp. 1197 - 1200.
 117. O. Lohne, O. Bauger, H. Gjestland, G. Nussbaum and G. Regazzoni, as ref. 68, pp. 163 - 168.
 118. F. Hehmann, Metastable Phase Transformation in Rapidly Solidified Magnesium-Base Mg-Al Alloys, Acta Met. Mater. 38, 1990, pp. 979 - 992.
 119. P. Vostry, I. Stulikova, B. Smola, W. Riehemann and B.L. Mordike, Mat. Sci. and Engng. A 137, 1991, pp. 87 - 92.
 120. O.S. Zarechnyuk and P.L. Kripyakevich, Izv. Akad. Nauk SSSR. Met. (4), 1967, p. 188; Russ. Metall. (4), 1967, p. 101.
 121. O.F. Zmy and E.I. Gladyshevsky, Kristallografiya 15 (5), 1970, p. 939; Sov. Phys. Crystallogr. 15 (5), 1970, p. 817.
 123. R.C. Weast, CRC Handbook of Chemistry and Physics, 66th edition, 1985 - 1986.
 124. R.S. Busk and T.E. Leontis, Trans AIME 188, 1950, pp. 297 - 306.
 125. I.J. Polmear, "Light Alloys - Metallurgy of the Light Metals", Edward Arnold, 1980.
 126. K.E. Bagnall, J.W. Steeds, P.G. Partridge and R.W. Gardiner, Proc. Int. Conf. Electron Microscopy, 17 - 22 July 1994, Paris, Edition Physiques, Les Ulis, Vol. 2B, pp. 711 - 712.
 127. G.H. Lu, K.E. Bagnall, C.M. Ward-Close, P.G. Partridge and J.W. Steeds, as ref. 79, Vol. 2A, pp. 625 - 626.
 128. S.K. Das and F.H. Froes, in "Rapidly Solidified Alloys", ed. H.H. Liebermann, Marcel Dekker, Inc., New York, 1993, p. 339.
 129. V. Radmilovic and G. Thomas, University of California, Berkeley, CA, to be published.
 130. P.S. Gilman and S.K. Das, as ref. 7, p. 27.1.
 131. R. Ayer, L.M. Angers, R.R. Mueller, J.C. Scaloni and C.F. Klein, Metall. Trans. 19A, 1988, p. 1645.
 132. D. Munsen, J. Inst. Metals 95, 1967, p. 217.
 133. B.A. Shaw, T.R. Schrecengost, W.C. Moshier and R.G. Wendt, Report AD - A 253 923, April 1, 1991, March 31, 1992, Office of Naval Research, Arlington VA, 22217 - 5000.
 134. A.L. Olsen, Metall 46(6), 1992, pp. 570 - 574.
 135. K. Bühler, Metall 44(8), 1990, pp. 748 - 753.
 136. G.L. Makar and J. Krüger, International Mat. Rev. 38(3), 1993, pp. 138 - 153.

137. G. Neite, "Corrosion Behaviour of Magnesium", in ref [99], by himself.
138. H. Kaesche, Die Korrosion der Metalle. Springer Verlag Berlin. New York, 2nd edn., 1979.
139. P. Marcus, Corrosion Science 36 (12), 1994, pp. 2155 - 2158.
140. A.G. Guy, Metallkunde für Ingenieure, Akad. Verlagsgesellschaft, Bad Soden am Taunus, 1978.
141. B. Chalmers, Phys. Metallurgy, Wiley & Sons, N.Y. 1959, pp. 445.
142. O. Kubachewski and B.E. Hopkins, Oxidation of Metals and Alloys, Academic Press, N.Y., 1962.
143. H.H. Uhlig and B.W. Revie, Corrosion and Corrosion Control, Wiley & Sons, N.Y. 1985.
144. W.H. Smyrl and J. Newmann, J. Electrochem. Soc. 123 (10), 1976, pp. 1423 - 1432.
145. A.G. Revesz and J. Kruger, "Passivity of Metals", eds. R.P. Frankenthal and J. Kruger. Electrochemical Society, Princeton, NJ, 1978.
146. O. Salas and C.G. Levi, Int. J. of Rapid Solidification 4, 1988, pp. 1 - 21.
147. P. Tsakiroopoulos, priv. communication, 21 July, 1994.
148. F. Sommer, J. Wachter, J. Rapid Solidification 3, 1988, pp. 223 - 236.
149. M.J. Couper and P.F. Singer, Rapidly Solidified Aluminium Alloys for Advanced Engineering Applications, as ref. 12, pp. 273 - 282.
150. S.K. Das, D. Raybould, R.L. Bye and C.F. Chang, US Patent 4718 475, Jan. 1988.
151. Rohklin, T.V. Dobatkina, I.G. Korol'kova and Yu.N. Grin, Russ. Metall. 5, (1991), p. 182 - 185.
152. K. Schild, Doctoral Thesis. University of Stuttgart, 1985.
153. H.R. Hilzinger and S. Hock, Proc. Conf. Metallic Glasses: Sciences and Technology, Budapest, 1980, p. 71.
154. R. Subramanian, S. Sircar and J. Mazumdar, J. Mat. Sci. 26, 1991, pp. 951 - 956.
155. R.K.H. Kalimullin and A.T. Berdnikov, Zashch Met. 22 (2), 1986, pp. 262 - 264.
156. R.K.H. Kalimullin, V.V. Valuev and A.T. V. Bernikov, Metalloved Term. Obrab. Met. 2, 1986, pp. 39 - 40.
157. R.K.H. Kalimullin, V.B. Spiridonov, A.T. Bernikov, A.A. Romanov and G.N. Pantikina, Metalloved Term. Obrab. Met. 5, 1988, pp. 18-24.
158. K. Schemme, Doctoral Thesis. University of Bochum, 1993, p. 52.
159. G. Neite, K. Kubota, K. Higashi and F. Hehmann, " Mg-Based Alloys ", in " Structure and Properties of Nonferrous Alloys ", ed. K.H. Matucha. Vol. 8 of Encyclopedia " Materials Science and Technology ", eds. R.W. Cahn, P. Haasen and E.J. Krämer, VCH Weinheim, P.O. Box 10 11 61, D - 6940 Weinheim, RFA. to be published in 1995.
160. P. Dobrinsky, G. Krakau and A. Vogel, Physik für Ingenieure, B.G. Teubner, Stuttgart. 4th edition. 1976.
161. F. Hehmann, F.W. Hugo, F. Müller and M. Raschke, German patent application P 44 06 333 4 [101].

162. F. Hehmann. "High performance light alloys by rapid quenching", European patent application EP 94111991.9, 1 August 1994.
163. F. Hehmann and F.H. Froes. "Advances in lightweight non-ferrous PM-metals", Proc. Int. Conf. PM '94, Powder Metallurgy World Congress, Vol. III, Les Editions de Physiques des Ulis, B.P. 112, F - 91944 Les Ulis Cedex A, 1994, pp. 1591 - 1604.
164. F. Hehmann, "Research on MgLi and a specifically German consequence" (in German), METALL 48 (5), 1994, p. 377-381.
165. F. Hehmann. Final report on SUMAC Job N° 37401, The University of Sheffield, 29 June 1985.
166. F. Hehmann, S. Krishnamurthy, E. Robertson, A.G. Jackson, S.J. Savage and F.H. Froes, in "Horizons of Powder Metallurgy", Part II, Verlag Schmid, Freiburg 1986, pp. 1001 - 1008.
167. F. Hehmann, Final Report on Contract F 33615-84-C-5127, Task n° 28 and 54, Wright-Patterson AFB, 15 Feb. 1986.
168. F. Hehmann, S. Krishnamurthy, E. Robertson, S.J. Savage, F.H. Froes and USAF, U.S. Patent 4,770,850, 13. Sept. 1988.
169. A. Inoue, U. Nakano, Y. Bizen, T. Masumoto and H.S. Chen, Jap. J. Appl. Physics 27 (6), 1988, pp. L944-L947.
170. A. Inoue, K. Ohtera, K. Kita and T. Masumoto, Jap. J. Appl. Physics 27 (12), 1988, pp. L2248-L2251.
171. A. Inoue, M. Kohinata, A.P. Tsai and T. Masumoto, Mat. Trans JIM 30 (5), 1989, pp.378-381.
172. A. Inoue, A. Kato, T. Zhang, S.G. Kim and T. Masumoto, Mat. Trans JIM 32 (7), 1991, pp. 609 - 616.
173. K. Aikawa and K. Taketani, European Patent 0407964, 16. 01. 1991.
174. T. Masumoto, A. Inoue, T. Sakuma and T. Shibata, US. Patent 5,118,368, June 2, 1992.
175. Y. Li, H.A. Davies and H. Jones, Proc. Conf. "Magnesium Alloys and Their Application", eds. B.L. Mordike and F. Hehmann, DGM, Oberursel, 1992, pp. 551 - 557.
176. F. Sommer, a) priv; communication to F. Hehmann; b) on-going work by F. Sommer.
177. W. Kurz, B. Giovanola and R. Trivedi, Acta metall. 35, 1987, pp. 823.
178. P. Lipton, W. Kurz and R. Trivedi, Acta metall. 35, 1987, pp. 957.
179. W.J. Boettinger, L. Bendersky and J.G. Early, Met. Trans. 17A, 1986, pp. 781-790.
180. R. Levoy and Chr. Mauhé report to the Secrétariat Général de la Défense Nationale, 51 Bld. de Latour-Maubourg, 75700 Paris, 31 January, 1992.
181. F. Hehmann, Diversity and Innovations: Key to the Structural Magnesium Market, JOM 45 (11), 1993, p. 27 - 29.
182. R. Sundaresan and F.H. Froes, Key Engng. Mater. 29-31, 1989, p. 199.
183. H. Kimura, M. Kimura and F. Takada, J. Less-Common Metals 140, 1988, p. 113.
184. C. Suryanarayana and F.H. Froes, J. Mater. Res. 5, 1990, p. 1880.
185. C. Suryanarayana, R. Sundaresan and F.H. Froes, in "Structural Applications of Mechanical Alloying", eds. F.H. Froes and J.J. deBarbadillo, ASM InterNational, p. 193.

186. E. Hellstern, H.J. Fecht, C. Garland and W.L. Johnson, in "Multicomponent Ultrafine Microstructure" eds. L.E. Mc Candish, D.E. Polk, R.W. Siegel and B.H. Kear, Mat. Res. Soc. Pittsburgh, PA, Vol. 132, 1989, p. 137.
187. H. Chang, H.J. Höfler, C.J. Altstetter and R.S. Averbach, Scripta Metall. Mater. 25, 1991, p. 1161.
188. J.H. Ahn, H.S. Chung, R. Watanabe and Y.H. Park, Mater. Sci. Forum 88-90, 1992, p. 347.
189. E. Gaffet, N. Malhouroux and M. Abdellaoui, J. All. Comp. 194, 1993, pp. 339-361.
190. R. Watanabe, H. Hashimoto and Y.H. Park, in "Advances in Powder Metallurgy 1991", compiled by L.F. Pease III and R.J. Sansoucy, MPIF Princeton, NJ, 1991, p. 119.
191. C. Suryanarayana, R. Sundaresan and F.H. Froes, Mater. Sci. & Engng. A150, 1988, p.117.
192. A. Frefer, C. Suryanarayana and F.H. Froes, aConf. Proc. 7th World Titanium Conference, San Diego, CA, TMS Warrendale, PA 1993, eds. F.H. Froes and I. Caplan, p. 933.
193. C.M. Ward-Close, P.G. Partridge, P. Holdway and A.W. Bowen, Conf. Proc. 7th World Conf. Titanium Conference, San Diego, Ca, eds. F.H. Froes and I. Caplan, TMS Warrendale, PA, 1993, p. 659.
194. F. Hehmann, Conf. Proc. "Advances in Production and Fabrication of Light Metals and Metal Matrix Composites", eds. M.M. Avedesian et al., Canadian Institute of Mining, Metallurgy and Petroleum (CIMMP), Montreal, 1992, pp. 305.
195. Z. Peng, C. Suryanarayana and F.H. Froes, Scr. Metall. Mater. 27 (4) 1992, pp. 475-480.
196. M.S. El-Eskandarany, K. Aoki and K. Suzuki, J. Less Common Met. 167, 1990, pp.113-118.
197. "Erzeugnisse der Pulvermetallurgie". company brochure, PEAK Werkstoff GmbH, Velbert RFA, 1995.
198. V. Arnhold, K. Hummert and R. Schattevoy, Conf. Proc. "Materials by Powder technology", PTM '93, edt. F. Aldinger, DGM, Oberursel, 1993.
199. K. Hummert, V. Arnhold, G. Brockmann, Proc. Conf. " PM Aerospace Materials", 2-4 Nov., 1987, Lucerne, Powder Metals Report, Shrewsbury, England.
200. T.B. Ameer, A.R. Yavari and J.M. Barandiaran, Mat. Sci. Engng. A134, 1991, p. 1402.
201. A. Calka and A.P. Radlinski, Mat. Sci. Engng. A118, 1989, pp. 131 - 135.
202. L.E. Hazelton. US. Patent 5 074 936. Dec 24, 1991.
203. J.F. King and F. Hehmann, Proc. Conf. "Magnesium Alloys and Their Application", eds. B.L. Mordike and F. Hehmann, DGM, Oberursel, 1992, p. 309.
204. Pulverisette 5^R, Product brochure and Manual. Fritsch GmbH Laborgerätebau, Idar-Oberstein, RFA; priv. communication. May, 1995.
205. Y. Chen, R. LeHazif and G. Martin, Solid St. Phen. 23&24, 1992, Trans Tech Publications Ltd., Zürich, 1992, pp. 271-283.
206. C.R. Clark, C. Suryanarayana, F.H. Froes, Int. Conf. Powder Metallurgical and Particulate Materials, May 14 - 17, 1995, Seattle, Washington, MPIF-APMI.
207. R.B. Schwartz, Mat. Sci. Engng. 97, 1988, pp. 71 - 78.
208. R. Brüning, Z. Altounian, J.O. Strom-Olsen and L. Schlutz, Mat. Sci. Eng. 97, 1988, pp. 317

- 320.

210. E. Hellstern and L. Schultz. Metall 41 (5), 1987.
211. L. Schultz. Mat. Sci. Engng. 27, 1988, pp. 15 - 23.
212. E. Hellstern and L. Schultz. J. Appl. Phys., 1988.
213. E. Gaffet, C. Louison, M. Harmelin and F. Faudot, Proc. 7th Int. Conf. on Rapidly Quenched Metals, Stockholm, 1990, in Mat. Sci. Engng. A134, 1991, pp. 1380 - 1384.
214. C.H. Lee, T. Fukunaga and U. Mizutani, Proc. 7th Int. Conf. on Rapidly Quenched Metals, Stockholm, 1990, in Mater. Sci. Eng. A134, 1991, pp. 1410 - 1413.
215. T. Fukunaga, M. Mori, K. Inoue and U. Mizutani, 7th Int. Conf. on Rapidly Quenched Metals, Stockholm, 1990, in Mat. Sci. Engng. A134, 1991, pp. 863 - 866.
216. E. Gaffet and M. Harmelin, a) Proc. Int. Conf. on Amorphization by Solid-State Reaction, Grenoble, February 21 - 23, 1990, in J. Phys. (Paris), Colloq. C4, Suppl. 14, 1990, T51, p. 139; b) Proc. Conf. on Structural Applications of Mechanical Alloying, Myrtle Beach, SC, 1990, ASM, Metals Park, OH, 1990, p. 257.
217. A.W. Weeber and H. Bakker, Z. Chem. Phys. N.F. 157, 1988, p. 221.
218. E. Gaffet and M. Harmelin, J. Less-Common Met. 157, 1990, p. 201.
219. E. Gaffet, Mat. Sci. Engng. A136, 1991, pp. 161 - 169.
220. E. Gaffet, F. Faudot and M. Harmelin, a) Mat. Sci. Engng. A149, 1991, pp. 85 - 94; b) Mat. Sci. For. 88-90, 1992, pp. 375-382.
221. E. Gaffet and J.P. Gaspard, J. Phys. Coll. Phys. C4, Suppl. 14, 51, 1990, p. 205.
222. R. Bormann and R. Busch, Conf. New Materials by Mechanical Alloying Techniques, E. Arzt and L. Schultz, DGM, 1988, p. 73-78.
223. M. Abdellaoui, Thèse de Doctorat de l'Université Paris VI, submitted on 4 July, 1994.
224. M. Abdellaoui and E. Gaffet, Acta metall. mater. 43 (3), 1995, pp. 1087 - 1098.
225. E. Gaffet and G. Martin, Coll. Phys. C4, Suppl. N° 14, 51, 1990, pp. 71 - 77.
226. H. Bakker and L.M. Di, Mater. Sci. For. 88 - 90, 1992, pp. 27 - 40.
227. A.R. Yavari, and P.J. Desré, Mater. Sci. For. 88 - 90, 1992, pp. 43 - 50.
228. H. Hashimoto and R. Watanabe, Mater. Trans. JIM 31 (3), 1990, pp. 219 - 224.
229. H. Hashimoto and R. Watanabe, Mater. Sci. For. 88 - 90, 1992, pp. 89 - 96.
230. A. Iasonna and M. Magini, Mat. Transactions JIM 36 (2), 1995, pp. 123 - 133.
231. R.S. Murthy, M. Mohan Rao and S. Ranganathan, Acta metall. mater. 43 (6), 1995, pp. 2443 - 2450.
232. J.S. Benjamin and T.E. Volin, Met. Trans. 5, 1974, p. 1929.
233. E. Gaffet and L. Yousfi, Mat. Sci. Forum 88 - 90, 1992, pp. 51 - 58.
234. E. Gaffet, Mat. Sci. Engng. A132, 1991, pp. 181 - 193.
235. J. Eckert, L. Schultz, E. Hellstern and K. Urbain, J. Appl. Phys. 64, 1988, pp. 3224.
236. A.R. Miedema, Philips Tech. Rev. 36(8), 1976, p.217.
237. E. Gaffet, M. Harmelin and F. Faudot, J. Appl. and Comp. 194, 1993, pp. 23-30.
238. M. Abdellaoui, T. Barradi and E. Gaffet, J. All. Comp. 198, 1993, pp. 155 -164.

239. E. Gaffet, P. Marco, M. Fedoroff and J.C. Rochaud, *Mat. Sci. For.*, 88-90, 1992, pp. 383-390.
240. M. Abdellaoui and E. Gaffet, *J. All. Compounds* 209, 1994, pp. 351-361.
241. R. Hultgren, P.D. Desai, D.T. Hawkins, M. Gleiser and K.K. Kelly, *Selected Value of the Thermodynamic Properties of Binary Alloys*, ASM Metals, OH, 1973.
242. M. Bolart, D. Brenet, F. Moret, CEREM, Laboratoire de Génie des Matériaux, CENG, 85X-38041, Grenoble, Cedex.
243. Technische Informationen FT0008, Netzsch Feinmahltechnik GmbH, Selb, RFA, 1992.
244. H. Zoz, *Mat. Sci. For.* 179 - 181, 1995, pp. 419 - 424.
245. E. Gaffet, N. Malhouroux-Gaffet, M. Abdellaoui and A. Malchère, *Révue de Métallurgie/CIT - Science et Génie des Matériaux*, 1994.
246. G.B. Schaffer and P.G. McCormick, *Mater.For.* 16, 1992, p. 91.
247. D.R. Maurice and T.H. Courtney, *Metall. Trans.* 21A, 1990, pp. 289 - 303.
248. Kirk-Othmer, *Encyclopedia of Chemical Technologies*, 3rd edition, Vol.8, John Wiley & Sons, N.Y., Chichester, Brisbane, Toronto, pp. 478 - 535, in particular p. 481 and p. 507.
249. A.W. Weeber, H. Bakker, H.J.M. Heijligers and G.F. Bastin, *Europhys. Lett.* 3, 1987, p.1261.
250. T. Tsuru, A.P. Tsai, A. Inoue and T. Masumoto, *Science Reports of the Research Institutes, Tohoku Universities Series A - Physics Chemistry and Metallurgy* 41 (1), 1995, pp. 69 - 75.
251. T.H. Courtney, *Mat. Transactions JIM* 36 (2), 1995, pp. 110 - 122.
252. S. Mayer, *Dipl. Thesis*, University of Stuttgart, 1985.
253. C.J. Smithells, *Metals Reference Book*, 2nd Edition, Interscience Publishers, 250 Fifth Avenue, New York 1, 1955; 6th edition, Butterworth, London and Boston, 1983.
254. R.C. Weast, *CRC Handbook of Chemistry and Physics*, 66th edition, 1985-86, CRC Press Inc., Florida.
255. A. Cottrell, *An Introduction to Metallurgy*, 2nd Edition, Edward Arnold Ltd, 41 Bedford Squares, London WC1B 3DQ, 1975.
256. C. Kittels, *Introduction into Solid State Physics*, 5th edition, John Wiley & Sons Inc., 1976, New York.
257. P. Dobrinsky, G. Krakau and A. Vogel, *Physik für Ingenieure*, B.G. Teubner, Stuttgart, 4th edition, 1976.
258. W. Kauzmann, *Chem. Reviews* 42, 1948, pp. 219 - 256.
259. *Interactive Lit. Res.*, ONERA, 1992.
260. I.J. Polmear, *Light Alloys*, Edition Edward Arnold Ltd, 41 Bedford Squares, London WC1B 3DQ, 1980.
261. E. Nassif, P. Lamparter, W. Sperl and S. Steeb, *Z. Naturforsch.* 38a, 1983, pp. 142 - 148; S. Falch, P. Lamparter and S. Steeb, *Z. Naturforsch.* 39a, 1984, pp. 1175 - 1183.
262. K. Aoki, X-G. Li and T. Masumoto, *Acta Met. Mater.* 40 (1992), pp. 1717 - 1726.
263. R.B. Schwartz, *priv. communication*, June 1990.
264. E.T. Brook-Levinson, A.A. Kolesnikov and I.V. Fine, *Mater. Sci. Forum* 88-90, 1992, pp. 113-120. (Fig.MA19)

265. E. Gaffet, M. Abdellaoui and N. Malhourouroux-Gaffet, Mater. Trans JIM 36 (2), 1995, pp. 196 - 207. (Fig.MA5)
266. M. Terzieva, M. Khrussanova, P. Peshev and D. Radev, Int. J. Hydrogen Energy, 20(1), 1995, pp. 53-58.
267. M.Y. Song, Int. J. Hydrogen Energy 20(3), 1995, pp. 221-227.
268. L. Zaluski, A. Zaluska, P. Tessier, J. O. Strom-Olsen and R. Schultz, J. All. Comp. 217, 1995, pp. 295 - 300.
269. L. Froyen, L. Delaey, X.P. Niu, P. LeBrun and C.Peytour, Journal of Metals 3, 1990, pp. 16 - 19.
270. L.E. Murr, Shock Waves for Industrial Applications. Noyes Publications, Park Ridges, NJ, USA, 1988.
271. R.V. Raman, S.V. Rele, S. Poland, J. Lasalvia, M.A. Meyers and A.R. Niiler, Journal of Metals, March 1995, pp. 23 - 25.
272. R.S. Busk, Magnesium Product Design, Marcel Dekker Inc., New York, 1988.
273. W.A. Baeslack and F.H. Froes, Journal of Metals, March 1995, pp. 13 - 15.
274. H.E. Friedrich, Journal of Metals, February 1995, pp. 33 - 35.

Fig. 1 (Colour photograph) Piston-and-anvil (PA) Mg-5 wt.% Si splat after eight years exposure to inland atmosphere with metallic shiny, pinkish-to-blueish surface film at bottom representing the (nearly) portionless surface zone of corresponding extended solid solution of 5 wt.% Si in cph-Mg. Worse contact between molten alloy droplet and chill has resulted in micro-segregations and resulting silver-to-dark surface as is represented by the remainder of the splat surface. Magnification 1.5 : 1. Note that the feathered rim of this PA-type of splats was removed prior to immersion tests of which the results are shown in the following figures.

Fig. 2 Piston-and-anvil (PA) Mg-4.7 wt.% Gd splats after eight years exposure to an aerated inland atmosphere, here showing essentially supersaturated solid solution as indicated by silver shiny metallic glamour coexisting with corroded interior (splat n° 2) and corroded circumference (splat n° 1 - 3).

Fig. 3 Piston-and-anvil (PA) Mg-4.7 wt.% Gd splats after eight years exposure to an aerated inland atmosphere, here showing the side with essentially the segregated dendritic zone resulting from uncontrolled fluid flow as indicated by the corrosive attack of splats n° 1 and 2. For splat n°3 corresponding segregation-free supersaturated zone (see **Fig. 2**) traverses the entire cross-section.

Fig. 4 Piston-and-anvil (PA) Mg-4.7 wt.% Gd splats after eight years exposure to an aerated inland atmosphere, here showing a more close look-up of the surface of the columnar featureless zone of the microstructure (left hand side) with virtually no degradation of the metallic surface film and of the dendritic segregated zone of the microstructure (right hand side) with uniform distribution of corrosive attack. Magnification is 2 : 1 (top) and 5 : 1 (bottom).

Fig. 5 As for **Fig. 4**, here showing unattacked supersaturated zone (top, left hand side), and an attack due to segregation inside the supersaturated zone resulting from uncontrolled fluid flow (center, right) and uniform attack in segregated zone where dendritic growth occurred due to recalescence (bottom, left). All magnifications: 37.5 : 1.

Fig. 6 Recalesced growth front advancing with V_f after an initial undercooling of 150 K for Mg - 0.74 at.% La alloy under adiabatic conditions. The resulting velocity required for solute trapping (i.e. as a function of increasing bath temperature after the onset of growth) is shown by the dashed curve resulting in free dendritic growth for dimensionless cross-sections > 0.3 (cf. **Fig. 9**).

Fig. 7 Schematic on efficiency of rapid solidification showing a drastic increase in the efficiency of rapid solidification processing in the range of critical fragmentation.
PM/RSP¹⁾: property-sensitive fragmentation range limiting efficiency of advanced processing

Fig. 7 / continued by the choice of materials. i.e. properties are very sensitive to chemical composition, process control etc. on a basis of a productivity which is usually very lousy.

PVD²⁾: productivity-sensitive fragmentation range which is immediately sensitive to productivity and quality of process on the basis of inherently best materials properties, where the efficiency of RSP-processing is primarily a question of design and performance of the PVD-process itself. Subsequent in-situ consolidation provides protection against contamination of the otherwise relatively unlimited surface area of the deposit and evaporated powder, respectively, by oxidization, inclusions due to processing etc. Therefore, any evaporation process for reactive and/or light metals and/or for pure, high performance aerospace applications requires vapour deposition by using a continuously chilled collector unit changing the materials property issue of advanced processing into a productivity-quality issue.

Fig. 8 Transverse cross-section of PA Mg-4.2 wt.% La splats with featureless surface chill zones representing the extended solid solution of La in cph-Mg and which shows inertness upon exposure to corrosive attack by the Machu-test.

In a) this surface chill zone coexists with a columnar dendritic microstructure at the chill-off side, while in b), left hand side with an equiaxed dendritic microstructure trapped by two featureless surface chill zones. Magnification: 500 : 1.

Fig. 9 Transverse cross-section of PA Mg-2.2 wt.% Ce splats showing a), b) featureless growth coexisting with predendrites and columnar dendritic chill-off zone and c) featureless columnar growth of which the grain boundaries are decorated with some microsegregation and trapping equiaxed central zone with large proportion of microsegregations. Magnification of a) to c) 500 : 1.

Fig. 10 As for Fig. 9, here with higher levels of light rare earth metals in PA Mg-splats:
a) 4.2 wt.% Ce, b) 6.2 wt.% Ce, c) 9.0 wt.% Nd. Magnification of a) to c) 500 : 1.

Fig. 11 PA Mg-4.2 wt.% La a) prior to and b), c) after 2 h immersion in 5% (0.3 H₂O₂) - 1% NaCl aqueous solution as to the modified Machu-test with a) and b) showing the side of the featureless surface chill zone. While this side remained silver shiny after 2 h, the dendritic chill-off zone was entirely obscured by a powder-like corrosion product (see c)). The feathered rim of the splat (cf. Figs. 1 to 3) was removed prior to immersion

Fig. 12 PA Mg-2.2 wt.% La splat a) after HF-activation, but prior to the Machu-test and after b) 0.5 h, c) 1h and d) after 3 h immersion in 5% (0.3 H₂O₂) - 1% NaCl aqueous solution as to

Fig. 12/cont'd the modified Machu-test showing the side of the featureless surface chill zone remaining silver shiny after 1 h and virtually unattacked after 3 h immersion. Corrosive attack started at rim and at 4 small sites in the central portion of the PA-splat.

Fig. 13 PA Mg-4.2 wt.% La splat heat treated for 1 h at 400°C and then immersed for 2h in 5% (0.3 H₂O₂) - 1% NaCl aqueous solution as to the modified Machu-test showing a) the side of the featureless surface chill zone and b) the side of the dendritic chill-off zone. While the attack in a) was limited to about 20% of the exposed surface area starting off at rim of the splat there, corrosive attack obscured nearly 100% of the chill-off dendritic zone.

Fig. 14 PA Mg-2.2 wt.% La splat heat treated for 1 h at 400°C and then a) HF-activated and prior to immersion and b) immersed for 0.5, c) for 1 and d) for 3h in 5% (0.3 H₂O₂) - 1% NaCl aqueous solution as to the modified Machu-test, here showing the side of the featureless surface chill zone for which the corrosive attack was triggered at rim of the splat and not by the predendritic surface islands shown in **Fig. 14a**. The corrosive attack was limited to about 30-35% of the exposed surface area at this side of the splat.

Fig. 15 As-solidified PA Mg-2.2 wt.% Ce splat h after a) HF-activation, but prior to immersion and b) immersed for 0.5, c) for 1 and d) for 3h in 5% (0.3 H₂O₂) - 1% NaCl aqueous solution as to the modified Machu-test, here showing the side of the featureless surface chill zone for which weak corrosive attack starting at rim of the splat and without exceeding 15% of the exposed surface area (**Fig. 15a**).

Fig. 16 As-solidified PA Mg-6.0 wt.% Ce splat a) after HF-activation prior to immersion as and b) after immersion for 3 h in 5% (0.3 H₂O₂) - 1% NaCl aqueous solution as to the modified Machu-test, here showing the effect on the side of the featureless surface chill zone for which the corrosive attack was triggered at rim of the splat as well as by the predendritic surface islands coexisting with the featureless chill zone. (cf. **Figs. 9a and 9b**). The corrosive attack was limited to about 15% of the exposed surface area at this side of the splat.

Fig. 17 PA Mg-2.2 wt.% Ce splat heat treated for 1 h at 400°C and then a) HF-activated and prior to immersion and b) immersed for 0.5, c) for 1 and d) for 3h in 5% (0.3 H₂O₂) - 1% NaCl aqueous solution as to the modified Machu-test, here showing the side of the featureless surface chill zone for which the corrosive attack was triggered at rim of the splat after immersion for 1h (**Fig. 17c**) then followed by rapidly progressing attack from the rim to the central portion of the heat treated splat (**Fig. 17d**) resulting in corrosive attack of about 65% of corresponding exposed surface area.

Fig. 18 PA Mg-6.0 wt.% Ce splat heat treated for 1 h at 400°C and then a) HF-activated and prior to

Fig. 18/ cont'd immersion and b) immersed for 0.5, c) for 1 and d) for 3h in 5% (0.3 H₂O₂) - 1% NaCl aqueous solution as to the modified Machu-test, here showing a side which contained a relatively large surface area with microsegregations coexisting with the featureless surface chill zone and triggering corrosive attack at arbitrary surface sites. The attack was limited to about 40% of the exposed surface area at this side of the splat.

Fig. 19 As-solidified PA Mg-15 and 20 wt.% yttrium splats, a) prior to immersion for 15 Y and b) and c) immersed for 3h in 5% (0.3 H₂O₂) - 1% NaCl aqueous solution as to the modified Machu-test (n.b. featureless columnar grains traversed the entire cross-sections of PA Mg-splats), where b) is 15 Y and c) is 20 Y in cph-Mg showing corrosive attack over the major fraction of corresponding surface splats.

Fig. 20 Evolution of corrosive attack on the surface of as-solidified PA Mg-La splats exposed to 5% (0.3 H₂O₂) - 1% NaCl aqueous solution of the modified Machu-test [19,20], where discs representing the extended solid solution of La in cph-Mg and squares representing the dendritic chill-off zone with equilibrium or nearly equilibrium volume fraction of microsegregations. X (straight bar): approximate volume fraction of predendrites coexisting with featureless chill-zone

Fig. 21 As for **Fig.20**, here PA Mg-La splats heat-treated for 1h at 400°C.

Fig. 22 Evolution of corrosive attack on surface of the featureless chill zone of PA Mg-Ce splats (i.e. the extended solid solution of Ce in cph-Mg) in the as-solidified state (discs) and after heat treatment for 1h at 400°C (squares) during exposure to 5% (0.3 H₂O₂) - 1% NaCl aqueous solution of the modified Machu-test [19,20]. X (straight bar): as for **Fig. 20**.

Fig. 23 PA Mg - 2.33 wt.% Nd splat with side of featureless chill-zone microstructure a) prior to and b) after 0.5, c) 1 and d) 3 hours immersion in 5 wt.% (0.3 H₂O₂) - 1 wt.% NaCl aqueous solution.

Fig. 24 PA Mg - 8.61 wt.% Sm splat in as-solidified condition a) prior to and b) after 0.5, c) 1 and d) 3 hours immersion in 5 wt.% (0.3 H₂O₂) - 1 wt.% NaCl aqueous solution, here side of featureless chill-zone microstructure.

Fig. 25 (Top) PA Mg - 6.99 wt.% Nd splat and (bottom) PA Mg - 8.61 wt. Sm splat heat-treated for 1 h at 400°C then immersed for 3 h in 5 wt.% (0.3 H₂O₂) - 1 wt.% NaCl aqueous solution, here side of chill-off zone of dendritic microstructure with strong black tarnish (thick layer of corrosion product).

Fig. 26 PA Mg - 4.0 wt.% Mn splat prior to immersion in 5 wt.% (0.3 H₂O₂) - 1 wt.% NaCl aqueous solution.

Fig. 27 PA Mg - 4.0 wt.% Mn splat with (left row) chill-off and (right row) chill-zone after (top) 0.5 h, (center) 1.0 h and (bottom) 3.0 h immersion in 5 wt.% (0.3 H₂O₂) - 1 wt.% NaCl aqueous solution.

Fig. 28 PA Mg - 6.0 wt.% Mn splat, here made from high purity Mg-feedstock (i.e. < 50 ppm Fe) with featureless chill-zone microstructure after (top) 0.5 h, (center) 1.0 h and (bottom) 3.0 h immersion in 5 wt.% (0.3 H₂O₂) - 1 wt.% NaCl aqueous solution, showing slight tarnish (cf. before).

Fig. 29 PA Mg - 6.0 wt.% Mn splat, here made from high purity Mg-feedstock, here after heat treatment for 4 hours at 350° to assure precipitation of β Mn from the supersaturated solid solution then developing black tarnish upon immersion as before (i.e. after a) 0, b) 0.5, c) 1 and d) 3 h immersion).

Fig. 30 PA Mg - 8.0 wt.% Mn splat with β Mn-dispersoids provoking local pits without destroying overall resistance to corrosive attack after b) 0.5, c) 1 and d) 3 h immersion (see above).

Fig. 31 PA Mg - splats with (top) 0.5 wt.% Si, (center) 1.0 wt.% Si and (bottom) 5.0 wt.% Si prior to immersion (cf. next pages).

Fig. 32 As for page before, here after 0.5 h immersion in 5 wt.% (0.3 H₂O₂) - 1 wt.% NaCl aqueous solution showing increasing corrosive attack with increasing Si-content according to the volume fraction of Mg₂Si-phase separated from the melt in particular at the outer splat zone (with worse contact with the piston).

Fig. 33 As for page before, here after 1 h immersion in 5 wt.% (0.3 H₂O₂) - 1 wt.% NaCl aqueous solution. A particular good contact resulting in featureless surface zone for PA Mg - 5 wt.% Si develops surprising corrosion resistance at splat center (see bottom, labelled with "FH703")..

Fig. 34 As for page before, here after 3 h immersion in 5 wt.% (0.3 H₂O₂) - 1 wt.% NaCl aqueous solution showing surprising resistance to corrosive attack for major part of splat containing 0.5 wt.% Si (top) and for central part of splat containing 5.0 wt.% Si (bottom).

Fig. 35 PA Mg-splat with 0.5 wt.% Si (top) and 5.0 wt.% Si (bottom) after heat treatment for 1 h at 400°C and (left row) prior to and (right row) after 3 h immersion (as before) showing

Fig. 35/cont'd entire breakdown of corresponding corrosion resistance. Supersaturation with Si of these materials did not exceed 0.5 wt.%. The breakdown is a result of coarsening of the Mg_2Si - phase either separated from the melt during solidification.

Fig. 36 PA Mg - 2.46 wt.% Sb splat, as-solidified condition and prior to immersion (cf. next page; n.b. scale is in [mm]).

Fig. 37 PA Mg - 2.46 wt.% Sb splat, as-solidified condition, after (top) 0.5, (bottom left) 1.0 and 3.0 immersion in 5 wt.% (0.3 H_2O_2) - 1 wt.% NaCl aqueous solution.

Fig. 38 PA Mg - 2.46 wt.% Sb splat, heat treated for 1 h at 400°C a) prior to and b) after 0.5, c) 1.0 immersion in 5 wt.% (0.3 H_2O_2) - 1 wt.% NaCl aqueous solution showing the effect of solid state precipitation and/or coarsening of Mg_3Sb_2 second phases, i.e. rapid solidification vs. the as-solidified condition (cf. Figs 36 and 37).

Fig. 39 PA Mg - 7.09 wt.% Sb splat in as-solidified condition and embrittled by Mg_3Sb_2 -dispersoids separated from the melt as indicated by cracks near rim and showing increasing pitting (in contrast to PA Mg-2.46 wt.% Sb) in regions of uncontrolled fluid flow and/or at splat rim after immersion as before (cf. Fig. 38).

Fig. 40 PA Mg - 3.5 wt.% Ca splat heat-treated for 1 h at 400°C (top) prior to and (bottom) after 2 h immersion in 5 wt.% (0.3 H_2O_2) - 1 wt.% NaCl aqueous solution with (bottom left) dendritic chill-off zone and (bottom right) featureless chill-zone in the as-splatted state.

Fig. 41 PA Mg - 2.0 wt.% Ca splat heat treated for 1h at 400°C with a) prior to and b) after 0.5, c) 1 and d) 3 h immersion in 5 wt.% (0.3 H_2O_2) - 1 wt.% NaCl aqueous solution with black islands representing predendritic features in featureless chill-zone. No corrosion was observed at this side of the splat.

Fig. 42 PA Mg - 5.0 wt.% Ca splat heat treated for 1h at 400°C, here chill-side (featureless) zone without showing corrosive attack a) prior to and b) after 0.5, c) 1 and d) 3 h immersion in 5 wt.% (0.3 H_2O_2) - 1 wt.% NaCl aqueous solution.

Fig. 43 PA Mg - 1.5 wt.% Sr splat, as-solidified condition, (top) prior to and (bottom) after 2 h immersion in 5 wt.% (0.3 H_2O_2) - 1 wt.% NaCl aqueous solution for (bottom left) featureless chill-zone microstructure and (bottom right) dendritic chill-off zone. Note the very low partition coefficient k_0 in the system Mg-Sr over Mg-Ca making it significantly more difficult to achieve substantial supersaturation of cph-Mg with Sr vs. cph-Mg with Ca.

Fig. 44 PA Mg - 4.23 wt.% Pd splat in as-splatted condition and immersed for 2 h in 5 wt.% (0.3 H₂O₂) - 1 wt.% NaCl aqueous solution with (top) corrosive attack localized to splat rim on side of featureless chill-zone microstructure and (bottom) excessive corrosion (black product) in dendritic chill-off zone.

Fig. 45 PA Mg - 3.91 wt.% Au splat in as-solidified condition, here featureless chill-zone microstructure (top) prior to and (bottom) after 3 h immersion in 5 wt.% (0.3 H₂O₂) - 1 wt.% NaCl aqueous solution showing localized corrosion at splat rim.

Fig. 46 PA Mg - 14.19 wt.% Au splat heat-treated for 1 h at 400° C after (top) 0.5 h and (bottom) 1 hour immersion in 5 wt.% (0.3 H₂O₂) - 1 wt.% NaCl aqueous solution with (all left) featureless chill-zone microstructure and (all right) dendritic chill-off zone microstructure.

Fig. 47 Test coupons of AZ91 and of vapour deposited Mg-4 wt.% Ti and Mg-7 wt.% Ce (both deposits here made at 60°C with the Ti and Ce held in the cph-Mg solid solution) prior to (top, with bend contrast for Mg-4 Ti) and after (bottom) 0.5 h immersion in 5% (0.3 H₂O₂) - 1% NaCl aqueous solution as to the modified Machu-test. The porosity (which was absent at deposition at higher temperatures, eg. > 100°C) leads to rapid attack of the VD-alloys and is at least as harmful as the microsegregations of corresponding melt processed alloys (see above), but the corrosive attack on Mg-7 Ce was less rapidly (75% of the exposed surface area) than on Mg- 4 Ti (> 90%) , while reference alloy AZ91 corroded more rapidly (100%) than both VD alloys.

Fig. 48 Optical microstructure of transverse section of vapour deposited (top, 1000:1) and chill cast (bottom, 200:1) Mg-8wt.% Ce alloy showing featureless columnar growth after vapour deposition and dendritic growth with two regimes of dendrite arm spacings after casting.

Fig. 49 Optical microstructure (1000:1) of transverse section of Mg-base gun splat containing 6.0 wt.% La showing featureless surface chill zone and banded cellular microstructure at the chill-off side of the splat. The degree of supersaturation of the banded microstructure is not very different compared to that of the featureless chill zone and is significantly larger compared to that of the dendritic chill-off zone of PA-splats (see above).

Fig. 50 Showing difference of heat flow between two successive differential scanning analyses (DSC) of gun splats of Mg-8wt.% Ce alloy. Heating rate: 40 K/min. Employed mass: 2.23 mg. A non-linear baseline drift was superimposed to the analyses that was not corrected for and is indicated by the difference between zero-line and dashed line.

Fig. 51 As for **Fig. 50**, here with employing Ta-foils to getter oxygen traces in the nitrogen used to purge the cell of the DSC-apparatus and evidently reducing the exothermal effect at temperatures above 400°C. Heating rate: 40 K/min. Employed mass: 2.05 mg.

Fig. 52 As for **Fig. 51**, here gun splats of Mg - 1 Nd (top) and Mg - 1 La (bottom, nom. [wt. %]). Heating rate: 40 K/min. Employed mass: 2.07 (top) and 1.94 (bottom) mg.

Fig. 53 Individual discrimination and subsequent evaluation as to **figure caption 50** to reduce the non-linear error of DSC-analysis of gun splats of Mg-8wt.% Ce alloy resulting in an exothermal enthalpy of transformation of -6.9 (top), - 9.8 (center) and - 31.8 (bottom) J/g for exothermal effects n° 1, 2 and 3. Heating rate: 40 K/min. Employed mass: 3.04 mg.

Fig. 54 Individual discrimination as to **Fig. 53**, here for the exothermal effect n° 2 of Mg-base gun splats with 1 Nd (top) and 1 La (center and bottom) (nom. [wt. %]) resulting in exothermal enthalpies of transformation of -9.7 (top), - 45.0 (center) and -30.1 (bottom) J/g. Heating rate: 40 K/min (top and center) and 20 K/min (bottom).

Fig. 55 Individual discrimination of exotherm n° 3 of gun splatted (top) and vapour deposited (bottom) Mg - 8 wt.% Ce alloy showing "Umklapp" process in transformation behaviour from exothermal (top, with superimposed endothermal) to endothermal transformation (bottom) as the degree of fragmentation had increased prior to solidification (cf. also **Fig. 53**, bottom). The gun splats were of thickness < 1 µm here, while thickness of the gun splats employed for the DSC-analysis in **Fig. 23** was > 1 µm. Heating rate: 40 K/min.

Fig. 56 DSC-analysis (top) including individual discrimination (center and bottom) of vapour deposited Mg - 8 wt.% Ce alloy resulting in an exothermal and endothermal enthalpy of transformation, respectively, of -15 (center) and + 68.5 (bottom) J/g and showing the complete conversion of exo- to endothermal transformation at temperatures > 400° C. Heating rate: 40 K/min.

Fig. 57 As for **Fig. 56** (top), here using a) another sample to employ a heating rate of 40 K/min (top) and b) to employ a heating rate of 20 K/min (bottom), both analyses showing excellent reproducibility of the thermal effects shown in **Fig. 56**.

Fig. 58 Individual discrimination of the DSC-analysis shown in **Fig. 57** (bottom) resulting in an exothermal enthalpy of transformation of -7.2 (top) and +42.8 (bottom) J/g for the exothermal effects n° 1, 2 and the endothermal effect at above 400°C.

Fig. 59 Showing DSC-analyses on Mg-La splats aged for eight years at ambient temperatures with
SUBSTITUTE SHEET (RULE 26)

Fig. 59 cont'd (top) rotating-wing (RW) Mg - 3.9 wt.% La splats of thickness $< 20 \mu\text{m}$, (center) Mg - 6.8 wt.% La splats of thickness $< 20 \mu\text{m}$ and (bottom) Mg - 4 wt.% La splats of thickness $140 \mu\text{m}$, the latter without evidence for an endothermal effect at around 150°C . ΔW = power, ΔH = enthalpy per gram (i.e. effective enthalpy of transformation). nb. endothermal effects are pointing downwards.

Fig. 60 As for **Fig. 59**, here for (top) rotating-wing (RW) Mg - 3.65 wt.% Ce splats and (center) RW Mg - 13.2 wt.% Ce splats and (bottom) Mg - 4 wt.% Ce splat by piston-and-anvil splat cooling. nb. endothermal effects are pointing downwards.

Fig. 61 Showing heat flow obtained by subtraction of DSC-analysis and subsequent in-situ baseline of RW Mg - 7.5 wt. Gd splats of thickness $30 \mu\text{m}$ aged for eight years at ambient temperature and resulting integration of corresponding enthalpy of transformation as before.

Fig. 62 As for **Fig. 61**, here RW Mg- splats with 17 wt.% Gd and thickness $30 \mu\text{m}$ (top) and for splats with approximately 8 wt.% Gd, but of thickness $200 \mu\text{m}$.

Fig. 63 (Top) TEM-diffraction pattern and (bottom) DSC-analysis using various heating rates as shown in [K/s] for melt-spun Mg - 23.4 wt.% Al ribbon after 12 months exposure to ambient temperatures. The endothermal transformation of the ordered room temperature phase is as strong as the transformation of the remaining supersaturated solid solution of aluminium in cpg-Mg after these conditions of natural ageing [118].

Fig. 64 X-ray spectrum of the "endothermal" solid solution of 8 wt.% Ce in cph-Mg made by vapour deposition using the sputtering method (cf. **Figs. 56 - 58**), here for two different deposits of thickness 70 and $250 \mu\text{m}$. The mean half width of the (002)-reflection of the $70 \mu\text{m}$ -sample was used to estimated the cell size of the microstructure via the formula by Scherrer (p. 17).

Fig. 65 Hall-Petch relationship for Vickers hardness numbers V.H.N. of Mg - 8 wt.% Ce made by conventional casting and by vapour deposition. For comparison, data of cph- αMgLi alloys and of alloy EA55RS are also included (cf. [64]). The slope of each relationship represents the Hall-Petch proportionality constant k_y .

Fig. 66 Tensile yield strength σ_y as a function of $d^{-0.5}$, with d = grain size for extruded Mg-alloys made by ingot processing (I/M. discs) and by rapid solidification processing (RSP, squares). The Hall-Petch relationship for Mg-Al-Zn base alloys is from [80], that for Mg - 10.9 Al after [84], for ZK60 after [82], that for ($\alpha+\beta$) Mg - 9 Li based alloys after

Fig. 66/cont'd [87,88], that for bcc- β Mg-40Li-2H [at.%] after [89] and that for pure Mg from [93].
If not indicated otherwise, alloy composition is in [wt.%].

Fig. 67 Tensile yield strength σ_y as a function of $d^{-0.5}$, with d = grain size for extruded Mg- and Al- alloys made by ingot processing and by rapid solidification processing, here without individual samples. Bold lines: k_y -values for Mg and Mg-alloys; dotted lines: k_y -values for Al and RSP-Al-alloys. Note that minimum grain size observed is represented by the end on the right hand side of each Hall-Petch relationship.

Fig. 68 (Top) Effect of Fe-content on the true weight loss - corrosion rate of \square rapidly solidified alloy Mg-15 wt.% Al and of \blacklozenge conventionally cast Mg - 10 wt.% Al (top) and (bottom) proposed mechanism of corrosion pit for a) conventionally cast Mg-Al alloy with large $\text{Mg}_{17}\text{Al}_{12}$ particles (not included here) and b) rapidly solidified microstructure with fine $\text{Mg}_{17}\text{Al}_{12}$ -dispersion. CP: corrosion pit, SCP: spalled corrosion product, both modified upon RSP to PC (i.e. (reduced) pit (size) containing corrosion product and passivated precipitates).

Fig. 69 a) Effect of grain size on temperature of ductility transition and on shape of transition curve and b) effect of gradual decrease of grain size on transition temperature, both for pure magnesium. After [50].

Fig. 70 Slip planes and slip directions of cph magnesium in order of thermal activability above ambient temperature (italics: conditions for operative slip mode). After [50].

Fig. 71 Showing agreement between intrinsic fault vector t_1 a) as derived from linear elasticity and b) from multi-body potential calculations, here for the γ -surface repeat cell $1/3 \langle 11\bar{2}0 \rangle \langle 1\bar{1}00 \rangle$ of the basal plane of pure magnesium with Burgers vector b (cf. [102]). Dark dotted arrow: t_1 ; bright dotted arrow: b ; solid discs: (0001) atoms; dotted discs: eg. (0002) atoms; double-hatched discs then (000 $\bar{2}$) atoms, accordingly.

Fig. 72 Hall-Petch proportionality constants k_y for light alloys based on Mg and Al and obtained from tensile tests (top) and microhardness data (down). While alloying of Al decreases the value of k_y of pure Al, almost all of the reported alloying of Mg decreases the k_y -value of pure magnesium.

Fig. 73 Stacking fault energy Γ (in $[10^{-2} \text{ Ryd/at.}]$) of closed packed hexagonal crystal lattices in (γ_b) corresponding basal plane and in (γ_p) corresponding prismatic plane as a function of filled d-band states, Z , showing $\gamma_p < \gamma_b$ for $Z = 1, 2$ and 6 to 8. From [109].

- Fig. 74** Potentiodynamic polarization curves of (essentially) monophasic Mg-alloys (a) - e) and of f) Cu-based Cu-Au solid solutions with typical anodic polarization plateaus except for e) where an active-to-passive transition (as for Cr-steels) had occurred.
- a,b: single phase solid solutions of (top) titanium and (bottom) zirconium in cph-magnesium made by magnetron sputtering and using a 1 mol NaCl electrolyte at pH9 at 30°C. The effect of this electrolyte on the pure elements is also shown [28].
- c: Potentiodynamic polarization of single phase solid solutions of 17.6 to 23.4 wt.% Al in cph-Mg made by melt-spinning and of chill-cast Al_8Mg_5 -phase containing 62.3 wt.% Al in an aggressive electrolyte (aerated 0.001 mol NaCl solution of pH4.9 at temperature of 25°C) using a scan rate of 6 mV/s. The resultant anodic polarization features were not evident for corresponding two-phase casting materials.
- d: as for c), here using PA Mg - 2.2 wt.% Ce (0.39 at.% Ce) splats and melt-spun ribbon containing 7.9 wt.% (1.35 at.%) and 18 wt.% (3.11 at.%) Ce.
- e: as for a), here sputtered Mg - 15.5 Al - 17.6 W (in [at.%], [133]) in 1 mol NaCl aqueous solution.
- f: effect of Au (in [at.%]) upon anodic polarization during potentiodynamic polarization of various Cu-Au solid solutions in 0.1 mol Na_2SO_4 / 0.01 n H_2SO_4 aqueous solution.

Fig. 75 Showing (top) cation and (bottom) anion fraction in the surface oxide of hypersaturated solid solutions of 47 at.% (63.6 wt.%) Ti and of 57 at.% (83.5 wt.%) Nb in cph-Mg upon polarization as in **Fig. 74a,b** [28].

Fig. 76 Effect of composition and resulting density on corrosion behaviour of characteristic Mg-TM alloys (TM = Ti, Zr, Nb and Ta) made by magnetron sputtering then exposed to aqueous 1 mol HCl solution [28].

Fig. 77 Schematic of evolution of surface reaction products on conventionally processed Mg-based alloys indicating area of interest for development of corrosion resistant Mg-alloys by advanced processing (upper left MgO-domain), while the rest is to be avoided. Penetration of hydroxyl-ions into MgO, for example, can result oxide thickening without developing any protective surface product (cf. **Fig. 80c**).

Fig. 78 Pitting corrosion is the most frequently observed form of corrosion of conventional Mg-alloys in real life. While it is common practise to attribute pitting corrosion to the microstructure including impurity inclusions of the Mg-alloy concerned, it is usually overlooked that an oxygen gradient (cf. **Fig. 78a**) is formed in front of the interface metal/electrolyte resulting in an increase in b) corrosion potential (ϵ_k)_R due to corresponding shift of the cathodic partial reaction from a_2 to k_2 (cf. **Fig. 78b**). **Fig. 78a** shows the stationary oxygen distribution with increasing distance from metal surface and decreasing distance from the

Fig. 78/cont'd surface of the electrolyte and Fig. 78c the resulting potential profile (solid lines) and current density lines (hatched lines) for a Zn-plate immersed in 1 N NaCl aqueous solution, the numbers in [mV] with 0-line as reference, i.e. the oxygen-rich part of the interface (cf. O in Fig. 78d) is the more noble (cathodic) part equivalent to an Fe-inclusion, while corrosion occurs in the oxygen depleted part of the interface depending on the amount of oxygen diffusing to the cathodic part. As a result, a topologically coherent iron oxide surface film (Fig. 78d) transforms locally into pits (P) which are surrounded by Fe_2O_3 or other corrosion products (cf. CP) depending on the details of the environment (cf. Fig. 79) and which build up in the vicinity of the pit as a result of local oxygen gradients under a droplet, for example, forming an aeration cell (local element) on top of the metal surface according to Fig. 78c. That is, the resulting pit would also form when the microstructure was absolutely homogeneous (i.e. one phase (equilibrium) alloy microstructure) showing that the reduction of pit falls requires also modification of the metal oxide via other means (cf. text and [138]).

Fig. 79 (Top) Transformation of topologically coherent iron oxide film (A) into pitting and surrounding corrosion product $\text{Fe}(\text{OH})_3$ (B: rust) building up around pit as a result of oxygen gradient in aeration cell (local element, i.e. C: electrolytic solution, D: diffusion and E: electrolytic transfer) on top of metal surface according to Fig. 78c (n.b. F: metallic shiny, G: tight layer of rust, H: loosely adherent rust). (Bottom) Corresponding result for rotating low alloyed steel disc exposed to 0.0003 mol Na_2CO_3 saturated with CaCO_3 in air at $T = 20^\circ\text{C}$, $\omega = 1 \text{ Hz}$ [138].

Fig. 80 Modelling of pit falls on I) metal surfaces resulting from a) penetration of anion (Cl^-) into metal oxide, b) island - adsorption of anions (Cl^-) on passive oxides and c) fissuring of passive surface oxides where A: attack of electrolyte and B: competition of growth between surface oxide and surface chloride, on II) iron oxide resulting from local perforation of oxide in Cl^- - containing solution at medium value of pH according to Heusler and III) on aluminium oxide according to Kaesche, the latter showing Al-hydrolysis in NaCl-solution resulting from Cl^- - and H_2O -transport to and H_2 -transport (bubbles) away from locally acitic pit fall (B, i.e. $\varepsilon < E_{\text{H}_2/\text{H}^+}$) despite overall $\text{pH} > 7$ (A, i.e. $\varepsilon > E_{\text{H}_2/\text{H}^+}$) more far away from pit [138].

Fig. 81 Synergy between heat of oxygen adsorption and easiness of disruption of like-like metal bonds and resulting clustering I, II and III of non-passive metals (I), passivity enhancing (enhanced) metals (II) and retarding their solution/reaction with oxygen due to relatively large internal forces (III), respectively [139].

Fig. 82 Showing equilibrium phase diagrams of a) binary system Fe-Cr including the effect of
SUBSTITUTE SHEET (RULE 26)

Fig. 82/cont'd 0.6 wt.% carbon on γ -phase field extension (dotted line) and b) ternary T - xNi - cut for Fe - 18 Cr alloys (cf. a)). Both diagrams show that monophasic α -ferritic and γ -austenitic iron alloys (and steels) are largely alloyed with passivating Cr (and Ni in b)), while any two phase ($\alpha + \gamma$ - microstructure provides relatively small microgalvanic gradients due to a relatively high alloying level involved in both phases [140].

Fig. 83 Showing schematic of a) typical binary Mg-base equilibrium phase diagram with relatively large concentration gradient between α and β in corresponding two phase microstructures and b) reduced concentration gradient by non-equilibrium processing resulting from (i) occurrence of non-equilibrium β -phase at intermediate concentration and/or (ii) phase field extension of corresponding terminal phases α and/or γ . Reduction of microstructural microgalvanic gradients due to non-equilibrium processing would be even more effective in ternary and higher order systems due to c) occurrence of intermediate (inter-metallic) γ -phases already at equilibrium processing so reducing the concentration range of Mg-based phases of interest and resulting density increment.

Fig. 84 Optical microstructure of melt-spun Mg-17.3 wt.% Ce ribbon showing columnar grains, here traversing a substantial part (i.e. about 75 %) of the cross-section of thickness 20 μm and trapping a more equiaxed microstructure along the center line of the ribbon. Magnification: 1200:1.

Fig. 85 Schematic showing effect of substitution of Mg and/or MgO in the surface film with higher valency-metal (here vanadium) and/or resulting oxide, i.e. introduction of n-conductance and reduced field gradients $\Delta\Psi/\Delta x$ for different PB-ratios indicating that both n-conductance and PB-ratios approaching 1 are complementary factors for passivation of bulk magnesium.

Fig. 86 Difference scan of two successive DSC-analyses of melt-spun Mg-17.3 wt.% Ce ribbon of thickness 20 μm showing exothermal peak effect (note that the exothermal effects are plotted downwards in this particular analysis) at around 425°C (698 K) and a relatively weak exothermal spectrum with respect to the baseline (dotted line). Heating rate: 40 K/min. Employed mass: 1.98 mg and assuming 44.341 g/mol for the accumulated enthalpy curve. The pivot of the ΔH -curve of the exothermal peak effect was used to estimate corresponding partial enthalpy.

Fig. 87 As-solidified PA Mg-6.0 wt.% Mn splat a) prior to and b), c) after 2 h immersion in 5% (0.3 H₂O₂) - 1% NaCl aqueous solution as to the modified Machu-test with a) and b) showing the side of the dendritic chill-off zone and c) that of the featureless chill-zone. While the letter remained essentially unaffected, the chill-off side was obscured by pitting corrosion (see **Fig. 87b**).

Fig. 88 Schematic of vapour deposition process controlled by suction flow via an external pumping system which generates elemental and alloyed vapour flow in chamber n and $n+1$ then driving the vapour towards a condensor (right hand side). For a given pumping speed S the actual throughput of vapour is controlled by the diaphragma. The resultant processing pressure and temperature gradient across the interface of the diaphragmas as well as the vapour velocity profile is shown schematically on the left hand side. The hatched area for the T-curve indicates the effect of radiation due to the positive temperature between chamber $n+1$ and $n+2$. The temperature in the " n "-unit to be used for the evaporation of magnesium and/or rare earth metals, for example, ranges eg. from 600° to 2000°C , while the temperature in the " $n+1$ " - unit to be used for the evaporation of rare earth and/or transition metals, for example, ranges eg. from 1400° to 2800°C .

Fig. 89 a) x-projection of "Pen stocks" as to [161], i.e. a "matrix of flow channels", b) x-projection of a resistor to flow with a defined resistor surface area A_R , which is strictly speaking a parallel resistor to flow, and c) x-projection of (the "element" c_1 of) a diaphragma as to the invention showing five vapour intakes here, each of them forming a basic "element" (cf. c_1) of the diaphragma. Only solution c) allows for a distinct pressure gradient dP/dx across the interface between chamber n and chamber $n+1$ as to Figs. 90 to 94.

Fig. 90 Bifurcations (B) as a basic diaphragma element used to control suction flow (see arrows pointing out of diaphragma) in vapour deposition processing to manufacture high performance light metals and alloys. The elements may consist of a single, or a single pair or a multiple, i.e. a series of single or pairs of bifurcations, the bifurcations either constructed in an angular way, or in a smoothed-out way or angular confined or smoothed out confined-to-channeled, but for all cases the overall pressure at the intake, p_i , is larger than the pressure at the backstreaming outlets, p_b . Diaphragmas consisting of bifurcations represent a depth-type of mass-filter in analogy to membranes used to chemically separate a component from a mixture. nb. e) and f) with trumpet-type (T) of vapour outlet to improve effect of suction on vapour flow as indicated by arrow*. l_i = length of interface of diaphragma.

Fig. 91 As for Fig. 90, here confined (or channelled) multiple bifurcations (type "octopus"). the hatched areas indicating alternative volumes to create turbulences so providing a solution which overlaps with those in Fig. 93 including heating elements for a progressive temperature increase. * = Δp_0 used to generate ("internal") turbulences for a T-controlled expansion of transmembranic vapour flow.

Fig. 92 Constructional elements (details) and element combinations to generate a turbulent-to-laminar flow transition at the periphery of the interface per diaphragma element. a) most

Fig. 92/ cont'd simple solution for which the retained vapour mass per diaphragma element, Δm_R is equal to the product " $k \cdot h$ " with k = a constant which is a function of length l , height h and angle α . The c_F -value of the control element is large in front of and small behind the vapour intake and/or diaphragma (see text). * = transition to adjacent diaphragma element. b) to d) show more massive control elements in front of the diaphragma with d) indicating an "external", i.e. "sieve"-type of bifurcation (voir letter "S"). T: transition to adjacent diaphragma element.

Fig. 93 A series of resistors, m , to vapour flow which can multiply the number of resistor elements per series thereby reducing the resistance to vapour flow per level m progressively towards chamber $n+1$. a) and b) showing the two basic solutions " $A_{0,1} > \Sigma A_{0,2} > \Sigma A_{0,3}$ " and " $A_{0,1} < \Sigma A_{0,2} < \Sigma A_{0,3}$ " including a "differential reservoir" DR to be extended in version c) by elements with large c_F -number in front of vapour intake and small c_F -number to direct vapour flow by reducing "internal" turbulent flow and turbulent flow at vapour outlet. d) shows a heating spiral H to locally heat vapour flow.

Fig. 94 For example, flow control elements with large c_F -number in front of vapour intake and small c_F -number at vapour outlet and a series resistor combined in such a way, that $m_1 = m_2$ so not providing a differential reservoir.

Fig. 95 As for Fig. 88, here with parallel arrangement of evaporation chambers in n -level (the height of which corresponding to the PD-controlled throughput Q_v as is for elements with similar vapour pressures) followed by a mixing chamber eventually designed as a funnel or macroscopic laval nozzle resulting in reduced cross-section of PD prior to vapour deposition in vapour deposition unit (21), the reduced PD-cross-section increasing freedom of transport of plank-condensators moving in a circuit batch process in level $(n+2)$, where (22): micro-rolls, (23): peening-system, (21a): outer wall of vacuum unit outside the vapour deposition unit (21); (27): transport system with rolls of adjustable height, (18): vacuum pump system. PD= porous membrane "diaphragma".

Fig. 96 "Parallel"-processing of evaporation in level " n " (the height of each evaporation chamber corresponding to the vapour pressure of corresponding element) in a porous membrane diaphragma (PD) - controlled and suction- and/or vapour pressure driven vapour deposition process, the evaporation chamber here arranged by way of a semi-circle around a mixing chamber (with baffle wall) in level $(n+1)$ so that a major suction effect is transferred to chamber n^3 in the center of the n -level. 24: movable separation wall; 25: flat hollow cylinder to accomodate (24).

Fig. 97 Discontinuous temperature intervals $\Delta T = T_{\max} - T_{\min}$ on deposit surface resulting from
SUBSTITUTE SHEET (RULE 26)

Fig. 97/cont'd reciprocating movement of flat "plank"-collector passing a vapour deposition unit (21) T_{\max} is attained during vapour impingement on the deposition surface, while T_{\min} is attained in the latest movement before the next following deposition pass. While a large absolute value of T_{\max} assures minimum porosity (i.e. prior to in-situ consolidation), T_{\max} may eventually exceed the transformation temperature of corresponding non-equilibrium alloy structure. Therefore, ΔT should be small, the control of which is best given by the condition $\delta\Delta T = 0$.

Fig. 98 Principle of continuous batch process using flat plank-collectors (PC): (top) showing "planar" - type of continuous process, i.e. condensers tilting (lateral) edge-on (le) by adapting (via tilt angle α) movement of velocity $V_{\text{Kon}}(2)$ which is larger than $V_{\text{Kon}}(1)$ during deposition pass (i.e. $V_{\text{Kon}}(1) < V_{\text{Kon}}(2)$), showing process principle $n_c^{\min} = 3/2 n_d$, where n_c^{\min} = minimum number of condensers, n_d = corresponding number of diaphragmas (PD) before deposition, while (bottom) showing "spatial" - type of continuous process with condensers tilting (front) face-on (ff) and requiring different planes (cf. tilt angle β) for the final diaphragma PD controlling the suction-driven overall VD-process.

Fig. 99 Evolution of compact construction of suction-driven and PD-membran controlled vapour deposition process (see a) to d)) for PC - condensor - circuit process providing $\delta\Delta T \rightarrow 0$ in deposition surface with a) each deposition unit (n+2) supplied with vapour from an individual mixing= and/or evaporation unit (n+1), and b) - d) common vapour source showing aerodynamic evolution of overall arrangement of process providing increasingly decreasing macroscopic coefficients of pressure loss, ζ , (see next patent).

Fig. 100 "Top"-view, i.e. projection of "planar" condensor level from evaporation part of process following principle $n_c^{\min} = 3/2 n_d$ with (top) $n_c^{\min} = 6$ and (bottom) $n_c^{\min} = 12$ (numbers in circles). (21) : deposition chamber as before (i.e. top view of diaphragma); (12,13) : condensor and corresponding deposit, respectively; (19d): wall of final mixing and/or evaporation chamber prior to diaphragma (see Fig. 101). (19): periphery of evaporation chamber more away from deposition / collector system. The process is g-independent.

Fig. 101 As for Fig. 100, here including further details such as (21a): vacuum chamber extension to provide sufficient freedom of condensor movement between two successive deposition passes (cf. also Fig. 102).

Fig. 102 Planar and vertical section of individual deposition unit as for Figs. 41, 43 - 46 (top) with (13d) rotating distributor and collector of chill medium for (13) condensor (substrate) with (60) meander tunnel to conduct the chill medium in the condensor by using separation

Fig. 102/cont'd walls as to (13g), the rotating distributor / collector being connected with the condensor (13) by (13c) a tube joint, (13a) rigid tubes, (13b) flexible (i.e. bendable and/or stretchable metallic) tubes connected with (13a) by means of a (13k) flange (gasket), the overall height / position of which being controlled by a microprocessing unit (13h), and (bottom) showing (31) upper and (34) lower part of vacuum chamber for deposition unit with (17): fix or movable, (17b): fix and (17c) movable separation wall between deposition unit and vacuum chamber for transport of the condensor with (12) in-situ consolidated deposit and (36) non-consolidated deposition layer.

Fig. 103 Schematic including overall vertical cross-section of g-independent condensor-level of g independent suction flow- or vapour pressure-driven vapour deposition plant of which the vapour throughput is controlled by a porous membrane PD as for **Fig. 102**, here furthermore including:

(33) = separation segment, (35) = scraper, (53) = top wall of vacuum chamber (deposition chamber), (13f) = cooling machine (refrigerating aggregate), (13i) = movable support bar, (13j) = tube accomodating support bar (13i), (13e) = motor drive for collector system, (58) = moving directions of (13i) and rest of collector system, (37) = barrier against flames, (38a) = vacuum pump system (eg. including roots booster), (38b) = filter, (38c) = container / collecting tank for powder, (38d) = various valves, (39a) = zyclone, (39b) = gas purification / gas separation / gas washe = (39c) collecting container for powder, (39d) = pumping system with trap for residual vapours.

Fig. 104 Specific tensile strength values of amorphous Mg-alloys by rapid solidification processing (RSP) reported between 1977 and 1992. From [159].

Fig. 105 Differential scanning calorimetry (DSC) - analyses of various Al-TM-based alloys (TM: transition metal) doped with ternary (X), quaternary (Y) and quinary (Z) alloying additions after milling at various conditions. From [194].

Fig. 106 DSC-analysis (scan 1 minus in-situ reference scan) of (WE54 + 9 wt.% Al_2O_3) ball milled for $t = 2$ h at $T = 20^\circ$ to 60°C without lubrifyer (i.e. "dry"). The actual (yet not published) milling variables were: $\Omega = 206$ rpm $\pm 10\%$ max.; $\omega_{\text{abs}} = 241$ rpm $\pm 10\%$ max.; $R = 12.5$ cm; $r = 3.275$ cm; $r_b = 0.50$ cm; $\rho_b = 7.60$ g/cm³; $n_b = 18$ milling balls of r_b and ρ_b as above. The precursor charge employed was 6g (WE54) and 0.54 g Al_2O_3 , i.e. $\Sigma m_{\text{charge}} = 6.54$ g.

Fig. 107 Vial and vial dimensions employed in the invention by using Fritsch's Pulverisette 5^R.

Fig. 108 Comparison of injected power by irradiation. mechanical and other forms of straining the

solid state showing overlap of mechanical alloying with all forms of mechanical loading and irradiation on the [eV/at.s] - scale. n.b. the term "solicitation" is taken from the French language eventually better translated into English language by the term "micro-stresses". From [100].

Fig. 109 Showing principal of planetary ball milling for (top) four vials rotating anti-clockwise while corresponding holder disc (large arrow circle) rotates clockwise and (bottom) horizontal cut of vial moving clockwise (V) with eight milling balls (of which two are in flight as indicated, see (F)) and milled powder during action as to schematic on top. A: movement of holder disc, here rotating anti-clockwise and B: centrifugal force.

Fig. 110 Velocity (amplitudes, i.e. V_c^2) of (solid bars) absolute velocity of milling balls after detachment using a planetary ball mill with $R = 12.5$ cm and $r^* = 2.775$ cm and (left hand side) three different ω -values (80, 180 and 280 rpm) at $\Omega = 206$ rpm and (right hand side) three different Ω -values (106, 206 and 306 rpm) at $\omega = 80$ rpm. Furthermore, the amplitudes of the normal (······, i.e. $V_{c,p}^2$) and tangential (x-x-x-x, i.e. $V_{c,\alpha}^2$) impact velocities of a milling ball as a function of impact angle α is given for $\Omega = 206$ rpm and $\omega = 80$ rpm (RHS).

Fig. 111 Impact energy for mass of milling ball, $m_b = 14$ g, as a function of disc rotation velocities Ω at various vial rotation velocities ω as indicated for two planetary ball mills with $R = 13$ (G5) and 7.5 cm (G7). Vial radius $r = 21$ mm, radius of milling ball, $r_b = 7.5$ mm. From [223].

Fig. 112 (Arbitrary) Flight trajectory $\overline{M_d M_c}$ (dashed line) between detachment M_d and collision event M_c of a milling ball during planetary ball milling and decomposition of corresponding velocities at M_d and M_c . For further details, see [224].

Fig. 113 Impact frequency of five milling balls as a function of disc rotation speed Ω at various vial rotation velocities ω as indicated for planetary ball mills with $R = 7.5$ (G7) and 13 cm (G5). The milling balls were of mass $m_b = 14$ g and size (radius) $r_b = 7.5$ mm; vial radius $r = 21$ mm. From [223].

Fig. 114 As for Fig. 113, here impact power as a function of disc rotation velocity Ω for planetary ball mills with $R = 13$ (G5) and 7.5 (G7) cm. From [223].

Fig. 115 Fraction amorphous of $Ni_{10}Zr_7$ alloy as a function of ball milling time using a vibrating ball mill with three milling "intensities" RT1 to RT3 at room temperature (solid symbols) and two milling intensities HT1 and HT2 at 200°C (open symbols) and showing that a)

Fig. 115/cont'd the amorphization rate increases with milling intensity and b) that milling intensity required for full amorphization requires to exceed a threshold (cf. RT3, n.b. milling "intensities" were: RT1 > RT2 > RT3 and HT1 > HT2).

Fig. 116 Mechanical power absorption $P_m = P'_m - P^\circ_m$ (where P'_m = for filled and P°_m = for empty vial) as a function of filling fraction $n_v = n_b / n_b(\max)$ with n_b = actual and $n_b(\max)$ = maximum number of milling balls per vial at two disc rotation velocities Ω , i.e. 240 and 300 rpm. From [230].

Fig. 117 Schematic showing qualitatively the relative freedom to manipulate impact energy and impact frequency with mass and number of milling balls per vial of planetary ball mill, type II, of a given product ωr and $\Omega^2 R$ as indicated (i.e. x_1, x_2, x_3 ; cf. Fig. 119).

Fig. 118 Disc rotation Ω as a function of vial rotation velocity ω for planetary ball mill with $R = 13$ cm showing minimum disc rotation for ball detachment (lowest line with solid circles) and decreasing friction-to-shock energy with increasing slope of the straight lines according to the figures given in the insertion. From [223].

Fig. 119 Showing rotation velocity (top) as a function of presetting of Pulverisette 5^R of motor, holder disc (Ω) and vial(s) (absolute and relative to Ω) and (bottom) resulting coupling factor $k_{\Omega/\omega} = 1.17$ for $\omega_{abs} = fn(\Omega)$ [204].

Fig. 120 As for Figs. 111, 113 and 114, here for Pulverisette 5^R, showing that for PBM, type II, the relationships shrink down to one graph (line) as a result of the coupling factor $k_{\Omega/\omega}$ (here -1.15) and showing also the effect of vial radius r in the range of 2.1 (small) to 3.3 (large) cm by using milling balls of size $r_b = 7.5$ mm, $\rho_b = 7.92$ g/cm³ resulting in $m_b = 14$ g. Evidently, the effect of vial radius r on impact power is very small in the lower Ω -regime. From [265].

Fig. 121 Ω - ω -T window for amorphous Ni₁₀Zr₇ by planetary ball milling with $R = 7.5$ cm of crystalline Ni₁₀Zr₇ intermetallic phase. Solid symbols represent fully amorphous Ni₁₀Zr₇, semi-solid symbols represent partially amorphous Ni₁₀Zr₇. From [233].

Fig. 122 As for Fig. 121, here including data from planetary ball mill with $R = 13$ cm, all at ambient temperature. Solid symbols: fully amorphous, open symbols: partially amorphous, squares : $R = 7.5$ cm, circles: $R = 13$ cm. From [224].

Fig. 123 Kinetic impact energy and impact frequency, the latter per five milling balls, as a function of disc velocity Ω for vial rotation 150 (1), 250 (2) and 350 (3) rpm of planetary ball mills

with $R = 7.5$ (G7) and 13 cm (G5) showing corresponding windows for amorphization of $\text{Ni}_{10}\text{Zr}_7$. $r = 2.1$ cm, $r_b = 7.5$ mm, $m_b = 14$ g. From [224].

Fig. 124 Impact power as a function of disc velocity Ω for vial velocities ranging from 150 (1) over 250 (2), 350 (3), 500 (4) and 600 rpm (5) of planetary ball mills with $R = 13$ (G5) and 7.5 cm (G7). Data points a to e for G5 and a' to d' for G7 represent fully amorphous $\text{Ni}_{10}\text{Zr}_7$, corresponding open squares and circles representing partially amorphous / crystalline $\text{Ni}_{10}\text{Zr}_7$ -alloy. $n_b = 5$, $r_b = 7.5$ mm; $m_b = 14$ g. From [224].

Fig. 125 a), d) side - and b), c) front - view of horizontal attritor technique with a) low and b) high filling fraction of corresponding milling container and c), d) corresponding rotor alone. From [244].

Fig. 126 Schematic of vertical attritor ball mill. After [244].

Fig. 127 Schematic of three principal vibrating ball mills [228]. a) 1-dim, b) 2-dim and c) 3-dim model; MV = mill vial; MOV = mode of vibration; B = milling ball(s).

Fig. 128 Schematic of industrial vibrating ball mills [228]. As for **Fig. 127**, here MC = mill container; UW = unbalanced weight.

Fig. 129 Schematic of horizontal ball mills. After [245].

Fig. 130 a) - c) Machined WE54 chips and turnings directly employed upon ball milling with Al_2O_3 , SiC, BN and Al_3Ti .

Fig. 130 / continued d) - f) Machined WE54 chips and turnings directly employed upon ball milling with Al_2O_3 , SiC, BN and Al_3Ti .

Fig. 131 Showing (top) X-ray diffraction of as-received Mg-alloy WE54 (ingot) and (center) DSC analysis with transformation peak at 613°C and (bottom) corresponding X-ray diffraction of (WE54 + 2.5 wt.% Al_2O_3) ball-milled for 2h at 20° to 70°C without lubrifyer (i.e. "dry"). Note that peak-intensities of as-milled (WE54 + 2.5 wt.% Al_2O_3) - powder amounted to 30 to 50% of the peak-intensities of as-received WE54 ingot. Milling variables: see **Table 10** , Alloy 2.

Fig. 132 Non-linear structural evolution with time as shown by a), c) enthalpy of transformation (crystallization) of a) amorphous $\text{Zr}_{80}\text{Fe}_{20}$, c) amorphous NiTi_2 with ΔH_x^{MG} made from crystalline intermetallic NiTi_2 (precursor with atomic configuration relatively close to

Fig. 132/cont'd amorphous NiTi_2) and with ΔH_x^{MA} made from elemental ($\text{Ni} + 2 \text{Ti}$) powder mixture (atomic configuration relatively far from amorphous NiTi_2) and b) X-ray intensities of amorphous $\text{Zr}_{50}\text{Fe}_{50}$ after different ball milling times. From [207,211].

Fig. 133 Evolution of volume fraction f_v^{ne} non-equilibrium (WE54 - 2.5 wt.% Al_2O_3) phase as a function of ball milling time employed (for further details, cf. **Fig. 131**) for low yield ($f_v^y < 0.5$) at dry milling conditions (upper curve) and high yield (f_v^y about 1), but low f_v^{ne} (bottom curve) including the use of "excessive" quantities of hexane resulting in $t_{\text{req}} =$ about 8 hours for $f_v^{\text{ne}} = 1.0$ at low yield and $t_{\text{req}} \gg 10$ hours for $f_v^{\text{ne}} = 1.0$ at high yield f_v^y . Note that straight line for $f_v^{\text{ne}} = 1.0$ represents an overall volume fraction $\Sigma f_v = f_v^y * f_v^{\text{ne}} = 0.3 * 0.95 =$ about 0.29 of resulting non-equilibrium powder.

Fig. 134 Schematic free-energy diagram with elemental components A (eg. Mg) and B (eg. TM, met, RE) and an intermetallic or ceramic compound C showing macroscopic ease by the addition of C to introduce non-equilibrium terminal phase (from position 3 to 2) rather than without (from position 1 to 2) provided, that a milling effect was attained without (excessive) "caking" before (cf. next figure).

Fig. 135 Variation of grain size as a function of milling time in mechanically alloyed γ -TiAl alloys (as to Al-content given in [at.%]). Any homogeneization on an atomic length scale as during part "b" of the above milling cycles would require the milling effect during "a" and also that no (excessive) "caking" would occurring during both (i.e. "a" and "b"). From [192].

Fig. 136 Powder particle size after eight effective impacts as a function of impact velocity of the alloys shown in the Table on top. Alloy 4 with the largest difference in hardness of precursor constituents develops the smallest powder size in the milling ball velocity regime of $> 3.5 \text{ ms}^{-1}$ as is typical for planetary ball milling. From [251].

Fig. 137 Evolution of non-equilibrium phase and yield of ball-milled Mg-10Ti-5B [wt.%] with increasing (ratio of) shock power (-to-friction) as controlled by increasing disc holder rotation Ω , here from 180 to 456 rpm. Employed milling conditions: $R = 13 \text{ cm}$, $r = 33 \text{ cm}$. $r_b = 7.5 \text{ mm}$. thus $r^* = 25.5 \text{ mm}$, $\omega = 200 \text{ rpm}$, $m_b = 14 \text{ g}$ (steel); $n_b = 5$; employed form of Mg: machined chips, that of Ti: sponge and that of B: broken lumps (coarse); dry milling conditions, resulting in exothermal doublet at around 600°C .

Fig. 138 Flow chart showing single (sMA) and double (dMA) mechanical alloying route, the latter including two distinct milling cycles before and after an heat treatment during which non-equilibrium phase formation and/or homogeneization of corresponding microstructure

Fig. 138/cont'd is enhanced due to the structural defects accommodated by the material during the first milling cycle (MA1). From [271].

Fig. 139 Showing in-situ annealing cycle achieved by employing increased friction-to-shock and an in-situ cooling system of a planetary type I - of ball mill with milling time including hysteresis (----) stemming from corresponding heat flow.

Fig. 140 Cross-sections of projectiles used for "ball"-milling in the present invention, here with particular effective impact energy transfer from projectile to the milled precursor and/or powder material. The surface of the projectiles consists of a discontinuous profile of curved and/or non-curved (i.e. flat) sections arranged to (T) quasi-triangle (here with two curvatures C1 and C2), (Q) quaternary (square), (P) pentagonal, (H) hexagonal ... (O) octagonal etc. cross-sections, the curved surface sections eventually embracing different curvatures per projectile (cf. T2) and/or partially (c) curved and (nc) non-curved (cf. O) surfaces.

Fig. 141 Universal diagram to employ economical and ecological balances on investments in advanced magnesium and Al-Li alloys (densities* as indicated in $[g/cm^3]$) to replace high strength conventional Al-7000 type of alloy in civil aeronautic applications. MEW: maximum empty ("dry") weight (i.e. aircraft weight without payload). ¹) Tonnage required to replace Al-7000 alloy. Note that a 10% increment in Mg-mass was employed to correct for specific strength (i.e. AlLi - to - Mg (or MgLi) - volume ratio 1 : 1.1), other properties assumed as equivalent to Al-7000 alloy. ²) 1kg kerosene : DM 0.38 or \$ 0.24. AEAP: Airbus-Equivalent Acquisition Price (in [Mio \$]). Δ = Revenue on \$ 10 Mio investment in AlLi. Note: the effect of snowball-factors, the return from rate of interests and rate of inflation of kerosene, the pay-back of replaced conventional Al-7000 type of alloy and possible CO₂-taxation has to be added to the scale on the right hand side of the diagramme.

Fig. 142 Universal diagram to employ economical and ecological balances on investments in advanced magnesium and Al-Li alloys to replace high-strength conventional Al-7000 type of alloy in aeronautical applications. MEW: maximum empty ("dry") weight (i.e. aircraft weight without payload). ¹) AEMI: Airbus-Equivalent Maximum Investment allowed to replace Al-7000 alloy with revenue equivalent to that obtainable by Al-Li. ²) AEMR: Airbus-Equivalent Maximum Revenue (including a return of \$30 per kg Al-7000 alloy replaced, but without including taxation on CO₂) obtainable with acquisition investments equivalent to the price of Al-Li. Remainder as for Fig. 141.

Fig. 143 Effect of magnesium on life-time fuel savings and resultant reduction of fuel costs and CO₂-emission. ¹) Savings relative to life-time investment in fuel.

Fig. 144 Different structural magnesium based products reported in 1966 (left column) and in the period from 1981 - 1992 (right). x : Deep See Diving Suit. For details, see [1].

Claims

It is claimed here:

1st claim. Pure magnesium or pure calcium or pure aluminum or pure Sr or pure Ba or pure rare earth metals La, Ce, Nd, Pr, Sm or Eu or pure gallium or pure (and porous !) silicon or any kind of water and/or aqueous solution or a magnesium based alloy in terms of any type a massive pre-form including flat and/or bent rectangular and/or round- and/or irregular shaped deposits including sheet- and/or disc form and/or plate- and/or disc-like forms and/or products, a deposited layer and/or a deposited thin film made by vapour deposition methods and techniques to result in as-deposited cross-sections (perpendicular, i.e. normal to the deposition contact surface) in the range from 20 nm to 800 nm, in particular in cross-sections from 0.5 μ m to 100 nm, the Mg-alloys containing:

rare earth metals:

0.1 to 30 % La by weight, in particular between 0.2 and 14 wt.% La, or

0.1 to 30 % Ce by weight, in particular between 0.2 and 16 wt.% Ce, or

0.1 to 30 % Pr by weight, in particular between 0.3 and 18 wt.% Pr, or

0.1 to 32 % Nd by weight, in particular between 0.3 and 20 wt.% Nd, or

0.1 to 35 % Sm by weight, in particular between 0.2 and 20 wt.% Sm, or

0.2 to 35 % misch-metal by weight, in particular between 0.3 and 25 wt.% misch-metal,

the misch-metal thereby in particular of compositions stemming from and/or corresponding to the ore composition of Monazite-, Bastnaesite- and Xun Wu-type of RE-ores, but in any case being dominated by corresponding compounds of La, Ce, Nd and Pr and, as a misch-metal, containing

5 - 97 % La by weight,

5 - 97 % Ce by weight and

5 - 98 % (Nd + Pr)

balance other rare earth metals such as Gd and Tb, but also Y,

and the sum of (La, Ce, Nd and Pr) totalling 40 - 100 % by weight, in particular 80 - 99 % by weight, or

0.2 to 30 % Y (and Eu) by weight, in particular between 0.5 and 7 wt.% Y (and Eu), or

0.1 to 30 % Sc by weight, in particular between 0.2 and 20 wt.% Sc, or

0.1 to 15 at.% Gd in cph-Mg, in particular 0.5 to 6 at.% Gd in cph-Mg, and/or

0.1 to 15 at.% Dy in cph-Mg, in particular 0.5 to 7 at.% Dy in cph-Mg, and/or

0.1 to 10 at.% Ho in cph-Mg, in particular 0.5 to 7 at.% Ho in cph-Mg, and/or

simple metals:

0.2 to 15 % Al by weight, in particular between 4 and 12 wt.% Al, or

0.2 to 15 % Ga by weight, in particular between 4 and 12 wt.% Ga, or

transition metals:

0.1 to 30 % Mn by weight, in particular between 0.2 and 18 wt.% Mn, or

0.1 to 30 % Zr by weight, in particular between 0.2 and 16 wt.% Zr, or

0.1 to 40 % Ti by weight, in particular between 0.2 and 25 wt.% Ti, or
 0.1 to 20 % Re by weight, in particular between 0.2 and 16 wt.% Re, or
 0.1 to 30 % Hf by weight, in particular between 0.2 and 16 wt.% Hf, or
 0.1 to 25 % Ta by weight, in particular between 0.2 and 10 wt.% Ta, or
 0.1 to 25 % W by weight, in particular between 0.2 to 20 wt.% W, or
 0.1 to 20 % Mo by weight, in particular between 0.2 and 15 wt.% Mo, or
 0.1 to 25 % Nb by weight, in particular between 0.3 and 17 wt.% Nb, or
 0.1 to 30 % Cr by weight, in particular between 0.2 and 18 wt.% Cr, or
 0.1 to 40 % V by weight, in particular between 0.2 and 25 wt.% V, or
 metalloids:

0.1 to 35 % B by weight, in particular between 0.5 to 15 wt.% B, or
 0.1 to 35 % Be by weight, in particular between 0.5 to 15 wt.% Be, or
 0.1 to 20 % Si by weight, in particular between 0.5 to 12 wt.% Si, or
 0.1 to 15 % Sb by weight, in particular between 0.5 to 10 wt.% Sb, or
 0.1 to 15 % Ge by weight, in particular between 0.5 to 10 wt.% Ge

1.1 an Mg-alloy according to claim 1., characterized further in that

- 1.1.1 the lanthanum, cerium, praesodymium, neodymium, samarium, europium, gadolinium and/or yttrium and/or the other heavy rare earth elements stemming from the mischmetals, the scandium or aluminium or gallium, the manganese or zirconium, titanium, rhenium, hafnium, tantalum, molybdenum, niobium, chromium, tungsten or vanadium or the boron, beryllium, silicon, antimon or germanium or dysprosium, gadolineum or holmium are or is substantially held in solid solution in the as-deposited state, corresponding solid solution being either (except for Ti) cph-Mg or (including Ti) any other metastable crystalline and/or amorphous phase and/or
- 1.1.2 an Mg-alloy according to one or more of claim 1. and 1.1.1, but also including cph-Mg-Ti alloys with up to 50 wt.% Ti and characterized further by an homogeneous distribution of the solute atom (alloying additions) on an atomic length scale and/or
- 1.1.3 an Mg-alloy according to one or more of claim 1. to 1.1.2, characterized further by an homogeneous distribution of the solute atom (alloying additions) on an atomic length scale with a distance of the like-like *alloying* atoms (i.e. B-B, C-C etc.) ranging from a minimum value of 1 to a maximum value of 10 atomic and/or ionic spacings of the alloying atom, and/or
- 1.1.4 an Mg-alloy according to claim 1.1.3, characterized further by an homogeneous distribution of the solute atom (alloying additions) on an atomic length scale with a distance of the like-like *alloying* atoms (i.e. B-B, C-C etc.) of a maximum value of up to 498 atomic spacings of the alloying atoms, and/or
- 1.1.5 an Mg-alloy according to one or more of claim 1 to 1.1.4, characterized further by an average length scale of the (homogeneous) distribution of a given number of matrix

atoms, N, which is given by $(N \cdot d_A \cdot c_A / 2 + N \cdot d_B \cdot c_B / 2)$ of atoms, where c_A, c_B and d_A, d_B = concentration and atomic and/or ionic spacing, respectively, of corresponding base metal A (eg. Mg or Al) and solute B (C for ternary alloys, see following claims for which the average length scale were given by $(N \cdot d_A \cdot A / 3 + N \cdot d_B \cdot B / 3 + N \cdot d_C \cdot C / 3)$ etc.) and/or

- 1.1.6 an Mg-alloy according to one or more of claim of 1 to 1.1.5, characterized further by an homogeneous solute distribution in the solid being either in an disordered and/or in an ordered atomic arrangement and/or
- 1.1.7 an Mg-alloy according to one or more of claim of 1 to 1.1.6, characterized further in that the number of like-like alloying atoms entitled to cluster without catastrophic effect on corrosion resistance ranges from 2 to 420, in particular from 3 to 20, and/or
- 1.1.8 an Mg-alloy according to one or more of claim of 1 to 1.1.7, characterized further in that these clusters have formed by natural ageing constituting trans- and/or intra-boundary elemental B-type of second phases and/or trans- and/or intraboundary superlattices (i.e. ordered and coherent phases) and/or trans- and/or interboundary equilibrium and/or non-equilibrium semicoherent and/or incoherent second phases and/or
- 1.1.9 an Mg-alloy according to one or more of claim of 1 to 1.1.8, characterized further in that the involvement of the at least one ordered phase requires a number of atomic and/or ionic B-B pairs per unit cell given by $N_{B-B} = (N \cdot Z / 2) \cdot p (1 - p)$, where $(1 - p)$ = fraction of B-atoms on α -site (which is the regular site of an A-atom in corresponding superlattice), Z = coordination number of atoms in corresponding superlattice and p = number of B-atoms on β -sites, N = number of atoms per unit cell of ordered (i.e. superlattice) structure with p ranging from 0.5 to 1.0 and resulting N_{B-B} ranging from 0.5 to 400, in particular from 1 to 200, and/or
- 1.2 a material according to one or more of claim 1. and 1.1.9, characterized further in that the materials being evaporated by using thermal evaporation methods including induction and/or resistance heating and melting and/or arc and/or electron beam heating and melting methods and/or microwave heating and/or melting methods and/or corresponding heating and sublimation methods and/or plasma and/or magnetron sputtering techniques, and/or
- 1.3 a material according to one or more of claim 1. to 1.2. characterized further in that the power input into any of the condensed phases involved in the process ranging from 0.1 to 300 W per cm^2 evaporation and/or sputtering surface, in particular from 0.5 to 50 W per cm^2 evaporation and/or sputtering surface and/or
- 1.4 a material according to one or more of claim 1. to 1.3. characterized further in that Mg, Ca and Ga is evaporated at vacuum pressures in the range of 1 to 0.001 bar, in particular at 0.1 to 0.01 bar, the rare earth elements, Sr and Ba being evaporated at vacuum pressures in the range from 1 to 0.001 bar, in particular at 0.1 to 0.005 bar, the transition metals and metal-loids being evaporated at vacuum pressures in the range from 0.1 to 0.0001 bar, in particu-

lar at vacuum pressures in the range from 0.1 to 0.001 bar and the aluminium being evaporated at vacuum pressures in the range of 1 to 0.001 bar, in particular at 0.1 to 0.005 bar and/or

- 1.5 a material according to one or more of claim 1. to 1.4, characterized further in that the Mg and Ga is evaporated at surface temperatures in the range of -50° to 1200°C, in particular at 200° to 900°C, the rare earth elements being evaporated at surface temperatures in the range from -20° to 1800°C, in particular at 200° to 1500°C, the transition metals and metalloids being evaporated at surface temperatures in the range from -20°C to 4000°C, in particular at surface temperatures in the range from 300° to 3200°C and the aluminium being evaporated at surface temperatures in the range of -20° to 2000°C, in particular at 200° to 1900°C and/or
- 1.6 a material according to one or more of claim 1. to 1.5, characterized further in that the material is deposited at a substrate temperature held at between -200° and 500°C, in particular between -10° and 200°C to control phase stability and/or porosity, and/or
- 1.7 a material according to one or more of claim 1. to 1.6, characterized further in that the driving force for mass transport between evaporation source and deposition surface of the element (alloy solvent and/or solutes and/or alloy constituents of corresponding equilibrium and non-equilibrium Mg-alloy or purified pure metal) is provided by the vapour pressure of at least one of the constituents concerned and/or the temperature difference providing condensation and resulting underpressure in the very next vicinity of the deposition surface where the vapour collapses into a condensed phase, either in the moment of adsorption and/or immediately before, so allowing the vapour pressure to control the above overall mass transport and/or
- 1.8 a material according to one or more of claim 1. to 1.7, characterized further in that the material is consolidated in-situ in vacuum during the deposition process after deposition of a differential layer of a thickness of at least two atomic monolayers and/or cold-isostatically pressed (CIPed) at pressures in both cases ranging from 50 - 1200 MPa, in particular ranging from 250 - 700 MPa, the in-situ consolidation technique being either micro-hammering, and/or a peening technique and/or rolling, and/or a micro-rolling technique and/or a micro-forging technique and/or a micro-swaging technique and/or
- 1.9 a material according to one or more of claim 1 to 1.8, characterized further in that the in-situ consolidated state is characterized by a porosity of 0.005 to 5 vol.%, in particular by a porosity of 0.01 to 1 vol.% and/or
- 1.10 an Mg - alloy according to one or more of claim 1. to 1.9, characterized further in that the magnesium used for the feedstock of the vapour-deposited Mg - alloy is (made) from commercially pure Mg including / and/or purity grade 2N5 to 5N (i.e. 99.5 to 99.999) and/or
- 1.11 an Mg - alloy according to one or more of claim 1. to 1.10, characterized further in that the magnesium used for the feedstock of the vapour-deposited Mg - alloy was made from

- commercially pure Mg and which is characterized by an impurity level by weight % of 0.001 - 0.1 Al, 0.0001 - 0.2 Mn, 0.0001 - 0.001 Ni, 0.0005 - 0.1 Si, 0.0005 - 0.005 Ca, 0.0001 - 0.005 Cd, 0.001 - 0.01 Zn, 0.0001 - 0.06 Fe, 0.0001 - 0.05 Cu, 0.0005 - 0.01 Pb, 0.0005 - 0.1 Sn, 0.0005 - 0.02 Na, 0.00002 - 0.1 B, 0.0001 - 0.1 Co, 0.0001 - 0.1 C, the remaining trace elements being less than 0.1 wt.% and/or
- 1.12 an Mg - alloy according to one or more of claim 1. to 1.9, characterized further in that the magnesium used for the feedstock of the vapour-deposited Mg - alloy was made from at least one-time vapour-deposited so at least one-time distilled and purified commercially pure Mg including / and/or purity grade 2N5 to 6N (i.e. 99.5 to 99.9999) and/or
- 1.13 an Mg - alloy according to one or more of claim 1. to 1.12, characterized further in that the magnesium used for the feedstock of the vapour-deposited Mg - alloy was made from at least one-time vapour-deposited so distilled and purified commercially pure Mg and which is characterized by an impurity level by weight %: 0.001 - 0.1 Al, 0.0001 - 0.1 Mn, 0.0001 - 0.002 Ni, 0.0005 - 0.05 Si, 0.0005 - 0.005 Ca, 0.0001 - 0.005 Cd, 0.001 - 0.01 Zn, 0.0001 - 0.05 Fe, 0.0001 - 0.04 Cu, 0.0005 - 0.01 Pb, 0.0005 - 0.1 Sn, 0.0005 - 0.02 Na, 0.00002 - 0.004 B, 0.0001 - 0.05 Co, 0.0001 - 0.1 C, the remaining trace elements being less than 0.1 wt.% and/or
- 1.14 an Mg - alloy according to one or more of claim 1. to 1.13, characterized further in that a major and/or minor part of the alloying element is taken into solid solution by an annealing and/or solid solution heat treatment, in particular by an annealing and/or solution heat treatment at temperatures between 80° and 600° C and/or
- 1.15 an Mg - alloy according to claim 1.14, characterized in that the annealing and/or solid solution heat treatment is employed after a thermo-mechanical treatment and/or hot forming operation and/or
- 1.16 an Mg - alloy according to one or more of claim 1. to 1.15, characterized further in that the Mg - alloy shows a better corrosion resistance than commercially pure Mg and/or high purity commercial alloy AZ91 and/or at least one of the other established commercial high purity Mg - base alloys (eg. high purity AM- and/or AS-series), all being made by casting techniques, in particular in an environment characterized by dry and/or humid air with 0.1% to 100% moisture and/or an aqueous solution (and/or humid air) covering the surface of the Mg-alloys either coherently (in that case either standing still and/or flowing) and/or in form of a spray (very fine condensed humidity) and/or droplets all containing at least 0.001 g/mol of at least one of the following acids HA and resulting conjugated base A⁻ known to provide the corresponding pKs-values as given in paranthesis (i.e. HA/base A⁻ (pKs)): HClO₄/ClO₄⁻(-9), HCl/Cl⁻(-6), H₂SO₄/HSO₄⁻(-3), H₃O⁺/H₂O(1.74), HNO₃/NO₃⁻(-1.32), HClO₃/ClO₃⁻(0), HSO₄⁻/SO₄²⁻(1.92), H₂SO₃/HSO₃⁻(1.96), H₃PO₄/H₂PO₄⁻(1.96), [Fe(H₂O)₆]³⁺/[Fe(OH)(H₂O)₅]²⁺(2.2), HF/F⁻(3.14), HCOOH/HCOO⁻(3.7), CH₃COOH/CH₃COO⁻(4.76), [Al(H₂O)₆]³⁺/[Al(OH)(H₂O)₅]²⁺(4.9), H₂CO₃/HCO₃⁻(6.46), H₂S/HS⁻(7.06), HSO₃⁻/SO₃²⁻(7.2), H₂PO₄⁻/HPO₄²⁻(7.21), HClO/HClO⁻(7.25), NH₄⁺/NH₃

(9.21), HCN/CN^- (9.4), $[\text{Zn}(\text{H}_2\text{O})_6]^{2+}/[\text{Zn}(\text{OH})(\text{H}_2\text{O})_5]^+$ (9.66), $\text{HCO}_3^-/\text{CO}_3^{2-}$ (10.40), $\text{H}_2\text{O}_2/\text{HO}_2^-$ (11.62), $\text{HPO}_4^{2-}/\text{PO}_4^{3-}$ (12.32), HS^-/S^- (12.9), $\text{H}_2\text{O}/\text{OH}^-$ (15.74), OH^-/O^- (24) and/or

- 1.17 an Mg - alloy according to one or more of claim 1. to 1.15, characterized further in that the Mg - alloy shows a better corrosion resistance than the commercial high purity AZ91 alloy in an environment containing any other acid/anion combination as given in claim 1.16 and which is characterized by a pKs-value ranging from -12 to +24, in particular from -9 to +16 and/or
- 1.18 a material according to one or more of claim 1. to 1.17, characterized further in that the as-deposited and/or in-situ consolidated state is characterized by a microstructure consisting of grains, cells and/or subcells of which the dimensions are $< 10\mu\text{m}$ in at least one dimension of the three translational directions x,y and z. and/or
- 1.19 a material according to one or more of claims 1. to 1.18, characterized by a grain (high angle boundary) and/or cell (low angle boundary) size in the range from 3 to 100 nm, in particular in the range from 5 to 50 nm and/or
- 1.20 a material according to one or more of claims 1. to 1.18, characterized by a grain and/or cell size in the range from 50 to 800 nm, in particular in the range from 60 to 500 nm and/or
- 1.21 a material according to one or more of claims 1. to 1.18, characterized by a grain and/or cell size in the range from 0.5 to 20 μm , in particular in the range from 0.6 to 10 μm and/or
- 1.22 an Mg-alloy according to one or more of claims 1. to 1.21, characterized by a volume fraction of second phases separated from vapour condensation and/or subsequent solid state precipitation during vapour deposition and/or in-situ consolidation ranging from 0.01 vol.% - 20 vol.% of the volume fraction corresponding to the equilibrium volume fraction of corresponding alloys, in particular ranging from 0.05 vol.% - 10 vol.% of the volume fraction corresponding to the equilibrium volume fraction of corresponding alloys and/or
- 1.23 an Mg-alloy according to one or more of claims 1. to 1.22, characterized by an intra- and/or transgranular intermetallic and/or elemental and/or equilibrium and/or non equilibrium alloy phase of a one-dimensional length scale (circumference, diameter, maximum 1-dim extension) in the range from 1 to 50 nm, in particular in the range from 2 to 35 nm and/or
- 1.24 an Mg-alloy according to claim 1.23, characterized by an intra- and/or transgranular second and/or ternary and/or quaternary etc. phase (see 1.23) in the range from 0.02 to 15.0 μm in particular in the range from 0.1 to 1.0 μm and/or
- 1.25 an Mg-alloy according to one or more of claims 1. to 1.24, characterized by virtual absence of porosity due to a thermo-mechanical treatment and/or forming operation according to claim to 1.15 and/or
- 1.26 an Mg-alloy according to one or more of claims 1. to 1.25, characterized by a maximum porosity after the final forming operation ranging from 0.001 to 5 vol.%, in particular from 0.01 to 3 vol.%, and/or
- 1.27 an Mg-alloy according to one or more of claims 1. to 1.26, characterized by a maximum

pore size after the final forming operation ranging from 0.001 to 10 μ m, in particular from 0.005 to 5 μ m, and/or

- 1.28 an Mg-alloy according to one or more of claims 1. to 1.27, characterized by a content of the impurities Fe, Ni, Cu, Co, Na, K, C, Cd, Zn, Pb, Sn, B and Si, the two letter except for the alloys to which it is deliberately alloyed and O₂ ranging from a factor of 0.1 to 10 compared to those levels currently accepted in the established high purity AZ- and AM-type of magnesium alloys made by casting from the liquid state, in particular ranging from a factor 0.2 to 5 of the levels of Fe, Ni, Cu, Co, Na, K, C, Cd, Zn, Pb, Sn, B and Si, and O₂ usually accepted in the established high-purity AZ- and AM-type of magnesium alloys and/or
- 1.29 an Mg-alloy according to one or more of claims 1. to 1.28, characterized by an impurity level (by weight %) of
- 1.29.1 0.00005 to 0.001 Ni and/or
 - 1.29.2 0.00005 to 0.05 Cu and/or
 - 1.29.3 0.00005 to 0.06 Fe and/or
 - 1.29.4 0.00005 to 0.1 Co and/or
 - 1.29.5 0.00005 to 0.1 Si (except for PVD Mg-Si alloys) and/or
 - 1.29.6 0.00005 to 0.1 B (except for PVD Mg-B alloys) and/or
 - 1.29.7 0.00005 to 0.1 Al (except for PVD Mg-Al alloys) and/or
 - 1.29.8 0.00005 to 0.2 Mn (except for PVD Mg-Mn alloys) and/or
 - 1.29.9 0.00005 to 0.02 Na and/or
 - 1.29.10 0.00005 to 0.005 Ca and/or
 - 1.29.11 0.00005 to 0.02 K and/or
 - 1.29.12 0.00005 to 0.5 C and/or
 - 1.29.13 0.00005 to 0.005 Cd and/or
 - 1.29.14 0.00005 to 0.01 Zn and/or
 - 1.29.15 0.00005 to 0.01 Pb and/or
 - 1.29.16 0.00005 to 0.1 Sn and/or
 - 1.29.17 0.0001 to 2.0 O (oxygen) and/or
- 1.30 an Mg-alloy according to one or more of claims 1. to 1.29, characterized by a level of Fe, Ni, Cu, Co, Na, K, C, Cd, Zn, Pb, Sn, B and Si which is not increased further by evaporation and/or vapour transport and/or deposition and/or in-situ consolidation compared to the employed feed stock due to the use of inert refractory metal, alloy and/or intermetallic phases in contact with condensed alloy constituents (eg. as crucible material), and in particular due to the use of tantalum (-based) materials, and/or
- 1.31 an Mg-alloy according to one or more of claims 1. to 1.30, characterized by a level of O₂ which is not increased further by the vapour deposition process compared to the oxygen level of the feed stock, in particular not more than by a factor of 5 due to the use of an inert gas atmosphere (in particular argon and/or nitrogen), high quality sealings and/or a getter vapour to purge the equipment prior to start the vapour deposition process and/or

- 1.32 an Mg-alloy according to one or more of claims 1. to 1.31, characterized by a size of an impurity inclusion (containing Fe, Ni, Cu, Co, Na, K, C, Cd, Zn, Pb, Sn, B, Si and oxides etc., cf. claim 1.28 - 1.31) with a one-dimensional length scale (circumference, diameter, maximum 1-dim extension) in the range of 1 - 50 nm, in particular in the range from 2 to 35 nm and/or
- 1.33 an Mg-alloy according to claim 1.32, characterized by a size of an impurity inclusion in the range from 0.04 to 5.0 μm , in particular in the range from 0.5 to 1.0 μm .

Claim 2. A magnesium based alloy made by a solid state synthesizing technique, in particular by ball and/or bar and/or rod milling via a mechanical alloying and/or chemical (reactive) alloying and mechanical grinding technique and/or cycles (sequences), the magnesium (based) alloy containing: at least one of the following rare earth metals (RE) and/or yttrium and/or scandium, i.e.

- 0.1 to 40 % La by weight, in particular between 0.2 and 14 wt.% La, and/or
- 0.1 to 40 % Ce by weight, in particular between 0.2 and 16 wt.% Ce, and/or
- 0.1 to 40 % Pr by weight, in particular between 0.3 and 18 wt.% Pr, and/or
- 0.1 to 40 % Nd by weight, in particular between 0.3 and 20 wt.% Nd, and/or
- 0.1 to 40 % Sm by weight, in particular between 0.2 and 20 wt.% Sm, and/or
- 0.2 to 40 % Y (and Eu) by weight, in particular between 0.5 and 7 wt.% Y (and Eu), and/or
- 0.2 to 40 % misch-metal by weight, in particular between 0.3 and 25 wt.% misch-metal, the misch-metal thereby in particular of compositions stemming from and/or corresponding to the ore composition of Monazite-, Bastnaesite- and Xun Wu-type of RE-ores, but in any case being dominated by corresponding compounds of La, Ce, Nd and Pr and, as a misch-metal, containing
 - 5 - 97 % La by weight,
 - 5 - 97 % Ce by weight and
 - 5 - 98 % (Nd + Pr)
 balance other rare earth metals such as Gd, Dy etc. through Tb, but also Y, and the sum of (La, Ce, Nd and Pr) totalling 40 - 100 % by weight, in particular 80 - 99 % by weight, and/or

- 0.1 to 20 Sc by weight in cph-Mg, in particular 0.5 to 15.0 wt.% Sc in cph-Mg, and/or
- 0.1 to 15 at.% Gd in cph-Mg, in particular 0.5 to 6 at.% Gd in cph-Mg, and/or
- 0.1 to 15 at.% Dy in cph-Mg, in particular 0.5 to 7 at.% Dy in cph-Mg, and/or
- 0.1 to 10 at.% Ho in cph-Mg, in particular 0.5 to 7 at.% Ho in cph-Mg, and/or

at least one of the following simple (i.e. simple electron structure) metals, i.e.:

- 0.2 to 20 % Al by weight, in particular between 4 and 12 wt.% Al, and/or
- 0.2 to 25 % Ga by weight, in particular between 4 and 16 wt.% Ga, and/or

at least one of the following transition metals (TM), i.e.:

0.1 to 30 % Mn by weight, in particular between 0.2 and 18 wt.% Mn, and/or
0.1 to 60 % Ni by weight, in particular between 0.2 and 55 wt.% Ni, and/or
0.1 to 20 % Pd by weight, in particular between 0.2 and 15 wt.% Pd, and/or
0.1 to 30 % Zr by weight, in particular between 0.2 and 16 wt.% Zr, and/or
0.1 to 20 % Ta by weight, in particular between 0.2 and 10 wt.% Ta, and/or
0.1 to 20 % Mo by weight, in particular between 0.2 and 15 wt.% Mo, and/or
0.1 to 25 % Nb by weight, in particular between 0.3 and 17 wt.% Nb, and/or
0.1 to 30 % Cr by weight, in particular between 0.2 and 18 wt.% Cr, and/or
0.1 to 40 % V by weight, in particular between 0.2 and 25 wt.% V, and/or
0.1 to 40 % Ti by weight, in particular between 0.2 and 25 wt.% Ti, and/or
0.1 to 40 % W by weight, in particular between 0.2 and 25 wt.% W, and/or
0.1 to 35 % Hf by weight, in particular between 0.2 and 20 wt.% Hf, and/or

at least one of the following metalloids (met) and/or beryllium, i.e.:

0.1 to 30 % B by weight, in particular between 0.2 to 20 wt.% B, and/or
0.1 to 30 % Si by weight, in particular between 0.2 to 20 wt.% Si, and/or
0.1 to 25 % Sb by weight, in particular between 0.2 to 10 wt.% Sb, and/or
0.1 to 25 % Ge by weight, in particular between 0.2 to 10 wt.% Ge and/or
0.1 to 30 % Be by weight, in particular between 0.5 to 10 wt.% Be,

and/ or an aluminium based alloy made by a solid state synthesising technique, in particular by ball milling via a mechanical alloying and/or chemical (reactive) alloying and mechanical grinding technique and/or cycles (sequences), the aluminium (based) alloy containing:

0.1 to 20% Fe by weight, in particular between 0.2 to 20 wt.% Fe and/or
0.0 to 15% Ce by weight, in particular between 0.2 to 12 wt.% Ce and/or
0.0 to 15% Mo by weight, in particular between 0.2 to 12 wt.% Mo and/or
0.0 to 40% V by weight, in particular between 0.2 to 30 wt.% V and/or
0.0 to 15% Si by weight, in particular between 0.2 to 12 wt.% Si and/or
0.0 to 15% Cr by weight, in particular between 0.2 to 12 wt.% Cr and/or
0.0 to 30% Zr by weight, in particular between 0.2 to 25 wt.% Zr and/or
0.0 to 15% B by weight, in particular between 0.2 to 10 wt.% B and/or
0.0 to 15% Mn by weight, in particular between 0.2 to 10 wt.% Mn and/or
0.0 to 50% Ti by weight, in particular between 0.2 to 40 wt.% Ti and/or
0.0 to 20% Hf by weight, in particular between 0.2 to 15 wt.% Hf and/or
0.0 to 30% Ta by weight, in particular between 0.2 to 25 wt.% Ta and/or
0.0 to 20% W by weight, in particular between 0.2 to 15 wt.% W and/or
0.0 to 30% Nb by weight, in particular between 0.2 to 25 wt.% Nb,

SUBSTITUTE SHEET (RULE 26)

the aforementioned alloys characterized in that in each case the density of 2.8 g/cm^3 is not exceeded and that the balance is made up by the impurities (for particular cases cf. below) and Mg and/or Al and:

2.1 the Mg- and/or Al-alloy according to claim 2 characterized further in that

2.1.1 the Mg- and/or Al-alloy was synthesized and/or ground and/or reacted by using elemental (commercially pure) and/or vapour distilled, purified and then deposited and eventually comminuted and/or pre-alloyed atomized, ground and/or ball-milled synthesized to ball-milled powders with powder size in the range from $0.05 \mu\text{m}$ to $500 \mu\text{m}$. in particular to powder-sizes ranging from $0.5 \mu\text{m}$ to $400 \mu\text{m}$ and/or

2.1.2 an Mg-alloy according to one or more of claims 2. to 2.1.1, characterized further in that the pre-alloyed precursors are Mg-containing alloys with 0.1 to 99.9 wt.% Mg and/or

2.1.3 an Al-alloy according to one or more of claims 2. to 2.1.2, characterized further in that the pre-alloyed precursors are Al-containing alloys with 0.1 to 99.9 wt.% Al and/or powders and/or machined chips and/or turnings and/or (broken) lumps to be

2.1.4 an Mg- and/or Al-alloy according to one or more of claims 2. to 2.1.3, characterized further in that the precursor powder or vapour distilled and -deposited Mg-base feed-stock, in particular the Mg- and/or Al- and/or RE-and/or Ga-containing powder(s) is (are) made by gas-atomizing using an inert atmosphere, in particular 5N and/or 4.8 argon and/or helium and/or nitrogen and/or eventually containing a deliberately added content of passivating oxygen containing 0.000005 to 5 wt.% O_2 , in particular 0.00001 to 3 wt.% O_2 and/or

2.2 an Mg- or Al-alloy according to one or more of claims 2. to 2.1.4, but by using at least one very hard ($> 80 \text{ V.H.N.}$) and eventually brittle precursor constituent, the hard precursor constituent either consisting of

2.2.1 at least one hard and eventually brittle elemental addition such as Mo, Cr, Si etc. and/or

2.2.2 at least one hard and brittle elemental addition such as Mo, i.e. the brittle state thereby achieved by:

2.2.2.1 the crystallography and/or large grains combined with employing the elemental addition at temperatures between -200° to 300°C . in particular at ambient or lower temperatures down to liquid nitrogen or so (-200°C) and/or

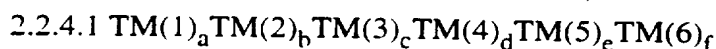
2.2.2.2 hydrogenization of the precursor solute and/or

2.2.2.3 enrichment of the solute precursor with (dissolved) oxygen, nitrogen or any other gaseous constituent dissolvable as an interstitial element in the crystal lattice of the precursor solute and/or

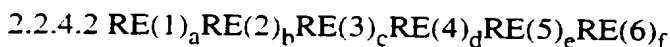
2.2.3 at least one hard and brittle intermetallic phase and/or alloy and/or

2.2.4 at least one brittle intermetallic phase and/or alloy of the following compositional

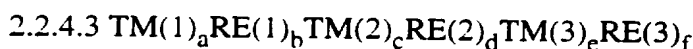
configurations (suffices a to f in atomic %):



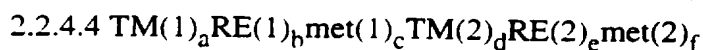
$a = 1 - 99, b = 1 - 99, c = 0 - 20, d = 0 - 10, e = 0 - 10, f = 0 - 5$ and/or



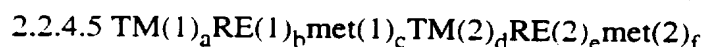
$a = 1 - 99, b = 1 - 99, c = 0 - 20, d = 0 - 10, e = 0 - 10, f = 0 - 5$ and/or



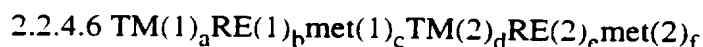
$a = 1 - 99, b = 1 - 99, c = 0 - 50, d = 0 - 50, e = 0 - 20, f = 0 - 20$ and/or



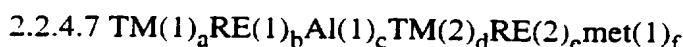
$a = 1 - 99, b = 1 - 99, c = 1 - 99, d = 0 - 50, e = 0 - 50, f = 0 - 50$ and/or



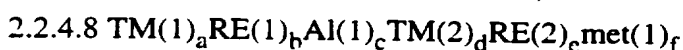
$a = 1 - 99, b = 0 - 99, c = 1 - 99, d = 0 - 50, e = 0 - 50, f = 0 - 50$ and/or



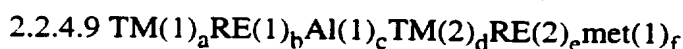
$a = 0 - 99, b = 1 - 99, c = 1 - 99, d = 0 - 50, e = 0 - 50, f = 0 - 50$ and/or



$a = 1 - 99, b = 1 - 99, c = 1 - 99, d = 0 - 50, e = 0 - 50, f = 0 - 50$ and/or



$a = 0 - 99, b = 1 - 99, c = 1 - 99, d = 0 - 50, e = 0 - 50, f = 0 - 50$ and/or



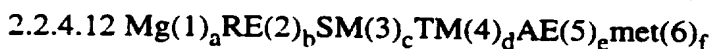
$a = 1 - 99, b = 1 - 99, c = 1 - 99, d = 0 - 50, e = 0 - 50, f = 0 - 50$ and/or



$a = 1 - 99, b = 1 - 99, c = 0 - 20, d = 0 - 10, e = 0 - 10, f = 0 - 5$ and/or



$a = 1 - 99, b = 1 - 99, c = 0 - 20, d = 0 - 10, e = 0 - 10, f = 0 - 5$ and/or



$a = 1 - 99, b = 0 - 99, c = 1 - 99, d = 0 - 10, e = 0 - 10, f = 0 - 5$ and/or



$a = 1 - 99, b = 0 - 99, c = 0 - 99, d = 0 - 10, e = 1 - 99, f = 0 - 5$ and/or

where TM are the transition metals of claim 2, RE the rare earth metals and yttrium and scandium in claim 2 and "met" the metalloids and Be in claim 2. and SM = simple metals such as Al, Ga, Hg, Zn and AE = alkaline earth metals (Ca, Sr, Ba) and/or

2.2.5 an intermetallic phase or alloy according to claim 2.2.4. but enhanced further for the use in the mechanical alloying technique for the preparation of passive magnesium by at least one of the methods under 2.2.2 and/or

2.2.6 at least one oxide, nitride, boride, silicide, carbide (under the condition that the carbon is tight up by another TM- or RE-based carbide), aluminide and/or

2.2.7 at least one of the following nitrides, borides, silicides, carbides (under the condition that the carbon is tight up by another TM- or RE-based carbide), oxides, aluminides: WC, Ta_xC_y (eg. Ta_2C), SiC, VC, B_4C , Cr_3C_2 , TiC, BN, TiB_2 , MgO, ZrO,

- BeO, Al_2O_3 , TM_aB_b , TiAl, TM_aAl_b , (Ti-Al, Fe-Al, Nb-Al), SiC_xN_y (powders), $\text{TM}_{1-x}\text{Ta}_x$ alloys, TiO_2 , SrTiO_3 , KNbO_3 , MoSi_2 , TiNi, TiB_2 , TiC, Si_3Ni_4 , TiC, TiN, TiC-MgO composites, CrO_2 , CrB_2 , VC, Al_2O_3 , SiC, SiAlON and Cr-base, Zr-base Nb-base, Ta-base, Hf-base, V-base, Ti-base, Mo-base and W-base alloys and/or
- 2.2.8 an Mg- and/or Al-alloy according to one or more of claims 2. to 2.27, characterized in that the weight ratio of hard and eventually brittle precursors to a ductile precursor ranges from 0.01 to 60 wt.%, in particular from 0.05 to 30 wt.% and/or
- 2.2.9 an Mg- and/or Al-alloy according to one or more of claims 2. to 2.28, characterized in that at least one of the ductile precursor is pure Mg and/or a terminal Mg-alloy and/or Mg-base alloying containing more than 50 at.% Mg and/or
- 2.2.10 an Mg- and Al-alloy according to claim 2.2.8 and/or 2.2.9, characterized in that the ductile precursor is represented by at least one of the constituents shown in Table 11 characterized as "ductile" and/or with elongation-to-fracture > 1%, and/or any of the intermetallic compounds of claim 2.2.4 with an elongation-to-fracture > 1%, and/or
- 2.3 an Mg- or Al-alloy according to one or more of claims 2., 2.1 to 2.2.10, characterized further in
- 2.3.1 that a substantial amount of the alloying addition of at least one of the solutes is held in the cph-solid solution or in any other metastable crystalline, quasi- and/or nano-crystalline or amorphous magnesium-based matrix phase, i.e. essentially in an homogeneous distribution of the alloying elements on an atomic length scale independent on the structure of the non-equilibrium (i.e. ne-) phase and/or
- 2.3.2 that the (micro-) structure consists of at least one of the characteristics given in claim 1.1 to 1.1.9 and/or
- 2.4 an Mg- or Al-alloy of a given (initial) alloy concentration according to one or more of claims 2., 2.1 to 2.3, characterized in that Mg- or Al-alloy is ball-milled by at least one of the following operating conditions and/or processing parameters:
- 2.4.1 an Mg- or Al-alloy according to one or more of claims 2., 2.1 to 2.3, made by ball-milling and milling with at least one (horizontally, vertically or oblique to gravity g operating) straight bar and/or rod, the cross-section of the balls and bar(s) either round (cf. Fig. 140) and/or rectangular and/or multifaceted and or irregular shaped and/or with irregular shaped impact bodies, and/or
- 2.4.2 an Mg- or Al-alloy according to one or more of claims 2., 2.1 to 2.4.1, by employing a horizontal and/or vertical and/or oblique vibrating milling technique and/or attritor milling technique with horizontally, vertically or oblique operating milling impellers or shafts and/or planetary ball milling technique with and without coupled rotation (velocity) of the relatively large holder disc and the relatively small milling containers (vials) and/or a corresponding tumbling ball milling technique and/or horizon-

- tal ball milling in the temperature range from -200°C to the Kauzmann temperature for glass transition + (0 to 200K) and/or
- 2.4.3 an Mg- or Al-alloy according to one or more of claims 2., 2.1 to 2.4.2. characterized in that it is synthesized by planetary ball milling employing $\omega^2 r^* / \Omega^2 R$ -ratios in the range from 0.01 to 1.5, in particular from 0.1 to 1.0 and/or
- 2.4.4 an Mg- or Al-alloy according to claim 2.4.3. characterized in that the employed planetary ball mill is characterized by a coupling factor $k_{\Omega/\omega}$ in the range from 0.05 to 4.0, in particular from 0.2 to 1.5 and/or
- 2.4.5 an Mg- or Al-alloy according to one or more of claims 2., 2.1 to 2.4.4. characterized in that the milling operation is carried out with an effective impact power P^* in the range of 0.02 to 2000 W/g. in particular in the range 0.05 to 500 W/g and/or
- 2.4.6 an Mg- or Al-alloy according to one or more of claims 2., 2.1 to 2.4.5. characterized in that the effective impact energy of milling balls employed ranges from 0.01 to 100 J/impact, in particular from 0.02 to 50 J/impact and/or
- 2.4.7 an Mg- or Al-alloy according to one or more of claims 2., 2.1 to 2.4.6. characterized in that the employed impact frequency of milling balls and/or milling bars employed ranges from 0.2 to 140 Hz, in particular from 0.05 to 80 Hz and/or
- 2.4.8 an Mg- or Al-alloy according to one or more of claims 2., 2.1 to 2.4.7, characterized in that the ratio of friction-to-shock power of the overall impact power employed ranges from 0.01 to 100%, in particular from 1.0 to 98% and/or
- 2.4.9 an Mg- or Al-alloy according to one or more of claims 2., 2.1 to 2.4.8. characterized in that milling cycles with minimized ratios of friction-to-shock powers are employed as a function of milling time in order to minimize friction and/or heating and/or caking and/or the milling time required to obtain a given volume fraction of corresponding non-equilibrium (i.e. ne-) Mg- or Al-base matrix phase, and/or
- 2.4.10 an Mg- or Al-alloy according to one or more of claims 2., 2.1 to 2.4.9, characterized in that the milling cycles with high ratios of shock-to-friction powers in the range from 50 to 100%, in particular from 80 to 100% are employed at any time during the overall milling cycle, the temperature thereby ranging up to temperatures characterized by the Kauzmann criterion for glass transition + (0 to 200°C) limiting the upper milling temperature while the lowest temperature is -200°C which is employed by an appropriate chill system and/or
- 2.4.11 an Mg-and Al-alloy according to one or more of claims 2., 2.1 to 2.4.10, characterized in that the overall milling period required to achieve the structural ne-state ranges from between 0.2 to 250 hours, in particular to between 0.3 to 40 hours depending on the tolerable volume fraction of second phases and/or dispersions in the as-milled state of the milled (powder) end-product and/or
- 2.4.12 an Mg-and Al-alloy according to one or more of claims 2., 2.1 to 2.4.11, characterized further in that during the first 0 to 15 h, in particular during the first 0 to 2 h at least

- one milling cycle is employed with a ratio in friction-to-shock power ranging from 40 to 100%, in particular from 50 to 95%, the milling operation thereby eventually chilled by a cooling system, and/or
- 2.4.13 an Mg-and Al-alloy according to one or more of claims 2., 2.1 to 2.4.12, characterized in that the employed planetary and/or horizontal and/or attritor and/or vibrating ball mill (container) is characterized by a distance and/or milling container radius R (R_A) in the range from 0.05 to 4 m, in particular from 0.075 to 2 m and/or
- 2.4.14 an Mg-and Al-alloy according to one or more of claims 2., 2.1 to 2.4.13, characterized in that the employed radius of the milling container (vial) of the planetary ball mill ranges from 0.01 to 2 m, in particular from 0.02 to 1.0 m, and/or
- 2.4.15 an Mg-and Al-alloy according to one or more of claims 2., 2.1 to 2.4.14, characterized in that the radius the rotational speed of the large holder disc of the planetary ball mill as is characterized by distance R , i.e. Ω , ranges from 10 to 1000 rpm, in particular from 15 to 1000 rpm, and/or
- 2.4.16 an Mg-and Al-alloy according to claim 2.4.15, characterized in that the rotational speed of the milling container (vial) as characterized by the vial radius r , i.e. ω , ranges from 10 to 1500 rpm, in particular from 15 to 1000 rpm, and/or
- 2.4.17 an Mg-and Al-alloy according to one or more of claims 2., 2.1 to 2.4.16, characterized in that the milling operation was performed by using a lubricating agent in particular an hydrocarbon of the series C_nH_{2n+2} such as hexan(e) and/or a silan-type of lubricifier such as SiH_4 , ethine (C_2H_2), and/or ethylene (C_2H_4), and/or C_3H_6 and/or metallo-hydrogens of one or more of the alloying additions of claim 2.4 including phosphine (PH_3) and/or
- 2.4.18 an Mg-and Al-alloy according to one or more of claims 2., 2.1 to 2.4.17, characterized in that the milling operation was performed by using a lubricating agent, in particular an alcohol such as methanol, ethanol, amylalcohols, glycols, glycerine, phenols, aldehydes, ketons, in particular Grignard-type of reaction products such as primary, secondary and tertiary alcohols and/or light oils and/or silicon oils and/or graphite and/or
- 2.4.19 an Mg-and Al-alloy according to one or more of claims 2., 2.1 to 2.4.18, characterized in that the quantity of the lubricating agent ranges from 0.001 to 15 wt.%, in particular from 0.01 to 8 wt.% relative to the initial precursor charge and/or
- 2.4.20 an Mg-and Al-alloy according to one or more of claims 2., 2.1 to 2.4.19, characterized in that the filling fraction f_{nb} of the (at least one) milling container (vial) of planetary ball mills with milling balls and that of horizontal ball mills ranges from 0.01 to 0.7, in particular from 0.02 to 0.5, and/or that of attritor and vibrating ball mills from 0.3 to 1.0, in particular from 0.5 to 0.95 and/or
- 2.4.21 an Mg-and Al-alloy according to one or more of claims 2., 2.1 to 2.4.20, characterized in that
- 2.4.21.1 the individual and/or average radius of the employed milling balls and

milling bars and/or rods including attritor impellers ranges from 2 to 60 mm, in particular from 3 to 300 mm, and/or

2.4.21.2 in that the geometry of the cross-section of the employed milling balls and milling bars is characterized by one of the geometrical elements and/or similar derivatives shown in Fig. 140 and/or

2.4.22 an Mg-and Al-alloy according to one or more of claims 2., 2.1 to 2.4.21, characterized in that the individual and average density of the milling balls and milling bars (rods) including attritor impellers ranges from 1.85 to 21.0 g/cm³, in particular from 2.6 to 17 g/cm³ including those materials to be introduced into Mg- and Al-alloys as an alloying element by being consumed away via friction and abrasion, for example.

2.4.23 an Mg-and Al-alloy according to one or more of claims 2., 2.1 to 2.4.22, characterized in that the massive bulk of the milling balls and/or milling bars and/or rods including attritor impellers, (irregular) and/or milling bodies and/or a (PVD- and/or CVD-) coating on the milling balls, bars and/or rods including attritor impellers and/or (irregular) milling bodies consists of at least one of the following materials, i.e. SiO₂, "Syalon" (90% Si₃N₄), sintered corundum (99.7% Al₂O₃), tungsten carbide 96%WC + 3%Co), hardened Cr-steel, stainless Cr-Ni-steel, Teflon with core of steel and 97% pure zirconia (ZrO₂), ZrC, TiC, NbC, V₂C, Cr₂₃C₆, Cr₇C₃, Mo₂C, Cr₃C₂, WC, MoC, W₂C, Mn₃C, intermetallics (Ti-Al, Fe-Al, Nb-Al), SiC_xN_y, non-equilibrium Cu_{1-x}Ta_x alloys, (nanocrystalline) oxides such as TiO₂, SrTiO₃, KNbO₃, dense MoSi₂, TiNi, TiB₂, TiC, Si₃Ni₄, TiC, TiN, TiO₂, TiC-MgO composites, CrO₂, CrB₂, VC, Fe₃C, Al₂O₃, SiC, SiAlON and Cr-base and/or bearing, Nb-base and/or bearing, Ta-base and/or bearing, Ti-base and/or bearing, Zr-base and/or bearing and/or W-base and/or bearing intermetallics and/or corresponding alloys or any other material based on those shown in Table 11 such as BN, TaC, Ta_xC_y, WC, W_xC_y, as well as (and/or) TiCN, AlN, Ni_xB_y, nitrided Fe-Al-alloys and/or steels and/or stainless steels,

2.4.24 an Mg-and Al-alloy according to one or more of claims 2., 2.1 to 2.4.23, characterized in that the surface (coating(s)) and/or the (massive) interior of the wall(s) of the employed milling containers (vial(s)) consist(s) of at least one of the materials claimed in claim 2.4.21. and/or

2.4.25 an Mg-and Al-alloy according to one or more of claims 2., 2.1 to 2.4.24, characterized in that the individual and/or average mass of the milling balls ranges from 0.15 to 11000 g, in particular from 1 to 50 g and/or

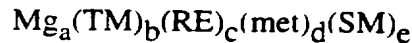
2.4.26 an Mg-and Al-alloy according to one or more of claims 2., 2.1 to 2.4.25, characterized in that the ratio of the mass of the milling balls to the mass of the (initial precursor) charge ranges from 2:1 to 40:1, in particular from 5:1 to 15:1 and/or

2.4.27 an Mg-and Al-alloy according to one or more of claims 2., 2.1 to 2.4.26, characterized in that the milling operation is carried out without artificial heating system and/or

- 2.4.28 an Mg-and Al-alloy according to one or more of claims 2., 2.1 to 2.4.27, characterized in that the milling operation is assisted by an artificial heating (such as via a Joule-effective system) and/or
- 2.4.29 an Mg-and Al-alloy according to one or more of claims 2., 2.1 to 2.4.28, characterized in that the milling operation comprises at least one milling cycle with in-situ heating via large ratios of friction-to-shock power of the overall impact power and/or via artificial heating such as via a Joule-effective system and/or
- 2.4.30 an Mg-and Al-alloy according to one or more of claims 2., 2.1 to 2.4.29, characterized in that the employed heating rate of the mean temperature of corresponding milling container during a heating cycle according to claim 2.4.29 ranges from 0.1 to 80 K/min. in particular from 0.2 to 40 K/min. the lower temperature in the range between -200K and ambient temperature, the higher temperature in the range between -50°C and the Kauzmann temperature for glass transition plus (0 to 200°C) and that the at least one milling cycle at higher temperatures lasting for 0.1 to 40 hours. in particular for 0.2 to 10 hours and/or
- 2.4.31 an Mg-and Al-alloy according to one or more of claims 2., 2.1 to 2.4.30, characterized in that the employed cooling rate of the mean temperature of corresponding milling container after a heating cycle according to claim 2.4.29 and for milling at temperatures lower than ambient ranges from 0.1 to 80 K/min, in particular from 0.2 to 40 K/min, the lower temperature in the range between -200K and ambient temperature, and that the at least one milling cycle at lower temperatures lasting for 0.1 to 100 hours, in particular for 0.2 to 10 hours and/or
- 2.4.32 an Mg-and Al-alloy according to one or more of claims 2., 2.1 to 2.4.31, characterized in that a (separate) annealing treatment without (in-situ) ball milling is employed, in particular the annealing treatments performed for 0.5 to 16 hours at temperatures in the range from 150° to 550°C at any time during and/or after the entire milling operation and/or
- 2.4.33 an Mg- or Al-alloy according to one or more of claims 2., 2.1 to 2.4.32, characterized in that a solution heat treatment at temperatures as to claim 1.14 is applied and/or
- 2.4.34 an Mg- or Al-alloy according to one or more of claims 2., 2.1 to 2.4.33, characterized in that a thermomechanical treatment is employed. the thermomechanical treatment being a combination of a solution treatment as to claim 2.4.33 and an extrusion and/or a forging and/or a drawing and/or a superplastic forming operation as to claim 12 is employed and/or
- 2.5 an Mg- and/or Al-alloy according to one or more of claims 2., 2.1 to 2.4.34, characterized by a (cph- or a metastable crystalline, quasi- and/or nanocrystalline and /or amorphous) matrix grain and/or cell size in the range from 0.02 to 50 μm , in particular in the range from 0.1 to 10 μm and/or
- 2.6 an Mg- and/or Al-alloy according to one or more of claims 2., 2.1 to 2.5, characterized by

a (cph- or a metastable crystalline, quasi- and/or nanocrystalline and /or amorphous) matrix grain and/or cell size in the range from 0.01 to 15 μm , in particular in the range from 0.03 to 3.0 μm and/or

- 2.7 an Mg- and/or Al-alloy according to one or more of claims 2., 2.1 to 2.6, characterized by a volume fraction of intermetallics of the type



where TM, RE, met and SM are defined according to claim 2.2.4, and $a = 0 - 99$, $b = 0 - 99$, $c = 0 - 99$, $d = 0 - 99$ and $e = 0 - 99$ and/or at least one of the elemental β -solute, the volume fraction ranging from 0.01 vol.% - 30 vol.%, in particular from 0.05 vol.% - 20 vol.% and/or

- 2.8 an Mg- and/or Al-alloy according to one or more of claims 2., 2.1 to 2.7, characterized by an intra- and/or transgranular intermetallic phase with a one-dimensional length scale (circumference, diameter, maximum 1-dim extension) in the range of 0.1 - 30 μm , in particular in the range from 0.5 to 15 μm , and/or
- 2.9 an Mg- and/or Al-alloy according to one or more of claims 2., 2.1 to 2.7, characterized by an intra- and/or transgranular intermetallic phase with a one-dimensional length scale (circumference, diameter, maximum 1-dim extension) in the range of 0.02 - 3 μm , in particular in the range from 0.03 to 1 μm , and/or
- 2.10 an Mg-and/or Al-alloy according to one or more of claims 2., 2.1 to 2.7, characterized by an intra- and/or transgranular intermetallic or metastable (crystalline, quasi-cristalline and /or amorphous) phase with a one-dimensional length scale (see 2.9) in the range of 0.01 - 0.1 μm , in particular in the range from 0.015 to 0.08 μm .
- 2.11 an Mg- and/or Al-alloy according to one or more of claims 2., 2.1 to 2.10, characterized by a virtual absence of porosity and/or
- 2.12 an Mg- and/or Al-alloy according to one or more of claims 2., 2.1 to 2.11, characterized by a virtual absence of porosity after a thermo-mechanical treatment as to 2.4.3 and/or
- 2.13 an Mg- and/or Al-alloy according to one or more of claims 2., 2.1 to 2.12, characterized by a maximum porosity after the final forming operation ranging from 0.001 to 3 vol.%, in particular ranging from 0.01 to 0.5 vol.%, and/or
- 2.14 an Mg- and/or Al-alloy according to one or more of claims 2., 2.1 to 2.12, characterized by a maximum pore size after the final forming operation ranging from 0.05 to 25 μm , in particular ranging from 0.08 to 5 μm , and/or
- 2.15 an Mg- and/or Al alloy according to one or more of claims 2., 2.1 to 2.12, characterized by a maximum pore size after the final forming operation ranging from 0.01 to 10 μm , in particular ranging from 0.02 to 1 μm , and/or
- 2.16 an Mg- and/or Al-alloy according to one or more of claims 2., 2.1 to 2.15, characterized by a content of impurities Fe, Ni, Cu, Si, Na and O₂ ranging from a factor of 0.1 to 10 compared to those levels currently accepted in the established high purity AZ- and

- AM-type of magnesium alloys made by casting from the liquid state, in particular, ranging from a factor 0.2 to 5 of the levels of Fe, Ni, Cu, Si, Na and O₂ usually accepted in the established high-purity AZ- and AM-type of magnesium alloys and/or
- 2.17 an Mg- and/or Al-alloy according to one or more of claims 2., 2.1 to 2.16, characterized by an impurity level (by weight %) introduced by feed-stock and/or processing amounting to with a minimum level as given in claim 1.29, but characterized further by a maximum impurity level of 0.01 Ni and/or 0.1 Cu and/or 0.1 Fe, in particular 0.05 Fe and/or 0.2 Co and/or 0.2 Si and/or 0.2 B and/or 0.02 Na and/or 0.1 Ca and/or 0.1 K and/or 3.0 C and/or 0.1 Cd and/or 0.1 Zn and/or 0.1 Pb and/or 0.1 Sn and/or 3.0 O (oxygen), in particular 0.05 to 2.0 oxygen and/or
- 2.18 an Mg- and/or Al-alloy according to one or more of claims 2., 2.1 to 2.17, characterized by a level of Ni, Cu, Fe, Co, Si, Na and/or Pb which is not substantially increased further by the milling operation compared to the feed stock due to the use of a shock- and/or wear-resistant and/or particularly hardened steel, refractory metal and/or refractory alloy and/or intermetallic phase as ball mill container material and/or ball mill container inner wall material and/or milling ball material, in particular tantalum, and/or
- 2.19 an Mg- and/or Al-alloy according to one or more of claims 2., 2.1 to 2.18, characterized by an impurity (Fe, Cu, Ni, Si, Co etc., cf. claim 2.17) inclusion size with a one-dimensional length scale (circumference, diameter, maximum 1-dim extension) in the range from 0.02 - 5 μm , in particular in the range from 0.05 to 1 μm and/or
- 2.20 an Mg- and/or Al-alloy according to one or more of claims 2., 2.1 to 2.18, characterized by an impurity (Fe, Cu, Ni, Si, Co etc., cf. claim 2.17) with a one-dimensional length scale (see claim 2.19) in the range of 0.01 - 0.5 μm , in particular in the range from 0.02 to 0.3 μm and/or
- 2.21 an Mg- and/or Al-alloy according to one or more of claims 2., 2.1 to 2.20, characterized by a level of O₂ which is not excessively increased further by the milling and/or powder handling operation compared to the feed stock due to the use of an inert gas atmosphere such as argon and/or nitrogen, in particular of an argon and/or nitrogen atmosphere of purity 4N8 and/or 5N, in order to protect the mechanically alloyed powder during the milling operation (which is performed at temperatures between -200°C and 300°C, in particular at between -50° to 140°C) in the milling cylinder and during opening/exposure of the powder to another (inert gas) atmosphere during preparation of hot and/or cold forming operations and during these operations themselves, the inert gas atmosphere used to protect the mechanically alloyed Mg-alloy powder against excessive oxidation and thereby being eventually purged continuously through a hot getter material such as a Cu- and/or Ta-grid to avoid even better oxidation and resulting oxide dispersions and/or fibre-type of oxides and/or oxidation layers in the final (eventually very fine) powders and/or product from mechanically alloyed powders, and/or
- 2.22 an Mg- and/or Al-alloy according to one or more of claims 2., 2.1 to 2.21, characterized

by containing MgO and oxides involving alloying constituents (both eg. as an impurity inclusion) with a one-dimensional length scale (see claim 2.19) in the range of 0.01 - 5 μm , in particular in the range from 0.02 to 0.5 μm and/or

2.23 an Mg- and/or Al-alloy according to one or more of claims 2., 2.1 to 2.22, characterized by a level of O_2 which is increased in a controlled manner to an oxygen content of up to 3 wt.% due to the controlled use of an inert gas atmosphere (in particular argon and/or nitrogen) eventually doped deliberately with oxygen to protect and/or reinforce the (as-)milled powder particles and/or

2.24 an Mg- and/or Al-alloy according to one or more of claims 2., 2.1 to 2.23, characterized by containing MgO-particles and oxides involving at least one alloying constituents, both type of oxides eg. as an impurity inclusion with a one-dimensional length scale (see claim 2.19) in the range of 0.01 - 5 μm , in particular in the range from 0.02 to 0.5 μm .

3rd claim A magnesium based alloy containing an element belonging to the "yttrics" (except of yttrium itself) with 0.1 wt.% solute to corresponding levels of approximately maximum equilibrium solid solubility, i.e.:

0.1 to 20 wt.% Sc in cph-Mg, in particular 0.5 to 15.0 wt.% Sc in cph-Mg, balance impurities, or
 0.1 to 7 wt.% Sm in cph-Mg, in particular 0.5 to 5.5 wt.% Sm in cph-Mg, balance impurities, or
 0.1 to 5 at.% Gd in cph-Mg, in particular 0.5 to 4.53 at.% Gd in cph-Mg, balance impurities, or
 0.1 to 7 at.% Dy in cph-Mg, in particular 0.5 to 6.0 at.% Dy in cph-Mg, balance impurities, or
 0.1 to 6 at.% Ho in cph-Mg, in particular 0.5 to 5.44 at.% Ho in cph-Mg, balance impurities, or
 0.1 to 7 at.% Tm in cph-Mg, in particular 0.5 to 6.3 at.% Tm in cph-Mg, balance impurities, or
 0.1 to 8 at.% Er in cph-Mg, in particular 0.5 to 6.9 at.% Er in cph-Mg, balance impurities, or
 0.1 to 9 at.% Lu in cph-Mg, in particular 0.5 to 8.5 at.% Lu in cph-Mg, balance impurities, or
 0.1 to 6 at.% Tb in cph-Mg, in particular 0.5 to 4.6 at.% Tb in cph-Mg, balance impurities, or
 transition metals with a at least some liquid and solid solubility in Mg and at the same time known to improve the corrosion resistance of magnesium and/or magnesium alloys, i.e.
 0.1 to 2.5 wt.% Zr in cph-Mg, in particular 0.5 to 2.0 wt.% Zr in cph-Mg, balance impurities, or
 0.1 to 3.0 wt.% Mn in cph-Mg, in particular 0.5 to 2.2 wt.% Mn in cph-Mg, balance impurities,

the aforementioned alloys characterized in that:

- 3.1 they are made from the liquid state by casting and/or thin-strip casting and/or thin-wall and/or pressure-die casting and/or spray forming (spray deposition) and/or rapid solidification and/or atomization to optimize the grain boundary strengthening effect, for example, so to result in cross-sections in the range from 200 nm to 500 mm, in particular in cross-sections from 1 μm to 50 mm and/or laser glazing (surface re-melting) and/or
- 3.2 an Mg-alloy according to one or more of claims 3. to 3.1, characterized further in that the alloying additions to cph-magnesium is substantially held in the equilibrium or non-equilibrium solid solution of cph-magnesium and/or

- 3.3 an Mg-alloy according to one or more of claims 3. to 3.2, the alloying additions are held in solid solution and characterized further in that corresponding microstructure was attained
- 3.3.1 in the as-solidified state due favorable solidification kinetics, i.e. equilibrium partition coefficients k_0 relatively (compared to the other Mg binary systems) close to unity where k_0 is the ratio of liquidus-to-solidus concentration of a given (initial) alloy concentration c_0 , and/or
- 3.3.2 after a solution heat treatment at temperatures at or in the vicinity of corresponding eutectic or peritectic temperatures including tolerance limits due to experimental error in phase diagramme assessment and/or scale effect of microstructure on the characteristic temperatures, i.e. for the:
- Mg-Sc alloys at 0.7 to $0.99 \cdot 983 \pm 3$ K, in particular at 0.8 to $0.95 \cdot 983 \pm 3$ K or
Mg-Sm alloys at 0.7 to $1.05 \cdot 815 \pm 3$ K, in particular at 0.8 to $1.03 \cdot 815 \pm 3$ K or
Mg-Gd alloys at 0.7 to $1.05 \cdot 819 \pm 3$ K, in particular at 0.8 to $1.03 \cdot 819 \pm 3$ K or
Mg-Dy alloys at 0.7 to $1.05 \cdot 823 \pm 4$ K, in particular at 0.8 to $1.03 \cdot 823 \pm 4$ K or
Mg-Ho alloys at 0.7 to $1.05 \cdot 838 \pm 4$ K, in particular at 0.8 to $1.03 \cdot 838 \pm 4$ K or
Mg-Tm alloys at 0.7 to $1.05 \cdot 858 \pm 4$ K, in particular at 0.8 to $1.03 \cdot 858 \pm 4$ K or
Mg-Er alloys at 0.7 to $1.0 \cdot 857 \pm 4$ K, in particular at 0.8 to $1.03 \cdot 857 \pm 4$ K or
Mg-Lu alloys at 0.7 to $1.0 \cdot 889 \pm 4$ K, in particular at 0.8 to $1.03 \cdot 889 \pm 4$ K or
Mg-Tb alloys at 0.7 to $1.05 \cdot 832 \pm 4$ K, in particular at 0.8 to $1.03 \cdot 832 \pm 4$ K or
Mg-Zr alloys at 0.7 to $0.99 \cdot 973$ K, in particular at 0.8 to $0.95 \cdot 973$ K or
Mg-Mn alloys at 0.7 to $0.99 \cdot 971$ K, in particular at 0.8 to $0.95 \cdot 971$ K and/or
- 3.3.3 after a thermo-mechanical treatment and/or hot forming operation at temperatures according to the solutionizing heat treatment regime in 3.3.2 and/or
- 3.4 an Mg-alloy according to one or more of claims 3., 3.1 to 3.3.3, characterized by a (cph-matrix) grain size in the range from 3 to $250 \mu\text{m}$, in particular in the range from 5 to $50 \mu\text{m}$ and/or
- 3.5 an Mg-alloy according to one or more of claims 3. to 3.4, characterized by a (cph-matrix) grain (high angle boundary) and/or cell (low angle boundary) size in the range from 0.2 to $10 \mu\text{m}$, in particular in the range from 0.5 to $8 \mu\text{m}$ and/or
- 3.6 an Mg-alloy according to one or more of claims 3. to 3.5, characterized by a volume fraction of intermetallics of the type $\text{Mg}_a(\text{yttrics})_b$ or elemental βZr or βMn ranging from $0.01 \text{ vol.}\%$ - $20 \text{ vol.}\%$ of the volume fraction corresponding to the equilibrium volume fraction of corresponding alloys, in particular ranging from $0.05 \text{ vol.}\%$ - $10 \text{ vol.}\%$ of the volume fraction corresponding to the equilibrium volume fraction of corresponding alloys where "a" ranging from 5 to 25 and "b" ranging from 1 to 6 and/or
- 3.7 an Mg-alloy according to one or more of claims 3. to 3.6, characterized by an intra- and/or transgranular intermetallic phase of a one-dimensional length scale (circumference, diameter, maximum 1-dim extension) in the range from 1 to $50 \mu\text{m}$, in particular in the range from 2 to $35 \mu\text{m}$ and/or

- 3.8 an Mg-alloy according to one or more of claims 3. to 3.7, characterized by an intra- and/or transgranular intermetallic phase of of a one-dimensional length scale (see claim 3.7) in the range from 0.01 to 8.0 μm , in particular in the range from 0.1 to 1.0 μm and/or
- 3.9 an Mg-alloy according to one or more of claims 3. to 3.8, characterized by virtual absence of porosity and/or
- 3.10 an Mg-alloy according to one or more of claims 3. to 3.9, characterized by virtual absence of porosity due to a thermo-mechanical treatment as to 3.3.3 and/or
- 3.11 an Mg-alloy according to one or more of claims 3. to 3.10, characterized by a maximum porosity after pressure die-casting or after the final forming operation ranging from 0.05 to 3 vol.%, in particular from 0.5 to 2 vol.%, and/or
- 3.12 an Mg-alloy according to one or more of claims 3. to 3.11, characterized by a maximum pore size after pressure-die-casting or after the final forming operation ranging from 0.05 to 10 μm , in particular from 0.1 to 5 μm , and/or
- 3.13 an Mg-alloy according to one or more of claims 3. to 3.12, characterized by a content of impurities Fe, Ni, Cu, Si, Na and O_2 ranging from a factor of 0.1 to 10 compared to those levels currently accepted in the established high purity AZ- and AM-type of magnesium alloys made by casting from the liquid state, in particular ranging from a factor 0.2 to 5 of the levels of Fe, Ni, Cu, Si, Na and O_2 usually accepted in the established high-purity AZ- and AM-type of magnesium alloys and/or
- 3.14 an Mg-alloy according to one or more of claims 3. to 3.13, but characterized by an impurity level (by weight %) as for claim 1.29 and/or
- 3.15 an Mg-alloy according to one or more of claims 3. to 3.14, characterized by a level of Fe, Ni, Cu, Co, Na, K, C, Cd, Zn, Pb, Sn, B and Si which is not increased further by the melting operation compared to the employed feed stock due to the use of inert refractory metal, alloy and/or intermetallic phases in contact with condensed alloy constituents (eg. as crucible material), and in particular due to the use of tantalum (-based) materials, and/or
- 3.16 an Mg-alloy according to one or more of claims 3. to 3.15, characterized by a level of O_2 which is essentially not increased further by the melting operation compared to the oxygen level of the feed stock, in particular not more than by a factor of 5 due to the use of an inert gas atmosphere (in particular argon and/or nitrogen), high quality sealings and/or a getter vapour to purge the equipment prior to start the vapour deposition process and/or
- 3.17 an Mg-alloy according to one or more of claims 1. to 3.16, characterized by a size of an impurity inclusion (containing Fe, Ni, Cu, Co, Na, K, C, Cd, Zn, Pb, Sn, B, Si and oxides etc., cf. claim 1.28 - 1.31) with a one-dimensional length scale (circumference, diameter, maximum 1-dim extension) in the range of 1 - 50 μm , in particular in the range from 2 to 35 μm and/or
- 3.18 an Mg-alloy according to claim 3.17, characterized by a size of an impurity inclusion in the range from 0.04 to 5.0 μm , in particular in the range from 0.05 to 2.0 μm , in particular in the range from 0.1 to 1.0 μm and/or

3.19 an Mg-based alloy according to one or more of the claims 3. to 3.18 characterized in that the alloy further contains ternary and/or higher order alloying elements, i.e.

- up to 5 wt.% lanthalam (La), in particular 0.1 to 2.0% wt.% La and/or
- up to 5 wt.% cerium (Ce), in particular 0.1 to 2.0% wt.% Ce and/or
- up to 5 wt.% praeodymium (Pr), in particular 0.1 to 2.0% wt.% Pr and/or
- up to 5 wt.% neodymium (Nd), in particular 0.1 to 2.0% wt.% Nd and/or
- up to 5 wt.% light rare earth misch-metal (LRE-MM), in particular 0.1 to 2.0% wt.% LRE-MM, the misch-metal thereby in particular of compositions stemming from and/or corresponding to the ore composition of Monazite-, Bastnaesite- and Xun Wu-type of RE-ores, but in any case being dominated by corresponding compounds of La, Ce, Nd and Pr and, as a misch-metal, containing
5 - 97 % La by weight, 5 - 97 % Ce by weight and 5 - 98 % (Nd + Pr)
balance other rare earth metals such as Gd and Tb, but also Y,
and the sum of (La, Ce, Nd and Pr) totalling 40 - 100 % by weight, in particular 80 - 99 % by weight, and/or
- up to 8 wt.% aluminium (Al), in particular 0.2 to 5.0% wt.% Al and/or
- up to 5 wt.% alkaline earth metal (AE) and up to 8 wt.% aluminium (Al), in particular 0.5 to 4.0% wt.% AE and 1 to 5 wt.% Al and/or
- up to 5 wt.% alkaline earth metal (AE) and up to 8 wt.% gallium (Ga), in particular 0.5 to 4.0% wt.% AE and 1 to 5 wt.% Ga and/or
- up to 5 wt.% calcium (Ca) and up to 8 wt.% aluminium (Al), in particular 0.1 to 4.0% wt.% Ca and 0.3 to 5 wt.% Al and/or
- up to 5 wt.% strontium (Sr) and up to 8 wt.% aluminium (Al), in particular 0.1 to 4.0% wt.% Sr and 0.3 to 5 wt.% Al and/or
- up to 5 wt.% barium (Ba) and up to 8 wt.% aluminium (Al), in particular 0.1 to 4.0% wt.% Ba and 0.3 to 5 wt.% Al and/or
- up to 5 wt.% calcium (Ca) and up to 8 wt.% gallium (Ga), in particular 0.1 to 4.0% wt.% Ca and 0.3 to 5 wt.% Ga and/or
- up to 5 wt.% strontium (Sr) and up to 8 wt.% gallium (Ga), in particular 0.1 to 4.0% wt.% Sr and 0.3 to 5 wt.% Ga and/or
- up to 5 wt.% barium (Ba) and up to 8 wt.% gallium (Ga), in particular 0.1 to 4.0% wt.% Ba and 0.3 to 5 wt.% Ga and/or
- up to 5 wt.% zinc (Zn), in particular 0.5 to 4.0% wt.% Zn for the Mg-"yttrics"-based alloys of claim 1, also and/or
- up to 5 wt.% manganese (Mn), in particular 0.1 to 2.0% wt.% Mn and/or
- up to 2 wt.% zirconium (Zr), in particular 0.1 to 1.8 wt.% Zr.

Claim 4. A Mg-based alloy according to one or more of the claims 1. to 2.24 characterized in that the alloy further contains ternary and/or higher order alloying elements, i.e. within which the

individual proportional limits by weight are as following:

4.1 metastable (non-equilibrium) Mg-base matrix phases including the (extended) solid solutions of rare earth metals and MM in Mg according to one or more of the claims

1. to 2.24. but also containing ternary and higher order alloying additions such as:

(if commata for elements. read "and/or" for claims 4.1 to 4.7)

- a) - 0.1 to 16 wt.% Al, in particular 0.5 to 6 wt.% Al, and
- b) - 0.0 to 8 wt.% Ca, Sr and/or Ba. in particular 0.2 to 3 wt.% Ca, Sr and/or Ba, and/or
- c) - 0.0 to 4 wt.% Zn, In, Sn and/or Pb in particular 0.2 to 2 wt.% Zn, In, Sn and/or Pb and/or
- d) - 0.0 to 10 wt.% Si, Ge, B, Be and/or Sb, in particular 0.2 to 5 wt.% Si, Ge, B, Be an/or Sb and/or
- e) - 0.0 to 12 wt.% V, Ti, Zr, Mn, Cr, Nb, Mo, Hf, Re, W and/or Ta. in particular 0.2 to 6 wt.% V, Ti, Zr, Mn, Cr, Nb, Mo, Hf, Re, W and/or Ta.

balance magnesium and impurities.

aimed at a partial transformation to very fine dispersions of precipitates (in particular <100 nm) after the final alloy conversion and/or forming operation via synergistic formation from a combination of higher order alloying additions and resulting metastable (non-equilibrium) Mg-base matrix phases possible between sub-groups a) to e),

in particular an alloy containing 0.2 to 14 wt.% MM, Ce, La, Pr, Nd, Sm, Gd, Dy, Ho and/or Er according to one or more of the claims 1. to 2.24, and of 0.5 to 8 wt.% Al and of 0.1 to 4 wt.% Ca, Sr and/or Ba, and of 0.2 to 10 wt.% V, Ti, Zr, Mn, Cr, Nb, Mo, Hf, Re, W and/or Ta. balance magnesium and impurities,

the alloys in any case not exceeding a density of 2.7 g/cm^3 , and/or:

4.2 metastable (non-equilibrium) Mg-base matrix phases including the (extended) solid solutions of rare earth metals and MM in Mg according to one or more of the claims 1. to 2.24, but also containing ternary and higher order alloying additions such as:

- a) - 0.1 to 30 wt.% V, Ti, Zr, Mn, Cr, Nb, Mo, Hf, Re, W and/or Ta in particular 0.3 to 15 wt.% V, Ti, Zr, Mn, Cr, Nb, Mo, Hf, Re, W and/or Ta or
- b) - as for a) but allowing for a combination of two or three of these transition metals with a common alloying level ranging from 0.3 to 30 wt.% and/or coexisting, at least substantially co-existing with the rare earth elements in extended solid solution or
- c) - as for a) or b), but also containing up to 15 % Al by weight and/or
- d) - in particular an alloy with 0.0 to 12 wt.% MM as defined under claim 2, Ce, La, Pr, Nd, Sm, Gd, Dy, Ho and/or Er and of 0.1 to 8 wt.% Al and of 0.05 to 8 wt.% of transition metals as defined under a) of this 4.2-group of alloys, or
- e) - as for a) through d), but also containing 0.1 to 4 wt.% Si, Ge, B, Be and/or Sb

balance magnesium and impurities.

the alloys in any case not exceeding a density of 2.7 g/cm^3 to produce higher order metastable (non-equilibrium) Mg-base phases including extended solid solutions plus fine dispersions of precipitates (in particular <100 nm) after the final alloy conversion and/or forming operation

via synergistic formation from a combination of higher order alloying additions to Mg as is possible between sub-groups a) to e), in particular an alloy containing 0.0 to 10 wt.% Ce, La, Pr, Nd and/or Sm and of 0.0 to 8 wt.% V, Ti, Zr, Mn, Cr, Nb, Mo, Hf, Re, W and/or Ta balance magnesium and impurities, and/or

f) - keeping any of the higher order additions possible from a combination of subgroups a) to e) in the metastable, essentially one-phase matrix including the (extended) solid solution of cph-Mg, or:

4.3 a metastable Mg - TM base matrix alloy including non-equilibrium crystalline, quasi- and/or nano-crystalline and/or amorphous Mg-base matrix phases according to one or more of the claims 1. to 2.24, but also containing ternary and higher order alloying additions such as:

a) - 0.2 to 15 wt. % Ce, La, Nd, Sm, Pr, Y and/or MM

b) - 0.0 to 10 wt.% Al, and/or

c) - 0.0 to 15 wt.% Si, Ge, B, Sb and/or Be and/or

d) - 0.0 to 8 wt.% Ca, Sr and/or Ba,

balance magnesium and impurities,

the alloys in any case not exceeding a density of 2.7 g/cm^3 , to produce higher order metastable (non-equilibrium) Mg-base phases including extended solid solutions plus fine dispersions of precipitates (in particular $<100 \text{ nm}$) after the final alloy conversion and/or forming operation via synergistic formation from a combination of higher order alloying additions to Mg and being embedded in and co-existing with metastable (non-equilibrium) Mg-base phases resulting from an alloy combination of sub-groups a) to d) of this 4.3-group of alloys, in particular an alloy containing 0.2 to 15 wt.% V, Ti, Zr, Mn, Cr, Nb, Mo, Hf, Re, W and/or Ta as defined under one or more of the claims 1. to 2.24, and also containing 0.5 to 6 wt.% Ce, Nd, La, Sm, Y and/or MM and 0.0 to 4 wt.% Al, and 0.0 to 3 wt.% Si, Ge, B, and/or Sb and/or 0.0 to 2 wt.% Ca, Sr and/or Ba, balance magnesium and impurities, and/or

e) - keeping any of the higher order additions possible from a combination of subgroups a) to d) essentially in (extended) solid solution of cph-Mg or any other metastable non-equilibrium Mg-base phase in the final product, and/or:

4.4 a metastable Mg - metalloid (and/or Be and/or B) base alloy including non-equilibrium crystalline, quasi- and/or nano-crystalline and/or amorphous phases according to one or more of the claims 1. to 2.24, but also containing ternary and higher order alloying additions such as:

a) - 0.2 to 25 wt. % Ce, La, Nd, Sm, Pr, Y and/or MM and

b) - 0.1 to 20 wt.% V, Ti, Zr, Mn, Cr, Nb, Mo, Hf, Re, W and/or Ta

c) - 0.0 to 10 wt.% Al, and/or

d) - 0.0 to 8 wt.% Ca, Sr and/or Ba,

balance magnesium and impurities,

the alloys in any case not exceeding a density of 2.7 g/cm^3 to produce higher order metastable

(non-equilibrium) Mg-base phases including extended solid solutions plus fine dispersions of precipitates (in particular <100 nm) after the final alloy conversion and/or forming operation via synergistic formation from a combination of higher order alloying additions to Mg and which are embedded in metastable (non-equilibrium) phases resulting from an alloy combination of sub-groups a) to d) of this 4.4-group of alloys. in particular an alloy containing 0.1 to 20 wt.% B and/or Si and/or Si and 0.2 to 15 wt.% V, Ti, Zr, Mn, Cr, Nb, Mo, Hf, Re, W and/or Ta as defined under one or more of the claims 1. to 2.24. and also containing 0.0 to 6 wt.% Ce, Nd, La, Sm, Y and/or MM and 0.0 to 4 wt.% Al. and 0.0 to 3 wt.% Si, Ge, B. and/or Sb and/or 0.1 to 2 wt.% Ca, Sr and/or Ba,

balance magnesium and impurities. and/or

e) - keeping any of the higher order additions possible from a combination of subgroups a) to d) essentially in solid solution of cph-Mg. and/or:

4.5 a metastable Mg - metalloid (and/or Be and/or B) base alloy including non-equilibrium crystalline, quasi- and/or nano-crystalline and/or amorphous phases according to one or more of the claims 1. to 2.24. but also containing ternary and higher order alloying additions such as:

a) - 0.1 to 20 wt.% V, Ti, Zr, Mn, Cr, Nb, Mo, Hf, Re, W and/or Ta

b) - 0.0 to 15 wt. % Ce, La, Nd, Sm, Pr, Y and/or MM and

c) - 0.0 to 10 wt.% Al. and/or

d) - 0.0 to 8 wt.% Ca, Sr and/or Ba,

balance magnesium and impurities,

the alloys in any case not exceeding a density of 2.7 g/cm³ to produce higher order metastable (non-equilibrium) Mg-base phases including extended solid solutions plus fine dispersions of precipitates (in particular <100 nm) after the final alloy conversion and/or forming operation via synergistic formation from a combination of higher order alloying additions to Mg and which are embedded in metastable (non-equilibrium) phases resulting from an alloy combination of sub-groups a) to d) of this 4.4-group of alloys. in particular an alloy containing 0.1 to 20 wt.% B and/or Si and/or Si and 0.2 to 15 wt.% V, Ti, Zr, Mn, Cr, Nb, Mo, Hf, Re, W and/or Ta as defined under one or more of the claims 1. to 2.24. and also containing 0.0 to 6 wt.% Ce, Nd, La, Sm, Y and/or MM and 0.0 to 4 wt.% Al. and 0.0 to 3 wt.% Si, Ge, B. and/or Sb and/or 0.1 to 2 wt.% Ca, Sr and/or Ba.

balance magnesium and impurities. and/or

e) - keeping any of the higher order additions possible from a combination of subgroups a) to d) essentially in solid solution of cph-Mg. and/or:

4.6 a metastable Mg - and/or Al-base early transition metal base alloy including non-equilibrium crystalline, quasi- and/or nano-crystalline and/or amorphous phases according to one or more of the claims 1. to 2.24. but also containing ternary and higher order alloying additions such as:

a) - 0.1 to 20 wt.% Si, B, Be and/or Ge

- b) - 0.0 to 15.0 wt.% of a second and/or ternary transition metals according to claim 1 and/or 2. thereby all elements essentially held in the non-equilibrium Mg-base matrix phase. and/or

4.7 an Mg-alloy as to the following commercial Mg engineering alloy compositions:

WE54, WE43, ZE63, ZE41, EZ33, EZ32, AE41, AE42, QE22, EQ21, AZ91D/E, AZ61A/B, AZ31A/B, AM20, AM50, AM60 or any other AM-base alloy as well as AS41 and AS42 including those made from high- and ultra-high purity feedstock (eg. X-, SX- and UX-series), these alloys being made by mechanical alloying in such a way that either a substantial or a minor fraction of the alloying additions is held in solid solution of cph-Mg or in any other resultant metastable structural (Mg-based) non-equilibrium matrix phase.

thereby either without or with complementary alloying additions to these alloys, the alloying additions being either

- ternary and quaternary additions according to claims 4.1 to 4.6. or
- with an increased content of the alloying additions present in the commercial alloy, the increase in alloying additions thereby corresponding to a factor ranging from 0.1 to 10 relative to the level in corresponding commercially established alloy composition.

in any case the alloy not exceeding a density of 2.7 g/cm^3 , and/or

the processing and/or quality of which correspond(s) to one or more of claims 1. to 2.24..

5nd claim. A gravity-independent vapour deposition process of which the driving force for the overall mass transport from evaporation source(s) to deposit(s) is provided by underpressure in successive levels of vacuum chambers which are eventually arranged in parallel, the (under-) pressure in the vacuum chamber(s) for deposition being maintained by an external pumping system resulting in a rate-controlling suction-type of vapour flow between evaporation sources and deposition surface of the evaporation unit and of which the actual throughput Q_v for a given pumping speed S is controlled by at least one heatable porous membran (diaphragma) for vapour flow, the (membran) diaphragma in particular heated by induction and/or resistance heating, and the evaporation sources being activated by thermal evaporation (resistance, induction, electron beam and/or microwave heating and/or sublimation, laser beam and/or arc evaporation methods) and/or magnetron sputtering methods and used to separate

- a) two adjacent evaporation chambers n and $(n+1)$ containing at least one individual evaporation source each or
- b) an evaporation chamber n with at least one individual evaporation source and a mixing chamber $(n+1)$ containing no or at least one individual evaporation source or
- c) an evaporation chamber as under a) or b), but followed by a chamber providing a facility for the deposition of the vapour and which follows into the direction of vapour flow lines (vapour trajectories) and/or

5.1 a vapour deposition process according to claim 5. characterized further in that the vapour transport from individual evaporation chambers (eg. to the mixing chamber) is driven by the

- vapour pressure of corresponding element(s) and/or
- 5.2 a vapour deposition process according to one or more of claim 5 and 5.1, the vapour deposition process characterized further in that a local pressure gradient dP/dx across the shortest separation length dx between two adjacent chambers of the evaporation process is generated, the magnitude of the local pressure gradient dP/dx in x-direction across the diaphragma being different, in particular larger in amount than the pressure gradients in adjacent vacuum chambers of the process resulting in a discontinuous pressure gradient profile between the evaporation source(s) and the substrate(s) used for deposition of the resultant alloy vapour and/or
- 5.3 a vapour deposition process according to one or more of claim 5 and 5.2, the vapour deposition process characterized further in that the local pressure gradient dP/dx provides the local driving force to allow a controlled fraction of the incoming vapour to be transferred into the next chamber following in the direction of the vapour condensation, i.e. deposition unit for both negative and positive temperature gradients across the diaphragma, the amount of the T-gradients ranging from 0 to 3000°C between evaporation and/or mixing and/or vapour deposition chamber and/or
- 5.4 a vapour deposition process according to one or more of claim 5 and 5.3, the vapour deposition process characterized further in that the specific traversing vapour volume is locally heated up and/or expanded and/or accelerated without compositional change, and/or
- 5.5 a vapour deposition process according to one or more of claim 5 and 5.4, the vapour deposition process characterized further in that the diaphragma *contains* at least one orifice(s) at the vapour intake and/or outlet of the flow channel(s) being symmetrically and/or assymetrically arranged around the x-normal of intake and/or outlet surface and/or the central y-/z-plane plane of the diaphragma which may, the x-normal being collinear or not with the center line of the adjacent evaporation and deposition chambers, the vapour flow resisting elements may form a matrix of equidistant or non-equidistant surfaces of equivalent or different surface area between the orifices at the intake and / or at the outlet of the diaphragma, and/or
- 5.6 a vapour deposition process according to one or more of claim 5 and 5.5, the vapour deposition process characterized further in that the diaphragma intake provides a ratio in surface area between the orifice surface(s) $(\Sigma)A_O$, and the surface around and/or between the orifice(s) A_R , acting as a resistor to flow, i.e. $(\Sigma A_O/A_R)*100\%$, ranging from 0.0001% to 99.5% relative to the overall (cross-sectional) surface of the diaphragma facing the incoming vapour flow, but in particular between 0.01 and 30% and including further engineering solutions to control condensation at and in the very and immediate vicinity of the diaphragma as well as away from the diaphragma and/or
- 5.7 a vapour deposition process according to one or more of claim 5 and 5.6, the vapour deposition process characterized further in that the bulk of the diaphragma is made from commercial steel and/or superalloys and/or one or more of the materials claimed under claim 2.4.21 and/or
- 5.8 a vapour deposition process according to one or more of claim 5 and 5.7, the vapour deposi-

tion process characterized further in that the surface of the diaphragma bulk is coated by a PVD- and/or CVD-coating of one or more of the materials claimed under claim 2.4.21.

6th claim. A vapour deposition process with a diaphragma according to claim 5. to 5.8, the diaphragma characterized further by individual diaphragma elements with at least one single and/or multiple bifurcation used as an anti-nozzle system (Fig. 90), the bifurcations being constructed in such a way that the individual backstreaming pressure, P_B , is smaller than the pressure at corresponding intake, P_I , i.e. $P_I > P_B$ so to allow for partial backstreamed vapour mass dm_B into the chamber n (or 1) where the vapour comes from, the bifurcations providing a solution for minimum turbulent flow inside the diaphragma and in conjunction with flow line elements at immediate intake area and as outlet configuration at rear of the diaphragma or in conjunction with trumpet-like nozzle geometries contrasting their use in gas-atomization and involving angular and smoothed out single and multiple bifurcations and resultant conductances arriving at single or multiple octopus-like configurations (Fig. 91), the angle δ between transmembranic flow channel and the flow for the backstreaming vapour at the bifurcations thereby ranging from 1 to 150° , in particular from 2° to 90° and/or

- 6.1. a vapour deposition process with a diaphragma according to one or more of claim 5. to 6., the diaphragma characterized further by constructional elements (profiles) to reduce laminar flow and to generate turbulent flow at a defined distance h in front of the vapour intake, the elements to generate turbulent flow providing coefficients of flow resistance, c_F , for flow surrounding a profile ranging from 0.25 to 5, in particular between 1.1 and 3, the higher values thereby obtained by a combination of comprising filigrane as well as relatively massive elements (Fig. 92) comprising rectangular and irregular plates, the c_F -value eventually increasing up to values of 50 for very small Reynold-numbers involved and/or
- 6.2 a vapour deposition process with a diaphragma according to one or more of claim 5. to 6.1, the diaphragma characterized further by constructional flow line elements (profiles) and design configurations to suppress turbulent flow at rear of the diaphragma as well as at the immediate intake area including trumpet-shaped in- and outlets and of which the resulting coefficients of flow resistance, c_F , being not larger than 0.3, in particular below 0.1, and/or
- 6.3 a vapour deposition process with a diaphragma according to one or more of claim 5. to 6.2, the diaphragma characterized further by a *series of successive resistor-to-flow levels* to surmount very large P- and T-gradients and which are represented by at least two levels of (a matrix of) resistor to flow levels according to a series electrical switch, each level thereby containing at least one transmembranic flow channel, the resultant matrix of resistor elements being arranged equidistantly between the flow channels or not, the resultant diaphragma element embracing one or more of the following characteristics:
 - a number m of resistor levels, where $100 > m > 1$ and/or
 - a decreasing, constant or increasing relative orifice area with increasing level m ,
i.e. $(\Sigma A_o / \Sigma A_R)_m > (\Sigma A_o / \Sigma A_R)_{m+1}$ or $(\Sigma A_o / \Sigma A_R)_m = (\Sigma A_o / \Sigma A_R)_{m+1}$

- or $(\Sigma A_o / \Sigma A_R)_m < (\Sigma A_o / \Sigma A_R)_{m+1}$ and/or
 - a nearly constant or a differentially increasing temperature with each discrete level of m and/or
 - a decreasing, constant or increasing orifice area with increasing level m. i.e. $(\Sigma A_o)_m$, $(\Sigma A_o)_{m+1}$ or $(\Sigma A_o)_m = (\Sigma A_o)_{m+1}$ or $(\Sigma A_o + \Sigma A_R)_m < (\Sigma A_o + \Sigma A_R)_{m+1}$ and/or
 - a decreasing, constant or increasing absolute surface area with increasing level m. i.e. $(\Sigma A_o + \Sigma A_R)_m > (\Sigma A_o + \Sigma A_R)_{m+1}$ or $(\Sigma A_o + \Sigma A_R)_m = (\Sigma A_o + \Sigma A_R)_{m+1}$ or $(\Sigma A_o + \Sigma A_R)_m < (\Sigma A_o + \Sigma A_R)_{m+1}$ and/or
 - a differential volume in front of level m which acts as a differential vapour reservoir likewise allowing the vapour to adapt the required partial temperature increase and which may include heating serpentine here to be traversed by the vapour volume released by the diaphragma. dm_D or dm , or not, and/or
 - flow line elements as under claim 6.2, but with coefficients of flow resistance, c_F , not larger than 1.0, employed in front of the differential resistor elements or in front of part of the resistor elements of a selected fraction of m-levels as well as at rear of the final outlet level m^{\max} in order to optimize turbulent with regard to traversing laminar flow or not and/or
- 6.4. a vapour deposition process with a diaphragma according to one or more of claim 5. to 6.3, the diaphragma characterized further by apertures to adjust the individual intake area A_o so local vapour flow and resultant magnitude of local vapour throughput per orifice at any location in the flow channel, in particular at the front face towards the incoming vapour flow, and/or
- 6.5 a vapour deposition process with a diaphragma according to one or more of claim 5. to 6.4, the diaphragma characterized further by transmembranic flow channels involving diffuser-jet nozzle transitions with continuous expansion and contraction of corresponding cross-sections and/or
- 6.6 a vapour deposition process with a diaphragma according to claim 6.5, the diaphragma characterized further by transmembranic flow channels involving diffuser- and/or jet nozzle transitions with discontinuous expansion and contraction of corresponding cross-sections and/or
- 6.7 a vapour deposition process with a diaphragma according to one or more of claim 5. to 6.6, the diaphragma characterized further by continuous diffuser and/or Laval-jet-nozzle type of outlets and/or
- 6.8 a vapour deposition process with a diaphragma according to one or more of claim 5. to 6.7, the diaphragma characterized further by continuous supersonic jet-nozzle outlets and/or
- 6.9 a vapour deposition process with a diaphragma according to one or more of claim 5. to 6.8, the diaphragma characterized further by diffuser- and jet-nozzle angles between the central axis of the diffuser or jet nozzle and the external peripheral wall ranging from 0° to 30° , in particular from 0.5° to 15°

resulting in any combination of possible solutions as shown in Fig. 94.

Claim 7 A vapour deposition process according to one or more of claim 5. to 6.9, the vapour deposition process characterized further in that the deposition unit comprises a continuous (batch) circuit process of at least one individual collector or of at least two individual flat planck condensators moving in one sense of the circuit process and/or

- 7.1 a vapour deposition process according to one or more of claim 5. to 7., the vapour deposition process characterized further in that the (eg. planck) collector/condensor provides a rectangular surface (projection) normal to the last diaphragma before vapour deposition and/or
- 7.2 a vapour deposition process according to one or more of claim 5. to 7.1, the vapour deposition process characterized further in that a condensor disc and/or at least one condensor with curved edges providing curved deposit edges is employed and/or
- 7.3 a vapour deposition process according to one or more of claim 5. to 7.2, the vapour deposition process characterized further in that a drum and/or at least one condensor with curved deposition surfaces (surface planes) is employed and/or
- 7.4 a vapour deposition process according to one or more of claim 5. to 7.3, the vapour deposition process characterized further in that the at least one individual condensor surface rotates in a given (horizontal, vertical or oblique to gravity g) plane with the lateral edges tilting (i.e. edge-on) around the central axis of the overall evaporation unit and/or
- 7.5 a vapour deposition process according to claim 7.4, the vapour deposition process characterized further in that the condensor surfaces embraces a tilt angle δ_{dep} with the central rotation axis of the condensor unit, the tilt angle ranging from $0^\circ < \delta_{\text{dep}} \leq 90^\circ$ and/or
- 7.6 a vapour deposition process according to one or more of claim 5. to 7.3, the vapour deposition process characterized further in that the at least one individual condensor (lateral) edge rotates in a given (horizontal, vertical or oblique to gravity g) plane with the at least one deposition surface moving in different surface planes per vapour deposition pass by tilting front-face-on around the central axis of the overall deposition unit and/or
- 7.7 a vapour deposition process according to claim 7.6, the vapour deposition process characterized further in that a tilt angle δ_{dep} between surface plan and central axis of the overall deposition unit is employed, the tilt angle ranging from $0^\circ < \delta_{\text{dep}} \leq 90^\circ$ and/or
- 7.8 a vapour deposition process according to one or more of claim 5. to 7.7, the vapour deposition process characterized further in that a constant ΔT -intervall is employed on the deposit surface at a given deposit surface position (x,y,z) between exposure to vapour impingement and a given transport position of the deposit outside the exposure and/or
- 7.9 a vapour deposition process according to one or more of claim 5. to 7.8, the vapour deposition process characterized further in that the $\delta\Delta T$ -deviation of a given deposit surface position (x,y,z) between exposure to vapour impingement and a given transport position outside the exposure ranges from 0.2 to 40K, in particular from 0.3 to 10 K, and/or
- 7.10 a vapour deposition process according to one or more of claim 5. to 7.9, the vapour deposi-

tion process characterized further by a constant lateral velocity v_{Kon} and/or ω_{Kon} on the entire deposition surface during exposure of the deposition surface to vapour impingement and/or

- 7.11 a vapour deposition process according to one or more of claim 5. to 7.10. the vapour deposition process characterized further by controlled Δv_{Kon} - and/or $\Delta \omega_{Kon}$ - intervalls of the deposition surface between exposure to vapour impingement of a given condensor and/or deposition surface position (x,y,z) and/or
- 7.12 a vapour deposition process according to one or more of claim 5. to 7.11. the vapour deposition process characterized further in that the at least on individual condensor is supplied with a (liquid) chill medium via a rotating disc distributor and/or collector and/or
- 7.13 a vapour deposition process according to one or more of claim 5. to 7.12. the vapour deposition process characterized further in that at least 1. in particular 1 to 20 independent meanders per condensor are employed and/or
- 7.14 a vapour deposition process according to one or more of claim 5. to 7.13. the vapour deposition process characterized further in that the number of individual deposition units, n_d , with one diaphragma per final mixing chamber ranges from 1 to 100. in particular from 2 to 32 and/or
- 7.15 a vapour deposition process according to one or more of claim 5. to 7.14. the vapour deposition process characterized further minimum ratio of the number of individual condensers, n_C , to individual diaphragmas, n_d , prior to deposition is given by the relationship $n_C = 1.5 * n_d$ and/or
- 7.16 a vapour deposition process according to one or more of claim 5. to 7.15, the vapour deposition process characterized further in that the lateral velocity of the condensor ranges from 10^{-3} cm/sec to 2 m/sec. in particular from 10^{-2} cm/sec to 50 cm/sec and/or
- 7.17 a vapour deposition process according to one or more of claim 5. to 7.16, the vapour deposition process characterized further in that the absolute pressure in the condensation / vapour deposition unit ranges from 10^{-6} to $7 * 10^{-1}$ bar. in particular from 10^{-4} to 10^{-2} bar and/or
- 7.18 a vapour deposition process according to one or more of claim 5. to 7.17. the vapour deposition process characterized further in that the effective hypermembranic distance h_{eff} between (rear) surface of the final diaphragma traversed by the vapour flow/stream/trajectories and the deposition surface ranges from 0.2 to 100 cm. in particular from 0.5 to 20 cm. and/or
- 7.19 a vapour deposition process according to one or more of claim 5. to 7.18. the diaphragma employed characterized further by a diameter d_z of the transmembranic flow channel at the x-level of rear outlet surface ranging from 0.05 to 100 cm. in particular from 0.08 to 30 cm and/or
- 7.20 a vapour deposition process according to one or more of claim 5. to 7.19. the vapour deposition process characterized further in that the surface ratio of diaphragma to individual

- (planck) condensator (projection to the diaphragma) ranges from 0.05 to 0.8 (i.e. 5 to 80 %), in particular from 0.1 to 0.3 (i.e. 10 to 30%) and/or
- 7.21 a vapour deposition process according to one or more of claim 5. to 7.20. the vapour deposition process characterized further in that the rectangular planck collector dimensions range from length 0.2 to 4 m by width 0.05 to 2 m. in particular from length 0.3 to 2 m by width 0.1 to 1 m. and/or
- 7.22 a vapour deposition process according to one or more of claim 5. to 7.21. the vapour deposition process characterized further in that the radius of the disc or drum condensor (collector) ranges from 7 to 400 cm. in particular from 12 to 250 cm and/or
- 7.23 a vapour deposition process according to one or more of claim 5. to 7.22. the vapour deposition process characterized further in that the condensor (surface) is kept at a (constant) temperature in the temperature regime between -200° to $+400^{\circ}\text{C} \pm 20^{\circ}\text{C}$. in particular at a (constant) temperature at between -190 to $+350^{\circ} \pm 20^{\circ}\text{C}$. and/or
- 7.24 a vapour deposition process according to one or more of claim 5. to 7.23. the vapour deposition process characterized further in that the relative surface roughness $\Delta = k/h_{\text{eff}}$ of the (in-situ consolidated) deposit prior to exposure to vapour impingement with k = mean height of surface protrusion (asperity) ranges from 0.000001 to 0.2, in particular from 0.001 to 0.1. and/or
- 7.25 a vapour deposition process according to one or more of claim 5. to 7.24. the vapour deposition process characterized further in that the fraction of vapour throughput reaching the deposit surface velocity boundary layer prior to accomodation. α_A . ranges from 0.5 to 1.0. in particular from 0.7 to 0.95, and/or
- 7.26 a vapour deposition process according to one or more of claim 5. to 7.25. the vapour deposition process characterized further in that the fraction of vapour throughput having reached the deposit surface velocity boundary layer prior to accomodation, α_A . and then being accomodated there. i.e. $\alpha_T(\alpha_A)$. ranges from 0.4 to 1.0, in particular from 0.5 to 0.95 and/or
- 7.27 a vapour deposition process according to one or more of claim 5. to 7.26. the vapour deposition process characterized further in that the overall mass transport is driven by the vapour pressure of the element with the highest vapour saturation pressure.

8th claim. A magnesium or aluminium based alloy according to one or more of claims 1. to 2.24 and claim 4. and made by vapour deposition techniques. but also including

- the extended solid solution of 0.1 to 95 % Ti by weight. in particular between 0.2 and 60 wt.% Ti. and including them for claim 4.3. and/or furthermore a subgroup
- f) of alloys of claim 4.3. in that a combination of two or three of corresponding transition metals of group 3 are possible with a common alloying level ranging from 0.3 to 30 wt.% and coexisting either in extended solid solution of cph-Mg or any other metastable non-equilibrium Mg-base alloy or being partially dispersed in corresponding microstructure

in terms of very fine intermetallic compounds.

all of these alloys made by vapour deposition involving one or more of the processes and/or process solutions possible by using diaphragmas according to one or more of claims 5 to 7, in order to control corresponding vapour synthesis and deposition for high reproducibility and productivity including yield and quality of the final as-deposited preform of these more complex higher order VD-Mg alloy systems.

thereby the specific vapour deposition techniques being those suitable for mass production by employing suction-type of overall driven mass transport using suitable diaphragmas as to at least one of the possibilities given under claim 2 and 3 and which allow to master and to control macroscopically and microscopically large vapour fluxes and the resultant throughput such as is possible by nature due to the high vapour pressure of magnesium metal as the base, of co-evaporated or separately evaporated light rare earth elements Mg-LRE due to their relatively low evaporation pressures as well as of metals known to be very different from magnesium such as early transition metals, metalloids, but also aluminium and other simple metals, and therefore never been alloyed to magnesium, at least not in a larger quantity, and these diaphragmas allowing all these elements to join the magnesium or aluminium base vapour in one or more mixing chambers, the entire evaporation being finally driven by an overall pressure gradient which is superimposed over the entire system by a pumping system located externally without interfering with the overall vapour between its origin, the evaporation sources and its destination, the at least one substrate and/or deposit surface on top of the substrate, thereby at least employing accommodation factors $\alpha_T(\alpha_A)$ and corresponding deposited / condensed yield ranging from 0.1 to 1.0, in particular from 0.3 to 0.8

9th claim A magnesium based alloy made by melt spinning techniques including twin-roller quenching and planar flow casting and containing

0.1 to 25 % La by weight, in particular between 0.2 and 14 wt.% La, or

0.1 to 25 % Ce by weight, in particular between 0.2 and 16 wt.% Ce, or

0.1 to 25 % Pr by weight, in particular between 0.3 and 18 wt.% Pr, or

0.1 to 28 % Nd by weight, in particular between 0.3 and 20 wt.% Nd, or

0.1 to 30 % Sm by weight, in particular between 0.2 and 20 wt.% Sm, or

0.2 to 14 % Y (and Eu) by weight, in particular between 0.5 and 7 wt.% Y (and Eu), or

0.2 to 30 % misch-metal by weight, in particular between 0.3 and 25 wt.% misch-metal,

the misch-metal thereby in particular of compositions stemming from and/or corresponding to the ore composition of Monazite-, Bastnaesite- and Xun Wu-type of RE-ores, but in any case being dominated by corresponding compounds of La, Ce, Nd and Pr and, as a misch-metal, containing 5 - 97 % La by weight, 5 - 97 % Ce by weight and 5 - 98 % (Nd + Pr) balance other rare earth metals such as Gd and Tb, but also Y, and the sum of (La, Ce, Nd and Pr) totalling 40 - 100 % by weight, in particular 80 - 99 % by weight, or

0.2 to 15 % Al by weight, in particular between 4 and 12 wt.% Al, or
 0.1 to 10 % Mn by weight, in particular between 0.2 and 8 wt.% Mn, or
 0.1 to 5 % Zr by weight, in particular between 0.2 and 3 wt.% Zr,

and thereby employing in all cases

- an inert atmosphere to protect molten feed stock, solidification operation and resultant ribbon, the inert gas in particular being commercially available helium or a mixture of helium with other suitable and inert gases, and/or

- a chill of highly conductive material such as (a) copper wheel(s) at a surface speed of at least 3.5 km / min, in particular at a surface speed of 5 to 7 km / min, and/or

and in particular for PFC-type of RS-processing employing

- a controlled distance between corresponding orifice for molten alloy supply and rotating chill to produce a constraint melt puddle between feed stock supply and rotating chill, and/or

- the distance between orifice and chill smaller than 4 mm, in particular smaller than 2 mm, and/or

- a scraper to reduce the inert gas film between liquid and resultant solidified ribbon and the chill,

in order to obtain a microstructural state

- within which the lanthanum, cerium, praeosodymium, neodymium, samarium, europium, gadolinium and/or yttrium and/or the other heavy rare earth elements stemming from the employed misch-metal, the aluminium, manganese or zirconium are or is substantially held in solid solution in the as-solidified state, corresponding solid solution being either cph-Mg or any other metastable crystalline or amorphous phase, the microstructure consisting of grains, cells and/or subcells of which the dimensions are < 10µm in at least one dimension of the three translational directions x,y and z, which are in particular columnar features and/or a microstructure that was formed by a completely partitionless mode of solidification from the melt,

corresponding binary alloys may contain minor higher order alloying additions in case of the binary extended solid solution alloys with La,Ce, Nd, Pr, Sm, Y (and Eu) or MM (as defined above):

a) - 0.1 to 15 wt.% Al, in particular 0.5 to 6 wt.% Al,

b) - 0.0 to 8 wt.% Ca, Sr or Ba, in particular 0.2 to 3 wt.% Ca, Sr or Ba,

c) - 0.0 to 4 wt.% Zn, in particular 0.2 to 2 wt.% Zn,

d) - 0.0 to 6 wt.% Si, Ge, B, Sb, in particular 0.2 to 3 wt.% Si, Ge, B, Sb,

e) - 0.0 to 6 wt.% Zr, Mn, in particular 0.2 to 3 wt.% Zr, Mn,

balance magnesium and impurities,

or the binary extended solid solutions of Mn or Zr containing group a) to d) of these higher order additions, balance magnesium and impurities,

all of which aimed at fine dispersions of precipitates synergistically formed from any of the combinations of higher order alloying additions possible between sub-groups a) to e) or to d).

in particular an alloy containing 0.2 to 10 wt.% Ce, La, Pr, Nd or Sm and of 0.5 to 3 wt.% Al and of 0.1 to 1 wt.% Ca, Sr or Ba, balance magnesium and impurities, by employing any of the alloy conversion routes claimed under claim n° 12, item 1a), 2a), 3a) and 4) to 7).

10th claim. A magnesium based alloy made by atomization methods, in particular by electro-hydrodynamic (EHD) atomization and containing the binary alloying additions according to claim 9, thereby adjusting processing conditions to produce powders with a frequency maximum in particle size distribution at particle sizes below 5µm, in particular at particle sizes below 1 µm, and a maximum particle size not exceeding 10 to 15µm, in particular not exceeding 5 µm, in order to employ chill conditions and resulting liquid undercoolings which allow to hold the binary alloying additions essentially in the cph-Mg solid solution or in any other metastable crystalline or amorphous phase in the advent of growth likely to be controlled by recalescence, in case of gas atomization employing an inert atomizing gas, the atomizing gas in particular helium or a mixture of helium with another inert gas, in any case employing an inert atmosphere to protect atomization, resultant powders and subsequent powder handling, these binary extendend solid solutions may contain the higher order alloying additions as to claim n° 8, but preferably a lower level of higher order alloying additions, in particular 50% of those claimed under claim n° 8, balance magnesium and impurities, all of the higher order additions aimed at fine dispersions of precipitates synergistically formed from any of the combinations of higher order alloying additions possible between sub-groups a) to e) or to d) in claim 8, in particular an alloy containing 0.2 to 10 wt.% Ce, La, Pr, Nd or Sm and of 0.5 to 3 wt.% Al and of 0.1 to 1 wt.% Ca, Sr or Ba, followed by employing the alloy conversion routes claimed by claim 11 and 12, but without communion, as well as those routes following claim n° 12.7.

Claim 11 Methods of producing a Mg- or Al-base alloy according to one or more of claims 1. to 4. and claims 8. to 10., the alloys made by ingot- and/or pressure die-casting methods and/or by vapour deposition, melt spinning, EHD-atomization and mechanical alloying / ball and/or bar and/or rod milling techniques, then making products including extruded bars and rods, fabrication of forgings, (rolling to) sheets, plates, foils and (eg. drawing to) tubes and wires, the fabrication of theses products eventually including (pre-) treating and/or (pre-) compaction methods such as degassing at temperatures up to 500°C, and/or the residual "free" hydrogen not exceeding levels of 2000 ppm, in particular 1 ppm preheating, hot (isostatic) pressing, in particular at 60° to 550°C, cold (isostatic) pressing at pressures between 50 and 1400 MPa, direct powder forging, explosive and/or shock consolidation, and metal powder injection molding providing parts of high complexity and accuracy at low costs, including

progressive decomposition during debinding at temperatures between 150° and 600°C allowing a wide range of geometric options including undercuts, tapered surfaces and cross holes (see claim n° 15).

12th claim Methods of producing a magnesium or aluminium based alloy according to one or more of claims 1. to 2.24 and claims 4. and claim 8. to 10. and resultant (eg. near-net shape) products according to claim 15.1 and/or claim 15.2. the methods are further characterized by employing at least one of the following alloy conversion routes:

12.1 extrusion of corresponding powders and/or in-situ-consolidated and/or CIPed and/or HIPed preforms, layers etc. and/or alloys:

- a) - for Mg-rare earth metal and/or - misch-metal according and/or - Sc and/or -Y based solid solutions and corresponding higher order alloy systems according to claims 4.1, 4.2 and 4.6 employing preheating cycles of 0.2 to 10 h at 35° to 450°C. the extrusion at reduction ratios between 3:1 and 45:1 at extrusion temperatures of 15° to 400°C. in particular at reduction ratios between 8:1 to 22:1 using extrusion temperatures of 50° to 250°C. the affordable ram speeds claimed herein ranging from 0.001 to 15 mm/sec, in particular from 0.01 to 4 mm/sec,
- then followed by at least one heat treatment at temperatures between 60° to 300° C, in particular at between 80° and 280°C for stress relieve and/or selected precipitation and/or (selected) dissolution of GP- zones and/or precipitates and other second phases without (substantially) reducing the passivating effect originating in corresponding extended solid solution of rare earth elements in cph-Mg or any other non-equilibrium Mg-base matrix phase,
- or not followed by such an heat treatment.
- b) - for Mg- or Al-transition metal based solid solutions and higher order Mg-TM-TM-TM and Al-based alloy systems as well as for higher order solid solutions with rare earth and transition metals and corresponding higher order alloy systems as well as for Mg-metalloid (Si, Ge, B, Sb, Be) based solid solutions with and without RE and TM according to claims 4.3 to 4.6. employing the extrusion at reduction ratios between 3:1 and 45:1 at extrusion temperatures of 15° to 500°C. in particular at reduction ratios between 8:1 to 22:1 at extrusion temperatures of 50° to 320°C. all after pre-heating for 0.1 to 10 h in corresponding temperature ranges. the affordable ram speeds claimed herein ranging from 0.001 to 15 mm/sec, in particular from 0.01 to 4 mm/sec,
- then followed by at least one heat treatment at temperatures between 60° to 400°C. in particular at between 80° and 280°C for stress relieve and/or selected precipitation and/or (selected) dissolution of GP-zones and/or precipitates and other second phases without (substantially) reducing the passivating effect originating in corresponding extended solid solution of the transition and/or rare earth metals and/or metalloid elements in cph-Mg, fcc-Al or any other non-equilibrium Mg-base or Al-base matrix phase,
- or not followed by such an heat treatment. and/or

12.2 rolling of corresponding powders and/or in-situ-consolidated and/or CIPed and/or HIPed preforms, layers etc. and/or alloys:

- a) - for alloy groups as to item 12.1a of this claim n°12. but forming corresponding alloy pre-form or billet into a rolling stock which is then preheated for 0.1 to 10 h to temperatures ranging from 90° to 520°C followed by rolling the heated stock at a rolling speed at the surface of the employed rolls, which ranges from 0.05 to 100 m/min, thereby adjusting the gaps of the rolls so to reduce thickness by 0.5 to 80% per pass and to arrive at sheet and plate thickness 0.1 to 10 mm, performed at temperatures ranging from 100° to 500°C, in particular at temperatures between 130° and 500°C, using no or at least one additional heat treatment between the required rolling passes, the rolling passes thereby involving a fixed or a variable thickness reduction ratio depending on the number of prior-rolling passes employed.
- then followed by an heat treatment at temperatures between 60° to 400° C, in particular at between 80° and 280°C for stress relieve and/or selected precipitation and/or (selected) dissolution of GP- zones and/or precipitates and other second phases without (substantially) reducing the passivating effect originating in corresponding extended solid solution of rare earth elements, MM and Sc in cph-Mg any other non-equilibrium Mg-base matrix phase,
 - or not followed by such an heat treatment,
- b) - for alloy groups as to item 12.1b of this claim n°12. but forming corresponding alloy pre-form or billet into a rolling stock which is then preheated for 0.1 to 10 h to temperatures ranging from 70° to 520°C followed by rolling the heated stock at a rolling speed at the surface of the employed rolls, which ranges from 0.05 to 100 m/min, thereby adjusting the gaps of the rolls so to reduce thickness by 0.5 to 80% per pass and to arrive at sheet and plate thickness 0.1 to 10 mm, performed at temperatures ranging from 50° to 450°C, in particular at temperatures between 110° and 500°C, using no or at least one additional heat treatment between the required rolling passes, the rolling passes thereby involving a fixed or a variable thickness reduction ratio depending on the number of prior-rolling passes employed,
- then followed by an annealing treatment at temperatures between 60° to 400°C, in particular at between 80° and 280°C for stress relieve and/or selected precipitation and/or (selected) dissolution of GP-zones and/or precipitates and other second phases without (substantially) reducing the passivating effect originating in corresponding extended solid solution of the transition and/or rare earth metals and/or metalloid elements in cph-Mg, fcc-Al or any other non-equilibrium Mg-base or Al-base matrix phase.
 - or not followed by such an heat treatment, and/or

12.3 forging operations of corresponding powders and/or in-situ-consolidated and/or CIPed and/or HIPed and/or (extruded) preforms, layers etc. and/or alloys:

- a) - for alloy groups as to item 12.1a of this claim n°12. the forging performed at temperatures ranging from 50° to 520°C eventually after pre-heating for 0.1 to 10 h at corresponding temperatures, the forging in particular at temperatures between 170° and 450°C, thereby deforming corresponding consolidated alloy (in particular cylindrical) preform or billet by

at least 10- 50% or by more than 50% by employing a closed-die or an open-die forging method.

- then followed by an heat treatment at temperatures between 60° to 400° C. in particular at between 80° and 280°C for stress relieve and/or selected precipitation and/or (selected) dissolution of GP- zones and/or precipitates and other second phases without (substantially) reducing the passivating effect originating in corresponding extended solid solution of rare earth elements, MM and Sc in cph-Mg any other non-equilibrium Mg-base matrix phase,
- or not followed by such an heat treatment.

b) - for alloy groups as to item 12.1b of this claim n°12. the forging performed at temperatures ranging from 50° to 520°C eventually after pre-heating for 0.1 to 10 h at corresponding temperatures. the forging in particular at temperatures between 150° and 450°C. thereby deforming corresponding consolidated alloy (in particular cylindrical) preform or billet by at least 10-50% or by more than 50% by employing a closed-die or an open-die forging method.

- then followed by an annealing treatment at temperatures between 60° to 400°C, in particular at between 80° and 280°C for stress relieve and/or selected precipitation and/or (selected) dissolution of GP-zones and/or precipitates and other second phases without (substantially) reducing the passivating effect originating in corresponding extended solid solution of the transition and/or rare earth metals and/or metalloid elements in cph-Mg, fcc-Al or any other non-equilibrium Mg-base or Al-base matrix phase,
- or not followed by such an heat treatment. and/or

12.4 drawing, deep drawing including direct and reverse redrawing, bending, and stretch forming of corresponding as-mechanically alloyed, as-extruded or as-rolled alloy products of the a)- or b)-type of Mg-base or Al-base non-equilibrium matrix phase alloy (cf. claim 12.1a) and claim 12.1b)) and at temperatures in the temperature ranges given for extrusion of the alloy of claims 12.1a or 12.1b of this claim n°12, and/or

12.5 superplastic forming of as-CIPed and/or as-HIPed (cf. claim 11) and/or as-extruded and/or as-rolled alloy products of the a)- or b)-type of Mg-base or Al-base non-equilibrium matrix phase alloy (cf. claim 12.1a) or 12.1b)) into simple and complex shapes by employing strain rates ranging from $8 \cdot 10^{-1}$ to 10^{-5} /sec at temperatures ranging from 20° to 450°C. in particular at temperatures ranging from 100° to 350°C employing strain rates ranging from 10^{-1} to 10^{-3} /sec. and/or

12.6 - mixing the (eventually from consolidated preforms communitied) powder with suitable reinforcement including particulates, short and long fibers and / or whiskers according to at least one of the compounds of claims 2.. 2.2.6 and/or 2.2.7. and/or a variant, in particular after a refinement by using a ball milling technique to particle sizes in the range of 0.2 to 5 μm . or no such mixing. then

- degassing for 0.5 to 10 hrs at temperatures ranging from 180° to 450°C and/or
- or no such degassing. and/or

- preheating for 0.5 to 6 hrs at temperatures in the range from 200°C to 450°C, and/or
 - hot-isostatic pressing for 1 to 6 h at 100°C to 450°C and/or
 - preheating for 1 to 4 hrs up to the temperatures required in one or more of claims 12.1 to 12.5 followed by an alloy conversion as is given by any combination of the claims under claim 12.1 to 12.5 and 12.7 of corresponding a)- or b)-type of Mg-base extended solid solution alloy and/or
- 12.7 after any one of the alloy conversion routes given under item 12.1 to 12.6 of this claim n°12 followed by directly quenching the said product form after finishing the forming operations in oil or water at temperatures ranging from 10°C to 90°C or by cooling in air, and then by
- a) either a final annealing treatment for 1 to 100 hrs at 60°C to 150°C, in particular for 1 to 5 hrs at 80 - 100°C, or
 - b) by an artificial ageing treatment for 1 to 1000 hrs, in particular for 1 to 300 hrs at temperatures between 130°C and 350°C, or
 - c) no further treatment and / or
 - d) an annealing treatment after application of corresponding alloy product at any time using the conditions as given under a)- and/or b)-type of methods of this claim n° 12.

Claim 13. A magnesium alloy according to claim 3 and/or a Mg-based product according to claim 15.1, corresponding processing is characterized further by holding the as-cast alloy for 0.5h to 1000 hrs at temperatures as to claim 3.3.2, to solutionize intermetallic and/or second phases separated from the melt during casting and/or solidification, or no such solution heat treatment, then followed by either

- no further treatment or
- an artificial ageing treatment at temperatures between 140 to 400°C, in particular at between 150°C and 280°C for 0.25 to 1000 hrs and/or
- quenching the said product form in oil or water at temperatures ranging from 10°C to 90°C, in particular from 20°C to 80°C, and/or quenching in air and/or

in all (three) cases followed by

- a final annealing treatment for 0.1 to 10 hrs at 60°C to 120°C, in particular for 1 to 5 hrs at 80°C to 100°C, the final annealing treatment to be repeated at any time during the life time of corresponding component in service in order to dissolve grain boundary phases and/or residual stresses accumulated by any loading and/or microstructural evolution or
- by no further treatment and/or

- 13.1 a magnesium alloy according to claim 3 and/or 13 and/or a Mg-based product according to claim 15.1, corresponding processing is characterized further by holding the as-cast alloy during a solution heat treatment for 0.25h to 1000hrs at temperatures as to claim 3.3.2, where the passivating component (cf. claim 3) and/or a substantial part of the ternary and/or higher order alloying addition is taken again and/or held in solid solution, or no such solution heat treatment, then followed by either no forming operation and/or

- extrusion at 280° to 550°C, in particular at 350° to 480°C using an extrusion ratio of 10:1 to 40:1, in particular of 12:1 to 25:1, and / or
 - either rolling at 360° to 560°C, in particular at 390° to 480°C using no or at least one additional heat treatment between the required rolling passes,
 - or forging operations at 360° to 560°C, in particular at 380° to 480°C using at least one additional heat treatment between the required forging operations,
- or no rolling or forging operation after extrusion, then followed
- either by directly quenching the said product form in oil or water at temperatures ranging from 10° to 90°C, in particular from 20° to 80°C and/or in air and/or
 - or by a second solution treatment for 0.1h to 300 hrs at temperatures as to claim 1, sub-item 1.3.2, and then quenching the said product form in oil or water at temperatures ranging from 10° to 90°C, in particular from 20° to 80°C and/or in air and/or
 - followed by an artificial ageing treatment at temperatures between 140 to 400°C, in particular at between 150°C and 280°C for 0.25 to 1000 hrs and/or
- in all (three) cases followed by
- a final annealing treatment for 0.1 to 10 hrs at 60° to 120°C, in particular for 1 to 5 hrs at 80° to 100°C, the final annealing treatment to be repeated at any time during the life time of corresponding component in service in order to dissolve grain boundary phases and/or residual stresses accumulated by any loading and/or microstructural evolution or
 - by no further treatment and/or

13.2 a magnesium alloy according to one or more of claim 3, 13, and 13.1 and/or a Mg-based product according to claim 15.1, corresponding processing is characterized further by a maximum level of claim 3-type of solutes multiplied by a factor of 1.5, the methods employed are characterized by fragmentation of the melt including solidification at intermediate and at relatively high growth rates as obtainable by (inert) gas atomization including spray forming and/or spray deposition techniques, especially those methods using a linear atomizer concepts, i.e. a linearly extended cross-over for atomization with improved productivity, as well as continuous chill-block quenching techniques such as planar flow casting, melt-spinning and twin-roller quenching and/or characterized by laser alloy surface re-melting with and without at least one of the additions of a passivating component as to claim 3, in order to produce a micrograined microstructure and large boundary strengthening effects, eventually associated with large solid solution strengthening and, in any case, with an enhanced passivating effect and a reduced time for solution heat treatments of the said (rapidly) solidified surface and/or microstructure as compared to corresponding as-cast 15.2-type of products) alloy conversion into products such as extrusion into bars and rods, fabrication of forgings, (eg. rolling to) sheets, plates, foils, and (eg. drawing to) tubes and wires and/or

13.3 a magnesium alloy according to one or more of claim 3 and 13 to 13.2 and/or a Mg-based product according to claim 15.1 and/or 15.2, corresponding processing is characterized

further by holding the as-solidified alloy during a solution heat treatment for 0.25h to 1000hrs at temperatures as to claim 3.3.2. where the passivating component and/or a substantial part of the ternary and/or higher order alloying addition (claim 3) is taken again and/or held in solid solution. or no such solution heat treatment. then followed by either

- comminution to flakelike powder in case of chill-block quenched foils. and/or by
- degassing for 0.5 to 10 hrs at temperatures ranging from 200° to 420°C. and/or by
- preheating for 0.5 to 4 hrs at 200° to 350°C. and/or by
- hot-isostatic pressing for 1 to 6 h at 200° to 500°C followed by
- preheating for 1 to 4 hrs at 200° to 400°C.

and / (or no comminution etc.. but the as-solidified or as-solutionized alloy directly)

- extruded at 100° to 550°C. in particular at 280° to 480°C using an extrusion ratio of 8:1 to 40:1. in particular of 10:1 to 25:1 at higher extrusion temperatures (i.e. 150° - 550°C). and / or
- a solutionizing treatment for up to 10 hrs at 340° to 500°C. in particular at 380° to 450°C in which the alloying elements are substantially held and/or taken again into solid solution. and/or followed by either
- rolling at 220° to 560°C. in particular at 390° to 480°C using no or at least one additional heat treatment between the required rolling passes, or
- forging operations at 200° to 560°C. in particular at 250° to 450°C using at least one additional heat treatment between the required forging operations, or

no rolling or forging operation after extrusion. and/or followed by

- directly quenching the said product form in oil or water at temperatures ranging from 10° to 90°C. in particular from 20° to 80°C and/or in air and/or
- by a second solution treatment for 0.1h to 300 hrs at temperatures as to claim 1, sub-item 1.3.2. and then quenching the said product form in oil or water at temperatures ranging from 10° to 90°C. in particular from 20° to 80°C and/or in air and/or
- followed by an artificial ageing treatment at temperatures between 140 to 400°C. in particular at between 150°C and 280°C for 0.25 to 1000 hrs and/or

in any case of the preceding processing alternatives followed by

- a final annealing treatment for 0.1 to 10 hrs at 60° to 120°C. in particular for 1 to 5 hrs at 80° to 100°C. the final annealing treatment to be repeated at any time during the life time of corresponding component in service in order to dissolve grain boundary phases and/or residual stresses accumulated by any loading and/or microstructural evolution or
- by no further treatment and/or

13.4 a magnesium alloy according to one or more of claim 3 and 13 to 13.3 and/or a Mg-based product according to claim 15.1 and/or 15.2. corresponding processing is characterized further by thin strip casting including fragmentation of the alloy melt such as by spray deposition techniques according to claim 8 and without fragmentation of the alloy melt to result in cross-sections ranging from 0.1 to 10 mm. in particular between 0.2 and 5 mm to

achieve sufficient boundary strengthening effect without the need to recur to fragmentation and subsequent consolidation methods as under claim 9, but with a reduced time for solution heat treatments of the said product and/or microstructure in the as-solidified state as compared to corresponding as-cast microstructure and products obtained by conventional casting methods (claim 15.2) and the products are characterized further by fabrication (eg. rolling) to sheets, plates, foils and (eg. drawing to) tubes and wires and/or

13.5 a magnesium alloy according to one or more of claim 3 and 13 to 13.3 and/or a Mg-based product according to claim 15.1 and/or 15.2, corresponding processing is characterized further by holding the as-cast alloy during a solution heat treatment for 0.25h to 1000hrs at temperatures as to 3.3.2, where the passivating component and/or a substantial part of the ternary and/or higher order alloying addition is taken again and/or held in solid solution, or no such solution heat treatment, and/or followed by

- rolling at 200° to 560°C, in particular at 250° to 500°C using no or at least one additional heat treatment between the required rolling passes, and/or
- by either directly quenching the said product form in oil or water at temperatures ranging from 10° to 90°C, in particular from 20° to 80°C and/or in air and/or
- by a second solution treatment for 0.1h to 300 hrs at temperatures as to claim 1, sub-item 1.3.2, and then quenching the said product form in oil or water at temperatures ranging from 10° to 90°C, in particular from 20° to 80°C and/or in air and/or
- quenching the said product form in oil or water at temperatures ranging from 10° to 90°C, in particular from 20° to 80°C and/or in air after the second solution heat treatment and/or
- followed by an artificial ageing treatment at temperatures between 140 to 400°C, in particular at between 150°C and 280°C for 0.25 to 1000 hrs and/or

in any of the preceding processing alternatives followed by

- a final annealing treatment for 0.1 to 10 hrs at 60° to 120°C, in particular for 1 to 5 hrs at 80° to 100°C, the final annealing treatment to be repeated at any time during the life time of corresponding component in service in order to dissolve grain boundary phases and/or residual stresses accumulated by any loading and/or microstructural evolution or
- by no further treatment.

Claim 14 A magnesium or aluminium based alloy and/or corresponding (semi-finished) product according to one or more of claims 1 to 13, the alloy and/or (semi-finished) product characterized further by being joined with like-like Mg-base or Al-base joints made by PVD and/or ball and/or bar and/or rod milling techniques, the mechanical joints being rivets, screws, bolts, self-clinching devices, HT-interference fits) and/or by adhesive bonding methods using rubber and/or epoxy base resin, ethoxyline resin, phenolic base materials) and/or by diffusion bonding (at pressures as high as 30 MPa) and/or by inertia and linear friction welding for high quality welds and joints and/or by thermal spraying (eg. on top of dissimilar metals and/or passive Mg-components and Mg-joints

all coping with like-unlike mechanical joints, and/or by employing high purity joint surfaces and/or adhesive intralayers, and/or cleaning, degreasing, thin coatings including anodizing, pickling and priming (eg. with chromate and dichromate).

Claim 15 Methods of producing a magnesium or aluminium based alloy according to one or more of the claims 1. to 14., the methods and resultant products are characterized further (in particular) by

- 15.1 a) pressure die-casting and/or thin-wall casting a magnesium based alloy according to one or more of claims 1. to 14., to wall thicknesses in the range of 0.2 to 20 mm, in particular in the range of 0.5 to 10 mm, the resultant products used in surface and airborne transport systems such as automobiles and aircrafts, in particular used in trains and/or for aeronautical (space and aerospace) components and/or applications which exposed to weathered conditions and also for computer applications and/or those where the alloy is exposed to oil (base environments), for example, and/or (if comma, read "and/or"):
- b) the resultant products including aircraft seats such as for passengers, pilots including pilot ejection seats, seats for navigators, seat and panels and joints for applications in automobiles, trains and/or aircrafts, signallers, first, second and economy class, all of which eventually to be combined with wrought product forms such as tubular components, and/or seatframes, (aeronautic) instruments and panels, window frames, doors and/or door frames such as for wheel cases, engine access, bomb bays, passenger cells, cockpit canopies and/or windscreen, undercarriage legs, large and/or small wheels including nose wheels, flanges, reelings, pulleys, furthermore brakes and/or brake components, fittings and/or partitions, oxygen bottle brackets, high precision mating components, rotor components such as stubs and/or rotor heads, welded frame structures including radio crate and/or reeling support structures, leading and/or tailing edges, top and/or bottom tips, nacelle upper cowl panels, and/or elevators, wing and/or stabilizer components such as spinners, jet pods, elevator trim tab, aft of spar, wing castings, waffle understructures and/or anti-icing components, for example, and/or housings (clutch, crankcase, gearbox, transmission, lock and pump housings, for example), covers (eg. engine block, engine peripheral and chassis covers) and supporting components (eg. subframe, suspension and bracket parts) and/or
- 15.2 a) ingot casting methods for a magnesium or aluminium based alloy and/or product according to one or more of claims 1. to 14., including extrusion to bars and rods, fabrication of forgings, sheets, plates and foils as well as products by drawing, the resultant products used in surface and airborne transport systems such as automobiles and aircrafts, in particular used in trains and/or for aeronautical (space and aerospace) components and/or applications which exposed to weathered conditions and also for computer applications and/or those where the alloy is exposed to oil (based environments), for example, and/or (if comma, read "and/or"):

b) the resultant products including large structural components, beam floorings, press forgings, intercostal components, door sheets such as for wheel cases, engine access, bomb bays, passenger cells, cockpit canopies and/or windscreen, undercarriage legs, large and/or small wheels including nose wheels, flanges, reelings, pulleys, furthermore brakes and/or brake components, tubes, fittings and/or partitions, oxygen bottle brackets, armament attachment plates, high precision mating components, rotor components such as stubs and/or rotor heads, tanks, components for welded frame structures including radio crate and/or reeling support structures, support profiles in missiles, launchers, satellites, and/or probes, instruments for space, fuselage skins including monocoque structures, fairing skins including those for gear cases, nacelles, doors, wing and/or stabilizer skins including those for monocoque structures, leading and/or trailing edges, top and/or bottom tips, nacelle upper cowl panels, and/or elevators, wing and/or stabilizer components such as spinners, jet pods, elevator trim tab, aft of spar, wing castings, tail unit components such as rudder trim tab, rudder, aileron leading edge, fin trailing and/or dorsal fin skin, inner sheet (and) waffle understructures, anti-icing components, air-ducting and/or inner door skins, for example, and/or any equivalent application in automobiles, trains, missiles, rockets and/or satellites.

16th claim. Laser or electron surface beam (re-)melting or traversing of

- a) the commercial Mg-alloys WE54, WE43, ZE63, ZE41, EZ33, EZ32, AE41, AE42, QE22, EQ21, AZ91D/E, AZ61A/B, AZ31A/B, AM20, AM50, AM60 or any other AM-base alloy, AS41, AS42, and EARS-type of Mg-base alloys including corresponding high purity variants (eg. AE42X1, AM50X1 etc.), EA55RS, EA65RS and resulting products (cf. claim 15) and/ or of
 - b) a novel Mg- and/or Al-alloy and product with compositions as given by one or more of claims n° 1 to 4 and made by either (i) conventional casting or by (ii) advanced processing according to one or more of claims n° 1 through n° 15 of this patent application, in particular corresponding automobile, train, ballistic and satellite applications and/or by (iii) any other advanced method of processing, balance magnesium and impurities, and/or of
- but only the surface microstructure is modified here by employing a laser or electron surface beam withdrawal speed ranging from 0.5 mm/sec to up to 6 m/sec, in particular a withdrawal speed ranging from 1 cm up to 4 m/sec, depending on the alloy employed, in order to obtain a microstructural surface layer with substantial and/or a minor fraction of the alloying elements to be held in the Mg- or Al-base solid solution or in any other resultant metastable structural variant in the surface layer of alloys of bulk compositions given in item a) and b) of this claim n° 16, and/or
- adding complementary (excess) elements to the surface of one or more of these alloys so to change the surface composition with regard to corresponding bulk composition given under item a) and b) of this claim n° 16 or not, the complementary element(s) and level(s) to be

added being either:

- c) - (high purity) Al, Ti, Zr, Mn, Cr, Nb, Mo, Hf, Re, W and/or Ta to result in surface layers with alloying levels from 0.1 to 100%, and/or
 - Si, Ge, B, Sb to result in surface layers with Si-, Ge-, B- and Sb- levels from 0.1 to 100% and/or
 - Zn, Zr, Mn, Ag, Cu, Ni to result in surface layers with Zn-, Zr-, Mn-, Ag-, Cu- and Ni-levels from 0.1 to 100% for the alloys given under item a) and b) of this claim n° 16, and/or being
- d) - the binary alloying elements claimed under one or more of claim n°2, 3, 4 and/or 9 which are employed to produce an Mg- or Al-base extended solid solution or any other Mg- or Al-base non-equilibrium matrix phase alloy at the surface and in the bulk of the alloy.

but here added only to the surface for the alloys given under item a) of this claim n° 16 and to the surface of established (eg. LA141) and novel Mg-Li-based alloys, and to result in surface layers with levels from 0.1 to 100% of these binary elements

and in any of the possibilities claimed under c) and d) of this claim n° 16, the surface excess alloying addition(s) being added by alloying (< 100 %) and/or cladding (100 %) to the surface via laser or electron beam surface (re-)melting or traversing, the purpose of which is

- a surface layer with at least a substantial part of the added and/or prior-bulk surface elements forming a monophase microstructure with minimum microgalvanic activity and maximum surface oxide passivity

or

- a fine dispersion of precipitates synergistically formed from any of the combinations of the surface additions under item c) and d) to the bulk alloys under item a) and the surface additions under item c) to the bulk alloys under item b), but tailored as by a heat treatment claimed under items 1a) and 1b) of claim n°12 so that the passivated Mg-base matrix phases as claimed under claim n° 9 can form and co-exist with these surface precipitates.

the resultant surface microstructures being in any case obtained by employing a laser or electron surface beam withdrawal speed ranging from 0.5 mm/sec to up to 6 m/sec. in particular a withdrawal speed ranging from 1 cm up to 4 m/sec. depending on the alloy employed.

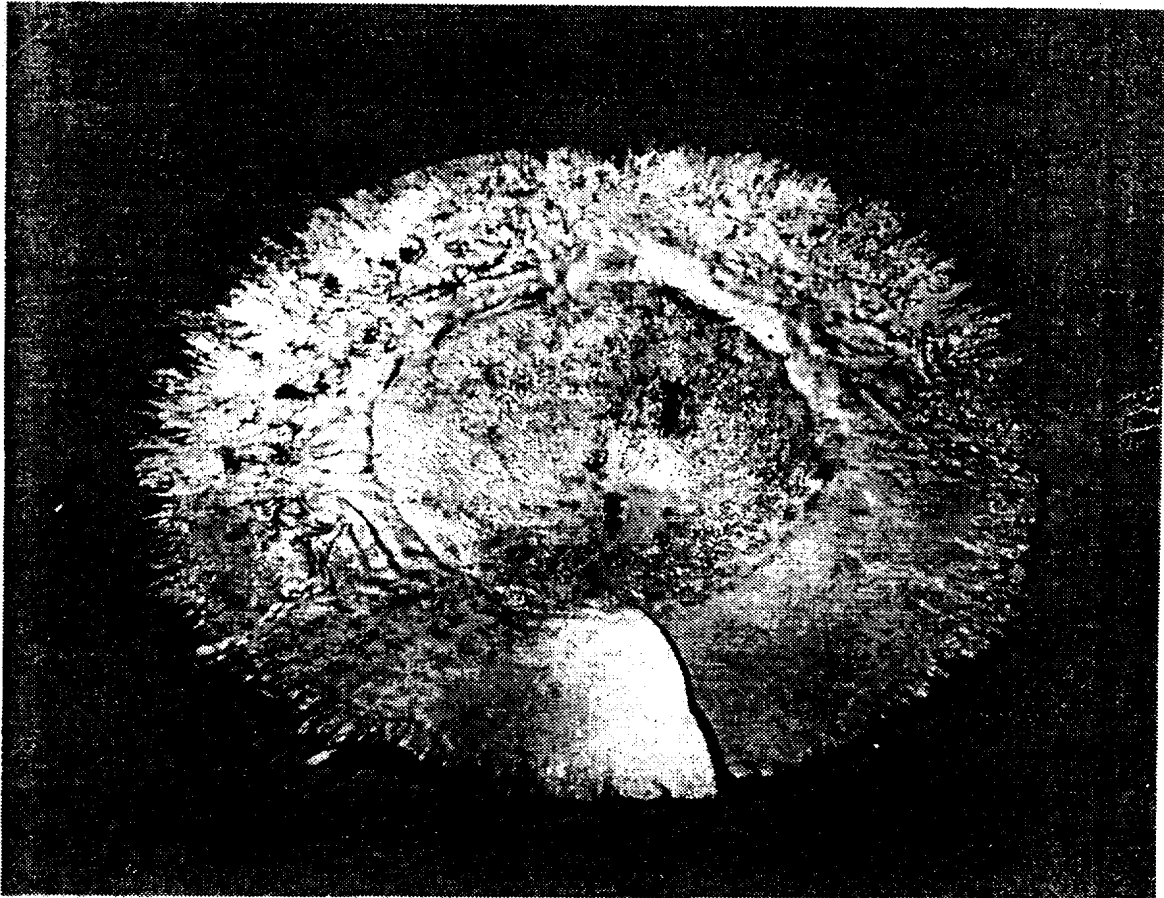


Fig. 1

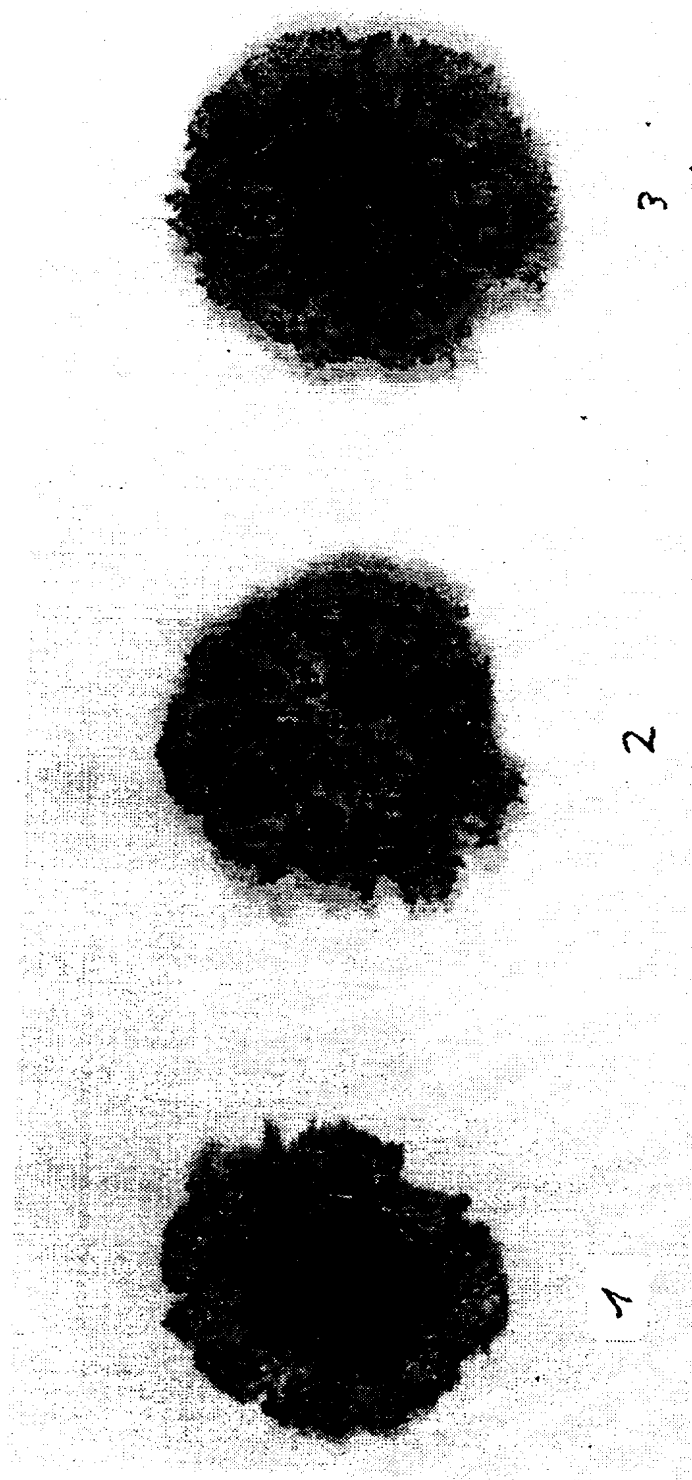


Fig. 2

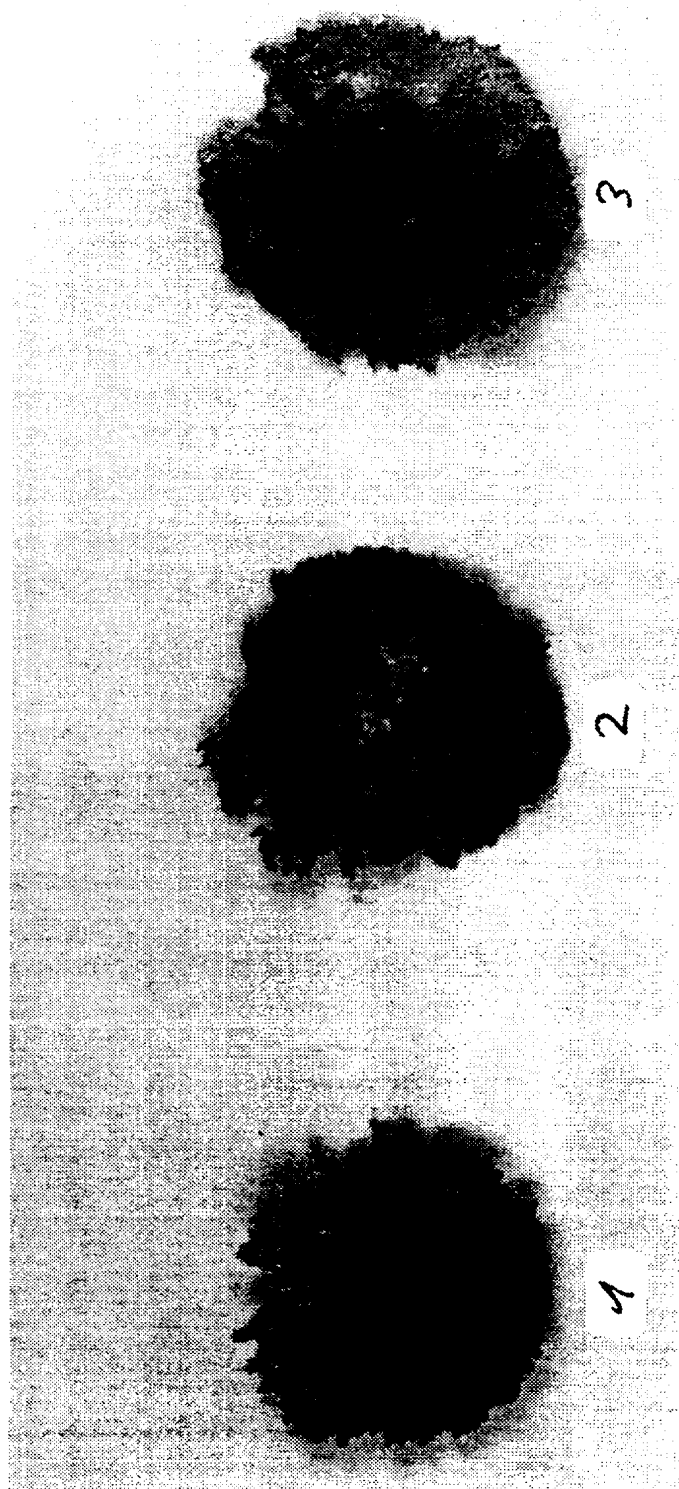


Fig. 3

SUBSTITUTE SHEET (RULE 26)

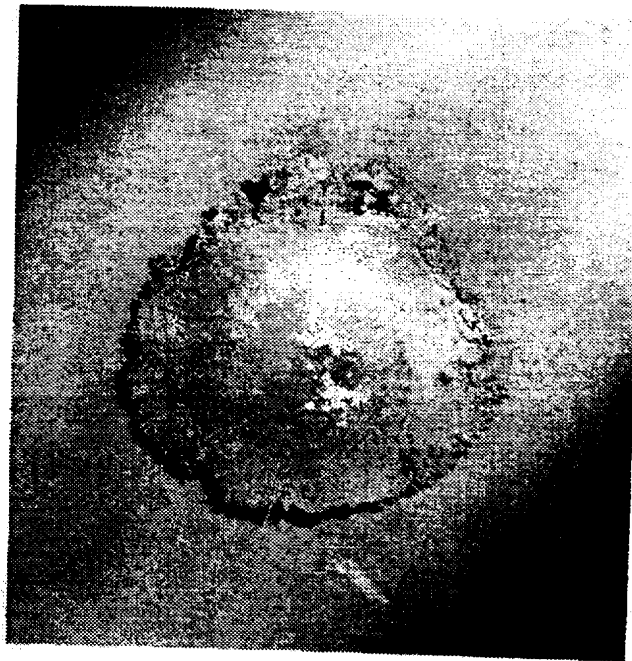


Fig. 4

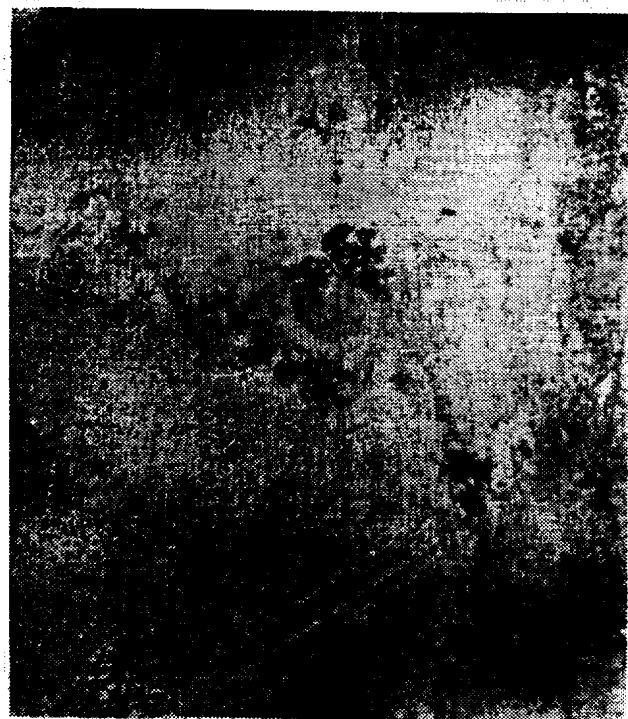
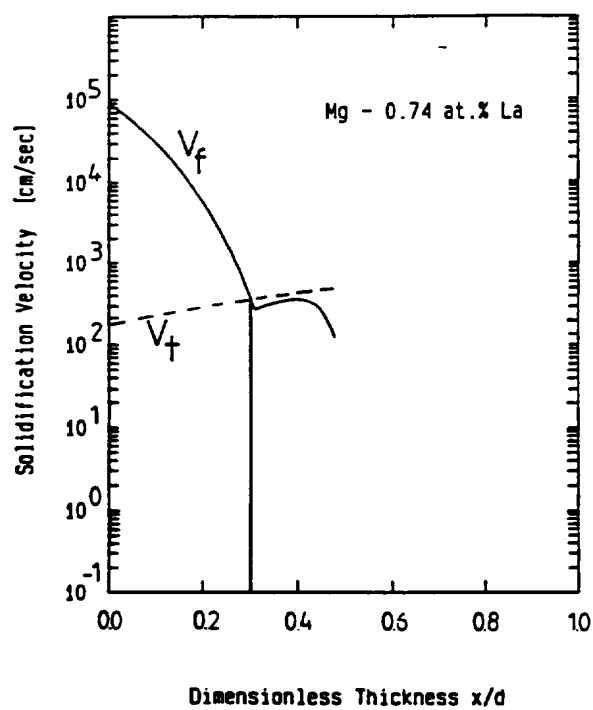


Fig. 5

Fig. 6

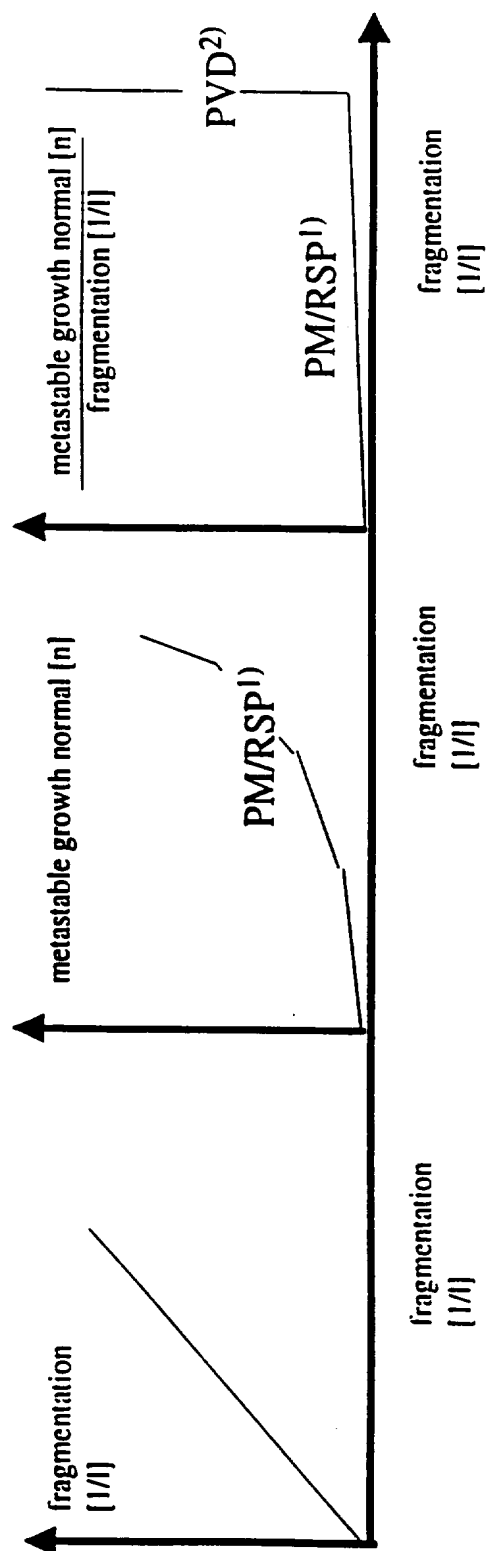
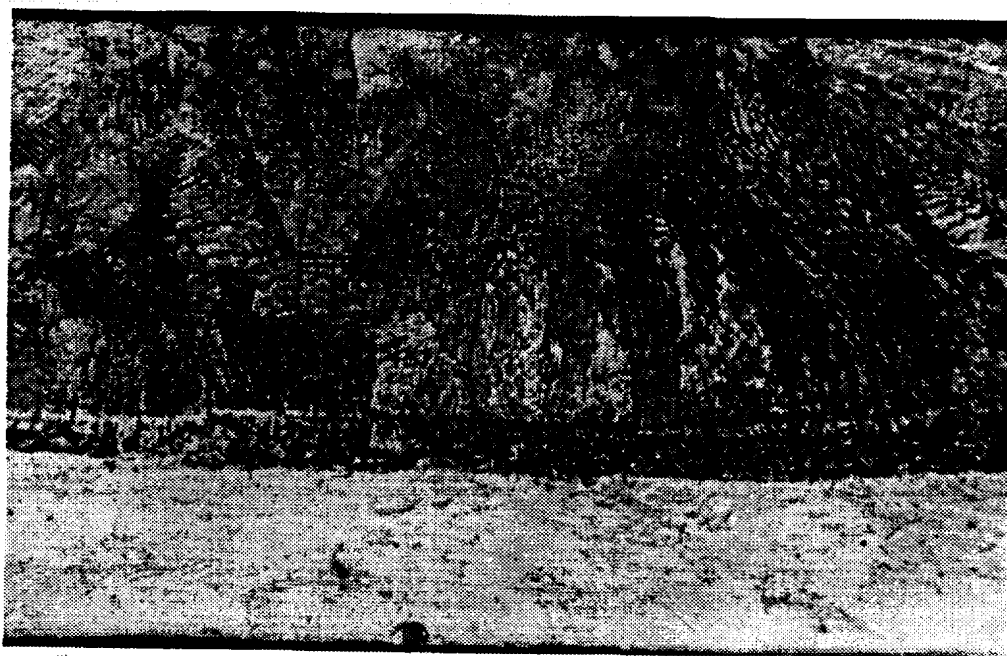


Fig. 7

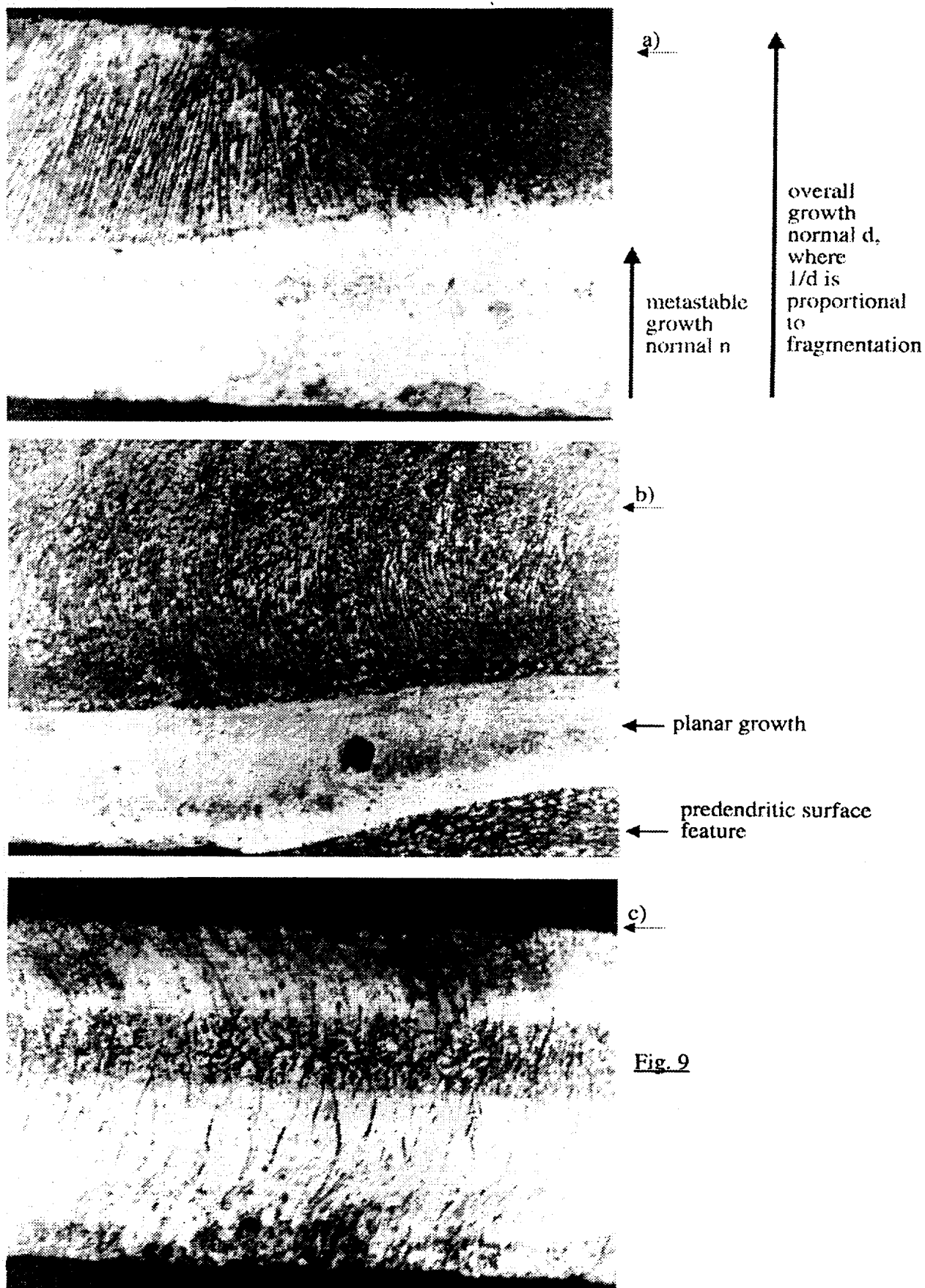


a)



b)

Fig. 8



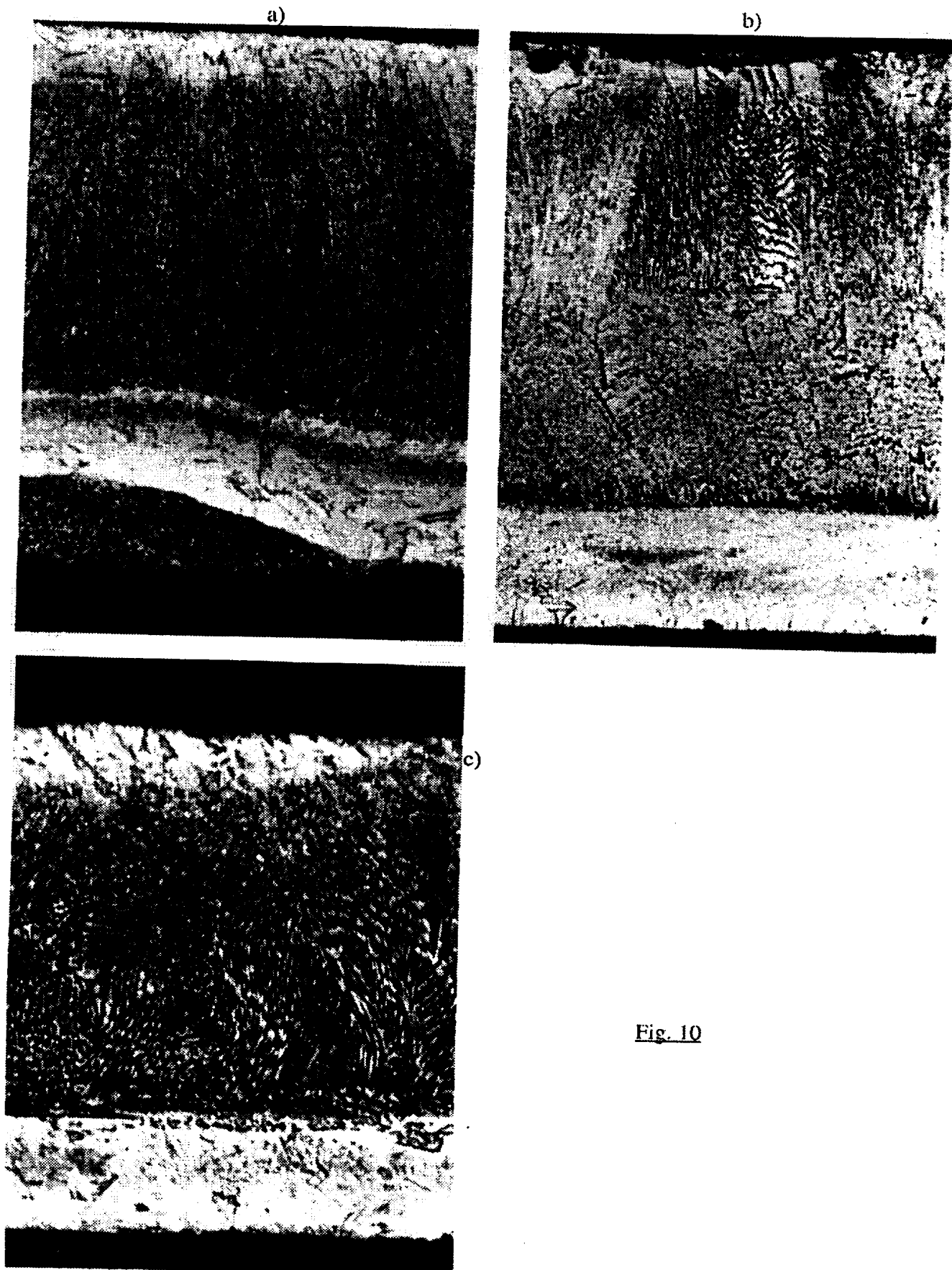


Fig. 10

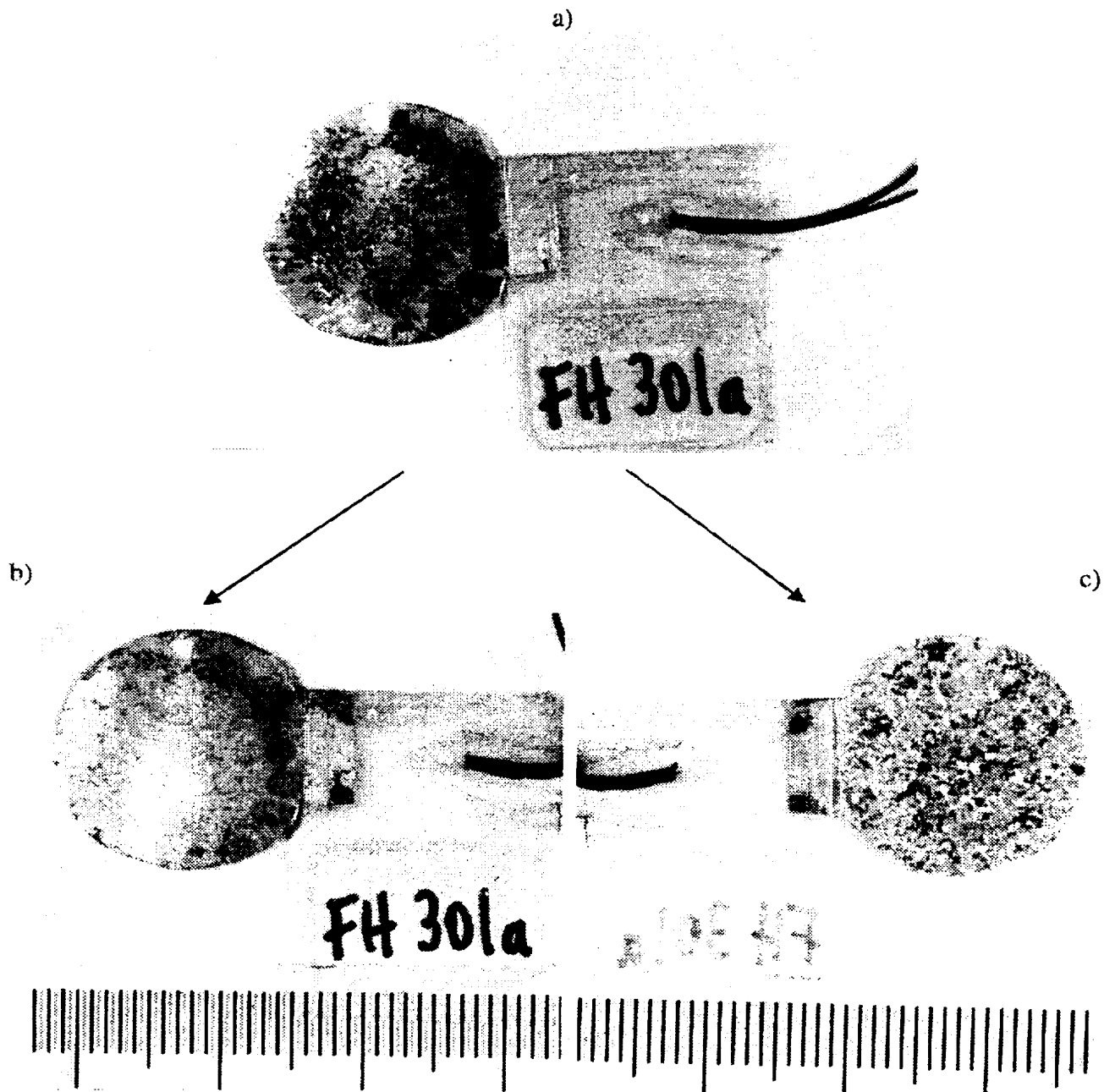


Fig. 11

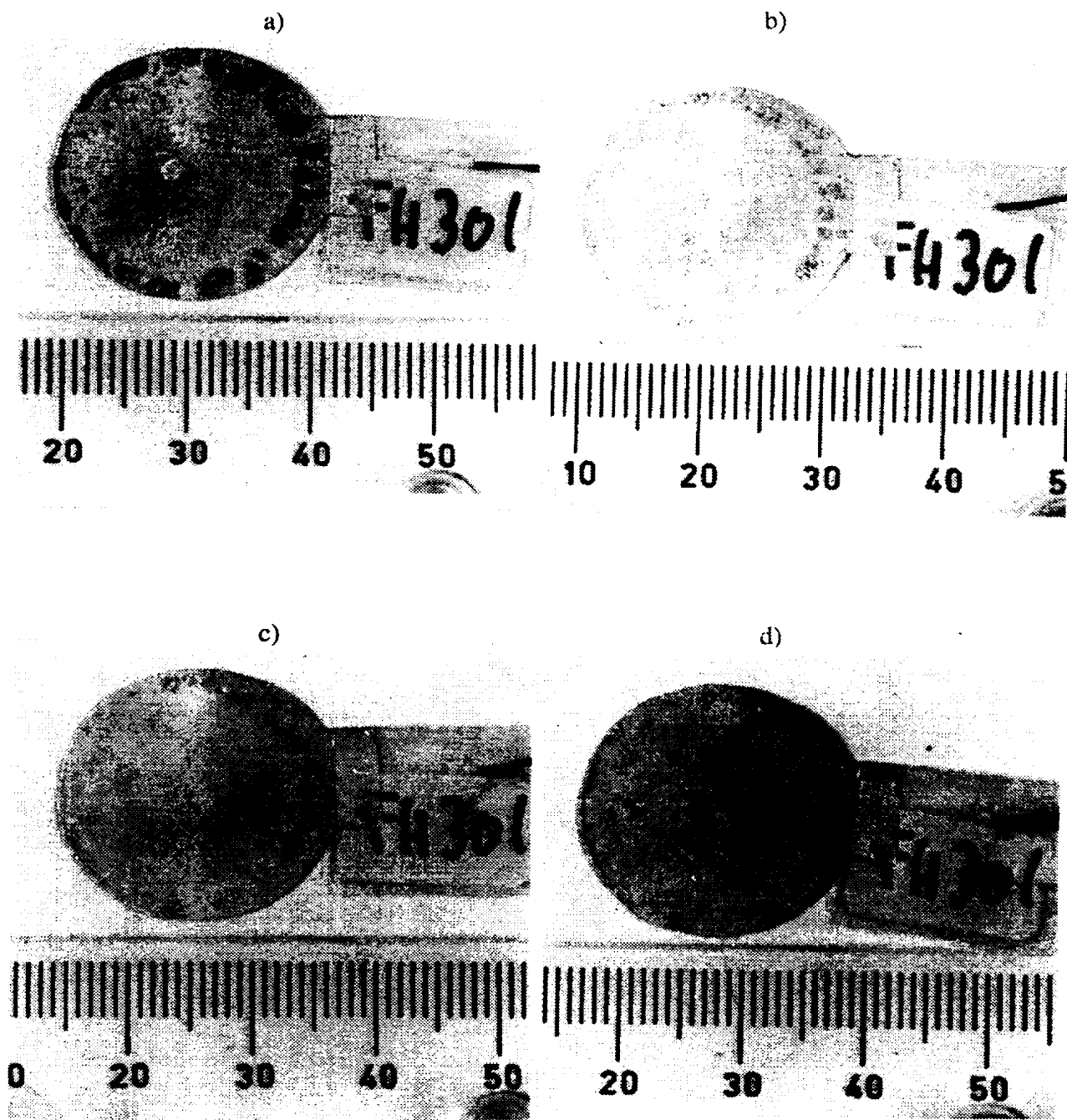
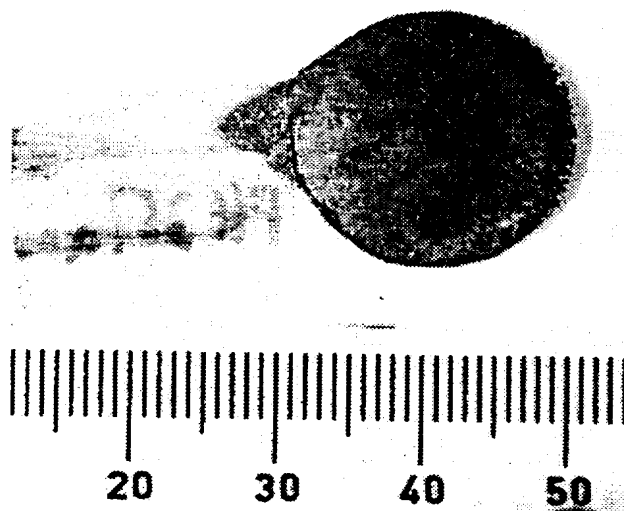


Fig. 12

a)



b)

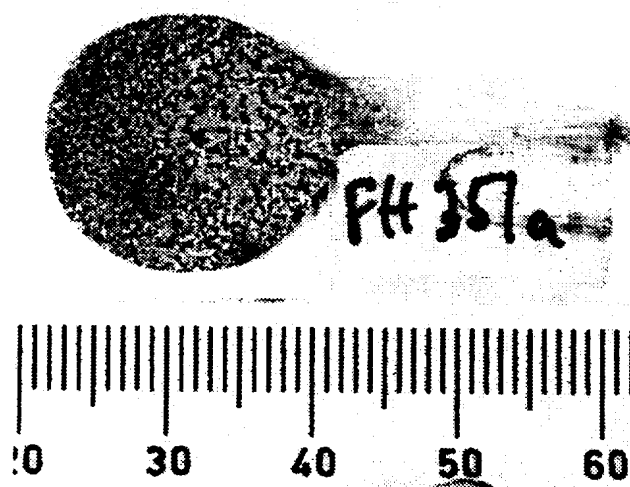


Fig. 13

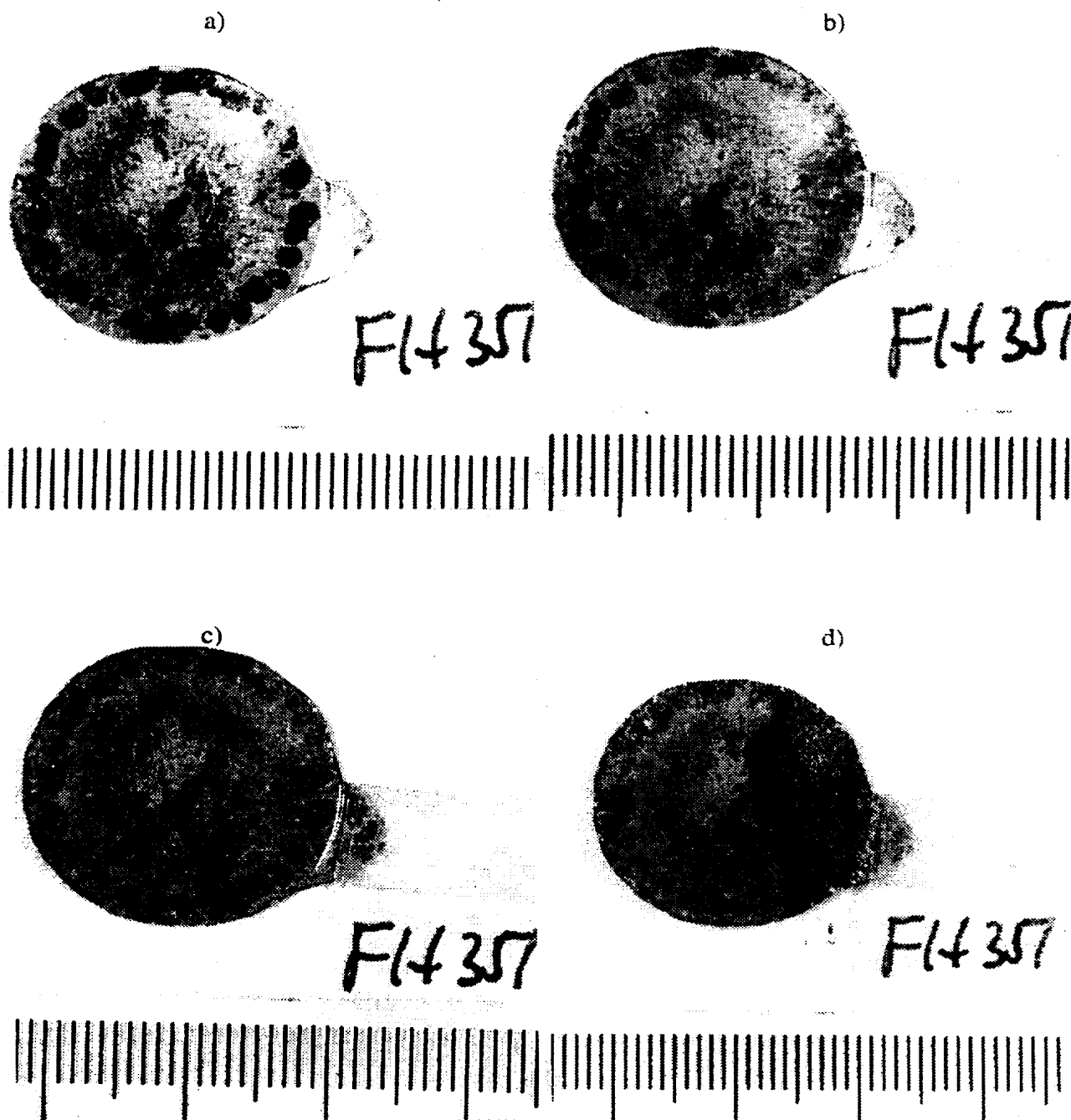


Fig. 14

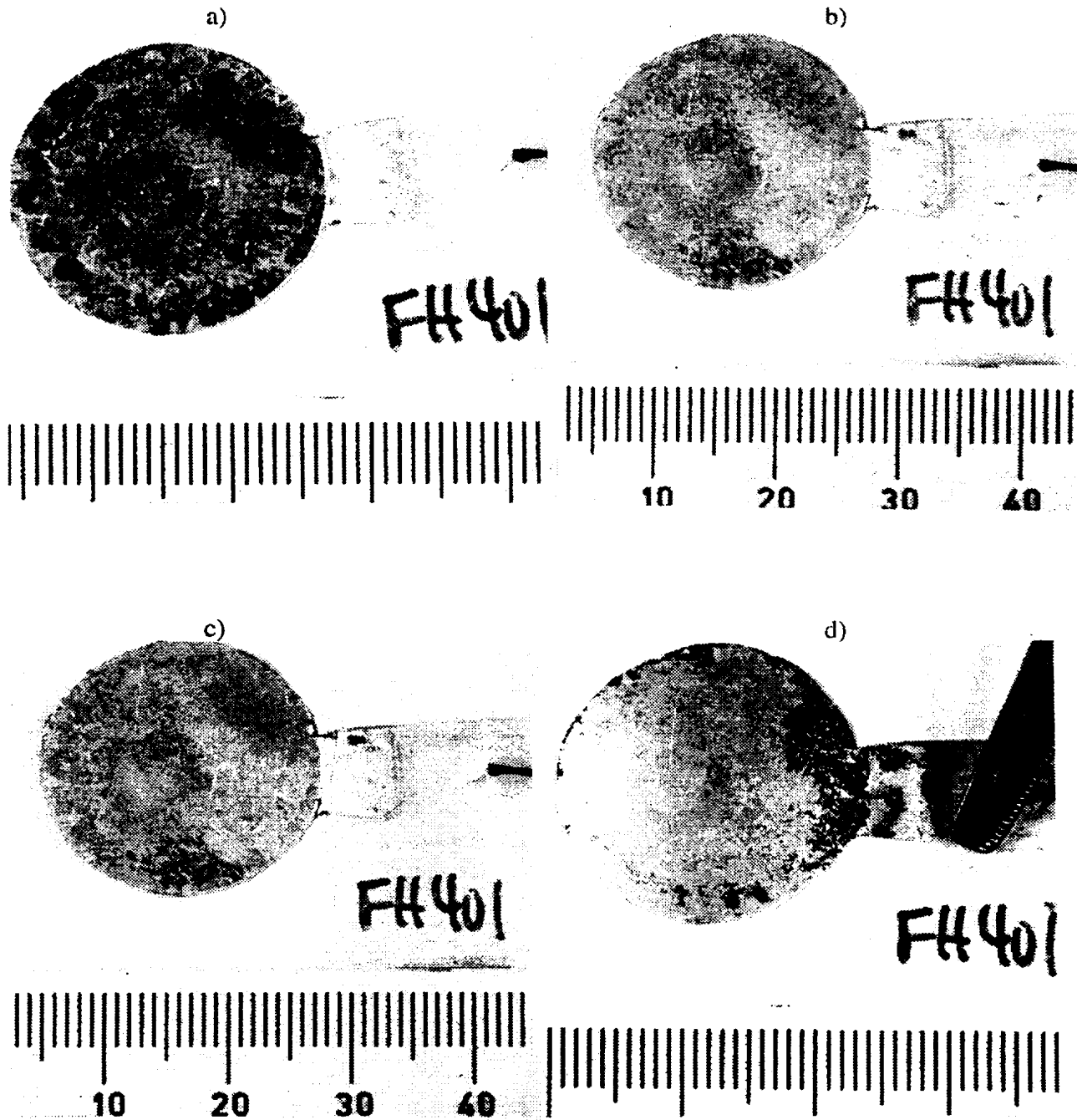
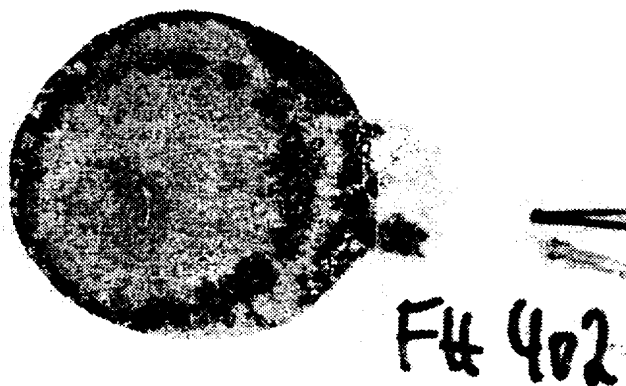


Fig. 15

a)



b)

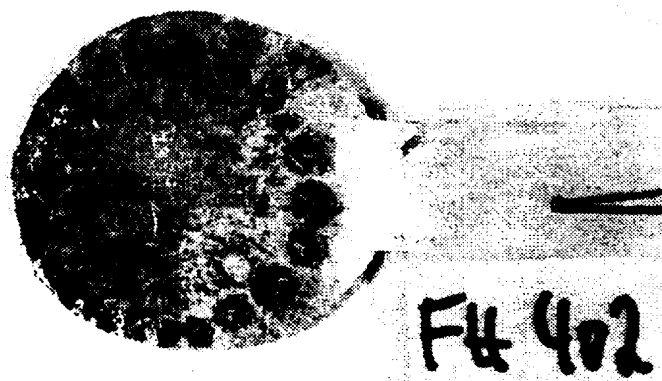


Fig. 16

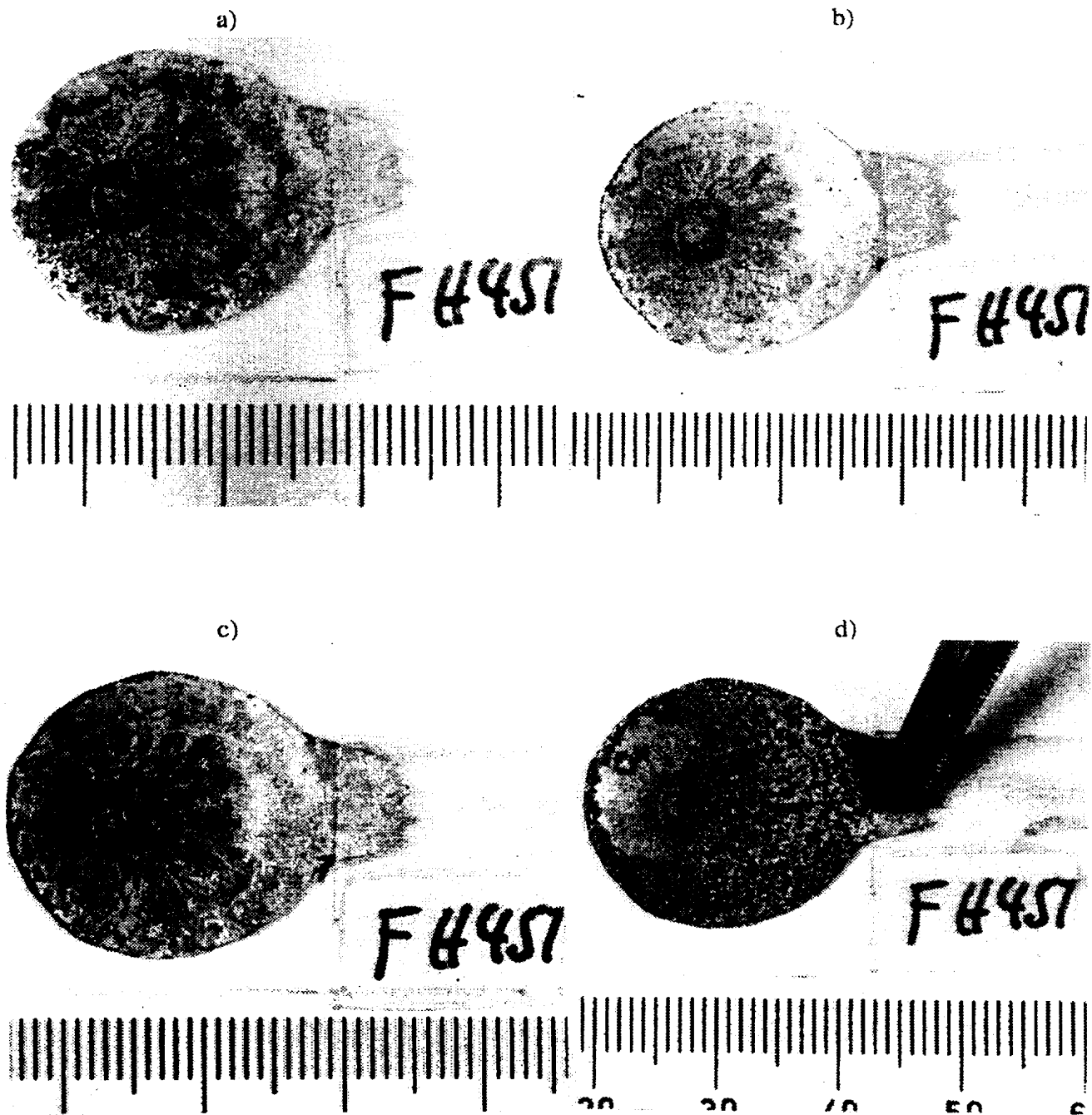


Fig. 17

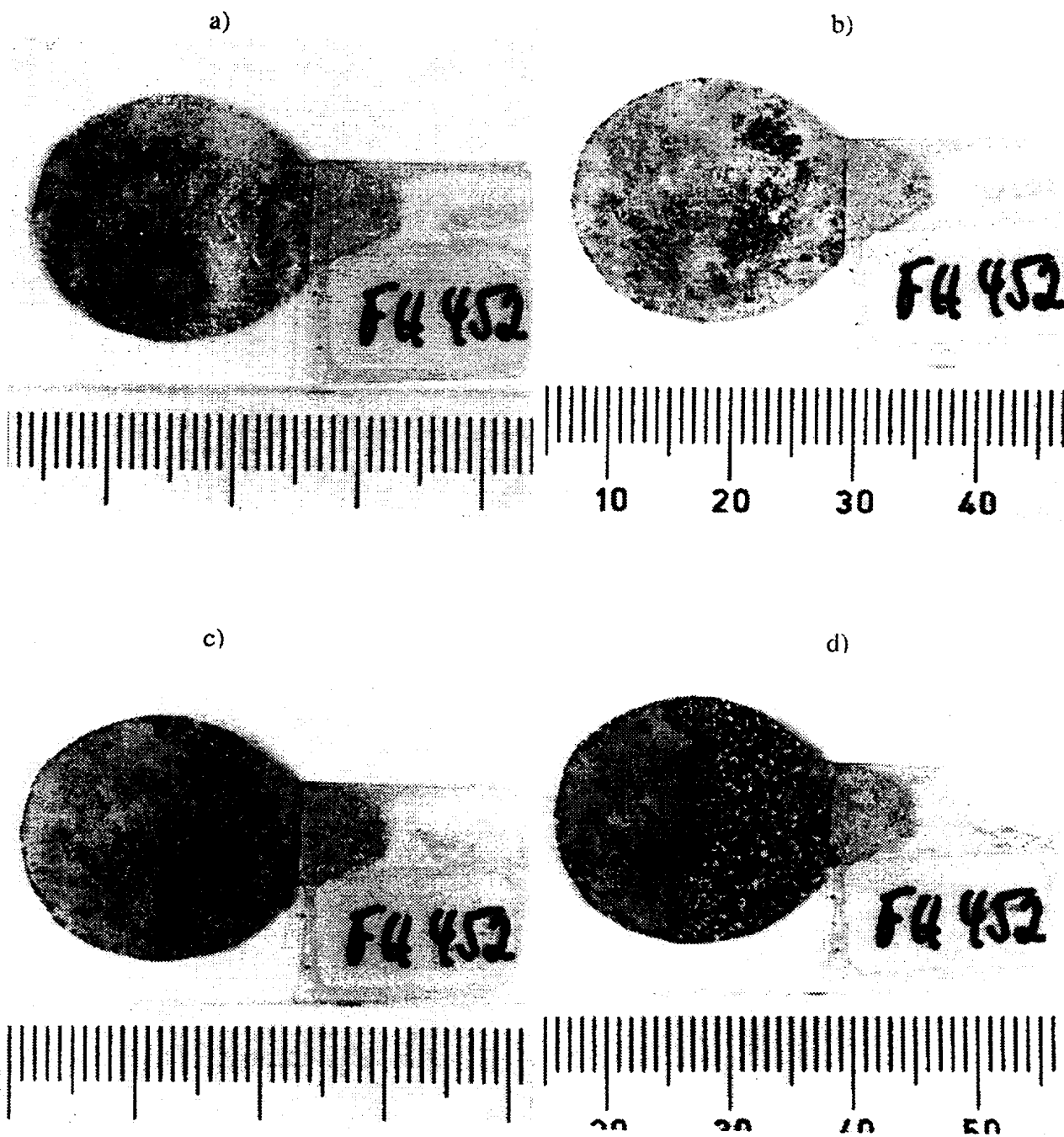
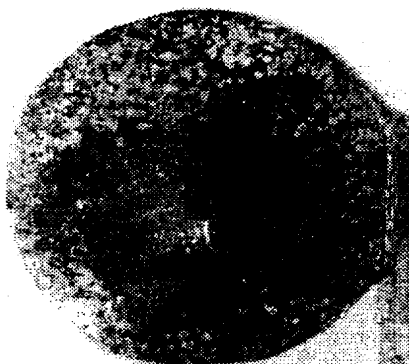


Fig. 18



FH1201a

a)



FH1201a

b)



FH1202

c)



Fig. 19

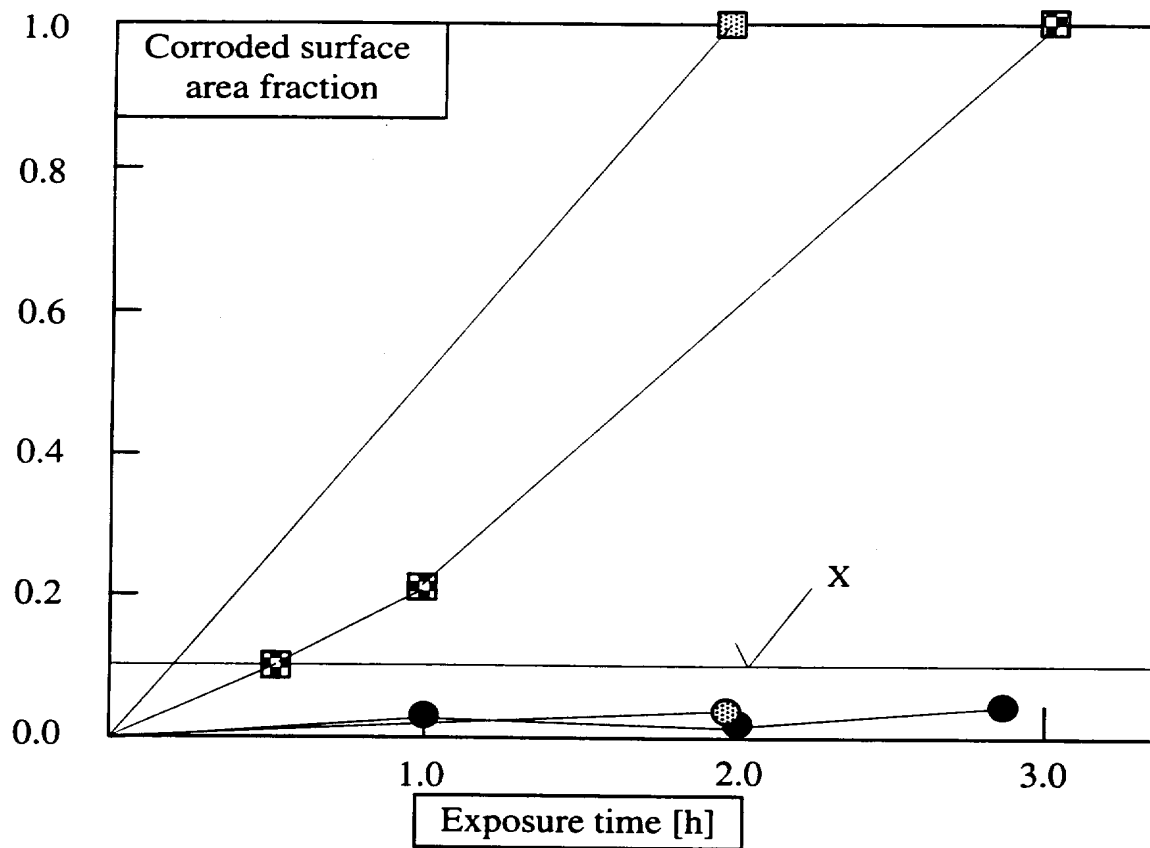
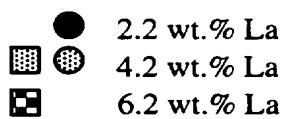


Fig. 20



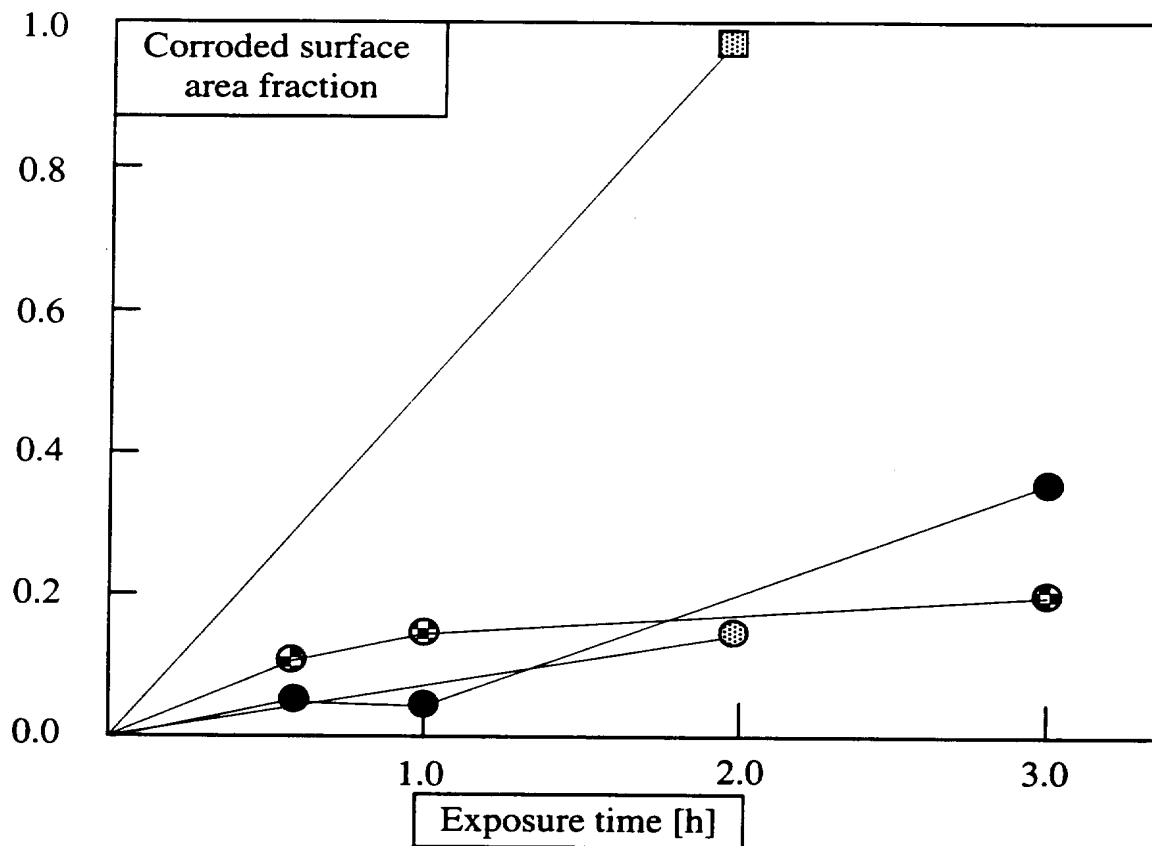


Fig. 21

- 2.2 wt.% La
- ◼ 4.2 wt.% La
- ⊕ 6.2 wt.% La

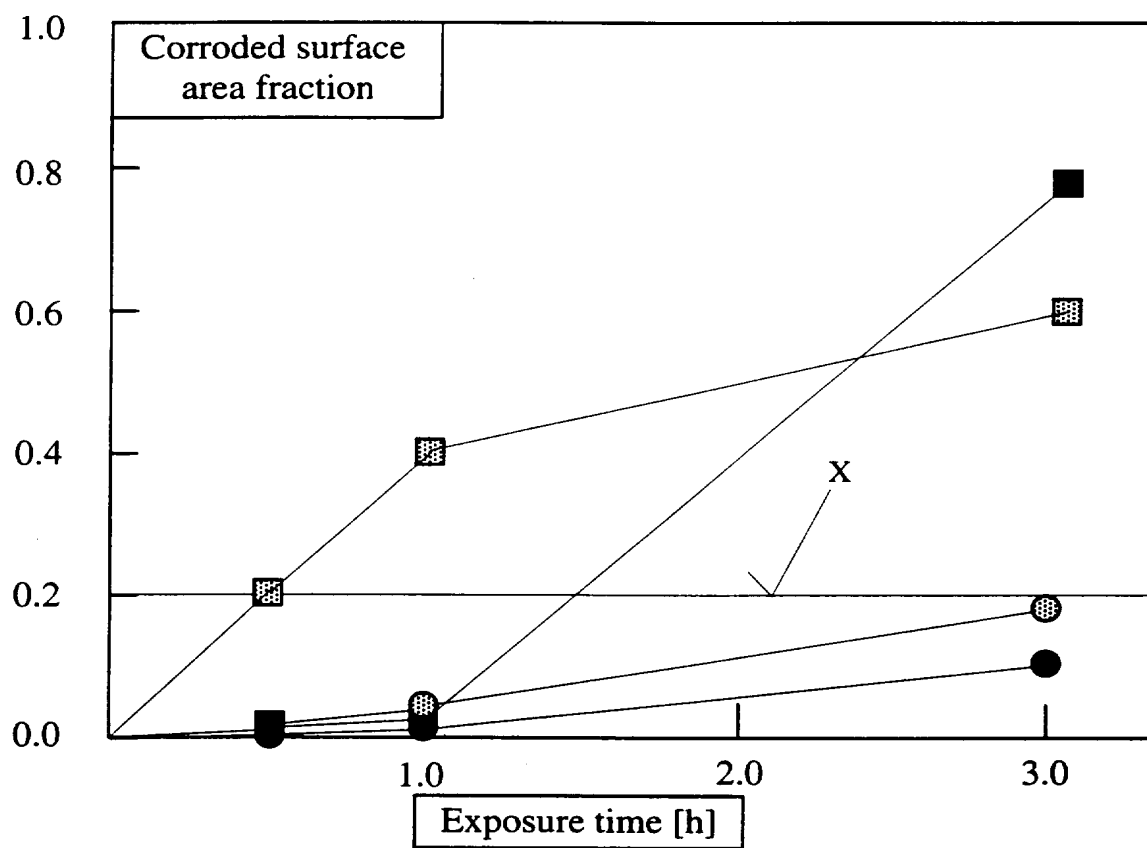


Fig. 22

■ ● 2.2 wt.% Ce
▣ ○ 6.0 wt.% Ce

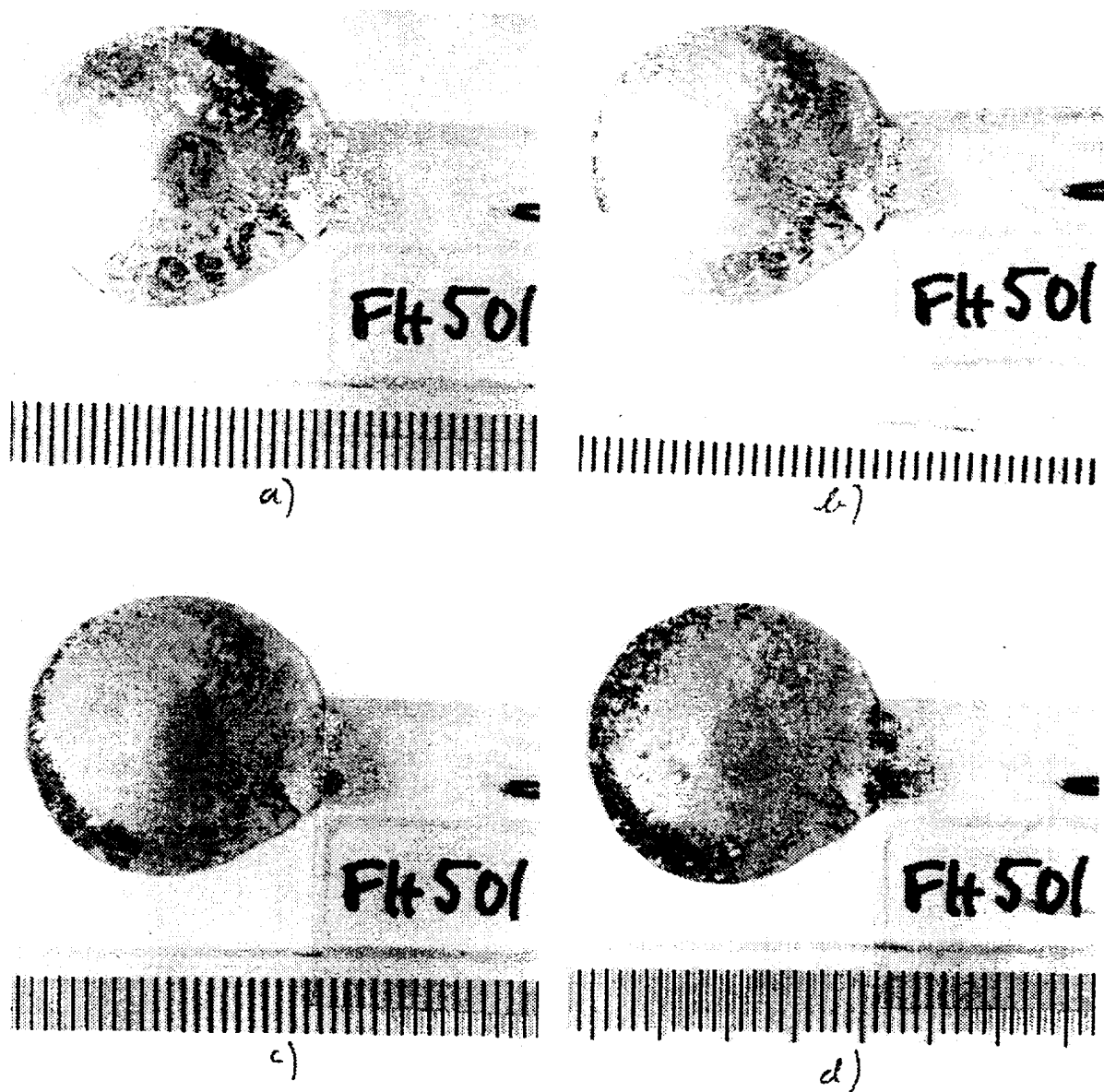


Fig. 23

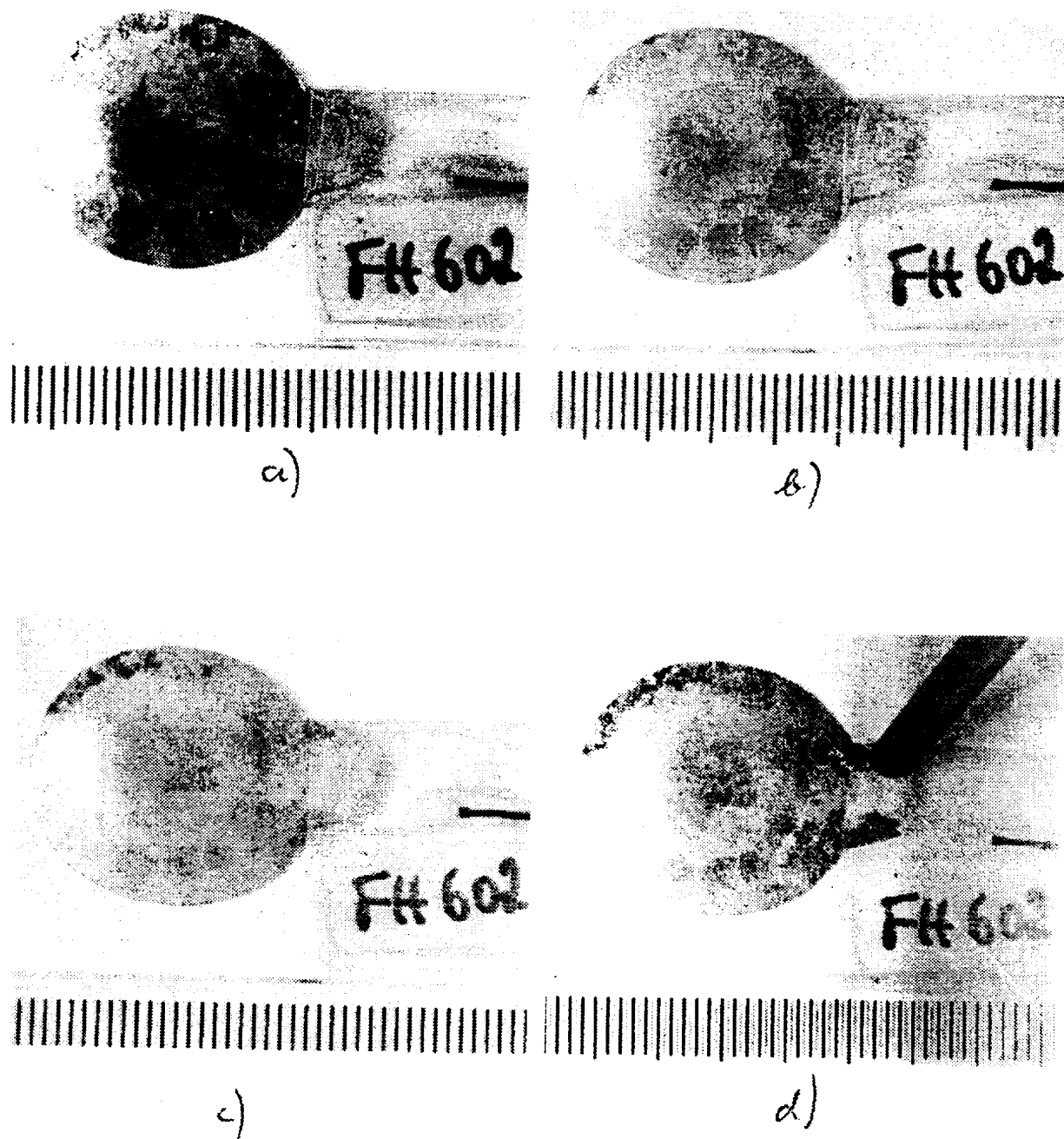


Fig. 24

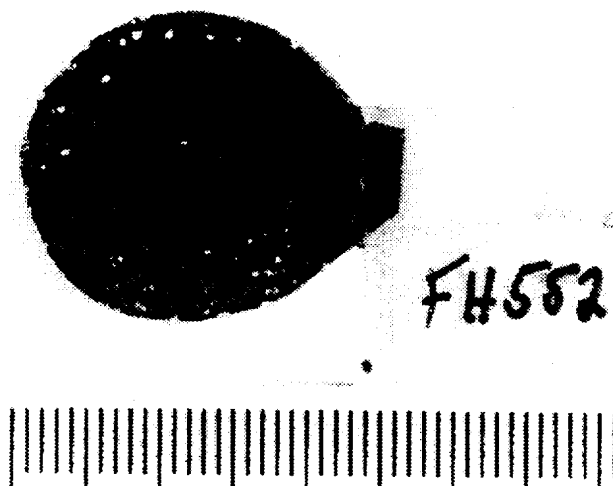


Fig. 25

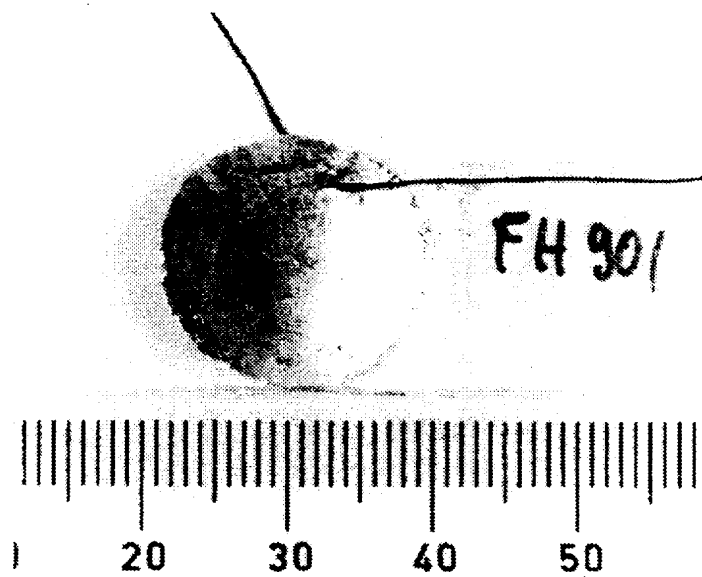


Fig. 26

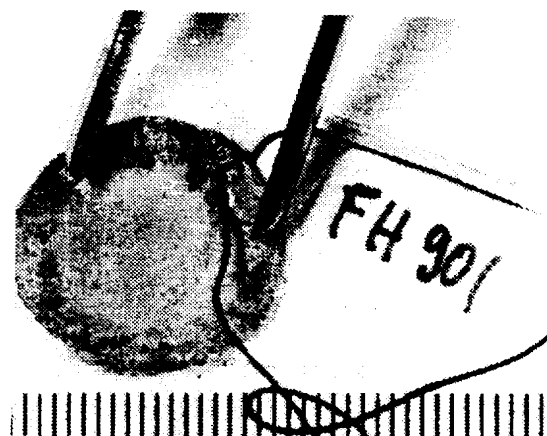
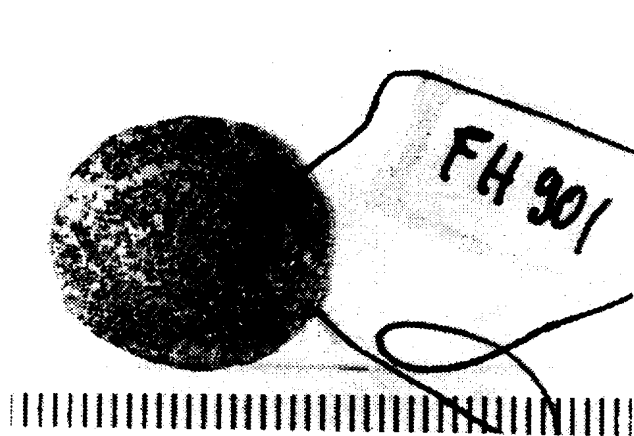
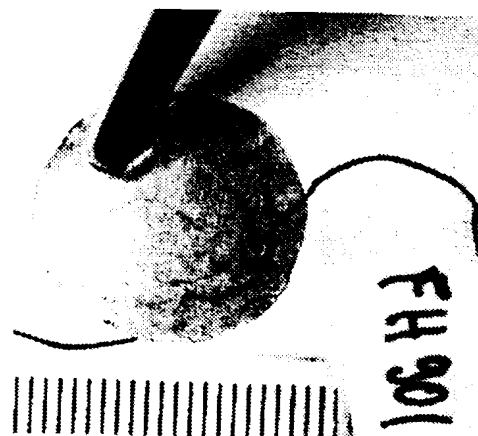
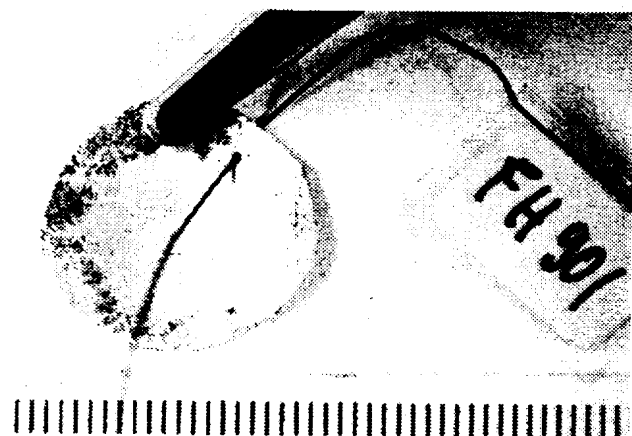


Fig. 27

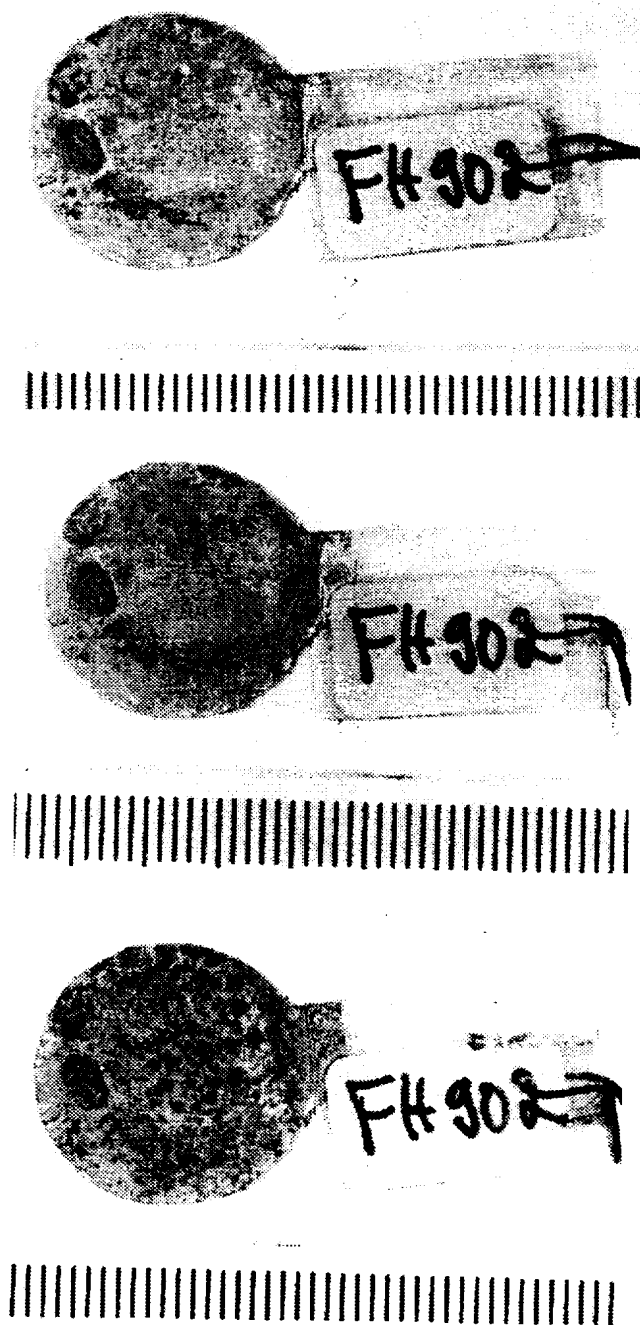


Fig. 28

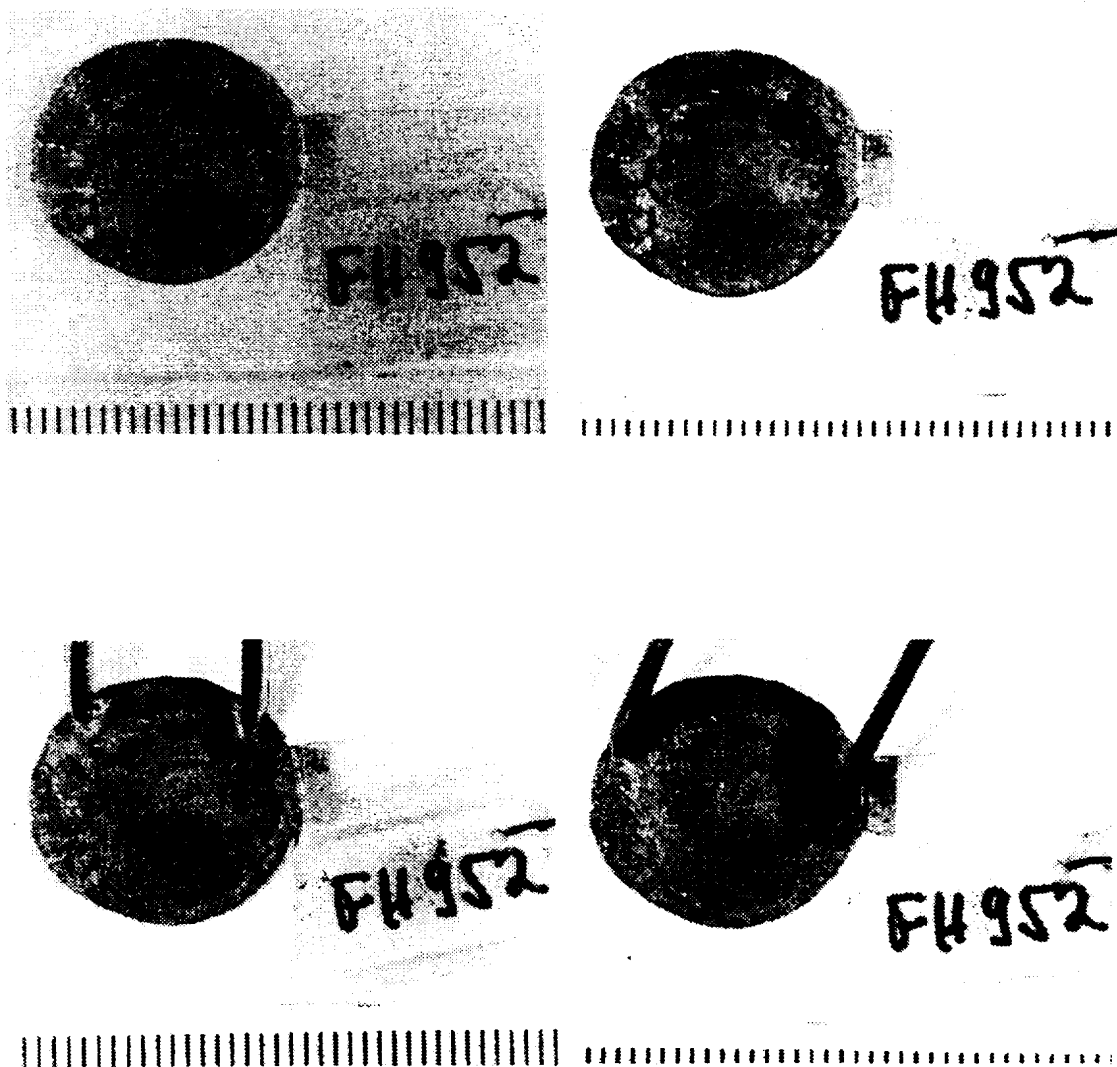


Fig. 29

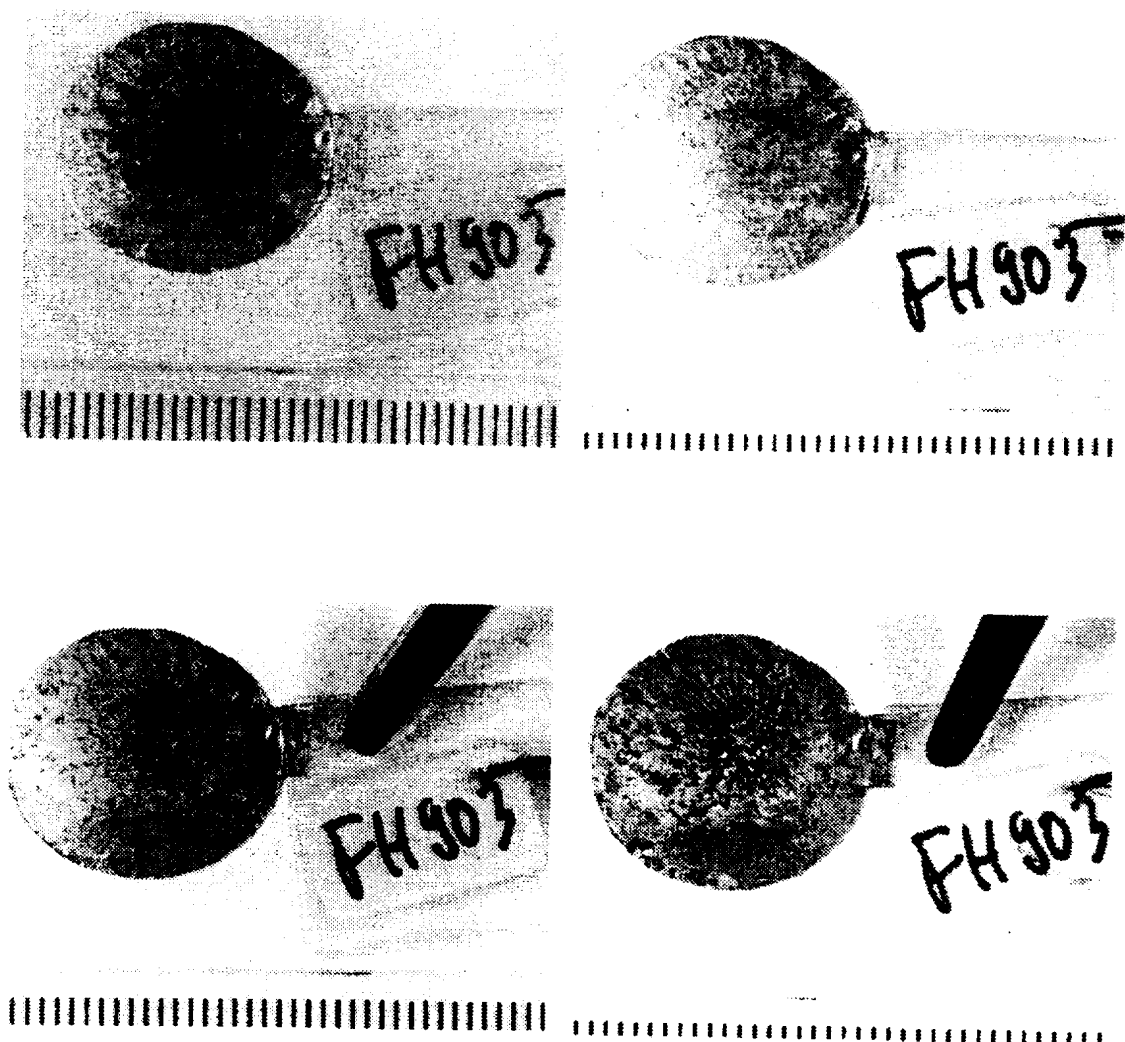


Fig. 30

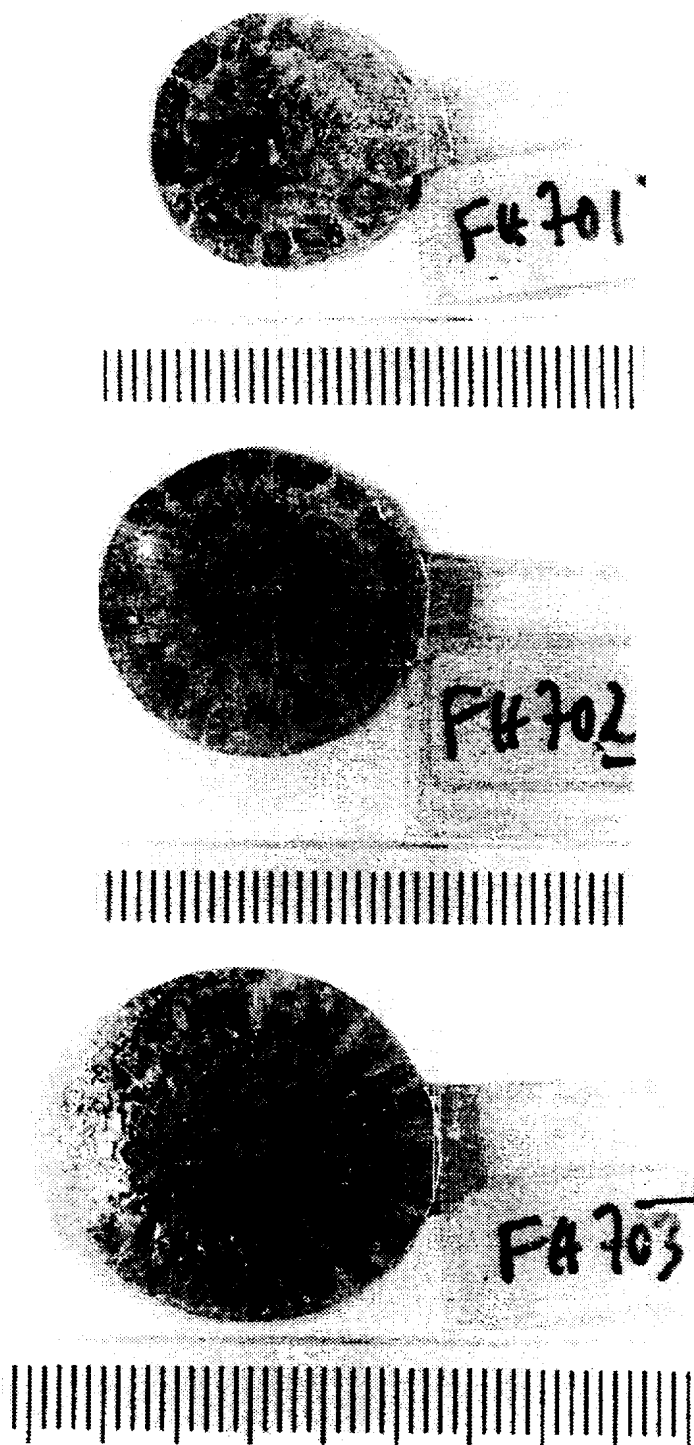


Fig. 31

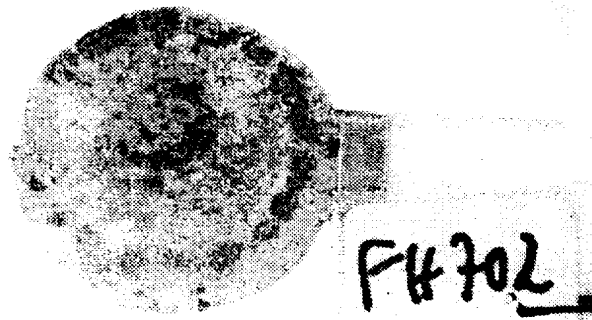


Fig. 32

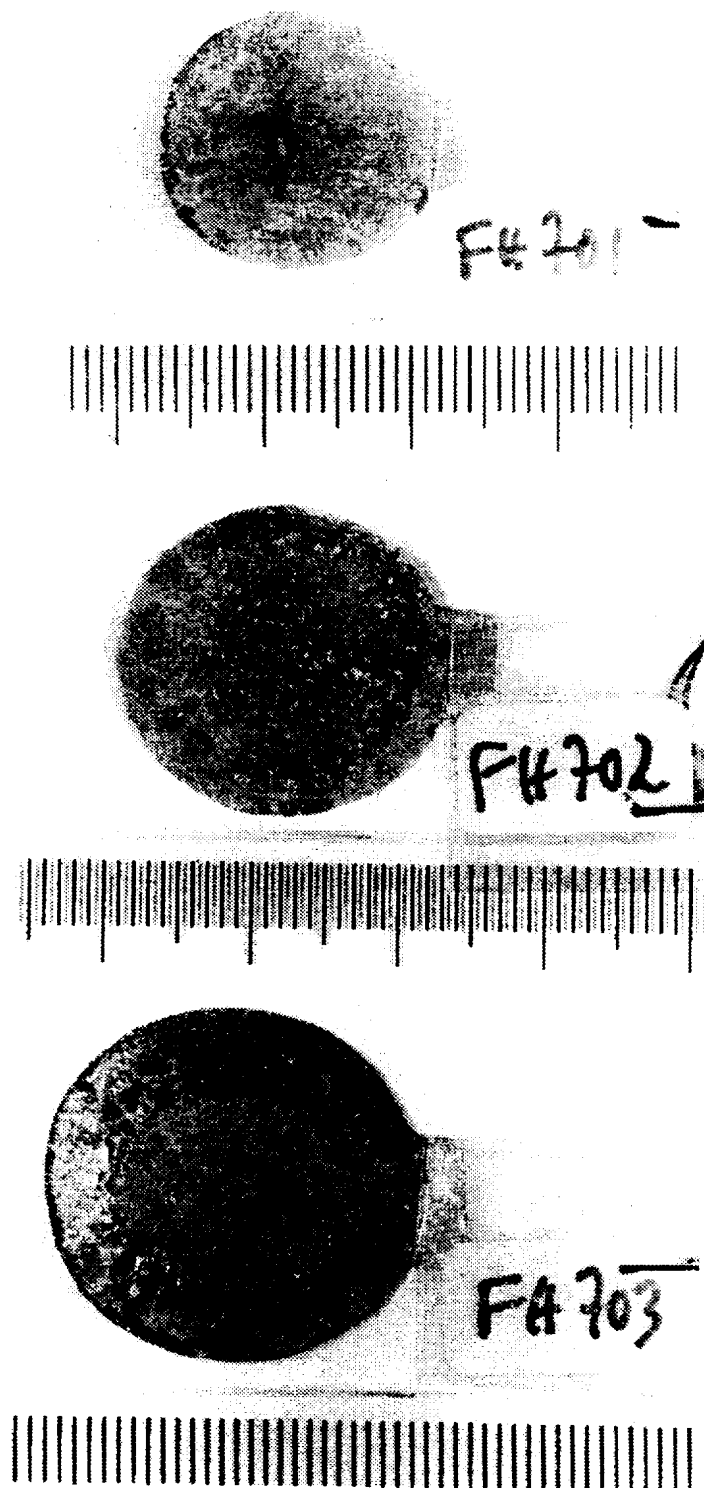


Fig. 33

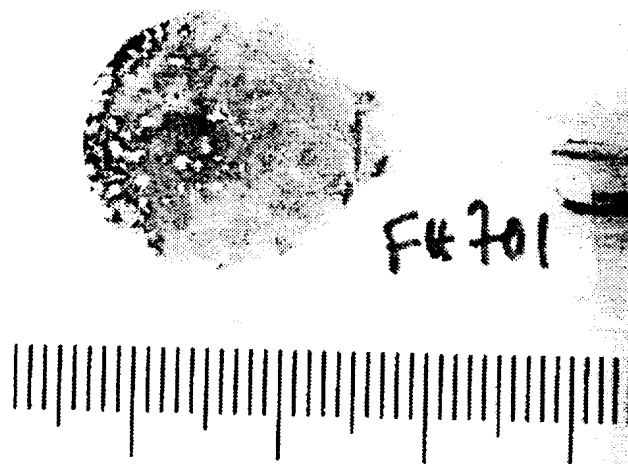


Fig. 34

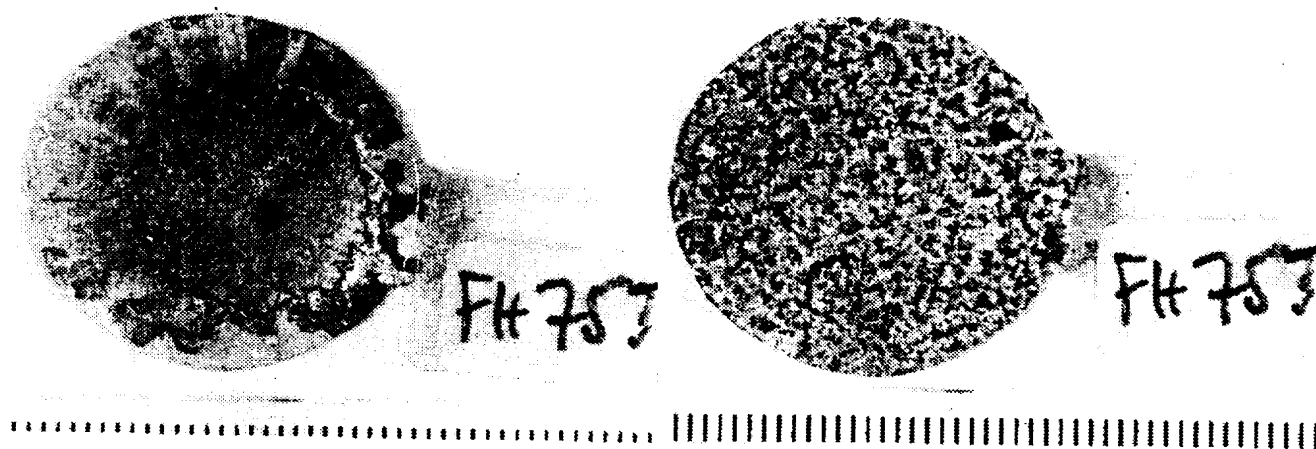
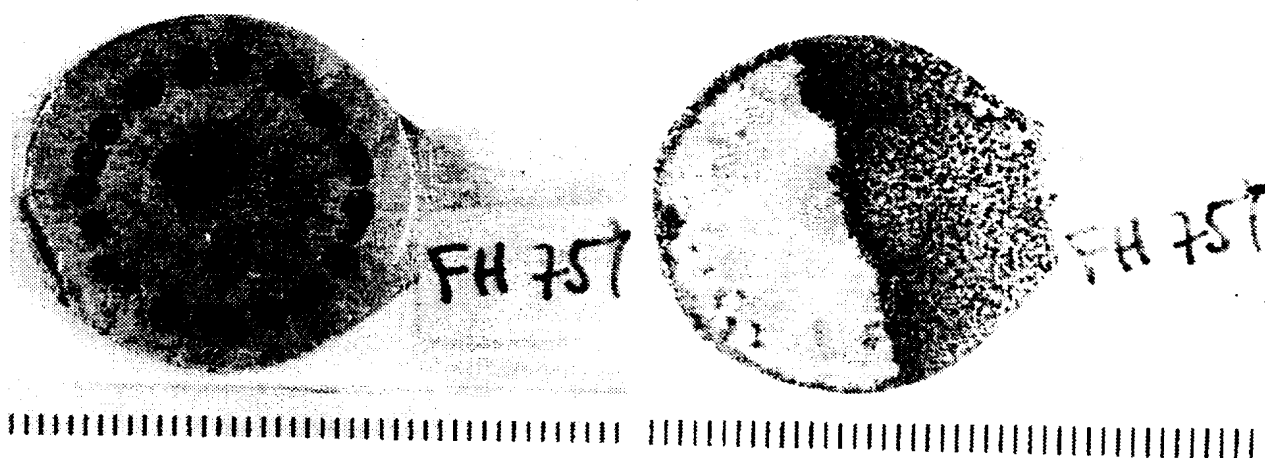


Fig. 35

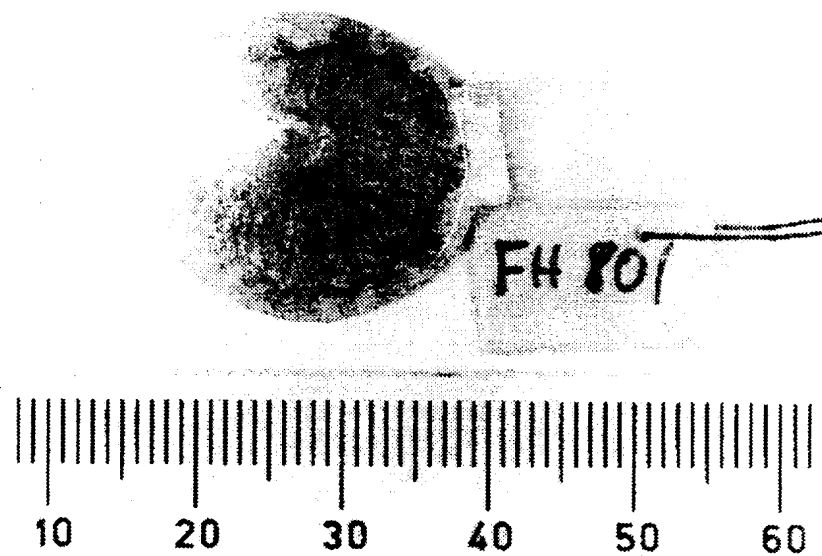


Fig. 36

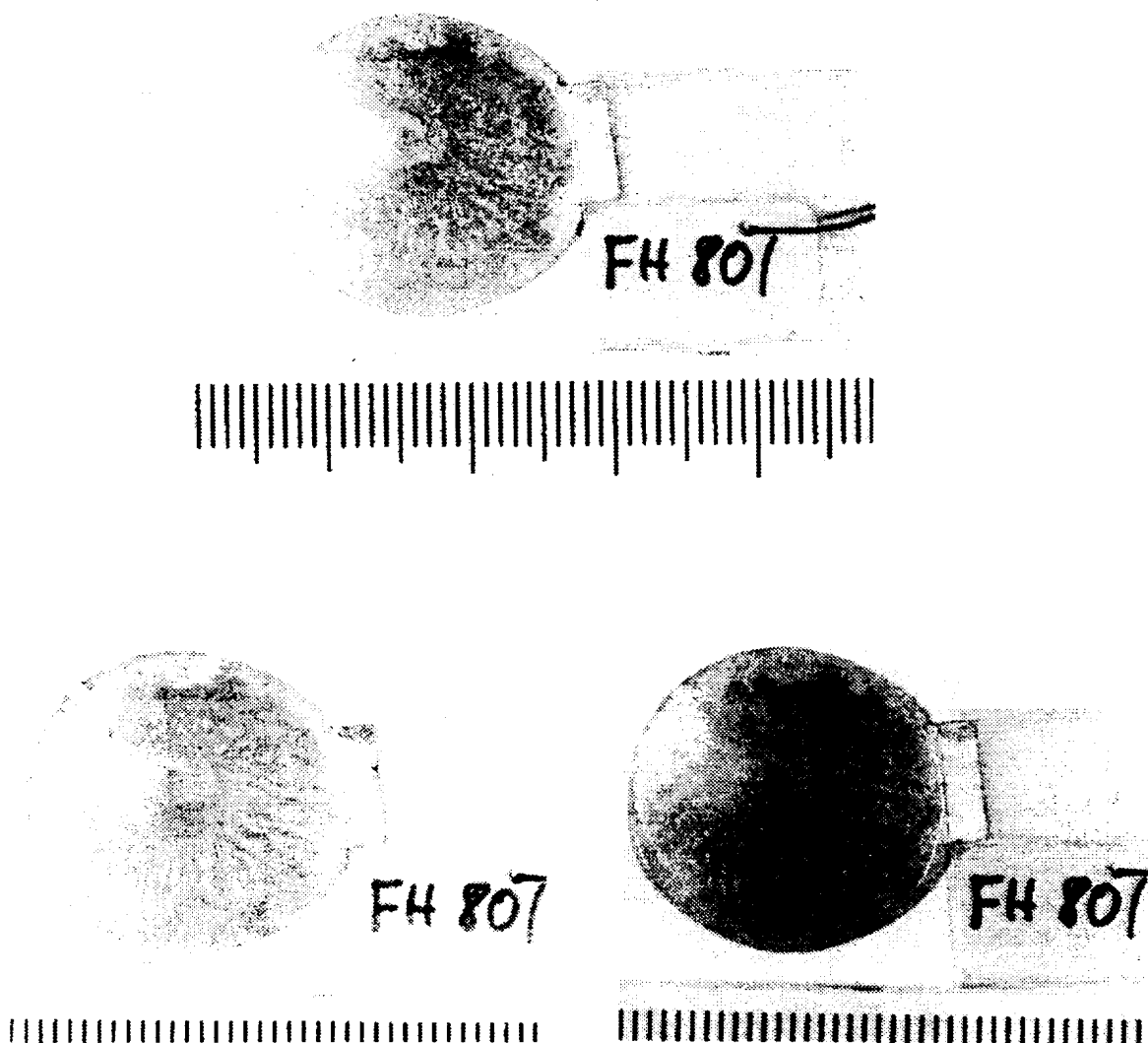
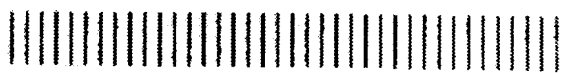
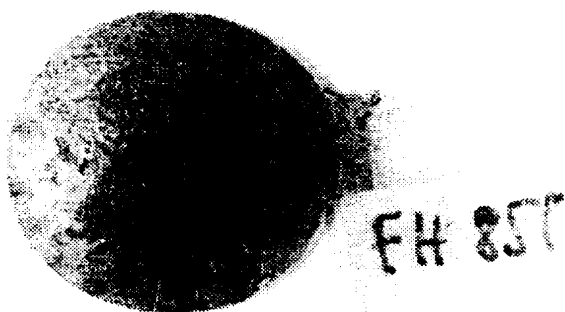
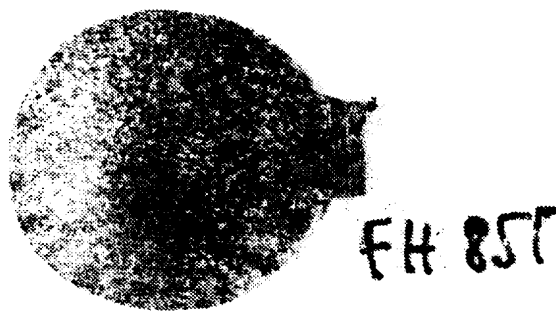


Fig. 37



a)



b)



c)

Fig. 38

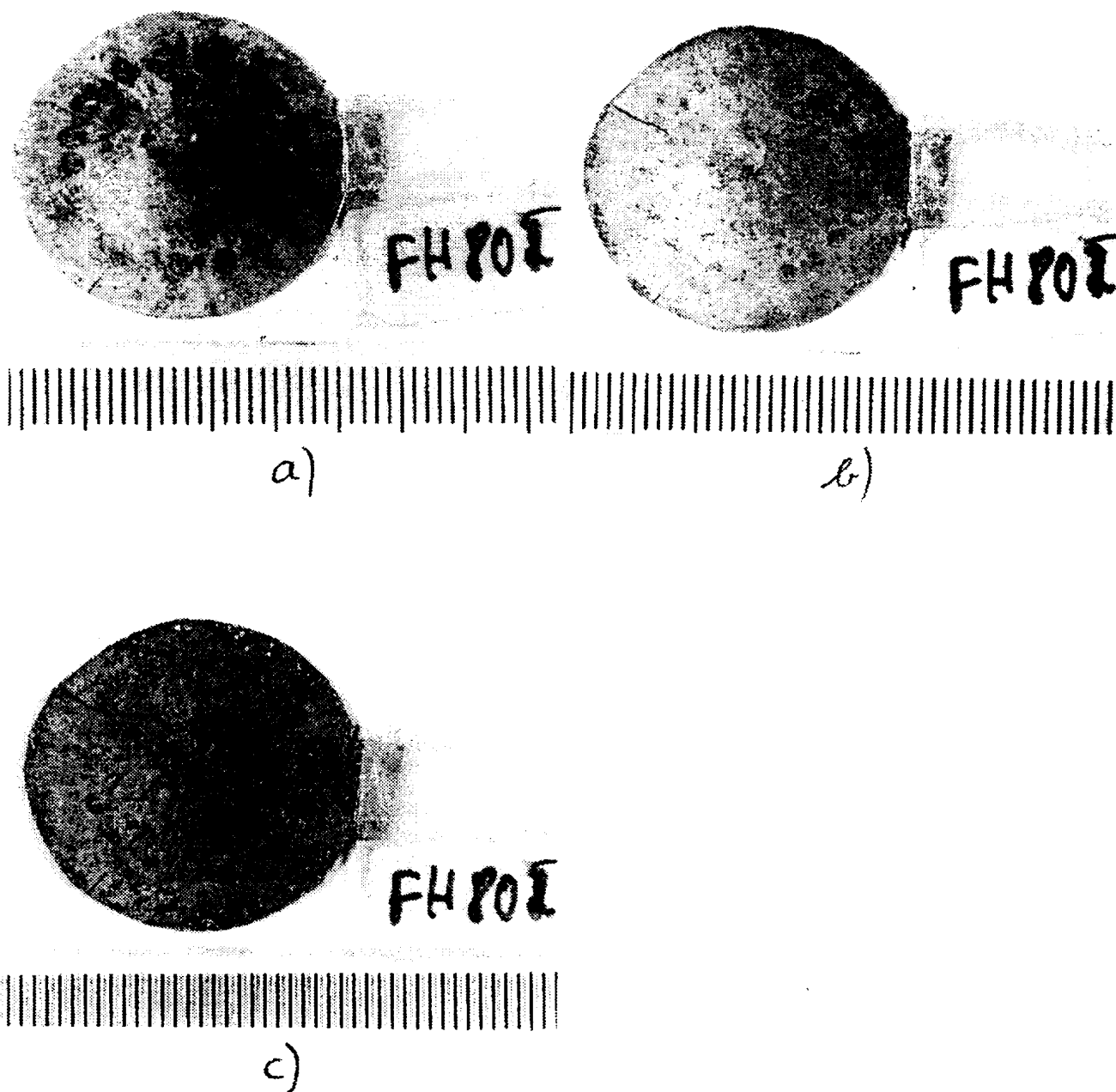


Fig. 39

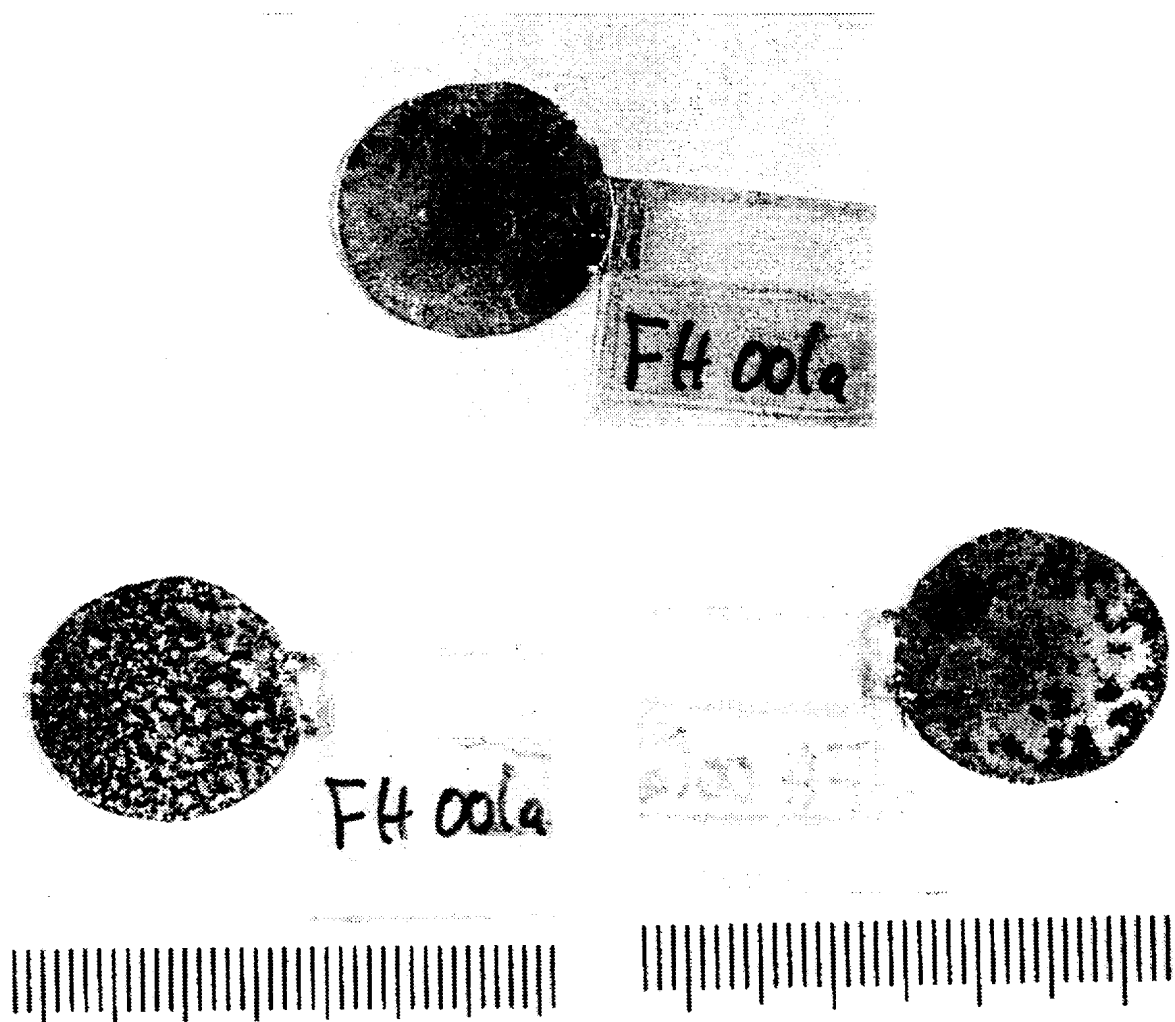
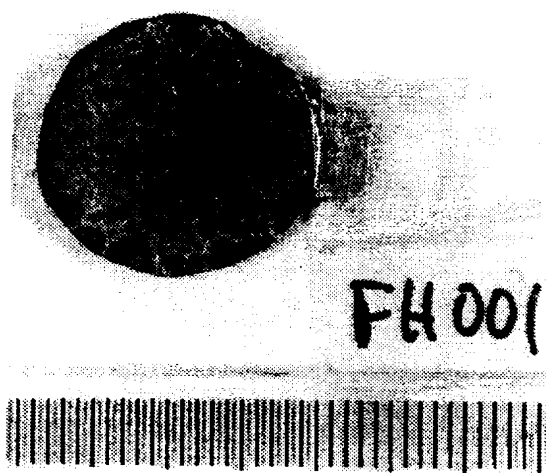


Fig. 40



a)



b)



c)



d)

Fig. 41

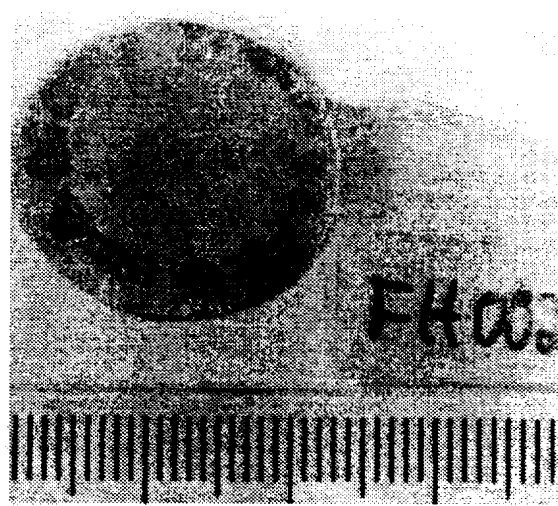
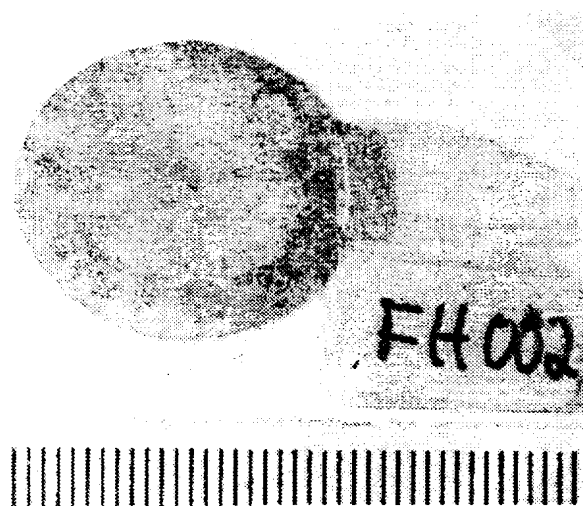
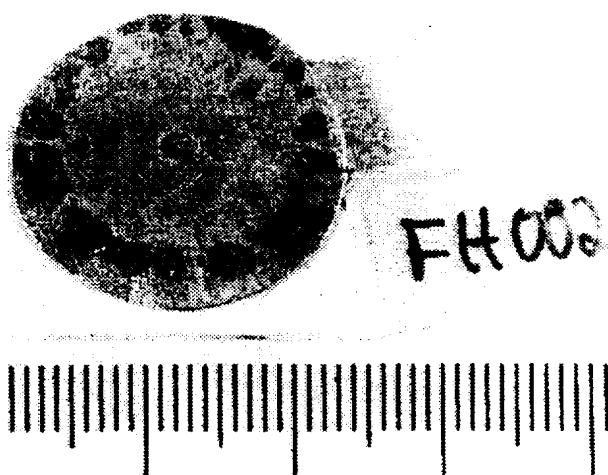


Fig. 42

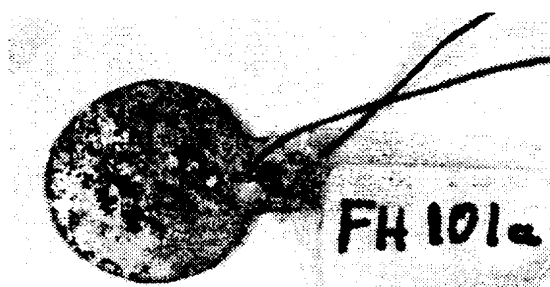
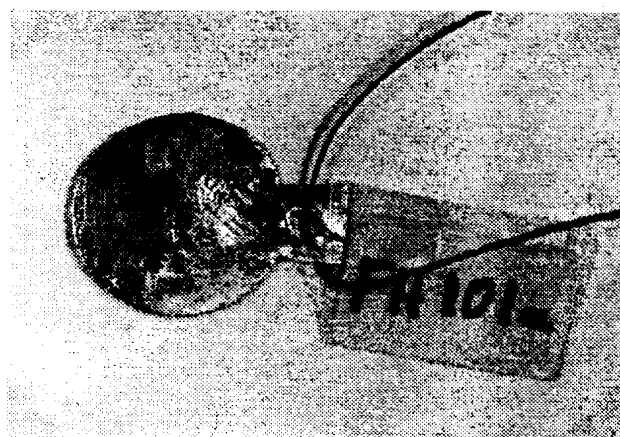


Fig. 43

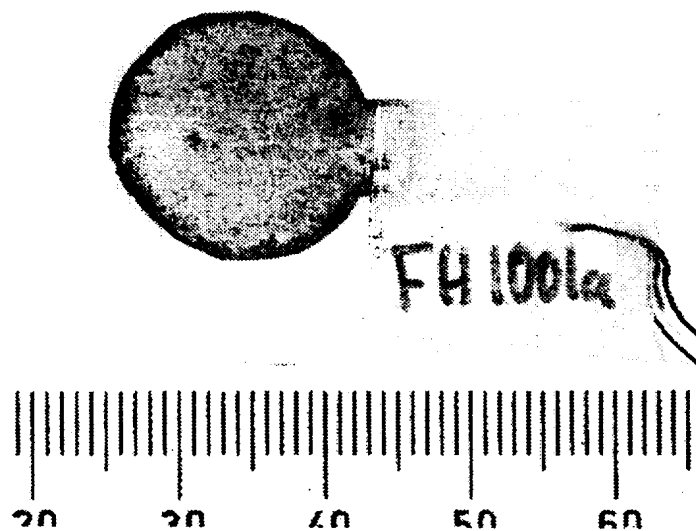


Fig. 44

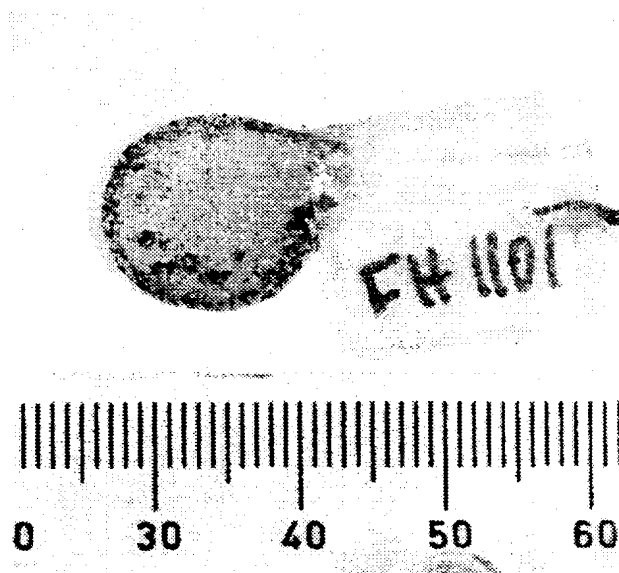
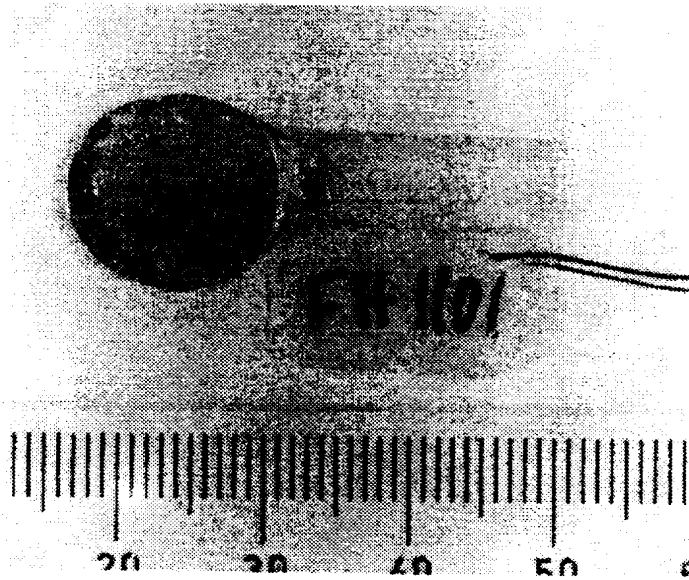


Fig. 45

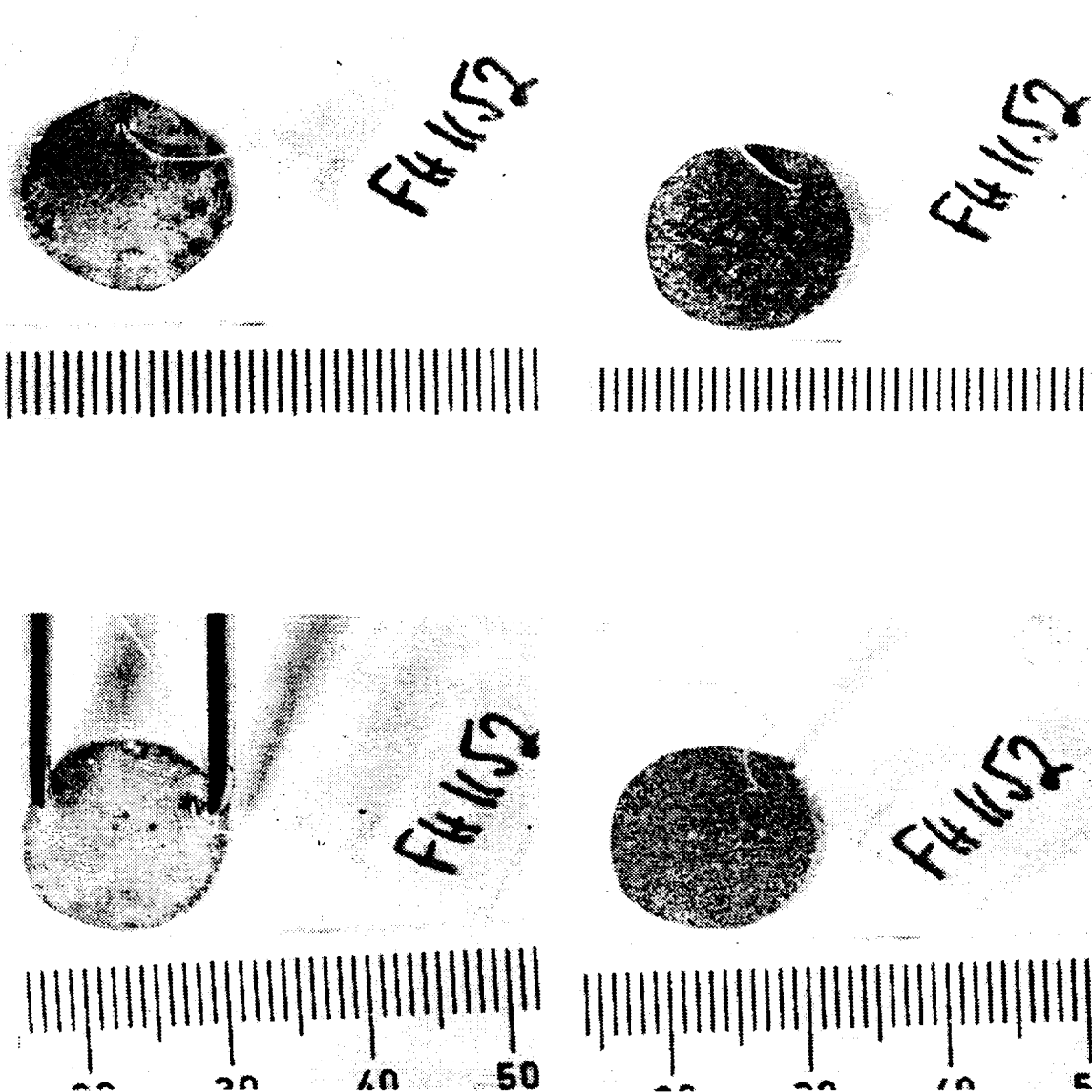
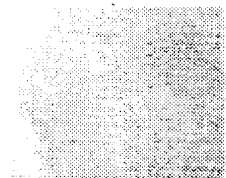


Fig. 46

Fig. 17 Composites used for modified immersion test after Machin.

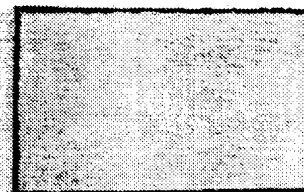
AZ 91



VD Mg - 4 Ti

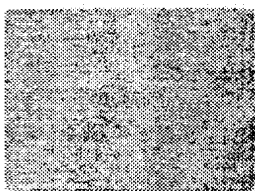


VD Mg - 7 Ce

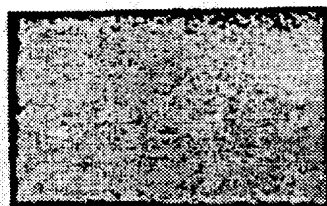


Prior to immersion

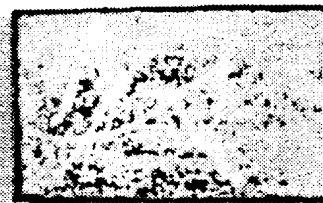
AZ 91



VD Mg - 4 Ti



VD Mg - 7 Ce



After immersion for 0.5 h

Fig. 47



Fig. 48

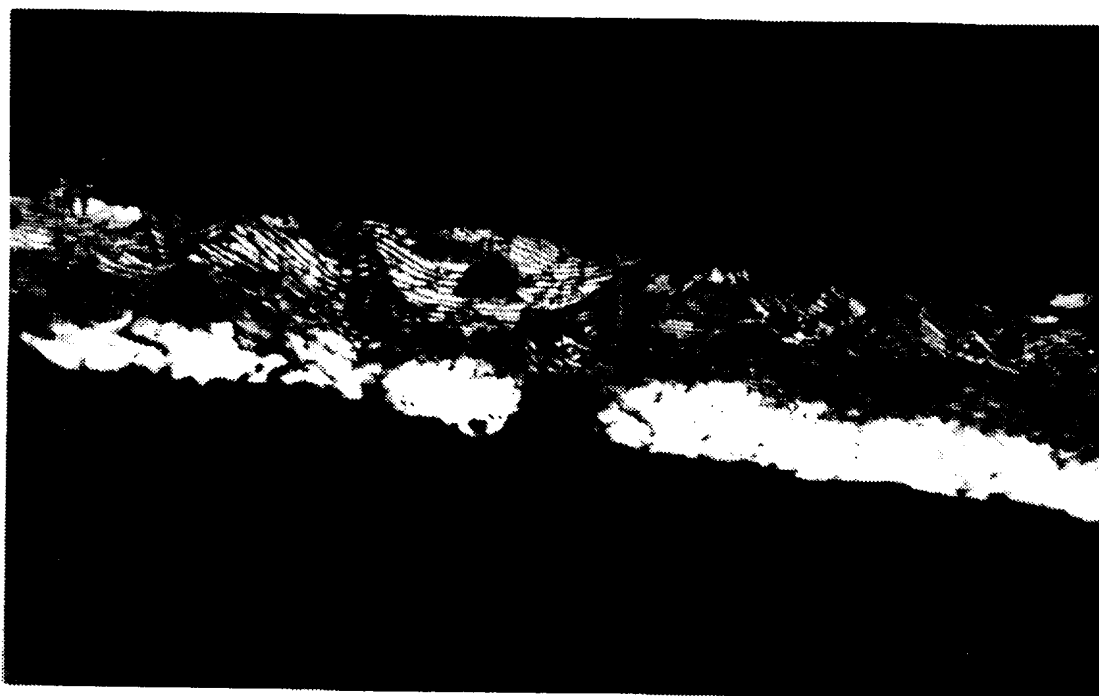
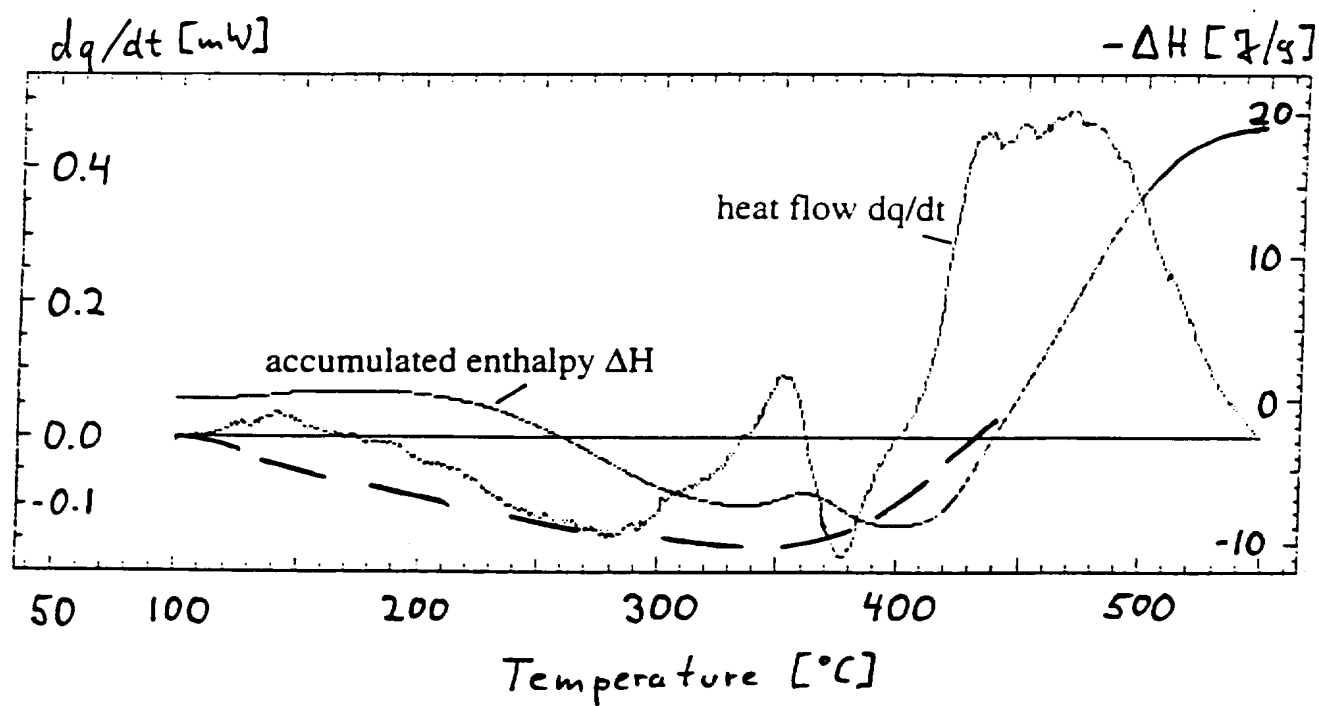
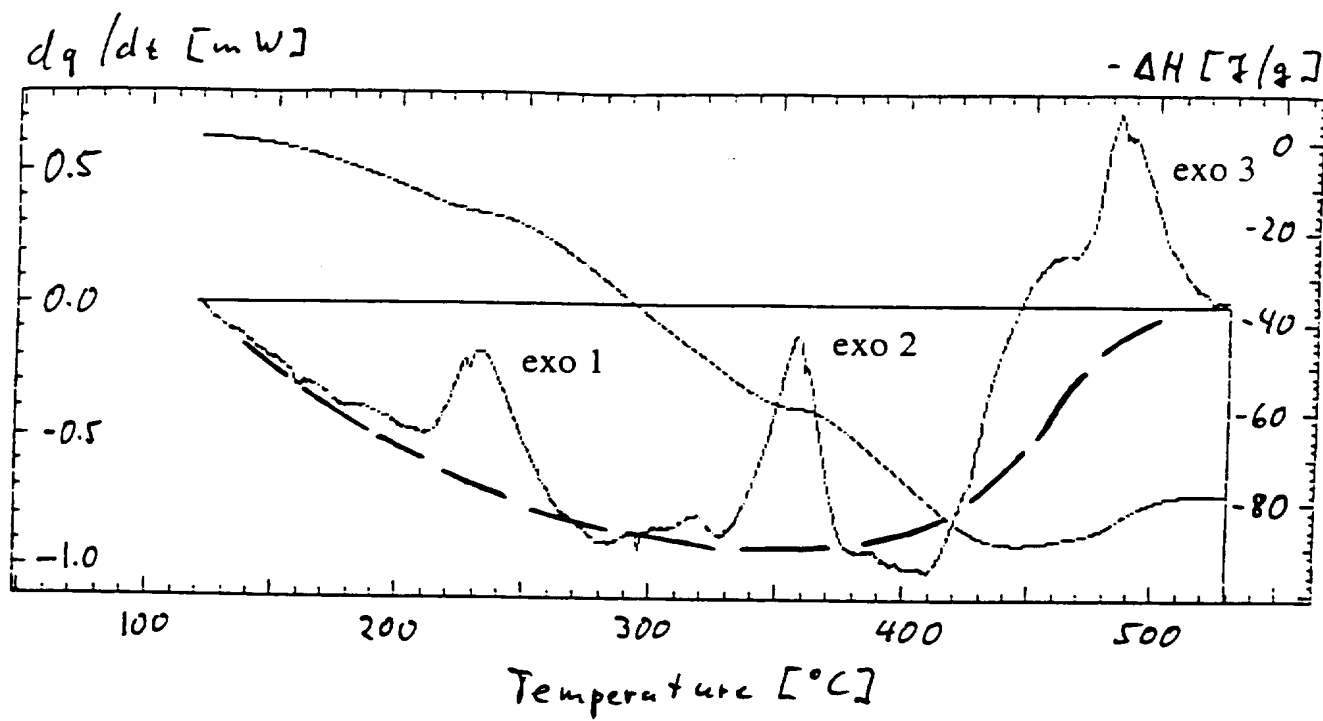
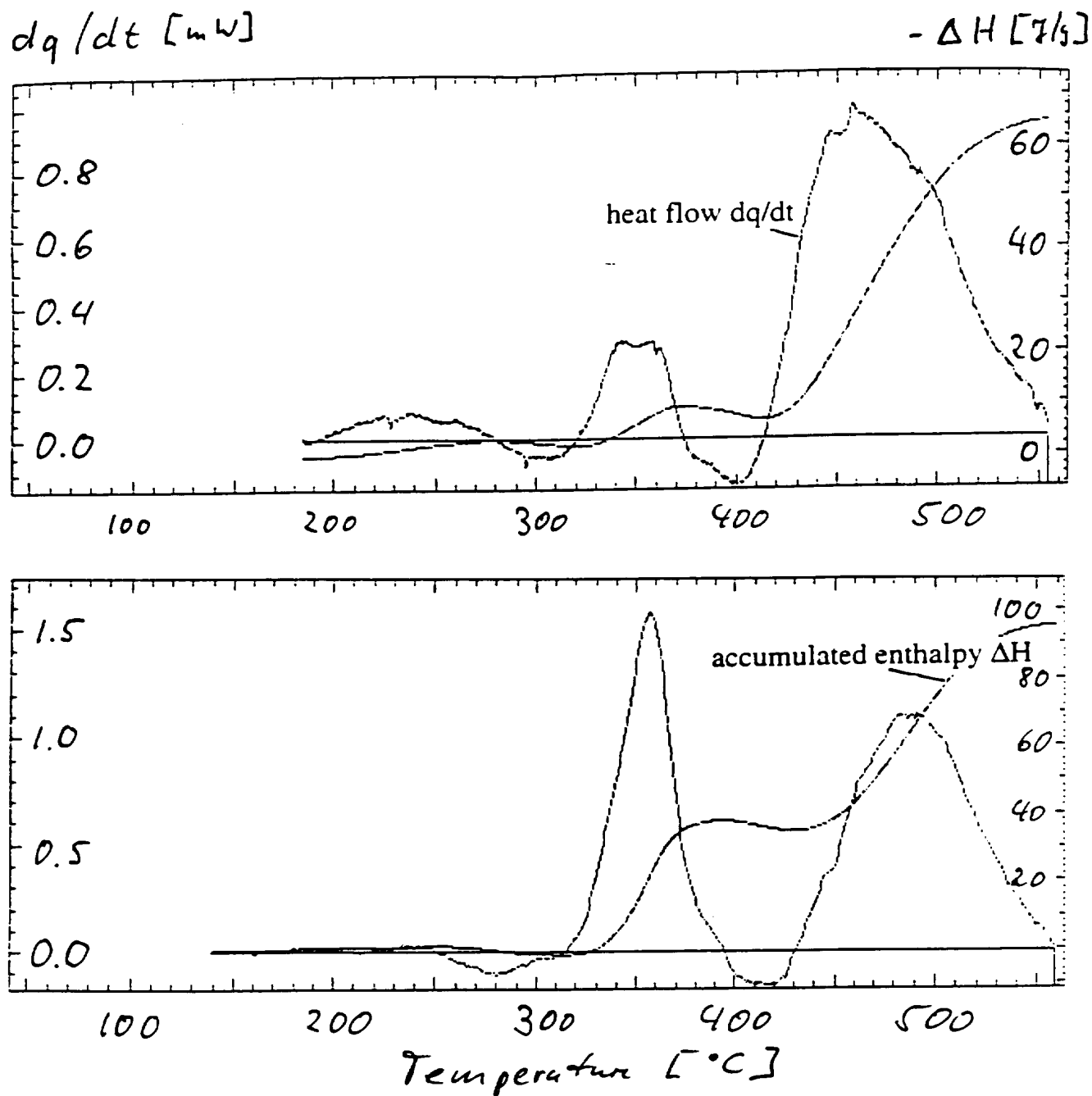
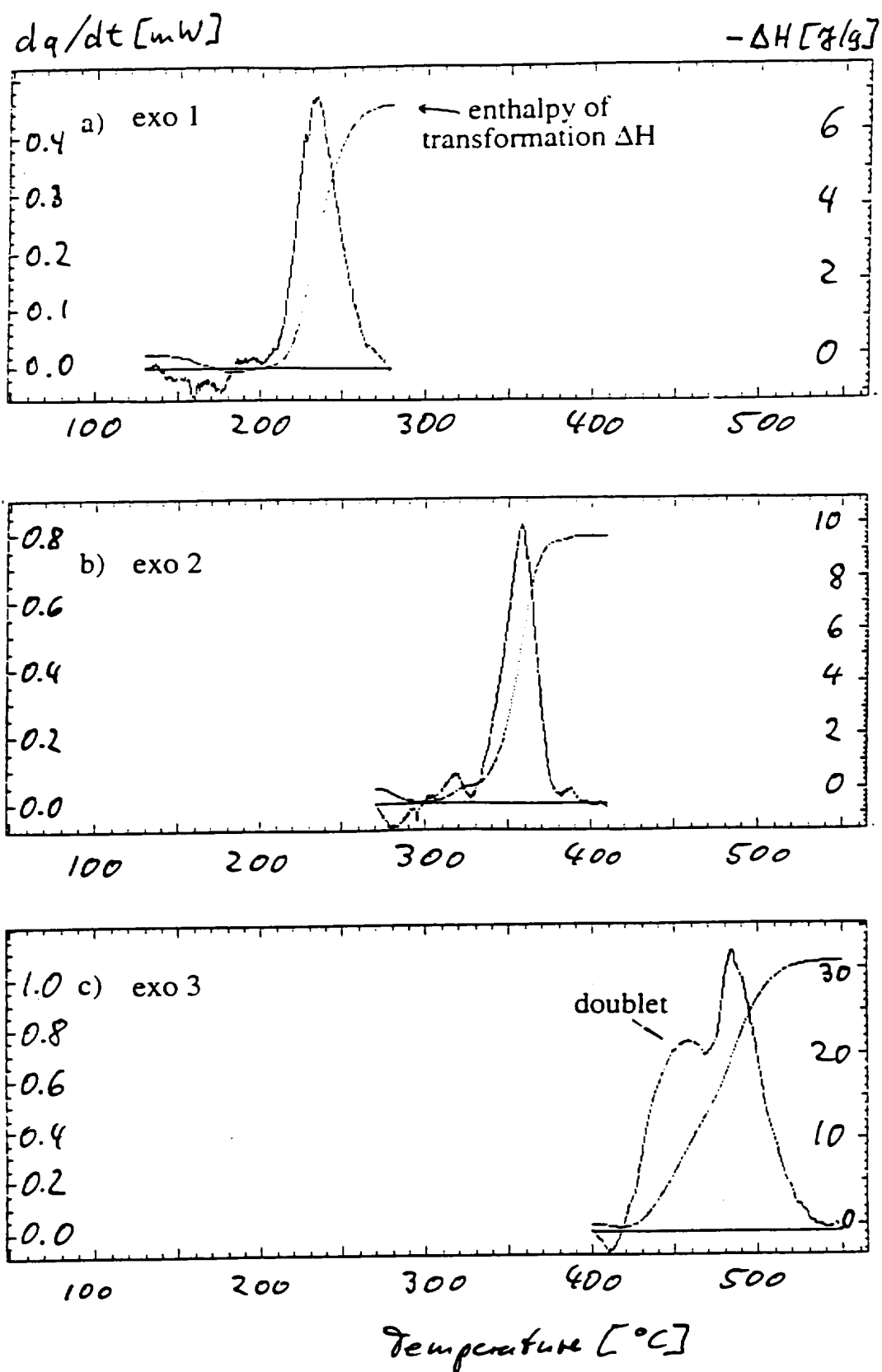


Fig. 49

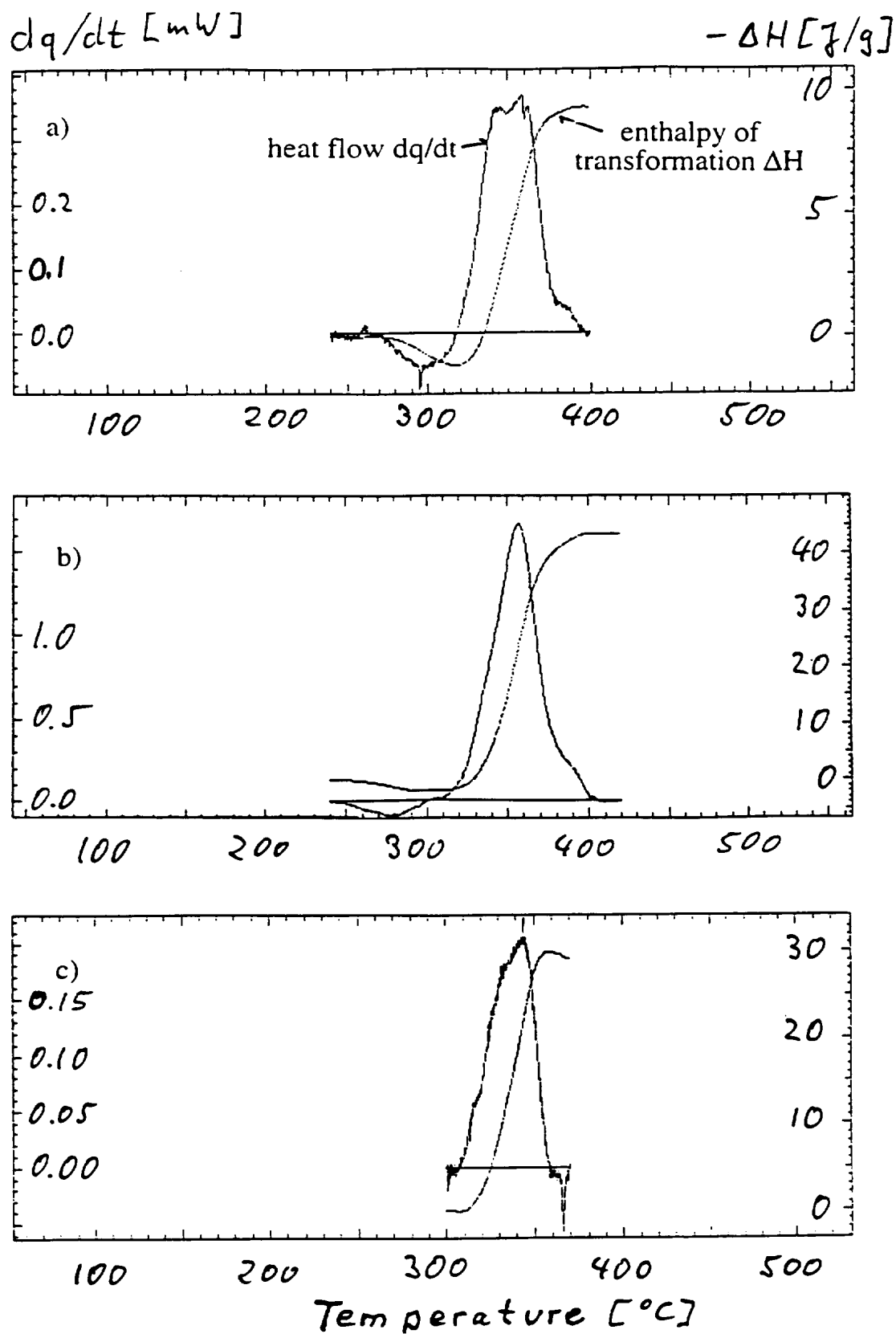
Fig. 50

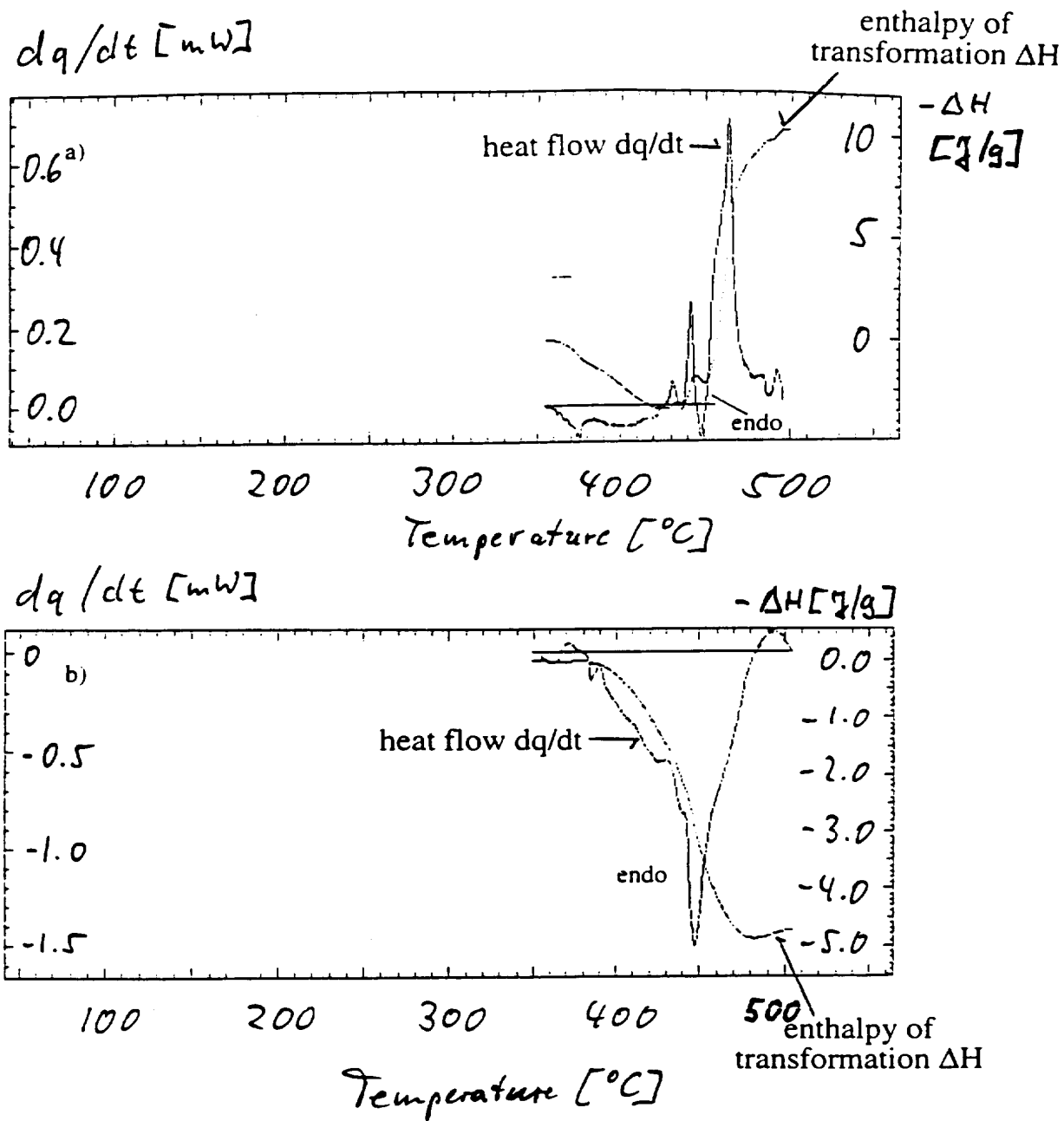
Fig. 51

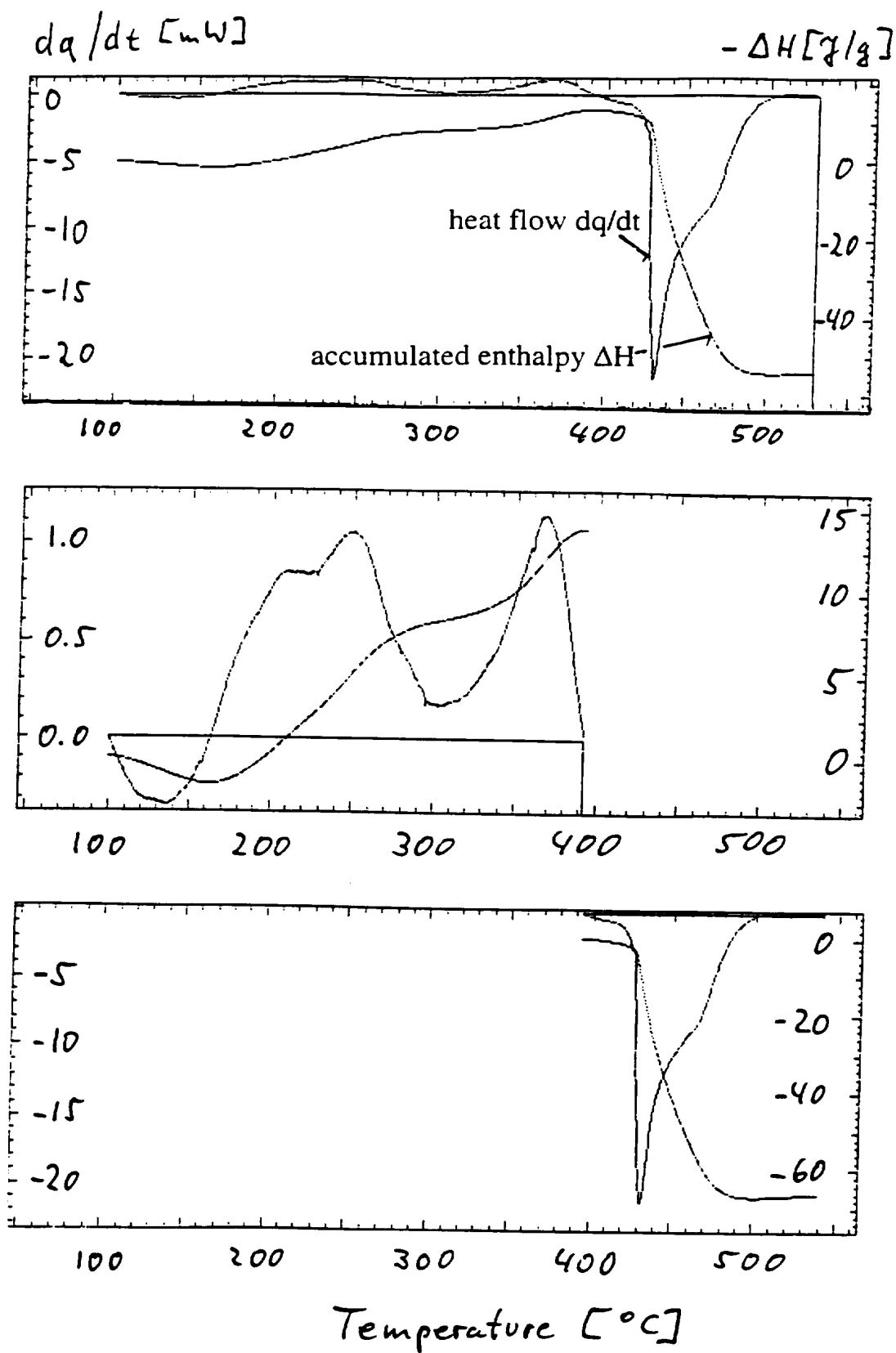
Fig. 52

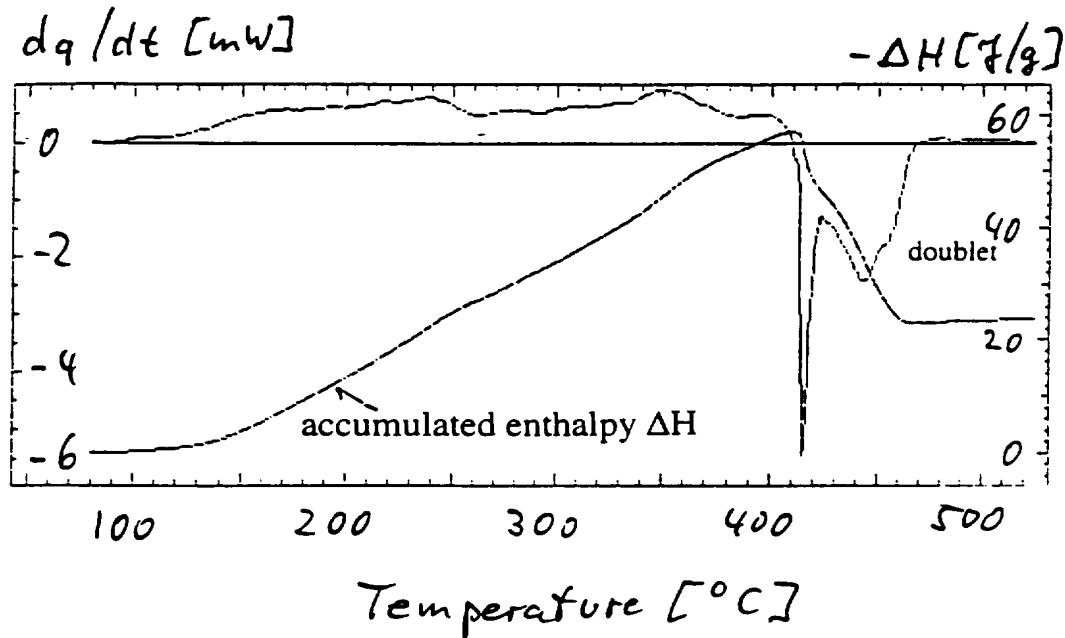
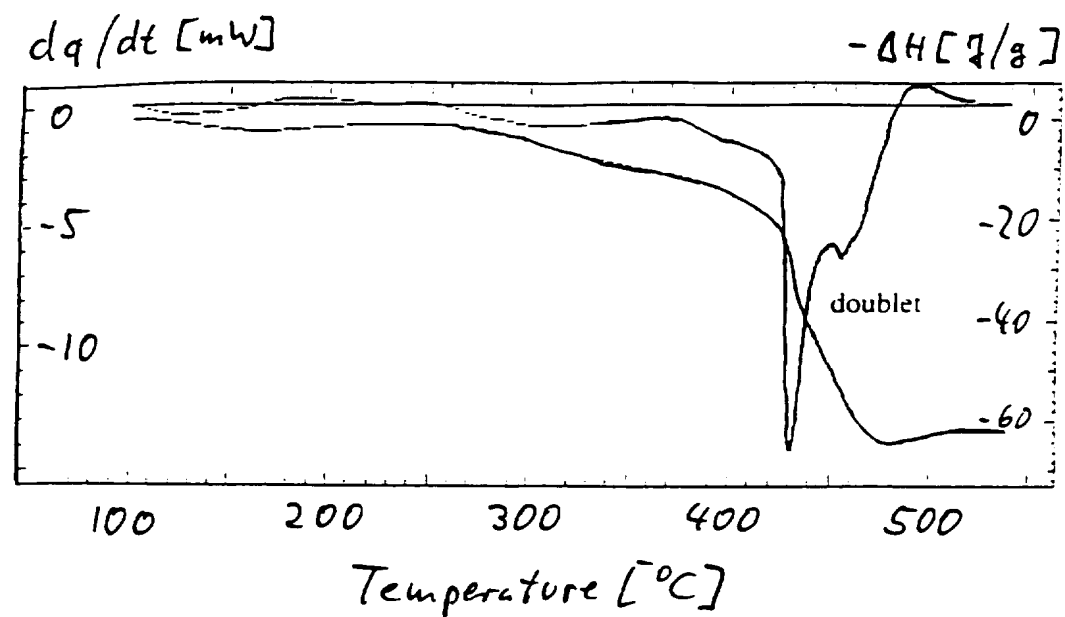
Fig. 53

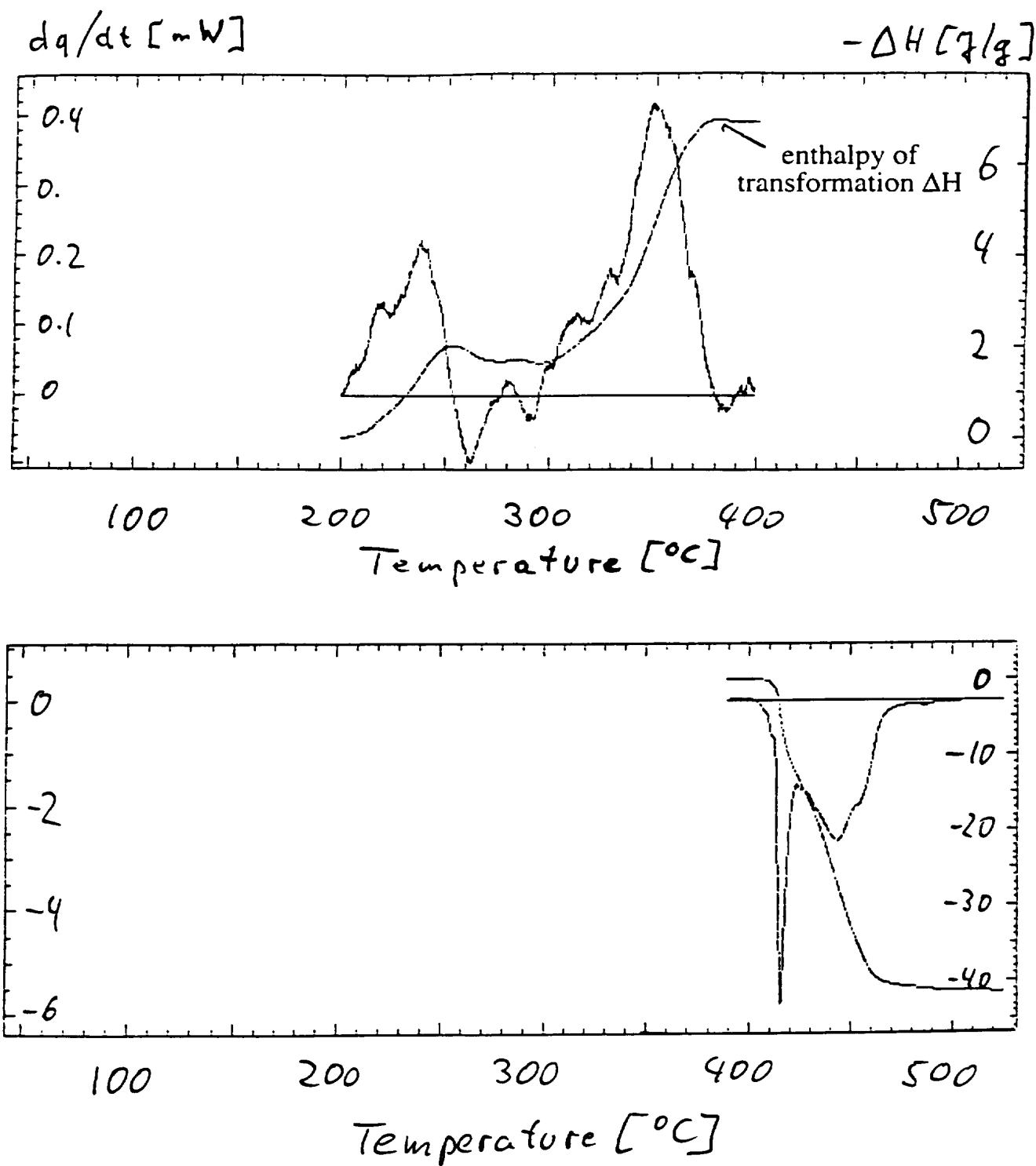
SUBSTITUTE SHEET (RULE 26)

Fig. 54

Fig. 55



Fig. 57

Fig. 58

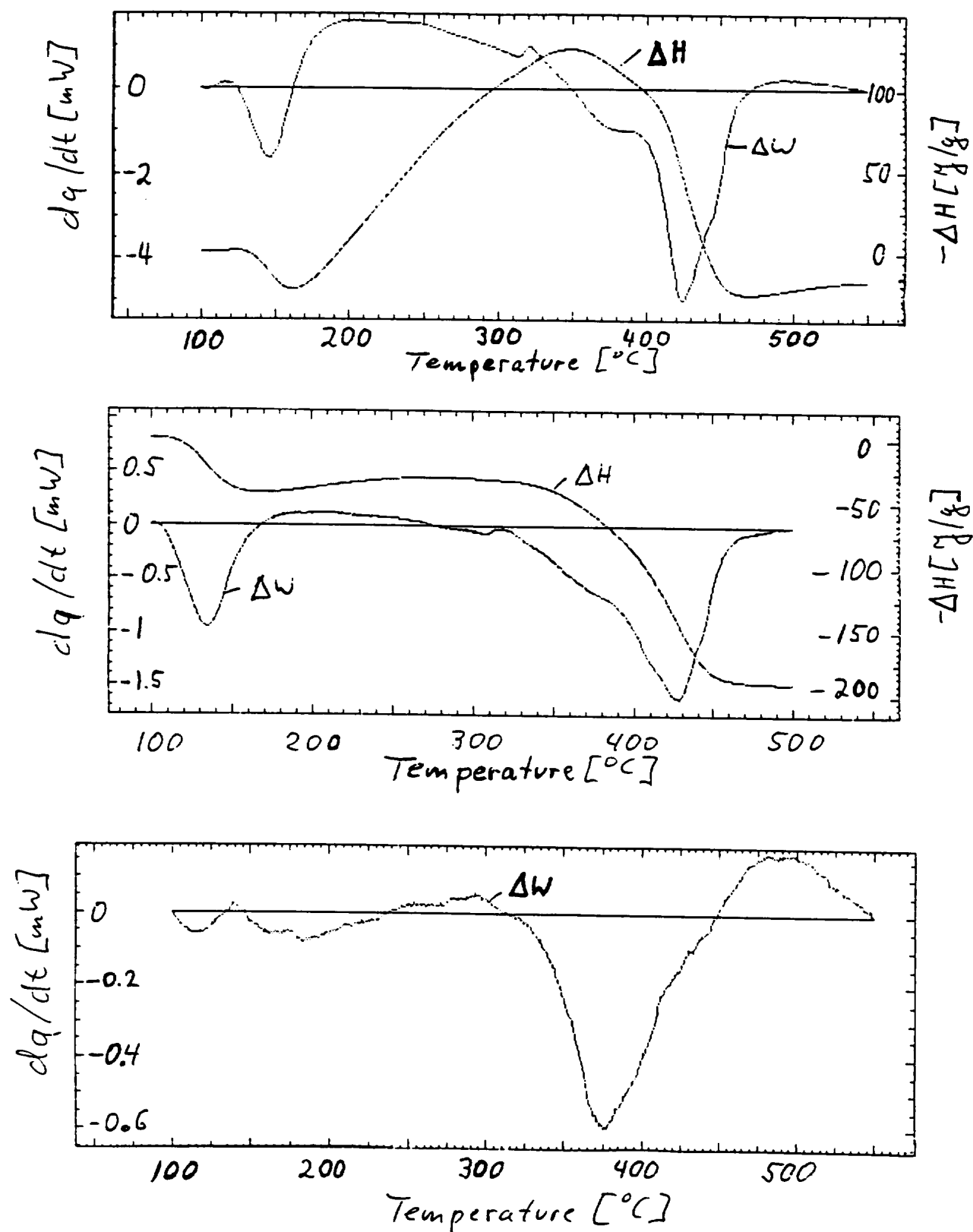


Fig. 59

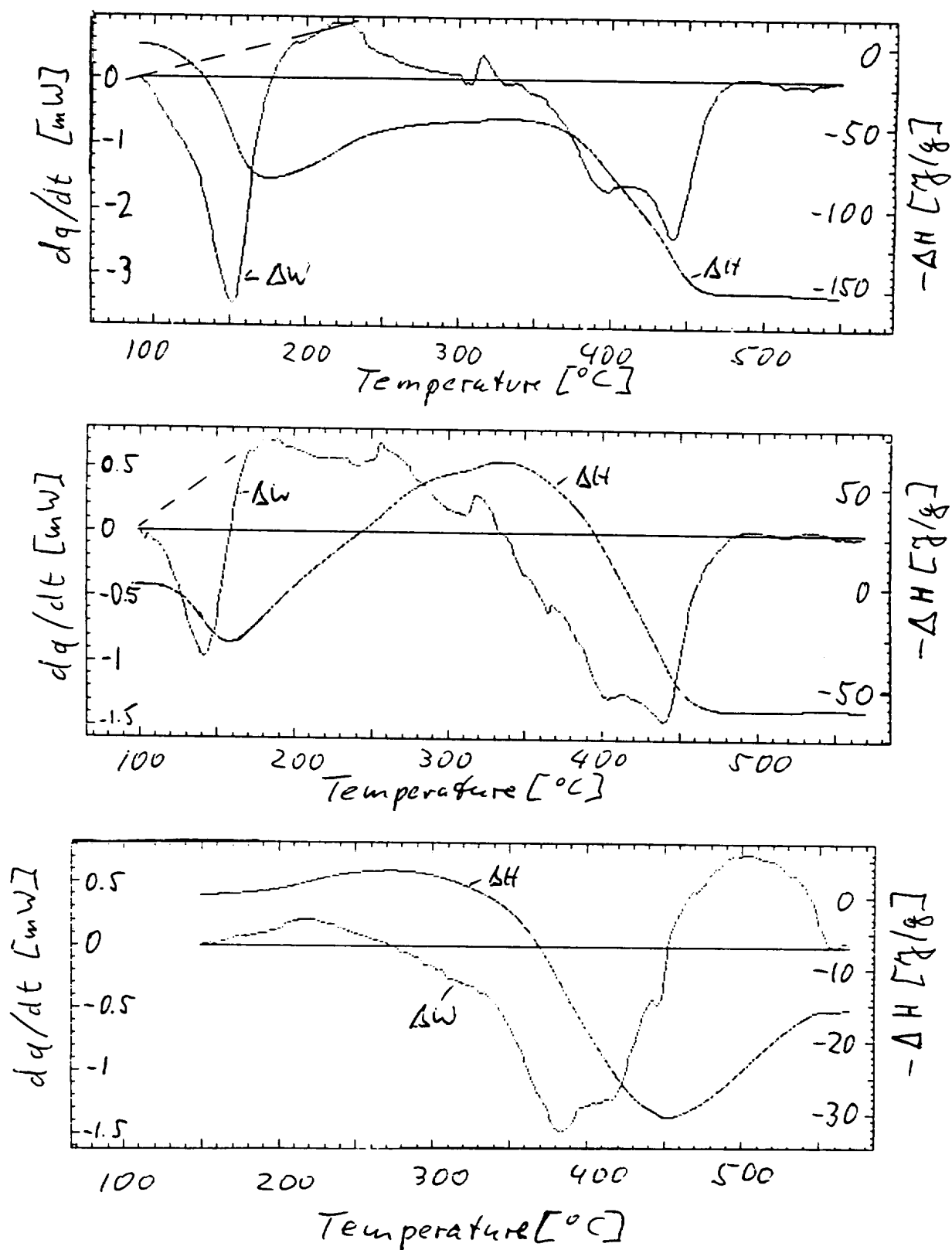
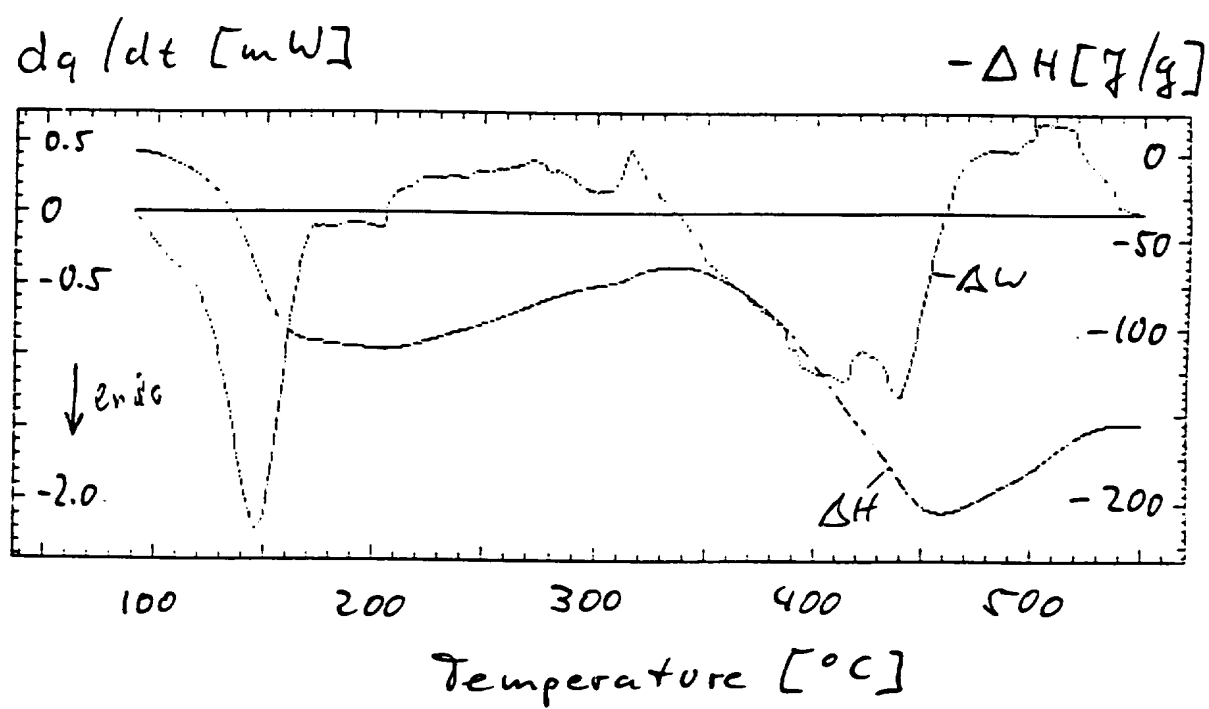
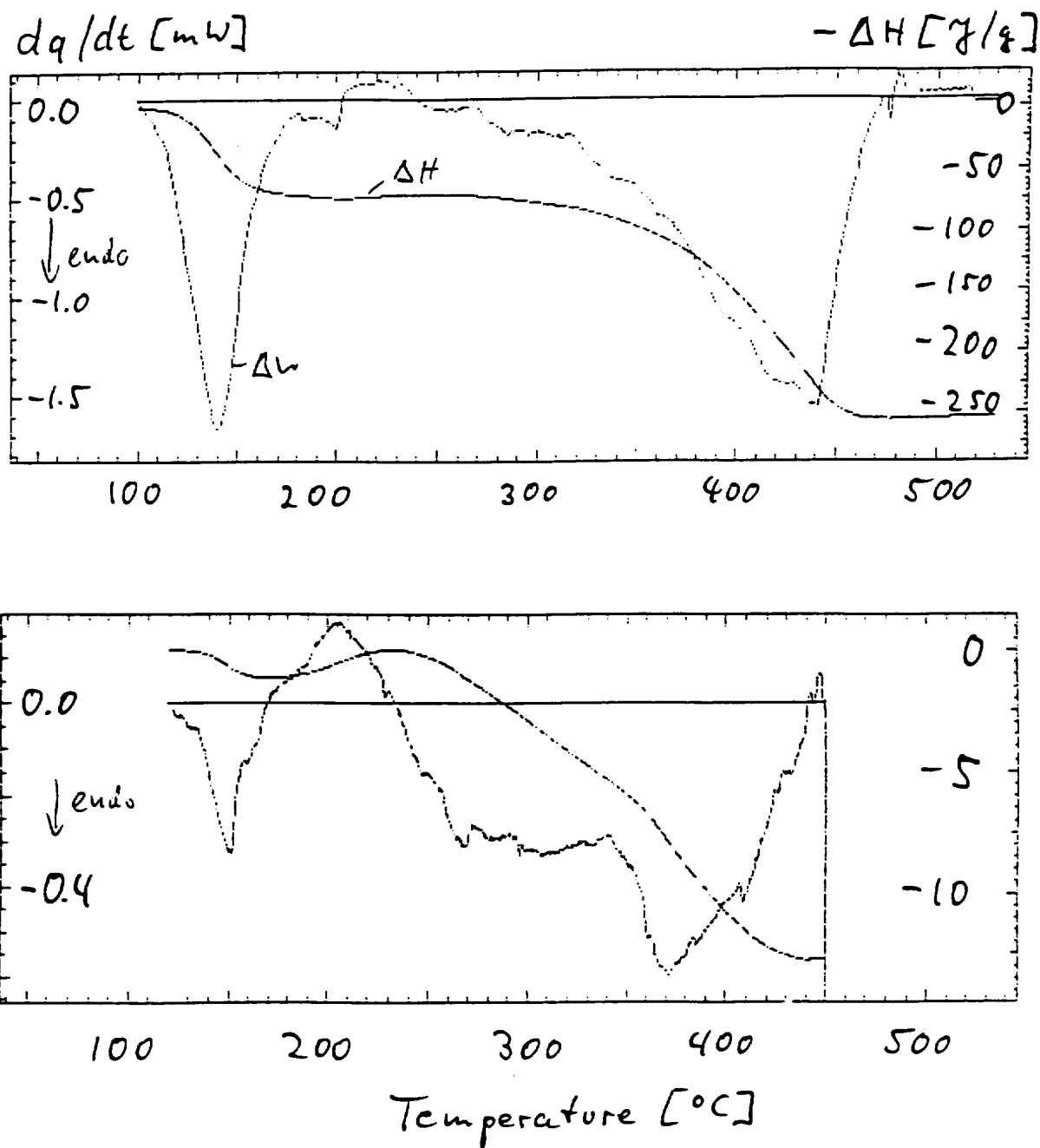


Fig. 60

Fig. 61

Fig. 62

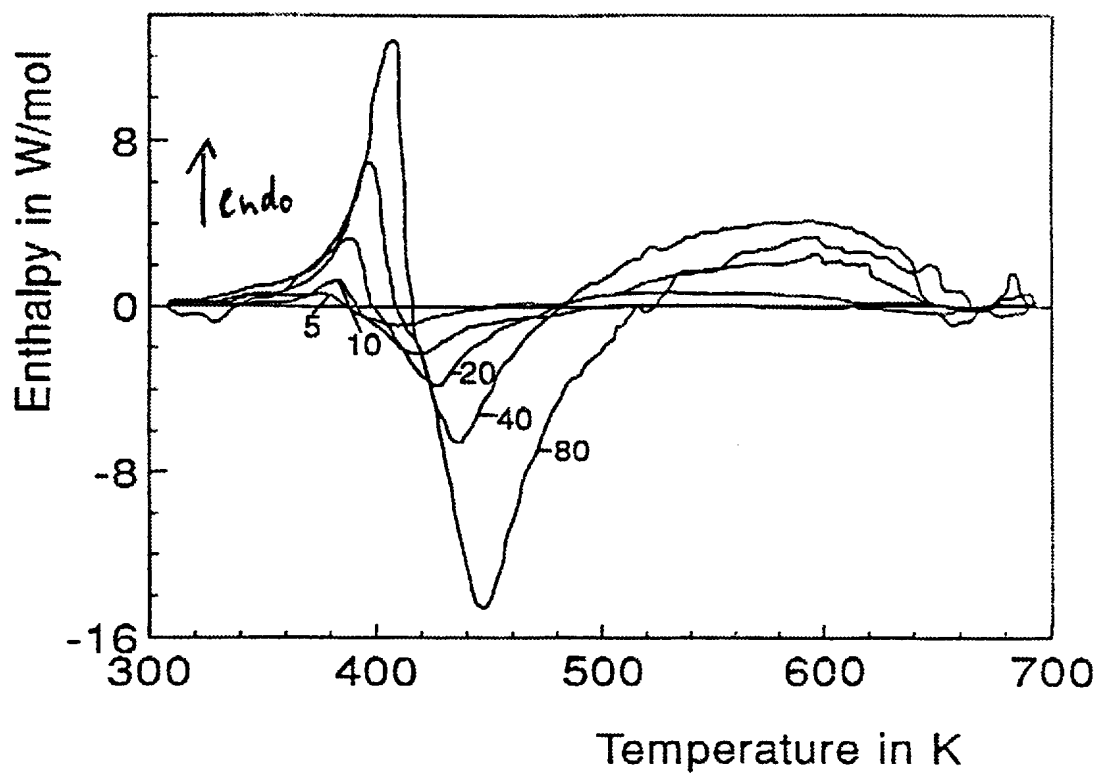
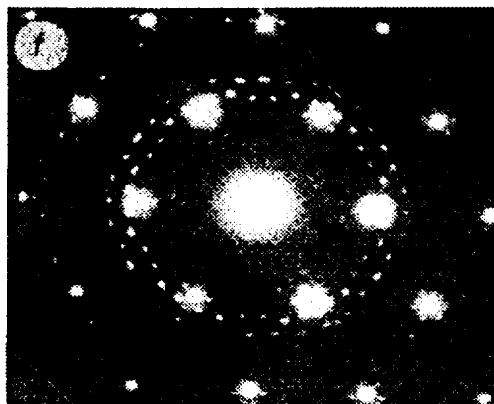


Fig. 63

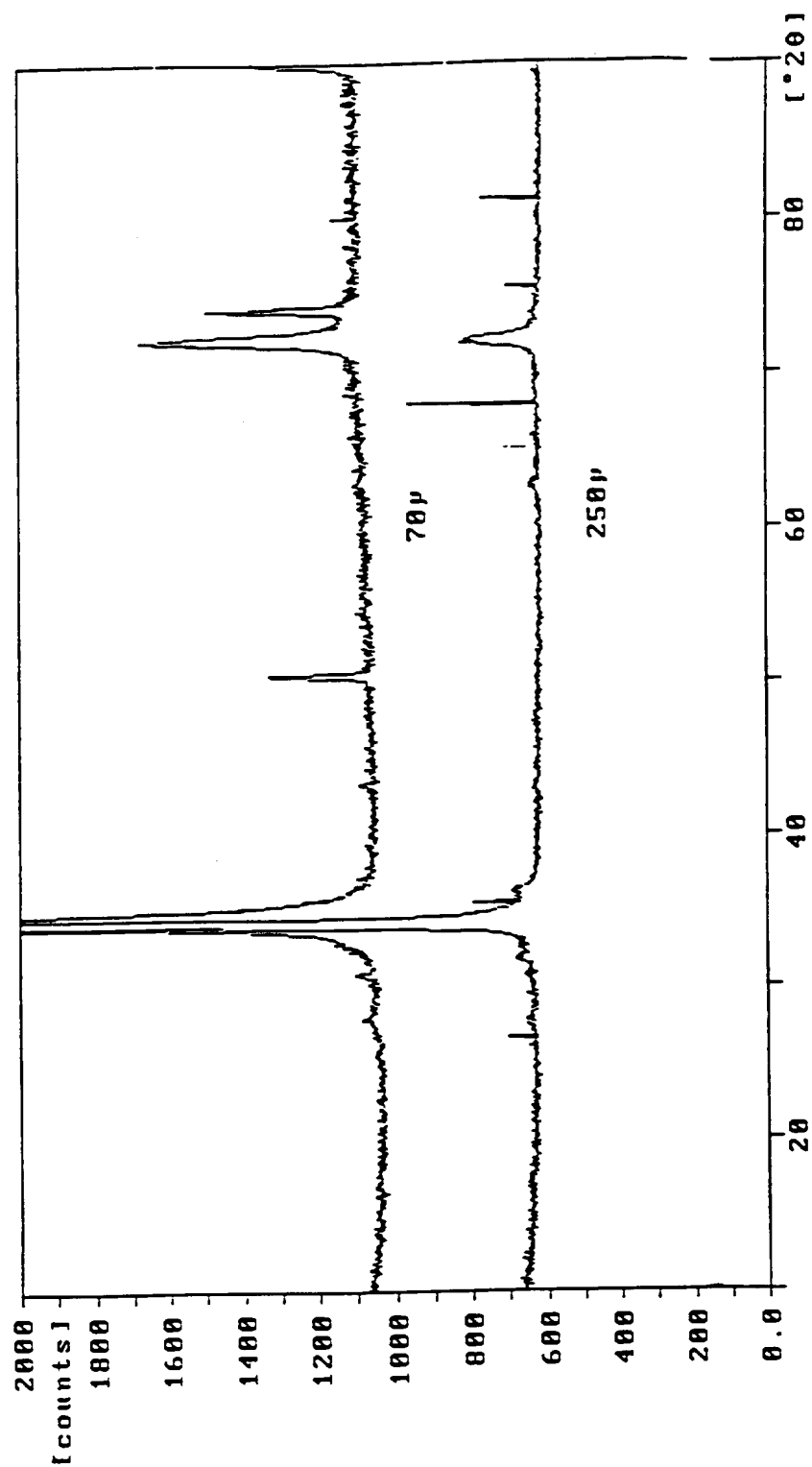


Fig. 64

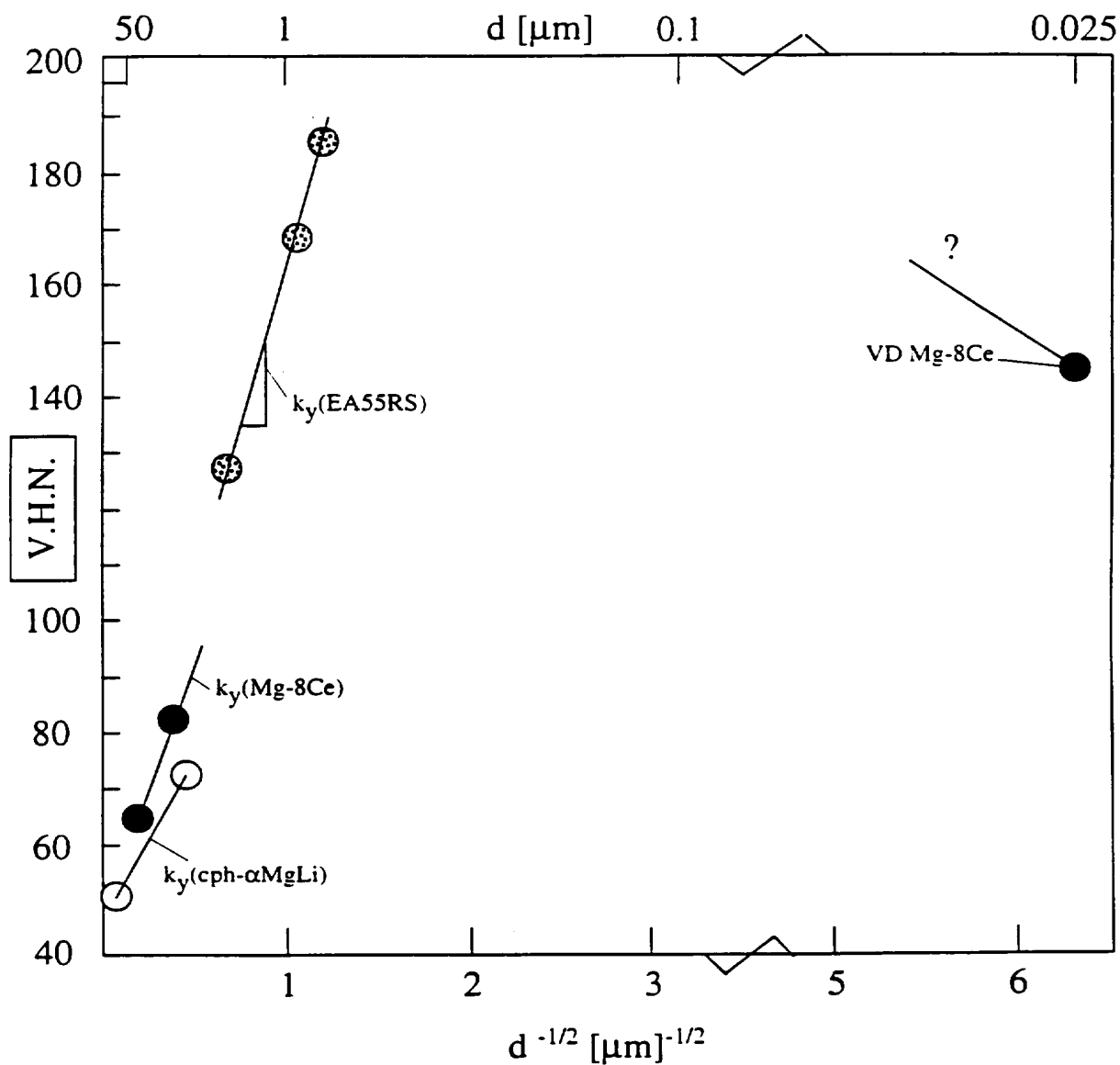


Fig. 65

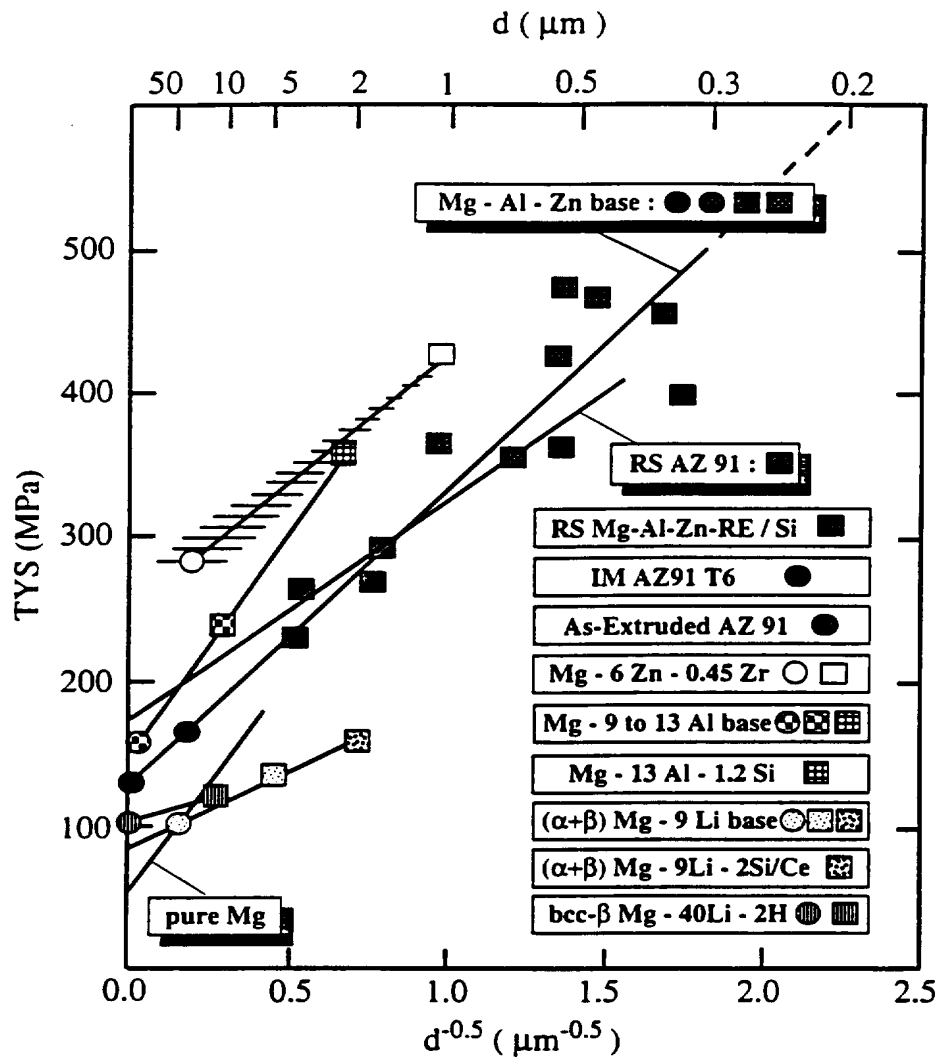


Fig. 66

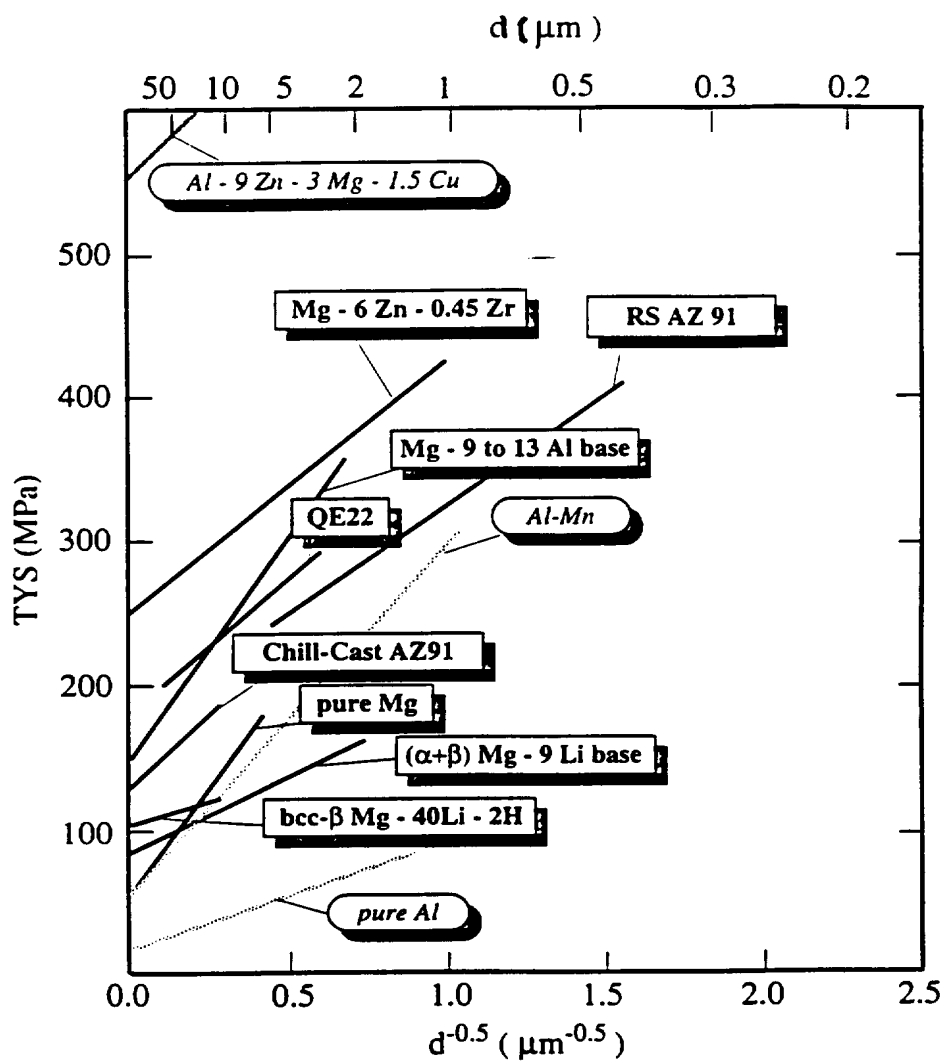
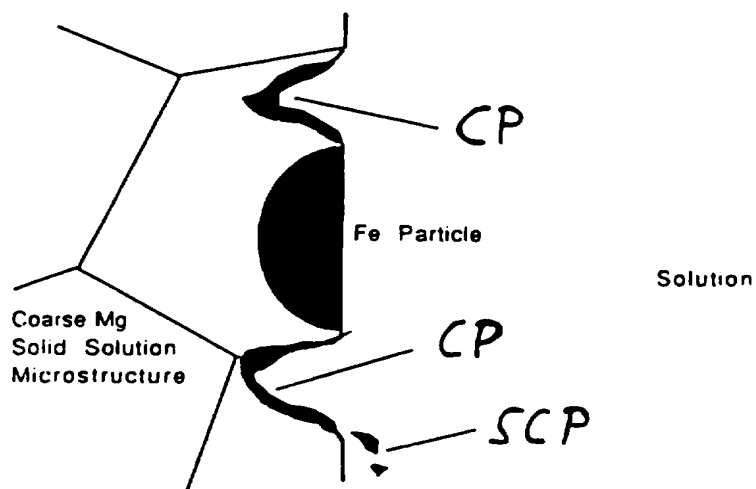
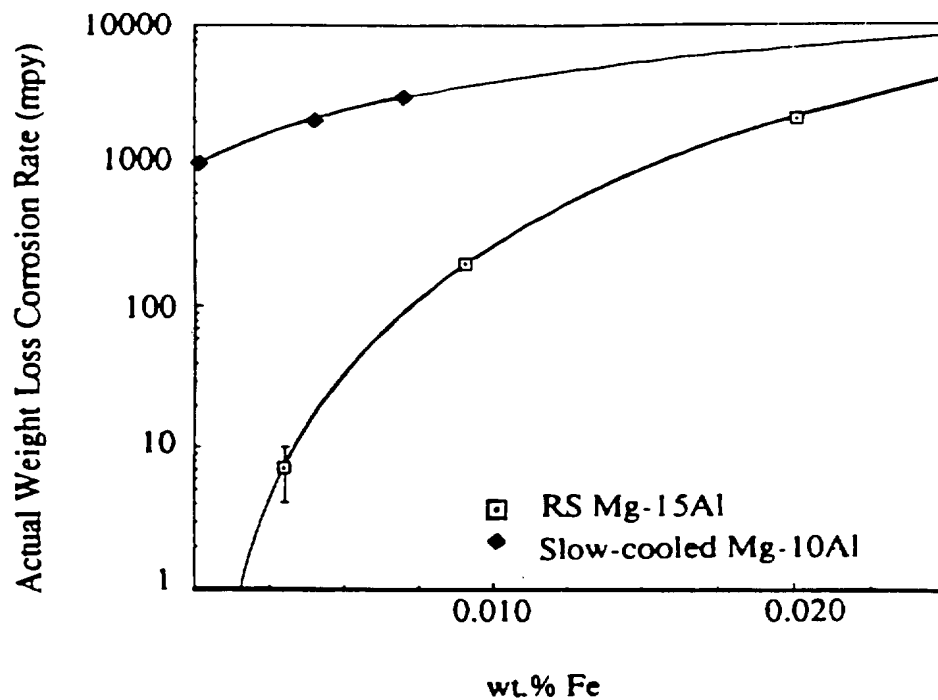
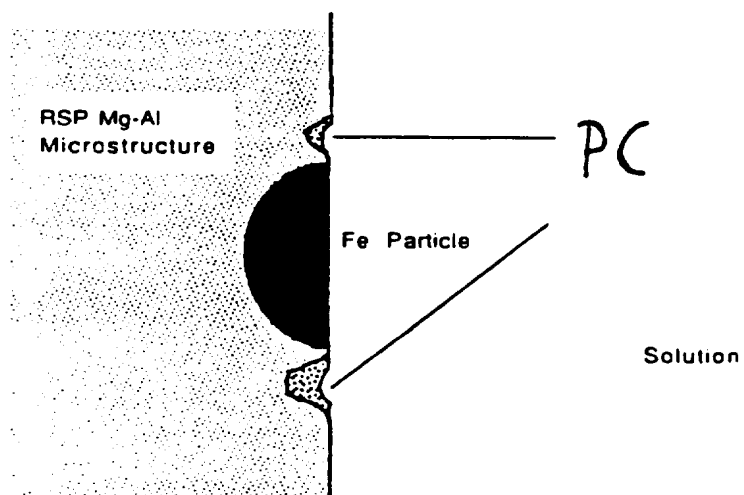


Fig. 67



(a)

Fig. 68

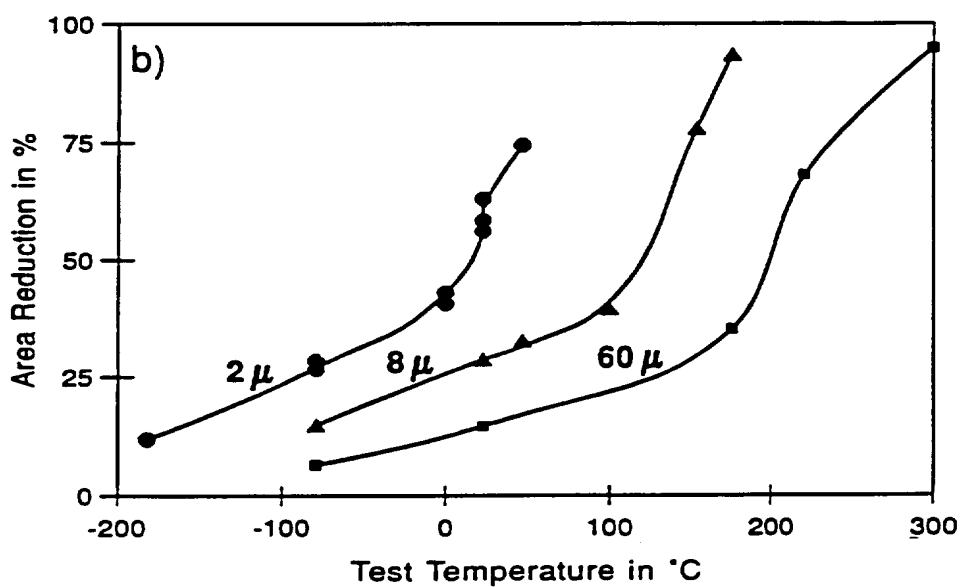
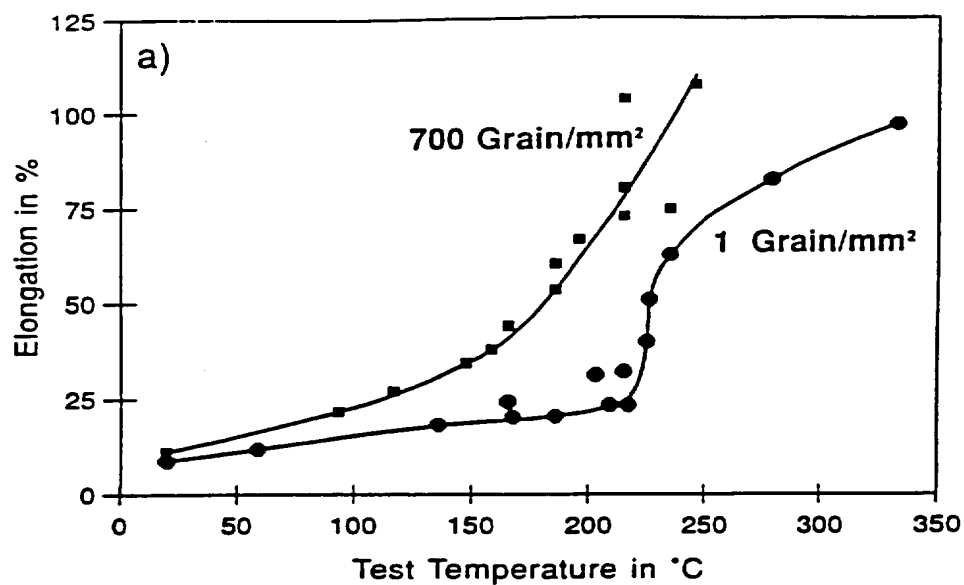
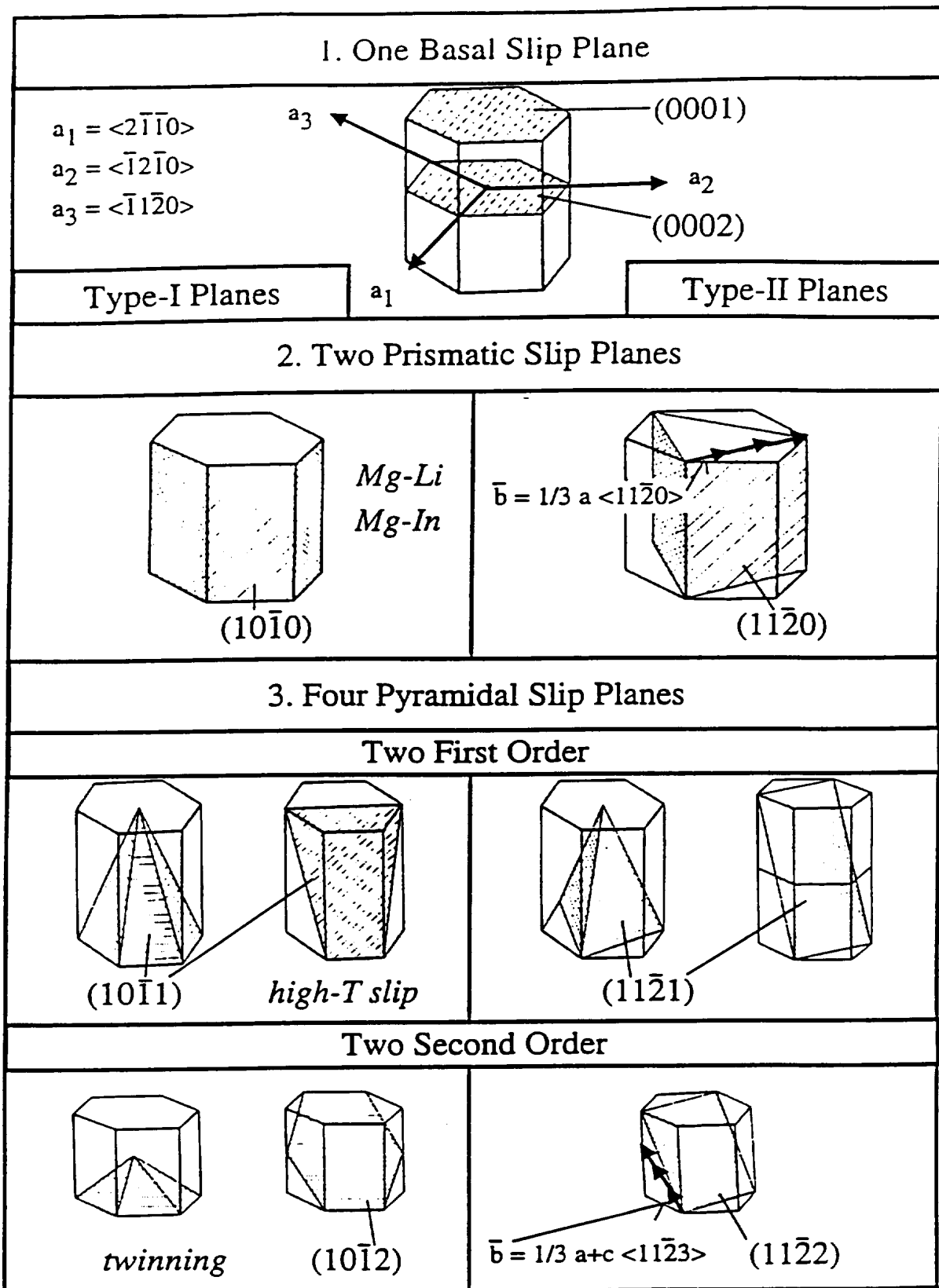


Fig. 69

Fig. 70

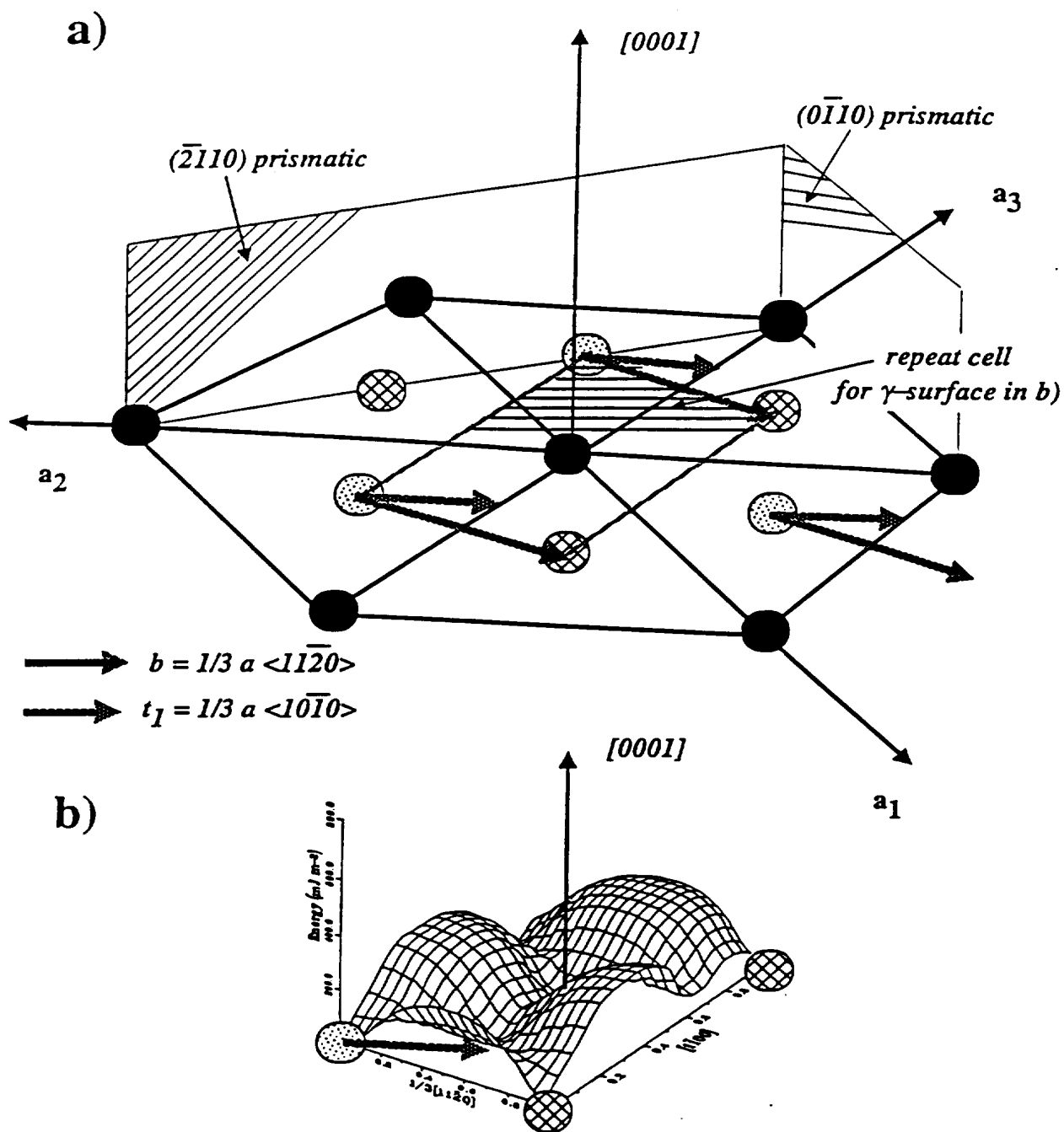


Fig. 71

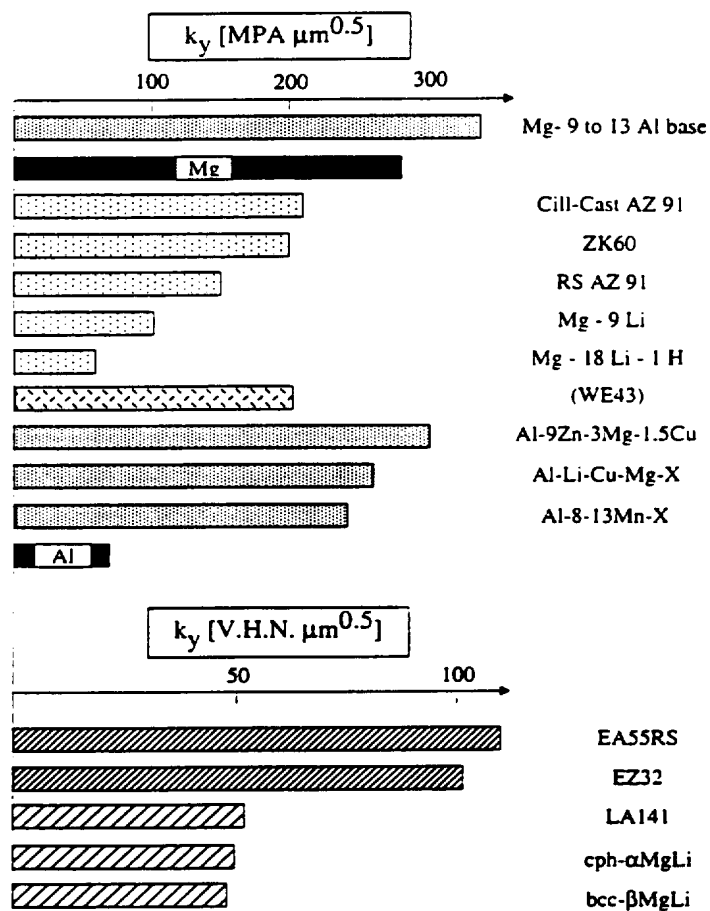


Fig. 72

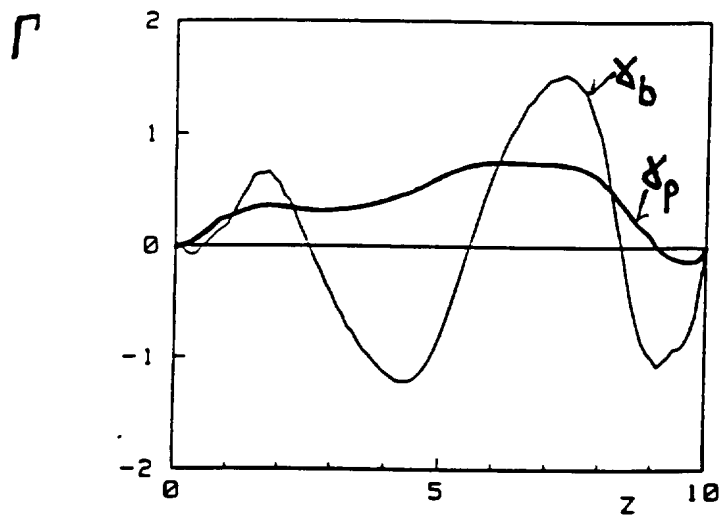
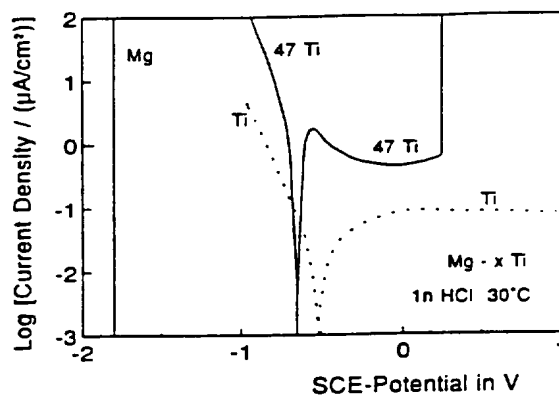
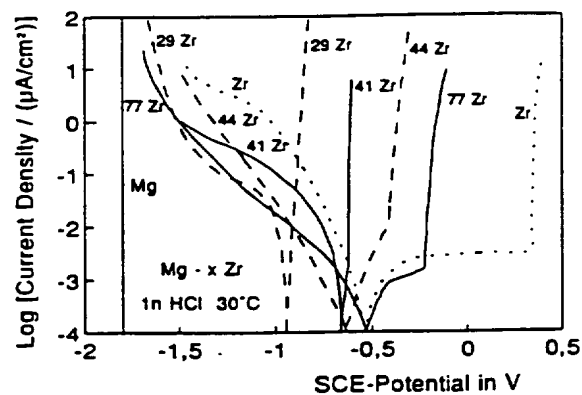


Fig. 73

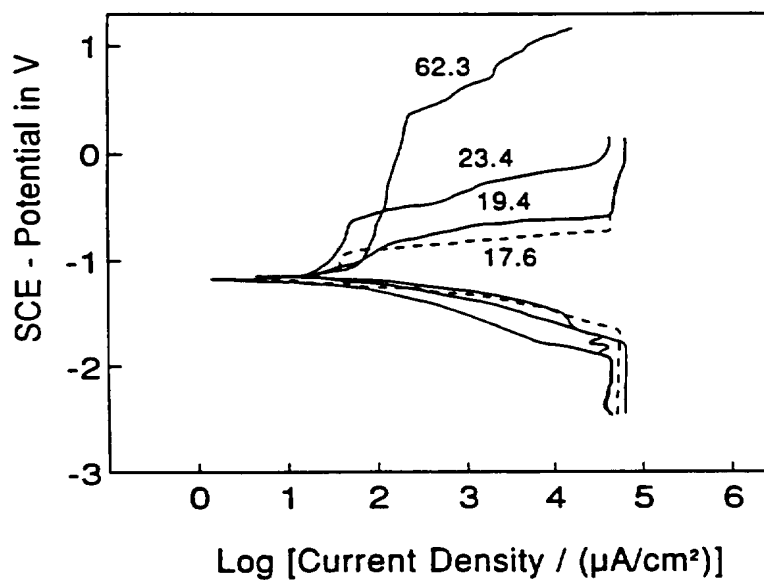
a)



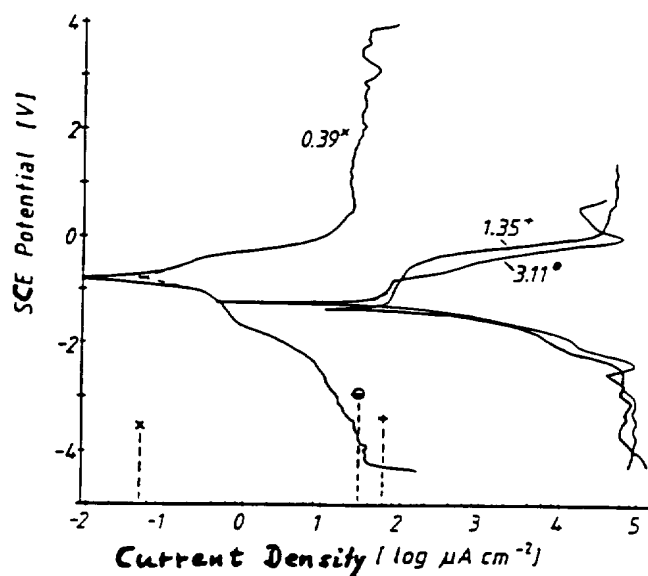
b)



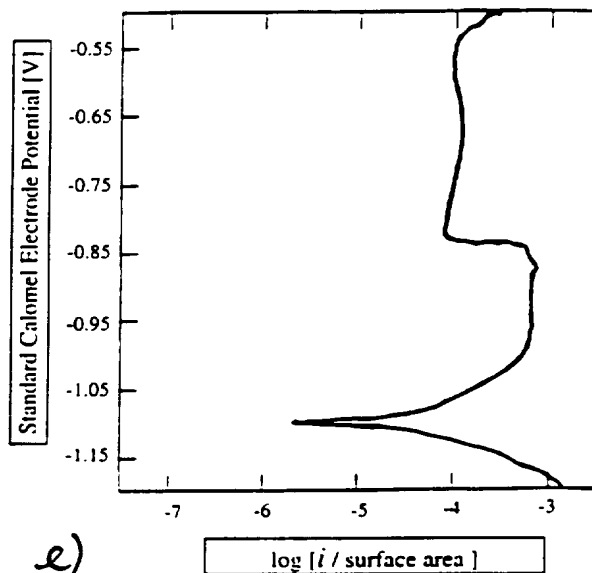
c)

Fig. 74

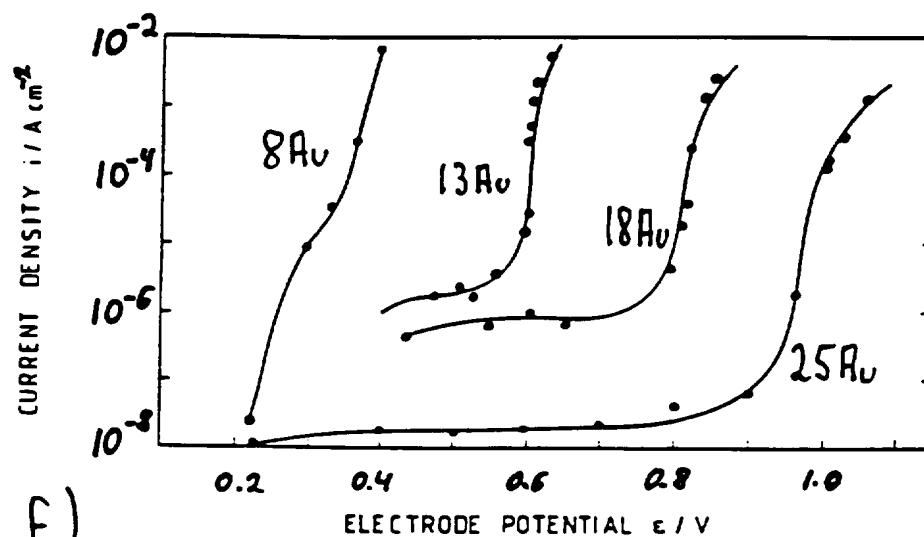
SUBSTITUTE SHEET (RULE 26)



d)

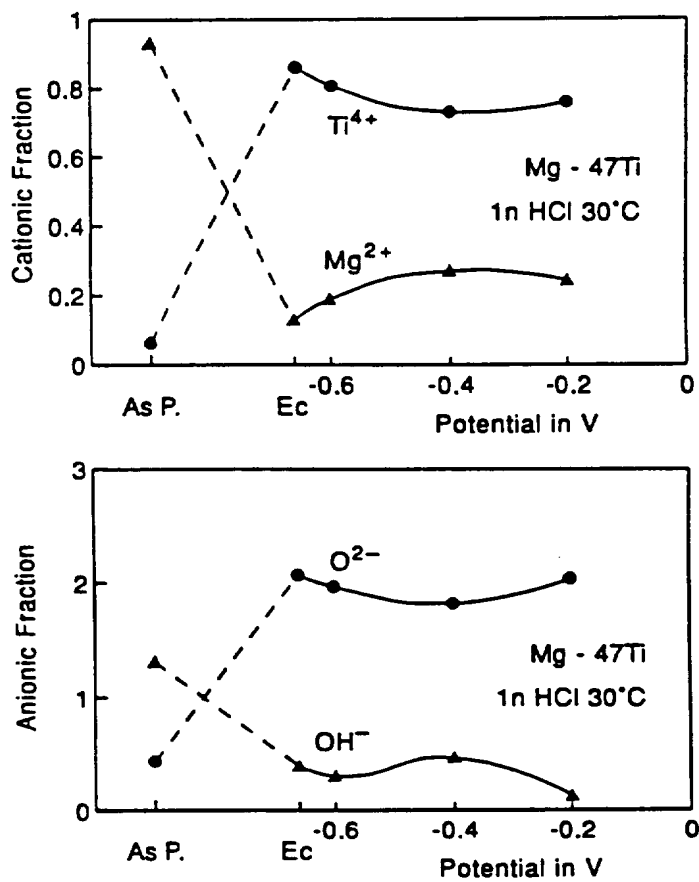


e)



f)

Fig. 74/cont'd

Fig. 75

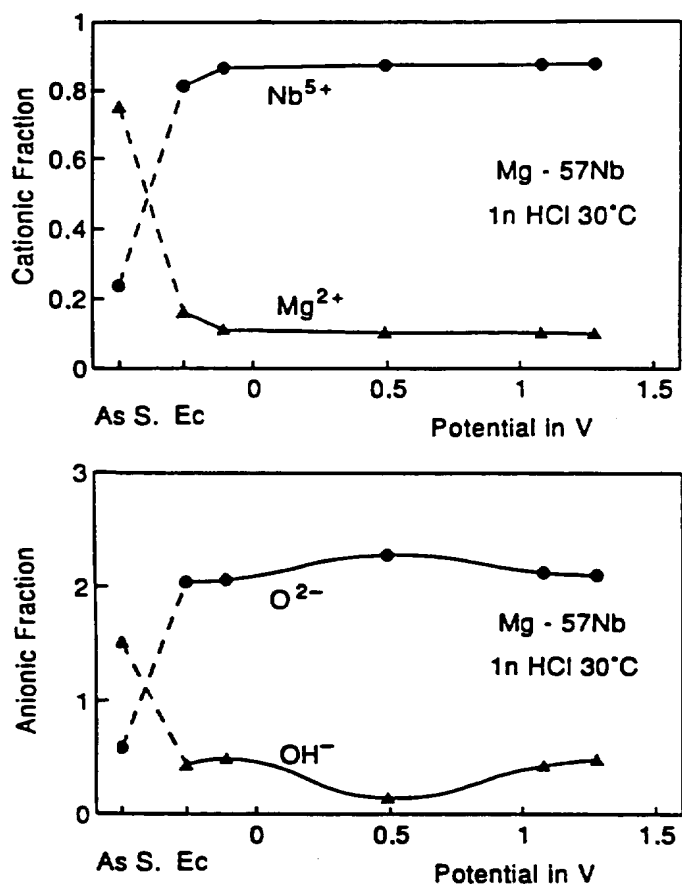
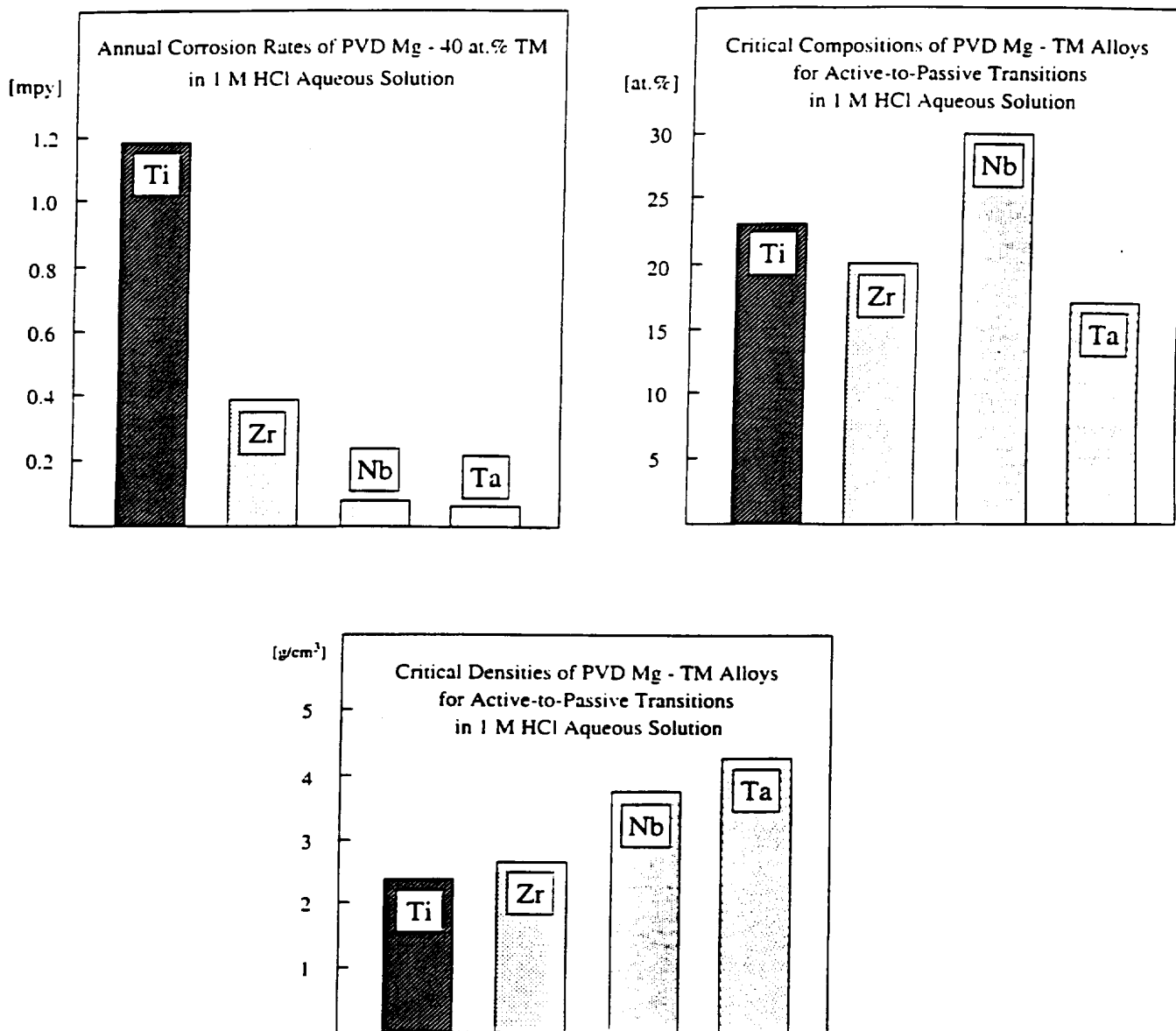


Fig. 75 / cont'd

Fig. 76

Corrosion of magnesium and its alloys with time

Pilling-Bedworth Ratio

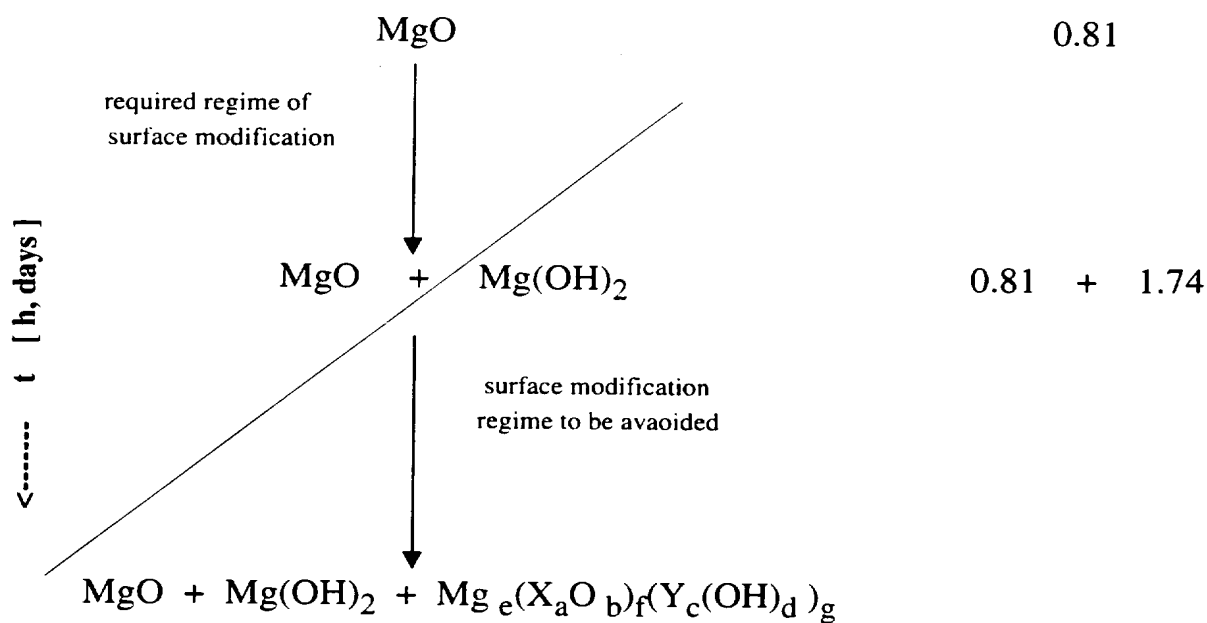
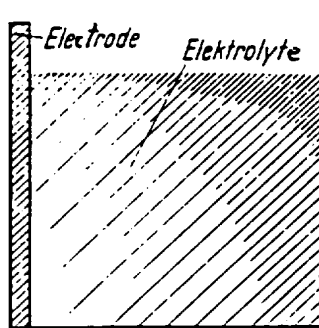
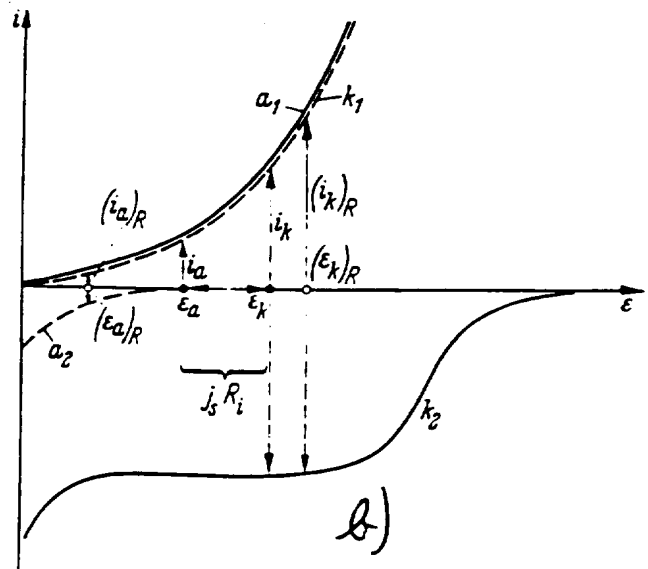


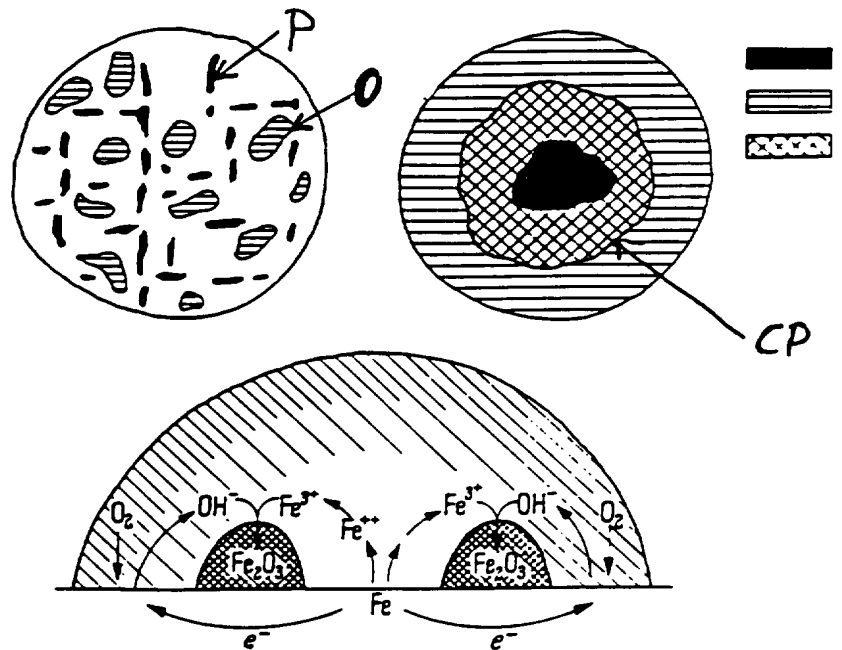
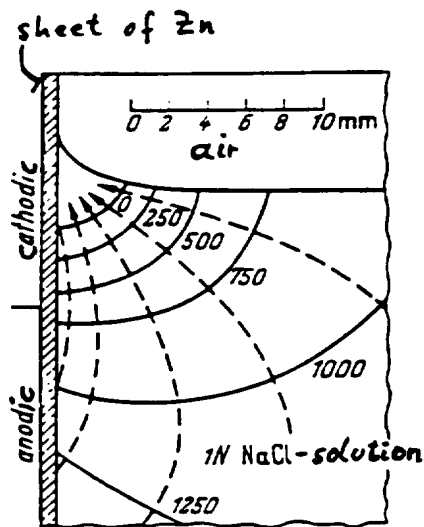
Fig. 77



a)



b)

Fig. 78

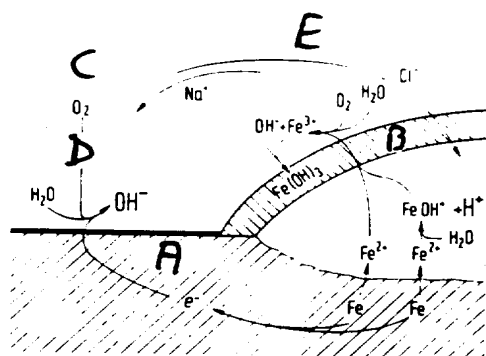
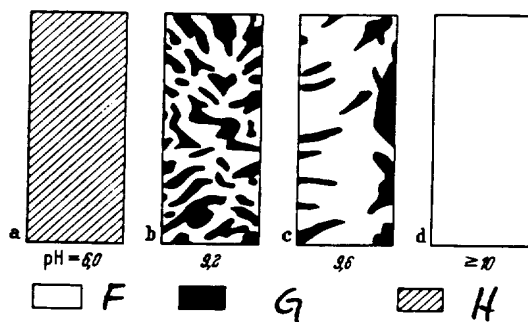


Fig. 79

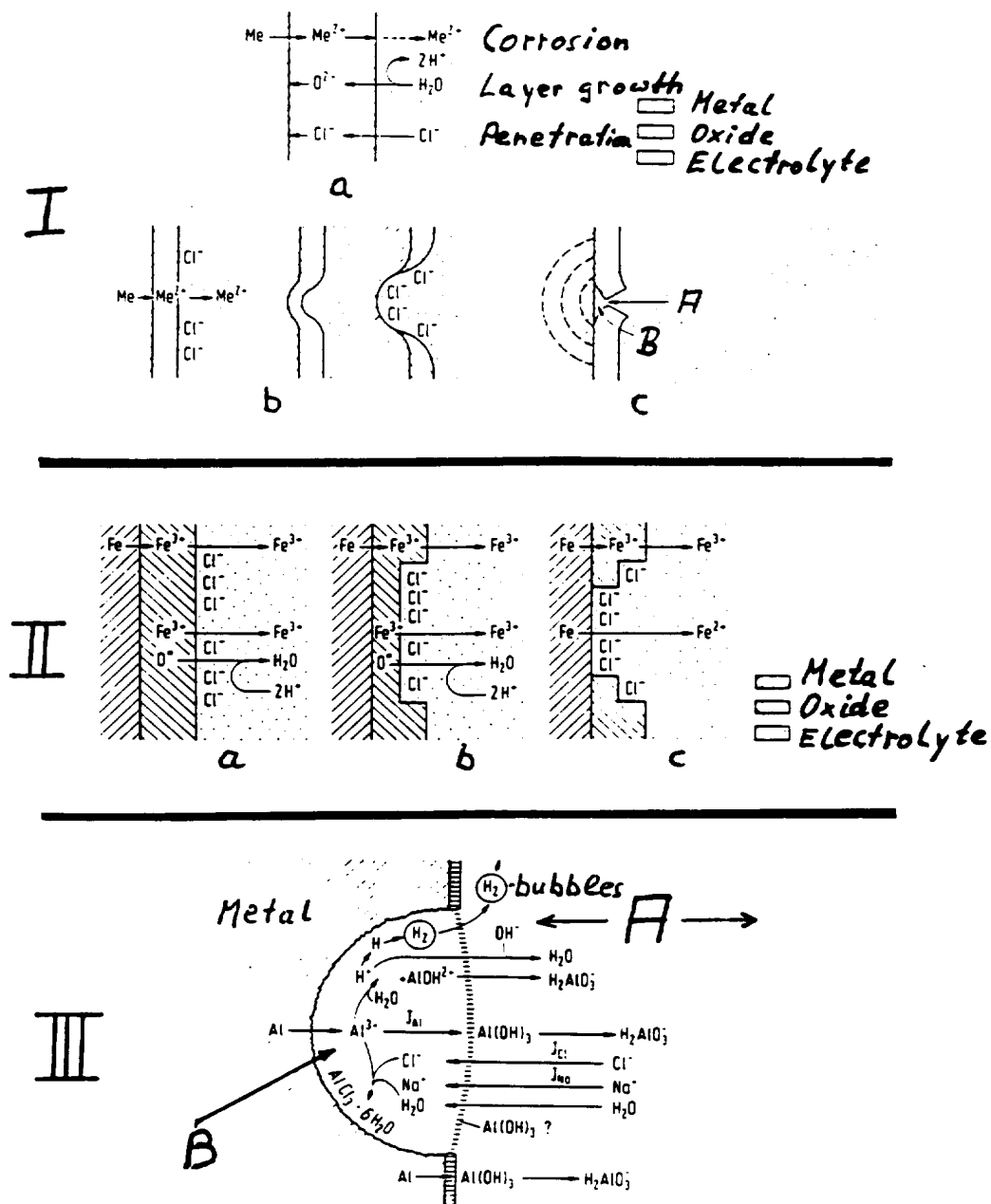
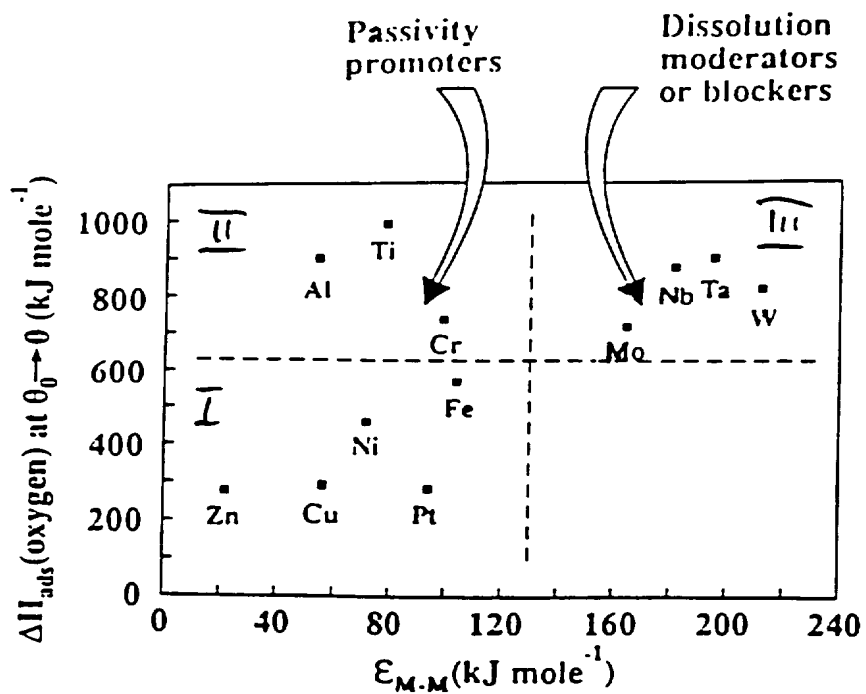


Fig. 80

Fig. 81

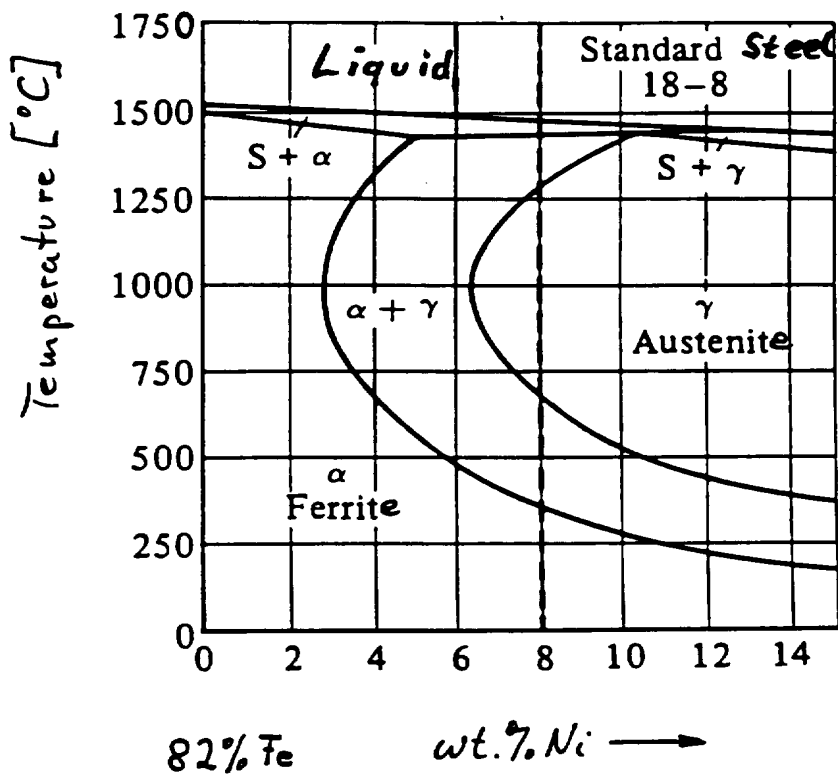
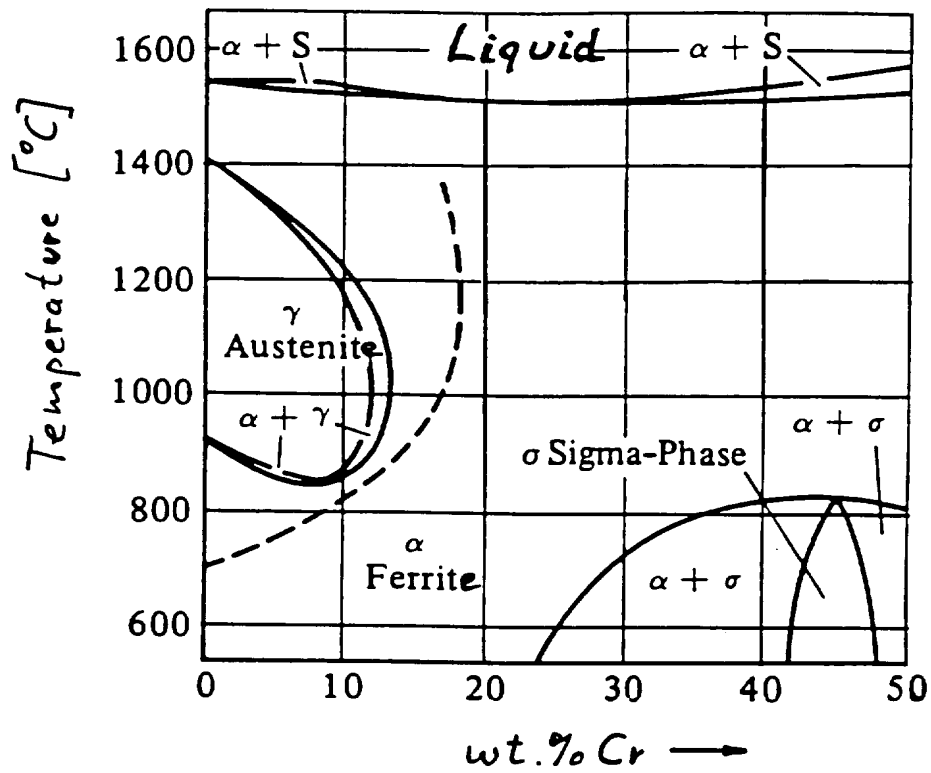
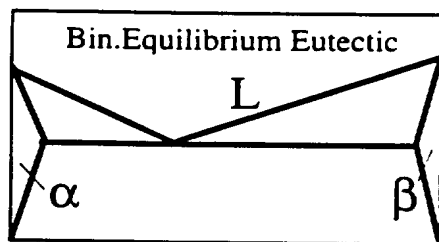
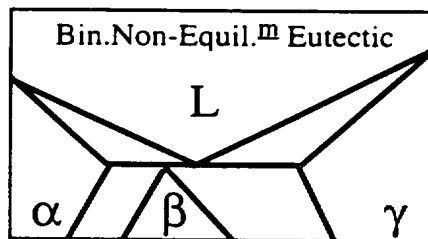


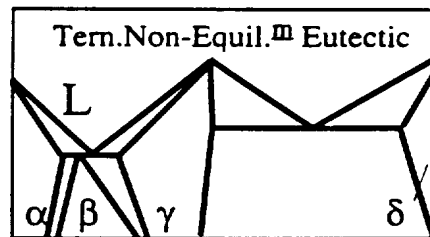
Fig. 82



a)



b)

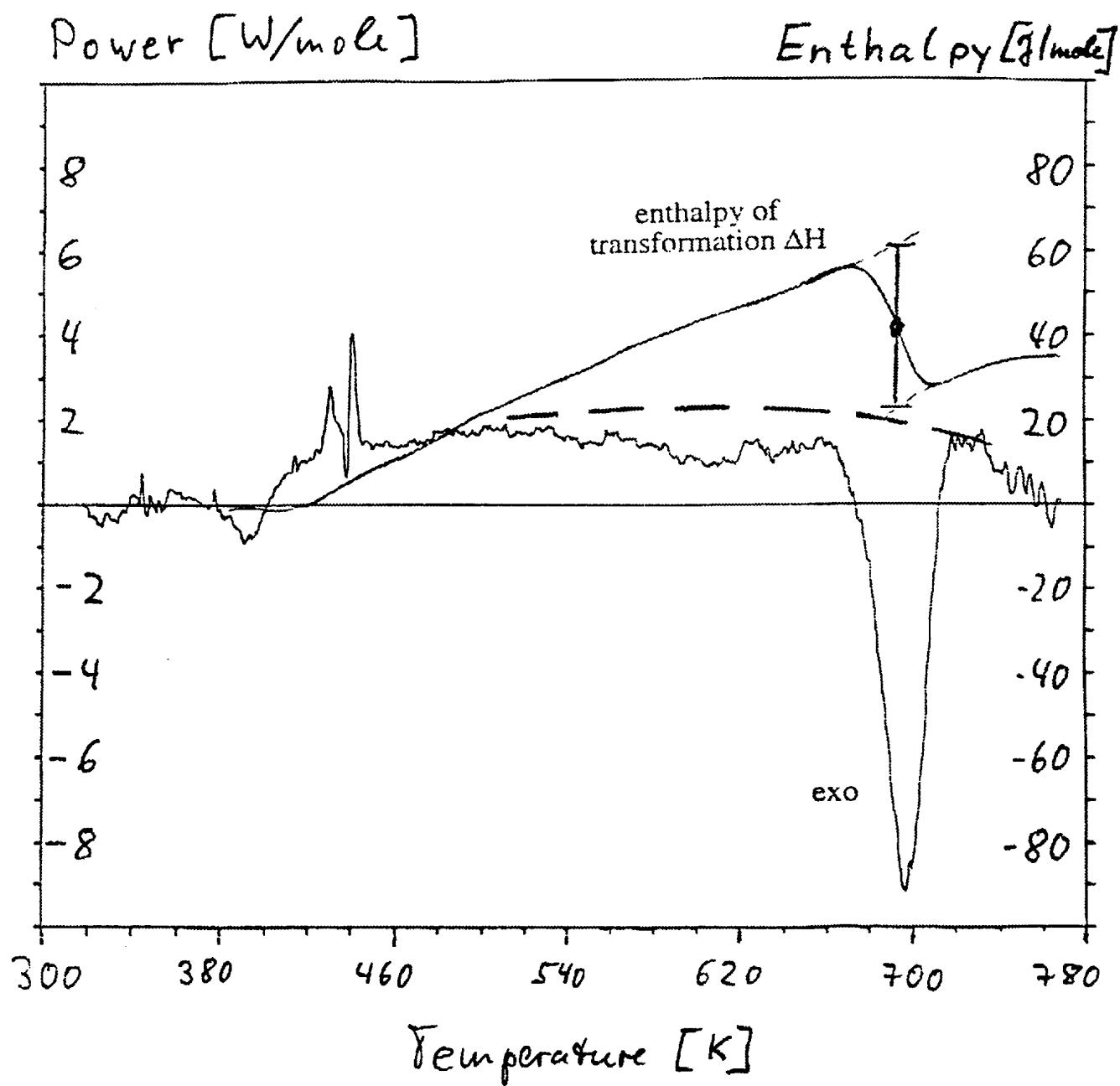


c)

Fig. 83



Fig. 85

Fig. 86

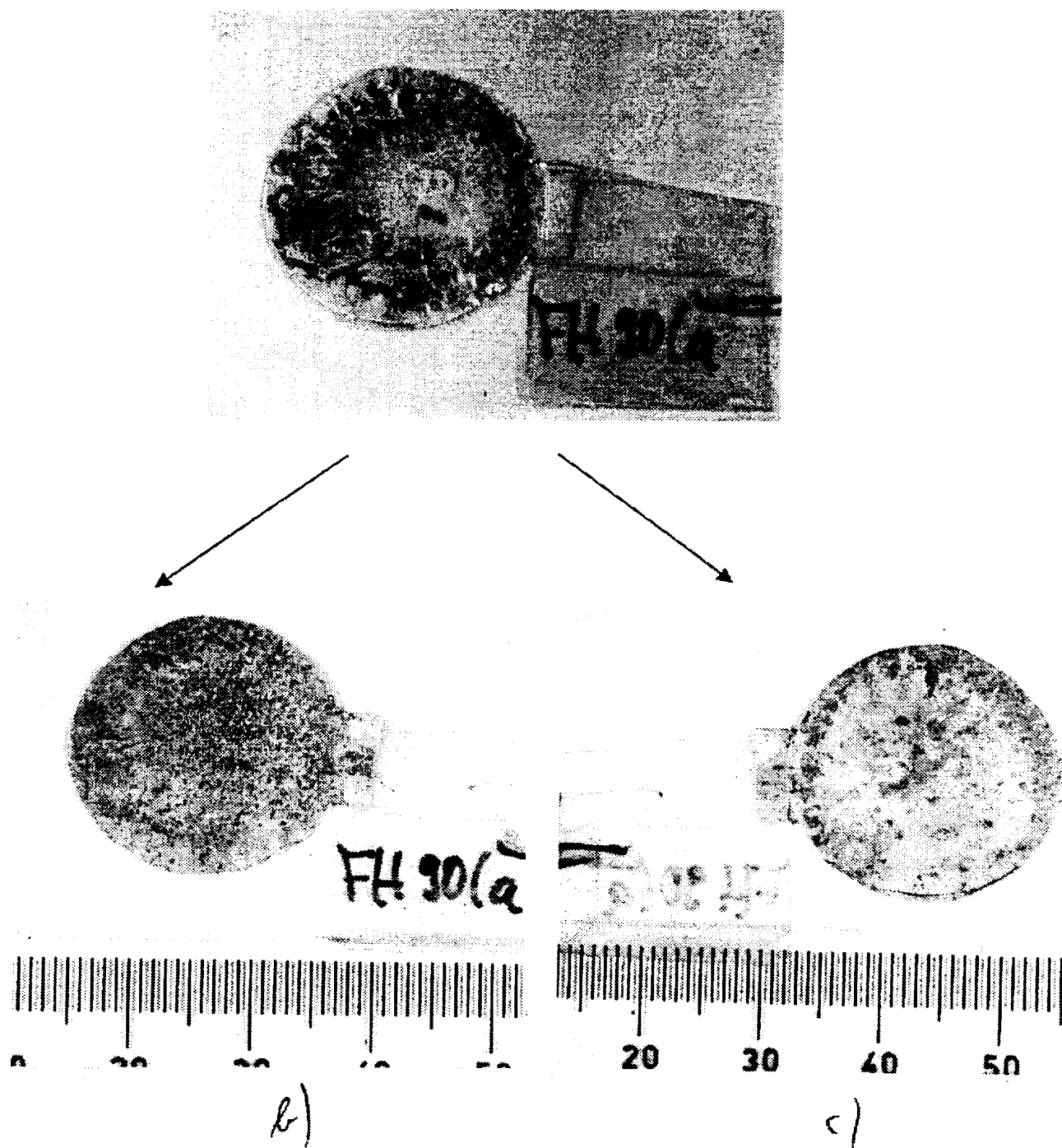


Fig. 87

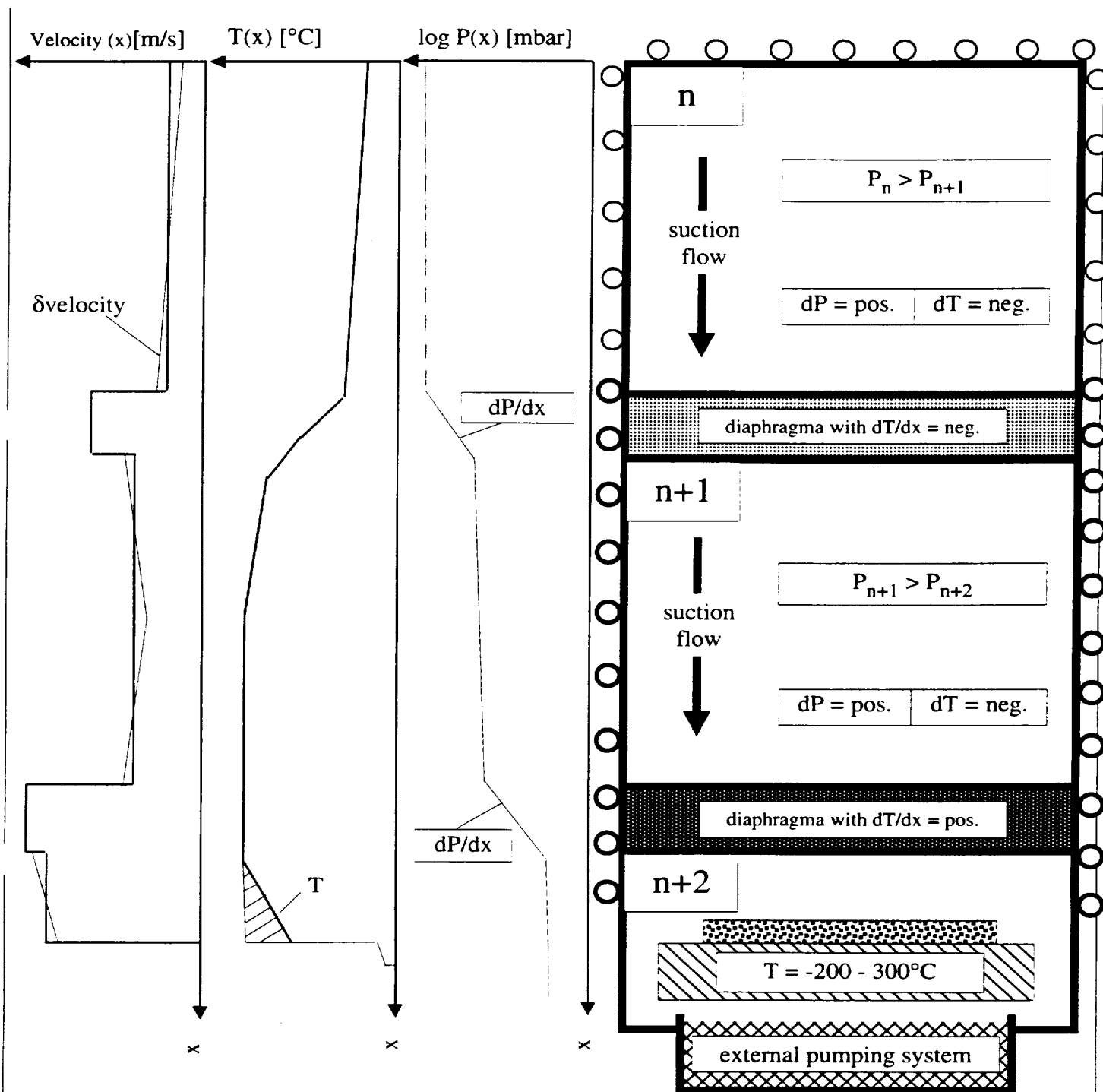


Fig. 88

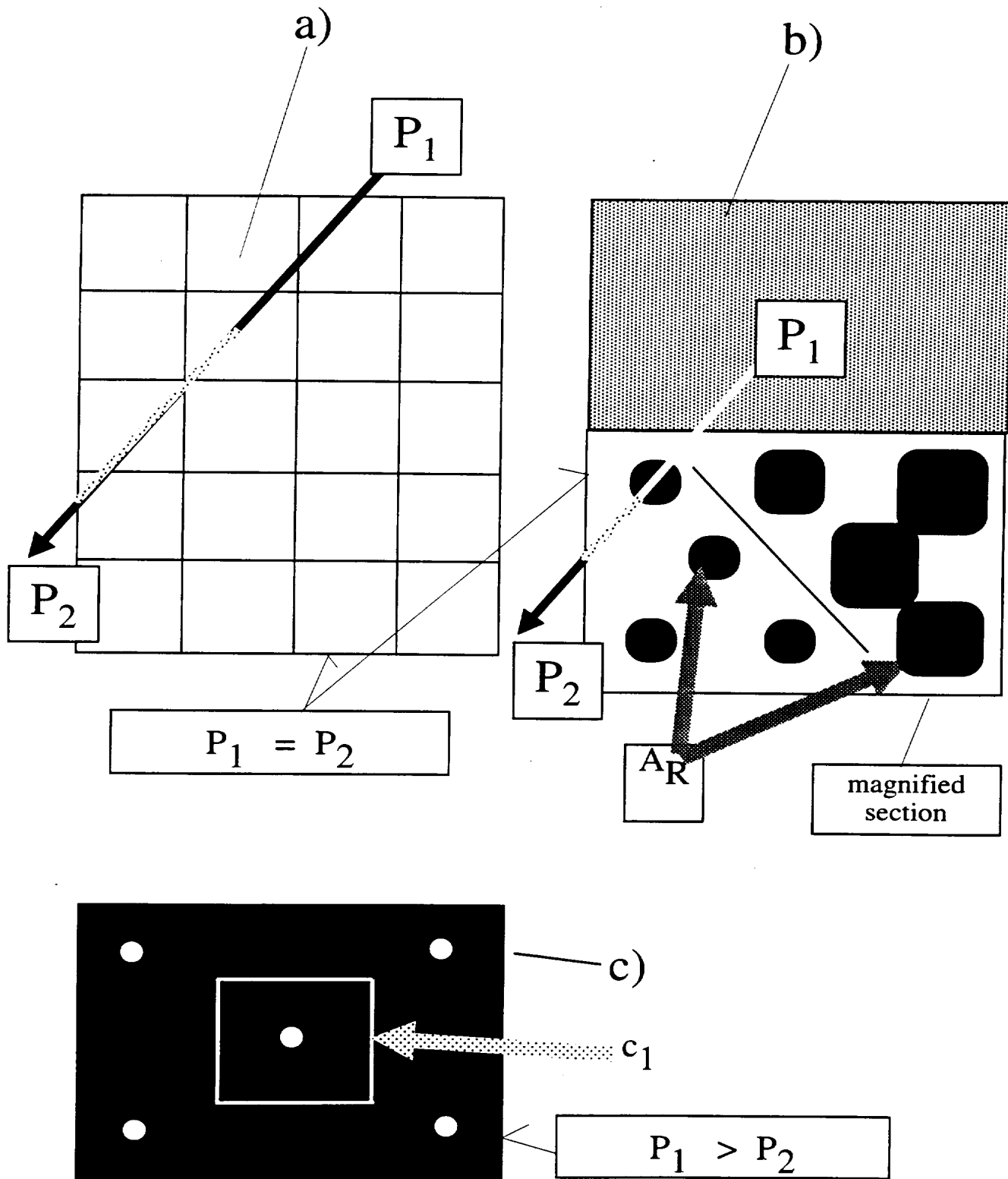


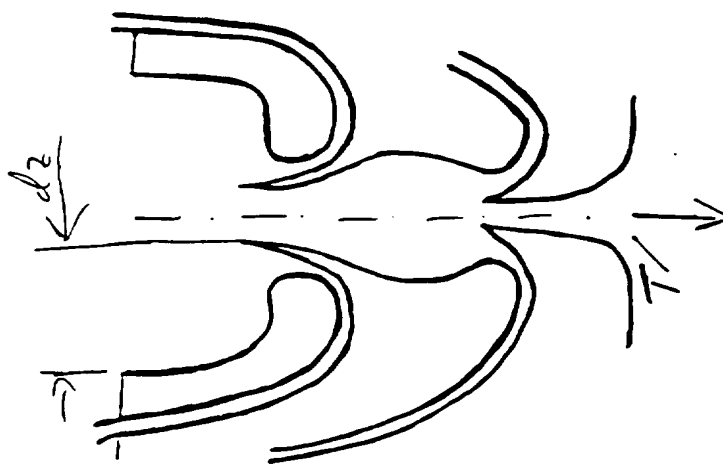
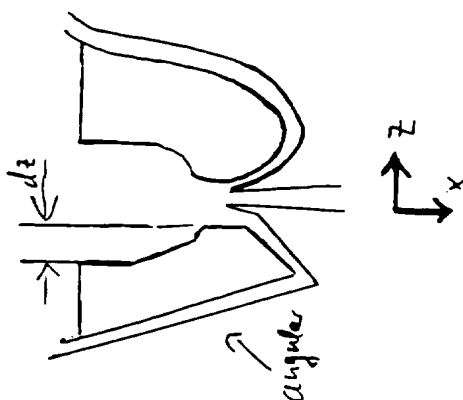
Fig. 89

Bifurcations

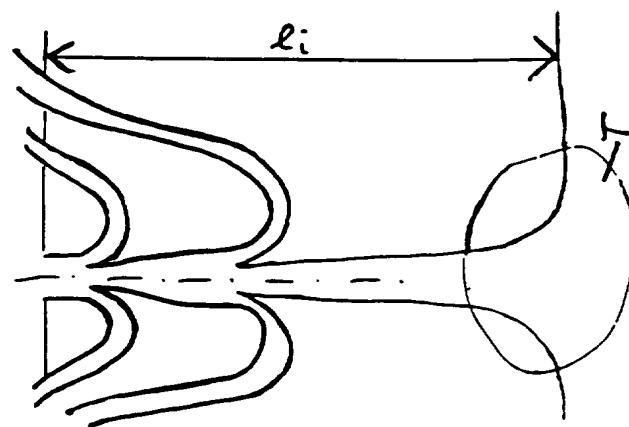
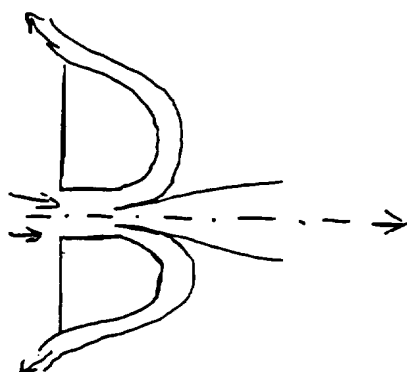
Single / single pair

Multiple / series

Channelled



Smoothed-out



Angular

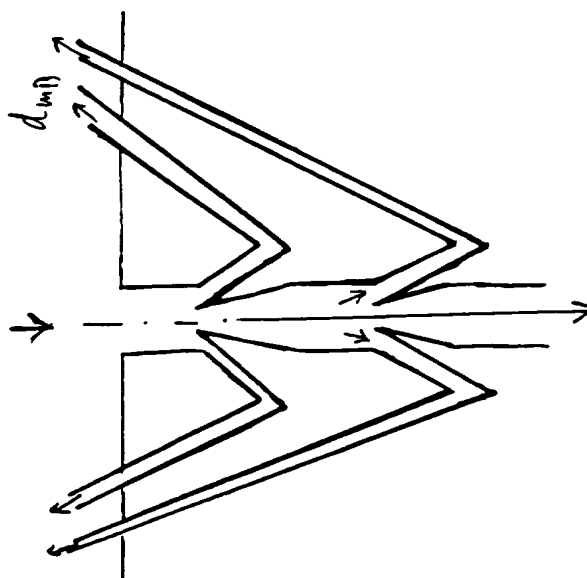
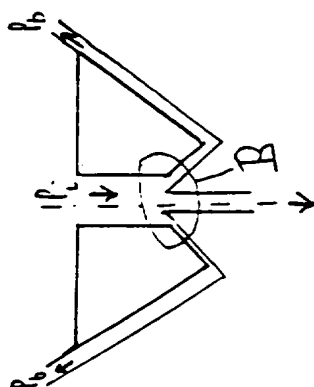


Fig. 90
SUBSTITUTE SHEET (RULE 26)

Bifurcations

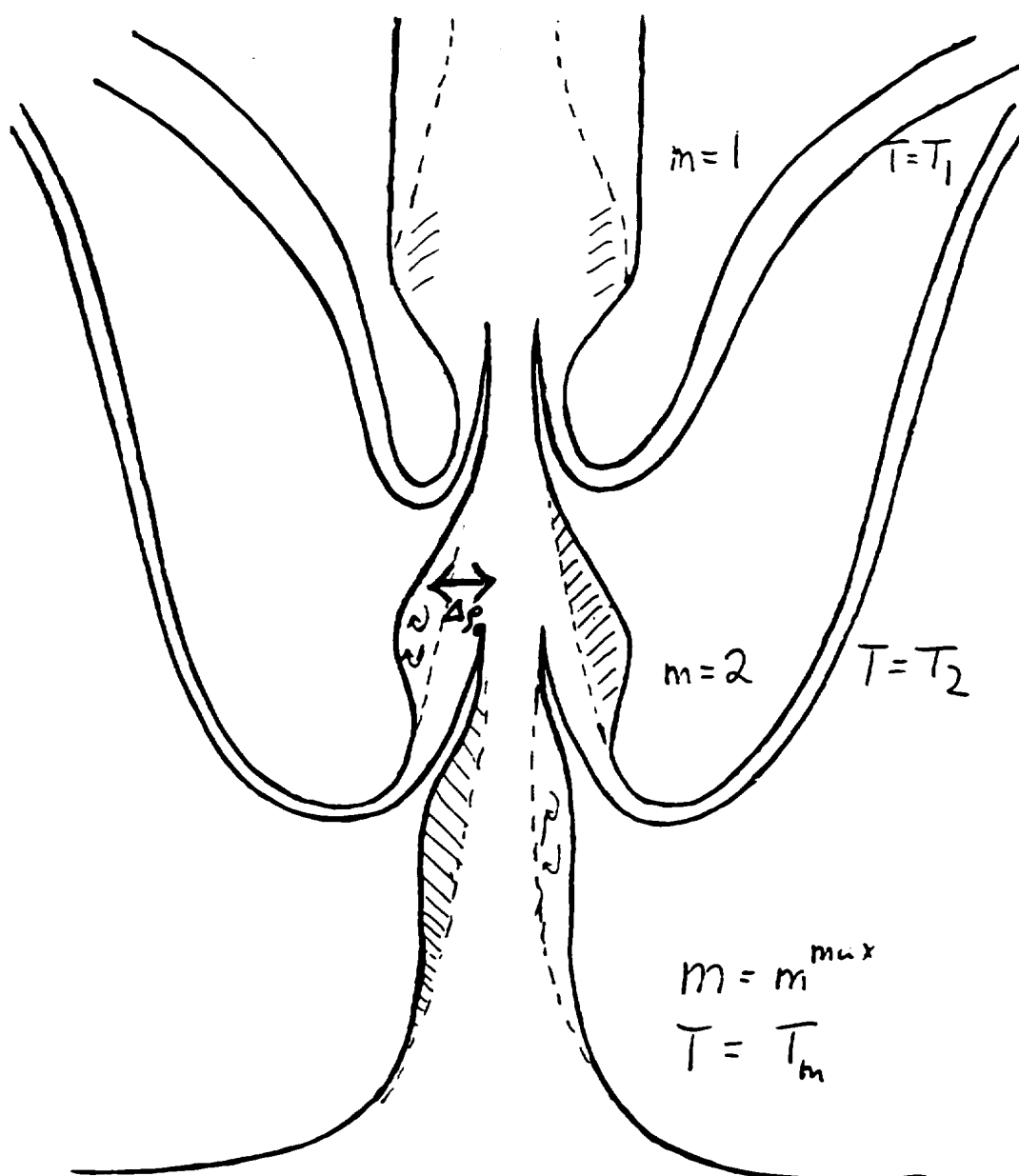


Fig. 91

Control elements for turbulent and laminar flow

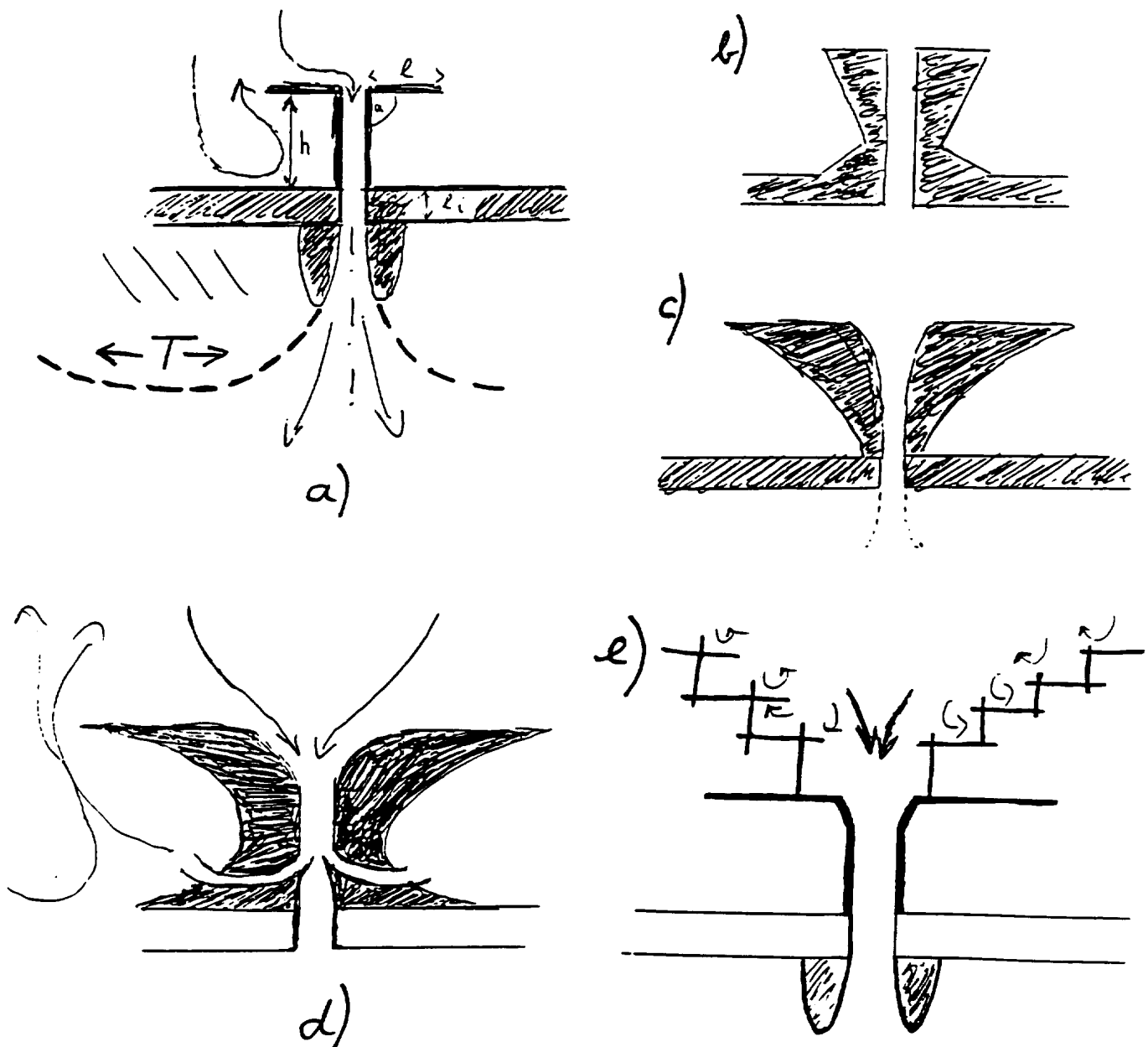


Fig. 92

SUBSTITUTE SHEET (RULE 26)

Series resistor to vapour flow

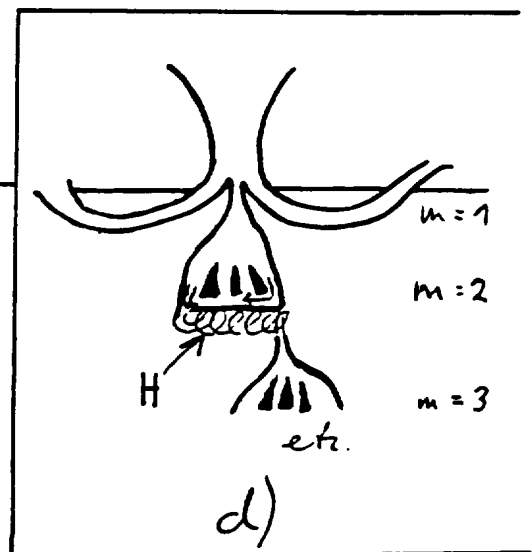
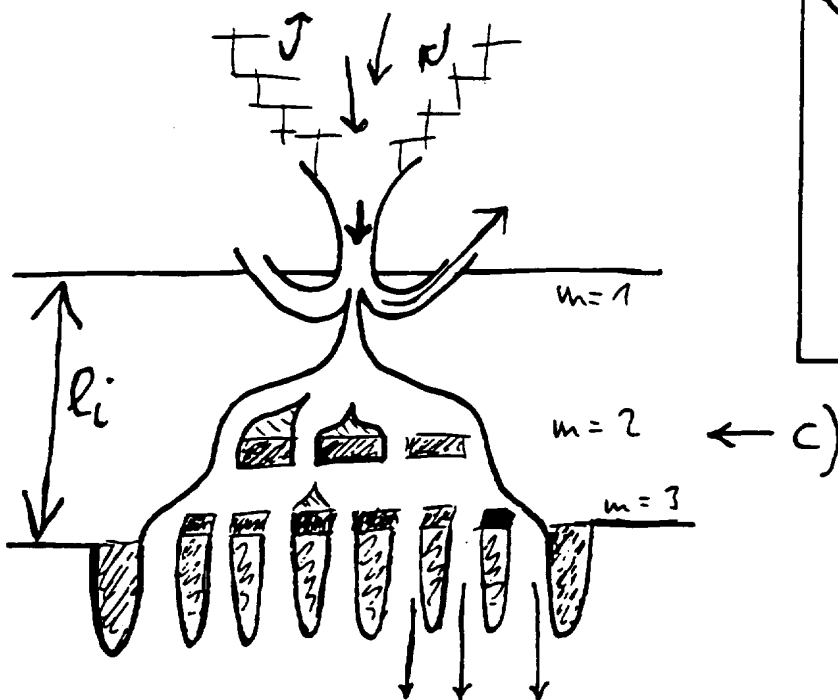
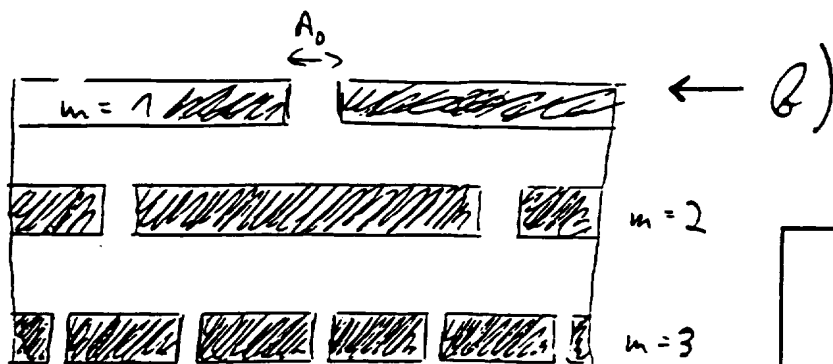
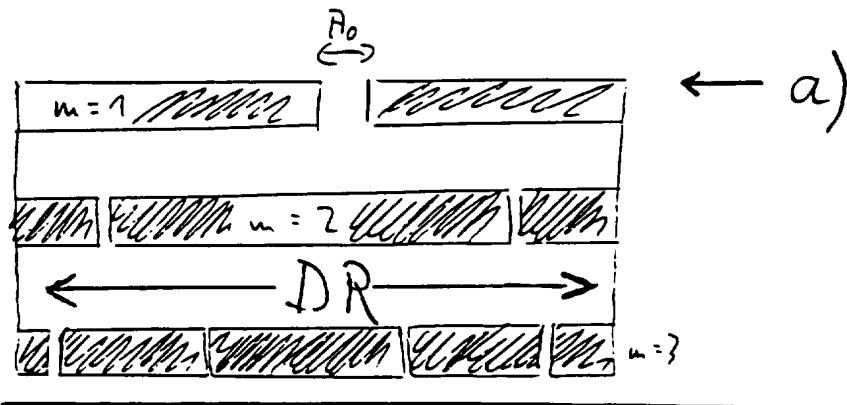


Fig. 93

Combinations of Principle Solutions

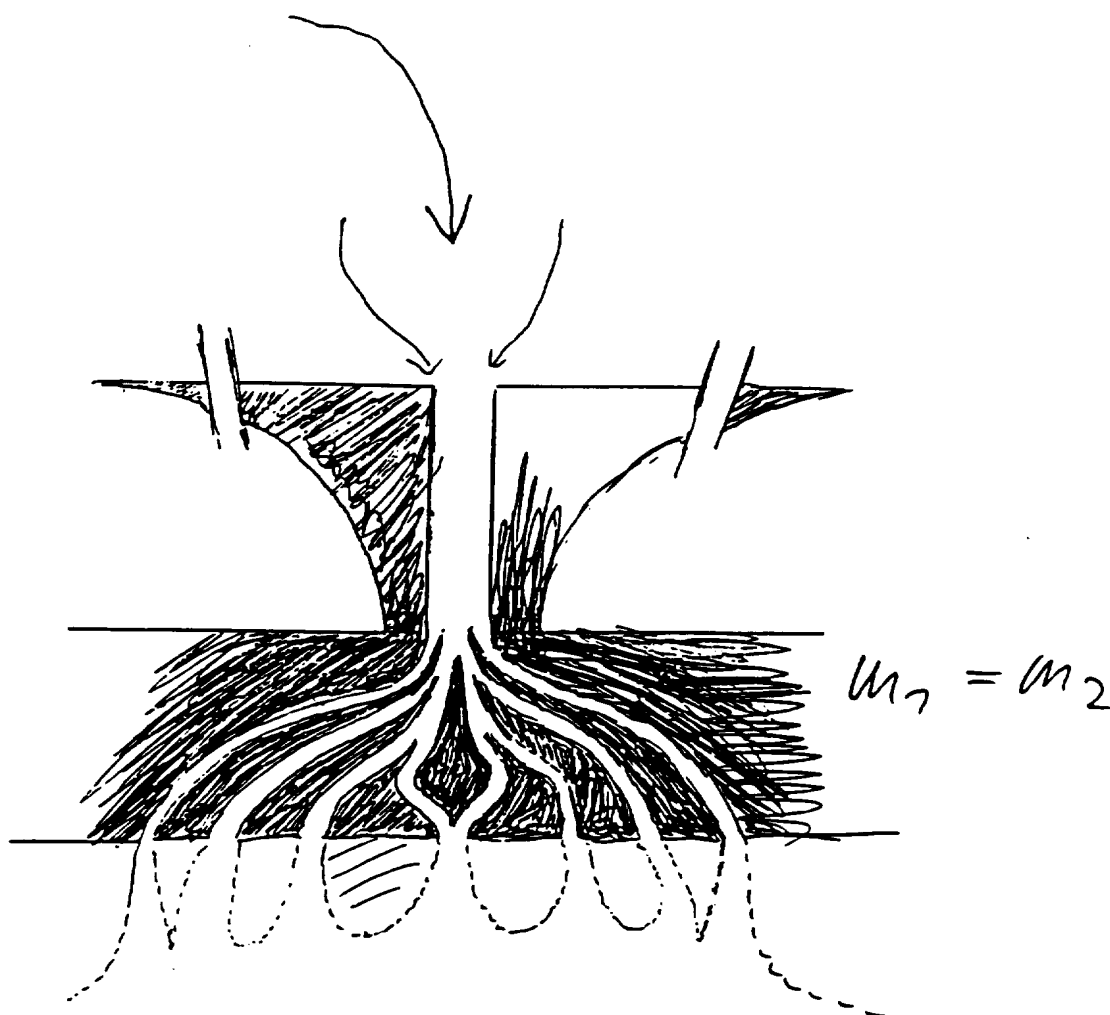


Fig. 94

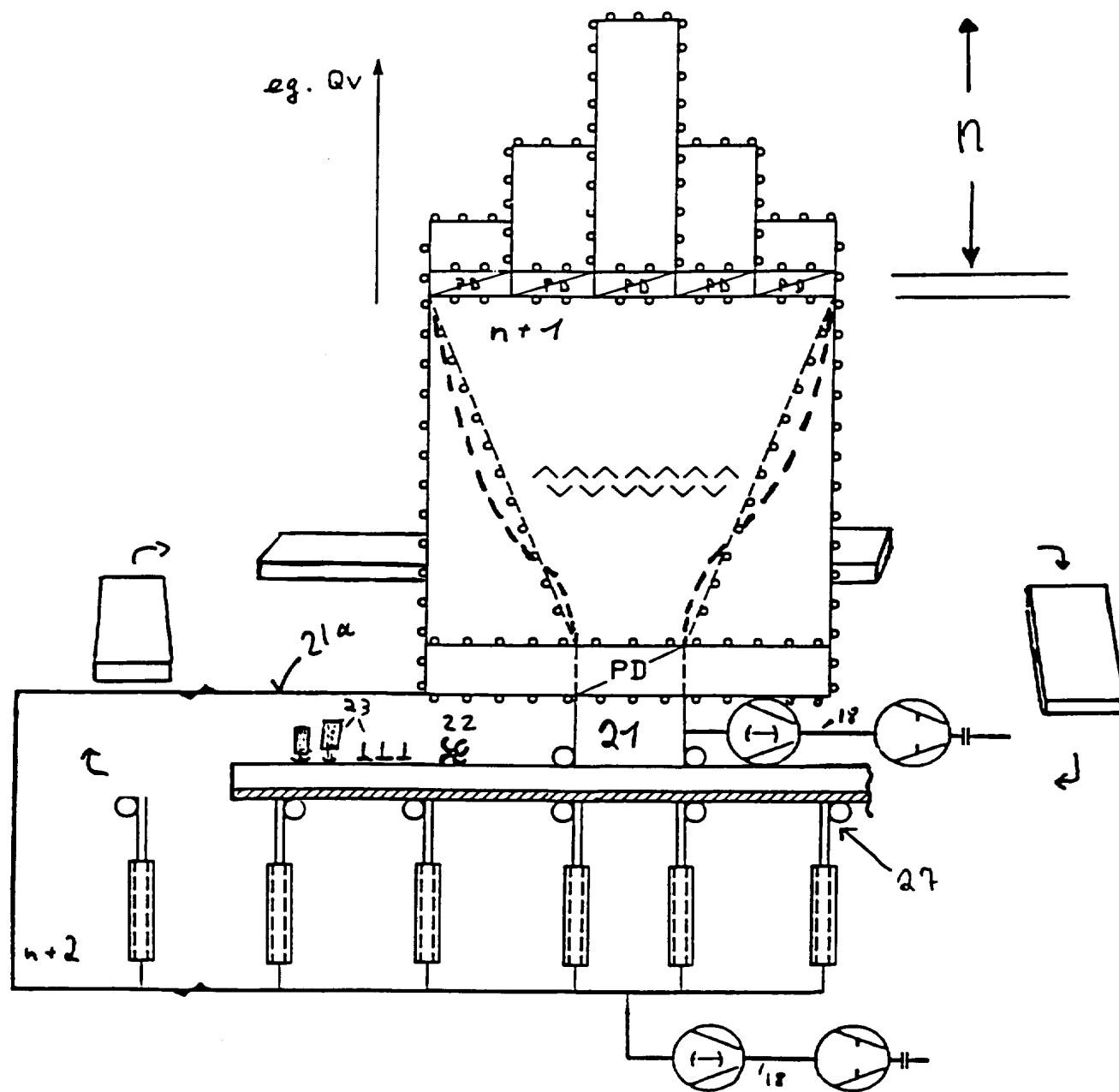


Fig. 95

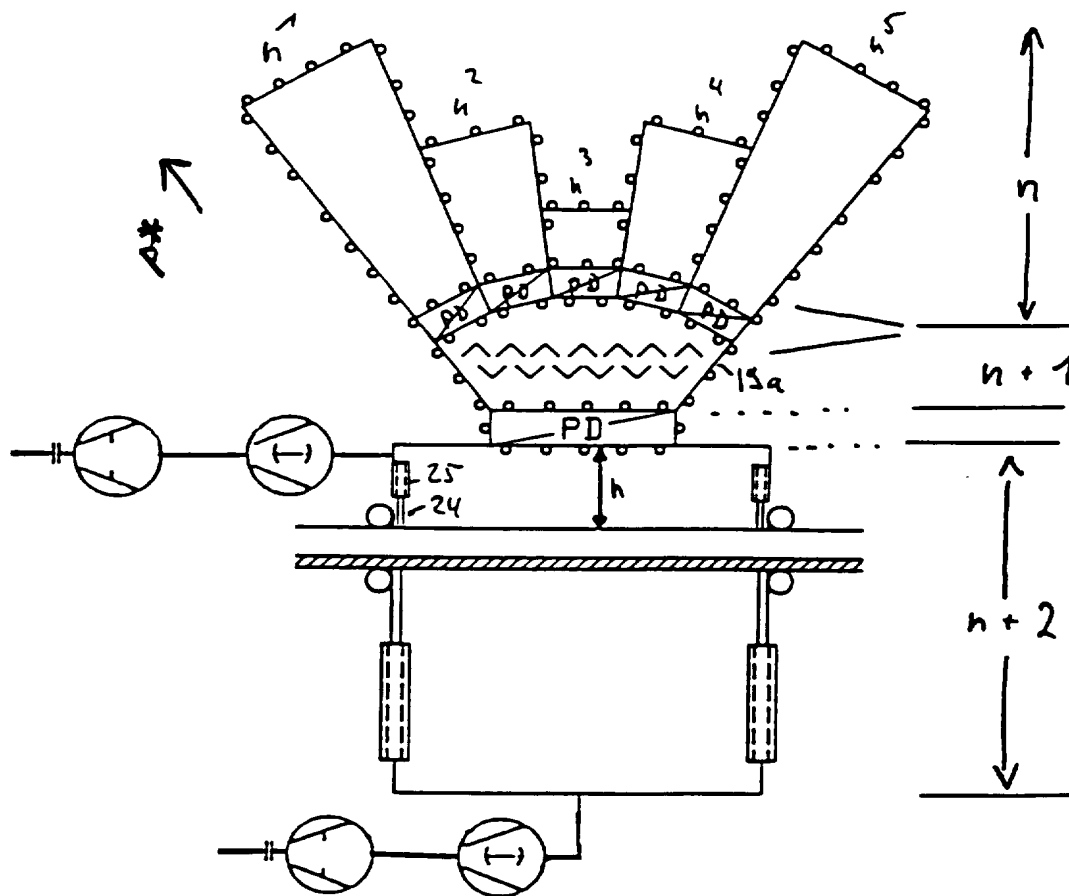
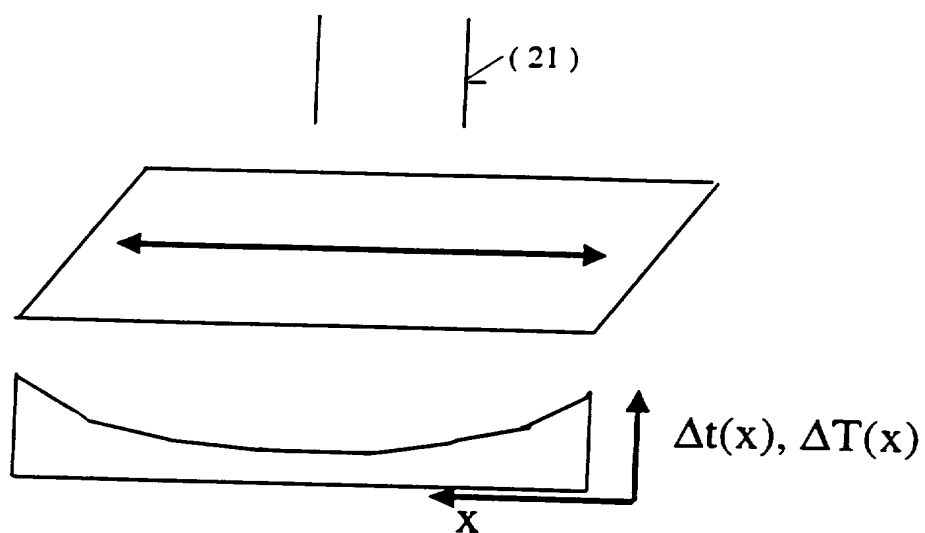


Fig. 96



i.e. $d\Delta T(x) \neq 0$

Fig. 97

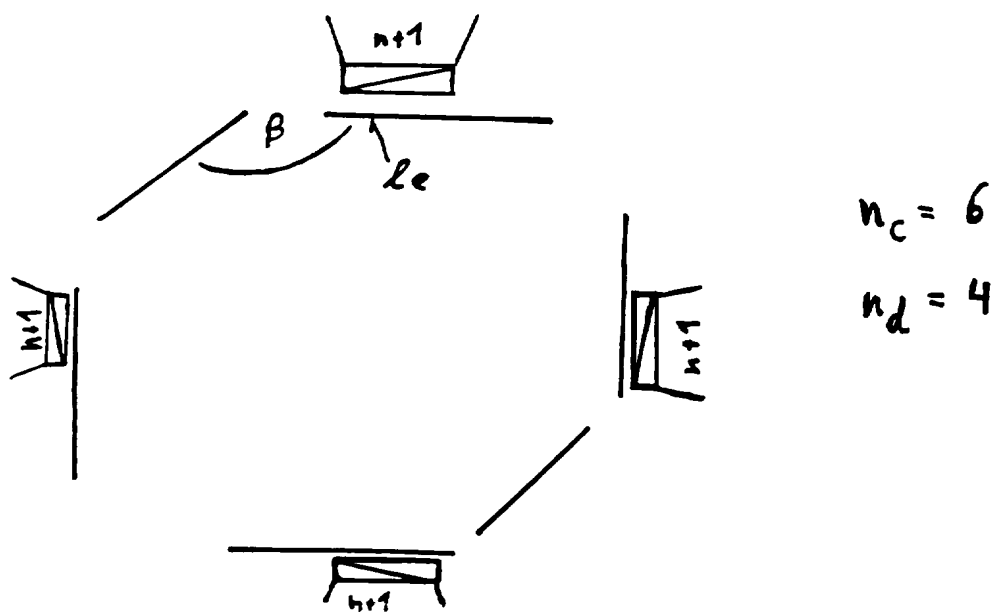
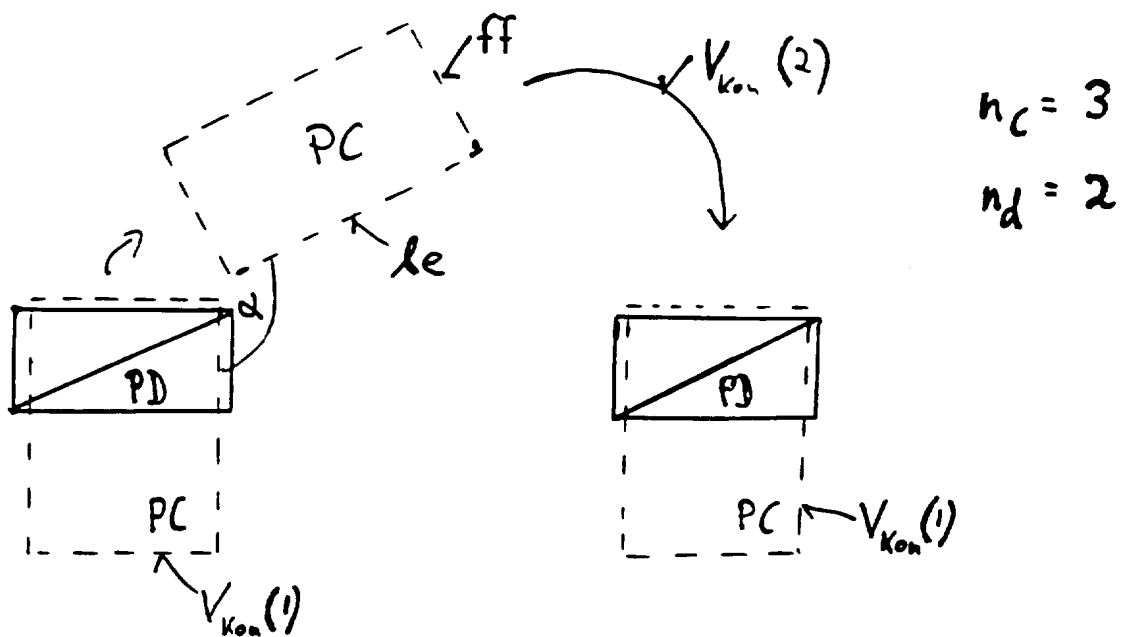


Fig. 98

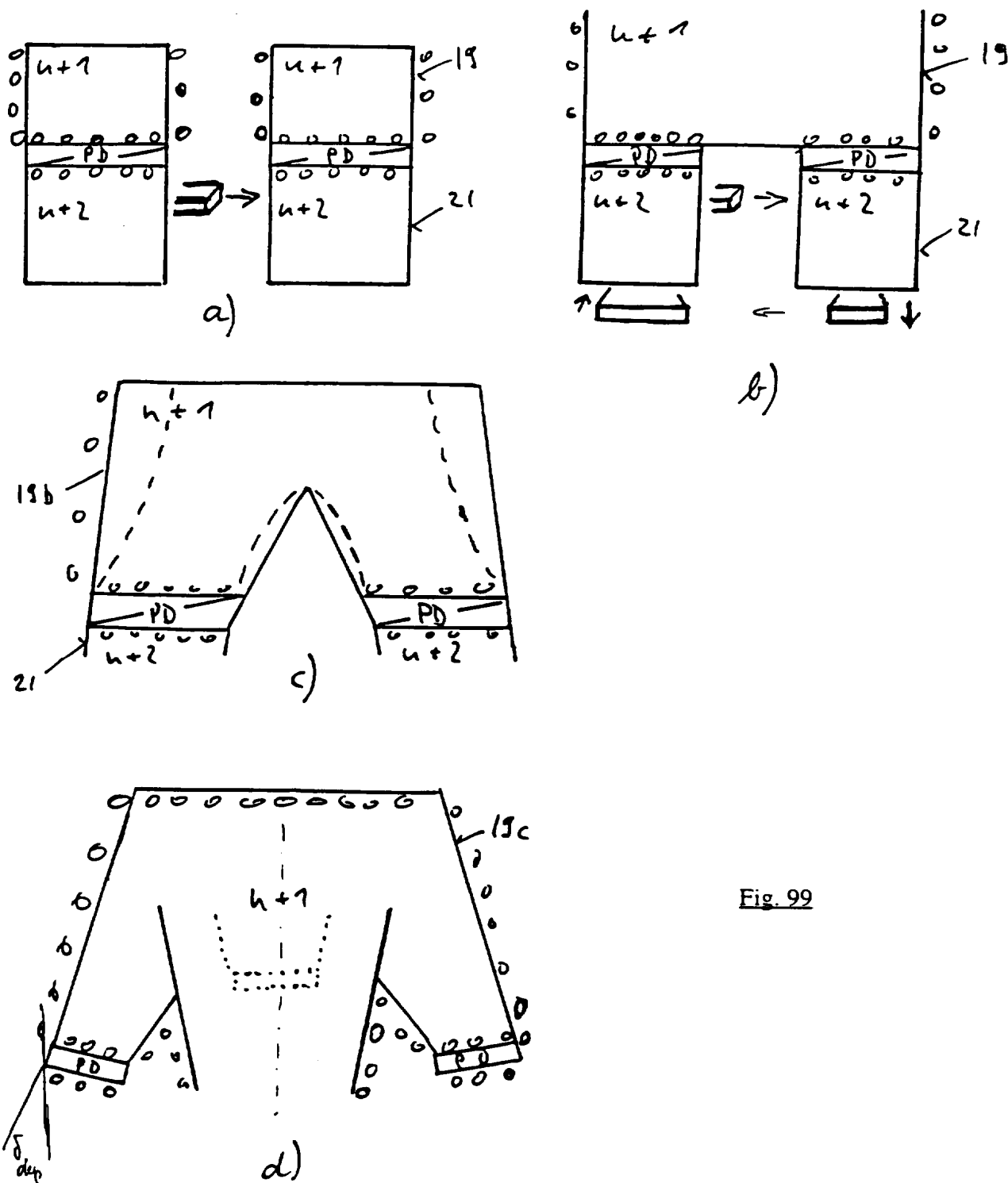


Fig. 99

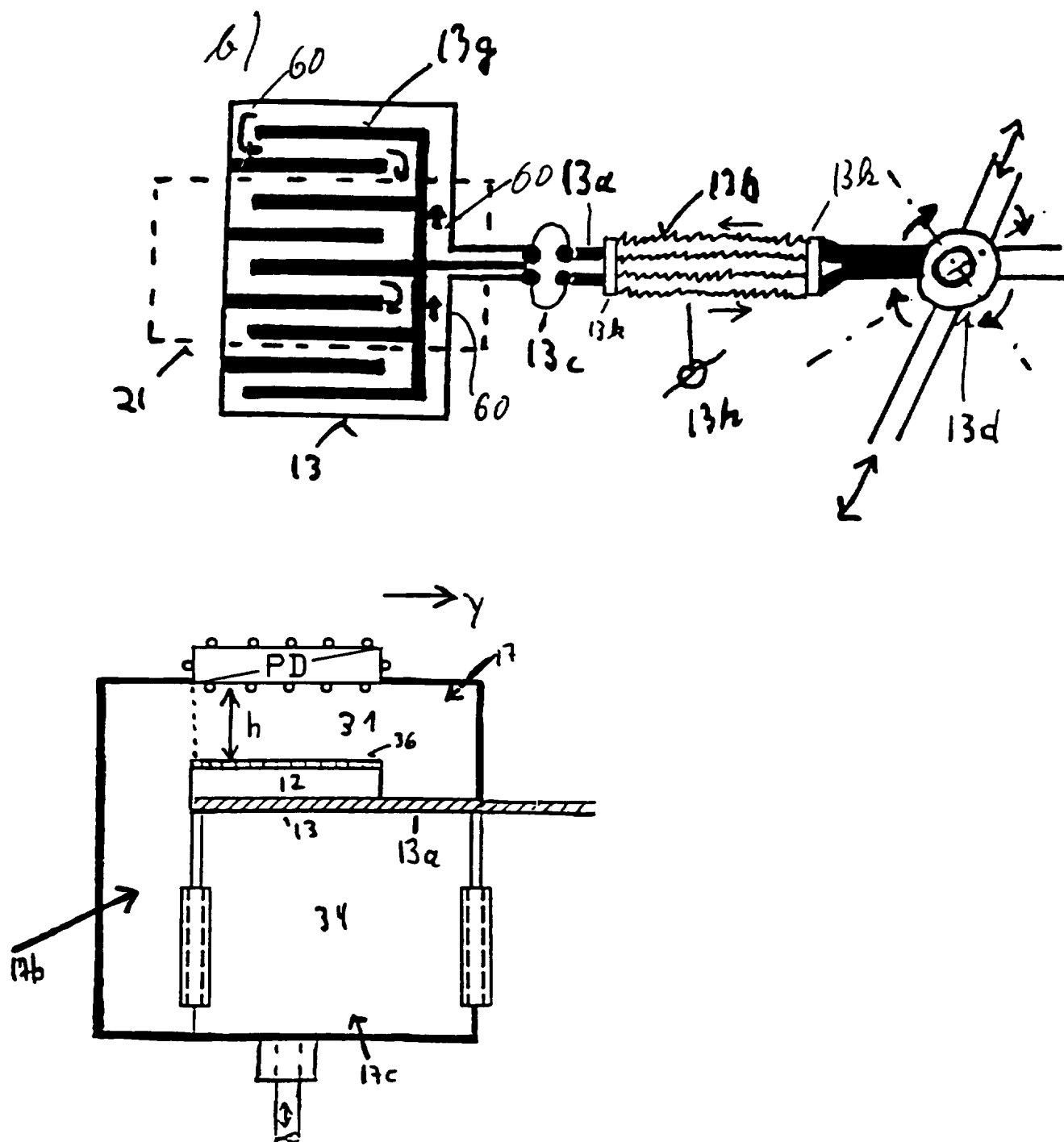
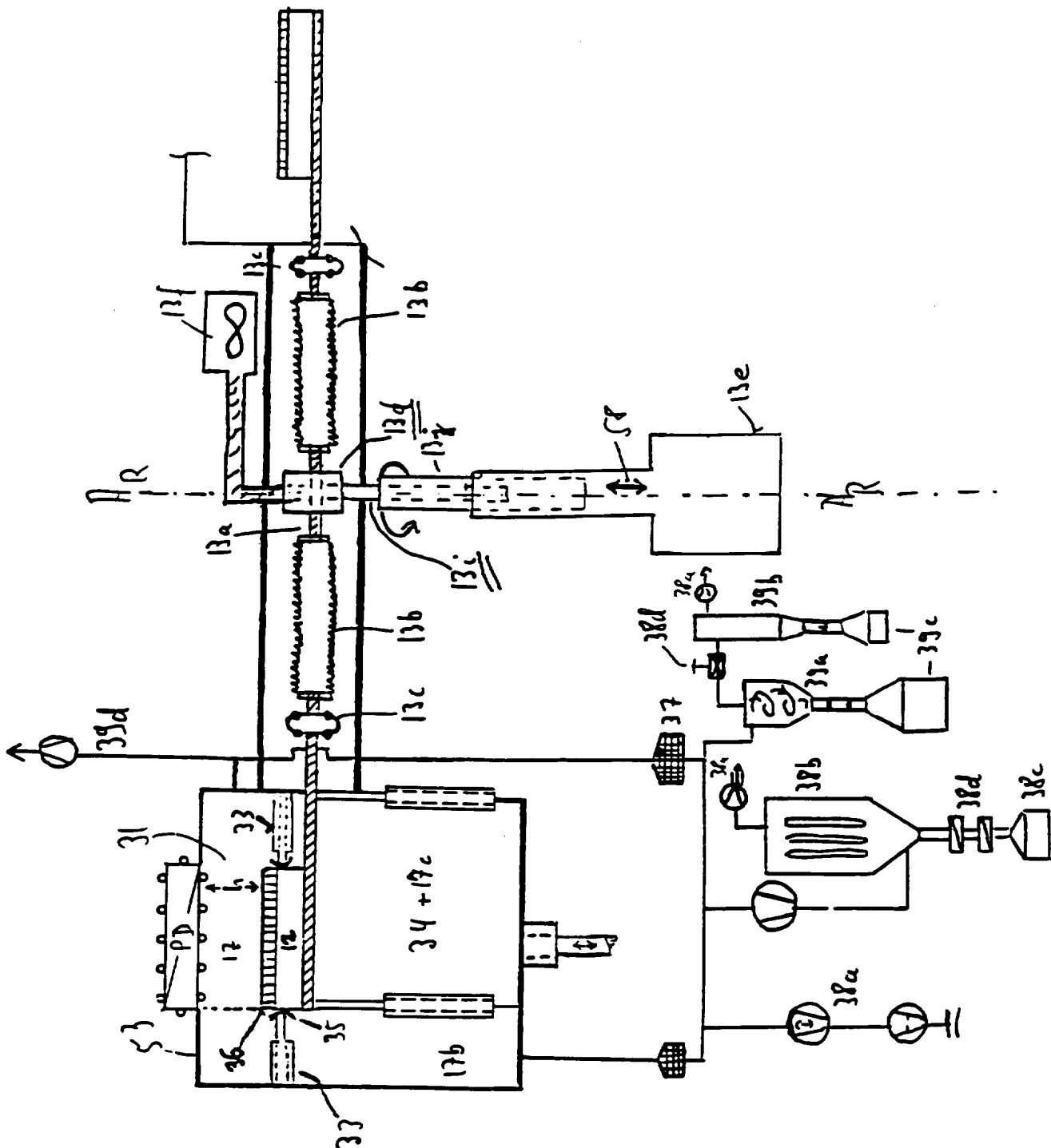


Fig. 102



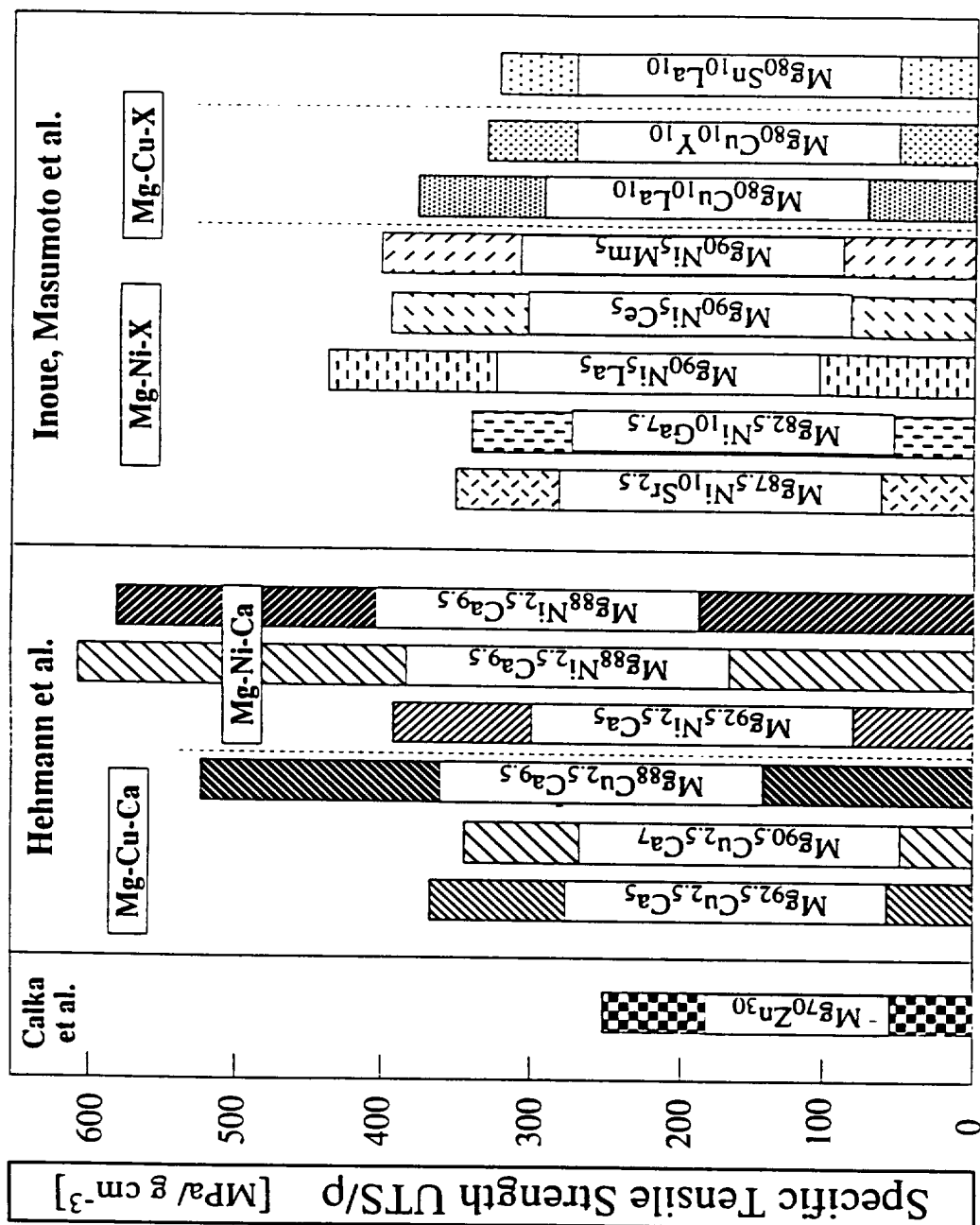
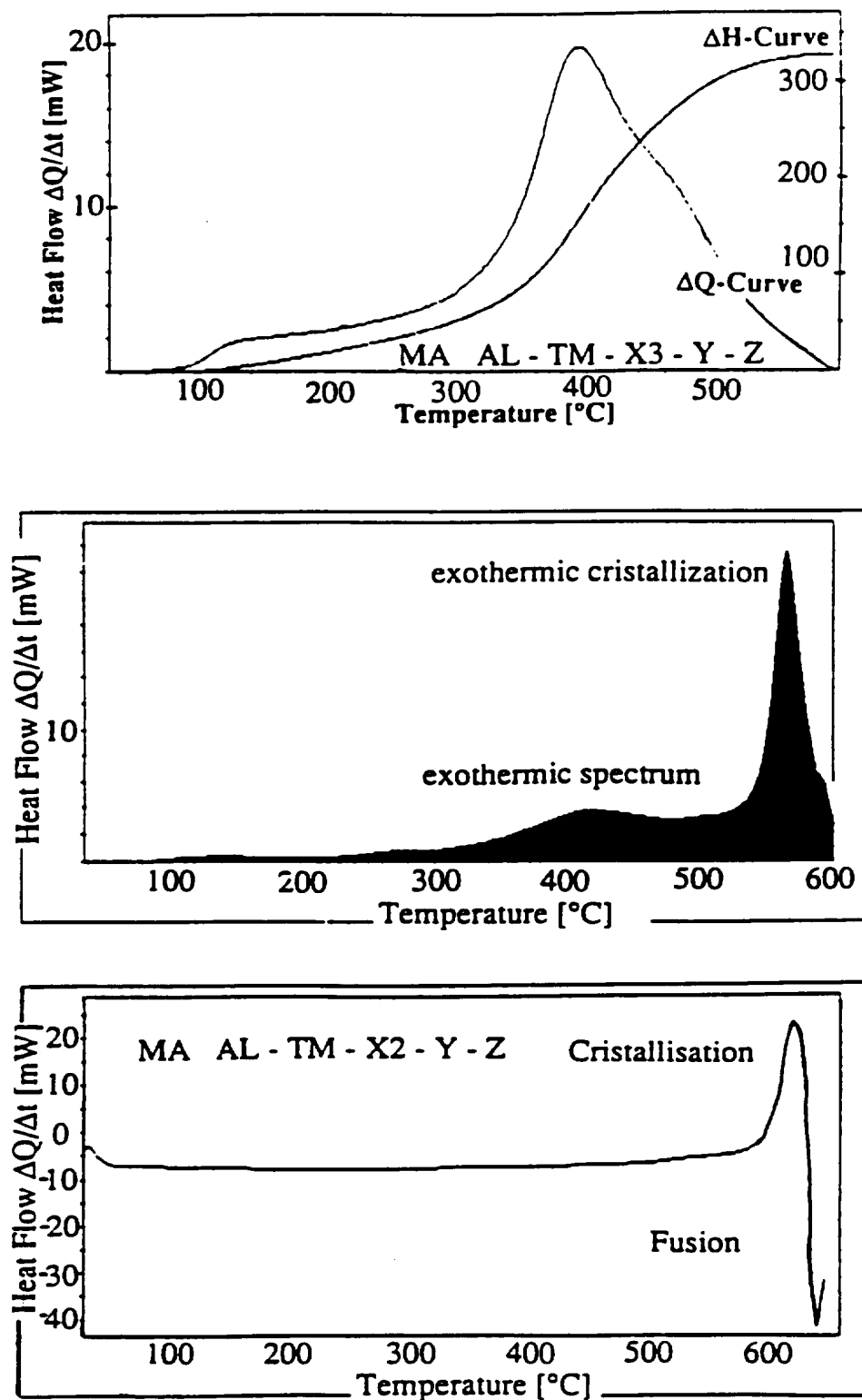


Fig. 104

Fig. 105

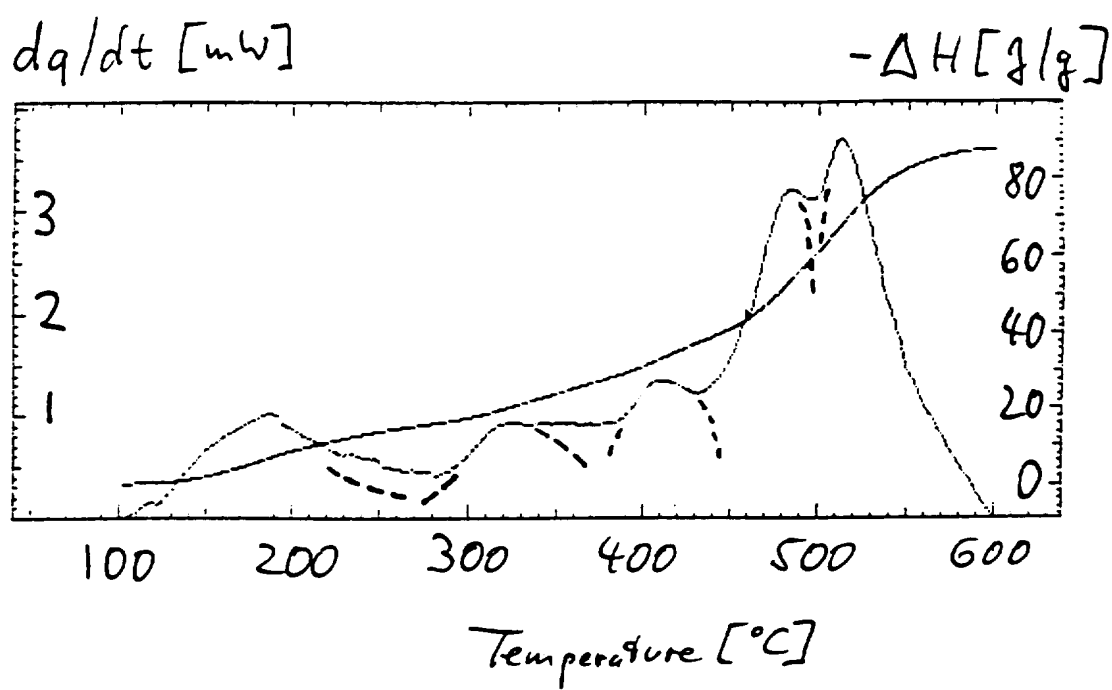


Fig. 106

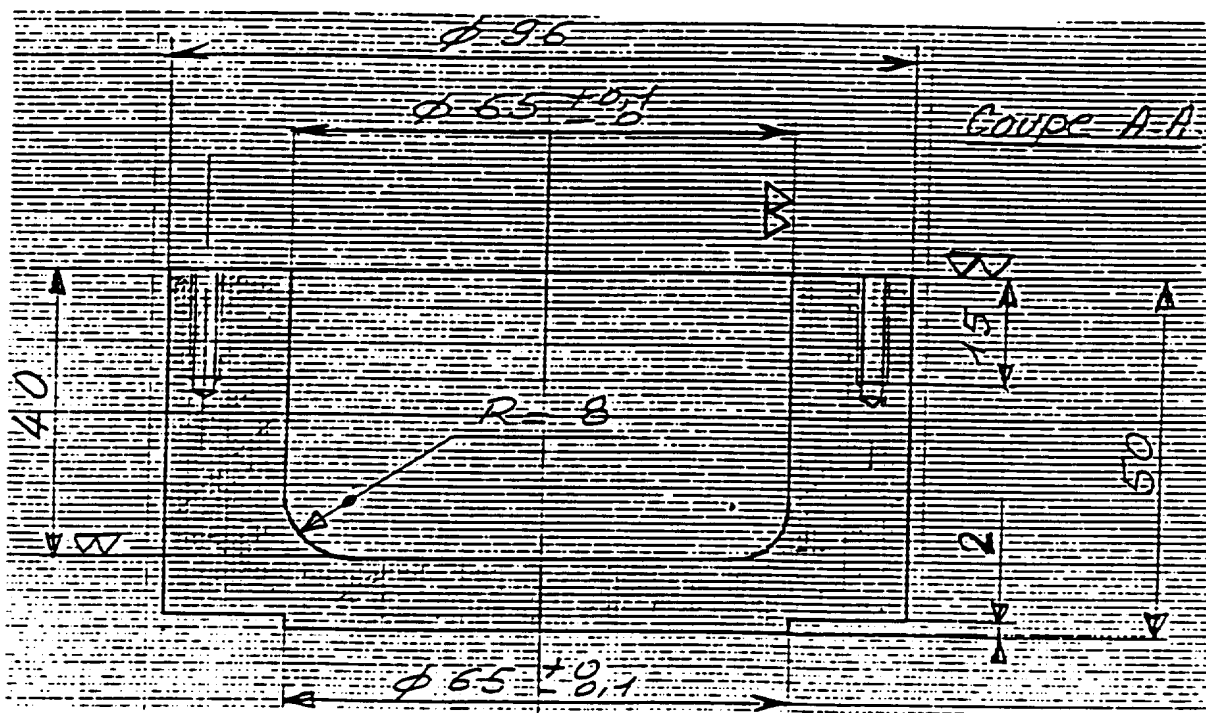
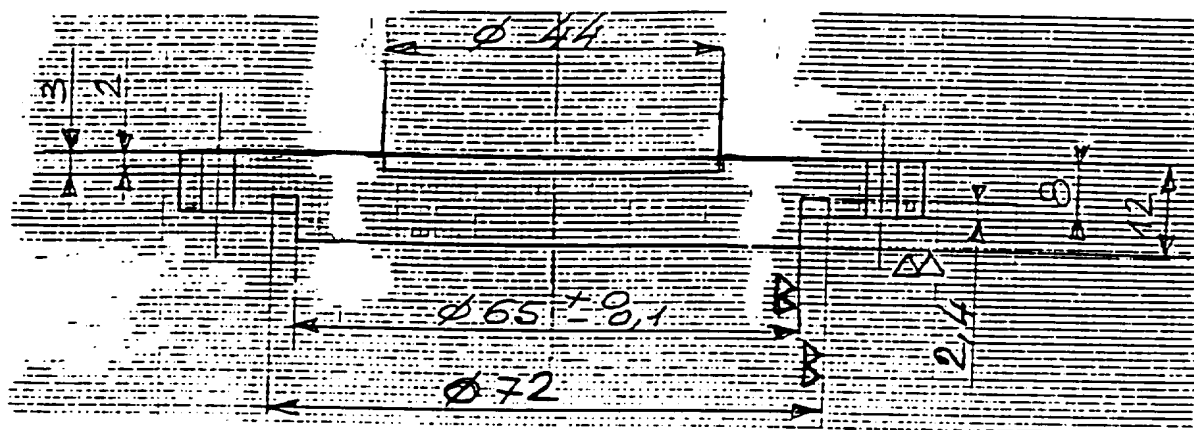


Fig. 107

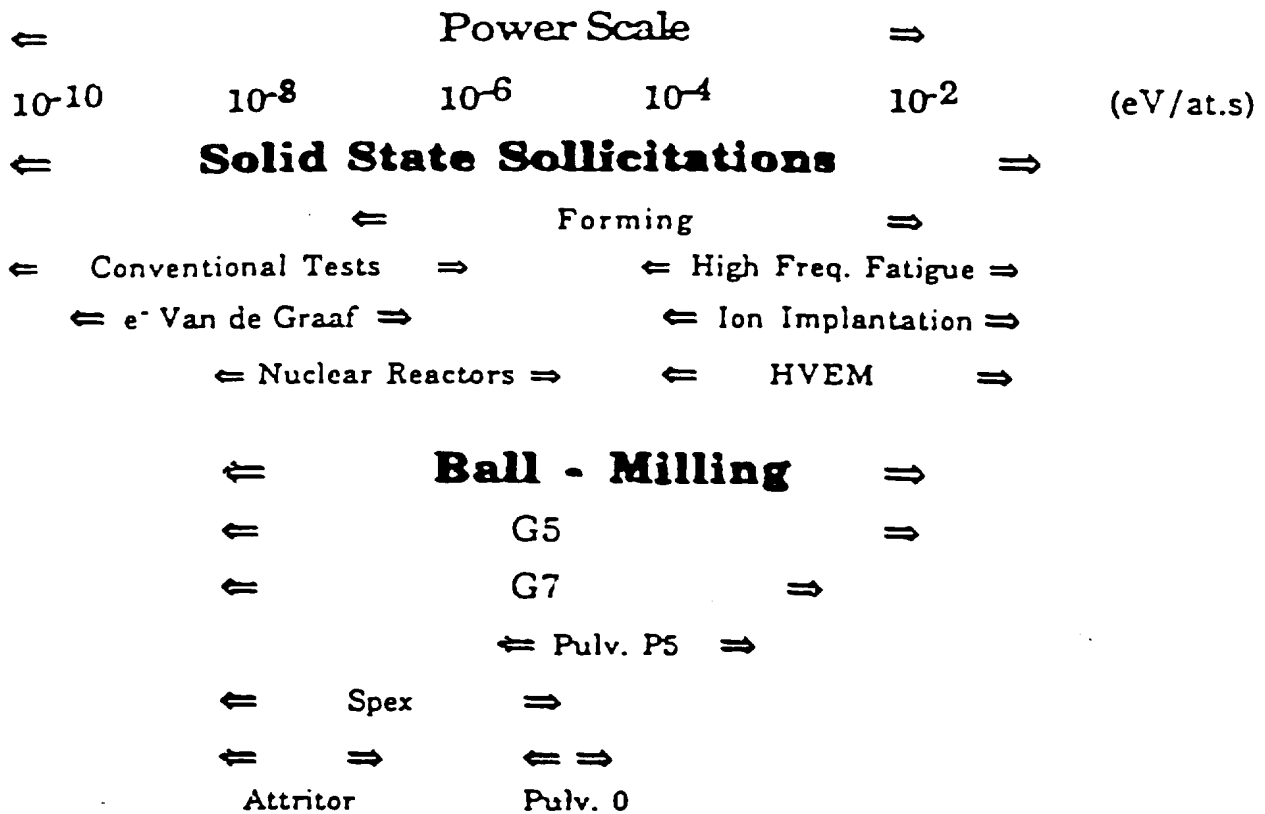


Fig. 108

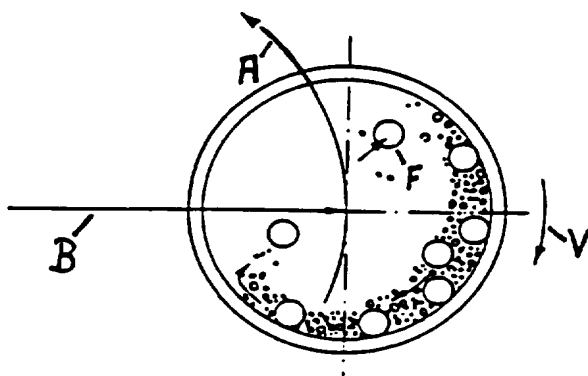
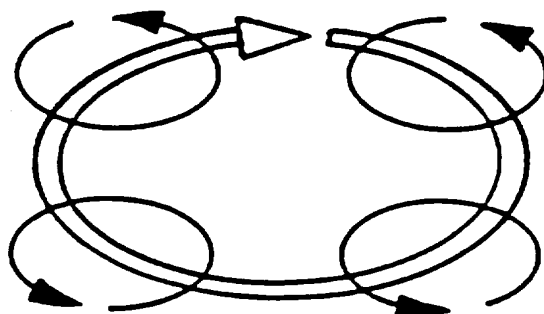
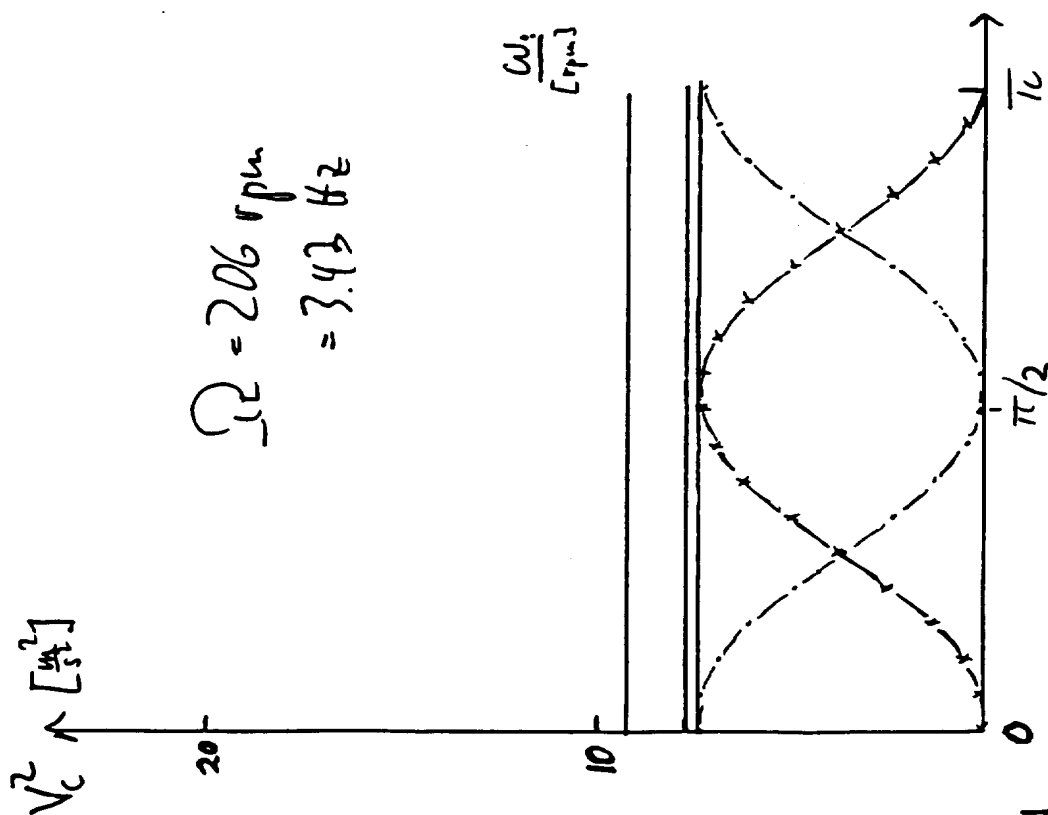
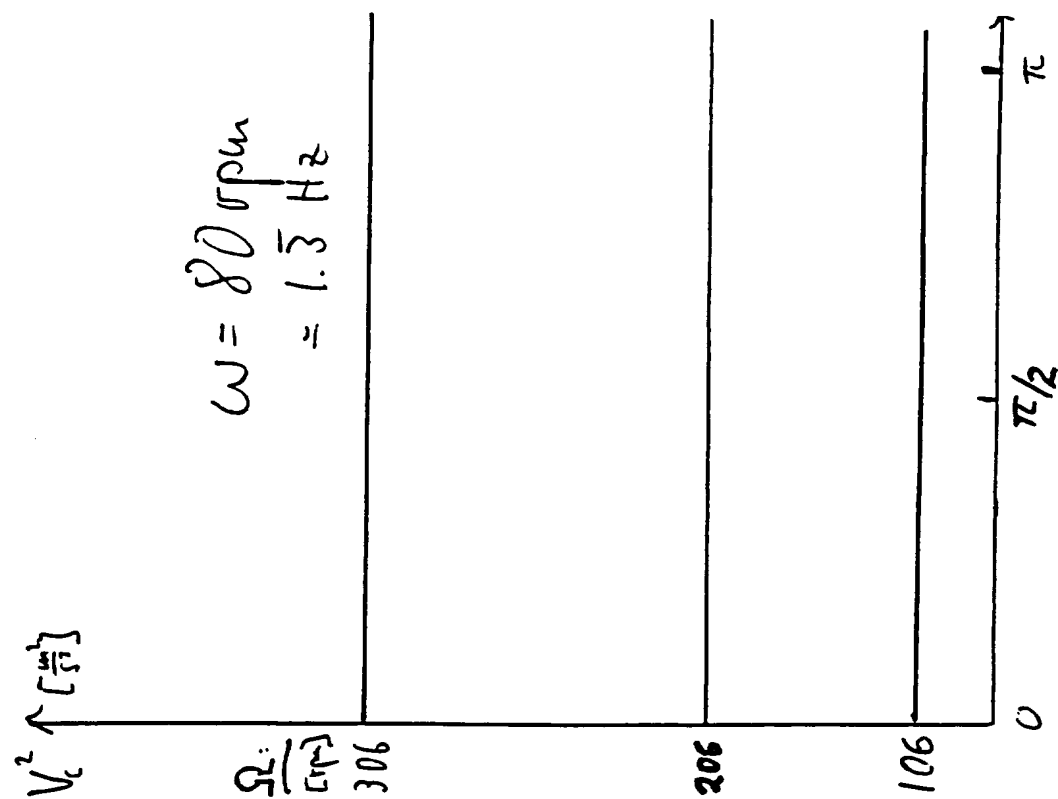


Fig. 109



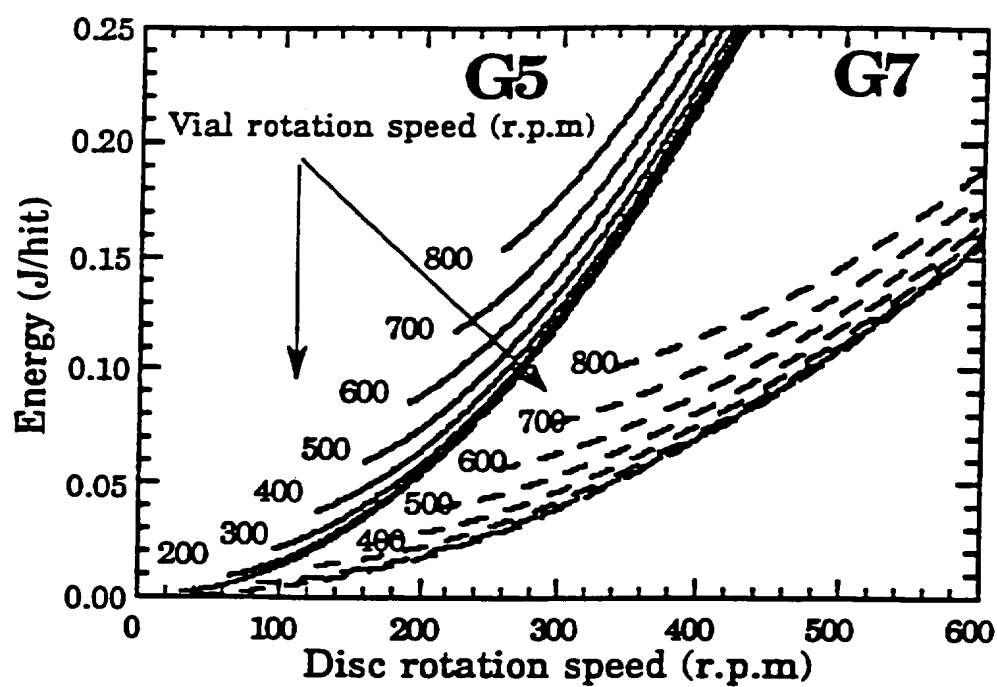


Fig. III

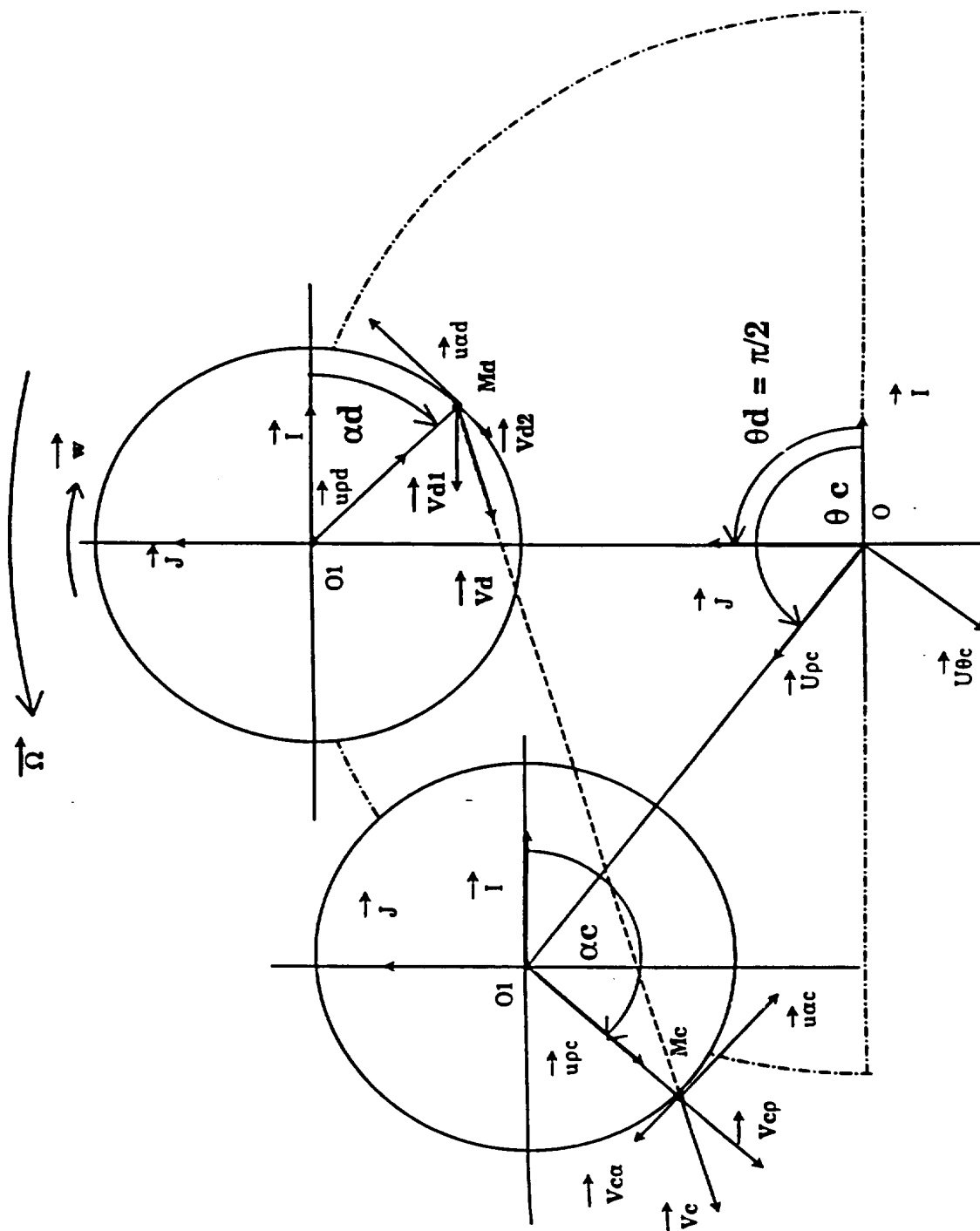


Fig. 112

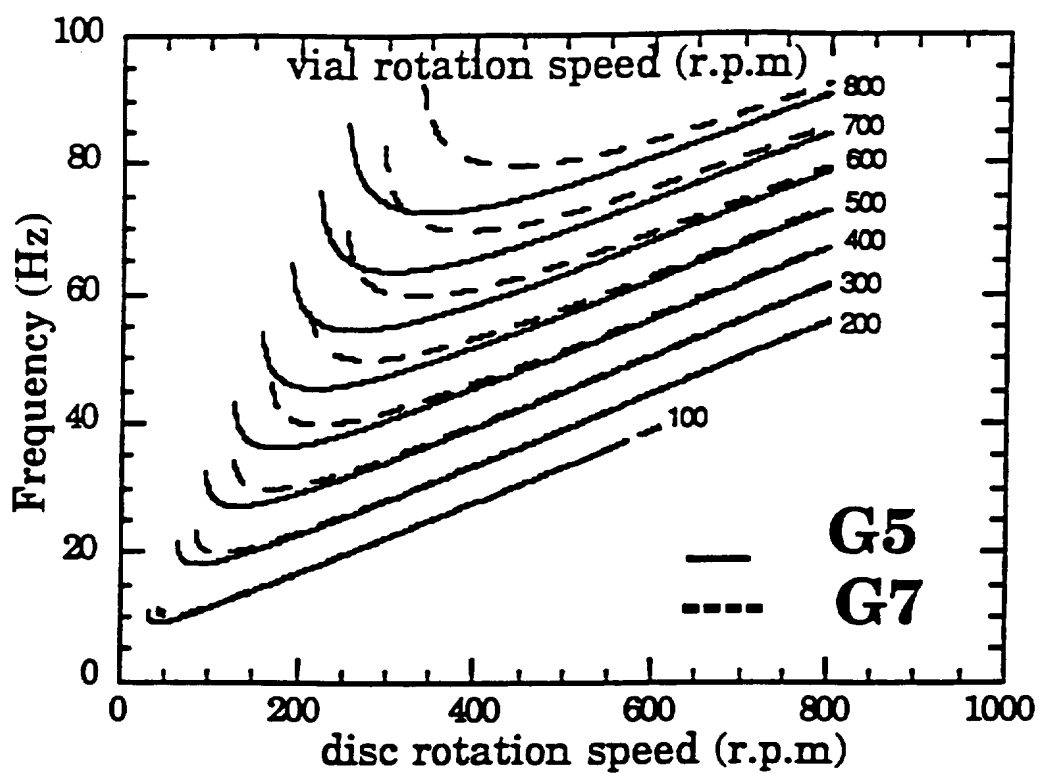


Fig. 113

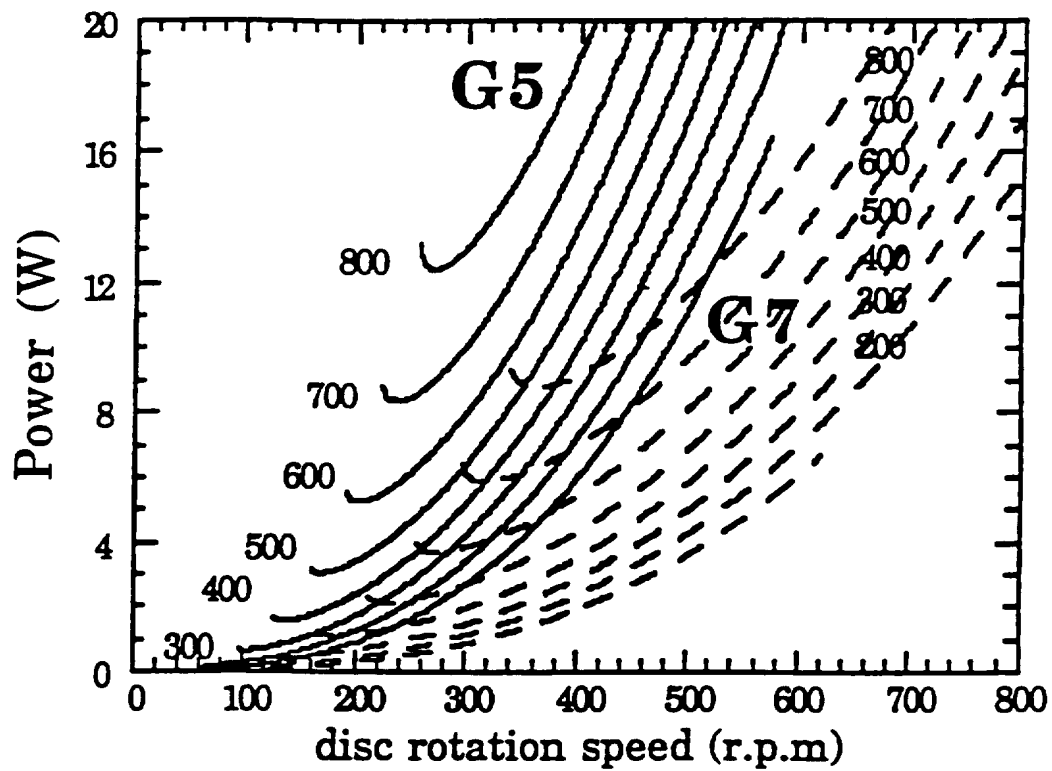
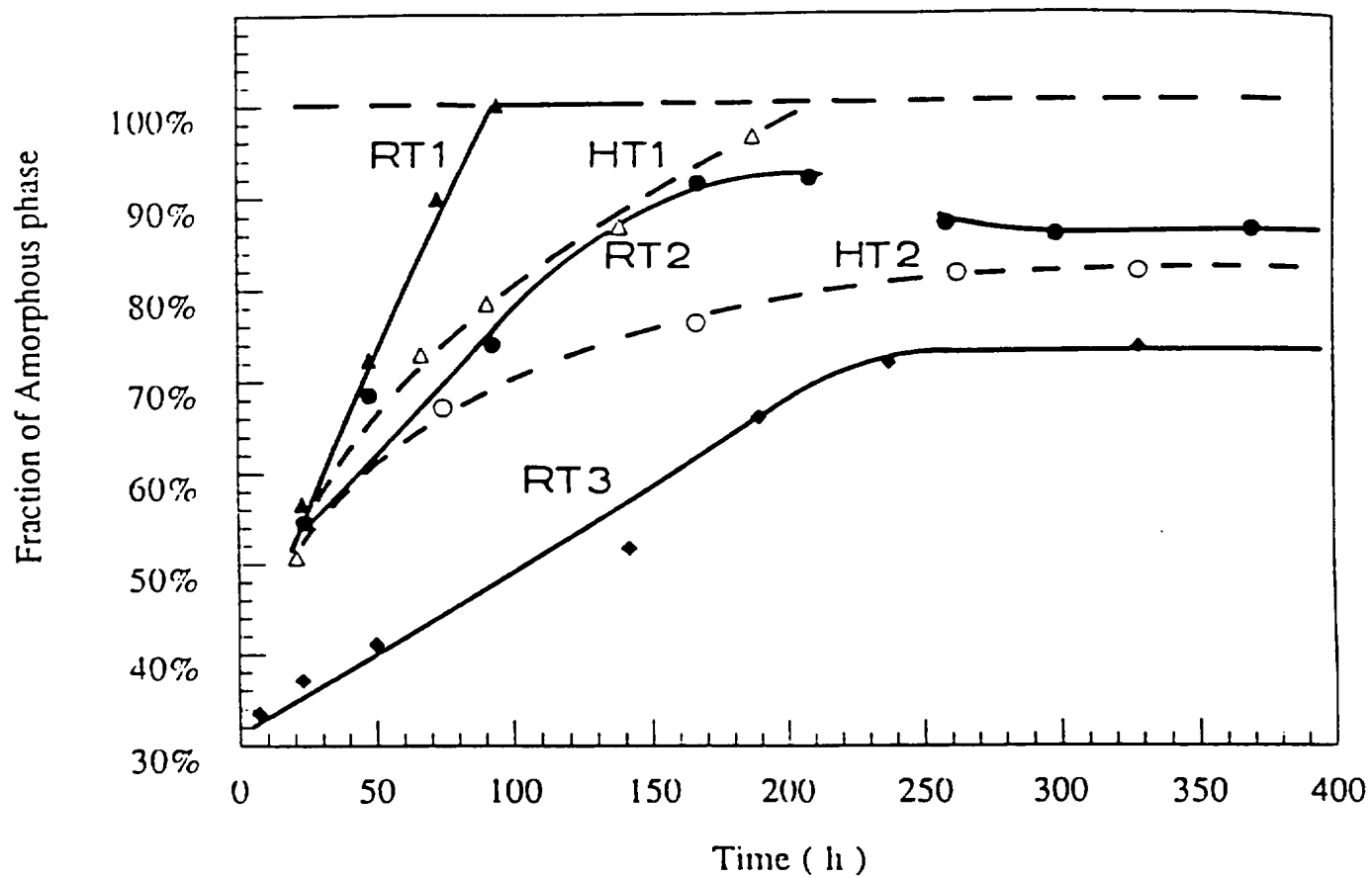


Fig. 114

Fig. 115

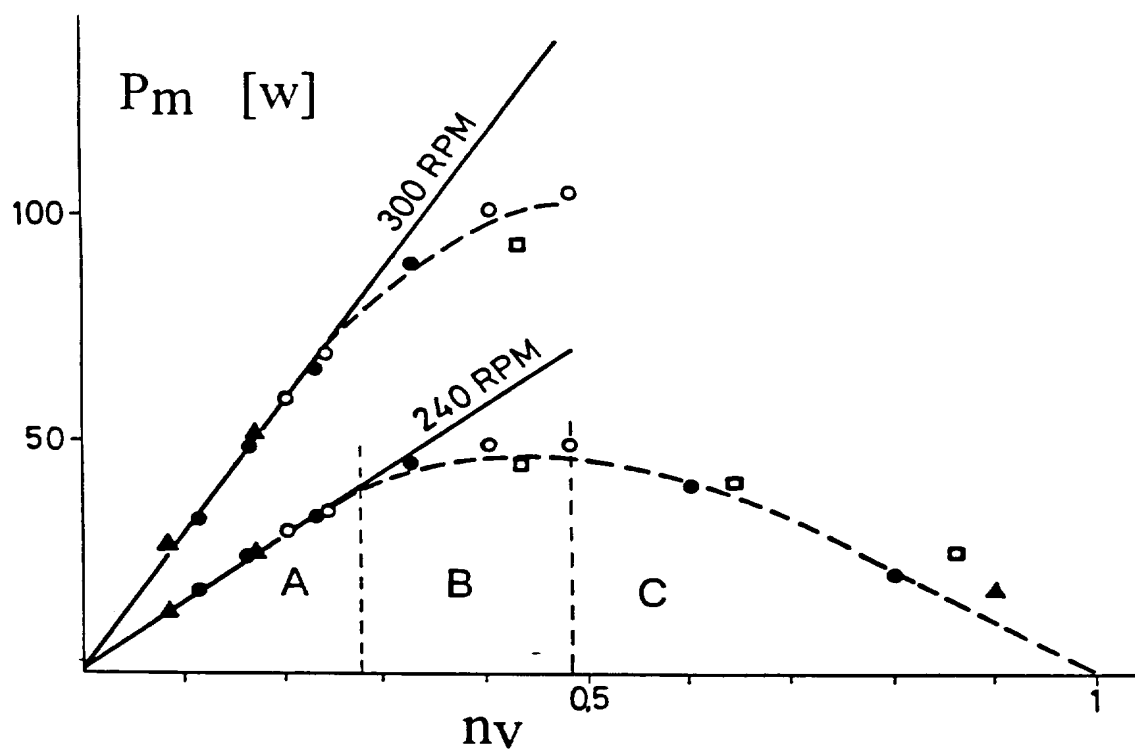
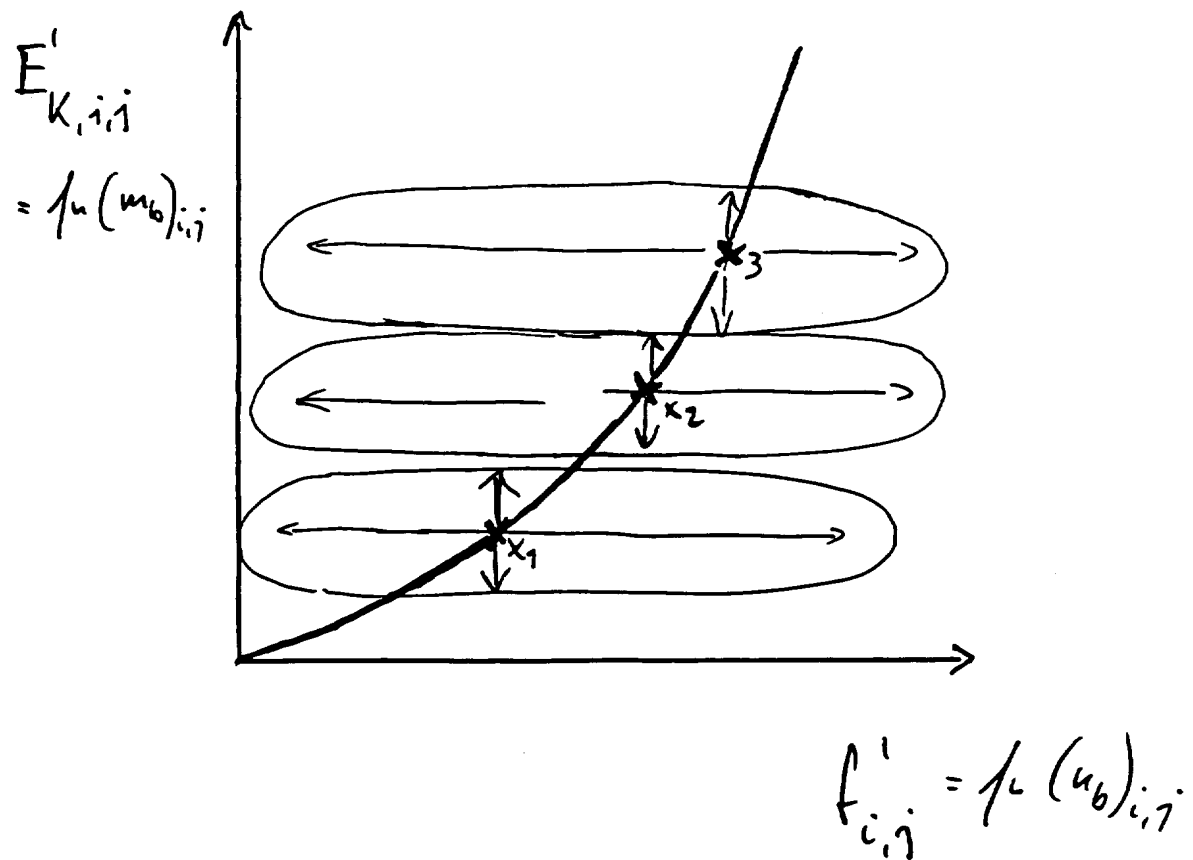


Fig. 116

Fig. 117

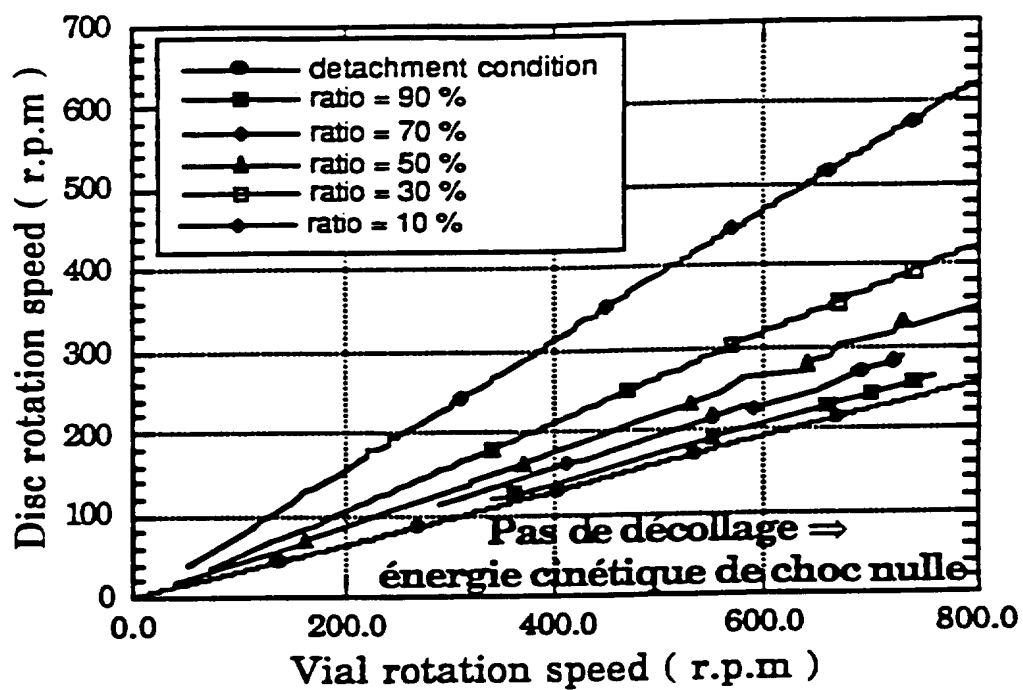
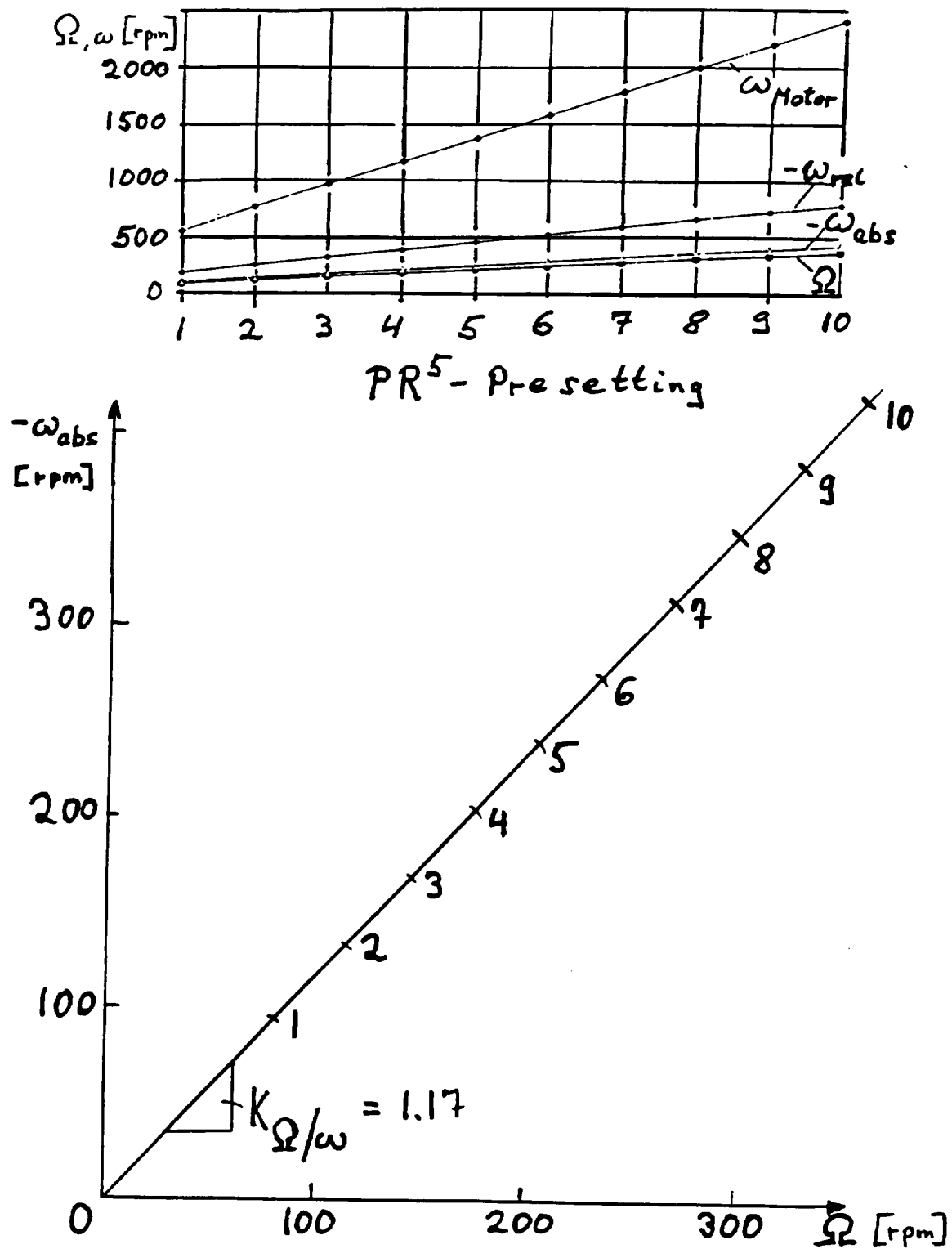
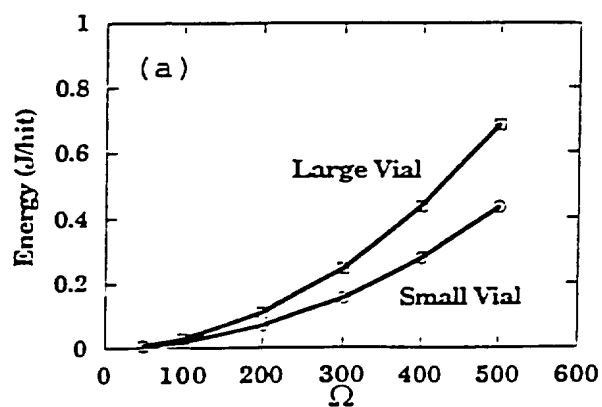


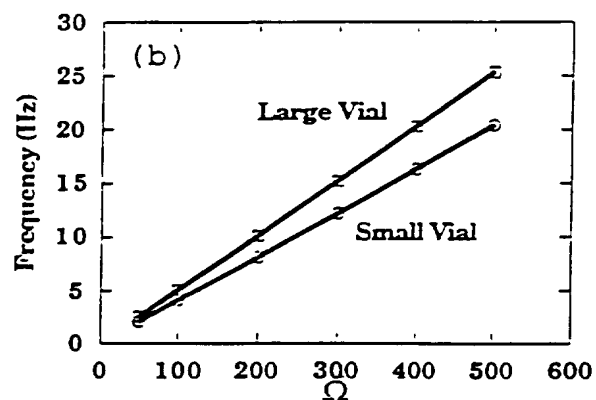
Fig. 118

Fig. 119

Energy(P5) = Fct (Vial Size)



Frequency (P5) = Fct (Vial Size)



Power (P5) = Fct (Vial Size)

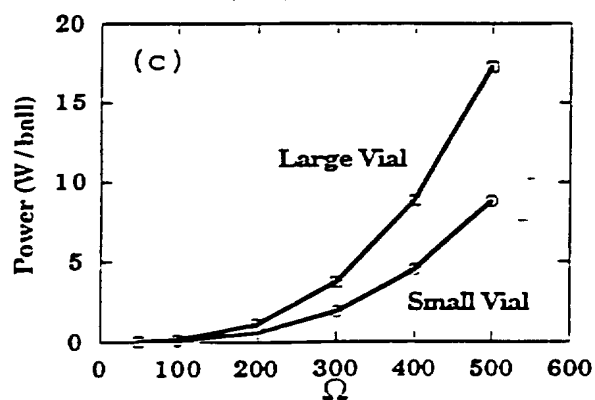


Fig. 120

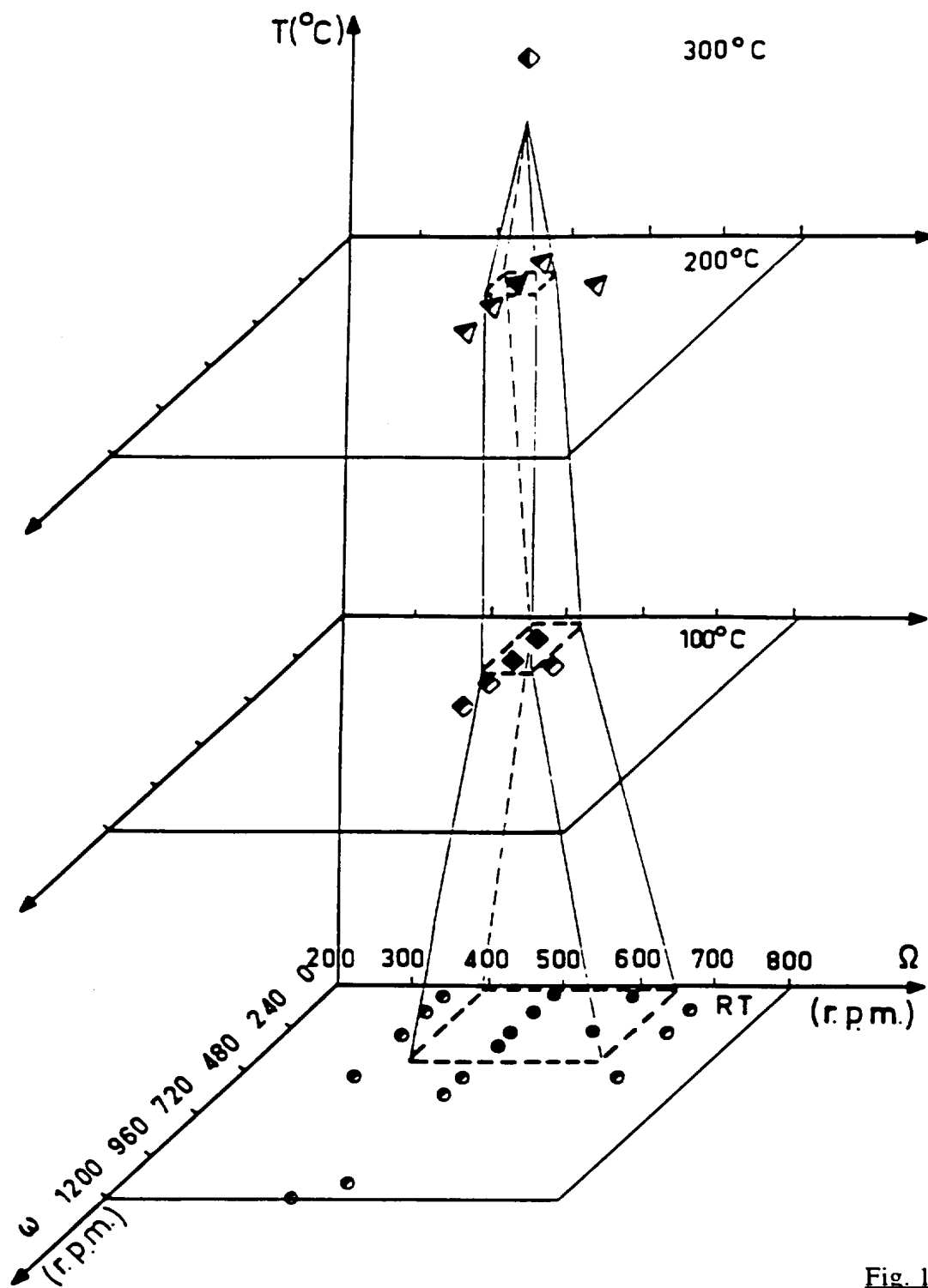


Fig. 121

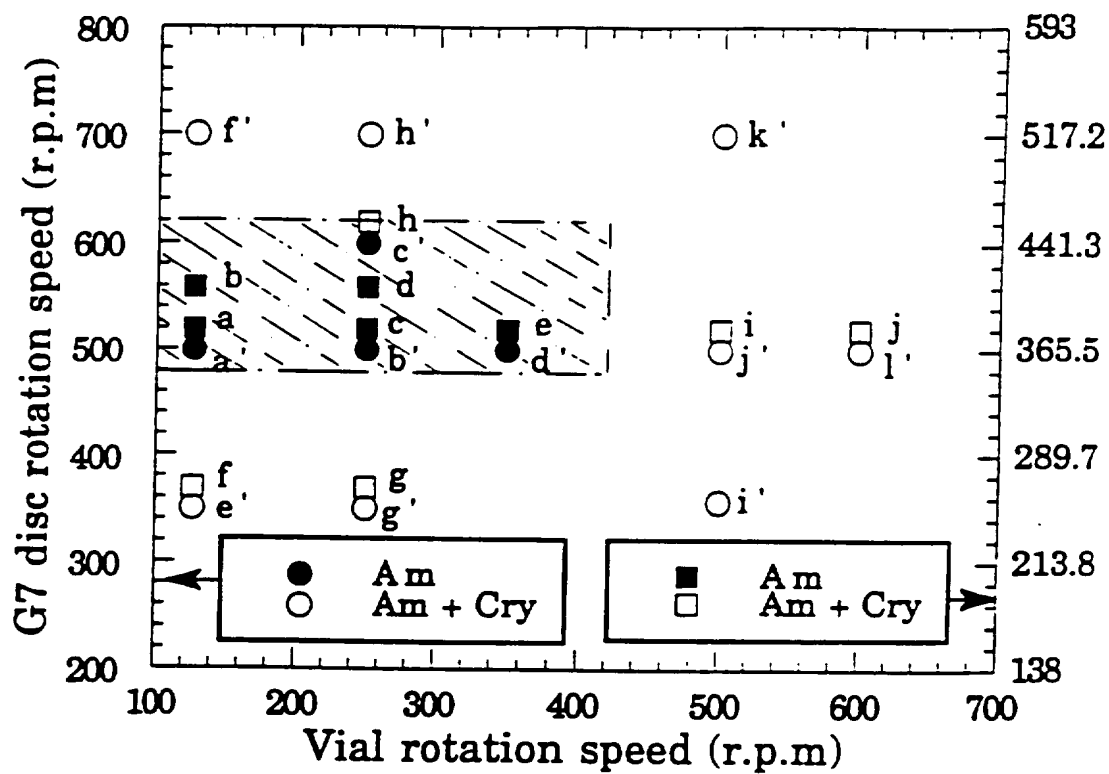
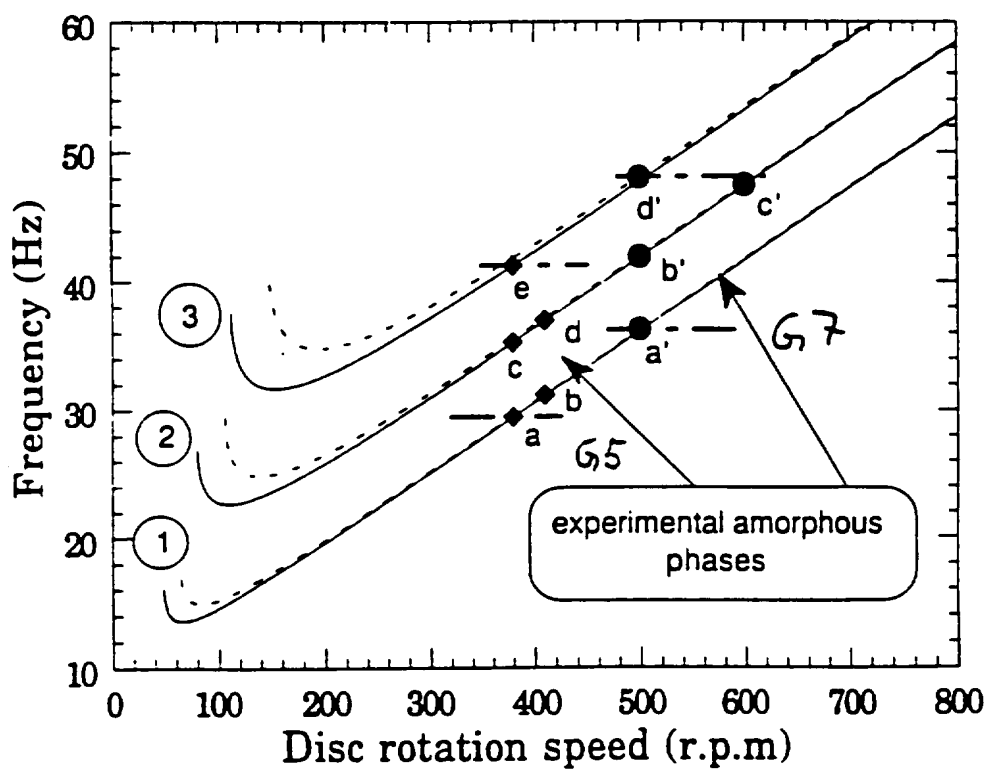
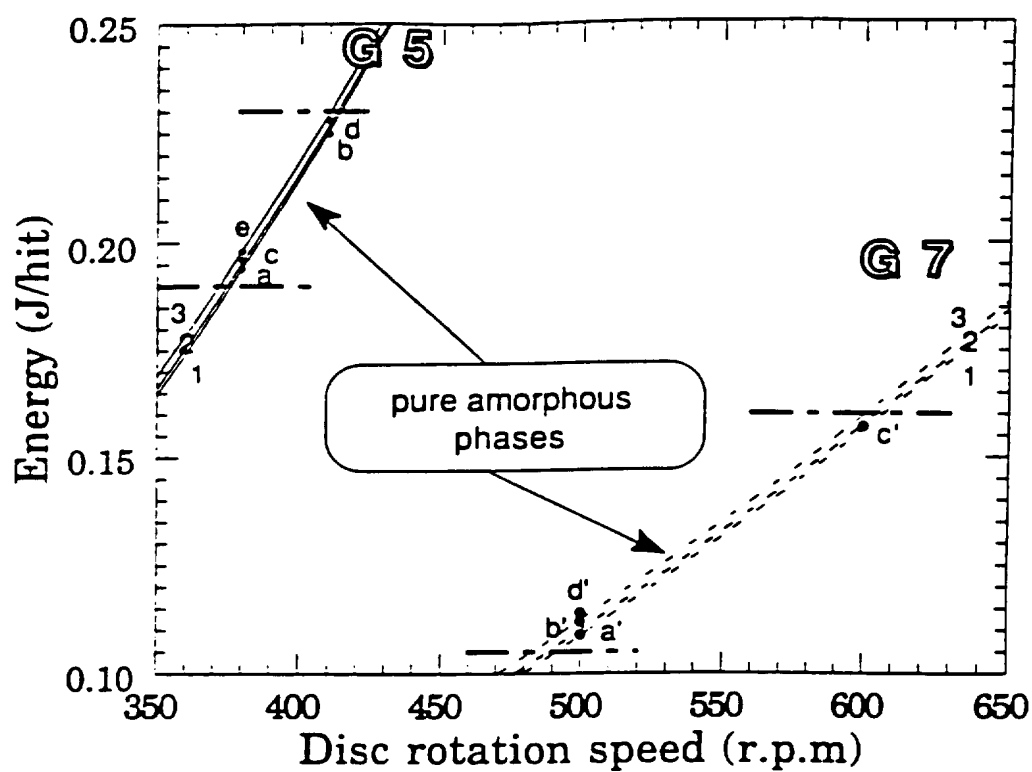
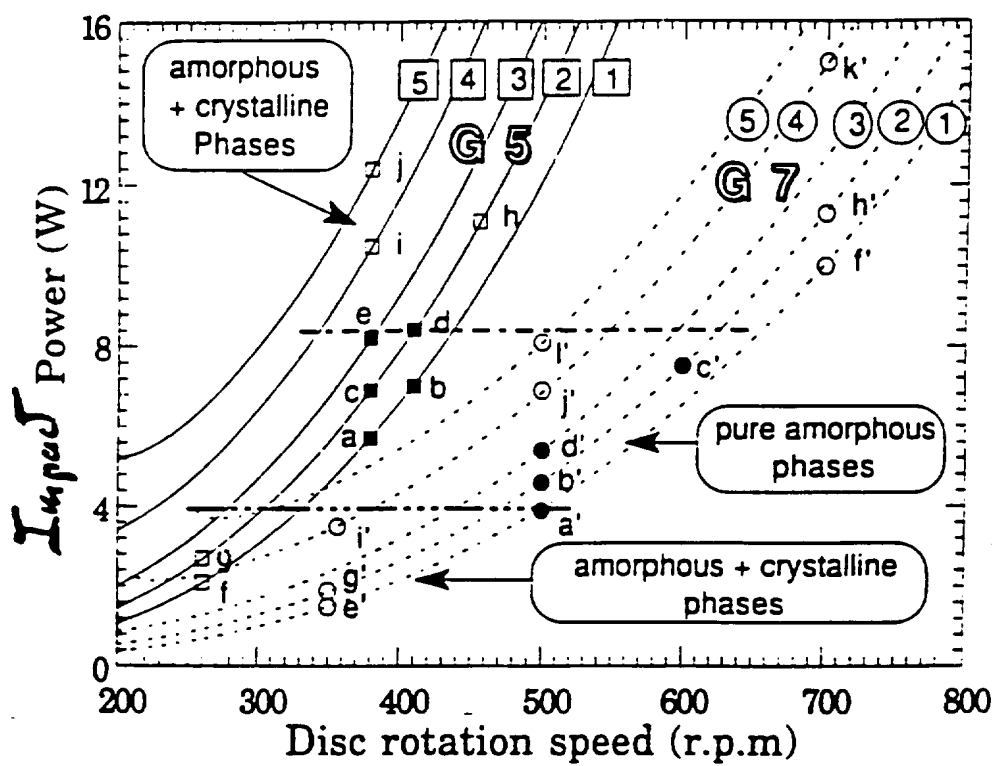


Fig. 122

Fig. 123

Fig. 124

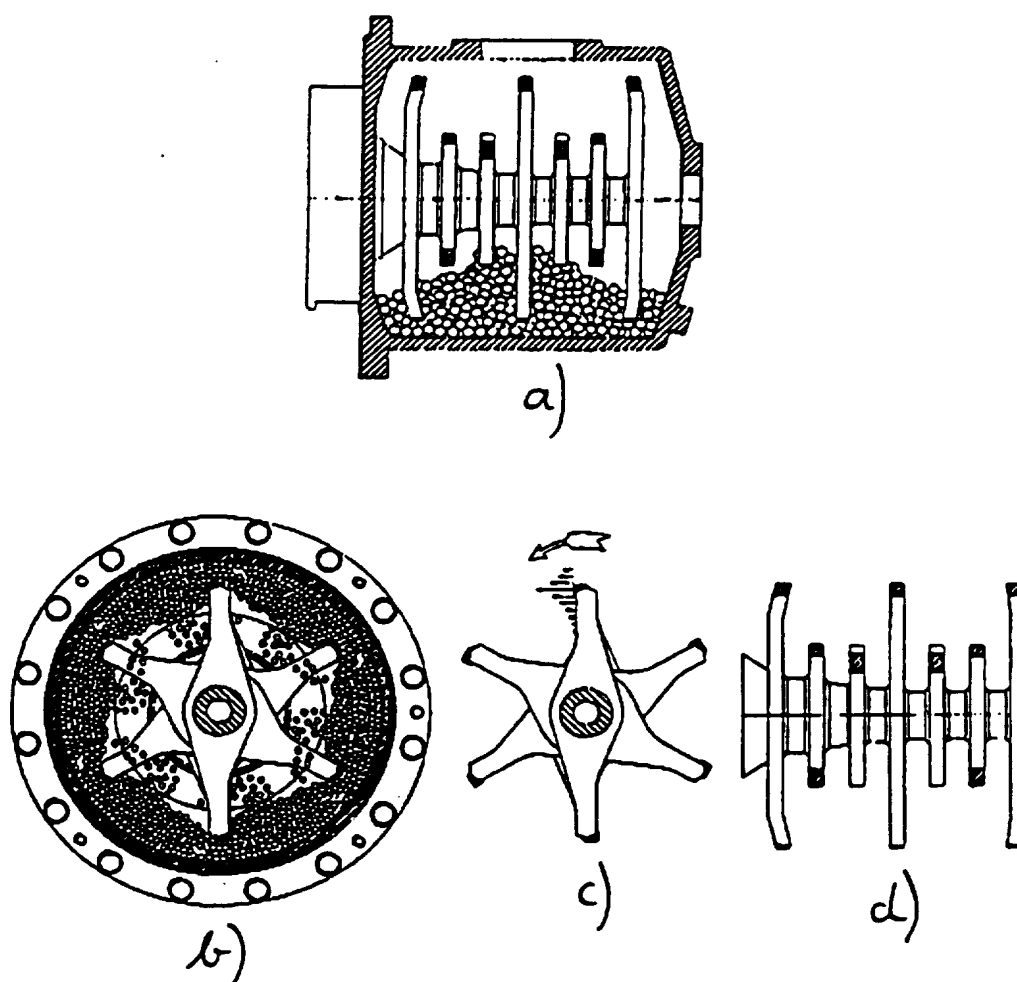
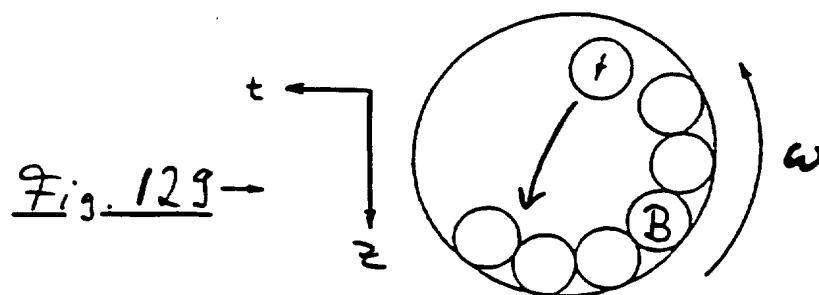
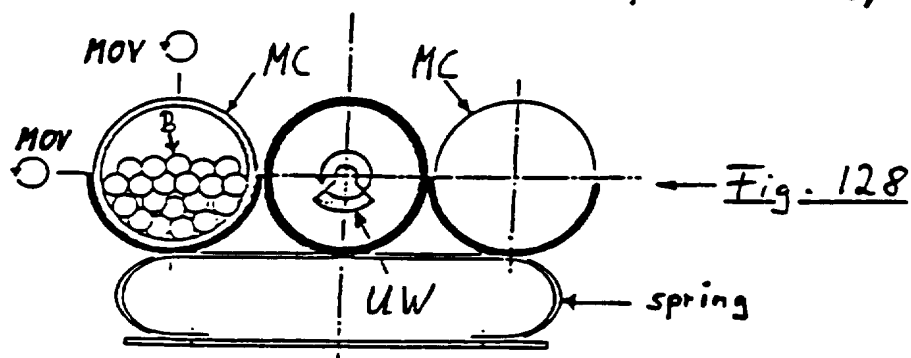
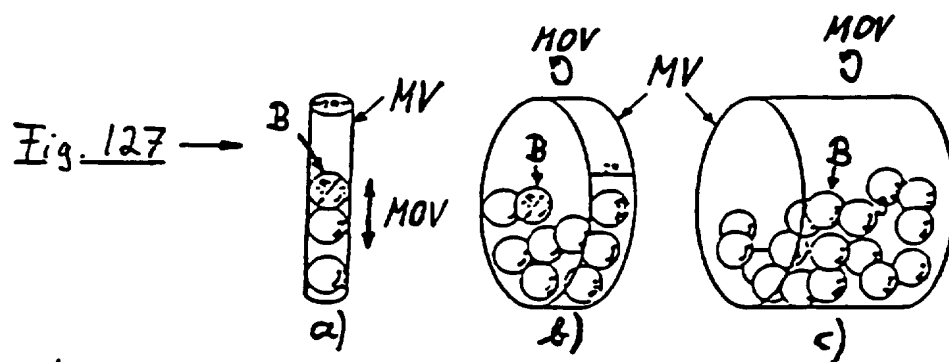
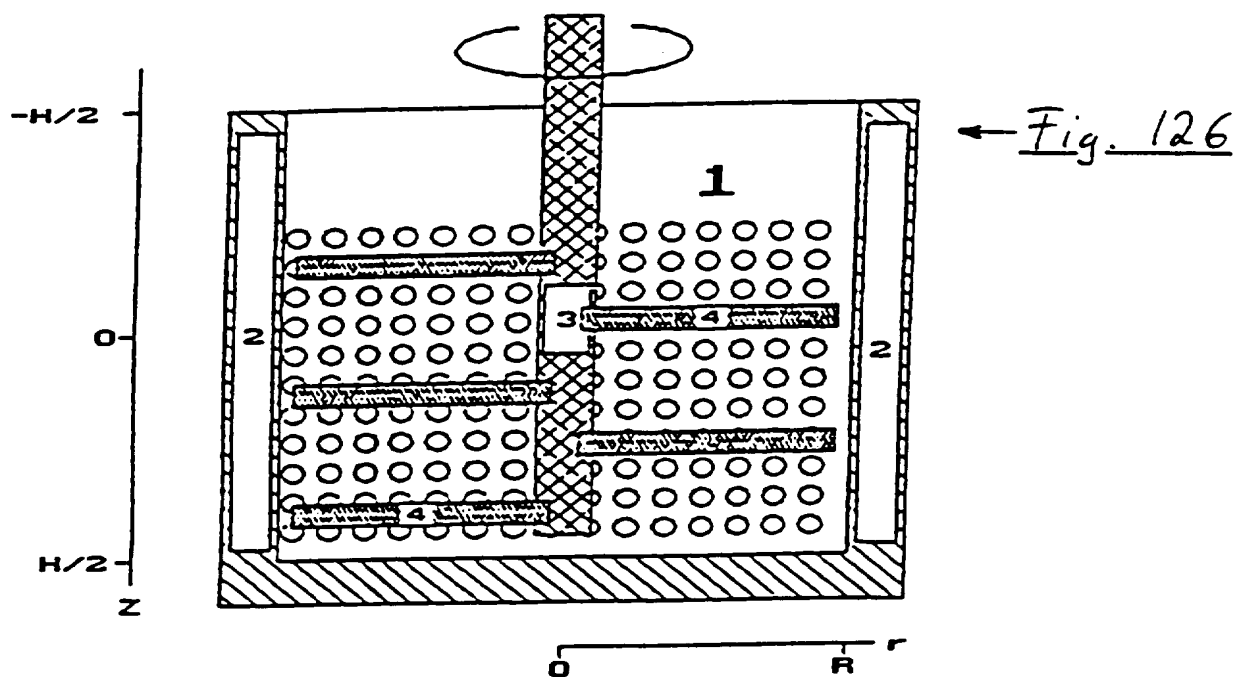
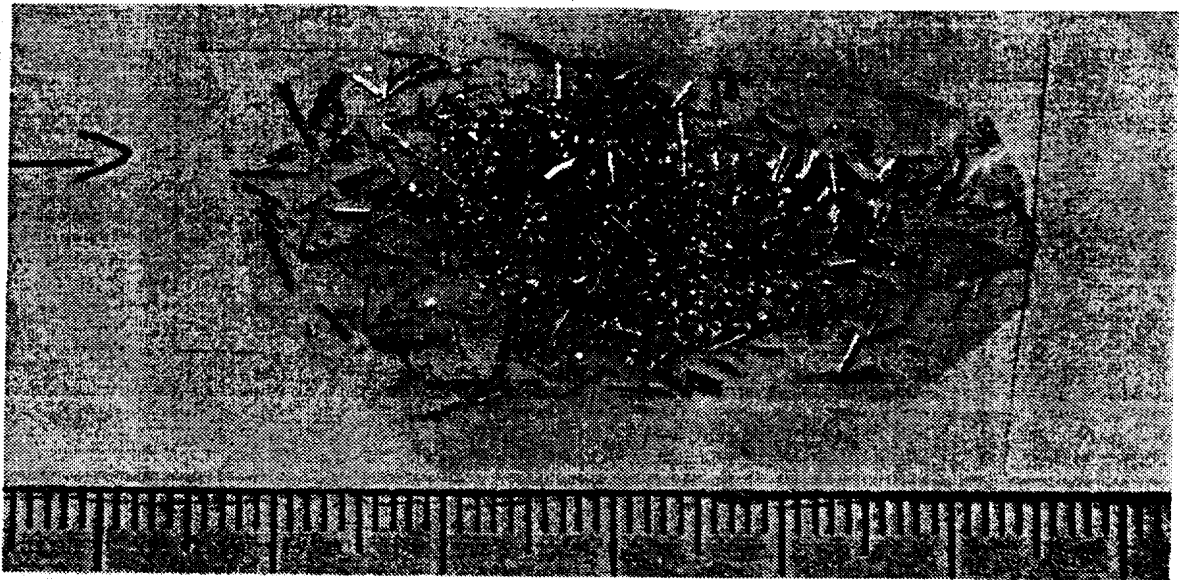


Fig. 125



a)



b)



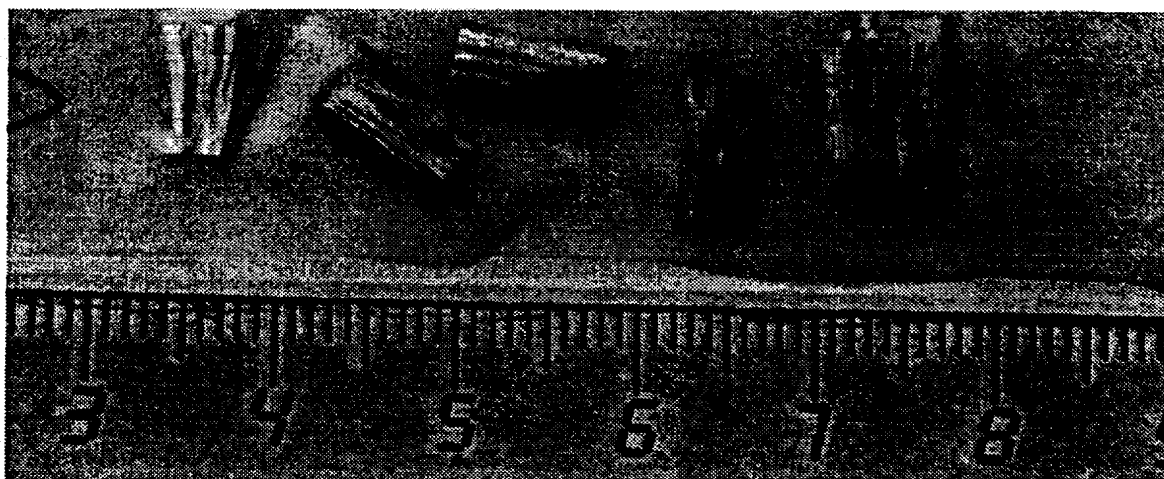
(großes Füllodermium)
(large filling mass)

c)

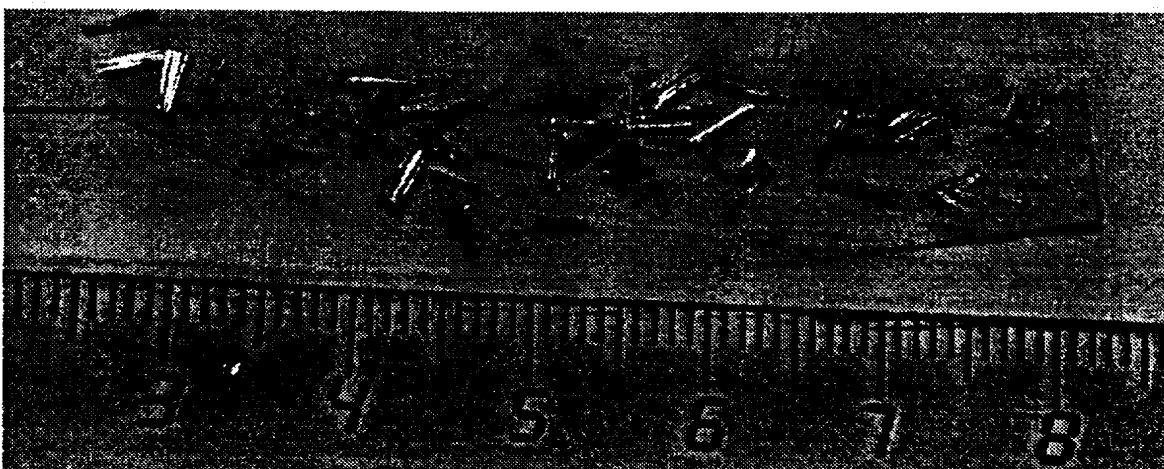


Fig. 130 a) - c)
SUBSTITUTE SHEET (RULE 26)

d)



e)



f)

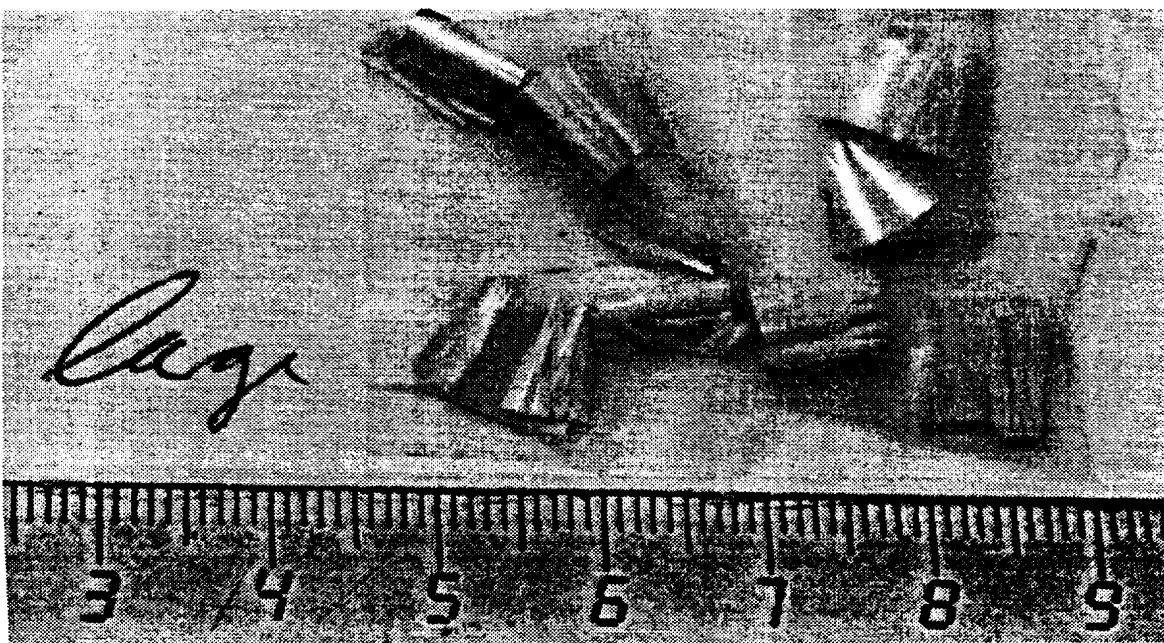


Fig. 130/cont'd d)-f)

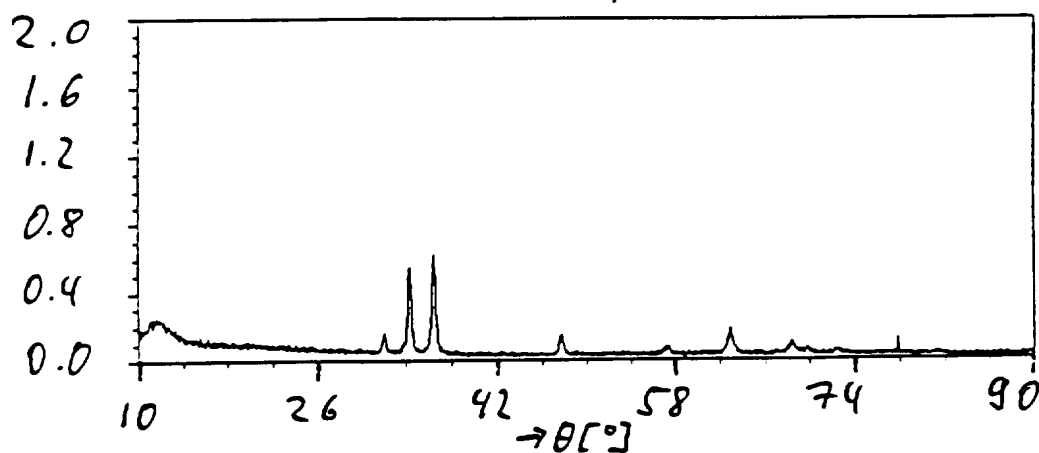
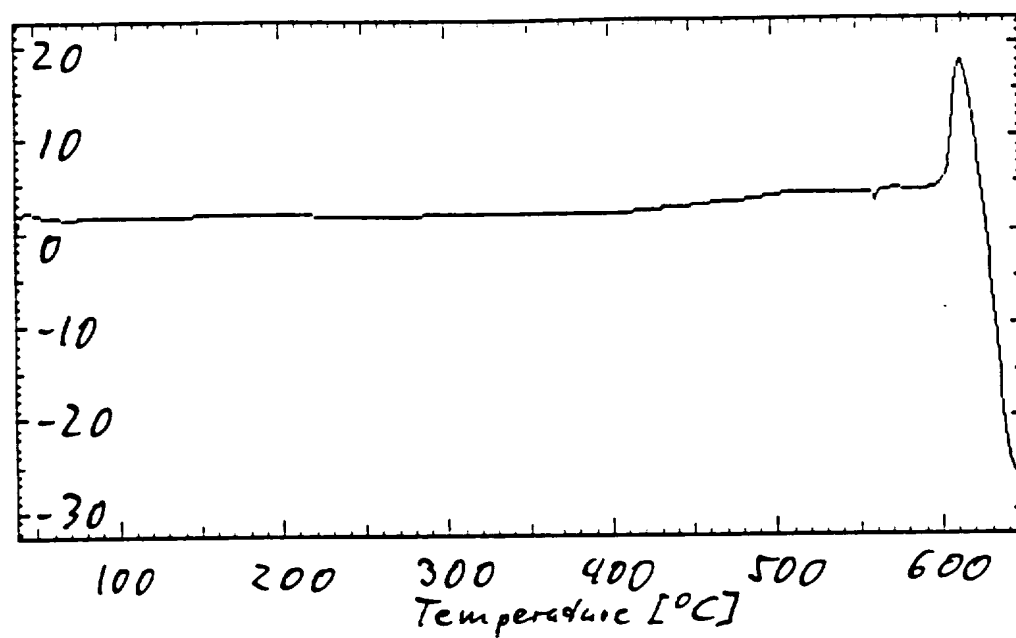
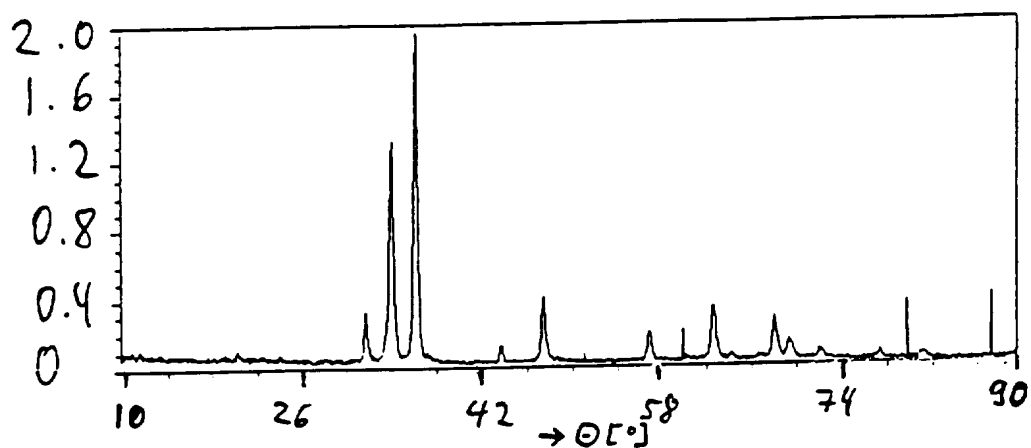
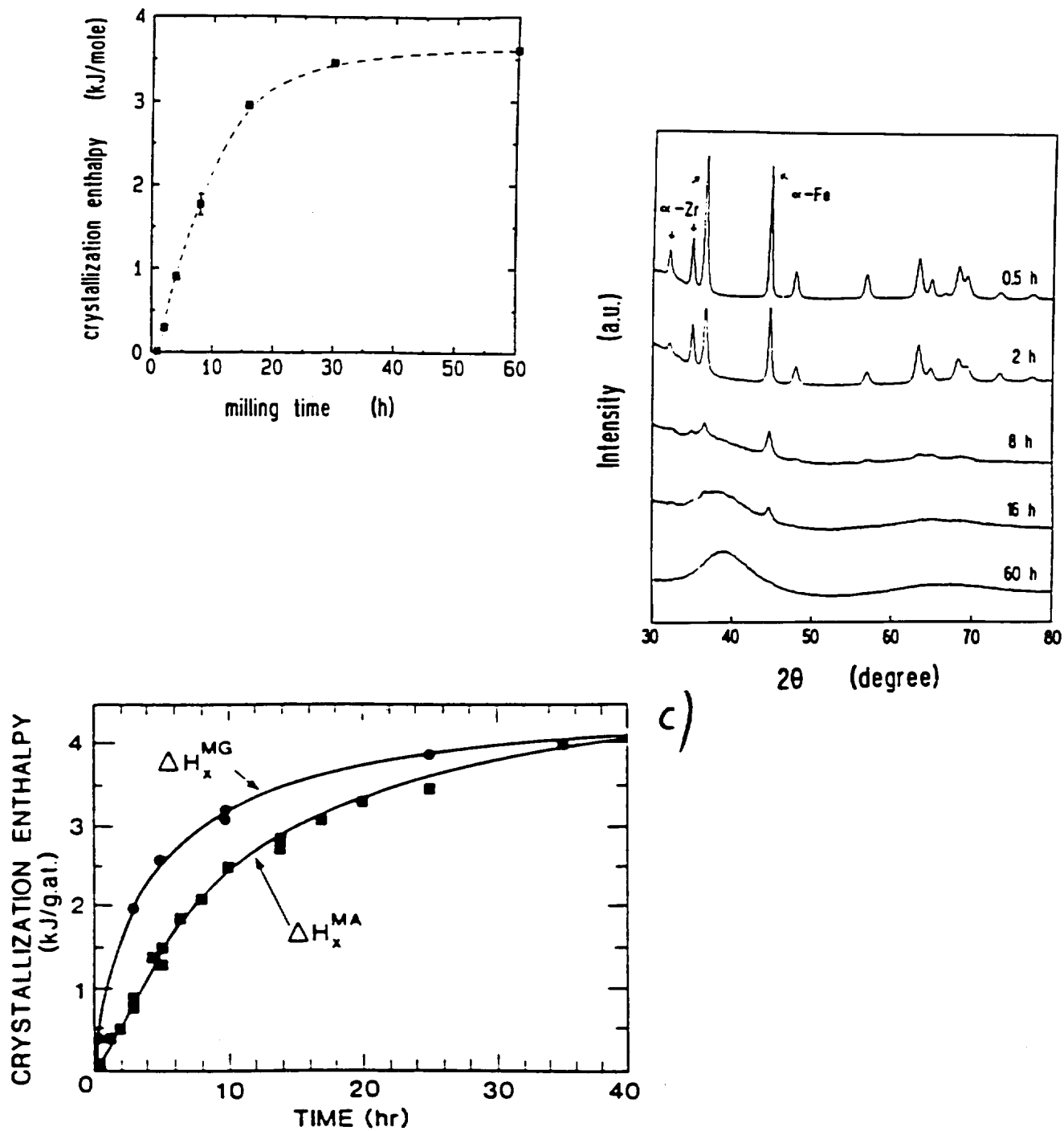


Fig. 131

Fig. 132

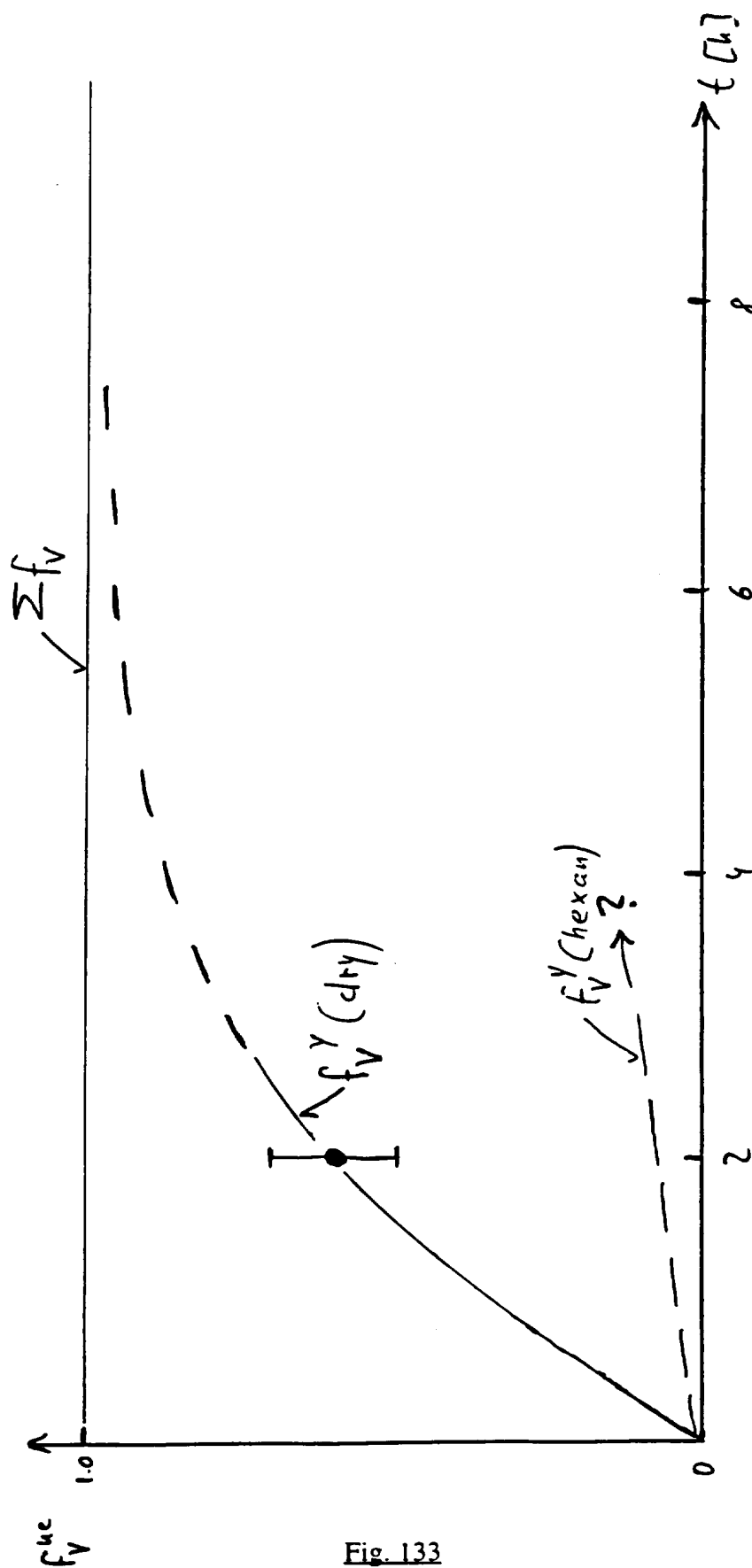
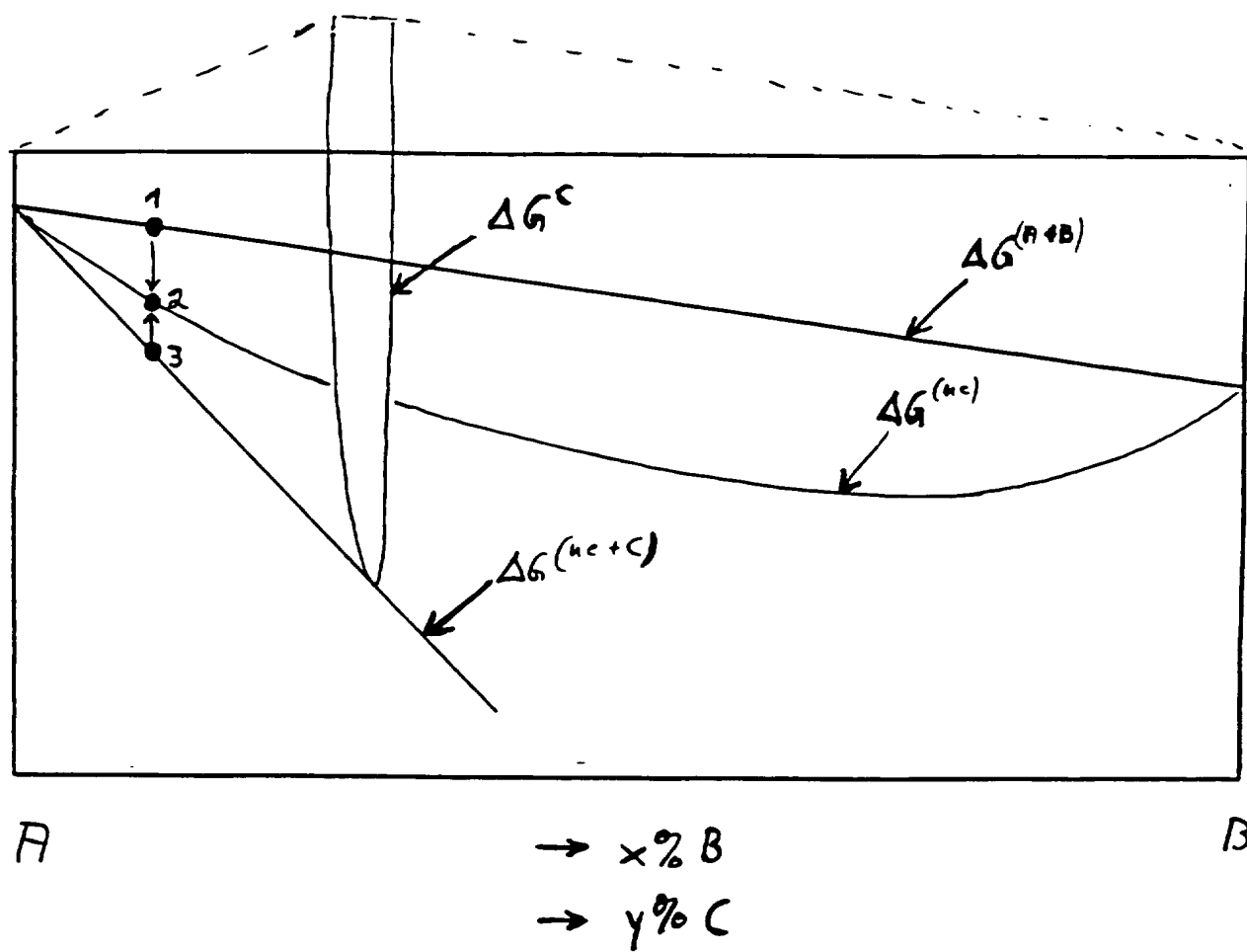


Fig. 133
SUBSTITUTE SHEET (RULE 26)

Fig. 134

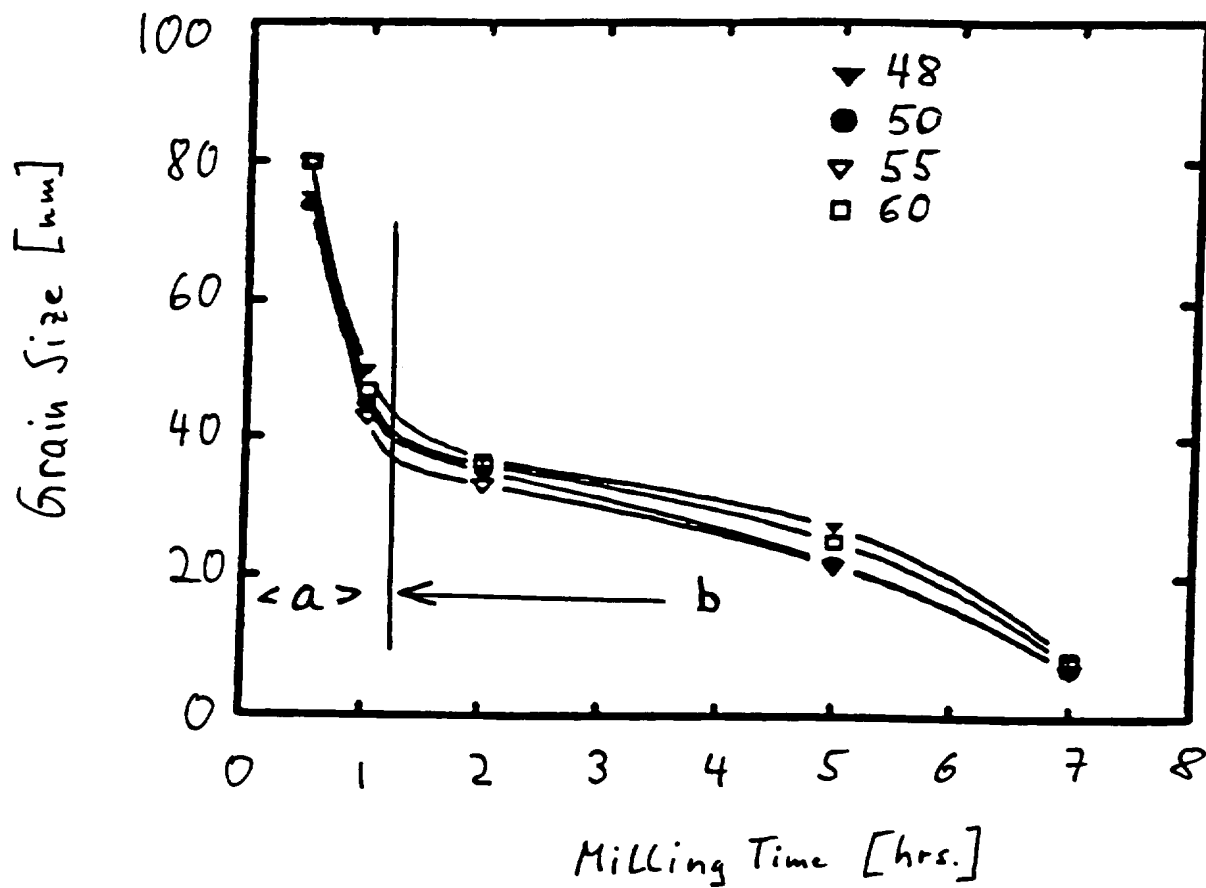


Fig. 135

Table 2 Properties of starting materials used in study of alloying kinetics.

Alloy	Property		Tensile strength (MPa)	Fracture strain	K_{IC} (MN/m ^{3/2})	H_v (KG/mm ²)	K (MPa)	n
	A	B						
0	A	B	275	0.37	85	54	275	0.42
	A	B	580	0.48	95	153	140	0.50
1	A	B	306	0.38	86	64	262	0.43
	A	B	550	0.47	94	143	154	0.49
2	A	B	336	0.39	87	74	248	0.43
	A	B	519	0.46	93	133	167	0.48
3	A	B	367	0.40	88	84	235	0.45
	A	B	489	0.45	92	123	181	0.47
4	A	B	397	0.41	89	94	221	0.45
	A	B	458	0.44	91	113	194	0.46

Notes: Simulation done for CR=10. Material "A" had modulus of 170 GPa; Material B had modulus of 200 GPa. K and n are constitutive equation parameters.

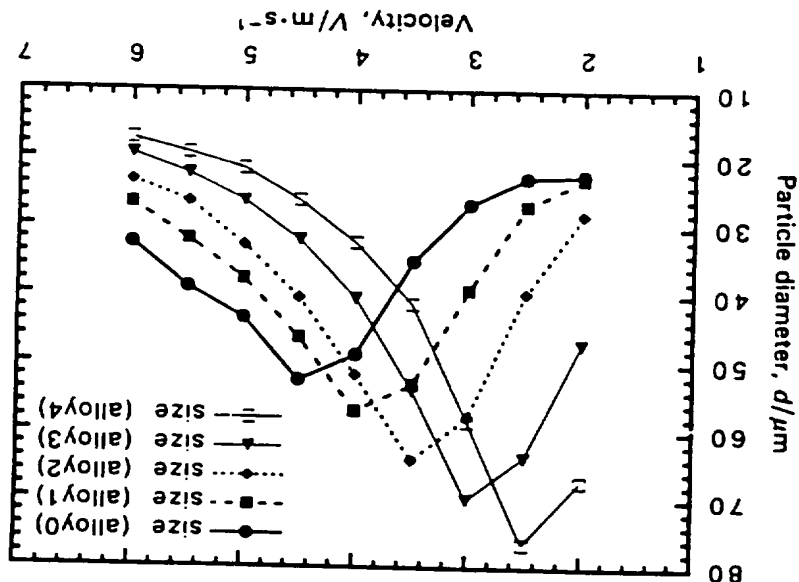


Fig. 136

$dp/dt [^{\circ}W]$

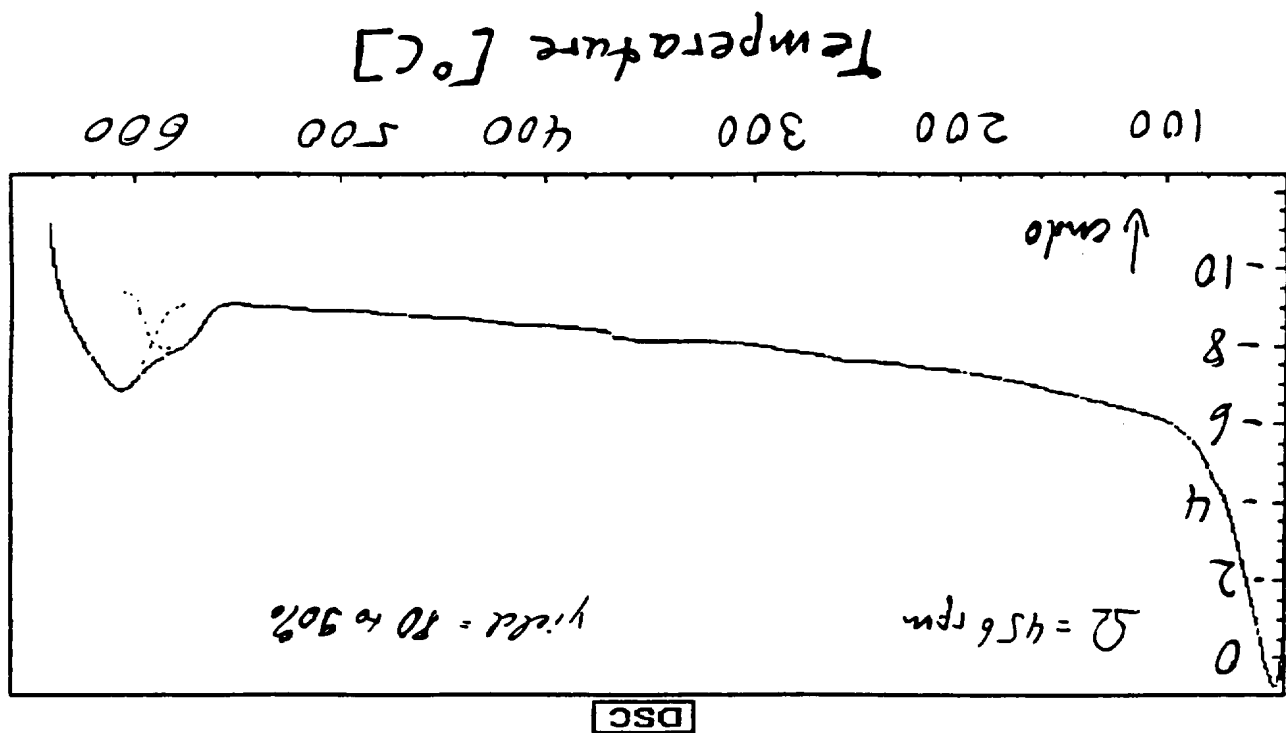
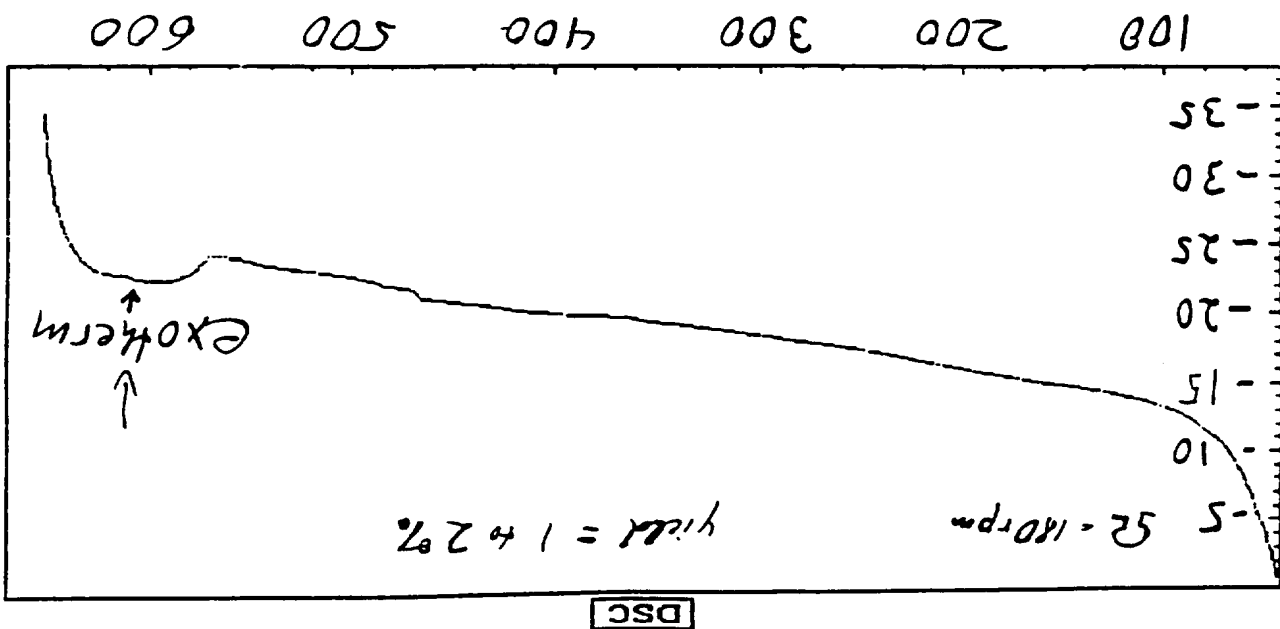


Fig. 137

SUBSTITUTE SHEET (RULE 26)

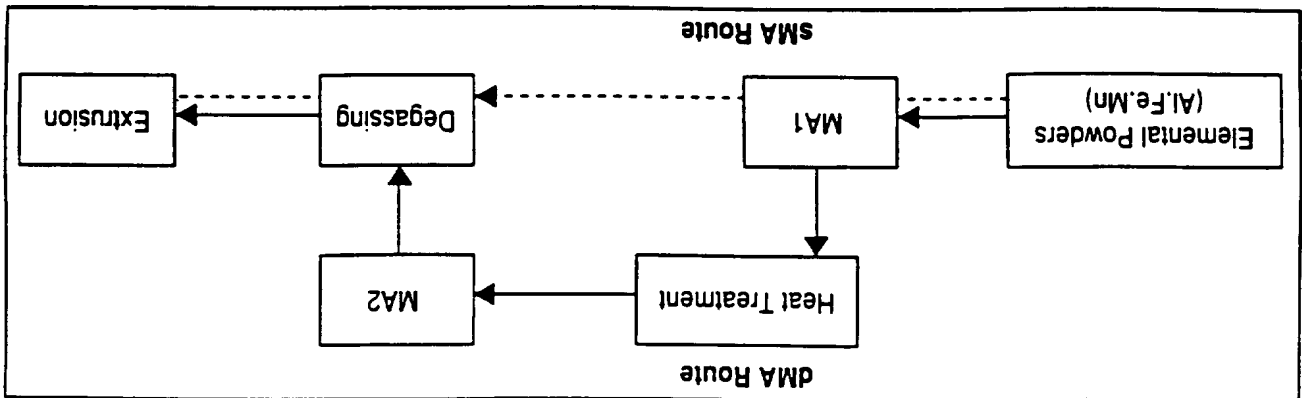


Fig. 138

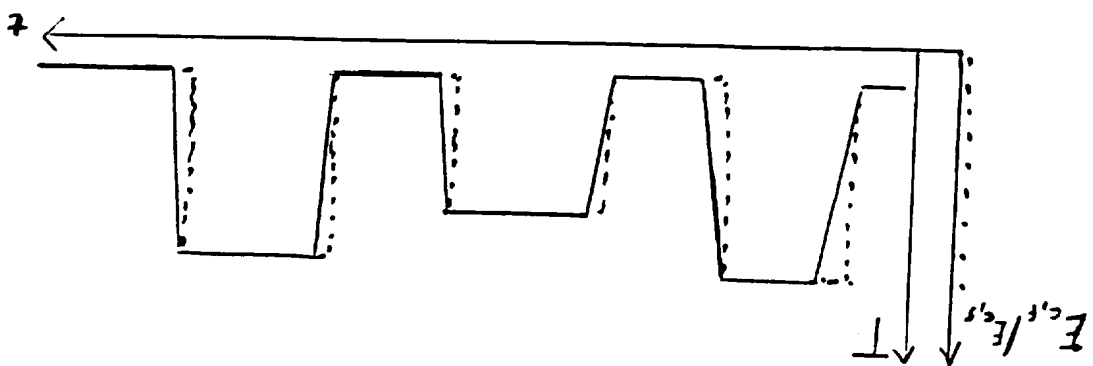


Fig. 139

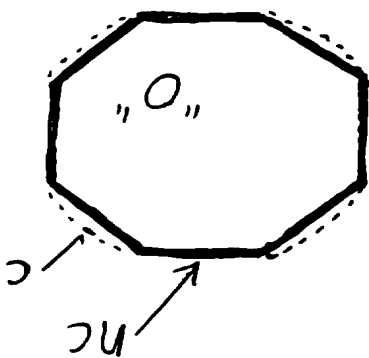
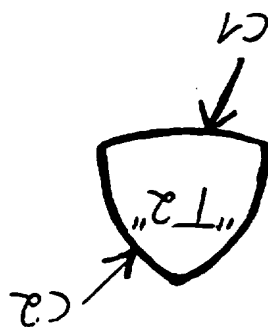
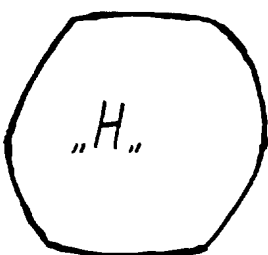
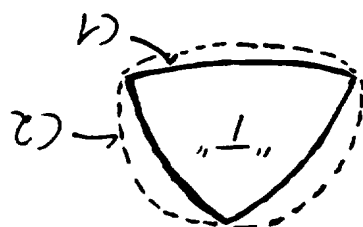
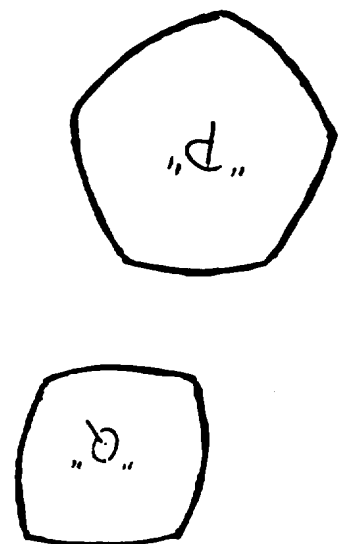


Fig. 140

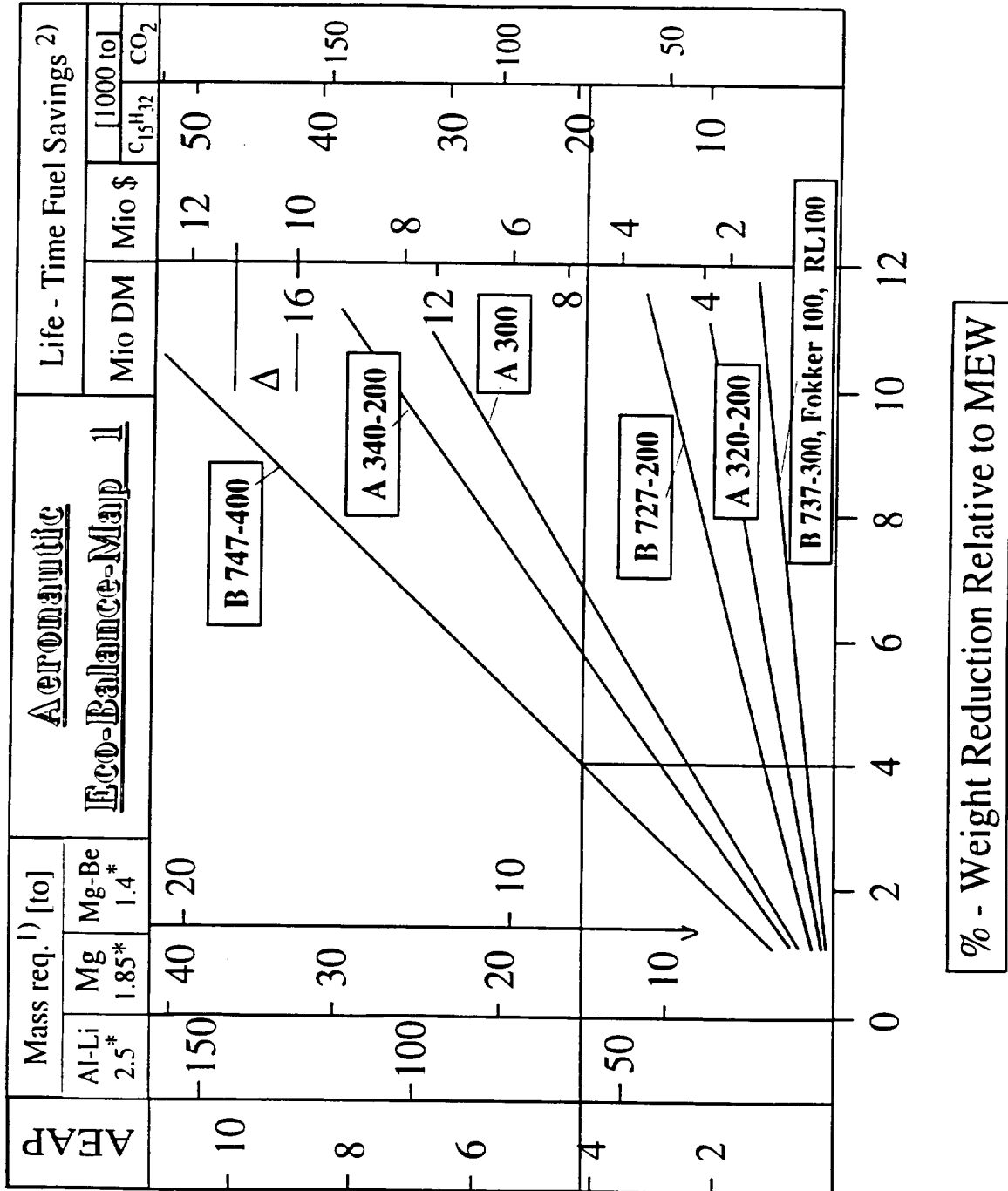


Fig. 141

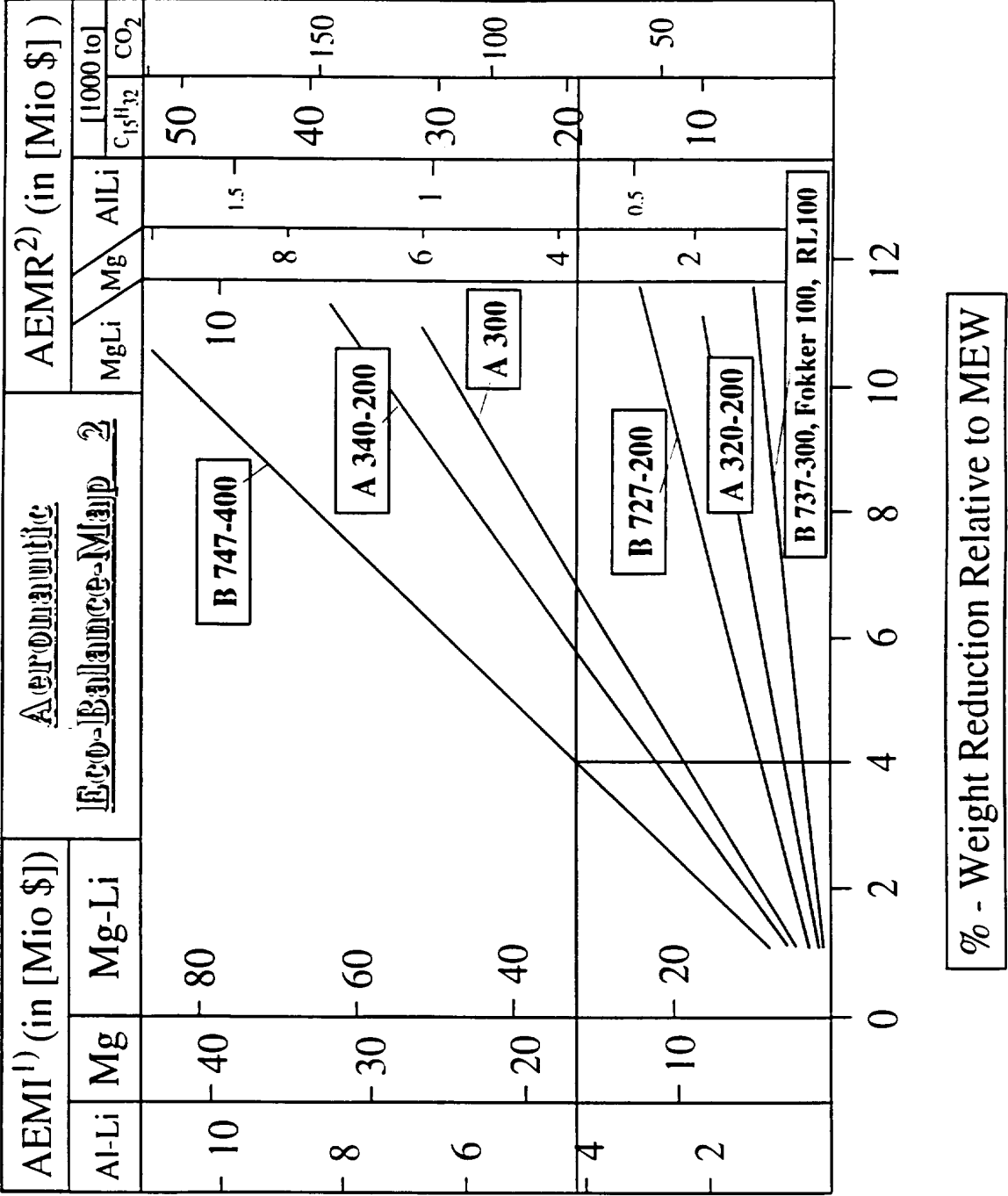


Fig. 142

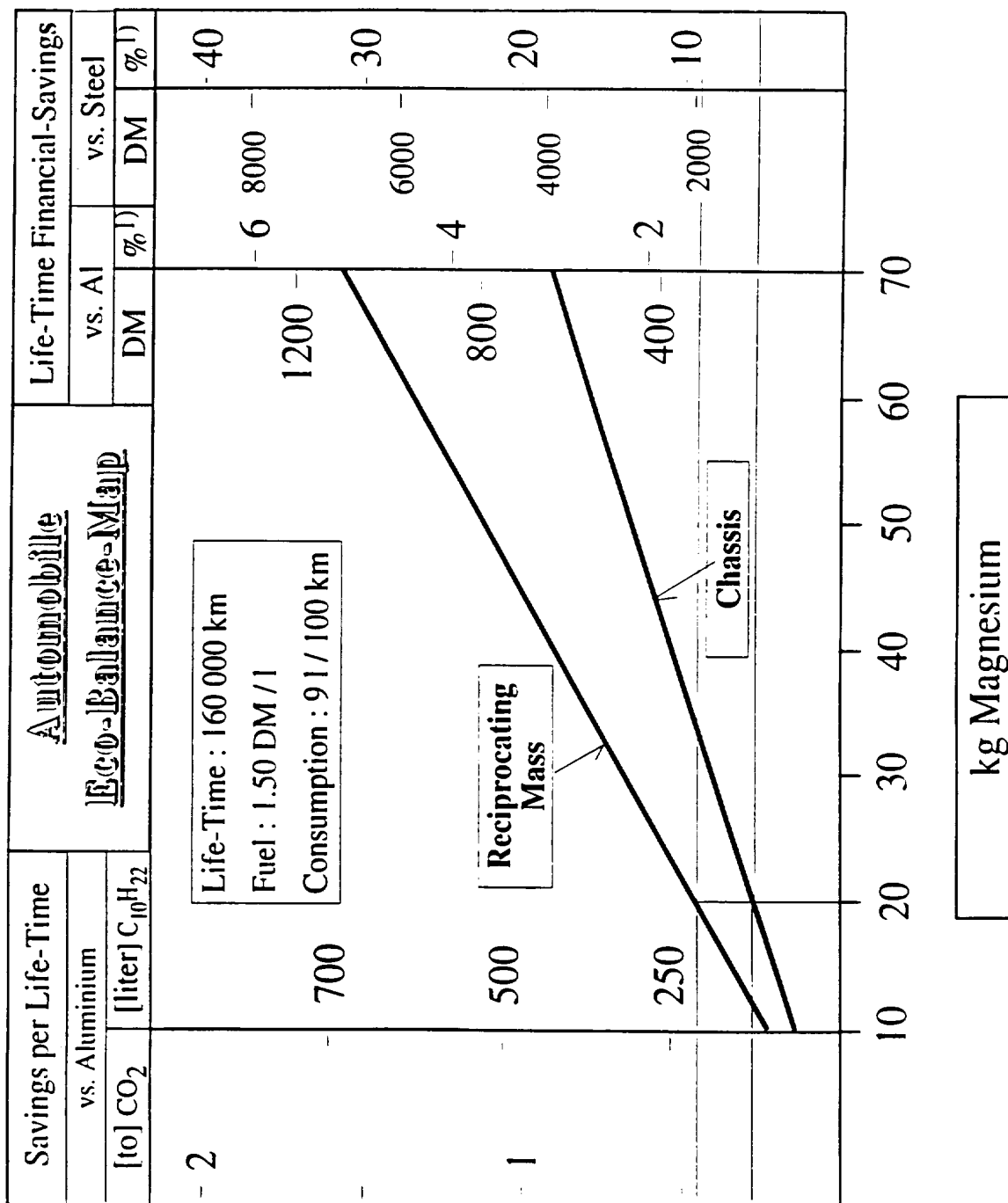


Fig. 143

Different Structural Magnesium Products

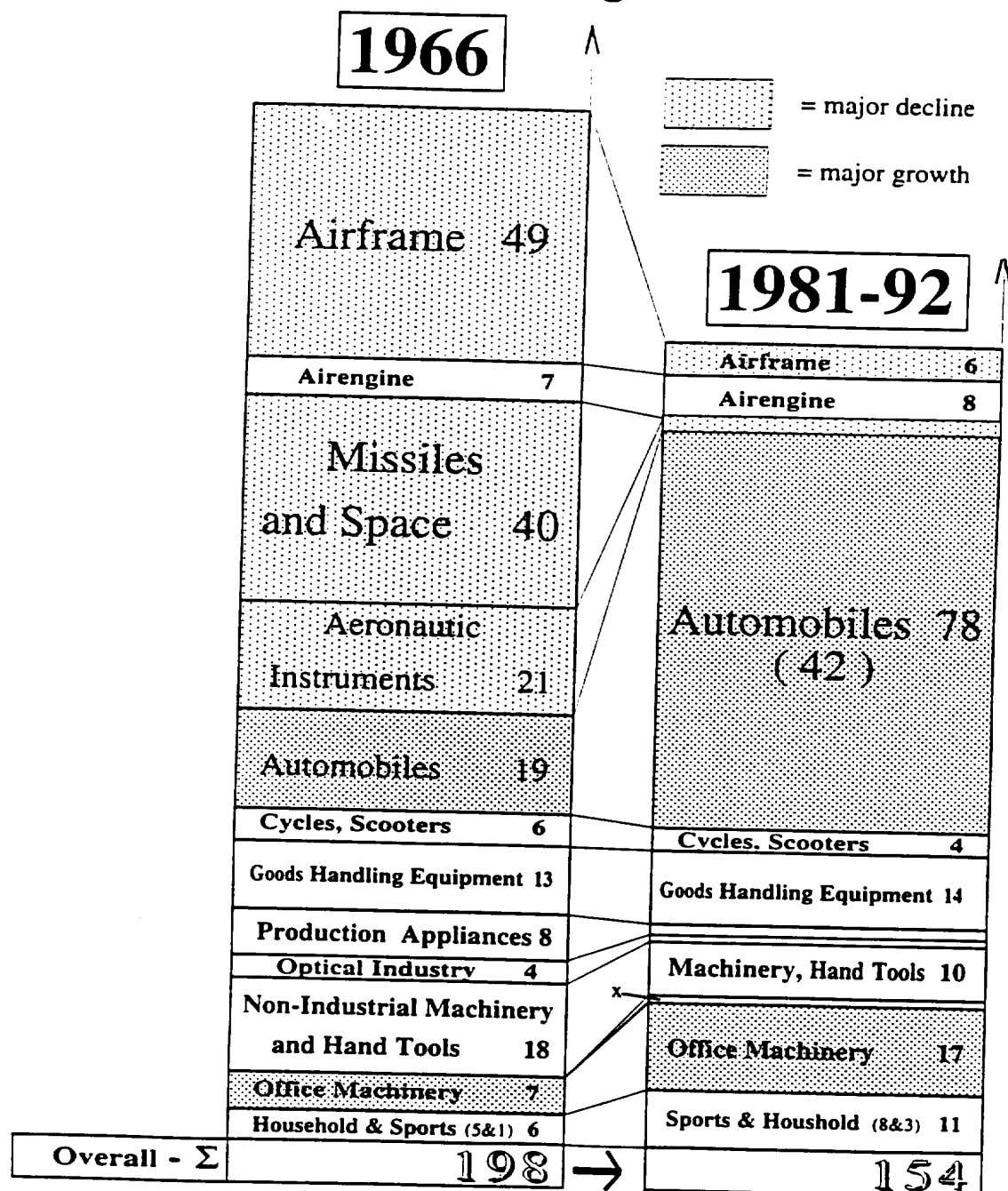


Fig. 144

SUBSTITUTE SHEET (RULE 26)

INTERNATIONAL SEARCH REPORT

Intern. Appl. No.

PCT/EP 95/02882

A. CLASSIFICATION OF SUBJECT MATTER

IPC 6 C23C14/14 C23C14/22 C22C23/06 C22C45/00

According to International Patent Classification (IPC) or to both national classification and IPC

B. FIELDS SEARCHED

Minimum documentation searched (classification system followed by classification symbols)

IPC 6 C23C C22C

Documentation searched other than minimum documentation to the extent that such documents are included in the fields searched

Electronic data base consulted during the international search (name of data base and, where practical, search terms used)

C. DOCUMENTS CONSIDERED TO BE RELEVANT

Category *	Citation of document, with indication, where appropriate, of the relevant passages	Relevant to claim No.
X	ANNUAL REPORT AD-A 253 923 OFFICE OF NAVAL RESEARCH, June 1992, ARLINGTON VA/USA pages 23 - 32 SHAW ET AL. 'Inhibiting corrosion in Gr/Al and Gr/Mg metal matrix composites using nonequilibrium alloying techniques' cited in the application see page 27, paragraph 4; table 4.2 ---	1
X	GB,A,2 262 539 (SECRETARY OF STATE FOR DEFENCE) 23 June 1993 cited in the application see claim 1; figures 1,2 ---	1,8,11
A	US,A,4 395 440 (ABE ET AL.) 26 July 1983 see claims 1-4; figures 1,2 ---	5-7
	-/--	

☒ Further documents are listed in the continuation of box C.

☒ Patent family members are listed in annex.

* Special categories of cited documents :

- "A" document defining the general state of the art which is not considered to be of particular relevance
- "E" earlier document but published on or after the international filing date
- "L" document which may throw doubts on priority claim(s) or which is cited to establish the publication date of another citation or other special reason (as specified)
- "O" document referring to an oral disclosure, use, exhibition or other means
- "P" document published prior to the international filing date but later than the priority date claimed

- "T" later document published after the international filing date or priority date and not in conflict with the application but cited to understand the principle or theory underlying the invention
- "X" document of particular relevance; the claimed invention cannot be considered novel or cannot be considered to involve an inventive step when the document is taken alone
- "Y" document of particular relevance; the claimed invention cannot be considered to involve an inventive step when the document is combined with one or more other such documents, such combination being obvious to a person skilled in the art.
- "&" document member of the same patent family

Date of the actual completion of the international search

13 November 1995

Date of mailing of the international search report

25.11.1995

Name and mailing address of the ISA

European Patent Office, P.B. 5818 Patentlaan 2
NL - 2280 HV Rijswijk
Tel. (+ 31-70) 340-2040, Tx. 31 651 epo nl,
Fax (+ 31-70) 340-3016

Authorized officer

Patterson, A

INTERNATIONAL SEARCH REPORT

International Application No

PCT/EP 95/02882

C.(Continuation) DOCUMENTS CONSIDERED TO BE RELEVANT

Category *	Citation of document, with indication, where appropriate, of the relevant passages	Relevant to claim No.
X	PROCESSING OF STRUCTURAL METALS BY RAPID SOLIDIFICATION; ASM SYMPOSIUM, October 1986, ORLANDO/USA pages 399 - 408 KRISHNAMURTHY ET AL. 'Magnesium-Neodymium alloys produced by rapid solidification.' see page 400 ---	1
X	US,A,5 087 304 (CHANG ET AL.) 11 February 1992 cited in the application see claims 1-5 ---	1
X	EP,A,0 414 620 (PECHINEY RECHERCHE) 27 February 1991 cited in the application see claims 1-6 ---	1
A	JOURNAL OF MATERIALS SCIENCE, vol.26, 1991, LONDON GB pages 951 - 956 SUBRAMANIAN ET AL. 'Laser cladding of zirconium on magnesium for improved corrosion properties' cited in the application *section 2, experimental procedure* ---	10
A	JOURNAL OF VACUUM SCIENCE AND TECHNOLOGY: PART A., vol.12, no.2, March 1994, NEW YORK US pages 282-298 - 298 HAGENA ET AL 'Magnesium cluster-beam deposition on glass and Si(111)' see page 283; figure 1 ---	16
A	GB,A,2 174 509 (CANON) 5 November 1986 see page 2; figures 1,2 ---	5-7
A	DATABASE WPI 20 May 1987 Derwent Publications Ltd., London, GB; AN 87-134058 'Evaporator for printed circuit boards manufacture...' & SU,A,440 428 (KIEV POLY) 15 September 1986 see abstract -----	5-7

INTERNATIONAL SEARCH REPORT

International application No.

PCT/EP 95/ 02882

Box I Observations where certain claims were found unsearchable (Continuation of item 1 of first sheet)

This international search report has not been established in respect of certain claims under Article 17(2)(a) for the following reasons:

1. ☐ Claims Nos.:
because they relate to subject matter not required to be searched by this Authority, namely:

2. ☒ Claims Nos.:
because they relate to parts of the international application that do not comply with the prescribed requirements to such an extent that no meaningful international search can be carried out, specifically:

Please see annex!

3. ☐ Claims Nos.:
because they are dependent claims and are not drafted in accordance with the second and third sentences of Rule 6.4(a).

Box II Observations where unity of invention is lacking (Continuation of item 2 of first sheet)

This International Searching Authority found multiple inventions in this international application, as follows:

1. ☐ As all required additional search fees were timely paid by the applicant, this international search report covers all searchable claims.

2. ☐ As all searchable claims could be searched without effort justifying an additional fee, this Authority did not invite payment of any additional fee.

3. ☐ As only some of the required additional search fees were timely paid by the applicant, this international search report covers only those claims for which fees were paid, specifically claims Nos.:

4. ☐ No required additional search fees were timely paid by the applicant. Consequently, this international search report is restricted to the invention first mentioned in the claims; it is covered by claims Nos.:

Remark on Protest

- ☐ The additional search fees were accompanied by the applicant's protest.
- ☐ No protest accompanied the payment of additional search fees.

INTERNATIONAL SEARCH REPORT

International Application No. PCT/EP95/02882

FURTHER INFORMATION CONTINUED FROM PCT/ISA/210

Claims searched incompletely: 1-16

Contrary to rule 6, PCT, the claims 1-16 are neither clear nor concise. The claims which refer to a product all contain one or more features which relate only to the process for manufacturing the respective product. All claims contain an unreasonable number of "and/or" alternatives so that it is virtually impossible to ascertain the extent of protection claimed. It is unclear whether the numerals 1.1.1, 1.1.2, ect represent separate claims - if so the total number of claims is very large. In fact it is not even certain how many claims the application contains.

INTERNATIONAL SEARCH REPORT

Information on patent family members

Intern. Application No

PCT/EP 95/02882

Patent document cited in search report	Publication date	Patent family member(s)		Publication date
GB-A-2262539	23-06-93	EP-A-	0571595	01-12-93
		WO-A-	9312262	24-06-93
		GB-A-	2267913	22-12-93
		JP-T-	6506505	21-07-94

US-A-4395440	26-07-83	JP-C-	1282389	27-09-85
		JP-A-	57065324	20-04-82
		JP-B-	59043988	25-10-84
		JP-C-	1253526	26-02-85
		JP-A-	57067165	23-04-82
		JP-B-	59029107	18-07-84

US-A-5087304	11-02-92	US-A-	5078807	07-01-92
		EP-A-	0548268	30-06-93
		JP-T-	6501056	27-01-94
		WO-A-	9205291	02-04-92
		US-A-	5129960	14-07-92
		US-A-	5316598	31-05-94

EP-A-0414620	27-02-91	FR-A-	2651244	01-03-91
		CA-A-	2023900	25-02-91
		DE-D-	69006293	10-03-94
		DE-T-	69006293	26-05-94
		JP-C-	1822336	10-02-94
		JP-A-	3097824	23-04-91
		JP-B-	5034411	24-05-93
		NO-B-	176483	02-01-95
		US-A-	5073207	17-12-91

GB-A-2174509	05-11-86	JP-A-	61218810	29-09-86
		JP-C-	1650121	30-03-92
		JP-B-	3016188	04-03-91
		JP-A-	61220763	01-10-86
		JP-A-	61220764	01-10-86
		JP-A-	61220765	01-10-86
		CA-A-	1272662	14-08-90
		DE-A-	3610291	02-10-86
		DE-A-	3610293	02-10-86
		DE-A-	3610294	02-10-86
		DE-A-	3610296	02-10-86

INTERNATIONAL SEARCH REPORT

Information on patent family members

Intern. al Application No

PCT/EP 95/02882

Patent document cited in search report	Publication date	Patent family member(s)	Publication date
GB-A-2174509		DE-A- 3610298	02-10-86
		DE-A, C 3610299	02-10-86
		FR-A- 2579486	03-10-86
		FR-A- 2579487	03-10-86
		FR-A- 2579488	03-10-86
		GB-A- 2175413	26-11-86
		GB-A- 2175414	26-11-86
		GB-A, B 2175709	03-12-86
		US-A- 4911805	27-03-90
